Stellar Iron Core Collapse in {3+1} General Relativity and The Gravitational Wave Signature of Core-Collapse Supernovae

Dissertation

eingereicht an der

Mathematisch-Naturwissenschaftlichen Fakultät
der Universität Potsdam

von

Christian David Ott

November 2006

Stellar Iron Core Collapse in {3+1} General Relativity and The Gravitational Wave Signature of Core-Collapse Supernovae

Christian David Ott

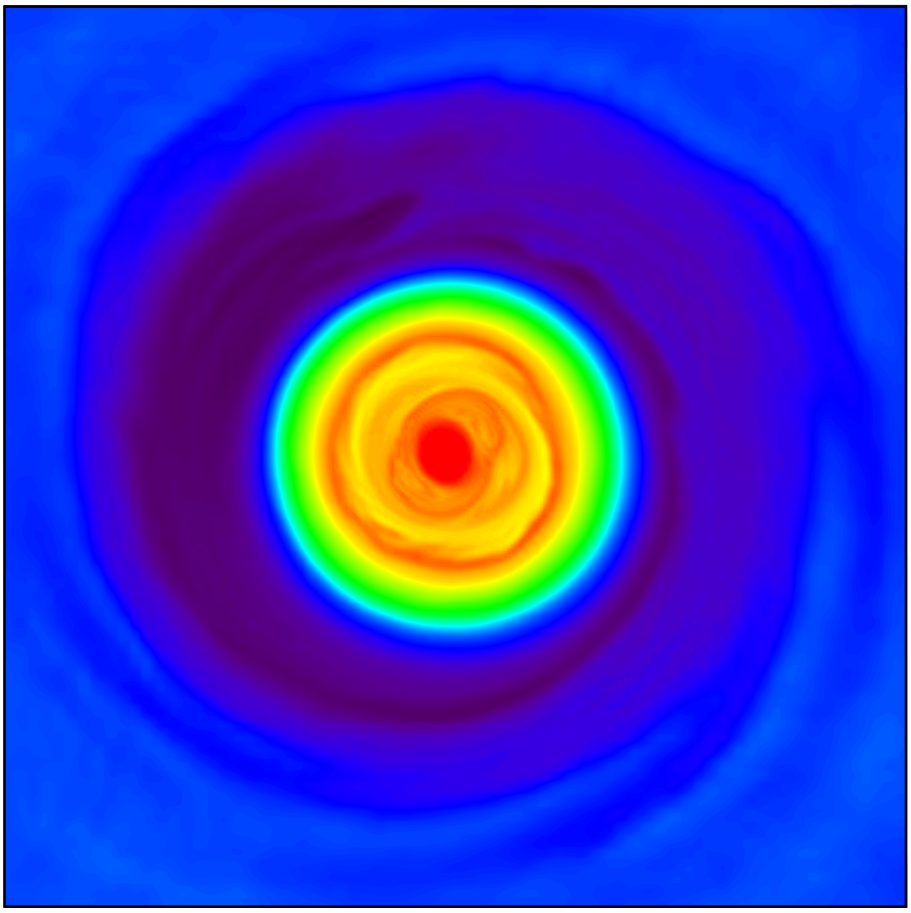

Dissertation

Albert-Einstein-Institut
Max-Planck-Institut für Gravitationsphysik

and

Mathematisch-Naturwissenschaftliche Fakultät
Universität Potsdam

2006

Cover figure: Color map of the specific entropy per baryon in the equatorial plane of a newborn rapidly rotating and nonaxisymmetrically deformed neutron star at 90 ms after core bounce. Shown are the inner 100×100 km^2. The color map ranges from $\sim0.8\ k_B$/baryon (red) to $\sim6\ k_B$/baryon (dark blue/purple).

Gravitational waves travel at the speed of thought.

Sir Arthur Eddington

I have no idea who first calculated the emission of gravitational radiation from a collapsing star with rotation. Ruffini and Wheeler may have been the first. It was certainly obvious to everyone who thought about it that a collapsing star with rotation would give rise to a strong pulse of gravitational waves. I make no claim to have thought of this first.

Freeman Dyson,
personal communication,
October 2006

I don't consider myself a pessimist. I think of a pessimist as someone who is waiting for it to rain. And I feel soaked to the skin.

Leonard Cohen

Abstract

Core-Collapse Supernovae are nature's grandest explosions, liberating $\sim 10^{53}$ erg, the colossal gravitational binding energy of a neutron star. Most of this energy, 99%, is emitted in neutrinos, 1% goes into the asymptotic explosion energy and becomes visible in the electromagnetic spectrum, and a tiny fraction, perhaps less than a millionth, is radiated in gravitational waves.

The work presented in this dissertation is concerned with the gravitational wave signature of core-collapse supernovae. Previous studies have identified rotating iron core collapse, core bounce and protoneutron star (PNS) ring-down pulsations, postbounce convection, anisotropic neutrino emission and postbounce nonaxisymmetric rotational instabilities as the primary processes and phases for the radiation of gravitational waves.

I perform the first ever calculations of rotating stellar iron core collapse in {3+1} general relativity (GR) that start out with presupernova models from stellar evolutionary calculations and include a microphysical finite-temperature nuclear equation of state, an approximate scheme for electron captures during collapse and neutrino pressure effects. Based on the results of theses calculations, I obtain the to-date most realistic estimates for the gravitational wave signal from collapse, bounce and early postbounce phases of core-collapse supernovae. My results show that (1) the collapse, bounce and early postbounce gravitational wave signal morphology is much more generic than previously estimated, (2) that the relevance of rotational effects is much smaller than thought and that rotational "multiple" core bounce does not occur in the range of physically plausible initial rotation rates and degrees of differential rotation, and (3) that all considered iron core rotational configurations undergo collapse, bounce and PNS ring-down in axisymmetry and none of these models reach ratios of rotational kinetic to gravitational potential energy ($\beta = T/|W|$) sufficiently high to experience a classical MacLaurin-type bar-mode instability at high-$T/|W|$. However, I find and analyze the development of nonaxisymmetric structures with a dominant $m = 1$ component that grow in a number of models due to a low-$T/|W|$ dynamical rotational instability and whose quadrupole components lead to prolonged narrow-band gravitational wave emission, significantly enhancing the gravitational wave signature of rapidly rotating iron core collapse.

I supplement my {3+1} GR simulations of rotating iron core collapse with 2D Newtonian neutrino radiation-hydrodynamic supernova calculations focussing on: (1) The late-postbounce gravitational wave emission in models of core-collapse supernovae with slowly or nonrotating progenitor cores. I find that the dominant emission process in such models may be the oscillations of the PNS core that are of predominantly g-mode character and that are excited hundreds of milliseconds after bounce and typically last for several hundred milliseconds while emitting strong gravitational waves in a narrow frequency band. (2) The gravitational wave emission in accretion induced collapse (AIC) of massive O/Ne/Mg white dwarfs to neutron stars, based on the first AIC calculations starting with rapidly rotating 2D equilibrium models. I find that efficient electron capture leads to rapid collapse largely unaffected by rotational effects, but owing to very small inner cores, to only modest gravitational wave emission from core bounce and PNS ring-down despite strong rotational flattening. At postbounce times the gravitational wave emission is dominated in amplitude by the low-frequency emission associated with rotation-induced anisotropies in the neutrino radiation fields.

Based on my results I surmise that the gravitational wave emission from rapidly rotating iron core collapse and AIC events should be detectable already by initial LIGO-class observatories throughout the Milky Way and with advanced LIGO-class observatories throughout the Milky Way and the Magellanic Clouds. If persistent nonaxisymmetric deformations occur, detection to distances out to the Virgo Cluster may be marginally possible. Nonrotating or slowly rotating core collapse does not lead to a detectable gravitational wave signal from core bounce, but gravitational waves from postbounce convection and shock deformations may be detectable by advanced LIGOs. Initial LIGOs would detect strong PNS core oscillations throughout the Milky Way and beyond.

Erratum

as of April 2, 2007

- Section 2.4.1, page 15. Discussion of equation (2.13). The terms $d\hat{t}$ and $d\hat{x}$ are imprecisely described as "physical time" and "physical distance". The more precise description of $d\hat{x} = \sqrt{(d\hat{x}^2)} = \sqrt{\gamma_{ij} d\hat{x}^i d\hat{x}^j}$ is the "proper distance on the spacelike 3-hypersurface Σ_t" (when $dt = 0$) while $d\hat{t} = \sqrt{d\hat{t}^2} = \sqrt{\alpha^2 dt^2}$ is the "advance in proper time along the vector $\alpha \boldsymbol{n}\, dt$".

- Section 3.6.4, page 81. Equations (3.133) and (3.134) are incorrect. The corrected equations (as implemented in the code) read:

$$s_i^{\text{momentum}} = -\alpha \sqrt{\gamma} (p_\nu)_{,i} \tag{3.133}$$

and

$$s^{\text{energy}} = v^i s_i^{\text{momentum}} = -v^i \alpha \sqrt{\gamma} (p_\nu)_{,i} \, . \tag{3.134}$$

- Section 5.2.5, page 141. Index error in equation (5.9). Correction:

$$Y^{ij} \equiv \epsilon^{ilm} \left(R_m{}^j - \frac{1}{4} \delta^j_m R \right)_{;l} = -\frac{1}{2} \epsilon^{ilm} \gamma^{jn} B_{nlm} \, . \tag{5.9}$$

- Section 7.3.2, page 248. The quoted numbers for the energies emitted in gravitational waves are incorrect owing to an error in the postprocessing analysis subroutine. The corrected numbers are $2.17 \times 10^{-10}\, \mathrm{M}_\odot c^2$ and $1.32 \times 10^{-9}\, \mathrm{M}_\odot c^2$ for the 1.46-$\mathrm{M}_\odot$ and 1.92-$\mathrm{M}_\odot$ model, respectively.

- Section 7.3.3, pages 249. In figure 7.19, the h_{char} graphs must be rescaled by factors of 0.62 (1.46-$\mathrm{M}_\odot$ model) and 0.14 (1.92-$\mathrm{M}_\odot$ model) to account for the corrected total emitted energies. This significantly reduces the prospects for detecting AIC events with current and future gravitational wave observatories. In addition, the quoted maximum values of h_{char} are incorrect. The corrected values are 1.45×10^{-21} (1.46-$\mathrm{M}_\odot$ model) and 2.80×10^{-21} (1.92-$\mathrm{M}_\odot$ model).

Table of Contents

Chapter 1

Overview

1.1 Preface and Motivation

Supernovae are nature's most powerful explosions. When marking the death of a massive star, a supernova in its first seconds emits the gravitational binding energy released in stellar collapse with 10^{53} erg s^{-1}, rivaling in power the rest of the observable universe combined. 99% percent of the total supernova energy is emitted in neutrinos, which are barely detectable, unless the *core-collapse supernova* occurs in our galaxy. About 1%, $\sim 10^{51}$ erg, goes into the kinetic and internal energy of the supernova ejecta, a fraction of which is converted into electromagnetic radiation [1].

The general picture of stellar evolution and of the nuclear fusion history of massive stars is relatively well established. We understand that the electron-degenerate iron cores of massive stars become unstable to electron capture and endothermic photo-dissociation of heavy nuclei. Collapse ensues and continues once the inner core has reached densities comparable to those in an atomic nucleus. At this point, nuclear repulsive forces lead to a stiffening of the nuclear equation of state and the collapse is dramatically reversed within a fraction of a millisecond. The core rebounds, "bounces". A shock wave is launched into the infalling outer core that quickly loses energy to dissociation of outer core material and to neutrinos that stream away. The shock stalls.

At this point a supernova theorist's problems set in. How is the stalled shock revived to finally explode the star? From first principles it is obvious that a fraction of the gigantic gravitational binding energy of the collapsed inner core that is now the *protoneutron star* and that slowly cools and *deleptonizes* to become a cold ultra-dense neutron star must be converted into the kinetic and internal energy of the exploding mantle.

The detailed mechanism of core-collapse supernova explosions is one of outstanding problems in astrophysics and it has resisted more than forty years of speculation, concerted theoretical work, and numerical exploration. But even more difficult questions are on the horizon: Recently, observers have found evidence that a special kind of core-collapse supernova might go along with the *long-soft* variety of gamma-ray bursts [2]. What is the core-collapse supernova–gamma-ray burst connection? Could it be that in core-collapse events, which do not produce a regular supernova, a black hole with an accretion disk forms and via accretion power, rotation, magnetic fields and/or neutrinos, a gamma-ray burst jet is launched that plows through the stellar envelope?

Virtually all we know about the universe and core-collapse supernovae is based on observations in the electromagnetic spectrum. From supernova 1987A that went off in the Large Magellanic Cloud, neutrino detectors on Earth detected about 20 neutrinos [3]. Modern day detectors are projected to detect thousands of neutrinos from a galactic supernova [1].

However, besides via electromagnetic waves and neutrinos there is a third way in which physical information from a core-collapse supernova can reach observers on Earth: Gravitational waves, predicted by Einstein's theory of gravity, *General Relativity* (GR) [4–7]. Gravitational waves are propagating vibratory disturbances, ripples, in spacetime, travelling through the universe at the speed of light. They are generated by time-changing mass quadrupole moments related to coherent, bulk motions of huge amounts of mass-energy at frequencies related to the dynamical timescale of their emitters. In contrast to electromagnetic waves, gravitational waves cannot be used to form an image of the radiating system since their wavelengths are comparable to or larger than their coherent, bulk-moving sources. Instead, gravitational waves are akin to sound and carry a stereophonic de-

scription of their source's dynamics in two independent polarizations. Gravitational waves interact very weakly with matter, thus can travel nearly unscathed from their source through intervening matter to distant observers. This makes them ideal carriers of information, but also means that gravitational waves interact very weakly with detectors on Earth.

To date, gravitational waves have never been observed directly, but there is strong evidence supporting their existence from the observed orbital shrinking of the Hulse-Taylor binary system [8]. The international array of first-generation large-scale light-interferometric gravitational wave observatories (LIGOs) is in the process of reaching fully operational state and design sensitivities. Current estimates (e.g., [9–14]) suggest that a galactic supernova would likely be visible to first-generation LIGOs.

The dawn of gravitational wave astronomy may be near and there is great potential that the physical information carried by gravitational waves emitted in a core-collapse supernova could be an important, possibly crucial piece in the supernova puzzle and may also boost our understanding of the core-collapse supernova–gamma-ray burst connection. However, detailed and accurate theoretical predictions of the gravitational wave signature of core-collapse supernovae / explosion mechanisms and a good theoretical understanding of the various possible gravitational wave emission processes in a core-collapse supernova will be indispensable for the extraction of physical information from an observed supernova gravitational wave signal.

It is my interest in both core-collapse supernova theory and general relativity that has led to the work culminating in this dissertation.

1.2 New Results obtained in this Work

This work is concerned with the gravitational wave signature of stellar iron core collapse and the subsequent core-collapse supernova evolution.

The new results presented in this dissertation and in part reported in [10, 15, 16] are my genuine contribution and have been obtained via general relativistic and Newtonian multi-dimensional numerical simulations of rotating and nonrotating stellar iron core collapse and core-collapse supernovae.

I acknowledge close collaboration with A. Burrows[1], L. Dessart[1], H. Dimmelmeier[2], I. Hawke[3], E. Livne[4], E. Schnetter[5], and B. Zink[6].

1.2.1 {3+1} GR Hydrodynamic Simulations of Stellar Iron Core Collapse

The major technical problem solved is the numerical simulation of stellar iron core collapse in 3D on mesh-refined Cartesian computational grids with GR hydrodynamics fully coupled with {3+1} spacetime evolution. I have accomplished this by combining and improving existing GR hydrodynamics, spacetime evolution and mesh refinement codes. In a first step, this was implemented and tested for simple polytropic iron core models. In a second step, I have extended the hydrodynamics treatment to include a microphysical finite-temperature nuclear equation of state (EOS), an approximate treatment of electron captures during collapse and state-of-the art presupernova stellar models from stellar evolutionary calculations. The approximations employed yield GR hydrodynamic and thermodynamic immediate postbounce protoneutron star (PNS) configurations that rival in realism those obtained with full neutrino radiation-hydrodynamics codes in axisymmetry and Newtonian gravity or approximate GR. Since postbounce deleptonization and neutrino radiation transport are neglected, the physical quality of the simulation results degrades with progressing postbounce time, but is still much more realistic than what can be achieved with polytropic models.

With the numerical codes and methods presented in this work (the CACTUS/CARPET/WHISKY code package; CCW) I have accomplished a first step towards connecting numerical relativity with core-collapse supernova theory in a multi-dimensional context.

1.2.2 Verification of the Conformally-Flat Approximation in the Core-Collapse Supernova Context

In the conformally-flat approximation (conformal-flatness condition; CFC) to general relativity the spatial 3-metric is replaced by the flat 3-metric multiplied by a position-dependent factor. In maximal slicing, the CFC ADM equations reduce to a set of elliptic equations. The CFC approximation is exact in spherical symmetry.

In a first application of the CCW code I have performed an extensive set of rotating collapse calculations with polytropic initial iron core models identical to those used in the 2D CFC study of Dimmelmeier et al. [12, 17, 18]. Via direct comparison of my results with data made available by H. Dimmelmeier, I find that CFC is an excellent approximation to full GR for tracking the collapse, bounce and early postbounce phases of axisymmetric stellar iron core collapse to a neutron star.

---

[1]Department of Astronomy and Steward Observatory, The University of Arizona, Tucson.

[2]Max-Planck-Institut für Astrophysik, Garching.

[3]School of Mathematics, University of Southampton; former member of the Albert-Einstein-Institut numerical relativity group.

[4]Racah Institute of Physics, Hebrew University, Jerusalem.

[5]Center for Computation & Technology, Louisiana State University, Baton Rouge; former member of the Albert-Einstein-Institut numerical relativity group.

[6]Center for Computation & Technology, Louisiana State University, Baton Rouge; former member of the Max-Planck-Institut für Astrophysik, Garching.

1.2.3 Gravitational Wave Signature of Rotating Iron Core Collapse

Using the newly developed technology and microphysics capability in the CCW code, I have performed a series of {3+1} GR collapse calculations with presupernova models from stellar evolutionary calculations, investigating the gravitational wave signature of rotating iron core collapse and its dependence on the initial rotation rate, on the initial degree of differential rotation, on the degree of deleptonization during collapse and on progenitor structure.

My results show that the deleptonization of the collapsing core is of central importance for the gravitational wave signature of fast rotating iron core collapse. Deleptonization leads to a density-dependent reduction of the effective adiabatic index of the collapsing core and reduces the size of the homologously collapsing and rebounding inner core. The combined effects of deleptonization and GR reduce the importance of centrifugal support and lead to a much more generic gravitational wave signal from core bounce and PNS ring-down pulsations than previously estimated.

1.2.4 Nonaxisymmetric Rotational Instabilities in Protoneutron Stars

The results of the above parameter study manifest that the rotation rates attainable during stellar core collapse with physically well-motivated initial rotation rates and degrees of differential rotation are generically too low to permit the growth of nonaxisymmetric structures via the classical dynamical nonaxisymmetric rotational instability that requires ratios of rotational kinetic to gravitational potential energy ($\beta = T/|W|$) above $\sim$27%.

Although all models stay axisymmetric throughout their infall, plunge, bounce and early postbounce phases, I observe the development of significant nonaxisymmetric structures and dynamics at postbounce times in a subset of models. The nonaxisymmetric rotational instability in these models is of dominant $m = 1$ character. It originates inside the PNS core and propagates through the postshock region, blending in with $m = \{2, 3\}$ spatial components and generating a spiral-density wave pattern in the region between PNS core and stalled supernova shock. I follow two models with postbounce $\beta\sim$9–13% that experience this instability out to late postbounce times of 70–90 ms. My analysis of the instability indicates a possible relationship with the recently proposed low-$T/|W|$ instabilities in differentially rotating compact stars that operate via resonant amplification of azimuthal modes at corotation points where their pattern speed equals the local fluid angular velocity [19–25]. The nonaxisymmetric instability leads to prolonged narrow-band gravitational wave emission at frequencies of $\sim$900–1000 Hz from the quadrupole components of the nonaxisymmetric structures. The emission is lower in amplitude, but owing to its high-frequency, narrow-band nature and long-term emission, significantly more energetic than the gravitational wave signal from axisymmetric core bounce.

1.2.5 Gravitational Wave Emission by Convection, Anisotropic Neutrino Radiation and PNS Core g-Modes

To supplement the aforementioned general relativistic calculations of the rotating collapse, bounce and early postbounce phases of core-collapse supernovae, I have performed, in collaboration with the Arizona supernova group, long-term postbounce supernova calculations in Newtonian gravity, using the axisymmetric neutrino radiation-hydrodynamics code VULCAN/2D [15, 26, 27]. These calculations extend to more than a second after core bounce and indicate the excitation of PNS core g-mode oscillations by accretion downstreams and turbulence at several hundred milliseconds after core bounce. The oscillations damp by the emission of strong sound waves. These deposit energy in the postshock region which may be sufficient to drive the explosion [26–29].

I find that the narrow-band gravitational wave emission from the quadrupole components of the PNS core oscillations may be the dominant gravitational wave emission process in slowly rotating core-collapse supernovae. It could easily rival in amplitude and energy the emission from the core bounce of quickly spinning iron cores.

1.2.6 Gravitational Wave Signature of Accretion-Induced Collapse

I have analyzed the gravitational wave emission in the accretion-induced collapse (AIC) of massive and high central-density O/Ne/Mg white dwarfs. The analysis considers gravitational wave signals of aspherical mass motions and of anisotropic neutrino emission and is based on the calculations of the Arizona supernova group (Dessart et al. [16]) who for the first time employed two genuinely 2D rapidly rotating precollapse white dwarf models and followed the collapse and postbounce evolution with the axisymmetric Newtonian radiation-hydrodynamics code VULCAN/2D. The simulation and analysis results show that the extremely efficient deleptonization in the AIC models allows collapse to nuclear densities largely unimpeded by rotational effects and leads to exceptionally small inner core masses at core bounce. They result in a matter gravitational wave signal qualitatively resembling that observed for large initial pressure depletion in previous studies with polytropic models [12, 30]. The model with the initially largest rotation rate reaches a postbounce β of $\sim$26% and might experience the rare case of a high-$T/|W|$ rotational instability if liberated on a 3D grid.

The AIC models show strong anisotropies in their neutrino radiation fields throughout their postbounce evolution and the gravitational wave signal at postbounce times $\gtrsim$ 50 ms is dominated in amplitude by low-frequency emission from anisotropic neutrino radiation. Due to its low-frequency, almost "DC" character, the neutrino component does not lead to significant energy emission.

1.3 Structure of this Dissertation

In chapter 2, I present a general introduction to supernova physics, numerical relativity, GR hydrodynamics, and gravitational wave theory and observation. In addition, I give an extensive overview on previous work concerning the gravitational wave signature of core-collapse supernovae.

Chapter 3 is devoted to a comprehensive and detailed description of the various components of the CACTUS/CARPET/WHISKY simulation code employed for the {3+1} GR hydrodynamics calculations that lie at the heart of the work presented here. Code tests of the CCW code are presented in chapter 4.

In chapter 5, I report on results from {3+1} GR core-collapse calculations that employ polytropic iron core models in rotational equilibrium and compare them in detail with previous results obtained by Dimmelmeier et al. [12, 17, 18] in conformally-flat GR in order to assess the qualitity of the conformal-flatness approximation in the core-collapse supernova context.

Chapter 6 contains an extensive discussion of the results obtained via today's most realistic calculations of rotating stellar iron core collapse in GR. These calculations employ a finite-temperature equation of state, an approximate scheme for deleptonization during collapse and incorporate state-of-the-art presupernova stellar models from stellar evolutionary calculations. I discuss new estimates for the gravitational wave signature of axisymmetric stellar iron core collapse and the development of nonaxisymmetric structure at post core-bounce times. The detectability of rotating core collapse events by current and future light-interferometric gravitational wave observatories is assessed.

In chapter 7, I present results on the gravitational wave emission from late postbounce PNS core oscillations and on the gravitational wave signature of the accretion induced collapse of massive O/Ne/Mg white dwarfs.

In chapter 8, I critically review the work presented in this dissertation and outline possible future lines of research directed towards a greater understanding of the core-collapse supernova phenomenon, black hole formation and the supernova–gamma-ray burst connection.

1.4 Conventions and Units

The unit system used in sections that discuss numerical relativity and GR hydrodynamics is fixed by assuming $c = G = M_\odot = 1$. For convenience, I list conversion factors to cgs and geometric units ($c = G = 1$) and values of physical constants in appendix A. All sections discussing numerical results and all sections related to astrophysics and supernova theory are kept in standard cgs units.

I chose Greek indices running from 0 to 3 to indicate 4-vectors and 4-tensors. Latin indices i, j, k, l, m running from 1 to 3 indicate spatial components. I abbreviate, where convenient, the partial derivative $\partial/\partial x^i$ with $,i$ and the covariant derivative ∇_i with $;i$. I adopt the abstract index notation with sum convention. Unless noted otherwise, I assume spacelike signature (-,+,+,+) throughout this dissertation. 4-vectors and 4-tensors in abstract notation are printed in bold letters. Abstract 3-vectors have the standard vector symbol placed on top. $g_{\mu\nu}$ is the 4-metric, while I use γ_{ij} for the spatial 3-metric.

Chapter 2

Introduction

2.1 Supernovae

The term *supernova* was coined by the two astronomers Walter Baade and Fritz Zwicky [31], when they realized that there is a class of objects showing a sudden burst in luminosity that slowly decays, similar to novae ("new star"), but much more luminous and rare. The high luminosities of supernovae (SNe), comparable to the integrated light of their host galaxies, and the broad lines in their spectra, led them to the correct conclusion that supernovae were very energetic explosions. Fritz Zwicky, famous for his prophetic vision (among other things, he postulated the existence of dark matter and extragalactic gravitational lensing), hypothesized [32, 33] that a supernova resulted from the "transformation of an ordinary star into a collapsed neutron star". This ground-breaking hypothesis lies at the heart of modern theoretical models of supernovae related to the gravitational collapse of the cores of evolved massive stars.

Core-collapse supernovae occur predominantly near star forming regions and have never been observed in elliptical galaxies [34]. This leads to the assumption that their progenitors are stars with masses larger than $\sim 8\ M_\odot$ which are relatively short-lived ($\sim 10^7$ years). Such stars go through all nuclear burning stages up to iron beyond which nuclear fusion would be endothermic. At the end of a massive star's thermonuclear life, it has an *onion-skin* structure where an electron-degenerate massive iron core is nested within layers comprised of elements of progressively lower atomic weight at progressively lower densities and temperatures [1, 35]. These massive stars undergo core collapse after the final stages of nuclear burning, leaving a neutron star (or a black hole) remnant. The gravitational binding energy of the remnant is liberated in neutrinos and in the kinetic energy of the explosion of the stellar envelope.

However, there is another type of supernovae, driven by a quite different physical mechanism: Thermonuclear explosion. Small carbon-oxygen white dwarfs, end products of low-mass stellar evolution, may be situated in tight binaries with a normal stellar or white dwarf companion. In a small subset of these systems, sufficient matter is accreted from the companion star onto the white dwarf to push it over the Chandrasekhar limit for relativistic electron degeneracy ($\sim 1.4\ M_\odot$; see, e.g., [35, 36]). Contraction ensues as in the core of a dying massive star. However, since these white dwarfs consist predominantly of carbon and oxygen which are far from the peak of the nuclear binding energy curve, compression and heating soon lead, not to continued implosion, but to the thermonuclear incineration of the white dwarf. Thermonuclear supernovae (type Ia supernovae, as shall be discussed below) are about ten times less prevalent than core-collapse supernovae, but are often more than ten times as luminous [34].

Alternatively to thermonuclear explosion, massive white dwarfs with O/Ne/Mg cores and high central densities that are accreting mass from a companion star could collapse to neutron stars. Such an accretion-induced collapse (AIC) event could produce a supernova in a similar fashion as iron core collapse in massive stars, but may have an observable signature more similar to type Ia events.

The cosmological relevance of supernovae as donors of heavy elements is indisputable: Both kinds of supernovae enrich the universe with freshly synthesized elements such as magnesium, silicon, calcium, sulphur, neon, and iron-peak elements. While most of the carbon and oxygen of an exploding white dwarf is burned to heavier elements, core-collapse supernovae eject their outer carbon and oxygen envelopes with little nuclear burning and thus are the major source of oxygen in the universe.

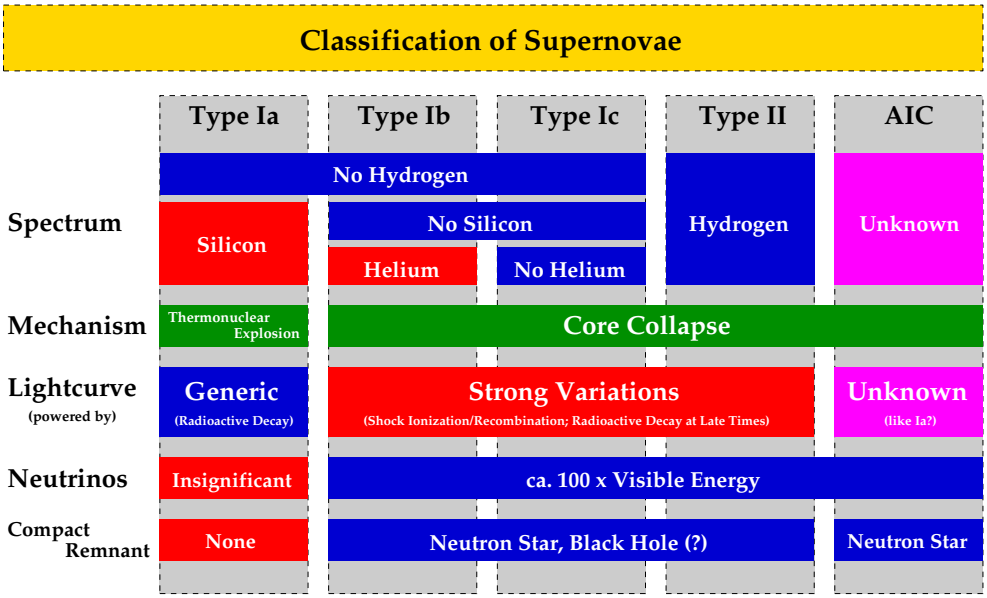

Figure 2.1: General classification scheme for Supernovae [1, 34, 37, 38]. Supernovae of type II, Ib, Ic, and of accretion-induced collapse (AIC) type are powered by the release of gravitational binding energy in stellar collapse. Type Ia supernova explosions are powered by exothermic thermonuclear reactions. The classification scheme is based on spectral characteristics.

Traditionally, SNe are not classified by theoretical considerations, but by their observed spectral characteristics (figure 2.1). By the time Baade & Zwicky introduced supernovae as an independent class of objects, spectra had already been obtained and Minkowski [39] observed two main supernova spectroscopic types: Type I SNe characterized by the absence of hydrogen in their spectra and type II SNe showing prominent hydrogen lines. As more spectra and better photometry became available, sub-types were introduced:

- **Type Ia**: Type Ia SN spectra show strong absorption lines attributed to Si II and no hydrogen lines. It has been determined observationally that the light curves (luminosity versus time) of all type Ia supernovae are quite similar, and, more importantly, can be made into cosmological standard candles for measuring distances (e.g., [40]). This type comprises all supernovae that are believed to be driven by thermonuclear incineration of a white dwarf. Thermonuclear supernovae produce $\sim 0.6\ M_\odot$ of ^{56}Ni. This element powers their optical light curves by its radioactive decay to ^{56}Co (τ = 8.8 days) and then to stable ^{56}Fe (τ = 111.3 days). Were it not for the radioactivity, the expansion of the exploding white dwarf would cool it adiabatically and its optical appearance would be much less spectacular. Type Ia SNe can be $\sim$10 times as luminous as type Ib, Ic, and II SNe and yield about ten times as much iron.

- **Type II**: Core-collapse supernovae. These objects have prominent hydrogen Balmer lines in their spectra. Their light curves are predominantly powered by the shock ionization (and subsequent recombination) of outer envelope material. Since this material is already at large radii, the adiabatic expansion effect does not cool it off much before the optical depths get sufficiently small to allow optical/IR photons to diffuse out (in contrast to the type Ia scenario). Hence, the shock energy is still available to power the light curve; how much depends on the initial radius of the progenitor. Core-collapse supernovae yield only $\sim 0.07\ M_\odot$ of ^{56}Ni. The radioactive decay of its daughter nucleus ^{56}Co powers the late-time light curve [34, 38]. Various subtypes have been introduced. The most frequently occurring type II-P ("plateau") is characterized by a long plateau in the lightcurve at high luminosities phase powered by hydrogen recombination. Type II-L ("linear") supernovae have a short plateau phase that merges into a ^{56}Co linear light curve tail. Type II-dw ("dense wind") supernovae are interacting with circumstellar material expelled by the progenitor before explosion. These SNe have strong radio emission caused by the interaction with that material and show strong hydrogen emission (Hα) and no absorption in the Balmer lines.

Neutron stars have been associated with remnants of core-collapse supernovae via pulsar radio emission and direct optical observation (e.g., the Crab pulsar associated with the supernova of 1054 AD in the Milky Way) [41].

- **Type Ib**: The spectra of type Ib SNe show no evident hydrogen Balmer lines, weak or absent Si II lines and strong He I lines. They are much less luminous than type Ia supernovae and are, in fact, core-collapse supernovae with massive single-star Wolf-Rayet progenitors or stripped stars in a binary system that have lost their hydrogen envelopes. Like type II-dw SNe they emit strongly at radio wavelength [34, 38].

- **Type Ic**: Type Ic SNe are core-collapse SNe whose spectra are similar to type Ib SNe, but, in addition, show weak or absent helium lines, indicating that their progenitor stars have lost their hydrogen and helium rich envelopes. Recently, signatures of exceptionally energetic type Ic supernovae (*hypernovae*) have been found in afterglows of the "long-soft" variety of gamma-ray bursts (GRBs) (see, e.g., [2] and references therein).

- **AIC**: The observational signature of supernova explosions resulting from the accretion-induced collapse of massive white dwarfs in binary systems is unknown, but could be similar to that of strongly subluminous type Ia SNe [42].

2.2 Supernova Rates

Within the last millennium, humans have witnessed and recorded 6 supernovae in our galaxy and one in the Large Magellanic Cloud (LMC, one of Milky Way's nearby satellite galaxies) [1]. Among them are the recent SN1987A in the LMC, 1987, type II), the supernova of the Crab Nebula (1054, type II) and the supernovae recorded by Tycho Brahe (1572, probably type Ia) and Johannes Kepler (1604, type Ia). Observers estimate that the six recorded supernovae make up only 20% of the galactic supernovae that exploded since AD 1000, because the majority were probably shrouded from view by the dust that pervades our galaxy, or were only observable from the southern hemisphere at times when there was no recording of astronomical events in that part of Earth. Examples are RX J0852-4642, a supernova remnant whose very nearby (~ 0.2 kpc) birth in historical times (~ 1300 AD) went unrecorded [43] and Cas A, a supernova remnant of a 17th-century explosion that was not recognized as a supernova.

Type Ia supernovae are not associated with star forming regions/galaxies. They are about 10 times less prevalent than core-collapse supernovae, primarily owing to their relation to close binary systems with mass transfer. Since this work is concerned with stellar core collapse, I focus in the following on core-collapse supernova rates.

Estimates of supernova rates can either be made based on galactic observations, star formation rates and the initial mass function (e. g., [44, 54, 55]) or on extragalactic supernova observations, statistics, galaxy morphology and mass (e. g., [45, 56, 57]).

Table 2.1: Summary of core-collapse supernova rate estimates for galaxies of the Local Group.

Galaxy	Distance (kpc)	Core-Collapse SN Rate $(100\ \mathrm{yr})^{-1}$	Reference
Milky Way	0–$\sim$15	0.50–2.50	[44–46]
LMC	$\sim$50	0.10 – 0.50	[44, 46–48]
SMC	$\sim$60	0.06 – 0.12	[44, 46, 48]
M31	$\sim$770	0.20 – 1.20	[44, 46, 49]
M33	$\sim$840	0.16 – 0.68	[44, 46, 50]
IC 10	$\sim$750	0.05 –0.11	[51]
IC 1613	$\sim$770	$\sim$0.04	[52, 53]
NGC 6822	$\sim$520	$\sim$0.04	[46, 52]

Of the ∼35 galaxies in the Milky Way neighborhood that form the Local Group of Galaxies (e.g., [58]), only the Milky Way, its satellites the Large and Small Magellanic Clouds (LMC/SMC), Andromeda (M31), Triangulum (M33), the starburst dwarf IC 10 and the dwarf irregular galaxies IC 1613 and NGC 6822 have significant core-collapse supernova rates. Table 2.1 summarizes the rate estimates found in the literature. Based on these estimates, even when being optimistic, one may expect not more than one core-collapse supernova within in ∼40 years in the Milky Way and (optimistically) within ∼17 years in the entire Local Group.

The nearest cluster of galaxies to the Local Group in the Local Supercluster is the Virgo Cluster at a distance of 10–20 Mpc. The Virgo Cluster contains a significant number of starburst galaxies with high star formation rates. Arnaud et al. [59], based on the Tully catalog [60] and the rates of Cappellaro et al. [45], estimated a rate of ∼5 core-collapse supernovae per year for the Virgo Cluster.

2.3 Core-Collapse Supernovae

Since this work is primarily concerned with the gravitational wave signature of core-collapse supernovae, it is expedient to review massive star evolution and the current state of core-collapse supernova physics.

2.3.1 Stellar Evolution and Progenitor Structure

Stars undergo a sequence of thermonuclear burning stages in their evolution, starting on the main sequence with core hydrogen ignition at temperatures above $\sim 2\times10^7$ K. With the exhaustion of core hydrogen, most stars proceed to shell hydrogen and successive core-helium ignition. The ashes of helium burning are predominantly carbon and oxygen. Stars with zero-age main-sequence (ZAMS) masses below ∼6–8 $M_\odot$ are not massive enough to contract to sufficiently high densities and temperatures for carbon burning. They develop electron-degenerate carbon-oxygen cores and eject their envelopes, losing enough mass to end their lives as quiescently cooling and contracting white dwarfs. More massive stars ignite carbon burning which leaves mostly oxygen, neon and magnesium as ashes [38]. In an intermediate mass range of ∼8–10 $M_\odot$ core temperatures are too low to ignite subsequent nuclear burning. Stars in that mass range either lose their envelopes and become O/Ne/Mg white dwarfs (that could become the progenitors of accretion-induced collapse SNe; e.g.,[16, 42, 61]) or experience collapse of their low-mass O/Ne/Mg cores [62].

Stars with ZAMS masses from ∼10 to ∼60–100 $M_\odot$ (depending, among other things, on ZAMS metallicity [38]) are able to ignite the ashes of carbon burning, most importantly oxygen and neon, fusing predominantly into silicon, sulphur, calcium, and argon. Silicon, in a final stage of exothermic nuclear reactions, is converted to iron-group nuclei in quasi-equilibrium via a series of photodisintegration reactions into neutrons, protons and α-particles, and nucleon rearrangement. The final core is electron degenerate and consists of ∼1.5 $M_\odot$ in iron-group nuclei near the peak of the nuclear binding energy curve and in nuclear-statistical equilibrium (NSE) [1, 3, 38]. It is embedded in an onion-skin structure of shells comprised of elements of progressively lower atomic weight at progressively lower densities and temperatures. A typical nesting is Fe→Si→O/C→He→H. Despite their high central temperatures, massive stars have, owing to their high central densities ($\gtrsim 5\times10^9$ g cm^{-3}) and ordered arrangement of their constituent nucleons into nuclei, low entropy [1, 3].

2.3.2 The Supernova Story from Collapse to Explosion (?)

The ultimate energy source of core collapse supernovae is the gravitational binding energy released when the iron core of a dying massive star contracts from an outer radius of ∼1500 km and central densities below $\sim 10^{10}$ g cm^{-3} to a radius of 10–30 km and densities above that in atomic nuclei (∼2–3×10^{14}g cm^{-3}). To first-order, the gravitational binding energy of the remnant neutron star is given by

$$|W| \sim \frac{GM_{\rm NS}^2}{R} = 3\times10^{53}\left(\frac{M_{\rm NS}}{M_\odot}\right)^2\left(\frac{10\,{\rm km}}{R_{\rm NS}}\right)^{-1}\ {\rm erg}\ , \tag{2.1}$$

where $M_{\rm NS}$ is the neutron star mass (typically $\sim$1.4 $M_\odot$) and $R_{\rm NS}$ is its radius (on the order of 10 km). 99% of this energy is liberated in the form of neutrinos throughout the supernova evolution and the late-time cooling of the protoneutron star (PNS). The kinetic energy of the material expelled in a supernova explosion accounts for about 1% ($\sim 10^{51}$ erg) of the binding energy and the energy emitted in optical wavelength is a fraction of this [1, 3, 37].

The precollapse iron core is stabilized against gravitational collapse by the pressure of relativisticly degenerate electrons,

$$p \propto Y_e^{4/3} \rho^\Gamma \ , \tag{2.2}$$

where Y_e is the number of electrons per baryon and Γ is the adiabatic exponent which assumes the value 4/3 for relativistic degeneracy [36]. Precollapse iron cores have $Y_e \sim 0.42$ at their center and $Y_e \sim 0.48$–0.5 at their outer edge. The contribution of the degenerate electrons to the total iron core pressure amounts to $\sim$90% in cores of intermediate mass in stars with ZAMS masses in the range of $\sim$12–20 $M_\odot$, in low-mass cores up to 99%, and less in the lower-density cores of higher-ZAMS-mass stars. Thermal and photon radiation pressure play only a minor role [3].

The Chandrasekhar mass

$$M_{\rm Ch} = 1.457\,(2Y_e)^2\,{\rm M}_\odot \tag{2.3}$$

is the maximum mass of a nonrotating fluid body that can be held in hydrostatic equilibrium by electron-degeneracy pressure in Newtonian gravity. $M_{\rm Ch}$ is increased by rotation and thermal pressure components and decreased by general relativity [36, 63]. Since the conversion of silicon-shell nuclei into iron-group nuclei continues after the iron core has formed, it is eventually pushed over its effective Chandrasekhar limit and becomes unstable to collapse when the additional thermal pressure support is lost by endothermic photo-dissociation of iron-group nuclei into α-particles, e.g.,

$$\gamma + {}^{56}_{26}{\rm Fe} \rightleftharpoons 13\alpha + 4n \ , \tag{2.4}$$

with an energy requirement of $\sim$125 MeV per reaction [36]. A second process involved in the onset of core collapse and prominent in low-mass cores is electron capture by heavy nuclei and free protons,

$$\begin{aligned} e^-\text{capture by nuclei nuclei:} &\quad e^- + (Z,A) \overset{(W)}{\rightarrow} \nu_e + (Z-1,A) \ , \\ e^-\text{capture by free protons:} &\quad e^- + p \overset{(W)}{\rightarrow} \nu_e + n \ . \end{aligned} \tag{2.5}$$

Electron captures reduce Y_e and consequently the pressure. The electron-type neutrinos created in the captures are able to stream freely out of the collapsing core until densities of $\sim 2\times10^{12}$ g cm^{-3} are reached at which point the neutrino scattering opacities become so large that the mean free path of neutrinos is quickly reduced to values much smaller than the core's size. Consequently, the diffusion timescale of the neutrinos becomes large compared to the dynamical timescale of collapse. The neutrinos are *trapped* and equilibrium of weak interactions (β-equilibrium, Bethe-equilibrium) prevails, keeping the lepton number $Y_l = Y_e + Y_{\nu_e}$ fixed [3, 35, 36, 64].

During the collapse of spherically symmetric iron cores[1], a subsonically and homologously ($v \propto r$; self-similar) collapsing *inner core* forms that interfaces with the supersonically collapsing *outer core* at the sonic point, where the local speed of sound equals the radial collapse velocity [3, 64–69]. At the onset of collapse and throughout the initial part of the infall phase during which the core contracts only slowly, the inner core encompasses $\gtrsim$ 1 $M_\odot$ of material. The mass of the inner core is well approximated by

$$M_{\rm ic} = M_{\rm ic} \simeq (K/K_0)^{3/2} M_0 \ . \tag{2.6}$$

Here K is the coefficient in the polytropic equation of state (EOS), approximately describing the electron-degenerate iron core, $p = K\rho^\Gamma$ with $\Gamma \approx 4/3$. The subscript 0 denotes the values of the corresponding quantities when collapse sets in [65, 66]. Considering the polytropic coefficient for the relativistically degenerate electron Fermi gas [36],

$$K = \frac{\hbar c}{4}(3\pi^2)^{1/3}\left(\frac{Y_e}{m_{\rm B}}\right)^{4/3} , \tag{2.7}$$

[1] Rotating, hence axisymmetric, iron cores collapse quasi-homologously with $v \simeq \alpha(t,\theta) r$, where the magnitude of α decreases with increasing polar angle θ [30].

it is straightforward to realize the strong Y_e^2 dependence of the inner core mass while keeping in mind that both (2.6) and (2.7) are simple estimates and only hold precisely if the EOS is polytropic.

Without sufficient angular momentum whose conservation may yield strong centrifugal support to halt collapse at lower densities, the iron core collapses until densities comparable to those in atomic nuclei are reached and nuclear repulsive forces lead to a stiffening of the EOS. This happens on a timescale of a few 100 ms after the onset of collapse. Within fractions of a millisecond, the homologously collapsing *inner core*'s collapse is halted and reversed. Due to its extremely large inertia, the inner core overshoots its equilibrium configuration and rebounds ("bounces") *into* the outer core which is still collapsing with velocities exceeding a tenth of the speed of light. At the surface of the rebounding inner core, a strong hydrodynamic shock wave forms and starts to propagate outward through the outer core material. The shock wave, initially having a multiple of the final observed kinetic supernova explosion energy, quickly loses strength to the dissociation of outer-core material into nucleons (at a cost of $\sim$8.8 MeV per nucleon [3]). Additional energy is lost when the shock breaks out of the neutrino-optically-thick regions which is accompanied by a prompt, ultra-luminous ($\sim 10^{54}$ erg s^{-1}) burst of neutrinos that decouple from the matter and begin to free-stream [70].

The size of the inner core at bounce does not only determine the mass of the infalling material that remains to be dissociated by the shock, but additionally, it determines (in a rotating core) the amount of angular momentum that may become dynamically relevant during the final phases of collapse and, perhaps most importantly, it determines the initial kinetic energy imparted to the bounce shock. Modern-day numerical calculations predict an inner core mass at core bounce below $\sim$0.5–0.6 M$_\odot$ for spherically symmetric collapse (see, e.g., [64]) which is too small to allow a *prompt explosion* as favored by early core-collapse supernova models [3]. Instead, losing energy to nuclear breakup and emitted neutrinos, the bounce shock stalls within only 10–20 ms of its birth and turns into a quasi-stationary accretion shock at radii of 100–200 km [1, 3, 37, 71].

At the time of shock stall, a hot and dense PNS has formed interior to the shock with an average lepton number $Y_l \lesssim 0.3$. It slowly contracts while deleptonizing and cooling as neutrinos of all flavors (μ and τ neutrinos are created by thermal processes) diffuse through the optically-thick regime to less dense, more transparent regions on a timescale of several hundred ms. Convective processes may enhance neutrino cooling and boost the PNS neutrino luminosity (e.g., [72, 73] and references therein). Furthermore, there is accretion-driven neutrino emission from the outer layers of the PNS onto which material accreted through the stalled shock at a rate of 0.5–1.0 M$_\odot$ s^{-1} settles.

In the so-called *delayed explosion mechanism* or *neutrino-driven mechanism*, first proposed by Hans Bethe and Jim Wilson [74, 75], the neutrinos emitted from the hot PNS star play a crucial role. Owing to a subtle imbalance between neutrino cooling of the postshock material and neutrino heating by the neutrinos that leak out of the PNS, net energy deposition in the *gain region* just below the stalled shock could lead to shock revival[2], resulting in a successful supernova explosion.

Although the existence of a neutrino heating region has been confirmed in many simulations (see, e.g., [77–80]), recent state-of-the-art *one-dimensional* calculations have not been able to demonstrate a robust shock revival and subsequent explosion [70, 81–85] (but see [62], who obtain neutrino-driven explosions in 1D for low-mass O/Ne/Mg stars). Two-dimensional axisymmetric simulations suggest that convection in the PNS star may play an important role by boosting its neutrino luminosity and thus leading to a higher heating rate in the gain region which may also be convectively unstable ([26, 27, 73, 77, 79, 80, 86–89] and references therein).

New multi-dimensional calculations [27, 73, 86, 87, 90–96] and analytic models [97–101] indicate the presence of a large-scale low-ℓ hydrodynamic/advective-acoustic instability of the standing accretion-shock (SASI) that leads to time-varying large-scale typically dipolar shock deformations and accretion downstreams that boost the neutrino luminosity. Buras et al. [73, 86] found that the neutrino-driven mechanism combined with the SASI can lead to explosions in low-mass progenitors with ZAMS masses $\lesssim$12 M$_\odot$, but fails for more massive stars. Bruenn et al. [93] found neutrino-driven SASI-related explosions in 15 and 11 M$_\odot$ progenitors.

Burrows et al. [26–29], on the other hand, found explosions not directly driven by neutrino energy depositions, but rather by acoustic power. In their simulations, these authors have observed that PNS core g-modes are excited by turbulence and by accretion downstreams through the unstable

[2]Note that the idea that the energy transfer to the ejecta is mediated by neutrinos goes back to Colgate & White [76].

and highly SASI-deformed stalled supernova shock at postbounce times of many hundreds of milliseconds. The oscillations continuously lose energy by the emission of strong sound waves, but do not ebb until accretion subsides. In this way the core g-modes act as transducers for the conversion of accretion gravitational energy into acoustic power that is deposited in the supernova mantle and may be sufficient to drive an explosion.

Up to the present, there is no agreement among supernova theorists on *the* core-collapse supernova mechanism. In fact, it may well be that there are multiple mechanisms that have varying relevance, depending on progenitor structure, rotational configuration, and magnetic field. Future 3D simulations including full Boltzmann neutrino radiation transport, magneto-hydrodynamics, general relativity, and multi-dimensional progenitor star models that consistently include rotation and magnetic fields will be needed to ultimately solve the supernova problem.

2.3.3 Black Hole Formation, Collapsars, and the SN–GRB Connection

The iron core of a dying massive star cannot directly collapse to a black hole[3] and always forms a PNS. This fact, although overlooked by many studies that focussed on the GR side of black hole formation (e.g., [103–105]), is a simple consequence of nuclear astrophysics and the basics of iron core collapse theory. Stars with masses from $\sim$10 to $\sim$60–100 $M_\odot$ form iron cores in the range of $\sim$1 to $\sim 2M_\odot$. During collapse, the precollapse iron core is separated into a subsonically collapsing and quickly deleptonizing inner core and a supersonically collapsing out core. Inner core mass of a nonrotating iron core[4] that is stabilized at nuclear densities by the stiff nuclear EOS is $\sim$0.5–0.6 $M_\odot$ [64, 106], spread out over a radial interval of not less than $\sim$5 km at greatest compression. These numbers correspond to $\frac{G}{c^2}\frac{M}{R} \lesssim 0.18$ which is too small for the inner core to be unstable to further collapse to a black hole. The inner core mass of $\sim$0.5–0.6 $M_\odot$ is determined by nuclear physics and weak interactions and *does not have a significant dependence on the progenitor star mass*.

Although direct collapse[5] to a black hole can be ruled out, black hole formation can occur in core collapse supernovae either when the supernova explosion is not successful and the PNS gains so much mass that it becomes unstable to GR collapse (type I collapsar, [108, 109]) or after a weak explosion and long-term fallback accretion (type II collapsar, e.g., [109, 110]). Type I collapsars may be the central engines of the long-soft variety of GRBs.

GRBs (see, e.g., [111] for a review) are intense beamed flashes of γ-rays. They are of cosmological origin and last between 0.5–200 s, with a bimodal distribution of durations, peaking at $\lesssim 1$ s and at ~ 50 s and indicating two distinct mechanism and/or central engines. The short-hard (hard, because their γ-ray spectra peak at shorter wavelength) GRBs are believed to be produced by the mergers of compact binaries. Long-soft GRBs appear to occur predominantly in star-forming galaxies, and recent observations [111] have found type Ic supernova characteristics in at least some of the afterglows of long-soft GRBs. This and the GRB energetics that – for highly-beamed emission by a jet with Lorentz factors $\Gamma \gtrsim 200$ and $\sim 5^\circ$ opening angle – come out to be on the order of a supernova explosion energy, suggest a direct relation between core-collapse supernovae and GRBs [2].

In the collapsar-GRB scenario [2, 108, 109] a black-hole with a stellar-mass accretion in combination with magnetorotational effects and/or neutrino–antineutrino pair creation and annihilation drive the baryon-poor ultra-relativistic GRB jet. However, it is not yet clear how exactly (collapsar-type) GRBs work, what decides between a more normal core-collapse supernova and a GRB, what fraction of long-soft GRBs have supernova characteristics in their afterglows, and what the structure and evolutionary track of GRB progenitor stars is [2, 38, 112–114].

[3] This is true for Population I/Population II stars and probably not for metal-less Population III stars that could form very massive iron cores. See, e.g., [102].

[4] Rotation – at least in all plausible/physically sensible cases – stabilizes against collapse and leads to decreased compactness at increased inner core mass.

[5] Unfortunately, Woosley and collaborators (e.g., [38, 107]) tend to use the term "direct black hole formation" incorrectly to denote collapse to a black hole *after* PNS formation, but *before* a successful supernova explosion. This has lead to significant confusion in the general astrophysics community.

2.4 Numerical Relativity

Einstein's Theory of General Relativity (GR) [4, 5] describes gravity in terms of the *curvature* of four-dimensional spacetime (one temporal, three spatial dimensions). GR is non-linear, since curvature is created by mass-energy and changed by variations in energy-momentum (including rest-mass energy, kinetic energy, electro-magnetic field energy etc.), but at the same time curvature governs the motion of mass-energy at least partly (completely in the case of vanishing other forces: strong, weak, electromagnetic). Unlike Newtonian theory where gravitational action is instantaneous, changes in the "gravitational field" described by curvature propagate at the finite speed of light.

The mathematical framework needed to describe GR is differential geometry which mathematically describes spacetime as a four-dimensional manifold $\mathcal{M}$ on which a metric $g_{\mu\nu}$ and its inverse $g^{\mu\nu}$ are defined. The invariant differential line element measuring the physical distance between two infinitesimally separated spacetime events is given by

$$ds^2 = g_{\mu\nu} dx^\mu dx^\nu \ , \tag{2.8}$$

where $\boldsymbol{dx}$ with components dx^α describes the separation vector between the two events. In the following, I shall assume that the reader is familiar with the basics of differential geometry. An easy-to-read introduction geared towards the physical aspects can, for example, be found in Schutz's book [115].

The Einstein equations describe the non-linear relation between spacetime curvature and the energy-matter fields and are given (here in dimensionfull units; in the following I assume $c = G = \mathrm{M}_\odot = 1$ unless noted otherwise) by

$$G_{\mu\nu} \equiv R_{\mu\nu} - \frac{1}{2} g_{\mu\nu} R = \frac{8\pi G}{c^4} T_{\mu\nu} \ , \tag{2.9}$$

where all tensors are symmetric. $G_{\mu\nu}$ is the Einstein tensor, $T_{\mu\nu}$ is the stress-energy tensor describing the matter and electro-magnetic components of spacetime. $R \equiv R^\rho_\rho$ is the Ricci (or curvature) scalar and $R_{\mu\nu}$ is the Ricci tensor obtained via the contraction $R_{\mu\nu} \equiv R^\rho_{\mu\rho\nu}$ of the Riemann curvature tensor which itself is constructed as

$$R^\sigma_{\mu\rho\nu} \equiv \Gamma^\sigma_{\mu\nu\,,\rho} - \Gamma^\sigma_{\mu\rho\,,\nu} + \Gamma^\sigma_{\tau\rho}\Gamma^\tau_{\mu\nu} - \Gamma^\sigma_{\tau\nu}\Gamma^\tau_{\mu\rho} \tag{2.10}$$

from the connection coefficients, the *Christoffel symbols*, which are defined in terms of the metric

$$\Gamma^\sigma_{\mu\rho} \equiv \frac{1}{2} g^{\sigma\tau} \left(g_{\rho\tau,\mu} + g_{\mu\tau,\rho} - g_{\mu\rho,\tau} \right) \ . \tag{2.11}$$

Note that, even though I have chosen to write them in index notation and not in abstract tensor notation, equations (2.9) – (2.11) are covariant, that is, they are independent of the choice of coordinates. In GR, all coordinate systems, and more tersely, all frames of reference, are treated on an equal footing. There is no such thing as global inertial frames of reference known in Special Relativity and Newtonian theory.

Despite their superficial simplicity (2.9), the Einstein equations form a complicated set of 10 coupled non-linear partial differential equations that have closed analytic solutions only for the most idealized physical settings (e.g. static spherically- or stationary axi-symmetric situations: Schwarzschild and Kerr solutions. A much more detailed discussion can be found in, e.g., [116]). In any astrophysically interesting scenario it is necessary to solve the Einstein equations numerically.

2.4.1 The Arnowitt-Desner-Misner {3+1} formalism

The Arnowitt-Desner-Misner formalism (ADM) [117, 118], based on the {3+1} splitting of spacetime first introduced by Lichnerowicz [119], is the basis of most modern formulations of the Einstein equations for numerical evolutions. In the following, I will only outline the most salient aspects of ADM. A much more thorough modern derivation and discussion may be found, for example, in York's seminal article from 1979 [118] and in the 1998 review article by Baumgarte and Shapiro [120]. Parts of the following discussion have already appeared in similar fashion in the dissertations of Thornburg [121], Dimmelmeier [18], Herrmann [122], and Baiotti [123].

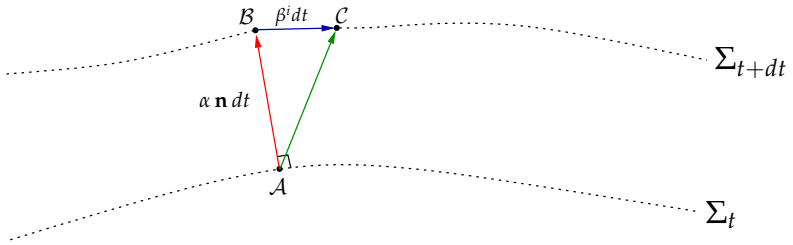

Figure 2.2: Schematic geometric interpretation of the {3+1} foliation of spacetime. Individual spacelike slices Σ are connected by (local) unit normal vectors n^μ along which time is evolved at rate α. In addition, the coordinate labels may change. This is expressed by the coordinate shift vector β^i. This figure is adapted from Thornburg's dissertation [121].

In its non-discretized form, the ADM {3+1} formalism decomposes (or *foliates / slices*) the four-dimensional spacetime manifold $\mathcal{M}$ into a continuous sequence of three-dimensional t-parametrized spacelike hypersurfaces (slices) Σ_t encompassing an entire three-dimensional space. Such a decomposition singles out "space" from "time", taking a step backwards from Einstein's elegant original formulation that treats time and space on an equal footing, but enabling GR to be viewed as a more conventional dynamical field theory. In this context, ADM defines a Cauchy problem, that is, if the appropriate initial data on some slice Σ_t and boundary conditions for all other $\Sigma_{t'>t}$ are specified, then the time evolution of the initial data is determined.

I define a future-pointing timelike vector $\boldsymbol{n}$ orthonormal to the slices Σ_t: $\boldsymbol{n} = -\alpha\boldsymbol{\nabla}t$, where α is the *lapse function* determining the *local* evolution of time along the unit normal through the latter's normalization constraint $\boldsymbol{n}\cdot\boldsymbol{n} = -1$. Furthermore, I introduce a coordinate basis for the entire spacetime manifold $\mathcal{M}$:

$$\{\mathbf{e}_{(\mu)}\} = \{\mathbf{e}_{(0)}, \mathbf{e}_{(i)}\} \ , \tag{2.12}$$

with $\mathbf{e}_i$ being purely spatial and tangent to the slices Σ_t at any point (orthogonal to the unit-normal $\mathbf{n}$ of Σ_t). In these coordinates, an event $\boldsymbol{x}$ has components $x^\mu = (t, x^i)$. The invariant differential line element connecting two events x^μ and x'^μ on infinitesimally separated slices Σ_t and Σ_{t+dt} is then given by

$$ds^2 = -(d\hat{t})^2 + (d\hat{x})^2 \ , \tag{2.13}$$

with $d\hat{t}$ and $d\hat{x}$ being the changes in physical time and physical distance, respectively. From the above definition of the lapse, one already knows

$$d\hat{t} = \alpha dt \ . \tag{2.14}$$

In general, for an observer momentarily at rest in Σ_t at coordinates labeled x^i, the same physical 3-location may be relabeled to x'^i on Σ_{t+dt} via $x'^i = x^i - \beta^i dt$, where β^i is an arbitrary spatial vector, tangent to Σ_t. Hence, it is necessary to recover the original coordinate labeling when considering the coordinate distances needed to measure physical distances from Σ_t to Σ_{t+dt}:

$$d\hat{x}^i = dx^i + \beta^i dt \ , \tag{2.15}$$

where dx^i is the coordinate distance and β^i represents the coordinate *shift*.

With the above choice of $\{\mathbf{e}_{(\mu)}\}$ and the definitions of α and β^i, the coordinate representation of the timelike contravariant unit vector n^μ normal to Σ_t is

$$n^\mu = \left(\frac{1}{\alpha}, -\frac{\beta^i}{\alpha}\right) . \tag{2.16}$$

Since arbitrary shifts β^i are allowed, the world line of a general coordinate observer need not be normal to Σ_t. Instead, its tangent is given by the timelike unit vector

$$t^\mu = \alpha n^\mu + \beta^\mu \ . \tag{2.17}$$

Figure 2.2 schematically depicts the geometrical interpretation of foliation, lapse and shift.

The general line element introduced in equation (2.8) can now be decomposed in {3+1} fashion:

$$ds^2 = g_{\mu\nu}dx^\mu dx^\nu = -\alpha^2 dt^2 + \gamma_{ij}(dx^i + \beta^i dt)(dx^j + \beta^j dt) \ . \tag{2.18}$$

Here, γ_{ij} is the 3-metric which is just the spatial part of the 4-metric: $\gamma_{ij} \equiv g_{ij}$. The 4-metric now assumes the following form:

$$g_{\mu\nu} = \left(\begin{array}{c|c} -\alpha^2 + \beta_i\beta^i & \beta_i \\ \hline \beta_j & \gamma_{ij} \end{array}\right) \ , \tag{2.19}$$

where $\beta_i = \gamma_{ij}\beta^j$ and the inverse metric reads

$$g^{\mu\nu} = \left(\begin{array}{c|c} -\alpha^{-2} & \alpha^{-2}\beta^i \\ \hline \alpha^{-2}\beta^j & \gamma^{ij} - \alpha^{-2}\beta^i\beta^j \end{array}\right) \ . \tag{2.20}$$

For projecting general four-dimensional vectors and tensors that live on $\mathcal{M}$ onto Σ_t, one must use the projector

$$\perp^\mu_\nu = g^\mu_\nu + n^\mu n_\nu \ , \tag{2.21}$$

which is naturally orthogonal to $\boldsymbol{n}$: $\perp \cdot \boldsymbol{n} = 0$.

2.4.2 Eulerian Observers, Eulerian 3-Velocities, Physical 3-Velocities

It is now convenient to introduce the concept of *Eulerian* observers (see, e.g., [124]). Eulerian observers have world lines that are normal to the spacelike hypersurfaces. Thus they are at rest with respect to the slicing of spacetime along the unit normal $\boldsymbol{n}$ and have $\boldsymbol{n}$ as 4-velocity. For example, the path $\mathcal{AB}$ in figure 2.2 is a portion of the world line of an Eulerian observer and the shift vector β^i represents the 3-velocity of the spatial coordinates with respect to the Eulerian observer. For future reference in the section on GR hydrodynamics (§2.5), I define the 3-velocity of an object (a fluid, for example) as measured by an Eulerian observer:

$$v^i = \frac{\perp^i_\rho u^\rho}{-\boldsymbol{n}\cdot\boldsymbol{u}} = \frac{u^i}{\alpha u^0} - n^i = \frac{u^i}{W} + \frac{\beta^i}{\alpha} \ , \tag{2.22}$$

where the object/fluid-intrinsic 4-velocity $\boldsymbol{u}$ is defined as $u^\mu = dx^\mu/d\hat{t}$ where $\hat{t}$ is the physical (or proper) time. I have used (2.16) and the fact that $n_\mu n^\mu = -1$ to write $-\boldsymbol{n}\cdot\boldsymbol{u} = \alpha u^0$. αu^0 which is the Lorentz factor W satisfying

$$W = \frac{1}{\sqrt{1 - v^i v_i}} \ . \tag{2.23}$$

For completeness, the covariant components of the Eulerian coordinate 3-velocity read

$$v_i = \frac{\perp^\rho_i u_\rho}{-\boldsymbol{n}\cdot\boldsymbol{u}} = \frac{u_i}{W} \ . \tag{2.24}$$

In general relativity with a general coordinate basis that is not necessarily orthonormal, the magnitude of the Eulerian 3-velocity vector is bounded by the speed of light, but its components, in general, are not. A trivial example that demonstrates this is Minkowski spacetime in spherical coordinates where $ds^2 = -dt^2 + dr^2 + r^2(d\theta^2 + \sin^2\theta d\varphi^2)$ and $\vec{v} = [v^r, v^\theta, v^\phi]^T$. In these coordinates, the angular velocity components may become arbitrarily large for $r \to 0$. It is now useful to define a *physical velocity* as the 3-velocity $\hat{v}^i$ measured by an Eulerian observer in a local orthonormal coordinate system which can be introduced at any point on the spacelike hypersurface Σ [116]. The components of

this $\hat{v}^i$ are individually bounded by the speed of light and, clearly, $\sqrt{\hat{v}^i\hat{v}_i} < c$ as well. To obtain $\hat{v}^i$ at a given coordinate location, one calculates a transformation tensor A^{ij} to diagonalize the 3-metric γ_{ij} (which is equivalent to transforming to an orthogonal coordinate basis). The physical velocity components are then

$$\hat{v}^i = \hat{v}_i = \sqrt{\hat{\gamma}_{ii}} A^{ij} v_j \ , \tag{2.25}$$

where $\hat{\gamma}_{ij}$ is the diagonalized 3-metric and no summation over index i is carried out. In this work I approximate the physical velocity components by $\hat{v}^i \approx \sqrt{\gamma_{ii}} v^i$ in situations in which the diagonal metric components dominate.

2.4.3 Extrinsic Curvature and the ADM Equations

Before discussing the actual time evolution of the Einstein equations in the ADM formalism, one must introduce the symmetric *extrinsic curvature* tensor which describes how the spacelike hypersurfaces are embedded in spacetime[6],

$$K_{ij} \equiv -\frac{1}{2}\mathcal{L}_{\boldsymbol{n}}\gamma_{ij} = -\gamma_i^l \gamma_j^k n_{(l\,;k)} \ , \tag{2.26}$$

where $\mathcal{L}_{\boldsymbol{n}}$ is the *Lie derivative* along the unit-normal vector $\boldsymbol{n}$ on Σ_t, where the semicolon denotes covariant differentiation $\nabla_\mu x^i = x^i_{\ ;\,i}$ with respect to the 3-metric γ_{ij} and where the round brackets around $_{(l;k)}$ denote symmetrization in l and k. Along a general vector w, the Lie derivative of a general tensor $T^{a_1,\ldots,a_n}_{b_1,\ldots,b_m}$ is defined (in component notation) as [125]

$$\mathcal{L}_{\boldsymbol{w}} T^{a_1,\ldots,a_n}_{b_1,\ldots,b_m} = w^r T^{a_1,\ldots,a_n}_{b_1,\ldots,b_m\ ;\,r} - \sum_{i=1}^{n} T^{a_1,\ldots,r,\ldots,a_n}_{b_1,\ldots,b_m}\ w^{a_i}_{\ ;\,r} + \sum_{i=1}^{m} T^{a_1,\ldots,a_n}_{b_1,\ldots,r,\ldots,b_m}\ w^r_{\ ;\,b_i} \ . \tag{2.27}$$

This definition of the Lie derivative is derived from the properties of parallel transport on general curved manifolds. An introduction to the Lie derivative and its geometric meaning can be found, for example, in Schutz's book [115].

The York form of ADM [118] recasts the Einstein equations (2.9) into a first-order in time and second-order in space system of partial differential hyperbolic *evolution equations* and a set of four elliptic *constraint equations*. The evolved dependent variables are the 3-metric γ_{ij} and the extrinsic curvature K_{ij}:

$$\left(\frac{\partial}{\partial t} - \mathcal{L}_{\boldsymbol{\beta}}\right)\gamma_{ij} = -2\alpha K_{ij} \ , \tag{2.28}$$

$$\left(\frac{\partial}{\partial t} - \mathcal{L}_{\boldsymbol{\beta}}\right)K_{ij} = -\alpha_{;ij} + \alpha\left[R_{ij} + K\,K_{ij} - 2K_{im}K^m_j - 8\pi\left(S_{ij} - \frac{1}{2}\gamma_{ij}S\right) - 4\pi\rho_{\rm ADM}\gamma_{ij}\right] \ . \tag{2.29}$$

Here, I have introduced the 3-Ricci tensor R_{ij}, the trace of the extrinsic curvature, $K \equiv \gamma^{ij}K_{ij}$, the total energy density as measured by an Eulerian observer, $\rho_{\rm ADM} \equiv n_\mu n_\nu T^{\mu\nu}$, and the projection of the stress-energy tensor onto Σ_t, $S_{ij} \equiv \gamma_{i\mu}\gamma_{j\nu}T^{\mu\nu}$ and $S \equiv \gamma^{ij}S_{ij}$. In this dissertation, I use exclusively the perfect-fluid stress-energy tensor, which I will introduce in Section 2.5.

Equation (2.28) illustrates the above interpretation of the extrinsic curvature as the "time derivative" of the 3-metric. From slice Σ_t to Σ_{t+dt} it may, however, still differ by an arbitrary coordinate shift. This is expressed by the Lie derivative along $\boldsymbol{\beta}$. Intuitively, equation (2.29) then represents the "acceleration", that is, the time variation of the time variation of the 3-metric.

In addition to the above evolution equations for the 3-metric and the extrinsic curvature, the ADM decomposition yields four elliptic constraint equations (the *constraints*) that must be satisfied on each spacelike hypersurface. The constraints are (intuitively) related to the conservation of energy and

[6] More precisely, the extrinsic curvature contains the information on time-derivatives of the four-dimensional metric (and, of course, also of the 3-metric) which is lost in the projection of the 4-Riemann tensor onto the three-dimensional hypersurfaces. See, e.g., Baumgarte & Shapiro [120] and York [118].

momentum[7]. The Hamiltonian constraint equation reads

$$R + K^2 - K_{ij}K^{ij} - 16\pi\rho_{\mathrm{ADM}} = 0 \ , \tag{2.30}$$

where R is the 3-Ricci scalar and the three momentum constraints are given by

$$K^{ij}_{\ \ ;j} - \gamma^{ij}K_{;j} - 8\pi S^i = 0 \ , \tag{2.31}$$

with $S^i \equiv -\gamma^{i\mu}n^\nu T_{\mu\nu}$ being the momentum density as seen by an Eulerian observer.

In the so-called ADM *free-evolution* scheme, initial data that satisfy the constraints are specified on the initial slice (that is, they are a solution to Einstein's equations; see, e.g., Cook [127] for a discussion of initial data) and then time-evolved by the evolution equations. In an ideal situation (continuum case, boundaries at infinity), the time-evolved data will satisfy the constraint equations on any future (or past) slice [118, 128–130]. In a discretized setting, numerical round-off errors, imperfect boundary conditions, and stability issues of the evolution system itself will lead to a deviation away from the *constraint hypersurface*, defined as the set of all field variables $\{\gamma_{ij}, K_{ij}, S_{ij}\}$ satisfying the constraints. The magnitude of the constraint deviation is frequently used to gauge the "quality" of a numerical evolution of Einstein's equations. The temporal behavior of the constraints is commonly monitored as well. A sudden exponential growth indicates an instability in the numerical evolution.

The observant reader may have noticed that I have so far not given a functional form of either the lapse function α or the shift vector β^i. In fact, since lapse and shift describe the time evolution of the coordinates (temporal and spatial, respectively), they must be provided as *inputs* to the time evolution. Einstein's equations are equally valid in *any* coordinate system. Hence, they cannot specify lapse and shift. In this sense, lapse and shift are pure gauge quantities that do not enter the physical solution. However, once the equations are discretized for numerical evolution on a computer, the choice of spatial and temporal gauge typically has, depending on the discretization chosen, a strong influence on the numerical stability of the evolution equations. As an example, special care must be taken not to "overuse" a numerical technique by trying to resolve very large coordinate gradients during the radial collapse of a neutron star to a black hole: even though the evolution equations will give the correct solution in the continuum limit, their ability to provide the physical solution will break down when the discretization scheme is not anymore able to capture the dynamics in a particular choice of coordinates. A better choice of coordinates may stabilize the evolution.

Ever since the first attempts to numerically evolve Einstein's equations, the stability of the free-evolution scheme has been a major concern. The ADM formalism has been in use for more than four decades now and detailed analysis of the ADM equations (see, e.g., [131, 132]) has shown them to have intrinsic stability issues related to their weakly-hyperbolic [133] nature[8].

One possible and straightforward approach to stabilize numerical evolutions is to make use of the constraint equations to "project" the evolution back onto the constraint hypersurface when the deviation of the constraints becomes too large [137, 138]. This, however, is on one hand computationally very expensive since a set of elliptic equations must be solved at each timestep. On the other hand and more importantly, it is impossible to do so straightforwardly if the evolved spacetime contains singularities. More practical approaches have been formulated by rewriting the ADM equations and introducing new variables that are combinations of the standard ADM variables and by adding constraint equations into the evolution equations. The latter is consistent, since in the continuum equations, the constraints are equal to zero and adding a zero does not - on an analytic level - change the evolution equations. On the numerical level, however, rearrangement of terms and addition of constraint equations at various places may well improve the numerical properties of the system and in this way, the stability of the numerical evolution. Examples of such modified evolution equations and their analysis can be found in [104, 135, 136, 139–143] and in references therein.

[7] Energy and momentum, in general, can only be measured locally by observers and hence cannot be defined unambiguously and globally in GR unless special conditions are met; see, e.g., the extensive discussion in Misner, Thorne & Wheeler [116]. In an asymptotically flat spacetime – a spacetime in which the curvature vanishes at large distances from some region so that at large distances the geometry becomes essentially that of a Minkowski spacetime – it is possible to define a total energy and a total angular momentum [116, 126].

[8] Also note that the traditional classification of hyperbolicity depends on the equation system to be first order in time and space (e.g. [133]). The ADM equations are first order in time, but second order in space. Only recently has the discussion of hyperbolicity been extended to mixed systems [134–136].

In the work presented here, I have used the spacetime evolution code [144] developed at the Albert-Einstein-Institut (in the following, I will refer to it as the BSSN_MOL code). It implements a conformal-traceless reformulation of the ADM equations first proposed by Nakamura, Oohara and Kojima [104] that subsequent studies [140, 141, 143–146] evaluated as robust enough to accomplish long-term stable evolutions of vacuum and matter spacetimes. This formulation of the {3+1} Einstein equations is frequently referred to as the BSSN evolution system. I chose to refer to it as the NOK-BSSN system, honoring the original authors that proposed the conformal-traceless recast. I will discuss the NOK-BSSN system and the BSSN_MOL code in Section 3.3.

2.4.4 Initial Data: The York-Lichnerowicz Procedure

Initial data for the ADM Cauchy free-evolution system must represent a physical solution[9] of the Einstein equations and, hence, must satisfy the momentum and Hamiltonian constraint equations. The minimal set of initial data that must be specified are the 3-metric γ_{ij} and the extrinsic curvature K_{ij}. Being symmetric tensors, they contain 6 degrees of freedom each. The Hamiltonian constraint constrains the 3-metric. The extrinsic curvature is constrained by the momentum constraints, leaving a total of 8 degrees of freedom [127], 5 for γ_{ij} and 3 for K_{ij}. Lapse and shift do not completely specify the coordinate gauge. Rather, they specify the time change of the coordinate gauge and, hence, there are 3 gauge degrees of freedom connected with the full 3-invariance of the 3-metric and 1 gauge degree of freedom which is usually associated with the trace of the extrinsic curvature [127]. There are 4 degrees of freedom left: 2 in γ_{ij} and 2 in K_{ij}. These correspond to the two physical dynamical degrees of freedom of gravitational waves when spelled out in first-order form.

As Cook has pointed out [127], the four constraint equations represent conditions which the 3-metric and extrinsic curvature must satisfy, yet they do not specify which components (or combination of components) are constrained and which are freely specifiable and there is no unique decomposition determining that. For general initial-data configurations, a widely used class of constraint decomposition are the York-Lichnerowicz conformal decompositions [119, 147, 148]. Their main features are a conformal decomposition of the 3-metric and of certain components of the extrinsic curvature plus a transverse-traceless conformal decomposition of the extrinsic curvature.

The 3-metric is rewritten in terms of a conformal factor Ψ and a conformally-related (also: conformal) 3-metric $\bar{\gamma}_{ij}$:

$$\gamma_{ij} \equiv \Psi^4 \bar{\gamma}_{ij} \ . \tag{2.32}$$

$\bar{\gamma}_{ij}$ carries five degrees of freedom and is typically chosen as

$$\bar{\gamma}_{ij} = \gamma^{-1/3} \gamma_{ij} \ , \tag{2.33}$$

leaving $\bar{\gamma} = 1$, but any normalization of $\bar{\gamma}$ is possible. A 3-metric that is conformally related to the flat spatial metric, $\gamma_{ij} = \Psi^4 \eta_{ij}$, is called *conformally flat*. Using (2.32), the Hamiltonian constraint (2.30) is rewritten as

$$\bar{\nabla}^2 \Psi - \frac{1}{8} \Psi \bar{R} - \frac{1}{8} \Psi^5 K^2 + \frac{1}{8} \Psi^5 K_{ij} K^{ij} = -2\pi \Psi^5 \rho_{\mathrm{ADM}} \ , \tag{2.34}$$

where $\bar{\nabla}^2 \equiv \bar{\nabla}^i \bar{\nabla}_i$, and $\bar{\nabla}_i$ is the covariant derivative with respect to x^i. All bar-ed variables are associated with the conformal metric $\bar{\gamma}_{ij}$. The extrinsic curvature is split into its trace and tracefree parts:

$$K_{ij} \equiv A_{ij} + \frac{1}{3} \gamma_{ij} K \ . \tag{2.35}$$

In addition, any symmetric tracefree tensor $\mathcal{S}^{ij}$ can be covariantly split [127] into a *longitudinal* and a *transverse-traceless* part according to

$$\mathcal{S}^{ij} \equiv (\mathbb{L}X)^{ij} + B^{ij} \ , \tag{2.36}$$

where B^{ij} is a symmetric, transverse-traceless ($B^{ij}{}_{;j} = 0$, $B^i_i = 0$) tensor, and

$$(\mathbb{L}X)^{ij} \equiv X^{j;i} + X^{i;j} - \tfrac{2}{3} \gamma^{ij} X^{\ell}_{\ ;\ell}. \tag{2.37}$$

[9] Solutions to the Einstein equations that are unphysical, that is, describing an unphysical situation, are certainly possible. Their evolution, though, does not make much sense.

This transverse-traceless decomposition is now applied to the tracefree part of the extrinsic curvature A_{ij} which eventually leads to a reduction of the momentum constraints to a set of elliptic equations based on differential operators with respect to the conformal 3-metric. This can be done in at least two ways, since it is natural to consider definitions of $(\mathbb{L}X)^{ij}$ and hence decompositions of A_{ij} with respect to both the physical and the conformal 3-metric, and there is no known advantage of one over the other [127]. In the following, I will only outline the conformal transverse-traceless decomposition. A more comprehensive discussion of both approaches is presented in [127].

The conformal tracefree extrinsic curvature $\bar{A}^{ij}$ is defined by

$$A^{ij} \equiv \Psi^{-10}\bar{A}^{ij} \text{ or } A_{ij} \equiv \Psi^{-2}\bar{A}_{ij} \,, \tag{2.38}$$

and it can be decomposed into

$$\bar{A}^{ij} \equiv (\bar{\mathbb{L}}X)^{ij} + \bar{Q}^{ij} \,, \tag{2.39}$$

where the longitudinal operator $\bar{\mathbb{L}}$ and the symmetric, transverse-traceless tensor $\bar{Q}^{ij}$ are both defined with respect to $\bar{\gamma}_{ij}$.

Applying (2.32, 2.35, 2.37 – 2.39) to the momentum constraints (2.31) and exploiting the fact that we demand $\bar{Q}^{ij}$ to be transverse and using the identity

$$\bar{\nabla}_j \mathcal{S}^{ij} = \Psi^{-10}\bar{\nabla}_j(\Psi^{10}\mathcal{S}^{ij}) \tag{2.40}$$

for any symmetric tracefree tensor $\mathcal{S}^{ij}$, yields [127] the momentum constraints with respect to $\bar{\gamma}_{ij}$:

$$\bar{\Delta}_{\mathbb{L}} X^i = \tfrac{2}{3}\Psi^6\bar{\nabla}^i K + 8\pi\Psi^{10}S^i \,, \tag{2.41}$$

where

$$\bar{\Delta}_{\mathbb{L}} X^i \equiv \bar{\nabla}_j(\mathbb{L}X)^{ij} = \bar{\nabla}^2 X^i + \tfrac{1}{3}\bar{\nabla}^i(\bar{\nabla}_j X^j) + \bar{R}^i_j X^j \,. \tag{2.42}$$

In general, one will not know if a given symmetric tracefree tensor $\bar{M}^{ij}$ is transverse. Its transverse-traceless part $\bar{Q}^{ij}$ must be obtained via

$$\bar{Q}^{ij} \equiv \bar{M}^{ij} - (\bar{\mathbb{L}}Y)^{ij} \,. \tag{2.43}$$

Since $\bar{Q}^{ij}$ is transverse, one also finds

$$\bar{\nabla}_j \bar{Q}^{ij} = 0 = \bar{\nabla}_j \bar{M}^{ij} - \bar{\nabla}_j(\bar{\mathbb{L}}X)^{ij} \,. \tag{2.44}$$

Defining $V^i \equiv X^i - Y^i$ and exploiting the linearity of $\bar{\mathbb{L}}$, (2.39) can be written as

$$\bar{A}^{ij} = (\bar{\mathbb{L}}V)^{ij} + \bar{M}^{ij} \,. \tag{2.45}$$

In the same way using the linearity of $\bar{\Delta}_{\mathbb{L}}$, (2.41) can be rewritten as

$$\bar{\Delta}_{\mathbb{L}} V^i = \tfrac{2}{3}\Psi^6\bar{\nabla}^i K - \bar{\nabla}_j \bar{M}^{ij} + 8\pi\Psi^{10}S^i. \tag{2.46}$$

Using (2.45) and (2.46) it is possible to solve directly for V^i. Including the Hamiltonian constraint, the full decomposition reads

$$\gamma_{ij} = \Psi^4\bar{\gamma}_{ij} \,, \tag{2.47}$$

$$K^{ij} = \Psi^{-10}\bar{A}^{ij} + \tfrac{1}{3}\Psi^{-4}\bar{\gamma}^{ij}K \,, \tag{2.48}$$

$$\bar{A}^{ij} = (\bar{\mathbb{L}}V)^{ij} + \bar{M}^{ij} \,, \tag{2.49}$$

$$\bar{\Delta}_{\mathbb{L}} V^i - \tfrac{2}{3}\Psi^6\bar{\nabla}^i K = -\bar{\nabla}_j \bar{M}^{ij} + 8\pi\Psi^{10}S^i \,, \tag{2.50}$$

$$\bar{\nabla}^2\Psi - \tfrac{1}{8}\Psi\bar{R} - \tfrac{1}{12}\Psi^5 K^2 + \tfrac{1}{8}\Psi^{-7}\bar{A}_{ij}\bar{A}^{ij} = -2\pi\Psi^5\rho_{\mathrm{ADM}} \,, \tag{2.51}$$

where one is free to specify a symmetric tensor $\bar{\gamma}_{ij}$ as the conformal 3-metric, a symmetric tracefree tensor $\bar{M}^{ij}$ and a scalar K. With appropriate boundary conditions and given matter energy ρ_{ADM} and momentum densities S^i, the coupled set of constraint equations are solved for Ψ and V^i, from which the physical initial data γ_{ij} and K^{ij} are easily constructed.

In the particularly simple case of conformally-flat time-symmetric initial data, where $\bar{\gamma}_{ij} = \eta_{ij}$ and $K^{ij} = 0$, (2.47 – 2.51) reduce to a single equation for the Hamiltonian constraint:

$$\bar{\nabla}^2\Psi = -2\pi\Psi^5\rho_{\mathrm{ADM}} \,. \tag{2.52}$$

2.5 General-Relativistic Hydrodynamics

In this section I describe the general-relativistic equations governing the dynamics of a single compressible fluid. The fluid is considered on a macroscopic scale as the set of many discrete fluid volumes, each being much smaller than the total size of the system, but at the same time larger than the collision mean free path of the physical fluid particles. I neglect fluid bulk and shear viscosities, microscopic heat transfer and magnetic fields, hence am only considering a single perfect fluid with zero magnetic field strength. The Newtonian dynamics of such a perfect fluid is governed by the Euler equations (see, e.g., [149]), a non-linear system of hyperbolic equations[10] derived from the Newtonian conservation laws of particle, momentum and energy conservation. By their very nature the Euler equations allow for discontinuities of arbitrary magnitude (that generically develop even from smooth initial data) in their solution and special care must be taken in their numerical treatment.

In the discussion of the general-relativistic Euler equations, I focus on the flux-conservative formalism (also referred to as the *Valencia formulation*) in the ADM {3+1} split of general relativity which was developed primarily at the Universitat de Valencia by José M. Ibàñez's group [153–156]. The frame of reference is that of an Eulerian observer at rest in a space-like 3-hypersurface Σ_t. For a historical overview on GR hydrodynamics and an introduction to different formulations I refer the interested reader to the extensive review by José A. Font [157] and to the discussions in Font et. al. [158] and Baiotti [123].

As I shall lay out, the flux-conservative formalism takes advantage of the hyperbolic and conservative character of the GR Euler equations and in this way allows for numerical schemes based on the *characteristic* information of the hyperbolic system. Such *high-resolution shock-capturing* (HRSC; also called Godunov-type methods [159]) are widely used in classical fluid dynamics (see, e. g., [152]) and their incorporation into general-relativistic hydrodynamics provides superior resolution of physical discontinuities (i.e. shocks) in the fluid flow than possible with the artificial-viscosity (AV) schemes traditionally used [158]. The Valencia formulation has been implemented in a number of modern general-relativistic codes, (among others) including MAHC/GRASTRO [146, 158], COCONUT [160–162], WHISKY [123, 163], and M. Shibata's code [164].

I begin with the definition of a few key quantities. The baryonic rest-mass density is given by

$$\rho = m_u n_B \ , \tag{2.53}$$

where m_u is the atomic mass unit (see Appendix A) and n_B is the baryonic particle number density. ϵ is the energy per unit mass, the specific internal energy of the fluid, including baryonic, leptonic and photonic contributions. The relativistic specific enthalpy is defined by

$$h = 1 + \epsilon + \frac{p}{\rho} \ , \tag{2.54}$$

where p is the fluid pressure (again including baryonic, leptonic and photonic contributions) as given by the general equation of state (EOS)

$$p = p(\rho, \epsilon, \{X_i\}) \ . \tag{2.55}$$

Here $\{X_i\}$ represents a set of mass fractions / compositional variables. I point out that the chosen set of independent variables for the EOS is not unique and that most realistic finite-temperature nuclear equations of state (see the discussion in §3.5.5 and §3.6.2) are given in terms of the fluid temperature rather than on its internal energy.

For completeness, I recall the definition (§2.4.2, equation 2.22) of the contravariant 3-velocity as seen by an Eulerian observer at rest in the spacelike hypersurface Σ_t:

$$v^i = \frac{u^i}{W} + \frac{\beta^i}{\alpha} \ , \tag{2.56}$$

[10] For an introduction to hyperbolic systems of conservation laws, I refer the reader to LeFloch [150], Toro [151] and LeVeque [152].

where u^i are the spatial components of the 4-velocity u^μ, α is the lapse function, β^i the shift vector and $W = \alpha u^0 = 1/\sqrt{1-\gamma_{ij}v^iv^j}$ is the Lorentz factor. Note that in the fluid rest frame $u^0 = 1$ and $u^i = 0$, and generally $u^\mu u_\mu = -1$.

The GR hydrodynamic equations in the standard covariant form under the assumption of an arbitrary coordinate basis $\{\mathbf{e}_{(0)}, \mathbf{e}_{(i)}\}$ and spacelike signature $(-1,1,1,1)$ consist of the local conservation laws of the stress-energy tensor, $T^{\mu\nu}$, and the matter-current density, J^μ:

$$J^\mu{}_{;\mu} = 0 \,, \tag{2.57}$$

$$T^{\mu\nu}{}_{;\mu} = 0 \,, \tag{2.58}$$

where $J^\mu = \rho u^\mu$ and $_{;\mu} = \nabla_\mu$ represents the standard covariant derivative with respect to the 4-metric $g_{\mu\nu}$. The perfect-fluid stress-energy tensor is given by

$$T^{\mu\nu} = \rho h u^\mu u^\nu + p g^{\mu\nu} \,. \tag{2.59}$$

In the following, I make use of the covariant divergence formula [115],

$$\nabla_\alpha a^\alpha = a^\alpha{}_{;\alpha} = \frac{1}{\sqrt{-g}}\left(\sqrt{-g}a^\alpha\right)_{,\alpha} \,, \tag{2.60}$$

where a^α is a contravariant vector, ∇_α is the covariant derivative with respect to the 4-metric $g_{\mu\nu}$ and $\sqrt{-g} = \alpha\sqrt{\gamma}$, while $g = \det(g_{\mu\nu})$ and $\gamma = \det(\gamma_{ik})$. The semicolon is used to denote covariant derivatives in short notation. I now rewrite equations (2.57) and (2.58) as

$$\frac{1}{\sqrt{-g}}\left(\sqrt{-g}\,J^\mu\right)_{,\mu} = 0 \,, \tag{2.61}$$

$$\frac{1}{\sqrt{-g}}\left(\sqrt{-g}\,T^{\mu\nu}\right)_{,\mu} = -\Gamma^\nu_{\mu\lambda}\,T^{\mu\lambda} \,. \tag{2.62}$$

To recast equations (2.61) and (2.62) in flux-conservative form, I follow Banyuls et al. [156] and the extensive discussion in Baiotti [123] and define a set of *conserved* variables in terms of the classical (now: *primitive*) variables ρ, ϵ, and v^i:

$$D = J^\mu n_\mu = \alpha\rho u^0 = \rho W \,, \qquad \text{(baryonic rest-mass density)}, \tag{2.63}$$

$$S^i = \perp^i_\nu T^{\mu\nu} n_\mu = \rho h W^2 v^i \,, \qquad \text{(momentum density)}, \tag{2.64}$$

$$\tau = T^{\mu\nu} n_\mu n_\nu - J^\mu n_\mu = \rho h W^2 - P - D \,, \qquad \text{(total energy density – rest-mass density)}, \tag{2.65}$$

where I have made use of the time-like unit-normal vector n^μ and the projection operator $\perp^\mu_\nu$ onto the spatial 3-hypersurfaces of {3+1} defined in §2.4. The equations of GR hydrodynamics can now be written as a first-order hyperbolic system of conservation laws:

$$\frac{1}{\sqrt{-g}}\left(\left(\sqrt{\gamma}\,\mathbf{U}\right)_{,0} + \left(\sqrt{\gamma}\,\mathbf{F^i}\right)_{,i}\right) = \mathbf{s} \,, \tag{2.66}$$

with the state vector

$$\mathbf{U} = (D, S_i, \tau)^T \,, \tag{2.67}$$

the flux vector

$$\mathbf{F}^i = \begin{pmatrix} (\alpha v^i - \beta^i)\, D \\ (\alpha v^i - \beta^i)\, S_j + \alpha p \delta^i_j \\ (\alpha v^i - \beta^i)\, \tau + \alpha p v^i \end{pmatrix} \,, \tag{2.68}$$

and the source vector

$$\mathbf{s} = \begin{pmatrix} 0 \\ T^{\mu\nu}(g_{\nu j,\mu} + \Gamma^\delta_{\mu\nu} g_{\delta j}) \\ \alpha(T^{\mu 0}\frac{1}{\alpha}\,\alpha_{,\mu} - T^{\mu\nu}\Gamma^0_{\mu\nu}) \end{pmatrix} \,. \tag{2.69}$$

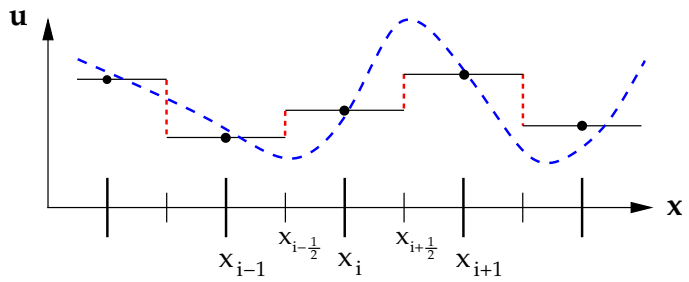

Figure 2.3: Finite-volume approximation to the continuous function $u(x)$ at cell centers x_i via cell averages u_i. Note that $u(x_i)$ is not necessary equal to u_i. The numerical data are piecewise constant and discontinuous at cell interfaces $i+\frac{1}{2}$ and $i-\frac{1}{2}$. This sketch was inspired by a similar figure in [157].

The explicit form of $\mathbf{s}$ in Cartesian {3+1} coordinates is given in the discussion of the WHISKY code in §3.5.4. Note that while the state vector $\mathbf{U}$ of the conserved variables is updated in time, the knowledge of the primitive variables (ρ, ϵ, v^i) is required for the calculation of the flux term $\mathbf{F}^i$ and for the computation of the characteristic fields and speeds discussed below. Hence, it is necessary to *recover* the primitive variables (ρ,ϵ,v^i) from the conserved ones after each time integration step. These variables cannot be obtained in closed functional form and must be recovered through a root-finding procedure as discussed in §3.5.3.

Equations (2.66) form a system of hyperbolic *balance* laws [152] that reduce to conservation laws if $\mathbf{s} = 0$ (i.e., in Cartesian special relativity!). For this reason, equations (2.66) are said to be flux-conservative. Since the right-hand side source vector $\mathbf{s}$ does not contain derivatives of the conserved variables in $\mathbf{U}$, it is generally numerically stable to first solve the homogeneous equations and apply the source term operator-split [152] or through the Method of Lines (MoL), as discussed in §3.2.

It is now straightforward to apply standard HRSC techniques that rely on hyperbolic and conservative properties to the homogeneous hyperbolic system.

2.5.1 HRSC Methods, the Riemann Problem, and the Characteristic Structure of the GR Hydrodynamic Equations

As mentioned in the introduction to this section, the non-linear hyperbolic character of the (Newtonian/GR) Euler equations may lead to so-called *weak solutions* containing discontinuities even for smooth initial data. An example at hand for this is the stellar collapse scenario in which the evolution of initially smooth density, velocity and internal energy distributions[11] leads to the formation of the supernova shock wave at core bounce.

However, in a numerical approximation based on finite volumes, smooth physical data are represented as discrete data that are interpreted as piecewise constant on the computational grid and that exhibit jumps of finite size at computational-cell interfaces in any non-trivial case. Figure 2.3 depicts a one-dimensional example for a finite-difference based approximation to a smooth solution $u(x)$. In each grid cell i the solution $u(x)$ is approximated at the cell center by the cell average u_i. This discretization leads to an approximation to the physical solution $u(x)$ with piecewise-constant data and finite discontinuous steps at cell interfaces which I denote by $i+\frac{1}{2}$ and $i-\frac{1}{2}$. In his seminal work from 1959 [159], Godunov realized that each individual cell-interface discontinuity may be viewed as a local Riemann problem whose solution is well known (see, e.g., [152, 165]). The series of the solutions to interface-local Riemann problems then constitutes a global solution of the conservation equations for the locally discrete initial data.

[11] Note, however, that the chemical abundances in an evolved stellar core exhibit an onion-shell structure with rather strong discontinuities (see § 3.7.3).

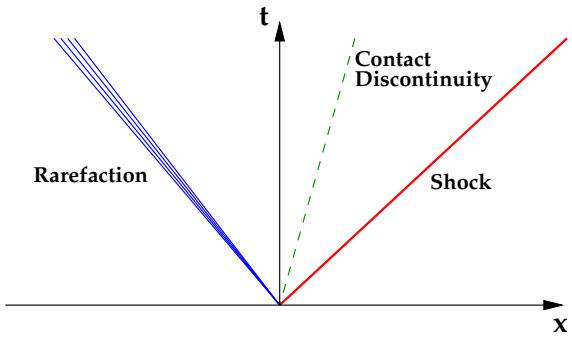

Figure 2.4: Schematic view of the possible waves resulting from a Riemann problem of the Euler equations at $t = 0, x = 0$.

The Riemann problem for the Euler equations (and, more general, for any hyperbolic system) is an initial-value problem with initial conditions (in one spatial dimension)

$$\mathbf{U}(x, t = 0) \begin{cases} \mathbf{U}_L \text{ if } x < a \ , \\ \mathbf{U}_R \text{ if } x > a \ , \end{cases} \tag{2.70}$$

where $\mathbf{U}_L$ and $\mathbf{U}_R$ are constant state vectors representing left (L) and right (R) states with respect to an interface at point a, respectively. The exact solution to the above Riemann problem in ideal hydrodynamics is typically formulated in terms of three elementary waves: a forward propagating non-linear shock wave, a contact discontinuity, and a non-linear backward propagating rarefaction wave. In the shock wave all state variables are discontinuous, in the rarefaction wave all variables are continuous, but change with time in self-similar fashion and the contact discontinuity carries a jump in density, while the other variables are continuous. Figure 2.4 depicts a schematic view of the three waves.

The three waves correspond to the *characteristic fields*, the eigenvectors of the three 5 x 5 Jacobi matrices of the GR Euler equations (2.66)

$$\mathbf{B}^i = \frac{\partial(\sqrt{\gamma}\mathbf{F}^i)}{\partial(\sqrt{\gamma}\mathbf{U})} = \frac{\partial(\mathbf{F}^i)}{\partial(\mathbf{U})} \ , \tag{2.71}$$

where the index i stands for the spatial direction considered. Each of the three Jacobi matrices $\mathbf{B}^i$ has 5 eigenvalues of which three are unique [156]:

$$\lambda^i_0 = \alpha v^i - \beta^i \quad \text{(3-fold degenerate)} \ , \tag{2.72}$$

$$\lambda^i{}_{\pm} = \frac{\alpha}{1 - v^2 {c_s}^2} \left\{ v^i(1 - {c_s}^2) \pm \sqrt{{c_s}^2(1 - v^2)\left[\gamma^{ii}(1 - v^2 {c_s}^2) - v^i v^i (1 - {c_s}^2)\right]} \right\} - \beta^i \ , \tag{2.73}$$

where c_s is the local speed of sound.

The physical information of the system is carried by the three characteristic waves (*characteristics*) at their *characteristic speeds*, corresponding to the three unique eigenvalues of the Jacobi matrices. In fact, in the case of an exact Riemann solver, only the knowledge of the characteristic speeds and the initial left and right states is required to solve for the new left and right states $\mathbf{U}^*{}_L$ and $\mathbf{U}^*{}_R$ (see, e.g., [151, 152, 159, 165]). However, in practice and in particular in multi-dimensional approaches, the exact solution of the Riemann problem becomes too computationally demanding. One resorts to approximate Riemann solvers, some of which make use of the characteristic fields in addition to the characteristic speeds and are highly competitive when compared with exact solvers. At this point, I postpone the discussion of numerical Riemann solvers to §3.5.2 and give the analytical expressions for the eigenvectors of the Jacobi matrices (2.71) in appendix C.

Godunov's original scheme uses piecewise-constant physical states as initial data for the Riemann problems at cell interfaces and hence is only first-order accurate in space. More modern HRSC schemes use interpolation procedures to *reconstruct* a higher-order approximation to the physical data at cell interfaces. Special care must be taken to ensure monotonicity and to avoid spurious oscillations introduced by the reconstruction method. I shall discuss details of this in §3.5.1.

2.5.2 Special Relativistic and Newtonian Limits

In special relativity where gravity cannot be included consistently, the general metric $g_{\mu\nu}$ reduces to the Minkowski case $g_{\mu\nu} = \eta_{\mu\nu} = \mathrm{diag}(-1, 1, 1, 1)$ and the source vector $\mathbf{s}$ in (2.66) vanishes in Cartesian coordinates, while the state vector $\mathbf{U}$ remains unaltered. For an extensive review of numerical methods for special relativistic hydrodynamics I refer the interested reader to Martí and Müller [165].

I take the Newtonian limit (Newtonian gravity, $v \ll 1$) of the GR state vector (2.67) by expanding the Lorentz factor W to first order in v^2:

$$W = 1 + \frac{1}{2}v^2 + \mathcal{O}(v^4) \ . \tag{2.74}$$

Following Landau & Lifshitz [166],

$$D = \rho W \overset{\text{Newt.}}{\longrightarrow} \rho \ , \tag{2.75}$$

since $\rho \gg \frac{1}{2}\rho v^2$. Analogously,

$$S^i = \rho h W^2 v^i = \rho(1 + \epsilon + \frac{p}{\rho})W^2 v^i \overset{\text{Newt.}}{\longrightarrow} \rho v^i \ , \tag{2.76}$$

and

$$\tau = \rho h W^2 - p - D \overset{\text{Newt.}}{\longrightarrow} \rho\epsilon + \frac{1}{2}\rho v^2 \tag{2.77}$$

with the safe assumption [166] in the non-relativistic limit, $\frac{1}{2}\rho v^2 \gg v^2(\rho\epsilon + p)$. Note that the energy equation (2.77) requires expansion to second order in v^2 to capture the Newtonian limit.

The Newtonian Euler equations in a Cartesian Eulerian frame now read:

$$\rho_{,t} + (\rho v^i)_{,i} = 0 \tag{2.78}$$

$$(\rho v^i)_{,t} + (\rho v_j v^i + p\delta^i_j)_{,i} = \rho g_j \tag{2.79}$$

$$\left(\rho\epsilon + \frac{1}{2}\rho v^2\right)_{,t} + \left([\rho\epsilon + \frac{1}{2}v^2 + p]v^i\right)_{,i} = \rho g_i v^i \ , \tag{2.80}$$

where $g_i = -\phi_{,i}$ is the Newtonian gravitational force and ϕ is the Newtonian gravitational potential.

2.6 Gravitational Waves

Gravitational waves are propagating vibratory disturbances, *ripples* in spacetime. They are a consequence of causality in general relativity: physical information cannot travel faster than by the speed of light, hence, any change in the curvature near a gravitating object must be communicated to distant observers no faster than the speed of light. This leads immediately to the idea that there must exist some notion of "gravitational radiation". In the non-linear strong-field regime near a compact source, it is extremely difficult to analyze the emission and propagation of gravitational waves (see, e.g. [116]). However, far away from the strongly gravitating source (in a *weak-field* region), GR can be linearized and Einstein's equations become a set of linear wave equations [5–7].

In the following, I will review linearized GR, linear wave solutions and gravitational wave generation in the weak-field, slow-motion limit by essentially-Newtonian matter sources. In addition, I will briefly touch on the detection of gravitational waves. For much more detailed discussions, I refer the reader to the standard text book by Misner, Thorne & Wheeler [116], to the recent review article by Flanagan and Hughes [167] and to the numerous scientific and semi-popular articles by Thorne (e.g., [168, 169]).

The discussion below is based on the lecture notes of Iring Bender's course on GR at the Ruprecht-Karls-Unversität Heidelberg which I attended as an undergraduate. A similar text appeared in my Diploma thesis [170]. In addition, I have used Schutz's book [115] and Flanagan and Hughes' review article [167]. In this section I work in standard cgs units, carrying along all factors of c and G for direct applicability of the expressions to astrophysical problems.

2.6.1 Linearized Theory

In regions of spacetime where curvature is small, $g_{\mu\nu}$ may be treated as deviating only slightly from the flat Minkowski metric $\eta_{\mu\nu} = \mathrm{diag}(-1, 1, 1, 1)$:

$$g_{\mu\nu} = \eta_{\mu\nu} + h_{\mu\nu} \ , \qquad ||h_{\mu\nu}|| \ll 1 \ . \tag{2.81}$$

Here, $h_{\mu\nu}$ is the metric perturbation. Note that the condition $||h_{\mu\nu}|| \ll 1$ requires both the gravitational field to be weak and the coordinate system to be approximately Cartesian. In linearized theory one only keeps terms linear in $h_{\mu\nu}$, hence indices are raised and lowered by the flat metric $\eta_{\mu\nu}$. $h_{\mu\nu}$ does not transform as a tensor under general coordinate transformations, but does so under Lorentz transformations.

In order to find the Einstein equations in the linear limit, one first rewrites the Riemann curvature tensor (2.10), using $h_{\mu\nu}$ ($\eta_{\mu\nu}$ drops out due to its additive-constant nature) and dropping all non-linear terms:

$$R_{\mu\nu\alpha\beta} = \frac{1}{2}(h_{\mu\beta,\nu\alpha} + h_{\mu\alpha,\nu\beta} - h_{\mu\alpha,\nu\beta} - h_{\nu\beta,\mu\alpha}) \ . \tag{2.82}$$

One defines $h \equiv h^{\alpha}_{\ \alpha}$ and the *trace reverse* tensor of $h_{\mu\nu}$:

$$\overline{h}^{\mu\nu} = h^{\mu\nu} - \frac{1}{2}\eta^{\mu\nu}h \ , \tag{2.83}$$

for which $\overline{h}^{\alpha}_{\ \alpha} = -h$ holds. In addition, one assumes the Lorentz gauge (analogously to electromagnetic theory) to exploit the remaining gauge freedom (see, e.g., [116, 167])

$$\overline{h}^{\mu\nu}_{\ \ ,\nu} = 0 \ . \tag{2.84}$$

Contracting the linearized Riemann tensor and inserting it into equations (2.9) and applying (2.83) and (2.84) then yields the *linearized Einstein equations*

$$G_{\mu\nu} = \Box\overline{h}^{\mu\nu} = -\frac{16\pi G}{c^4}T^{\mu\nu} \ , \tag{2.85}$$

where

$$\Box := \frac{\partial}{\partial x_\sigma}\frac{\partial}{\partial x^\sigma} \tag{2.86}$$

is the d'Alembert operator.

2.6.2 Wave Solutions - Vacuum

The linearized field equations are wave equations much like those known from electromagnetic theory. In the homogeneous case ($T_{\mu\nu} = 0$) (2.85), reduces to

$$\Box \overline{h}^{\mu\nu} = 0 \tag{2.87}$$

and has the well-known plane wave solutions

$$\overline{h}^{\mu\nu} = A^{\mu\nu} \exp(ik_\lambda x^\lambda) \ . \tag{2.88}$$

Inserting these solutions into (2.87) yields $k_\lambda k^\lambda = 0$ which means that gravitational waves travel along null geodesics, i.e. at the speed of light. Due to the symmetry of $h^{\mu\nu}$, the polarization tensor $A^{\mu\nu}$ initially has ten independent components. Enforcing Lorentz gauge and the choice of a special generator for the gauge transformation (ξ^μ, see, e.g. [167]) with $\Box \xi^\mu = 0$ reduces the wave fields to two independent physical degrees of freedom, identified as polarizations:

$$A^{\mu\nu} k_\lambda = 0, \qquad A^\lambda_\lambda = 0, \qquad \text{and} \qquad A_{\mu\lambda} U^\lambda = 0 \tag{2.89}$$

with an arbitrary, light-like ($U_\nu U^\nu = 0$) unit 4-vector U^μ. This choice of gauge is called *transverse-traceless*. I will use it in the following and denote it by superscript TT. From the above gauge conditions follows:

$$h^{TT}_{\mu 0} = 0, \qquad h^{TT}_{ij,j} = 0, \qquad \text{and} \qquad h^{TT}_{jj} = 0, \tag{2.90}$$

where latin characters indicate spatial indices. One directly sees that $\overline{h}^{TT}_{\mu\nu} = h^{TT}_{\mu\nu}$. Furthermore, all non-spatial components of $h^{TT}_{\mu\nu}$ are zero. Hence, I will use h^{TT}_{ij} in the following.

2.6.3 Polarization of Gravitational Waves

The dimensionless gravitational wave field tensor h^{TT}_{jk} of a gravitational wave propagating in the positive z-direction can be written as a linear combination of two independent, transverse-traceless unit tensors that correspond to the two possible polarization modes of gravitational waves:

$$\begin{aligned} h^{TT}_{jk} = h_+ \boldsymbol{e}_+ + h_\times \boldsymbol{e}_\times \text{ with } \boldsymbol{e}_+ &= (\vec{e}_x \otimes \vec{e}_x - \vec{e}_y \otimes \vec{e}_y) \ , \\ \boldsymbol{e}_\times &= (\vec{e}_x \otimes \vec{e}_y + \vec{e}_y \otimes \vec{e}_x) \ , \end{aligned} \tag{2.91}$$

where $\vec{e}_x$ and $\vec{e}_y$ are Cartesian unit vectors and $\otimes$ is the outer product. For a given h^{TT}_{jk}, the two scalar dimensionless gravitational wave amplitudes or *strains*, h_+ ("plus") and $h_\times$ ("cross"), are obtained by evaluating the scalar product of h^{TT}_{jk} with the appropriate unit tensor.

Gravitational waves act tidally, stretching and squeezing space and thus any object that they pass through. Figure 2.5 shows the two polarizations of a gravitational wave and the lines of force associated with them.

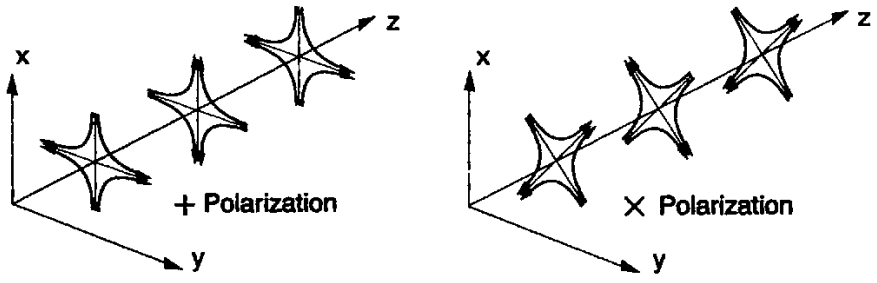

Figure 2.5: The lines of force associated with the two polarizations of a gravitational wave. Figure taken from [169].

2.6.4 Generation of Gravitational Radiation in the Weak-Field Slow-Motion Limit

Quadrupole Nature of Gravitational Radiation

Before I discuss wave solutions to the inhomogeneous linearized Einstein equations (2.85), let me first consider a basic fact about gravitational radiation: Its quadrupole nature. For my quite intuitive discussion I follow the text of Misner, Thorne and Wheeler [116]. Note that the arguments presented below must be regarded with due caution. They rely on global conservation of linear and angular momentum, both of which are not generally guaranteed in non-linear GR [116]. The arguments do, however, apply in the here considered weak-field limit.

The simplest and strongest radiating configuration in electromagnetic theory is an electric dipole with a dipole moment that experiences acceleration. Its luminosity is given by

$$L_{\text{el.dipole}} = \frac{2}{3}\frac{d^2}{dt^2}\vec{d}^{\,2} \,, \tag{2.92}$$

where $\vec{d}$ is the dipole moment. Thus, electromagnetic radiation is of leading order dipole radiation.

The gravitational analog of the electric dipole moment is the mass-dipole moment

$$\vec{d} = \sum_{\text{particles } i} m_i \vec{x}_i \,. \tag{2.93}$$

Its first time derivative

$$\frac{d}{dt}\vec{d} = \sum_{\text{particles } i} m_i \frac{d}{dt}\vec{x}_i = \vec{P} \,, \tag{2.94}$$

is just the total momentum of the system. The second time derivative of the mass dipole moment must vanish because of momentum conservation: $\frac{d^2}{dt^2}\vec{d} = \frac{d}{dt}\vec{P} = 0$.

In electromagnetic theory the next strongest types of radiation are magnetic-dipole and electric-quadrupole. Magnetic-dipole radiation is proportional to the second time derivative of the magnetic moment, $\vec{\mu}$. The gravitational analog, the mass-current dipole moment, is defined as

$$\vec{\mu} = \sum_i (\text{position of mass } i) \times (\text{current due to mass } i) = \sum_i \vec{x}_i \times (m_i \vec{v}_i) = \vec{J} \,. \tag{2.95}$$

This is the total angular momentum, a constant of motion of an isolated system. Its time derivative is zero. Thus, according to these simplistic arguments, there can be no gravitational dipole radiation of any kind. Gravitational radiation of leading order must be (at least) quadrupole radiation.

Solution to the Inhomogeneous Wave Equation - Quadrupole Radiation

The time-retarded solution of the inhomogeneous wave equation (2.85) is found analogously to electromagnetic theory via the convolution of the inhomogeneity in equation (2.85) with a time-retarded Green function which yields

$$h_{jk}^{TT}(t,\vec{x}) = \left[\frac{4\,G}{c^4}\int \frac{T_{ik}(t-\frac{|\vec{x}-\vec{x}'|}{c},\vec{x}')}{|\vec{x}-\vec{x}'|}d^3x'\right]^{TT} \,. \tag{2.96}$$

I now consider a finite source stress-energy tensor T_{ik} whose center is located at the origin of the coordinate system. $|\vec{x}|$ is the distance from the observer to the source. The source shall conform to the weak-field limit ($\frac{G}{c^2}\frac{M}{R} \ll 1$, R be the extent of the source) and to the slow-motion approximation ($|\vec{v}| \ll c$). In these limits, an expansion in powers of $\vec{x}'/|\vec{x}|$ yields in lowest order the so-called *quadrupole formula*

$$h_{jk}^{TT}(t,\vec{x}) = \left[\frac{2}{c^4}\frac{G}{|\vec{x}|}\ddot{I}_{jk}(t-\frac{|\vec{x}|}{c})\right]^{TT} \,, \tag{2.97}$$

with $\ddot{I}_{jk}$ being the second time derivative of the mass quadrupole moment

$$I_{jk} := \int \rho\, x_j x_k\, d^3x \,. \tag{2.98}$$

To make the right hand side of equation (2.97) match the gauge conditions of the transverse-traceless gauge, I define the *reduced mass quadrupole moment*

$$I_{jk} \equiv I_{jk} - \frac{1}{3}\,\delta_{jk} I^{l}{}_{l} \tag{2.99}$$

and the projector

$$P_{jklm} \equiv P_{jl}P_{km} - \frac{1}{2}P_{jk}P_{lm} \text{ with } P_{ij} \equiv \delta_{ij} - \frac{x_i\,x_j}{|\vec{x}|^2}\ . \tag{2.100}$$

Finally, I can write out what is called the *standard quadrupole formula* (SQF):

$$h^{TT}_{jk}(t,\vec{x}) = \frac{2}{c^4}\frac{G}{|\vec{x}|}P_{jklm}\,\ddot{I}_{lm}(t-\frac{|\vec{x}|}{c})\ . \tag{2.101}$$

Higher-order radiation is strongly suppressed by powers of 1/c (see, e.g., [116, 171]) and shall not be considered here. Importantly, note the source-independent $1/|\vec{x}|$ fall-off behavior of the quadrupole wave strain. The quadrupole part of the total energy radiated in gravitational waves is given by [116]

$$E_{\rm GW} = \frac{1}{5}\frac{G}{c^5}\int_{-\infty}^{\infty} \dddot{I}_{ij}\,\dddot{I}_{ij}dt\ . \tag{2.102}$$

The definition of the reduced mass quadrupole moment reveals that spherically symmetric configurations cannot emit gravitational radiation: their mass quadrupole moment is a scalar multiplied with the unit tensor. Hence, I_{ij} will be zero, and, if spherical symmetry is maintained, will remain so. According to Birkhoff's theorem [172], this fact is independent of the quadrupole approximation: "A spherically symmetric gravitational field is always static exterior to the stress-energy distribution causing it and given by the external Schwarzschild solution."

There are a number of issues associate with the SQF (2.101) and its use:

1. The SQF describes the gravitational wave generation by an essentially Newtonian, slowly moving object as seen by an asymptotic (= far away) observer. SQF waves live in the *distant wave zone*, that is, they are fully formed and linear. From electrodynamic theory one knows that electromagnetic waves that are still very close to their source do not yet have their asymptotic wave shape. The same is true for gravitational waves – with the complication that not only their shape is not linear-wave like, but that they non-linearly interact with the strong curvature near their source, because GR, in contrast to electrodynamics, is a non-linear theory.

2. Using the SQF to extract gravitational wave information from a general relativistic simulation must be done with great care; the result must be regarded as questionable. It relies on coordinate quantities that are not covariant/gauge invariant. A change of coordinates (different choice of lapse and/or shift vector) will affect the results and there is no unique definition for the mass quadrupole tensor in fully non-linear general relativity. However, for pulsating neutron star models, Balbinski et al. [173] have shown that the Newtonian quadrupole approximation yields good results for neutron stars with moderate compactness ($(GM)/(c^2R) \lesssim 0.04$). Recently, Shibata and Sekiguchi [174] have compared their implementation of the SQF to the gauge-invariant Zerilli-Moncrief method (see [175–177] and below discussion) for extracting gravitational waves from oscillating neutron stars. Interestingly, they found very good qualitative agreement between the two methods. In addition, they found very good agreement of the wave phase and amplitude modulation while the SQF appeared to underestimate the magnitude of the wave amplitude consistently by $\sim$20%.

3. The SQF contains second time derivatives of the mass quadrupole tensor components. Second time derivatives are numerically cumbersome. Finn & Evans [178] and, independently, Blanchet and collaborators [171] have derived quadrupole radiation formulae in which one or even both time derivatives are eliminated by means of the (Newtonian) Euler equations.

Despite these issues and problems, I resort to a variant of the SQF for extracting gravitational waves from the matter motions in my general relativistic simulations[12]. The reasons for this will be explained in the following.

[12]Note that I use an SQF-like prescription also in the Newtonian simulations described in § 7 for which there is clearly no argument about SQF's applicability

2.6.5 Gravitational Waves from not-so Weak-Field not-so Slow-Motion Sources and Gravitational Wave Extraction in Numerical Relativity

In situations where the weak-field slow-motion approximation breaks down, one possibility is to use post-Newtonian extensions to the quadrupole formalism [168, 171]. This approach however fails ultimately for spacetimes in which the gravitational wave emission is dominated not by matter stresses, but by the non-linear dynamics of curvature itself. This is for example the case in the collapse of a supermassive neutron star to a black hole or in the plunge and merger phases of a binary-black hole (or neutron star) coalescence event[13].

In simulations numerically evolving the full {3+1} Einstein equations, the gravitational wave information is present in the curvature variables. Instead of trying to estimate the gravitational wave emission from matter stresses (or via point-mass assumptions) based on approximate formulae, it is more natural and – in principle – much more accurate to *extract the gravitational waves directly from the spacetime*[14]. Ideally, such a treatment would also be gauge invariant. Over the past decades, a number of approaches have been proposed in the literature [175–177, 180–187]. In the following, I will outline only three of them. For more details I refer the reader to the extensive review in F. Herrmann's dissertation [122].

Radiation Gauge Approach

The most straightforward way of extracting gravitational wave content from a numerical spacetime is to choose a special coordinate system which allows one to directly "read" the waves off the metric. This is only possible far away from the source where the waves have their asymptotic shape (i.e., in the *wave zone*) and where the rest-mass density is practically zero. This method is *not* gauge invariant and is realized by choosing the minimal-distortion shift condition by Smarr and York [132, 188] which leads to a conformal 3-metric $\tilde{\gamma}_{ij} = \gamma^{\frac{1}{3}}\gamma_{ij}$ that is approximately transverse and traceless (TT) in the wave zone [132]. The disadvantages of this method include the computational expensiveness of the elliptic minimal-distortion shift condition and the gauge and boundary-condition dependence of the extracted waves. The former problem could be alleviated by using an approximate hyperbolic version of minimal distortion (see the discussion in section 3.3). This would, however, spoil the approximation to TT and make the extracted waveforms even more unreliable.

Newman-Penrose Formalism

The *Weyl* tensor (see, e.g., [189]) is defined by

$$C_{\alpha\beta\gamma\delta} = R_{\alpha\beta\gamma\delta} - \frac{1}{2}(g_{\alpha[\gamma}R_{\delta]\beta} - g_{\beta[\gamma}R_{\delta]\alpha}) + \frac{1}{3}R\, g_{\alpha[\gamma}g_{\delta]\beta} \,, \tag{2.103}$$

where $[\,]$ denotes anti-symmetrization in the bracketed indices. The Weyl tensor is the traceless component of the Riemann curvature tensor. It obeys the same symmetries as the former, but all its contractions vanish. Importantly, $C_{\alpha\beta\gamma\delta} = R_{\alpha\beta\gamma\delta}$ in vacuum. The Weyl tensor can furthermore be interpreted as that part of curvature which is not determined locally by the matter distribution, or, in other words, it represents the curvature at a point that may depend on the matter distribution at other points or on gravitational radiation independent of matter sources [189]. Newman and Penrose exploited this feature of the Weyl tensor to analyze the gravitational wave content of spacetimes [186]. They introduced a reformulation of Einstein's equations using a vierbein (tetrad) and complex scalars describing the Weyl tensor. The tetrad frame is composed of a set of null (light-like) vectors $\{\boldsymbol{l}, \boldsymbol{n}, \boldsymbol{m}, \overline{\boldsymbol{m}}\}$ which obey

$$l^\alpha n_\alpha = -m^\alpha \overline{m}_\alpha = -1 \,. \tag{2.104}$$

[13] For large separations, the two black holes / neutron stars can be treated as point masses in post-Newtonian theory. After merger, perturbation theory can be applied to predict the ring-down wave emission of the resultant black hole. See, e.g., [122, 179].

[14] In the following I will gloss over the details and call wave estimation via the above SQF *and* the extraction of wave information from the numerical {3+1} spacetime *wave extraction*.

Using those one can construct the 5 complex *Weyl scalars*, denoted by Ψ_0 through Ψ_4. They contain the same physical information as the 10 real independent components of the Weyl tensor [186, 190] and are particularly useful for gravitational wave studies since one of the five, namely

$$\Psi_4 = -C_{\mu\nu\tau\delta} n^\mu \overline{m}^\nu n^\tau \overline{m}^\delta \tag{2.105}$$

represents outgoing gravitational waves [186] and has the correct asymptotic $1/r$ fall-off behavior if the tetrad is chosen appropriately. A decomposition of Ψ_4 into spherical harmonics yields the usual radiation multipoles (see, e.g., [168, 191]). The Ψ_i are gauge invariant, but depend on the tetrad choice [190]. Only if the chosen tetrad is appropriate (i.e., leads to the correct fall-off behavior of the Ψ_i – the *peeling property* [186]) for the spacetime considered, will the full outgoing gravitational wave content be contained in Ψ_4. Otherwise, it will live in linear combinations of the Ψ_i [122, 186, 192]. Performing an accurate analysis of the emitted gravitational waves will then be nearly impossible. Unfortunately, finding an appropriate tetrad is not easy and testing the peeling property is only possible very far from the source and thus difficult in numerical simulations encompassing a finite volume of spacetime. Nevertheless, there are a number of recent studies of binary black-hole spacetimes [122, 191, 192] that have quite successfully used the Newman-Penrose formalism. However, note that these studies have relied on either a simplified "radial" tetrad [192] or used the Kinnersley tetrad [191, 193] appropriate for Kerr-like rotating black-hole spacetimes.

To my knowledge there is no published result on gravitational waves extracted with this method from matter spacetimes. This is most likely owing to the fact that gravitational waves emitted by matter sources (neutron stars, stellar core collapse etc.) are orders of magnitude smaller in amplitude and total emitted energy (see, e.g., [169]) than those from black holes (binary black hole coalescence, black hole formation in neutron star collapse events etc.). A slightly wrong choice of tetrad and numerical errors associated with the computation of the Weyl scalars easily bury weak signals. In addition, wave extraction has to be performed in the wave zone at coordinate locations of many times the radius of the source. Only there do the waves have their asymptotic shape and the Weyl scalars their asymptotic meaning. Even with mesh refinement this is still very difficult in today's simulations of extended matter sources.

Zerilli-Moncrief Formalism

The Zerilli-Moncrief approach [175, 176], which is based on gauge-invariant perturbation theory of Schwarzschild black holes originally developed by Regge and Wheeler [194], has so far been the most successful approach to radiation extraction in non-vacuum numerical relativity. In the first-order gauge-invariant formulation[15] [176] it was first implemented and applied in 1988 by A. Abrahams [180, 181] and has subsequently been used in a multitude of studies dealing with vacuum spacetimes with wave content (e.g. [122, 177, 192, 195–201]) and recently also in matter spacetimes with particularly strong gravitational wave content such as neutron star collapse to a black hole [202, 203], neutron star oscillations (e.g. [146, 174]), dynamical rotational instabilities of neutron stars (e.g. [204]), and neutron star binary coalescence (e.g. [205–207]). In the following, I will outline the most salient features and formulae of Zerilli-Moncrief extraction as presented in the recent reviews by Nagar & Rezzolla [208] and Herrmann [122].

In the Zerilli-Moncrief formalism the physical metric is split into a spherically symmetric background $g^{\mathbf{s}}_{\mu\nu}$ metric (typically: Schwarzschild) and non-spherical perturbations $h_{\mu\nu}$:

$$g_{\mu\nu} = g^{\mathbf{s}}_{\mu\nu} + h_{\mu\nu} \ , \tag{2.106}$$

where $|h_{\mu\nu}|/|g_{\mu\nu}| \ll 1$. Assuming a background Schwarzschild metric of the form

$$g^{\mathbf{s}}_{\mu\nu} = \begin{bmatrix} -\mathcal{S}(r) & 0 & 0 & 0 \\ 0 & \mathcal{S}(r) & 0 & 0 \\ 0 & 0 & r^2 & 0 \\ 0 & 0 & 0 & r^2 \sin^2\theta \end{bmatrix} \ , \tag{2.107}$$

[15] First-order gauge invariant means that the results do not change under (small and) linear gauge changes (coordinate transformations). First-order gauge invariant quantities are not necessarily invariant under more general gauge changes

where $\mathcal{S}(r) = 1 - \frac{2M}{r}$, the metric perturbation is expanded into odd-parity and even-parity Regge-Wheeler tensor spherical harmonics [194, 208]

$$h_{\mu\nu} = \sum_{\ell,m} \left[\left(h_{\mu\nu}^{(\ell m)} \right)^{(\mathrm{o})} + \left(h_{\mu\nu}^{(\ell m)} \right)^{(\mathrm{e})} \right] , \tag{2.108}$$

where $\ell \geq 0$ and $m = -\ell, ..., \ell$ and (o) and (e) denote odd and even parity, respectively. There are seven even-parity components ($\mathcal{H}_0^{(\ell m)}$, $\mathcal{H}_1^{(\ell m)}$, $h_0^{(\ell m)}$, $\mathcal{H}_2^{(\ell m)}$, $h_1^{(\ell m)}$, $\mathcal{K}^{(\ell m)}$, $\mathcal{G}^{(\ell m)}$) and three odd-parity components ($c_0^{(\ell m)}$, $c_2^{(\ell m)}$, $c_3^{(\ell m)}$). A complete list and the definition of the individual components in terms of metric components in spherical coordinates are given by Allen in [209]. The even-parity perturbations are given by [194]

$$h_{\mu\nu}^{(\mathrm{e})} = \begin{bmatrix} \mathcal{S}\mathcal{H}_0 Y_{\ell m} & \mathcal{H}_1 Y_{\ell m} & h_0 Y_{\ell m,\theta} & h_0 Y_{\ell m,\phi} \\ . & \mathcal{S}^{-1}\mathcal{H}_2 Y_{\ell m} & h_1 Y_{\ell m,\theta} & h_1 Y_{\ell m,\phi} \\ . & . & r^2(K Y_{\ell m} + \mathcal{G} Y_{\ell m,\theta\theta}) & r^2(Y_{\ell m,\theta\phi} - \cot\theta Y_{\ell m,\phi}) \\ . & . & . & r^2(\mathcal{K}\sin^2\theta Y_{\ell m} + \mathcal{G}(Y_{\ell m,\phi\phi} + \sin\theta\cos\theta Y_{\ell m,\theta})) \end{bmatrix} . \tag{2.109}$$

And the odd-parity perturbations read [194]:

$$h_{\mu\nu}^{(\mathrm{o})} = \begin{bmatrix} 0\,0 & -c_0 \frac{1}{\sin\theta} Y_{\ell m,\phi} & c_0 \sin\theta Y_{\ell m,\theta} \\ .\,0 & -c_1 \frac{1}{\sin\theta} Y_{\ell m,\phi} & c_1 \sin\theta Y_{\ell m,\theta} \\ .\,. & c_2 \frac{1}{\sin\theta}(Y_{\ell m,\theta\phi} - \cot\theta Y_{\ell m,\phi}) & c_2 \frac{1}{2}\left(\frac{1}{\sin\theta} Y_{\ell m,\phi\phi} + \cos\theta Y_{\ell m,\theta} - \sin\theta Y_{\ell m,\theta\theta} \right) \\ .\,. & . & c_2(-\sin\theta Y_{\ell m,\theta\phi} + \cos\theta Y_{\ell m,\phi}) \end{bmatrix} . \tag{2.110}$$

Here "." denotes a symmetry entry and the superscripts of the odd-parity and even-parity components have been dropped. Following Moncrief [176], one can now construct from the above two independent and first-order gauge invariant quantities $Q^{\times}$ and Q^{+}, the so-called scalar *wave indicators*. The odd-parity part $Q^{\times} = Q^{\times}(c_1, c_2)$ depends only on odd-parity components and the even-parity part $Q^{+} = Q^{+}(\mathcal{K}, \mathcal{G}, \mathcal{H}_2, h_1)$ depends only on even-parity components:

$$Q^{+} = \sqrt{\frac{2(\ell-1)(\ell+2)}{\ell(\ell+1)}} \frac{4r\mathcal{S}^2 k_2 + \ell(\ell+1) r k_1}{\Lambda} \tag{2.111}$$

$$Q^{\times} = \sqrt{\frac{2(\ell+2)!}{(\ell-2)!}} \left[c_1 + \frac{1}{2}(c_{2,r} - \frac{2}{r} c_{2,r}) \right] \frac{\mathcal{S}}{r} , \tag{2.112}$$

where

$$k_1 = \mathcal{K} + \mathcal{S} r \mathcal{G}_{,r} - 2\frac{\mathcal{S} r}{h_{\ 1}} \tag{2.113}$$

$$k_2 = \frac{\mathcal{H}^2}{2\mathcal{S}} - \frac{1}{2\sqrt{\mathcal{S}}} (r\mathcal{S}^{-1/2}\mathcal{K})_{,r} \tag{2.114}$$

$$\Lambda = \ell(\ell+1) - 2 + \frac{5M}{r} . \tag{2.115}$$

Re-introducing the dropped (ℓm) superscripts, the gravitational-wave amplitudes in the two polarizations h_+ and $h_\times$ are then given [202, 208] by

$$h_+ - i h_\times = \frac{1}{2D} \sum_{l,m} \left[Q^{+(\ell m)} - i \int_{-\infty}^{t} Q^{\times(\ell m)} dt' \right] {}_{-2}Y^{\ell m} , \tag{2.116}$$

where ${}_{-2}Y^{\ell m}$ is the $s = -2$ spin-weighted spherical harmonic (see, e.g., [168]) and D is the distance to the observer.

In principle, the Qs may be extracted at any distance from the source at which the gravitational waves can be viewed as perturbations on a Schwarzschild background. For an isolated perturbed black hole this could be as close in as right on the horizon. However, note that for the interpretation of the

extracted Q^+ and $Q^\times$ as indicators for gravitational wave information as seen by an observer at large distances, the wave extraction has to be performed at a distance as large as possible from the source on the computational grid. In addition, in matter spacetimes without singularities, the assumption of a Schwarzschild background generally does not hold. Shibata and collaborators thus frequently use the flat-space Minkowski metric in spherical coordinates [174, 204] as the static background.

Gauge-Invariant Extraction vs.
Quadrupole Formula-Based Approaches for Matter-Dominated Spacetimes

Historically, the (quasi)[16] gauge-invariant wave extraction techniques highlighted above have been formulated in the context of vacuum black-hole spacetimes. The Newman-Penrose formalism relies on the asymptotic nature of the Weyl scalars, requiring an extraction far from an ultra-compact (= black hole) source. An extended matter source – such as a collapsing stellar core or an oscillating neutron star – will most likely require much larger extraction radii, and since even those are not in the ideal sense close to "asymptotic", the radiation tetrad choice will be ambiguous. The Zerilli-Moncrief formalism relies on the fact that the gravitational waves can be treated as small perturbations on a static background spacetime. In addition, Zerilli-Moncrief is only invariant under linear gauge-induced coordinate transformations, hence, e.g. coordinate shifts with $|\beta^i| > |\gamma_{ij}|$ (for any ij) may spoil the extracted quantities. The Zerilli-Moncrief assumptions will hold only at very large distances from an extended matter source.

In contrast to the gauge-invariant extraction formalisms, wave extraction via the Newtonian quadrupole formula does not and cannot aim at a direct and local representation of the gravitational wave content of a considered spacetime. Instead, it is a working approximation to the gravitational waves emitted by an extended (yet compact; not ultra-compact) matter source *as seen by an asymptotic observer*, directly based on matter dynamics and not requiring extraction at large physical distances from the source. In this way the quadrupole formalism evades the problems associated with the above quasi gauge-invariant methods. It *does not* have the potential of giving *the* accurate description of the gravitational wave content of a given spacetime. It provides, however, a first-order approximation to the waves emitted by a matter source as observed at asymptotic distances [174] and may — for matter-dominated spacetimes — be regarded as superior to the above described gauge-invariant methods. These have the potential of being highly-accurate, but only under certain very special conditions that cannot generally be met in numerical simulations with grid boundaries at finite (and close) radii from the extended matter source.

I have experimented with both Zerilli-Moncrief and Weyl extraction, but have not been able to extract numerically convergent gravitational-wave information from the weakly-relativistic stellar core-collapse spacetimes considered here in which the gravitational-wave energy content is on the order of 10^{-10} to 10^{-8} $M_\odot c^2$. This satisfies the weak-perturbation constraint for Zerilli-Moncrief, but is $\sim$1 to 3 orders-of-magnitude smaller than the (relative) weakest waves Abrahams et al. [177] were able to extract from their black-hole spacetimes. Furthermore, Shibata & Sekiguchi report [174], that gravitational waves from core-collapse supernovae cannot be extracted reliably with the present Zerilli-Moncrief technique: Systematic offsets, non-linear gauge effects and numerical errors dominate over the weak gravitational waves emitted from stellar core-collapse to neutron star densities. This confirms my finding. Shibata & Sekiguchi [174] also point out that, while underestimating the physical amplitudes, the Newtonian quadrupole formalism adequately captures the phase and frequency information of the gravitational-wave emission.

All gravitational waveform estimates published in this dissertation are obtained with the Newtonian quadrupole formula in the way described in § 3.8. It may be possible – in future work beyond this dissertation – to extract gravitational waves from stellar core-collapse spacetimes via the *Observers approach* proposed by Erik Schnetter [210] in which a second coordinate frame with trivial lapse ($\alpha = 1$) and shift ($\beta^i = 0$) is evolved via appropriate transformation from the dynamically evolved spacetime in parallel to the latter. Gravitational waves can then be extracted from the Observer frame which only has trivial gauge content. Another alternative would be the technique proposed and tested by Abrahams & Evans [181] which matches the gravitational-radiation field around a compact source to linear analytic solutions that allow the determination of asymptotic waveforms.

[16] linearly and/or under special conditions

2.6.6 Gravitational Wave Astronomy

Although this dissertation is a theoretical work, I find it important to give at least an overview on the ongoing experimental efforts to observe gravitational waves with detectors on Earth and in space.

Detectability: General Considerations

In contrast to electromagnetic radiation whose observables are in most cases energy fluxes, and hence fall off $\propto 1/r^2$, the gravitational wave strain h^{TT} is directly observable, and, being an amplitude, falls off only $\propto 1/r$.

The measurement of gravitational radiation is based on the fact that the physical distance $\Delta L = \sqrt{(\eta_{\mu\nu} + h_{\mu\nu})\, dx^\mu\, dx^\nu}$ between two free point masses will undergo changes when a gravitational wave passes them. The relative change in distance $\Delta L/L$ is, in an optimal setting, directly given by the gravitational wave strain $|h^{TT}|$.

With the help of the quadrupole formula (2.97 and 2.101), I can make a first order-of-magnitude estimate of the relative displacement:

$$|h^{TT}| \sim \frac{2}{D}\frac{G}{c^4}\frac{MR^2}{\tau_{\rm dyn}^2}\ , \tag{2.117}$$

where r is the distance to the source and the *dynamical time* $\tau_{\rm dyn}$ is given [116] by

$$\tau_{\rm dyn} := \frac{\text{characteristic size R}}{\text{mean velocity}} \sim \frac{R}{\sqrt{(GM/R)}} = \sqrt{\frac{R^3}{GM}}\ . \tag{2.118}$$

For stellar core collapse of a star with core mass M = 2 $M_\odot$ and radius R = 2000 km, taking place at $r = 10$ kpc a *first estimate* of the gravitational wave strain with equation (2.117) is $|h^{TT}_{\text{core collapse}}| \simeq 3.2 \times 10^{-21}$. The results presented in this work verify this as the right order of magnitude.

Resonant-Mass Detectors

The first-ever gravitational-wave detector was conceived and built by Joseph Weber at the University of Maryland in the 1960's [211], when still very little was known theoretically about astrophysical gravitational wave sources. Weber used a massive aluminum cylinder (*bar*) and aimed at exploiting the fact that the fundamental longitudinal frequency of such a bar is very sharply defined, allowing for resonant driving of mechanical oscillations by incident gravitational waves at the bar's resonant frequency and in a very narrow bandwidth around it (usually one to a few Hertz). After a decade of effort constructing and improving his detector technology, Weber announced [212] in 1969 to the world tentative evidence that two of his detectors, one based at the University of Maryland, one near Chicago, had detected gravitational waves in coincidence. In the years following 15 other research groups around the world tried to confirm Weber's results, but even with markedly improved detector sensitivities, these efforts gave no convincing evidence that gravitational waves were seen [169].

Nevertheless, the search for gravitational waves continued and over the past decades resonant-bar detectors have been developed further. State of the art detectors (for a review see, e.g., [213] and [214] and references therein) use new improved bar materials and cryogenic technology and are sensitive in a relatively broad bandwidth of ∼50 to 100 Hz around their resonance frequencies (typically around ∼1 kHz). As of 2004 [213], there are five large resonant-bar detectors in operation: **ALLEGRO** at Louisiana State University (LSU), **AURIGA** at the Italian INFN Legarno Laboratories, **EXPLORER** at CERN, **NAUTILUS** at the Italian INFN Frascati Laboratories, and **NIOBE** at the University of Western Australia in Perth.

A prototypical bar detector (for a more detailed discussion see, e.g., [214] or [169]) consists of a cylinder of very high-Q material[17] and length L ∼1 m and mass $M \sim 1000$ kg. A short gravitational-

[17] The Q or *quality factor* is a measure of the rate at which a vibrating system dissipates its energy. It is defined as the number of oscillations per e-folding time of the system's energy. For a driven oscillation, it is given by $Q = f_0/\Delta f$, where f_0 is the resonant frequency and Δf is the spectral bandwidth the resonant frequency that is excited by the driving force.

wave burst of $h \sim 10^{-21}$ cm will excite the bar to vibrate with an amplitude (to zeroth order)

$$\Delta L \sim hL \sim 10^{-21}\,\mathrm{m}\ . \tag{2.119}$$

To measure such a minute amplitude, the observers must fight against three main sources of noise:

- **Thermal noise**: Thermal noise is due to Brownian motion of the detector atoms. The rms amplitude of Brownian vibration is on the order of $\sim 10^{-16}$ m at room temperature [214]. State-of-the-art bar detectors are cooled down to $\sim$0.1K and use very high Q material ($Q \sim 10^7$). For a 1-ms signal at their resonance frequency such detectors have a thermal-noise limited strain sensitivity of $\sim 5\times 10^{-21}$ m [214].
- **Sensor noise**: A transducer is used to convert the bar's mechanical energy into electrical energy, and an amplifier increases the signal level to record it. Both components introduce additional noise, limiting the sensitivity to frequencies near the resonance frequency, and, in fact, the transducers are the largest limiting factor on the bandwidth of present-day bars [213]. State-of-the-art transducer-amplifier units have a bandwidth of some tens of Hz, but there is potential to increase this to 100 Hz or more [213, 214].
- **Quantum noise**: The zero-point vibrations of a bar with a resonance frequency of 1 KHz is given by Heisenberg's uncertainty principle [214, 215]:

$$\langle \Delta L^2 \rangle^{1/2}_{\mathrm{quant}} = \left(\frac{\hbar}{2\pi M f_0}\right)^{1/2} \sim 5 \times 10^{-21}\,\mathrm{m}\ . \tag{2.120}$$

  This number is comparable to the thermal limits and it will be very difficult, though not impossible [215], to push bars to higher sensitivities than 10^{-21}.

Light-Interferometric Detectors

Interferometric gravitational wave detectors measure the gravitational wave field by observing its action upon a widely separated set of test masses. The experimental setup is very much like that of a two-armed Michelson-Interferometer as shown in figure 2.6 and has first been proposed in the 1970's [216–218]. Detailed reviews of interferometric detector design can be found in [169, 219, 220].

At the end of each arm a test mass with a mirror is suspended as freely as possible with a sophisticated pendular isolation system to minimize the effects of local ground vibrations. A second test mass with a semi-transparent mirror is suspended close to the beam splitter in each arm, thus creating two Fabry-Perot cavities (one in each arm) that allow for laser beam recycling (see, e.g., [214]).

A gravitational wave incident perpendicular to the detector plane with $+$ polarization aligned with the detector arms increases the length of one arm while reducing that of the other. Each arm oscillates between being stretched and squeezed as the wave itself oscillates. The gravitational wave is thus detectable by measuring the separation between the test masses in each arm and searching for this oscillation by means of monitoring changes in the interference pattern of the recombined laser beams in the photo detector. In general, both polarizations, $+$ and $\times$, of incident gravitational waves influence the test masses. The general detector output $h(t)$ is written as

$$\frac{\Delta L(t)}{L} = F_+ h_+(t) + F_\times h_\times(t) \equiv h(t)\,, \tag{2.121}$$

where L is the detector arm length and the *response functions* F_+ and $F_\times$ weigh the two polarizations in a quadrupolar manner on the direction of the source and the orientation of the detector [169].

In practice [214], the phase difference of the two laser beams is monitored by a nulling method in which one keeps the light returning from the two arms always π out of phase so that the output is dark. The error signals of the servo-loop control applied to the mirrors to maintain the dark fringe are directly proportional to the action of an incident gravitational wave. The sensitivity of a light-interferometric gravitational wave antenna depends on the arm length and the amount of light energy stored in the arms [214]. To exclude acoustic disturbances and fluctuations in the local index of refraction, the interferometers operate in ultra-high vacuum at pressures below $\sim 10^{-13}$ bar.

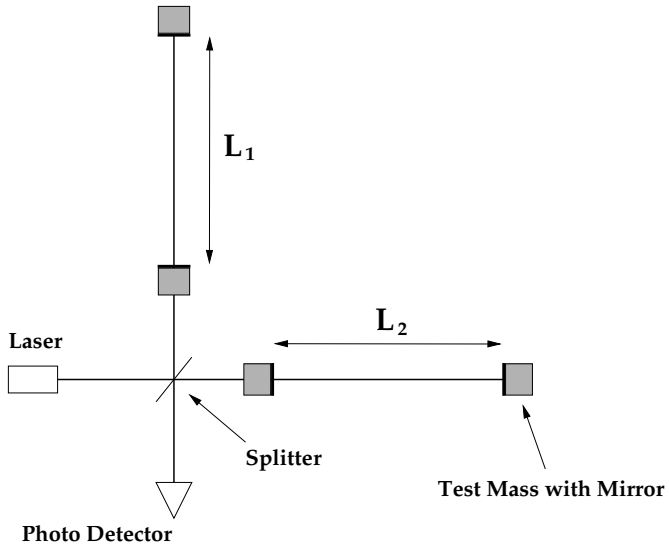

Figure 2.6: Sketch of a light-interferometric gravitational wave detector. Adopted from [221].

The main sources of noise competing with physical signals are [214, 215]:

- **Seismic Noise**: External mechanical vibrations lead to displacements of the mirrors and are typically many orders of magnitude larger than an astrophysical signal. Seismic noise is the limiting noise below ∼10 Hz and a combination of active filters (piezo-electric actuators), passive filters (alternate layers of steel and rubber) and a multi-stage pendulum suspension of the optical components allow effective filtering above ∼10 Hz.

- **Thermal Noise**: Brownian motion of the mirrors and excitation of violin modes of the suspension can mask gravitational waves. The pendulum suspensions have thermal noise at a few Hz and internal vibrations of the mirrors have natural frequencies of several khz. To ensure that most of the vibration energy of both kinds of oscillations is confined to a small bandwidth around their natural frequencies, extremely high Q material and low temperatures around 1 K are desirable. However, present-day detectors operate at room temperature. Thermal noise is the limiting noise between 50–250 Hz.

- **Photon shot noise**: Photons arrive at random and make random fluctuations in the light intensity that could be misinterpreted as gravitational wave information. As a random process, the measurement error improves with $\sqrt{n}$, where n is the number of photons. The shot noise related error displacement is given by [214]

$$\delta\tilde{l}_{\rm Shot} = \left(\frac{\hbar c}{2\pi}\frac{\lambda}{\eta P}\right)^{1/2}, \tag{2.122}$$

  where η is the efficiency of the photo detector, λ the laser wavelength and P the circulating light power. In order to obtain $\tilde{l}_{\rm Shot} < 10^{-22}$, $\eta P \sim 1$ kW is necessary. Photon shot noise is the principal limitation to sensitivity for frequencies above ∼250 Hz. Present-day detectors operate with lasers with output on the order of 10 W and the necessary high light power is obtained via resonant cavities and beam recycling [214].

- **Quantum effects**: Besides photon shot noise, additional quantum effects like zero-point vibrations of mirror surfaces affect the detector sensitivity. For present-day detectors these quantum noise effects are small and limit the sensitivity to $h{\sim}10^{-25}$ [214].

- **Gravity gradient noise**: Changes in the local gravitational field on the timescale of the measurements lead to tidal forces on a gravitational wave detector that cannot be screened out. The environmental noise comes from human activities (e.g., lumbermen cutting trees near a detector) and seismic waves, surf of the sea and changes in air pressure/density. Gravity gradient noise is the dominant noise component in the frequency band below ∼1 Hz and is the primary

reason why the detection of gravitational waves in that frequency band must be carried out in space [214, 215].

At this point, six large laser-interferometric gravitational wave detectors are in operation.

- **LIGO**: The MIT/Caltech Laser Interferometer Gravitational Wave Observatory [221, 222] operates since 2001 with two 4 km interferometers located at Hanford, Washington and Livingston, Louisiana and one 2 km interferometer located at Hanford, Washington. In 2006, LIGO has reached its design sensitivity[18] of $\tilde{h} \sim 10^{-21}$–10^{-22} Hz$^{-1/2}$ within a frequency band of $\sim$60–$\sim$1000 Hz.
- **GEO600**: GEO600 is a joint British-German detector with 600 m arm length that operates since 2001 near Hannover, Germany under the auspices of the Albert-Einstein-Institut's section at Hannover University. GEO600 incorporates more modern and improved detector design to make up for its short arm length [214, 223]. By June 2006 GEO600 had not yet reached its design sensitivity [224].
- **TAMA300**: TAMA300 operates since 1999 at Tokyo, Japan. The 300 m arm length interferometer's sensitivity is $\sim 10^{-20}$ Hz$^{-1/2}$ within a frequency band 300 Hz–8 Khz [225].
- **VIRGO**: VIRGO is French-Italian 3 km interferometer that has started taking data in 2006. It incorporates advanced interferometer design features, including improved test mass suspensions, allowing for sensitivities similar to the LIGO detectors down to frequencies of $\sim$10 Hz [226].

Planned detectors that have already received (partial) funding include *advanced LIGO* [214, 227, 228] that is designed to be ten times as sensitive as the initial LIGO detectors and the space-based LISA detector for low-frequency sources (e.g., [215, 220, 229] that is currently scheduled to be launched around 2015.

[18] Often the performance of a detector is given by the frequency-dependent noise that limits its sensitivity. For stochastic noise, the amplitude spectral density $\tilde{h}$ is used. It is the the square root of the power spectrum: $\tilde{h} = \sqrt{S(f)}$ in units of $1/\sqrt{Hz}$.

2.7 Historical Overview on Previous Work: Gravitational Wave Emission in Core-Collapse Supernovae

The core-collapse supernova – neutron star connection was first drawn by Baade & Zwicky in the mid to late 1930s [31–33]. Nevertheless it took more than 20 years until core-collapse supernovae became popular as potential emission sites for gravitational radiation. The reason for this delay is most likely linked to the doubts that many theoretical physicists had in the time from $\sim$1925 to $\sim$1960 about the nature of gravitational waves and their capability to carry energy. Once these issues were finally resolved (see, e.g., [116, 230–236]), relativists began to speculate on potential astrophysical gravitational wave sources.

The first refereed publication to mention gravitational wave emission from core-collapse supernovae is a 1966 Physical Review Letter by Joseph Weber [237]. In this article Weber referred to work by Freeman Dyson [235, 238, 239] on astrophysical sources of gravitational waves, including binary neutron star systems and non-spherical stellar core collapse[19].

Extensive review articles on the gravitational wave emission processes in core-collapse supernovae have been published by Fryer & New [240] and by Kotake [241]. For a more concise review, see Kokkotas & Stergioulas [242].

2.7.1 Rotating/Aspherical Collapse and Core Bounce

The earliest published work on the gravitational wave emission of nonspherical stellar collapse was carried out by Ruffini & Wheeler [243] in 1971. They provided the first order-of-magnitude estimates. Thuan and Ostriker [244] performed semi-analytic calculations of the pressureless aspherical (dust) collapse of cold, uniformly rotating Newtonian spheroids in 1974 and estimated the frequency spectrum of the emitted gravitational waves and the total radiated energies. Novikov [245] and Shapiro [246] improved upon their calculations by including internal pressure, and Epstein [247] in addition included post-Newtonian effects. In an extensive study spanning three articles published in 1978, 1979, and 1981, Saenz & Shapiro [248–250] carried the work on collapsing and bouncing ellipsoids to full blossom by including more realistic initial conditions, equations of state, and even to limited extent weak interaction physics. They were the first who published gravitational waveforms (the time evolution of the dimensionless strain amplitudes h_+ and/or $h_\times$) from stellar iron core collapse. In 1979, Moncrief [251] employed the ellipsoid model to study the gravitational wave emission from oscillating axisymmetric and nonaxisymmetric spinning ellipsoids in the core collapse context. Detweiler & Lindblom [252] in 1981 also followed the ellipsoidal approach and computed the gravitational wave emission from axisymmetrically and nonaxisymmetrically collapsing ellipsoids.

In 1979, Turner & Wagoner [253] employed a perturbative approach to calculate the gravitational wave emission produced by rotationally-induced perturbations of spherically symmetric iron core collapse models of Van Riper [254] and Wilson [255]. Seidel and collaborators followed along those lines and pertubatively analyzed detailed spherically symmetric GR core collapse calculations with a hot nuclear EOS and presupernova models from stellar evolutionary calculations in the late 1980s [256–259]. Their approach, though only valid for small deviations from sphericity (and, hence, slow rotation), is remarkably competitive with multi-dimensional hydrodynamic calculations. This is apparent from figure 2.7 that compares examples of gravitational waveforms from rotating collapse and bounce obtained in the last three decades.

In 1982, Müller published [260] the first (Newtonian quadrupole) waveform estimates that were extracted from the fluid motions in non-linear 2D (axisymmetric) hydrodynamic calculations of rotating iron core collapse that included a realistic EOS and an approximate treatment of electron capture [261]. Almost 8 years later, Finn [262] and Finn & Evans [178] derived improved variants of the Newtonian quadrupole formula tailored for numerical calculations[20] and applied them to the

[19] Note that F. Dyson himself does not claim to have been the first to propose gravitational wave emission from core-collapse supernovae: "I have no idea who first calculated the emission of gravitational radiation from a collapsing star with rotation. Ruffini and Wheeler may have been the first. It was certainly obvious to everyone who thought about it that a collapsing star with rotation would give rise to a strong pulse of gravitational waves. I make no claim to have thought of this first." [239]

[20] Note that Blanchet et al. [171] independently derived similar variants of the Newtonian quadrupole formula.

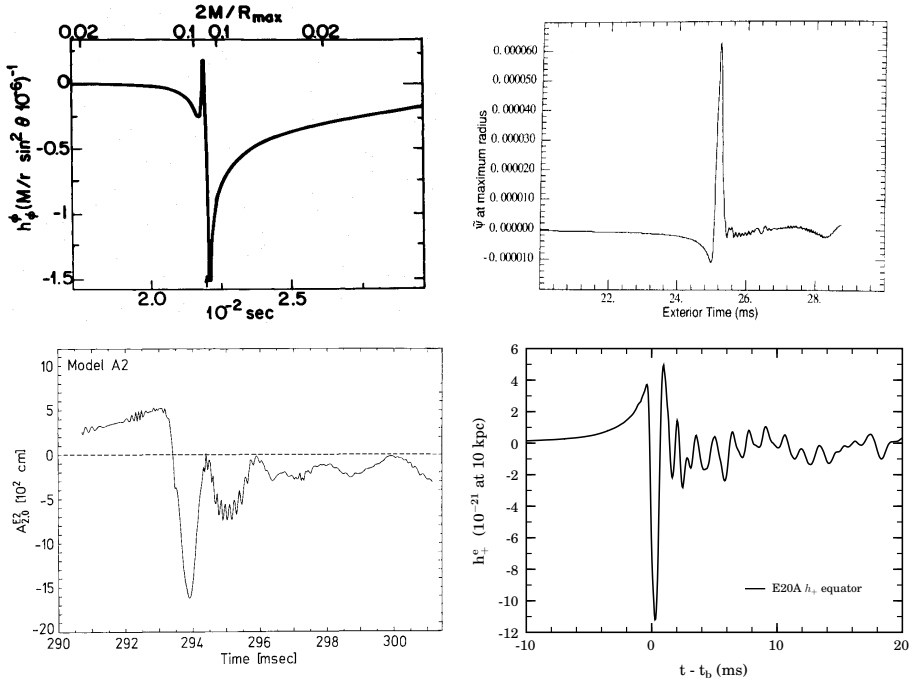

Figure 2.7: Example gravitational waveforms of moderately fast rotating collapse and core bounce obtained over a period of almost 30 years and computed with various methods. Top left: Gravitational waveform estimate computed with a Newtonian ellipsoidal model by Saenz & Shapiro in 1978 (figure 4b of [248]). Top right: Waveform estimate by Seidel & Moore [256] obtained via the perturbative approach from spherically symmetric detailed GR core collapse calculations in 1987. Bottom left: Waveform extracted by Müller [260] from the fully non-linear 2D Newtonian hydrodynamic calculations by Müller & Hillebrandt [261] carried out in 1981. Bottom right: Example waveform extracted from a {3+1} GR hydrodynamics model calculation presented in §6 of this work.

extraction of gravitational wave information from adiabatic axisymmetric hydrodynamic collapse calculations starting with rotating $n = 3$ polytropic progenitor models, a simple Γ-law EOS, and no weak interaction physics.

In 1991, Mönchmeyer & Müller published [11] collapse, bounce, and early postbounce waveforms that they extracted from their 2D Newtonian core collapse calculations [263] that started out with progenitors from stellar evolutionary calculations, employed a finite-temperature nuclear EOS, and a neutrino trapping / leakage scheme. They performed only four model calculations with varying rotation laws, degree of differential rotation, and initial rotation parameter β, defined as

$$\beta = \frac{T}{|W|} \ , \tag{2.123}$$

where T is the rotational kinetic and $|W|$ is the gravitational potential energy. They identified the waveform characteristics of rotation dominated core bounce and introduced the nomenclature to distinguish between "type I" (not rotation dominated) and "type II" (rotation dominated) dynamics and waveforms.

In 1993, Bonazzola & Marck [264] attempted the first Newtonian hydrodynamic iron core collapse calculations in 3D. They were limited to $n = 3$ polytropes, a simple EOS, no neutrino physics, and were only able to capture the infall phase of collapse for which they computed gravitational waveform estimates.

Burrows and Hayes [265] considered nonrotating, but asymmetrical collapse in 1996 by artificially increasing the density in a 40° wedge around one of the poles. Their simulations were 2D Newtonian, but included a flux-limited diffusion (along radial rays) treatment of the neutrinos, a finite-temperature EOS, and started out with a presupernova model from stellar evolutionary calculations. They extracted the gravitational wave signals of aspherical matter motions *and* anisotropic neutrino emissions (see §2.7.2 below).

Yamada & Sato [266] (1995) and Zwerger & Müller [30] (1997) performed extensive 2D Newtonian parameter studies of the collapse of $n = 3$ polytropes in rotational equilibrium with a hybrid polytropic/ideal-fluid EOS (see §3.5.5) and investigated the dependence of the gravitational wave signal on the value of the initial rotation parameter β, the degree of differential rotation, and on the adiabatic coefficient $\Gamma \leq 4/3$ used during the collapse phase. They found that the considerably simpler physical model qualitatively reproduced the results obtained by Mönchmeyer & Müller [11], including type I and type II waveforms. In addition, Zwerger & Müller [30] identified a third kind of dynamics / waveform (type III) that obtains only for large initial pressure reductions ($\Gamma \lesssim 1.28$).

In 1998, Rampp, Müller & Ruffert [267] performed the first 3D Newtonian calculations of the bounce and early postbounce phase and investigated nonaxisymmetric instabilities in extremely differentially rotating polytropic initial models of Zwerger & Müller [30]. Their results were (in part) confirmed by Brown [268] in 2001 and showed no enhancement of the collapse and immediate bounce wave signature by nonaxisymmetric dynamics.

In 2001 and 2002, Dimmelmeier et al. [12, 17, 18, 160] followed up on the work by Zwerger & Müller [30] and included a conformally-flat treatment of GR and relativistic hydrodynamics. Their results, which have since been confirmed by Shibata & Sekiguchi [13] in full GR in 2004 and by Cerdá-Durán et al. [162] with a second-order post-Newtonian extension of the conformal-flatness approximation in 2005, indicate that in GR higher initial values of β and degrees of differential rotation are required for a given model to yield type II dynamics and waveform. Before Shibata & Sekiguchi, Siebel et al. [269] performed the first multi-dimensional full GR core collapse simulation in 2003. They employed a characteristic formulation of GR which is optimized for the propagation of gravitational waves, but is suboptimal in strong-field regions.

In 2002, Fryer, Holz, and Hughes published an overview article [270] on gravitational wave emission from core-collapse supernovae and accretion-induced collapse with analytic estimates and a small set of quantitative estimates based on detailed Newtonian numerical simulations [42, 88]. In 2004, the same authors extended their analysis [271] to the 3D Newtonian calculations of [89]. In 2003, Kotake, Yamada, and Sato performed [14, 272] 2D Newtonian calculations with a finite-temperature EOS, progenitor models from stellar evolutionary studies, and a neutrino treatment similar to that of the more than ten years earlier work by Mönchmeyer & Müller [11]. Their (larger) set of models did not show significant qualitative differences to the Mönchmeyer & Müller models. Also in 2003/2004, Ott et al. [9, 170] performed an extensive parameter study of rotating core collapse in 2D Newtonian context. They employed a finite-temperature nuclear EOS and progenitor models from stellar evolutionary calculations, but neglected electron capture during collapse. They investigated the effects of variations in progenitor structure and the degree of differential rotation on the collapse/bounce gravitational wave signal. In addition, they studied the gravitational wave emission from slowly rotating presupernova models that have been found to yield neutron stars consistent with pulsar birth spin estimates [273] and determined that the core bounce gravitational wave signal of such progenitors would be too weak to be detected even from a galactic supernova. These results were confirmed by the more microphysically detailed 2D calculations of Müller et al. [95] that included an approximate GR description of gravity.

In 2005, Shibata & Sekiguchi extended their hybrid-EOS GR calculations to a 3D treatment of the postbounce phase with an emphasis on nonaxisymmetric rotational instabilities [204] and, in a separate study [105] again using idealized initial models and EOS, investigated black hole formation with and without prior formation of a PNS.

The effects of magnetic fields on the collapse dynamics and gravitational wave emission have been considered in Newtonian gravity by Kotake et al. [274] (2004), Yamada & Sawai [275] (2004), and Obergaulinger et al. [276, 277] (2006, with an approximate GR potential in [277]). The latter authors identified a new magnetic-field induced type of collapse / bounce dynamics and gravitational waveform that they refer to as type IV. In 2006, Shibata et al. [278] performed the first GR MHD calculations of the collapse of polytropic iron core models and computed gravitational waveforms for a subset of their models. Of the aforementioned studies, only Kotake et al. went beyond the hybrid EOS and employed a finite-temperature EOS and an approximate treatment of deleptonization.

2.7.2 Convective Overturn, Shock Instability, Anisotropic Neutrino Emission

It is theoretically well established that convective overturn in the PNS and in the postshock region of core-collapse supernovae is likely to occur and may play an important role in the explosion mechanism (e.g., [26, 72, 73, 77, 79, 86, 86, 88, 89, 96, 279, 280]. Recent simulations [26, 27, 73, 87, 90, 92–95] and analytic models [97–101] indicate the presence of a large-scale low-ℓ instability of the standing accretion-shock (SASI[21]). Time-varying quadrupole and higher-order multipole components of postshock flow lead to gravitational wave emission. In addition and as pointed out by Epstein in 1978 [281], anisotropic neutrino emission may also lead to gravitational wave emission at significant strain amplitudes.

Burrows & Hayes [265] carried out the pioneering study on gravitational wave emission from flow asphericities not induced by rotation and anisotropic neutrino radiation fields. They perturbed the precollapse density distribution of an iron core model by 15% in a 20° wedge around one pole and studied its collapse and postbounce evolution in 2D Newtonian gravity with gray flux-limited neutrino diffusion along radial rays. Their results indicate that a 15% initial $l = 1$ density perturbation would be sufficient to obtain neutron star kick velocities $\sim$500 km s^{-1}. They computed the gravitational wave signal emitted by the time-varying quadrupole components of the fluid motion and by anisotropic neutrino emission. In accordance with analytic estimates [282], they found that the gravitational wave emission from the neutrino radiation anisotropies leaves behind a zero-frequency offset (*memory effect*, [283]) in the gravitational wave strain.

In 1997, Janka & Müller [284] performed 2D and the first 3D Newtonian calculations of the postbounce (pre-explosion) phase of nonrotating core-collapse supernovae. Their calculations started out with profiles from detailed 1D collapse calculations and included a realistic EOS and a simplified scheme for neutrino transport and neutrino energy deposition. They computed the gravitational wave signal of convective overturn inside the PNS and in the convectively unstable outer postshock layers and estimated the gravitational wave emission from neutrino radiation anisotropies.

In 2004, Müller et al. [95] performed 2D calculations with ray-by-ray spectral Boltzmann transport, approximate GR gravity and an approximate treatment of general relativistic effects in neutrino transport, but treated the hydrodynamics in Newtonian fashion. Müller et al. considered one nonrotating and one very slowly rotating precollapse model and found that the gravitational wave emission from postbounce convective mass motions affected by the SASI[22] is significantly more energetic than that from slowly rotating core bounce. In addition, they computed the gravitational wave emission from convection-induced anisotropic neutrino emission.

Based on 3D Newtonian smoothed-particle hydrodynamics and gray multi-species flux-limited diffusion neutrino transport calculations by Fryer & Warren [89], Fryer, Holz, and Hughes [271] (2004) studied the gravitational wave emission in asymmetric rotating and nonrotating core-collapse supernovae. Besides the gravitational wave emission from rotating core bounce, they also considered the postbounce gravitational wave signal owing to convective mass motions and anisotropic neutrino emission, but did not consider the possibility of postbounce rotational instabilities in their models.

In 2005/2006, Kotake and collaborators performed a series of 2D Newtonian gray flux-limited diffusion neutrino radiation-hydrodynamics calculations in which they considered the gravitational wave signal of rotationally-induced neutrino anisotropies in the collapse of iron cores spinning much faster than those considered by Müller et al. [95]. Their results, which indicate that the degree of precollapse iron core differential rotation is central in determining the gravitational waveform, have so far been published only in a review article [241]. In another study [94], Kotake et al. focussed on the gravitational wave emission from mass motions and neutrino radiation field anisotropies induced by the SASI.

The gravitational wave emission from anisotropic neutrino radiation and mass motions in the SASI phase of core-collapse supernovae was also captured by the calculations of Ott et al. [15] in 2006 that I discuss below in the context of PNS oscillations and in §7.2 of this dissertation.

[21] SASI: **S**tanding **A**ccretion **S**hock **I**nstability

[22] Note that although their models exhibit SASI-like feature, they did not identify them as being related to the SASI at the time the paper was written.

2.7.3 Nonaxisymmetric Rotational Instabilities

From the classical theory (see, e.g., [285, 286]) of Newtonian axisymmetric incompressible, uniform density fluid bodies in rigid rotation, so-called MacLaurin spheroids, it is known that for sufficiently high rotation rates (described by the rotation parameter β), lower-energy nonaxisymmetric configurations exist. At the threshold values of β beyond which such configurations become favorable, MacLaurin spheroids become unstable to nonaxisymmetric deformations, and one speaks of a *nonaxisymmetric rotational instability* which arises in MacLaurin spheroids from non-radial azimuthal modes/perturbations $\propto \exp(im\varphi)$ in the $\ell = m$ Kelvin f-mode[23], the fundamental pressure mode of the spheroid.

For MacLaurin spheroids a purely *dynamical rotational instability* sets in at $\beta_{\rm dyn} \approx 27.38\%$, leading to a transformation of a MacLaurin spheroid into a Riemann ellipsoid with bar-like $m = 2$ shape. At lower rotation rates that are still above $\beta_{\rm sec} \approx 13.75\%$, MacLaurin spheroids can experience a *secular rotational instability* [287–290] under the influence of dissipation-driven angular momentum redistribution. A MacLaurin spheroid subject to normal fluid viscosity will deform into a rigidly rotating Jacobi ellipsoid while gravitational radiation reaction (via the Chandrasekhar-Friedman-Schutz [CFS] instability [289, 290]) can drive the MacLaurin spheroid to assume a differentially-rotating Dedekind ellipsoid shape [286, 291].

Axisymmetric MacLaurin spheroids do not emit gravitational waves, yet their nonaxisymmetric bar-deformed counterpart ellipsoids are strong emitters: A top-over spinning massive solid rod (or bar) emits gravitational waves with dimensionless strain amplitudes $h \propto MR^2\Omega^2/D$, where D is the distance to the observer, M is the mass, R the length, and Ω the angular velocity of the spinning rod. Note that owing to the π-symmetry of the rod its gravitational wave emission occurs at $2f$, with $f = 2\pi/\Omega$ [115, 116]. For a bar-deformed cold neutron star, one can make the estimate [242, 270]

$$h \approx 3.6 \times 10^{-22} \left(\frac{\epsilon}{0.2}\right) \left(\frac{f}{3\,\mathrm{kHz}}\right)^2 \left(\frac{D}{15\,\mathrm{Mpc}}\right)^{-1} \left(\frac{M}{1.4\,M_\odot}\right) \left(\frac{R}{10\,\mathrm{km}}\right)^2 , \qquad (2.124)$$

where ϵ is the ellipticity parameter of the bar and f its rotation frequency. For a 1 $M_\odot$ PNS that extends out to 30 km and spins with a 2 ms period with $\epsilon \sim 0.1$, one finds $h \sim 5\times10^{-21}$ if the PNS is located at 10 kpc distance from Earth.

Collapsing iron cores (e.g., [204, 267, 268]), accretion-induced collapse (e.g., [292, 293]), centrifugally-hung iron cores (so-called fizzlers) (e.g., [294–296]), hot early and late postbounce PNS (e.g., [204, 267, 268, 291, 297]), as well as old neutron stars and neutron star remnants of binary neutron star mergers (e.g., [20, 21, 23–25, 291, 298–311] and references therein) have been proposed as objects that might be subject to dynamical and/or secular rotational instabilities.

The literature on rotational instabilities in fluid bodies is extensive and cannot be reviewed here in the necessary detail. I refer the reader to recent reviews on rotational instabilities in compact stars in [242, 286, 312]. In the following I list only a number of key studies that are dealing directly with rotational nonaxisymmetric instabilities in stellar iron core collapse and core-collapse supernovae. Most but not all of the following studies (numerically) considered the gravitational wave emission by nonaxisymmetric structures and dynamics.

Nonaxisymmetric deformations of collapsing iron cores were first considered quantitatively in the late 1970s using an ellipsoidal model for nonspherical stellar collapse by Shapiro and collaborators [248–250] and by Detweiler & Lindblom in the early 1980s [252]. In 1984, Ipser & Mangan [298] employed an ellipsoid model to investigate the gravitational wave emission by nonaxisymmetrically deformed rotating ellipsoids along the Jacobi sequence [285, 290]. They provided estimates of the gravitational wave energy emission from such configurations. These early studies were primarily concerned with the gravitational wave emission of initially present nonaxisymmetric deformations and did not track the development of nonaxisymmetric rotational instabilities.

In 1995, Lai & Shapiro [297] investigated viscosity and gravitational radiation driven rotational instabilities in nascent neutron stars by means of a compressible ellipsoid model and linear perturbation theory, and estimated the gravitational wave emission from bar-like deformations.

[23] The fundamental pressure mode of a self-gravitating fluid body was first studied by Lord Kelvin in 1863.

In the context of rapidly rotating iron cores that become rotationally supported at subnuclear densities and whose collapse "fizzles" [11, 313–317], Imamura and collaborators [294–296] considered dynamical and secular nonaxisymmetric rotational instabilities and found that such fizzlers[24] may become nonaxisymmetrically unstable only at late times and not immediately during or immediately after rotationally-induced core bounce. In addition, they found that secular instability could occur in fizzlers at β much lower than the classical threshold value.

The first full 3D Newtonian non-linear hydrodynamics calculations of the bounce and early postbounce phase of a rotating iron core were carried out by Rampp, Müller and Ruffert [267] with a hybrid polytropic/ideal-fluid EOS. They investigated the growth of nonaxisymmetric structures and dynamics in the most extreme differentially-rotating polytropic model of Zwerger & Müller [30] with a quasi-toroidal density distribution[25] and $\beta \sim 35\%$ at core bounce. They found the growth of nonaxisymmetric modes with $m = \{1, 2, 3\}$ character and, depending on the spatial structure of the initial perturbations, dominant $m = 3$ or late-time dominant $m = 2$ structures. Rampp et al. did not find a significant enhancement of the gravitational wave emission by the nonaxisymmetric structures.

In 2001, Brown [268] carried out 2D collapse and 3D bounce and postbounce calculations in Newtonian gravity in many ways similar to those of Rampp et al. [267]. He numerically evolved the same initial model as Rampp et al. and in addition considered a variety of less differentially rotating initial models. Brown's results showed dominant $m = 2$ bar-mode growth and no substantial growth in the $m = \{1, 3, 4\}$ modes. Like Rampp et al., Brown did not find strong gravitational wave emission associated with the nonaxisymmetric structures and dynamics in his models.

In 2002, Liu [293], in part based on the work of Liu & Lindblom [292], investigated the possibility of nonaxisymmetric rotational instability in postbounce accretion-induced collapse (AIC) models by means of differentially rotating equilibrium model sequences and linearized Newtonian hydrodynamics. Liu found that dynamical bar-mode instability in differentially-rotating AIC remnants may set in at $\beta \sim 25\%$ which accords with estimates for moderately differentially rotating cold neutron stars (e.g., [300, 302, 304] and references therein).

In 2005, Shibata & Sekiguchi [204] performed 2D GR collapse calculations of differentially rotating polytropes with the hybrid polytropic/ideal-fluid EOS and mapped to 3D shortly before core bounce. They followed core bounce and the early postbounce phase in 3D for models with β near the classical threshold for dynamical instability. In their models that developed non-negligible nonaxisymmetric dynamics, the authors found a dominant and fastest growing $m = 2$ bar-mode component and at late times a subdominant $m = 1$ contribution.

In the years between 2000 and 2005, strong evidence for a dynamical rotational instability in differentially rotating neutron stars at β significantly below the classical threshold value was found by studies of strongly differentially rotating equilibrium compact star models [20, 21, 308, 309, 311]. In contrast to the classical high-$T/|W|$ instability, this new kind of dynamical instability at low-$T/|W|$ appears to be related with resonant amplification of azimuthal modes at corotation points where the pattern speed of the mode coincides with the local angular velocity [19, 23–25].

In 2004, Villain et al. [318] considered the axisymmetric early postbounce evolution of rigidly and differentially rotating PNS by means of sequences of GR stationary equilibrium configurations based on the postbounce rotational configurations of Dimmelmeier et al. [12]. They employed a realistic finite-temperature EOS and found that early-postbounce PNS rotation rate is too low for PNSs to be subject to a classical bar-type dynamical instability, but sufficiently fast (and differentially) rotating for a secular or low-$T/|W|$ instability. They did, however, not track the 3D evolution and made no estimates of the gravitational wave emission.

Motivated by the results on low-$T/|W|$ instabilities, Ott et al. [22] performed 3D Newtonian calculations of the postbounce phase of a moderately-fast stellar core collapse model with postbounce $\beta \sim 9\%$ that was adiabatically collapsed in 2D with a finite-temperature nuclear EOS. The 3D calculations were carried out with a hybrid polytropic/ideal-fluid EOS. They found the unstable growth of an $m = 1$ one-armed spiral deformation accompanied by quadrupole components that leads to copious emission of gravitational waves.

[24] Note that fizzlers may represent extreme cases of type II dynamics [30]

[25] I denote stellar models with the maximum rest-mass density located in a ring about the origin as quasi-toroidal.

2.7.4 PNS Pulsations

PNS/NS can pulsate in a multitude of ways. In relativistic theory, PNS normal[26] modes, owing to the emission of gravitational waves, generally have complex frequencies with the real part specifying the actual frequency of oscillation and the imaginary part representing the damping (or driving) [179]. Thus, they are called *quasi-normal modes* and are categorized (e.g., [179, 286, 312]) as follows:

- **Polar fluid modes** (i.e., modes having even parity) encompass the classical f(undamental)-modes, p(ressure)-modes and g(ravity)-modes. The unstable nonaxisymmetric rotational modes discussed in the previous section are polar modes.

- **Axial/hybrid fluid modes** (i.e., modes having odd or mixed parity) including inertial modes whose restoring force is the Coriolis force [312, 320]. They are degenerate at zero frequency in nonrotating stars. r(otation)-modes are a special group of inertial modes that are purely axial (at least in Newtonian theory) and generically unstable to the CFS instability [286]. Work on r-modes and their gravitational wave emission in the core-collapse supernova context is briefly discussed in the next section.

- **Polar and axial spacetime modes** are w(ave)-modes of curvature analogous to the quasi-normal modes of black holes (e.g., [179, 286, 321]) that are weakly coupled to matter.

Non-radial pulsations of nonrotating and rotating PNSs or cold neutron stars could be excited in a number of astrophysical scenarios, including iron core collapse, AIC, hypermassive neutron star formation in merger events, accretion from binary companion stars, and in neutron star core quakes owing to phase-transitions in the nuclear EOS (see, e.g., [312, 322, 323]). The observation and analysis of gravitational waves from neutron star pulsations would lead to an entirely new field of research — *gravitational wave asteroseismology* — which, similar to what helioseismology does for solar physics, would allow (nuclear) astrophysicists to observationally validate models for neutron star internal structure, EOS, magnetic fields etc. [324].

The early and ground-breaking work on non-radial pulsations of relativistic stars and their gravitational wave emission was carried out by Thorne and collaborators in the late 1960s and early 1970s [325–330] and by Detweiler and collaborators [331–333] in the early to mid 1970s. Since these early contributions an extensive literature on quasi-normal modes of compact stars has developed and has been thoroughly reviewed by Andersson et al. [324] (1995), Kokkotas & Schmidt [179] (1999) and with an emphasis on rotating stars, by Stergioulas [312] (2003). In the following, I list key studies concerned with the polar pulsations of rotating and nonrotating PNSs.

In 1983 Lindblom & Detweiler [334] computed the eigenfrequencies and gravitational wave damping timescales of quadrupole oscillations of neutron stars with a variety of microphysical, though cold nuclear EOSs. McDermott et al. [335–337] considered general non-radial pulsations of young finite-temperature neutron stars / PNSs, including buoyancy-related g-modes.

Beginning in the mid 1990s, Andersson, Kokkotas, and collaborators [324, 338–341] improved upon the results of Lindblom & Detweiler [334] with more modern techniques and EOSs. Their results were again updated by Benhar et al. [342] in 2004.

In a series of papers, Ferrari, Pons, and collaborators [343–348] investigated the pulsational spectrum of hot newborn neutron stars, in part based on perturbative analyses of PNS profiles from detailed, spherically-symmetric radiation-hydrodynamics calculations.

In 2001, Font et al. [349] performed GR hydrodynamics calculations in the Cowling approximation[27] and computed axisymmetric quasi-radial and non-radial modes of rigidly rotating polytropic neutron stars. In 2004, Stergioulas et al. [322] extended this work to differentially rotating stars and considered the mode spectrum of neutron stars near the mass-shedding limit. Shibata & Sekiguchi [174] performed fully coupled GR hydrodynamics calculations of the gravitational wave emission from axisymmetric non-radial pulsations in rotating and nonrotating neutron stars with a polytropic EOS.

[26] A normal mode in an oscillating system is the frequency at which a deformable structure will oscillate when disturbed. Normal modes are also known as natural frequencies or resonant frequencies [319].

[27] In the Cowling approximation the GR field equations are not evolved.

In 2005, Passamonti et al. [350], based on previous suggestions by Eardley [351], investigated the excitation of non-radial pulsations via non-linear mode coupling with radial pulsations (e.g., [352–354]) that could be active in the ring-down phase of nonrotating or slowly rotating PNSs.

In 2006, Dimmelmeier et al. [323] performed an extensive study of axisymmetric pulsations, their gravitational wave emission, and non-linear mode couplings in rotating compact polytropic stars via non-linear 2D hydrodynamics calculations in the conformal-flatness approximation of GR.

Recently, evidence for the potential importance of non-radial pulsations of PNSs for the core-collapse supernova explosion mechanism was found in the 2D Newtonian radiation-hydrodynamics supernova simulations of Burrows et al. [26–29]. The calculations show that at late times and when the SASI has reached its non-linear phase, PNS core g-mode oscillations are excited by accretion downstreams and postshock turbulence. Burrows et al. furthermore found that the PNS core oscillations damp via the emission of strong sound waves that are absorbed in the postshock region and by the stalled shock, and eventually drive the supernova explosion. The gravitational wave emission from $\ell = 2$ components of the core oscillations is discussed in §7.2 of this dissertation.

2.7.5 r-Modes

A nonrotating star has no non-trivial axial modes[28]. As briefly mentioned above, this situation is changed by rotation, which leads to the presence of axial inertial modes whose restoring force is the Coriolis force [286].

In 1998, Andersson [355] found that $l = m = 2$ r-modes, a subclass of axial modes, are in GR unstable to growth for *all* rotation rates via the CFS [289, 290] instability. Friedman & Morsink [356] soon after confirmed Andersson's results. This discovery sparked the interest of relativistic astrophysicists in the *r-mode instability* and over a period of five years more than 200 articles[29] on r-modes were published. Reviews on the r-mode instability can be found in [242, 312, 357].

The gravitational wave amplitudes, the emitted energy, and amount of angular momentum radiated depend sensitively on the r-mode dimensionless saturation amplitude $\alpha_{\max}$. If not limited by viscosity or magnetic fields, early optimistic estimates by Lindblom et al. [358–361] saw the r-mode amplitude grow to $\alpha_{\max} \sim 1$ within $\sim$10 minutes of core bounce for a millisecond neutron star. Similar results were found by Stergioulas & Font [362] in 2001.

More recent studies of non-linear mode couplings between the unstable r-mode and higher-order inertial modes by Arras et al. [363, 364] and non-linear 3D Newtonian hydrodynamics simulations by Gressman et al. [365] suggest that $\alpha_{\max} \ll 1$. If $\alpha_{\max}$ is indeed $\ll 1$, then the gravitational wave emission from r-modes in compact stars is likely undetectable.

[28] Strictly speaking, it can have axial w-modes in GR[286].

[29] The number is based on the number of articles with "r mode" in their abstract published between 1998 and 2003 as returned by NASA ADS (`http://adswww.harvard.edu`). The estimate is conservative given that `http://scholar.google.com` found 1880 entries for "r modes" and 5280 for "r-mode" on November 10, 2006.

Chapter 3

GR Core-Collapse Simulations: Implementation

In this Chapter I give an overview of the numerical methods and tools that I have used in my research. This includes a discussion of the computational framework CACTUS, the mesh-refinement driver CARPET, the AEI spacetime evolution code, and the general-relativistic hydrodynamics code WHISKY. In Section 3.6 of this Chapter I detail the features with which I have augmented WHISKY's capabilities for performing astrophysical simulations in the core-collapse supernova context. Finally, I describe various analysis tools including gravitational-wave extraction methods.

Note that all of CACTUS, CARPET, and WHISKY is to be seen as a collaborative effort to which I have contributed in the course of my dissertation research. This involved technical code development, including the idea, the first implementation and the first use of progressive mesh refinement in CARPET (see §3.4) which greatly reduced the average runtime needed for a collapse simulation from the standard fixed mesh-refinement case and for the first time allowed fully self-consistent core collapse simulations in {3+1} numerical relativity. In addition, I have added code for chemical species advection in collaboration with I. Hawke, coupled a finite-temperature equation of state to WHISKY and implemented a simple yet effective deleptonization treatment for the collapse phase of core-collapse supernovae.

3.1 The Cactus Code

The CACTUS code [366, 367] is an open-source framework for scientific computing. CACTUS development began in the mid 1990s at the National Center for Supercomputing Applications (NCSA) in Urbana-Champaign, Illinois, USA when researchers in the center's numerical relativity group around Edward Seidel realized that it would be advantageous to separate scientific (numerical relativity) code development into *framework*, *infrastructure/driver* and *physics application* parts. In this way, scientists would only have to write physics-related code and could rely on a well-tested generic infrastructure for parallelization and standard tasks like input/output. CACTUS 1 was released on April 24, 1997 when Seidel's group had moved to the AEI. Development has continued since then at the AEI and, since 2003, also at the Center for Computation and Technology (CCT) at Louisiana State University (LSU) in Baton Rouge, Louisiana, USA.

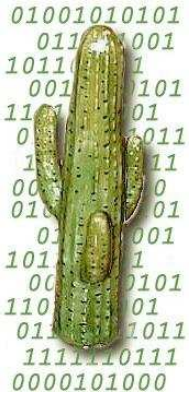

The core of CACTUS, its *Flesh*, only provides an interface for and the management of infrastructure/driver and physics modules (*Thorns*). Infrastructure thorns provide input/output functionality, manage and apply boundary and symmetry conditions, carry out numerical time integration, facilitate numerical grid setup, and provide additional high-level features such as web-based application control. Driver thorns are of exceptional importance. The driver controls the overall evolution of a simulation (scheduling of routines/thorns to be called, memory allocation), parallelization (interprocessor communication, domain decomposition) and mesh refinement. The physics thorns interface through the CACTUS application programming interface (API) with the driver and infrastructure and other physics thorns.

Currently, CACTUS is actively used by the numerical relativity community, by fluid-dynamics specialists and quantum gravity researchers. Specifically for the numerical relativity community, CACTUS includes the CACTUSEINSTEIN [368] arrangements of thorns that provide basic variables and functionality (e.g., for analysis and curvature–matter coupling) for {3+1} evolutions.

3.2 The Method of Lines

The NOK-BSSN system and the equations of general-relativistic hydrodynamics are discretized via standard finite-difference/finite-volume methods, but are kept semi-discrete in the sense that on the physics-module level, the equations are finite differenced only in space, retaining the continuous time derivatives. The time integration is then performed in an independent generic step. This procedure is referred to as the *Method of Lines* (MoL) and is equivalent to transforming a set of partial differential equations (PDEs) into ordinary differential equations (ODEs) in time that then can be integrated with standard ODE integrators. MoL is a widely used scheme in numerical relativity and fluid dynamics and has been extensively discussed by Hyman [370–372] and Thornburg [121]. Here I shall only delineate its most salient features and limit the discussion of MoL to one dimension in space and time, geared towards numerical hydrodynamics. The generalization to multiple spatial dimensions is straightforward.

As an example, I consider the simple continuum PDE,

$$q(x,t)_{,t} + f(q(x,t))_{,x} = s(q(x,t)) \ , \tag{3.1}$$

where $q = q(x,t)$ is the evolved variable, $f = f(q(x,t))$ is the flux term, and $s(q(x,t))$ is a source term. This could be interpreted as an advection equation for a chemical species with a source/sink term. In order to transform (3.1) into an ODE, I now perform the spatial discretization. I rewrite the equations in terms of cell averages located at the cell center of cell i at x_i:

$$\bar{q}_i \equiv \frac{1}{\Delta x_i} \int_{x_{i-1/2}}^{x_{i+1/2}} q(x)\, dx \, , \tag{3.2}$$

with $\Delta x_i = x_{i+1/2} - x_{i-1/2}$. This is necessary because spatial discontinuities in q_i may be present in which case the spatial derivative of q_i becomes undefined. The spatial derivative of the cell average $\bar{q}_i$, however, remains well defined even if a discontinuity is present. Equation (3.1) now reads

$$\frac{1}{\Delta x_i} \int_{x_{i-1/2}}^{x_{i+1/2}} \left[q_{,t} + f_{,x} \right] dx = \bar{s}_i \, . \tag{3.3}$$

By pulling out the partial time derivative, integrating the flux term and moving it to the right-hand side, the resulting ODE reads

$$\frac{d}{dt}\bar{q}_i = \bar{s}_i - \frac{1}{\Delta x_i}\left[f_{i+1/2} - f_{i-1/2} \right] \equiv L(\bar{q}_i). \tag{3.4}$$

The order of spatial accuracy of this scheme depends on the accuracy to which the source terms $\bar{s}_i$ and the cell-interface fluxes, $f_{i+1/2}$ and $f_{i-1/2}$, are determined. If the cell-interface fluxes and the source terms are obtained with first order accuracy in time then the overall temporal accuracy is determined by the ODE integrator employed to integrate equation (3.4). The transformation from PDE to ODE form and the spatial discretization of the ADM and NOK-BSSN system is considerably simpler (see, e. g., [121]) and is performed with standard second-order or fourth-order finite differencing.

In CACTUS, all right-hand side contributions $L(\bar{q}_i)$ are calculated by the physics module (*thorn*) responsible for the physical variable q_i. Time integration is then performed by the CACTUS thorn `CactusBase/MoL` with standard Runge-Kutta or iterative Crank-Nicholson time integrators. The physics thorn is called at each intermediate step (in multi-level schemes) to provide an updated $L(\bar{q}_i)$.

3.2.1 ODE Time Integrators implemented in `CactusBase/MoL`

For completeness and future reference I list the implemented ODE time integrators.

Runge-Kutta Integrators

The first-order accurate Runge-Kutta method (the standard Euler method; matching a first-order Taylor series expansion) to numerically integrate f from time step n to $n+1$ is given by:

$$\begin{aligned} f^{(0)} &= f^n \\ f^{(1)} &= f^{(0)} + \Delta t\, L(f^{(0)}) \\ f^{n+1} &= f^{(1)} \,. \end{aligned} \tag{3.5}$$

Here indices in parentheses indicate intermediate steps / levels. The second-order method (in the formulation of Shu [373, 374]) is

$$\begin{aligned} f^{(0)} &= f^n \\ f^{(1)} &= f^{(0)} + \Delta t\, L(f^{(0)}) \\ f^{(2)} &= \frac{1}{2}\left[f^{(0)} + f^{(1)} + \Delta t\, L(f^{(1)})\right] \\ f^{n+1} &= f^{(2)} \,. \end{aligned} \tag{3.6}$$

The third-order Runge-Kutta reads

$$\begin{aligned} f^{(0)} &= f^n \\ f^{(1)} &= f^{(0)} + \Delta t\, L(f^{(0)}) \\ f^{(2)} &= \frac{1}{4}\left[3f^{(0)} + f^{(1)} + \Delta t\, L(f^{(1)})\right] \\ f^{(3)} &= \frac{1}{3}\left[f^{(0)} + 2f^{(2)} + 2\Delta t\, L(f^{(2)})\right] \\ f^{n+1} &= f^{(3)} \,. \end{aligned} \tag{3.7}$$

And the fourth-order integrator as given in [373, 374] reads

$$\begin{aligned} f^{(0)} &= f^n \\ f^{(1)} &= f^{(0)} + \frac{1}{2}\Delta t\, L(f^{(0)}) \\ f^{(2)} &= f^{(0)} + \frac{1}{2}\Delta t\, L(f^{(1)}) \\ f^{(3)} &= f^{(0)} + \Delta t\, L(f^{(2)}) \\ f^{(4)} &= \frac{1}{6}\left[-2f^{(0)} + 2f^{(1)} + 4f^{(2)} + 2f^{(3)} + \Delta t\, L(f^{(3)})\right] \\ f^{n+1} &= f^{(4)} \,. \end{aligned} \tag{3.8}$$

The time step size Δt has to obey the Courant-Friedrich-Lewy (CFL) stability criterion [375] and is – in the case of dynamical General Relativity – bounded by the light-crossing time through the grid cell with smallest physical extent and by the time it takes for gauge information to propagate through the smallest cell. This may well be shorter than the light-crossing time [120]. In addition, stability properties of the evolved equations and the discretization scheme chosen impinge on the maximal time step size and the stability of the chosen ODE integration scheme.

Iterative Crank-Nicholson Integrators

The second class of ODE integrators in `CactusBase/MoL` are of iterative Crank-Nicholson (ICN) type. ICN is an explicit version of the standard implicit Crank-Nicholson (CN) scheme [376]. ICN replaces

the implicit time integration by an iterative procedure, where each iteration is an explicit operation depending only on previous data. It retains the good stability properties of the implicit CN scheme.

$$\begin{aligned} f^{(0)} &= f^n \\ f^{(i)} &= f^{(0)} + \frac{\Delta t}{2} L(f^{(i-1)}) \\ f^{(N)} &= f^{(0)} + \frac{\Delta t}{2} L(f^{(N-1)}) \\ f^{n+1} &= f^{(N)} \ . \end{aligned} \tag{3.9}$$

Alcubierre et al. [144] and Teukolsky [377] (see also Leiler & Rezzolla [378]) have shown that $N = 3$ results in a stable, second-order accurate scheme, given a time step Δt that obeys the Courant-Friedrich-Lewy (CFL) stability criterion [375].

Total-Variation Diminishing Property

An important property of any numerical integration scheme to be used with nonlinear systems is its ability to preserve monotonicity, that is, to not introduce artificial high-frequency oscillations into the solution. A way of measuring the amount of numerical oscillations introduced by a numerical scheme is to consider the *total variation* for a discretized function f^n at time step n [151, 152]:

$$TV(f^n) \equiv \sum_i |f_i^n - f_{i-1}^n| \ , \tag{3.10}$$

where i is the cell index. A scheme is total-variation diminishing (TVD) if

$$TV(f^{n+1}) \leq TV(f^n) \ \ \forall n \ . \tag{3.11}$$

Harten [379] (see also the discussion in Toro [151]) has demonstrated that any scheme that is TVD is also monotonicity preserving.

The first (Euler), second and third-order Runge-Kutta schemes are TVD, while the fourth-order is not [380]. Since ICN is constructed as a sequence of simple Euler steps, it is TVD. In the high-resolution shock-capturing approach to numerical fluid dynamics, the TVD nature of cell-interface reconstruction schemes is of ultimate importance. More details are discussed in §3.5.1.

3.3 The BSSN_MoL Spacetime Evolution Code

BSSN_MoL evolves the {3+1} Einstein equations in the NOK-BSSN [104, 140, 141] formulation with the Method of Lines (MoL) time discretization scheme which I have discussed in § 3.2 of this dissertation. The spatial discretization is performed via standard centered second- or fourth-order accurate finite differences. BSSN_MoL is a CACTUS thorn and was developed and is maintained at the AEI. The original code was written by Miguel Alcubierre and Gabrielle Allen. Code details, tests and analyses were published in Alcubierre et al. (2000) [144]. Ian Hawke has converted the code to use MoL and Denis Pollney added fourth-order accurate finite differencing.

My original contribution to the BSSN_MoL code is the implementation of a hyperbolic coordinate shift condition approximating the well-known elliptic minimal distortion condition of Smarr and York [381]. My implementation is similar to the shift condition proposed by Shibata [381].

In the following, I will briefly introduce the NOK-BSSN evolution system as implemented in the BSSN_MoL code. I will also present an overview of the gauge and boundary conditions used in this dissertation.

3.3.1 The NOK-BSSN Evolution System

As already mentioned in §2.4.3, the ADM equations have undesirable stability properties that render long-term stable numerical evolutions nearly impossible, and the numerical relativity community has invested great effort into finding better formulations of Einstein's equations for numerical relativity. One evolution system which is empirically found to behave relatively stable is NOK-BSSN[1] (Nakamura-Oohara-Kojima – Baumgarte-Shapiro-Shibata-Nakamura) [104, 140, 141].

NOK-BSSN makes use of a conformal decomposition (see §2.4.4 for a similar conformal-type decomposition that is, however, primarily used for initial data generation) of the ADM 3-metric and the trace-free part of the extrinsic curvature 3-tensor. I now follow the discussion in Alcubierre et al. [144]. The conformal 3-metric $\tilde{\gamma}_{ij}$ is related to the 3-metric via

$$\tilde{\gamma}_{ij} \equiv e^{-4\phi}\gamma_{ij}\,, \tag{3.12}$$

with the conformal factor fixed by

$$\Psi^4 \equiv e^{4\phi} = \det(\gamma_{ij})^{\frac{1}{3}} = \gamma^{\frac{1}{3}}\,, \tag{3.13}$$

yielding $\det(\tilde{\gamma}_{ij}) = 1$. The trace-free part of the extrinsic curvature K_{ij}, defined by

$$A_{ij} \equiv K_{ij} - \frac{1}{3}\gamma_{ij}K\,, \tag{3.14}$$

where $K = K^i_i$, is also conformally decomposed:

$$\tilde{A}_{ij} \equiv e^{-4\phi}A_{ij}\,. \tag{3.15}$$

The evolved variables of NOK-BSSN are [144]

$$\phi = \ln\Psi = \frac{1}{12}\ln\gamma\,, \tag{3.16}$$

$$K = K^i_i = \gamma^{ij}K_{ij}\,, \tag{3.17}$$

$$\tilde{\gamma}_{ij} = e^{-4\phi}\gamma_{ij}\,, \tag{3.18}$$

$$\tilde{A}_{ij} = e^{-4\phi}A_{ij}\,. \tag{3.19}$$

[1] Note that I choose to call NOK-BSSN what is in the literature widely known as BSSN. I do this in honor of the original proposition of a conformal-traceless recast of the ADM equations by Nakamura-Oohara-Kojima [104].

In terms of these variables, the ADM equations (2.28) and (2.29) are split into

$$\left(\frac{\partial}{\partial t} - \mathcal{L}_{\boldsymbol{\beta}}\right)\tilde{\gamma}_{ij} = -2\alpha\tilde{A}_{ij} \tag{3.20}$$

$$\left(\frac{\partial}{\partial t} - \mathcal{L}_{\boldsymbol{\beta}}\right)\phi = -\frac{1}{6}\alpha K \tag{3.21}$$

$$\left(\frac{\partial}{\partial t} - \mathcal{L}_{\boldsymbol{\beta}}\right)K = -\gamma^{ij}\tilde{\nabla}_i\tilde{\nabla}_i\alpha + \alpha\left(\tilde{A}_{ij}\tilde{A}^{ij} + \frac{1}{3}K^2 + \frac{1}{2}(\rho_{ADM} + S)\right) \tag{3.22}$$

$$\left(\frac{\partial}{\partial t} - \mathcal{L}_{\boldsymbol{\beta}}\right)\tilde{A}^{ij} = e^{-4\phi}[-\tilde{\nabla}_i\tilde{\nabla}_j\alpha + \alpha(R_{ij} - S_{ij})]^{TF} + \alpha(K\tilde{A}_{ij} - 2\tilde{A}_{il}\tilde{A}^l_j)\,, \tag{3.23}$$

where the evolution equation for the trace of the extrinsic curvature (3.22) is obtained via using the Hamiltonian constraint to eliminate the Ricci scalar R [144] and TF denotes the trace-free part of the term in brackets. Note that I am here not using the short notation for covariant derivatives and instead denote covariant derivatives with respect to the conformal 3-metric $\tilde{\gamma}_{ij}$ by $\tilde{\nabla}_i$. As shown in [140, 141], it is desirable to rewrite equation (3.23) using the conformally decomposed Ricci tensor,

$$R_{ij} = \tilde{R}_{ij} + R^{\phi}_{ij}\,, \tag{3.24}$$

where the term involving the logarithm of the conformal factor ($\phi = \ln\Psi$) is given by the computation of the derivatives of ϕ:

$$R^{\phi}_{ij} = -2\tilde{\nabla}_i\tilde{\nabla}_j\phi - 2\tilde{\gamma}_{ij}\tilde{\nabla}^l\tilde{\nabla}_l\phi + 4\tilde{\nabla}_i\phi\ \tilde{\nabla}_j\phi - 4\tilde{\gamma}_{ij}\tilde{\nabla}^l\phi\ \tilde{\nabla}_l\phi\ . \tag{3.25}$$

The conformal part $\tilde{R}_{ij}$ is computed in the standard way from the conformal 3-metric. To simplify notation, it is convenient to define *conformal connection functions* [141] by contracting the 3-Christoffel symbols via the conformal 3-metric[2]:

$$\tilde{\Gamma}^i \equiv \tilde{\gamma}^{jk}\tilde{\Gamma}^i_{jk} = -\tilde{\gamma}^{ij}_{,j}\ . \tag{3.26}$$

Here the latter equality only holds if the determinant of the conformal 3-metric $\tilde{\gamma}$ is actually unity (which holds analytically, but possibly not numerically). The conformal Ricci tensor then reads:

$$\tilde{R}_{ij} = -\frac{1}{2}\tilde{\gamma}^{lm}\tilde{\gamma}_{ij,lm} + \tilde{\gamma}_{k(i}\partial_{j)}\tilde{\Gamma}^k + \tilde{\Gamma}^k\tilde{\Gamma}_{(ij)k} + \tilde{\gamma}^{lm}\left(2\tilde{\Gamma}^k_{l(i}\tilde{\Gamma}_{j)km} + \tilde{\Gamma}^k_{im}\tilde{\Gamma}_{klj}\right). \tag{3.27}$$

Alcubierre et al. [144] found it advantageous for numerical stability to time-evolve the $\tilde{\Gamma}^i$ as independent variables. An evolution equation is straightforwardly obtained from definition (3.26) and the evolution equation for the conformal 3-metric (3.20), and writing out the Lie-derivative terms:

$$\frac{\partial}{\partial t}\tilde{\Gamma}^i = -\frac{\partial}{\partial x^j}\left(2\alpha\tilde{A}^{ij} - 2\tilde{\gamma}^{m(j}\beta^{i)}_{,m} + \frac{2}{3}\tilde{\gamma}^{ij}\beta^l_{,l} + \beta^l\tilde{\gamma}^{ij}_{,l}\right). \tag{3.28}$$

However, as demonstrated by Alcubierre et al. [144] it is crucial for stability to eliminate the divergence of $\tilde{A}^{ij}$ by means of the momentum constraint. Alcubierre et al. [144] then obtain (as implemented in BSSN_MoL)

$$\begin{aligned}\frac{\partial}{\partial t}\tilde{\Gamma}^i = &-2\tilde{A}^{ij}\alpha_{,j} + 2\alpha\left(\tilde{\Gamma}^i_{jk}\tilde{A}^{kj} - \frac{2}{3}\tilde{\gamma}^{ij}K_{,j} - \tilde{\gamma}^{ij}S_j + 6\tilde{A}^{ij}\phi_{,j}\right)\\ &-\frac{\partial}{\partial x^j}\left(\beta^l\tilde{\gamma}^{ij}_{,l} - 2\tilde{\gamma}^{m(j}\beta^{i)}_{,m} + \frac{2}{3}\tilde{\gamma}^{ij}\beta^l_{,l}\right).\end{aligned} \tag{3.29}$$

To summarize: NOK-BSSN rewrites the ADM variables and evolves the set $\{\phi, K, \tilde{\gamma}_i j, \tilde{A}_{ij}, \tilde{\Gamma}^i\}$ of independent variables with a first-order-in-time, second-order-in-space evolution system. NOK-BSSN's greater stability has been determined empirically (see, e.g., [144]). Note, however, that, leaving the stability issue aside, for the same numerical accuracy (measured in terms of constraint deviation), NOK-BSSN requires finer numerical grid resolution than ADM [144]. A detailed analysis of the system's hyperbolicity and stability properties is very involved and has only recently been approached [143, 383].

[2]Note that the $\tilde{\Gamma}^i$ – like the Christoffel symbols – are not tensors and have a rather complicated transformation behavior, a derivation of which can be found in Thornburg[382].

3.3.2 Gauge Conditions

BSSN_MoL and WHISKY have been designed to handle arbitrary choices of lapse and shift. Given the knowledge of the covariance of the continuum Einstein equations, a naive first choice is setting $\alpha = 1$ (geodesic slicing) and $\beta^i = 0$ for all times. Again, at first glance and in the limit of infinite spatial and temporal resolution, there is no whatsoever problem related to this choice[3]. Now, in any realistic setting, resolution will be finite and the coordinates must be chosen in such a way that the physical problem in question (stellar core collapse) can be solved numerically, given the chosen formulation of the equations and discretization methods. In direct consequence of GR's covariance, it is very difficult (if not impossible) to predict mathematically what set of coordinates is most appropriate for a given physical problem. The answer is left to empirical investigation and, importantly, *physical intuition*.

In binary black hole merger simulations, for example, numerical relativists try to exploit symmetries of the system: only one black hole is evolved on an octant of a cubical spacetime volume. In addition, a co-rotating coordinate system is chosen via an appropriate shift condition. A similar choice of shift could be adopted for a rigidly rotating neutron star[4]. For a differentially rotating neutron star or, more extreme, for a collapsing (rotating / nonrotating) star, simple symmetry-based coordinate choices become impossible and must be replaced by more involved choices of lapse function and shift.

Slicing Conditions

The above mentioned simplest possible lapse function, geodesic slicing, creates a "synchronous" reference system with time advancing at the same rate everywhere. Eulerian observers are freely falling and for $\beta^i = 0$ coordinate and Eulerian observers coincide. However, geodesic slicing is a particularly poor choice for most numerical simulations. In a numerical black hole spacetime, for example, every coordinate observer will fall into the singularity in a finite time, leading to the focussing of geodesics and the inevitable break down of the numerical simulation (for a more detailed discussion see, e.g., [120] and B. Reimann's dissertation [384]). Even in the – when compared to a black hole – mildly relativistic collapse of a stellar iron core to a neutron star, geodesic slicing leads to numerical instabilities at early times (see the code test Sections in Chapter 4) and is hence not an appropriate choice.

To avoid the pathologies associated with geodesic slicing, so-called *singularity avoiding* slicings have been introduced. The prime example for singularity avoiding slicings is the *maximal slicing* condition

[3] A detailed analysis [384], however, shows that even in the analytic limit, geodesic slicing can lead to gauge pathologies.

[4] Note that such a choice, since based on a global coordinate-frame assumption, does not take into account frame dragging by the rotating compact object(s) and thus typically does not allow long-term stable evolutions.

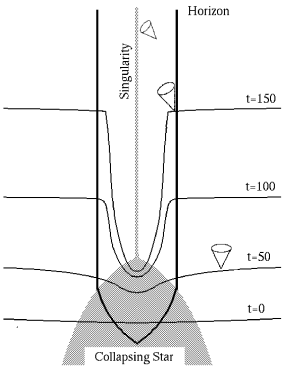

Figure 3.1: Schematic diagram of singularity avoiding slicings. As the evolution progresses from $t = 0$ to $t = 150$ the lapse function α "collapses" at the center of the collapsing star, slowing down the evolution (as seen from an asymptotic observer). However, the large gradients in the lapse may lead to numerical problems (slice stretching). Figure taken from [385].

which leads to an elliptic condition for the lapse function, fixing the trace of the extrinsic curvature to $K = 0$ and $K_{,t} = 0$. Singularity avoiding slicings "slow down" evolution close to strongly gravitating objects while allowing the exterior evolution to continue practically unhindered. However, as shown in figure 3.1, singularity avoiding slicings also lead to large gradients in the lapse function. This effect is frequently referred to as *slice stretching*. Slice stretching due to singularity avoiding slicing may be a major problem in numerical simulations of black hole spacetimes [384].

For the generalized maximal slicing condition $K = \text{const.}$, the *K*-freezing condition, Alcubierre et al. [144] and Baumgarte & Shapiro [120] give the following elliptic equation for the lapse:

$$\Delta\alpha = \beta^i K_{,i} + \alpha\left(K_{ij}K^{ij} + 4\pi(\rho_{\mathrm{ADM}} + S)\right) \tag{3.30}$$

with Δ being the Laplacian operator for the ADM 3-metric γ_{ij}. For $K = 0$ maximal slicing is recovered. The numerical solution of the elliptic equation (3.30) is computationally very expensive and, for 3D numerical simulations, one typically resorts to hyperbolic variants of maximal slicing. Implemented in BSSN_MoL is the hyperbolic *K-driver* condition:

$$\partial_t\alpha = -\alpha^2 f(\alpha)(K - K_0)\,, \tag{3.31}$$

where $f(\alpha)$ is an arbitrary function of the lapse and $K_0 = K(t = 0)$. With the choice

$$f(\alpha) = \frac{2}{\alpha} \tag{3.32}$$

one obtains the standard singularity avoiding $1 + \log$ slicing[5] [139, 386] which I use in the simulations presented in this thesis. Another frequently used choice is $f(\alpha) = 1$ which is known as *harmonic* slicing and is only marginally singularity avoiding. This means that a singularity will be reached at infinite coordinate time in the continuum limit [387].

Shift Conditions

For most astrophysically interesting problems (e.g. collapse scenarios, [differentially] rotating stars, inspiralling compact objects) it is impossible to prescribe the change of coordinates for a numerical simulation from one spacelike hypersurface to the next based on global coordinate-frame assumptions. Naive choices of the coordinate shift vector β^i, for example, $\beta^i = 0$, quickly lead to numerical instabilities. As an example why this is the case, consider a rotating compact object (e.g. a rotating neutron star or a Kerr black hole) which "drags" spacetime in a swirl-like fashion (see, e.g., [116]) with it. Because of this, the physical grid cells in a numerical simulation become distorted (stretched and bent). Eventually, the distortion will become too large to be handled accurately by the numerical evolution scheme and the evolution will go unstable. Exactly when this happens depends, of course, on the quality of the discretization, the properties of the evolution equations and the physical model parameters. For long-term stable evolutions it is necessary to use a local prescription of the coordinate shift that adjusts the coordinates in such a way that the numerical evolution remains accurate and stable.

A geometrically motivated *local* choice for the shift vector is minimal distortion proposed by Smarr and York [188]. They define the distortion tensor Σ_{ij} by

$$\Sigma_{ij} = \frac{1}{2}\gamma^{\frac{1}{3}}\tilde{\gamma}_{ij\,,t}\,. \tag{3.33}$$

The distortion tensor quantifies the change in shape of a test volume dragged along from hypersurface Σ_t to Σ_{t+dt}. Via minimizing the *shear stretching energy* given by $S = \frac{1}{2}\int_{\Sigma_t}\Sigma_{ij}\Sigma^{ij}\sqrt{\gamma}d^3x$, Smarr and York obtain the minimal distortion condition,

$$\Sigma^{ij}{}_{;i} = 0\,, \tag{3.34}$$

[5] The name $1 + \log$ stems from the integrated form of the slicing condition given by $\alpha = h(x^i) + \ln(\gamma)$, where $h(x^i)$ is a time-independent function and γ is the determinant of the 3-metric. [122, 139]

which yields a set of coupled elliptic equations for β^i which are computationally very demanding to solve. Minimal distortion can also be viewed as adjusting the coordinates in such a way as to minimize the purely coordinate-dependent changes of the 3-metric γ_{ij} [120]. Interestingly, the original minimal distortion condition was not very successful in numerical black hole simulations [388].

In the NOK-BSSN context, the elliptic *Gamma-freezing* condition, $\tilde{\Gamma}^i{}_{,t} = 0$, is closely related to minimal distortion [389]. For consistency, frequent computations of the shift vector are necessary and should – preferably – be carried out for every time step. Since elliptic equations are computationally very demanding – especially in 3D simulations relying on domain decomposition – non-elliptic approximations to minimal distortion have been derived. The *Gamma-driver* shift conditions introduced by Alcubierre et al. [389] and implemented in BSSN_MOL, for example, used the $\tilde{\Gamma}^i$ evolution equations (3.29) to derive a shift evolution that "drives" the $\tilde{\Gamma}^i$ to a constant, approximating Gamma freezing. The hyperbolic Gamma-driver shift reads

$$\frac{\partial^2}{\partial t^2}\beta^i = F\,\tilde{\Gamma}^i{}_{,t} - \eta\beta^i{}_{,t}\ , \tag{3.35}$$

where F and η are arbitrary positive functions of space and time. F is usually chosen to be $(3/4)\,\alpha$ in order to have the longitudinal part of the shift propagate with the speed of light [389]. $-\eta\beta^i{}_{,t}$ is a dissipation term introduced by Alcubierre et al. [389] to avoid strong oscillations of the shift. It should be set to $\sim 1/\tau_D$, τ_D being a characteristic dynamical time scale of the system.

Recently, Shibata [381] has introduced the dynamical first-order-in-time hyperbolic shift condition

$$\beta^i{}_{,t} = \tilde{\gamma}^{il}(F_l + \Delta t F_{l\,,t}) \tag{3.36}$$

where $F_l = \delta^{jk}\tilde{\gamma}_{ik\,,j}$ are his equivalents to the $\tilde{\Gamma}^i$ used in BSSN_MOL. I have implemented

$$\beta^i{}_{,t} = (\tilde{\Gamma}^i + \Delta t\,\tilde{\Gamma}^i{}_{,t})\ , \tag{3.37}$$

which is equivalent to the above up to derivatives of the conformal 3-metric. Similarly to Shibata, I find that the shift condition specified by equations (3.37) and (3.36) lead to excellent code stability in my core collapse simulations. For a series of test simulations with different shift conditions see section 4.3.3 in this dissertation.

3.3.3 Boundary Conditions

In the {3+1} simulations discussed in this thesis, the computational domain covers only a finite region of the spatial 3-hypersurfaces and hence only a finite volume of spacetime. Hence, it is necessary to specify boundary conditions. Ideally, the boundary conditions should satisfy the constraint equations and allow gravitational waves coming from any direction to leave the grid without reflections. In the case of ADM/NOK-BSSN finding appropriate boundary conditions is highly non-trivial, in particular, because some of the evolved variables are tensors, some are tensor densities and the $\tilde{\Gamma}^i$ have their own special transformation behavior.

In BSSN_MOL the boundary conditions for the NOK-BSSN Einstein field variables are treated in a simplistic fashion by assuming the Sommerfeld outgoing-radiation boundary condition implemented by Alcubierre et al. [122, 389]:

$$f = f_0 + \frac{u(r - vt)}{r}\,. \tag{3.38}$$

Here f is the boundary value of the considered field variable, f_0 is its asymptotic value and v is the wave speed. For most field variables $f_0 = 0$ and $v = 1$ are chosen to approximate the Minkowski values. For the lapse and the diagonal 3-metric components $f_0 = 1$ is used. For α, $\phi = \ln\Psi$ and K the wave speed $v = \sqrt{2}$ is used since they travel at the gauge speed set by the $1 + \log$ slicing [389]. The boundary condition (3.38) is constraint violating and a wave of constraint violation emerges from the outer boundary and propagates through the grid. This is a major concern in black hole simulations, especially in binary merger simulations with ad-hoc shift for co-rotating coordinates [122]. In the stellar core collapse problem the grid boundaries prove unproblematic since they are located at $\sim$3000 km distance from the grid center. That distance corresponds to $\sim$100 times the radius of the formed protoneutron star, hence, the grid boundaries are sufficiently far away from the strong-field region for the spacetime to be close to Minkowski.

3.3.4 Artificial Dissipation

Due to the nonlinearity of the ADM / NOK-BSSN equations (as for any set of nonlinear PDEs), artificial high-frequency noise enters the solution in any second or higher-order standard finite difference scheme and may, in the presence of large gradients or shocks, drive the system to instability[6]. In addition, in the presence of discontinuities in the matter variables, the curvature-matter coupling leads to discontinuities in the second spatial derivatives of the curvature variables ([390] and see, e.g., equation (2.52) in §2.4.4). Since the coupling occurs on the level of the second spatial derivatives, the 3-metric itself remains differentiable even in the presence of hydrodynamic shocks and essentially smooth for the strength of shocks encountered in the core-collapse supernova problem. Hence, it is sufficient and accurate to use a small amount of artificial dissipation to suppress high-frequency modes in the numerical evolution (see, e.g., [391, 392]).

In my simulations I use the Kreiss-Oliger [392] fourth-order dissipation operator Q^4, defined for evenly spaced grids by

$$Q^4 = \epsilon h^3 D^4 \ , \tag{3.39}$$

where h is the grid spacing, ϵ is a small constant which I typically chose to be 0.2 and D^4 is the symmetric fourth-order difference operator given by

$$D^4 u^n_j \equiv \frac{1}{16} \frac{u^n_{j+2} - 4u^n_{j+1} + 6u^n_j - 4u^n_{j-1} + u^n_{j-2}}{h^4} \ . \tag{3.40}$$

Here u^n_j is the discretized quantity at time level n and at grid point j. Due to the h^3 factor, Q^4 is third-order convergent. Hence, it reduces the numerical convergence of the fourth-order variant of BSSN_MoL to third order, but does not affect the convergence behavior of the second-order BSSN_MoL.

Dissipation is added as an additional right-hand side update term in the MoL time integration according to

$$u_{,t} = u_{,t} - Q^4 u \ . \tag{3.41}$$

[6] A first-order accurate finite-difference approximation acts similarly to a low-pass filter in this context; higher-order methods allow higher-frequency spatial modes to enter the solution, some of which are unphysical and may grow without bounds.

3.4 Mesh Refinement and the Carpet Code

Stellar core-collapse is a problem of multiple length scales. A typical stellar iron core has a mass of $\gtrsim 1.5\,M_\odot$ and extends out to $\sim$1500 – 2000 km. It has a precollapse central density of a few times 10^9 – 1×10^{10} g cm^{-3}. During collapse, the innermost part of the iron core (roughly $\sim 0.7\,M_\odot$) contracts to a radius of $\sim$15 – 20 km and reaches densities on the order of 10^{13} – 10^{14} g cm^{-3}. Based on the experience gained over many decades of core-collapse simulations (see also the resolution study tests in Section 4.3 of this dissertation), a central computational cell size of not greater than $\sim$500 m is required to adequately cover the final collapse phase (the *plunge*) and core bounce during which velocities of up to 20% of the speed of light and extremely large accelerations are encountered. In addition, the formed protoneutron star must be covered with a sufficient number of grid cells ($\gtrsim 20$) to allow for its stable evolution on the numerical grid (also: *mesh*).

A Cartesian coordinate grid that is equally spaced with $\sim$ 500 m cell size (on a side) and that extends out to 2000 km would have to be composed of $(4000)^3$ cells – a grid size that would fit only into the main memory of today's biggest supercomputers. Performing a simulation with such a grid would also require an outrageous amount of CPU hours on today's fastest supercomputers. It would be impossible to complete even a single simulation run within a 3-year dissertation period.

One approach to evade this problem is to use spherical-polar coordinate grids with non-equidistant *radial* cell sizes[7], providing high resolution in the central region of the mesh where it is needed most and putting fewer cells at large radii, where densities, velocities and accelerations are small. Such a non-equidistant zoning may be seen as an example of *fixed mesh refinement* (FMR): optimizing the distribution of grid cells based on an *a priori* knowledge of how much resolution and where the resolution is required. For {3+1} numerical relativity, spherical coordinates are suboptimal, since their coordinate singularity on the z-axis requires special treatment (see, e.g., [393]). Hence, one – as in this work – resorts to Cartesian meshes that do not contain coordinate singularities, but for which even fixed mesh refinement poses a considerable technical challenge.

In contrast to fixed mesh refinement, *adaptive mesh refinement* (AMR) does not rely on prior knowledge of where in the computational domain what resolution is needed, but refines the mesh in response to some criterion such as the local finite-difference truncation error (see, e.g., [394–396] and references therein). AMR provides, ideally, a very high degree of computational efficiency for a given problem: resolution is added and removed where suitable, leading to the optimal number of numerical cells at any point during a simulation. However, if the truncation error criterion is not chosen with great care (the criterion may have to be modified dynamically during the course of a simulation), AMR can lead to large computational overhead (refining where no refinement is needed) or large numerical errors (not refining where refinement is needed).

In the stellar core-collapse problem, the resolution requirements are known beforehand, but the full resolution is not needed until the plunge phase of collapse. Hence, I have – in collaboration with Burkhard Zink, Ian Hawke, and Erik Schnetter – introduced the concept of *progressive mesh refinement* (PMR). In PMR, the mesh hierarchy (the mesh resolutions, positions and nesting of refined meshes) is predefined, but the simulation is started only with the resolution needed for the initial phase of collapse. Additional levels of refinement are activated when a simple, empirically determined criterion is met; for example, when certain threshold values of the maximum rest-mass density on the grid are reached. The PMR method, which has also been used in the context of neutron-star collapse to black holes by Baiotti et al. [163], provides high computational efficiency to the stellar-core collapse problem in {3+1} numerical relativity in Cartesian coordinates while maintaining numerical accuracy and numerical convergence.

CARPET

CARPET [391, 397] is a mesh refinement driver thorn for Cactus written mainly in C++. CARPET uses the Berger-Oliger approach [394] to mesh refinement, where the computational domain as well as all refined subdomains consist of a set of rectangular grids. The grid points are located on a Cartesian

[7] Note that applying non-equidistant radial cell sizes to a Cartesian mesh leads to distorted cells for which standard finite-difference / finite-volume methods are not applicable.

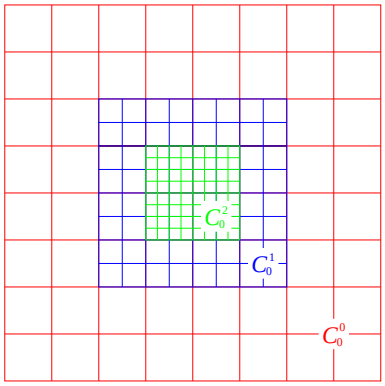

Figure 3.2: Two-dimensional exemplary box-in-box refinement hierarchy with three refinement levels, each having only one component. For a typical model simulation, I use 9 refinement levels with one component each and each comprising 64^3 grid points. This figure has been adapted from [391].

grid and the grid boundaries are aligned with the grid lines. CARPET currently only supports vertex-centered refinement, that is, coarse-grid points coincide with fine-grid points. The concept of a grid point is somewhat confusing in this context. For WHISKY, grid points mark computational *cell centers*, while CARPET assumes grid points to lie on cell vertices. This discrepancy does not cause problems in the interior of refined regions, but leads to small errors at the refinement boundaries which bisect WHISKY's cells located there.

Following [391], I introduce *refinement levels* L^k that encompass one or multiple grid *component(s)* C_j^k with a grid spacing (in one dimension) Δ^k. The grid spacings are related by $\Delta^k = \Delta^{k-1}/N_{\text{refine}}$. In this dissertation I use exclusively a refinement factor $N_{\text{refine}} = 2$. In the setup that I use, the base level (the *basegrid*) L^0 covers the entire domain with the coarse grid spacing Δ^0 and a single component. The refined grids have to be properly nested: Any C_j^k must be completely contained within the components of the next coarser refinement level L^{k-1}. For the stellar core-collapse problem considered here, I choose a simple fiducial box-in-box-like refinement hierarchy in which I nest consecutively more refined grids, each refined grid being centered in the next coarser grid and encompassing $1/8$ of the latter's coordinate volume[8]. In this simple and effective setup there is no need for more than one component per refinement level. Figure 3.2 depicts an example refinement hierarchy with three refinement levels.

CARPET's time evolution scheme follows that of the original Berger-Oliger AMR scheme [394], in which one evolves coarse grid data forward in time before any time evolution on finer grids. The evolved coarse grid data can then be used to provide boundary conditions for the evolution of data on the finer grids via *prolongation*, that is, interpolation of coarse grid data into boundary zones of the fine grids in space and *time*[9]. For hyperbolic systems of equations, where the timestep is limited

[8] The refinement hierarchy slightly varies from simulation to simulation. Grid setup details can be found in Appendix E

[9] Typically, one uses third-order Lagrangian interpolation in space and second-order Lagrangian interpolation in time for spacetime variables and second-order ENO interpolation in space and time for all hydrodynamic variables to minimize numerical oscillations introduced by interpolation.

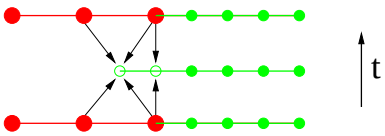

Figure 3.3: $\{1 + 1\}$ dimensional display of the prolongation scheme for a two-grid refinement hierarchy. The large circles represent coarse grid data, and smaller filled circles represent data on the fine grid. The arrows indicate interpolation of coarse grid data in space and time. Note that this figure only provides a schematic picture and does not show the actual interpolation stencil used. This figure has been reproduced from [391] with kind permission of the authors.

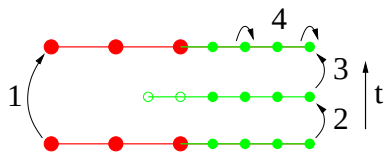

Figure 3.4: Similar schematic view in {1 + 1} dimensions as in figure 3.3, but depicting the time evolution scheme. The algorithm proceeds in the following order: (1) Coarse grid timestep, (2) and (3) fine grid timesteps, (4) restriction from fine grid onto coarse grid. Since the fine grid is always nested inside a coarse grid, there are also coarse grid points (not shown) spanning the fine grid region at locations of "every other" fine grid point. The data at these coarse grid points are restricted (copied directly) from the fine grid data after steps (2) and (3). This figure is reproduced from [391] with kind permission of the authors.

by the CFL criterion [375], a refinement by a factor of N_{refine} requires timestep sizes that are smaller by a factor N_{refine}, hence N_{refine} fine grid timesteps on level $k+1$ are necessary for each timestep on level k. After the fine-grid evolution, the fine grid data are *restricted* onto the coarse grid via a simple copy operation.

For time evolution schemes that consist only of a single step (like the standard first-order Euler scheme), the fine grid boundaries need only be updated once via prolongation. Higher-order integrators, such as Runge-Kutta or iterative Crank-Nicholson (see section 3.2.1), are multi-step schemes, and require consistent fine grid boundary conditions at each intermediate step. CARPET realizes this not by performing prolongation at each intermediate integration step, but, instead, by using a larger fine grid boundary, a so-called buffer region, as extensively discussed in [391][10].

With the above discussed subcycling of fine grids and $N_{\text{refine}} = 2$, each coarsest grid timestep involves $2^n - 1$ individual grid evolutions with n being the total number of present refinement levels (not considering time-integrator substeps). If the entire refinement hierarchy is evolved with the finest grid timestep then time interpolation and buffer regions become unnecessary. However, without subcycling of fine levels, the number of individual grid evolutions is given by $n2^{n-1}$. For $n = 9$, subcycling in time is computationally less demanding by a factor of 4 (minus the fraction of computational time spent in time interpolation) and not using subcycling should only be considered when computer memory limitations make the use of buffer regions impossible.

Parallelization

CARPET follows the domain-decomposition paradigm of parallelization and employs the message-passing interface (MPI) [398–400] for interprocessor communications. The box-in-box refinement hierarchies employed in this work are distributed onto l CPUs by dividing each refinement level into l chunks (in CARPET terminology, these are also referred to as components) of approximately equal number of grid points.

For a fixed load per CPU, CARPET scales to approximately 64 CPUs before the time spent in interprocessor communication becomes significant. More details and performance measurements can be found on the CACTUS benchmark page [401].

To conclude my discussion of CARPET, I point out that the fixed/progressive mesh refinement approach to stellar core collapse currently implemented with CARPET leads to excellent results for the collapse phase during which the flow is smooth[11]. However, as the hydrodynamic bounce shock is formed, propagates outwards and crosses mesh refinement boundaries, the quality of the results obtained with CARPET is reduced. This is because:

(1) The sudden jump in grid resolution leads to reflections of the strong shock that propagate back inwards and are sometimes referred to as *grid scattering* effects. Even though they con-

[10] The number of buffer cells in one direction for a three-step time integrator is three times the number of ghost cells in that direction. For a GR hydrodynamic simulation with HRSC and third-order reconstruction, the buffer region encompasses 9 cells in one direction.

[11] See §5.2.3 where CACTUS/CARPET/WHISKY is compared to the COCONUT code in spherical symmetry.

verge away with increasing resolution, some reflections will always be created at finite resolutions [402].

(2) As mentioned above, CARPET provides vertex-centered mesh refinement, while WHISKY employs a cell-centered finite-volume scheme. This leads to errors and loss of conservation to machine accuracy in the hydrodynamics scheme at mesh refinement boundaries. When a shock passes a mesh refinement boundary the errors can become large. As in (1), this problem should converge away with increased resolution.

(3) The numerical fluxes computed on the coarse and on the fine level at a refinement boundary do not necessarily agree. This is related to but independent of (2). To guarantee conservation and monotonicity, so-called *refluxing* must be carried out to find the correct fluxes for the cell interfaces next to the refinement boundary [394, 402]. This is currently not implemented in CARPET and would be technically very difficult to realize because of the vertex/cell-centered clash between CARPET and WHISKY. Flux errors are systematic and are not expected to converge away with increased resolution.

(1) – (3) lead to the excitation of spurious high-frequency oscillations in the hydrodynamics quantities that develop when the bounce shock passes through a mesh refinement boundary and damp only slowly. Obvious examples of this can be found in §5.2.3 and in the results of the relativistic shock tube test calculations with mesh refinement presented in §4.1. In general, it would be best to employ fully adaptive mesh refinement at postbounce times to ensure that the finest grid covers the shock at all times. This must be left to future work.

3.5 The WHISKY Code: General-Relativistic Hydrodynamics

The core of the WHISKY code was primarily developed between the years 2001 and 2003 within the European Union Research Training Network on Sources of Gravitational Waves [403]. Some of its components were previously part of the MAHC/GRASTRO GR hydrodynamics code [146, 158]. WHISKY is being used in a growing number of studies [25, 123, 163, 202, 404–406].

WHISKY implements the equations of GR hydrodynamics introduced in Section 2.5 with high resolution shock capturing methods (e.g., [151, 152]) in the Method of Lines (MoL) context (see §3.2). My original contribution to WHISKY is the advection of scalar compositional tracer variables and the implementation of a very efficient variant of the HLLE [407] approximate Riemann solver proposed by Kurganov & Tadmor [408, 409]. In addition, I have for the first time coupled a finite-temperature nuclear equation of state to WHISKY.

In the following, I describe how WHISKY works and give details on its various components. My description is based primarily on the WHISKY *Thorn Guide* [410] and on Luca Baiotti's dissertation [123], yet I omit the discussion of spacetime/hydrodynamics singularity excision within WHISKY since it is not relevant here. A discussion can be found in [406].

It is important to stress that WHISKY uses *densitized* conserved variables:

$$\begin{aligned} \hat{D} &= \sqrt{\gamma} D = \sqrt{\gamma}\rho W \ , \\ \hat{S}^i &= \sqrt{\gamma} S \ = \sqrt{\gamma}\rho h W^2 v^i \ , \\ \hat{\tau} \ &= \sqrt{\gamma}\tau \ = \sqrt{\gamma}(\rho h W^2 - P) - \hat{D} \ , \end{aligned} \tag{3.42}$$

where γ is the determinant of the 3-metric. This is consistent with WHISKY's predecessor MAHC/-GRASTRO and simplifies the set of GR hydrodynamics equations (2.66) slightly while yielding directly the integral conservation law from the continuity equation (and vice versa!)[12]

$$\Big(\int \hat{D}\, d^3x \Big)_{,t} = 0 \ . \tag{3.43}$$

Because of non-zero curvature source terms, $\hat{S}^i$ and $\hat{\tau}$ do not obey such a conservation law.

In order to solve the equations of GR hydrodynamics in 3D and Cartesian coordinates, WHISKY makes use of dimensional splitting in which the solution of the 3D problem is approximated by the solution of a sequence of three 1D problems in the x, y, and z directions (see, e.g., [152]). WHISKY is semidiscrete in the sense that it only evaluates the spatial terms in the system (2.66) and relies on MoL for the simultaneous time integration with the spacetime curvature equations. In particular, the entire system of GR hydrodynamics is rewritten in a way analogous to equation (3.4) in §3.2. With MoL, the general 3D flux-conservative PDE,

$$\mathbf{q}_{,t} + \mathbf{f}^{(a)}(\mathbf{q})_{,a} = \mathbf{s}(\mathbf{q}) \ , \tag{3.44}$$

is transformed to the ODE for cell averages $\bar{q}_{ijk}$ defined at cell centers (x_i, y_j, z_k),

$$\frac{d}{dt}\bar{\mathbf{q}}_{ijk} = \mathbf{L}(\bar{\mathbf{q}}_{ijk}) \ , \tag{3.45}$$

where WHISKY evaluates the right-hand side according to

$$\begin{aligned} \mathbf{L}(\bar{\mathbf{q}}_{ijk}) = \mathbf{s}(\bar{\mathbf{q}}_{ijk}) & \\ & -\frac{1}{\Delta x}\big(\mathbf{f}^{(x)}(\mathbf{q}(x_{i+1/2}, y_j, z_k)) - \mathbf{f}^{(x)}(\mathbf{q}(x_{i-1/2}, y_j, z_k))\big) \\ & -\frac{1}{\Delta y}\big(\mathbf{f}^{(y)}(\mathbf{q}(x_i, y_{j+1/2}, z_k)) - \mathbf{f}^{(y)}(\mathbf{q}(x_i, y_{j-1/2}, z_k))\big) \\ & -\frac{1}{\Delta z}\big(\mathbf{f}^{(z)}(\mathbf{q}(x_i, y_j, z_{k+1/2})) - \mathbf{f}^{(z)}(\mathbf{q}(x_i, y_j, z_{k-1/2}))\big) \ . \end{aligned} \tag{3.46}$$

[12] Note that the conservation law holds only if the system under consideration is isolated.

In WHISKY, the cell averages $\bar{\mathbf{q}}_{ijk}$ are approximated to second-order accuracy in space by the midpoint rule. That is, in 1D,

$$\bar{q}_i = \frac{1}{\Delta x_i} \int_{x_{i-1/2}}^{x_{i+1/2}} q(x)\, dx \; = (\Delta x_i)\, q\left(\frac{x_{i+1/2} + x_{i-1/2}}{2} \right) + \mathcal{O}(\Delta x_i^2) \approx q(x_i) \; . \tag{3.47}$$

The evaluation of equations (3.46) splits into the following two parts:

(1) Calculation of the source terms $\mathbf{s}(\bar{\mathbf{q}}_{ijk})$. Derivatives of the curvature variables are approximated with fourth-order or second-order central finite differences depending on the finite-differencing order used in the curvature evolution thorn.

(2) In each coordinate direction $a \in \{x, y, z\}$ calculation of the intercell fluxes $\mathbf{f}^{(a)}$ at the cell interfaces. This requires two steps and, for conciseness, I consider here only the x direction; the procedures for y and z directions are identical:

   (a) Reconstruction of the data at the cell interfaces. Based on the known cell averages $\bar{\mathbf{q}}_{ijk}$, the data at the cell boundaries $(\mathbf{q}_{i+1/2,j,k})$ and $(\mathbf{q}_{i-1/2,j,k})$ can in smooth parts of the flow be reconstructed to any required accuracy in space. In the vicinity of shocks the accuracy is dropped to first order to avoid spurious oscillations. I introduce the following nomenclature: $\mathbf{q}_L = (\mathbf{q}_{i+1/2,j,k})$, $\mathbf{q}_R = (\mathbf{q}_{i+1-1/2,j,k})$, $\mathbf{q}^+ = (\mathbf{q}_{i+1/2,j,k})$, $\mathbf{q}^- = (\mathbf{q}_{i-1/2,j,k})$. Constructing the flux $\mathbf{f}^{(x)}$ at the cell interfaces from the reconstructed data alone would yield only a zeroth-order approximation in time [151, 152]. In order to attain first-order accuracy in time, local Riemann problems are solved in the next step.

   (b) Solution of local Riemann problems at the cell interfaces with $\mathbf{q}_L$ and $\mathbf{q}_R$ as initial data. This allows a first-order accurate in time and, depending on the reconstruction step, high-order in space computation of the cell-interface fluxes $\mathbf{f}^{(x)}(\mathbf{q}_L, \mathbf{q}_R)$.

3.5.1 Reconstruction

For consistency and stability of the hydrodynamics scheme, the reconstruction procedure for the cell-interface data must retain conservation and must not introduce spurious oscillations. In the late 1950's, Godunov [159] has demonstrated that any linear[13] reconstruction method of higher than first-order accuracy generically will introduce spurious oscillations. In his original scheme he hence used *piecewise-constant* reconstruction:

$$q^{\text{first}}(x) = \bar{q}_i, \qquad x \in [x_{i-1/2}, x_{i+1/2}], \tag{3.48}$$

which is the only conservative first-order reconstruction method and where I have made the simplification of considering 1D data along the x direction.

Since WHISKY aims to construct a scheme that is globally higher than first-order accurate for smooth flow and drops to first order only near discontinuities, reconstruction should be carried out with at least second-order accuracy. WHISKY implements slope-limited total-variation diminishing (TVD) piecewise-linear reconstruction [411], essentially non-oscillatory (ENO) reconstruction [379] and the piecewise-parabolic reconstruction method (PPM) [412]. I will briefly describe these three methods in the following, simplified to one spatial dimension and constant grid spacing. A generalization is straightforward.

Note that WHISKY reconstructs the primitive variables ρ, ϵ, and v^i at the cell interfaces since they are needed for the computation of the numerical fluxes. After reconstruction, the equation of state is called in order to obtain consistent values of the pressure and the local speed of sound. Only then the conversion to the conserved variables (3.42) is carried out.

[13] Linear in the sense that the reconstruction method is independent of the data to be reconstructed.

Slope-Limited TVD

A straightforward conservative second-order reconstruction method is given in terms of a slope Δ_i by

$$q^{\text{second}}(x) = \bar{q}_i + \frac{x - x_i}{x_{i+1/2} - x_{i-1/2}}\Delta_i, \qquad x \in [x_{i-1/2}, x_{i+1/2}] \,. \tag{3.49}$$

However, the above inevitably leads to spurious oscillations near extrema where both q and q' change abruptly [151, 152]. In other words, (3.49) does not preserve monotonicity and may lead to an unphysical increase in the total variation (TV) of the discretized function q (see §3.2 for a definition of TV). A TV-diminishing (TVD) scheme that retains second-order accuracy in smooth parts of q can be constructed by introducing a *slope limiter* function $\sigma_i(\bar{q}_{i-1}, \bar{q}_i, \bar{q}_{i+1})$ and writing

$$q(x) = \bar{q}_i + \frac{x - x_i}{x_{i+1/2} - x_{i-1/2}}\sigma_i, \qquad x \in [x_{i-1/2}, x_{i+1/2}] \,. \tag{3.50}$$

At discontinuities, $\sigma_i = 0$ and the piecewise-constant reconstruction is recovered. Away from discontinuities, the second-order form (3.49) is obtained. The simplest though most diffusive slope is given by the *minmod* limiter,

$$\sigma_i = \text{minmod}\left(\bar{q}_i - \bar{q}_{i-1}, \bar{q}_{i+1} - \bar{q}_i\right) \,, \tag{3.51}$$

where the minmod function of two arguments is defined by

$$\text{minmod}(a,b) = \begin{cases} a & \text{if } |a| < |b| \text{ and } ab > 0 \,. \\ b & \text{if } |b| < |a| \text{ and } ab > 0 \,. \\ 0 & \text{if } ab \leq 0 \,. \end{cases} \tag{3.52}$$

Hence, the minmod limiter compares the magnitude of the upwind slope $(\bar{q}_i - \bar{q}_{i-1})$ with that of the downwind slope $(\bar{q}_{i+1} - \bar{q}_i)$ and picks the one that is smaller in magnitude, or, in the case of a local extremum where the two slopes have different sign, returns 0.

Van Leer's monotonized centered (MC) limiter [413, 414] provides considerably sharper resolution of discontinuities while still preserving the TVD property. It is defined by a minmod function of three arguments (defined analogously to (3.52)),

$$\sigma_i = \text{minmod}\left(\frac{1}{2}(\bar{q}_{i+1} - \bar{q}_{i-1}), 2(\bar{q}_i - \bar{q}_{i-1}), 2(\bar{q}_{i+1} - \bar{q}_i)\right) \,. \tag{3.53}$$

In addition to minmod and the MC limiter, Roe's superbee limiter [415] is implemented in WHISKY.

ENO

The essentially non-oscillatory (ENO) reconstruction methods introduced by Harten et al. [379] have a large number of variants. In WHISKY, only the simplest ENO reconstruction method of accuracy p is implemented following the outline provided by Shu [374]. The fundamental idea of ENO reconstruction is to choose of all possible stencils of size p (for pth order reconstruction) the one that is least oscillatory and gives the smoothest reconstruction. For stability, the stencil must include the cell that is to be reconstructed and it is set up by starting in cell i and adding a cell j, $j = i \pm 1$, where j is chosen to minimize the Newton undivided differences[14]

$$q[i-1, i] \equiv \bar{q}_i - \bar{q}_{i-1} \,, \tag{3.54}$$

$$q[i, i+1] \equiv \bar{q}_{i+1} - \bar{q}_i \,. \tag{3.55}$$

[14] In the case of non-uniform grids it is necessary to consider Newton divided differences

Then more cells are added recursively, at each step minimizing the subsequent Newton undivided differences, recursively defined by

$$q[i-s, i+t] = q[i-s+1, i+t] - q[i-s, i+t-1] \ , \tag{3.56}$$

until the stencil is sufficiently large: $p = s + t + 1$. Once the smoothest stencil,

$$S(i) = \{i-s, ..., i, ..., i+t\} \ , \tag{3.57}$$

is determined, a p-polynomial interpolation gives the reconstructed values on the cell interfaces of cell i:

$$q_{i+1/2} = \sum_{l=0}^{p-1} c_{sl}\, \bar{q}_{i-s+l} \ , \qquad q_{i-1/2} = \sum_{l=0}^{p-1} c_{s-1,l}\, \bar{q}_{i-s+l} \ , \tag{3.58}$$

where the interpolation coefficients are given by

$$c_{sl} = \sum_{m=l+1}^{p} \frac{\Pi_{k=0;k\neq m}^{p} \Pi_{n=0,n\neq m,k}^{p} (s-n+1)}{\Pi_{r=0,r\neq m}^{p} (m-r)} \ . \tag{3.59}$$

Numerical tests [123] indicate that increasing the order of accuracy beyond $p = 4$ does not improve significantly the reconstruction quality while becoming computationally very expensive due to the large stencil and the correspondingly large number of comparisons necessary to find the smoothest stencil.

PPM

The piecewise-parabolic method (PPM) as introduced by Colella and Woodward [412] and first applied to relativistic flows by Martí and Müller [416], is a composite reconstruction method that provides third-order accuracy in space. In the following, I present only the simplified variant of the original method implemented in WHISKY that is specialized for the case of an evenly-spaced grid. The fundamental idea behind PPM is to construct an interpolating parabola $a(x)$ in each computational cell $x_{i-1/2} < x < x_{i+1/2}$ such that no new artificial extrema appear in the interpolated function and such that its integral averages coincide with the known cell averages $\bar{q}_i$ (and at timestep n)

$$\frac{1}{\Delta x} \int_{x_{i-1/2}}^{x_{i+1/2}} a(x) dx = \bar{q}_i \ . \tag{3.60}$$

The three coefficients of the parabola are determined by imposing (3.60) and by demanding that the parabola pass through the points $(x_{i-1/2}, a_{i-1/2})$ and $(x_{i+1/2}, a_{i+1/2})$. The interface values $a^- = a_{i-1/2}$ and $a^+ = a_{i+1/2}$ are found by demanding: (i) that they do not fall outside the ranges $[\bar{q}_{i-1}, \bar{q}_i]$, $[\bar{q}_i, \bar{q}_{i+1}]$ for a^- and a^+, respectively; (ii) that in smooth parts of q, $a_{i+1}^- = a_i^+ \equiv q_{i+1/2}$; and (iii) that $a(x)$ is monotone in each cell. The first step in order to find a^+ and a^- is to consider the indefinite integral $I(x) = \int^x a(\xi) d\xi$ whose values are known at the cell interfaces:

$$I(x_{i+1/2}) = I_{i+1/2} = \sum_{k<i} \bar{q}_k \Delta x \ . \tag{3.61}$$

To find $q_{i+1/2}$, the above quartic polynomial is interpolated through the points $(x_{i+r+1/2}, I_{i+r+1/2})$, $r = 0, \pm 1, \pm 2$, which, after some algebra [412], yields from its differentiation:

$$a_i^+ = q_{i+1/2} = \frac{1}{2}\left(\bar{q}_{i+1} + \bar{q}_i\right) + \frac{1}{6}\left(\delta_m \bar{q}_i - \delta_m \bar{q}_{i+1}\right) , \tag{3.62}$$

where

$$\delta_m \bar{q}_i = \begin{cases} \min(|\delta\bar{q}_i|, 2|\bar{q}_{i+1} - \bar{q}_i|, 2|\bar{q}_i - \bar{q}_{i-1}|)\ \mathrm{sign}(\delta\bar{q}_i) & \text{if } (\bar{q}_{i+1} - \bar{q}_i)(\bar{q}_i - \bar{q}_{i-1}) > 0 \\ 0 & \text{otherwise.} \end{cases} , \tag{3.63}$$

and

$$\delta\bar{q}_i = \frac{1}{2}(\bar{q}_{i+1} - \bar{q}_{i-1}) \ . \tag{3.64}$$

Analogously, a_i^- can be determined and the interpolating parabola then reads

$$a(x) = a_i^- + x\left((a_i^+ - a_i^-) + 6\left[\bar{q}_i - \frac{1}{2}(a_i^+ - a_i^-)\right](1-x)\right) . \tag{3.65}$$

At this point, the left and right states at the interfaces $i+1/2$ (and analogously at $i-1/2$) are set equal to the interpolated values,

$$q_i^+ = q_{i+1}^- = q_{i+1/2} . \tag{3.66}$$

This reconstruction will be oscillatory near discontinuities. Monotonicity is enforced by the replacements [412]:

$$\begin{aligned} q_i^+ &= q_i^- \;=\; \bar{q}_i \;\text{ if } (q_i^+ - \bar{q}_i)(\bar{q}_i - q_i^-) \le 0 \\ q_i^- &= 3\bar{q}_i - 2q_i^+ \;\text{ if } (q_i^+ - q_i^-)\left(\bar{q}_i - \tfrac{1}{2}(q_i^- + q_i^+)\right) > \tfrac{1}{6}(q_i^+ - q_i^-)^2 \\ q_i^+ &= 3\bar{q}_i - 2q_i^- \;\text{ if } (q_i^+ - q_i^-)\left(\bar{q}_i - \tfrac{1}{2}(q_i^- + q_i^+)\right) < -\tfrac{1}{6}(q_i^+ - q_i^-)^2 . \end{aligned} \tag{3.67}$$

On a Cartesian grid, a spherically symmetric configuration (such as a TOV star; discussed in §3.7.1), will appear to PPM to have a local extremum along the coordinate axes. Hence, the above monotonicity enforcement will be carried out, reducing the accuracy to first-order along the coordinate axes even if no physical discontinuity is present. This effect is called *clipping* and cannot be avoided in the current implementation of PPM in WHISKY.

Before monotonicity is actually enforced, two other steps may optionally be applied: Firstly, one may *steepen* discontinuities. This is to ensure sharp profiles and is only applied to contact discontinuities (i.e., discontinuities in ρ and continuous v and p). The steepening procedure replaces the cell interface values of the density with

$$\rho_i^- = \rho_i^-(1-\eta) + \left(\bar{\rho}_{i-1} + \frac{1}{2}\delta_m\bar{\rho}_{i-1}\right)\eta \tag{3.68}$$

$$\rho_i^+ = \rho_i^+(1-\eta) + \left(\bar{\rho}_{i+1} - \frac{1}{2}\delta_m\bar{\rho}_{i+1}\right)\eta . \tag{3.69}$$

Here η is defined as

$$\eta = \max(0, \min(1, \eta_1(\tilde{\eta} - \eta_2))), \tag{3.70}$$

where η_1, η_2 are constants and

$$\tilde{\eta} = \begin{cases} \dfrac{\bar{\rho}_{i+2} - \bar{\rho}_{i+2} + 4\delta\bar{\rho}_i}{12\delta\bar{\rho}_i} & \text{if } \begin{cases} \delta^2\bar{\rho}_{i+1}\delta^2\bar{\rho}_{i-1} < 0 \\ |(\bar{\rho}_{i+1} - \bar{\rho}_{i-1})| - \epsilon_{\rm PPM}\min(|\bar{\rho}_{i+1}|, |\bar{\rho}_{i-1}|) > 0 \end{cases} \\ 0 \qquad\qquad \text{otherwise} \end{cases} ,$$

with $\epsilon_{\rm PPM}$ being another constant and

$$\delta^2\bar{\rho}_i = \frac{\bar{\rho}_{i+1} - 2\bar{\rho}_i + \bar{\rho}_{i-1}}{\Delta x^2} . \tag{3.71}$$

In addition to the above rules, $\rho_i^{-,+}$ are only modified if

$$K\frac{|\delta\bar{\rho}_i|}{\min(\bar{\rho}_{i+1}, \bar{\rho}_{i-1})} \ge \frac{|\delta p_i|}{\min(\bar{p}_{i+1}, \bar{p}_{i-1})} , \tag{3.72}$$

where $\bar{p}_i$ is the cell average of the pressure in cell i. The above ensures that the discontinuity is predominantly a contact discontinuity. K is another positive parameter.

The second additional step that may be performed before monotonicity enforcement is the flattening of the zone structure near strong shocks. This adds simple dissipation to all reconstructed variables, is always active in WHISKY, and avoids postshock oscillations:

$$q_i^{-,+} = \nu_i q_i^{-,+} + (1-\nu_i)\bar{q}_i, \tag{3.73}$$

where

$$\nu_i = \begin{cases} \max\left[0, 1 - \max\left(0, \omega_2\left(\frac{\bar{p}_{i+1}-\bar{p}_{i-1}}{\bar{p}_{i+2}-\bar{p}_{i-2}} - \omega_1\right)\right)\right] & \text{if } \omega_0 \min(\bar{p}_{i-1}, \bar{p}_{i+1}) < \bar{p}_{i+1} - \bar{p}_{i-1} \\ & \text{and } \bar{v}^x_{i-1} - \bar{v}^x_{i+1} > 0 \\ 1 & \text{otherwise} \end{cases} , \tag{3.74}$$

and $\omega_0, \omega_1, \omega_2$ are constants.

The implementation of PPM in WHISKY has seven tunable parameters whose default values are taken from Colella & Woodward [412] and summarized in Table 3.1

Table 3.1: Parameters of the PPM implementation within WHISKY. See text and [412] for details. Γ is the adiabatic exponent provided by the EOS.

Parameter:	$\epsilon_{\rm PPM}$	η_1	η_2	K	ω_0	ω_1	ω_2
Value:	0.01	20	0.05	$0.1\,\Gamma$	0.33	0.75	10

3.5.2 Riemann Solvers / Flux Formulae

Once the left and right states, $\mathbf{q}_L = (\mathbf{q}_{j+1/2})$ and $\mathbf{q}_R = (\mathbf{q}_{j+1-1/2})$, at the cell interfaces are obtained via the outlined reconstruction procedures, they can be used as initial data for a local Riemann problem whose solution yields a highly accurate approximation of the intercell flux. *Exact* or *approximate* Riemann solvers may be used. Exact solvers exploit the details of the characteristic wave structure (see §2.5.1) and continuity conditions at discontinuities and iteratively solve the non-linear Riemann problem. Exact Riemann solvers are discussed at length in [151, 152, 417]. The exact solution of the 1D Riemann problem in relativistic hydrodynamics is extensively discussed by Martí & Müller [418] (also see the review in [165] and [419, 420] for a recent proposal of an efficient exact relativistic Riemann solver). For multi-dimensional GR hydrodynamics, even the most efficient exact Riemann solvers are computationally too expensive to be employed in practice. Hence, one turns to approximate Riemann solvers which solve a simplified and usually linearized Riemann problem. Alternatively, flux formulae are used which provide an approximation to the flux obtained with an exact Riemann solver, but do not provide information about the intermediate states in the Riemann problem.

Implemented in WHISKY is Roe's approximate Riemann solver [421], the Harten–Lax–van Leer–Einfeldt (HLLE) solver [407, 422], the HLLE flux-formula variant of Kurganov & Tadmor [408, 409] and the approximate Marquina flux formula [423–425]. The various Riemann solvers / flux formulae in WHISKY in combination with the previously discussed reconstruction methods were extensively tested and compared in [123, 163]. The Marquina flux formula appears to perform best in a large variety of problems and is hence used by default in WHISKY.

Roe's Solver

The Roe Riemann solver considers a linearized Riemann problem and solves it exactly. The Roe intercell flux reads

$$\mathbf{f}^{\rm Roe}_{i+1/2} = \frac{1}{2}\left[\mathbf{f}(\mathbf{q}_L) + \mathbf{f}(\mathbf{q}_R) - \sum_{i=1}^{5} |\lambda_i| \Delta w_i \, \mathbf{r}_i\right]. \tag{3.75}$$

Here $\mathbf{f}(\mathbf{q}_L)$ and $\mathbf{f}(\mathbf{q}_R)$ are the direct numerical fluxes as obtained from the left and right states, respectively. The 5 λ_i are the eigenvalues of the linearized Jacobian $\tilde{\mathbf{B}}(\mathbf{q}^{\rm Roe})$ and the $\mathbf{r}_i$ are its right eigenvectors (see §2.5.1 and Appendix C). The characteristic variables w_i are defined as the scalar product of the left eigenvectors with the state vector:

$$w_i = \mathbf{l}_i \cdot \mathbf{q} \ , \tag{3.76}$$

and the jumps in the here relevant characteristic variables at the cell interface are then given by

$$\Delta w_i = \mathbf{l}_i \cdot (\mathbf{q}_L - \mathbf{q}_R) \ . \tag{3.77}$$

There is a choice of which intermediate state $\mathbf{q}^{\mathrm{Roe}}$ the Jacobian should be evaluated at. Roe gives criteria that are meant to ensure consistency and stability of the Roe flux:

(1) $\tilde{\mathbf{B}}(\mathbf{q}^{\mathrm{Roe}})\,(\mathbf{q}_R - \mathbf{q}_L) = \mathbf{f}(\mathbf{q}_R) - \mathbf{f}(\mathbf{q}_L)$,

(2) $\tilde{\mathbf{B}}(\mathbf{q}^{\mathrm{Roe}})$ is diagonalizable with real eigenvalues,

(3) Consistency with the exact Jacobian: $\tilde{\mathbf{B}}(\mathbf{q}^{\mathrm{Roe}}) \to \partial\mathbf{f}/\partial\mathbf{q}$ smoothly as $\mathbf{q}^{\mathrm{Roe}} \to \mathbf{q}$.

Although it is possible to find the consistent state $\mathbf{q}^{\mathrm{Roe}}$ for the GR hydrodynamics equations [426, 427], it is in most cases sufficient [156] to use the simple arithmetic mean of the left and right states:

$$\mathbf{q}^{\mathrm{Roe}} = \frac{1}{2}(\mathbf{q}_L + \mathbf{q}_R) \ . \tag{3.78}$$

The Roe solver provides a very good approximation to the Riemann solution, except at sonic points[15] in rarefaction waves that cannot be adequately captured by the linearized system [152] and where the Roe solver leads to an entropy violation.

Marquina Flux Formula

The Marquina flux formula [423–425] can be regarded as an improved version of the Roe solver, since it yields identical results everywhere, except at sonic points where it removes the entropy violation at rarefactions of the Roe solver. Implemented in WHISKY is the variant proposed by Aloy et al. [425]. The procedure consists of computing the left $\mathbf{l}_i$ and $\mathbf{r}_i$ eigenvectors and the eigenvalues λ_i for the left ($\mathbf{q}_L$) and right ($\mathbf{q}_L$) states. Next, the left and right characteristic variables $(w_i)_{L,R}$ and fluxes $(\phi_i)_{L,R}$ are defined by

$$(w_i)_{L,R} = \mathbf{l}_i(\mathbf{q}_{L,R}) \cdot \mathbf{q}_{L,R}\,, \qquad (\phi_i)_{L,R} = \mathbf{l}_i(\mathbf{q}_{L,R})\mathbf{f}(\mathbf{q}_{L,R}) \ . \tag{3.79}$$

The flux formula is then given by

$$\mathbf{f}^{\mathrm{Marquina}}_{i+1/2} = \sum_{i=1}^{5} \left[(\phi_i)_+ \mathbf{r}_i\,(\mathbf{q}_L) + (\phi_i)_-\,\mathbf{r}_i(\mathbf{q}_R) \right] \tag{3.80}$$

where the $(\phi_i)_{+,-}$ are chosen according to the sign of the eigenvalues:

- $(\phi_i)_+ = (\phi_i)_L$ and $(\phi_i)_- = 0$, if both $\lambda_i(\mathbf{q}_L)$ and $\lambda_i(\mathbf{q}_R)$ are positive. That is, when both waves move to the right and so the flux has to be computed from the left state.
- $(\phi_i)_- = (\phi_i)_R$ and $(\phi_i)_+ = 0$, if both eigenvalues are negative.
- While, if the eigenvectors have opposite sign:

$$\begin{aligned} (\phi_i)_+ &= \frac{1}{2}\left[(\phi_i)_L + \max\left(|\lambda_i(\mathbf{q}_L)|, |\lambda_i(\mathbf{q}_R)| \right)\ (w_i)_L \right] \\ (\phi_i)_- &= \frac{1}{2}\left[(\phi_i)_R + \max\left(|\lambda_i(\mathbf{q}_L)|, |\lambda_i(\mathbf{q}_R)| \right)\ (w_i)_R \right] \ . \end{aligned} \tag{3.81}$$

HLLE and Kurganov-Tadmor

The Harten–Lax–van Leer–Einfeldt (HLLE) solver [407, 422] approximates the full Riemann problem by considering only the fastest wave moving to the left and the fastest wave moving to the right, disregarding the central contact wave.

[15] At sonic points the fluid velocity equals the local speed of sound.

The HLLE flux formula reads

$$\mathbf{f}^{\rm HLLE}_{i+1/2} = \frac{\xi_+ \mathbf{f}(\mathbf{q}_L) - \xi_- \mathbf{f}(\mathbf{q}_R) + \xi_+\xi_-(\mathbf{q}_R - \mathbf{q}_L)}{\xi_+ - \xi_-} \,, \tag{3.82}$$

where ξ_+ and ξ_- are chosen in WHISKY as

$$\xi_- = \min(0, (\lambda_i)_R, (\lambda_i)_L) \,, \qquad \xi_+ = \max(0, (\lambda_i)_R, (\lambda_i)_L) \,. \tag{3.83}$$

This ensures that the physical maximum and minimum characteristic velocities are contained within $[\xi_-, \xi_+]$ [152].

Kurganov and Tadmor [408, 409] proposed a semi-discrete conservative scheme with a flux-formula similar to that of HLLE:

$$\mathbf{f}^{\rm KT}_{i+1/2} = \frac{1}{2}\left[\mathbf{f}(\mathbf{q}_L) + \mathbf{f}(\mathbf{q}_R)\right] + \frac{\alpha}{2}(\mathbf{q}_R - \mathbf{q}_L) \,, \tag{3.84}$$

where $\alpha_{i+1/2} = \max((\lambda_i)_R, (\lambda_i)_L) = \max(|\xi_+|, |\xi_-|)$. Equation (3.84) is obtained from equation (3.82) by setting $\alpha = \max(|\xi_+|, |\xi_-|)$ and $\xi_\pm = \pm\alpha$.

3.5.3 Conserved–to–Primitive Variable Conversion

As discussed in §2.5, the Valencia formulation of GR hydrodynamics relies on the knowledge of the primitive variables (ρ, ϵ, v^i) at the cell interfaces for the computation of the intercell fluxes. While there exists a straightforward analytic conversion from the primitive to the conserved evolved variables (specified by equation (3.42)), there is no such simple general relationship for converting back to the physical primitive variables. Instead, they must be recovered by an iterative root-finding procedure. For an overview on different methods, see [165]. In WHISKY, a Newton-Raphson type iteration operating on the pressure is used. This works for general equations of state (EOS) of the type $p = p(\rho, \epsilon)$. The following also works for EOSs of the type $p = p(\rho, \epsilon, \{X_i\})$, if the dependence of p on the compositional variables (or mass fractions) X_i is much weaker than its dependence on ρ and ϵ.

First the conserved variables are *undensitized*: $D = \gamma^{-1/2}\hat{D}$, $S^i = \gamma^{-1/2}\hat{S}^i$, and $\tau = \gamma^{-1/2}\hat{\tau}$. Given an initial guess for the pressure $\bar{p}$ from the previous step, the root of the function

$$f = \bar{p} - p(\bar{\rho}, \bar{\epsilon}), \tag{3.85}$$

is sought, where the approximate density and specific internal energy are given by

$$\bar{\rho} = \frac{D}{\tau + \bar{p} + D}\sqrt{(\tau + \bar{p} + D)^2 - S^2} \,, \tag{3.86}$$

$$\bar{W} = \frac{\tau + \bar{p} + D}{\sqrt{(\tau + \bar{p} + D)^2 - S^2}} \,, \tag{3.87}$$

$$\bar{\epsilon} = D^{-1}\left(\sqrt{(\tau + \bar{p} + D)^2 - S^2} - \bar{p}\bar{W} - D\right). \tag{3.88}$$

where $S^2 = S^i S_i$. The derivative of f with respect to the dependent variable $\bar{p}$ is given by

$$f' = 1 - \frac{\partial p}{\partial \rho}\frac{\partial \rho}{\partial \bar{p}} - \frac{\partial p}{\partial \epsilon}\frac{\partial \epsilon}{\partial \bar{p}} \,, \tag{3.89}$$

where $\frac{\partial p}{\partial \rho}$ and $\frac{\partial p}{\partial \epsilon}$ must be provided by the EOS routines, and

$$\frac{\partial \rho}{\partial \bar{p}} = \frac{DS^2}{\sqrt{(\tau + \bar{p} + D)^2 - S^2}(\tau + \bar{p} + D)^2} \,, \tag{3.90}$$

$$\frac{\partial \epsilon}{\partial \bar{p}} = \frac{\bar{p}S^2}{\rho\left((\tau + \bar{p} + D)^2 - S^2\right)(\tau + \bar{p} + D)} \,. \tag{3.91}$$

Once the pressure is known to satisfactory precision, the other variables follow straightforwardly.

For a polytropic EOS, the procedure is simpler and one iterates over $\bar{\rho}\bar{W}$:

$$f = \bar{\rho}\bar{W} - D, \tag{3.92}$$

where $\bar{\rho}$ is the variable solved for. The pressure, specific internal energy, and enthalpy $\bar{h}$ are set from the EOS and the Lorentz factor is found from

$$\bar{W} = \sqrt{1 + \frac{S^2}{(D\bar{h})^2}} \ . \tag{3.93}$$

The derivative is given by

$$f' = \bar{W} - 2\frac{\bar{\rho}S^2\bar{h}'}{\bar{W}D^2\bar{h}^3}, \tag{3.94}$$

where

$$\bar{h}' = \bar{\rho}^{-1}\frac{\partial p}{\partial \rho} \ . \tag{3.95}$$

3.5.4 Hydrodynamic Curvature Source Terms and Coupling with Curvature

The GR hydrodynamics equations contain curvature related source terms in the momentum and energy equations. The ADM (and the NOK-BSSN) equations contain matter source terms. The coupling of hydrodynamics with the curvature evolution in BSSN_MoL is done via simultaneous time update through the Method of Lines (see §3.2) and the actual passing of variables is done via the CACTUS thorns CACTUSEINSTEIN/ADMBASE [428] and CACTUSEINSTEIN/ADMCOUPLING [429]. The coupling is implemented via the standard ADM variables introduced in §2.4.

Stress-Energy Tensor

WHISKY provides the energy-momentum right-hand side of the Einstein equations for the curvature evolution carried out by BSSN_MoL. This is done straightforwardly by computing the 4-stress-energy tensor

$$T^{\mu\nu} = \rho h u^\mu u^\nu + p g^{\mu\nu} \ . \tag{3.96}$$

at every (intermediate) time integration step. BSSN_MoL then carries out the necessary projections of $T^{\mu\nu}$ onto the 3-hypersurface Σ_t for the source terms in equations (3.22) and (3.23).

Curvature Source Terms

In WHISKY, the source terms given by (2.69) in §2.5 are not implemented directly, but in a modified form to avoid time derivatives of the ADM 3-metric. In the source term computation it is necessary to know the expression of some of the 4-Christoffel symbols ${}^{(4)}\Gamma^\rho_{\mu\nu}$ in terms of the {3+1} variables. In order to remove time derivatives, the ADM evolution equation for the 3-metric in the form

$$\gamma_{ij\,,t} = -2\Big(\alpha K_{ij} - \beta_{(j\,,i)} - \Gamma^k_{ij}\beta_k\Big) \tag{3.97}$$

is employed. In addition, it is useful to recall that

$$\gamma^{jk}_{\ \ ;i} = \gamma^{jk}_{\ \ ,i} + 2\,\Gamma^j_{il}\gamma^{lk} = 0 \ . \tag{3.98}$$

One begins with expanding ${}^{(4)}\Gamma^0_{00}$:

$${}^{(4)}\Gamma^0_{00} = \frac{1}{2\alpha^2}\Big[-(\beta_k\beta^k)_{,t} + 2\alpha\alpha_{,t} + 2\beta^i\beta_{i\,,t} - \beta^i(\beta_k\beta^k)_{,i} + 2\alpha\beta^i\alpha_{,i}\Big] \ . \tag{3.99}$$

The explicitly expanded derivatives read

$$\begin{aligned}(\beta_k\beta^k)_{,t} &= (\gamma_{jk}\beta^j\beta^k)_{,t} = 2\gamma_{jk}\beta^j\beta^k{}_{,t} + \beta^j\beta^k\gamma_{jk,t} \\ &= 2\beta_k\beta^k{}_{,t} - 2\alpha K_{jk}\beta^j\beta^k - 2\beta^j\beta^k\beta_{k,j} + 2\Gamma^i_{kj}\beta_i\beta^j\beta^k \end{aligned} \tag{3.100}$$

and

$$(\beta_k\beta^k)_{,j} = (\gamma^{jk}\beta_j\beta_k)_{,i} = 2\gamma^{jk}\beta_j\beta_{k,i} + \beta_j\beta_k\gamma^{jk}{}_{,i} = 2\beta_k\beta_{k,i} - 2\Gamma^j_{ik}\beta_j\beta^k \ . \tag{3.101}$$

Equation (3.99) simplifies now considerably:

$${}^{(4)}\Gamma^0_{00} = \frac{1}{\alpha}\left(\alpha_{,t} + \beta^i\alpha_{,t} + K_{jk}\beta^j\beta^k\right) \ . \tag{3.102}$$

The other 4-Christoffels simplify in a similar fashion [123]:

$${}^{(4)}\Gamma^0_{i0} = -\frac{1}{2\alpha^2}\left[(\beta^k\beta_k - \alpha^2)_{,i} - \beta^j(\beta_{j,i} - \beta_{i,j} - \gamma_{ij,t})\right] = -\frac{1}{\alpha}\left(\alpha_{,i} - \beta^j K_{ij}\right) \ , \tag{3.103}$$

$${}^{(4)}\Gamma^0_{ij} = -\frac{1}{2\alpha^2}\left[\beta_{j,i} + \beta_{i,j} - \gamma_{ij,t} - \beta^k(\gamma_{kj,i} + \gamma_{ki,j} - \gamma_{ij,k})\right] = -\frac{1}{\alpha}K_{ij} \ , \tag{3.104}$$

$${}^{(4)}\Gamma_{00j} = {}^{(4)}\Gamma^\nu_{0j}\,g_{\nu 0} = \frac{1}{2}(\beta_k\beta^k - \alpha^2)_{,j} \ , \tag{3.105}$$

$${}^{(4)}\Gamma_{l0j} = {}^{(4)}\Gamma^\nu_{lj}\,g_{\nu 0} = \alpha K_{lj} + \beta_{j,l} + \beta_{l,j} - \beta_k\Gamma^k_{lj} \ , \tag{3.106}$$

$${}^{(4)}\Gamma_{0lj} = {}^{(4)}\Gamma^\nu_{0j}\,g_{\nu l} = -\alpha K_{jl} - \beta_{j,l} + \beta_k\Gamma^k_{lj} \ , \tag{3.107}$$

$${}^{(4)}\Gamma_{lmj} = {}^{(4)}\Gamma^\nu_{lj}\,g_{\nu m} = \Gamma_{lmj} \ . \tag{3.108}$$

It is now possible to write out the source terms with little effort. The momentum source contributing to the evolution of the momenta S_j is given by [156, 157]

$$s_{S_j} = T^{\mu\nu}(g_{\nu j,\mu} + {}^{(4)}\Gamma^\delta_{\mu\nu}g_{\delta j}) = T^\mu_\nu\,{}^{(4)}\Gamma^\nu_{\mu j} = T^{\mu\nu}\,{}^{(4)}\Gamma_{\mu\nu j} \ . \tag{3.109}$$

Note that in WHISKY the above is multiplied by $\sqrt{-g} = \alpha\sqrt{\gamma}$ which slightly simplifies equation (2.66). $\sqrt{-g}$ is not carried along in the following. The coefficient of T^{00} can be written as

$${}^{(4)}\Gamma_{00j} = \frac{1}{2}\beta^l\beta^m\gamma_{lm,j} - \alpha\alpha_{,j} + \beta_m\beta^m{}_{,j} \ , \tag{3.110}$$

the coefficient of T^{0i} is given by

$${}^{(4)}\Gamma_{0ij} + {}^{(4)}\Gamma_{i0j} = \beta^l\gamma_{jl,i} + \gamma_{il}\beta^l{}_{,j} \ , \tag{3.111}$$

and the coefficient of the T^{lm} term is the standard Γ_{lmj}. This then yields the expression implemented in WHISKY:

$$s_{S_j} = T^{00}\left(\frac{1}{2}\beta^l\beta^m\gamma_{lm,j} - \alpha\alpha_{,j}\right) + T^{0i}\beta^l\gamma_{il,j} + T^0_i\beta^i_{,j} + \frac{1}{2}T^{lm}\gamma_{lm,j} \ . \tag{3.112}$$

The energy source term is given by

$$s_\tau = \left(T^{\mu 0}\alpha_{,\mu} - \alpha T^{\mu\nu\,(4)}\Gamma^0_{\mu\nu}\right) \ . \tag{3.113}$$

As for the momentum source, the energy source is multiplied by $\alpha\sqrt{\gamma}$ in WHISKY. Again, it is easiest to consider the coefficients of various $T^{\mu\nu}$ components individually. The coefficient of the T^{00} component is

$$(\alpha_{,t} - \alpha\,{}^{(4)}\Gamma^0_{00}) = -(\beta^i\alpha_{,i} - \beta^k\beta^l K_{kl}) \ . \tag{3.114}$$

The T^{0i} coefficient is given by

$$(\alpha_{,i} - 2\alpha\,{}^{(4)}\Gamma^0_{i0}) = 2\beta^j K_{ij} - \alpha_{,i} \ , \tag{3.115}$$

and, finally, the T^{lm} coefficient can simply be expanded to

$$\begin{aligned} -\alpha\,{}^{(4)}\Gamma^0_{lm} &= \frac{1}{2\alpha}\left(2\alpha K_{lm} + \beta_k\Gamma^k_{lm} - 2\beta^j\Gamma_{jlm}\right) \\ &= K_{lm} \ . \end{aligned} \tag{3.116}$$

3.5.5 Equations of State

WHISKY features a general EOS interface, allowing for EOSs of the general type $p = p(\rho, \epsilon, \{X_i\})$, where the X_i are compositional scalars. Traditionally, multi-dimensional studies in general relativity have tended to put an emphasis on the spacetime dynamics and have largely neglected astrophysically important details such as a realistic finite-temperature EOS.

In the following I will describe the "classical" EOSs implemented for use in WHISKY while I postpone the discussion of the finite-temperature nuclear EOS to §3.6 where it is discussed in the context of the astrophysical extensions to the original code that I have implemented.

Each EOS constitutes an independent CACTUS thorn that is called through a generalized interface provided by thorn EOSBASE_GENERAL and may also be used by thorns other than WHISKY.

Polytropic and Ideal Fluid EOSs

The polytropic/isentropic EOS, $p = p(\rho)$,

$$p = K\rho^{\Gamma} , \tag{3.117}$$

$$\epsilon = \frac{K\rho^{\Gamma-1}}{\Gamma - 1} , \tag{3.118}$$

is adequate for modelling fluids that are dominated by Fermi degeneracy pressure of electrons [36] and that only experience adiabatic flow and exhibit no shocks. K and Γ are constants that depend on the fluid composition (neutrons/electrons) and on the degree of degeneracy. A cold neutron star that is supported by the pressure of degenerate neutrons can, for example, be modelled with $\Gamma = 2$ and $K = 7.904 \times 10^5$ [cgs] [158, 161]. A pre-collapse stellar iron core supported by relativistically degenerate electrons can be described by $\Gamma = 4/3$, $K = 4.897 \times 10^{14}$ [cgs] [30, 36]. Frequently, the polytropic index $n = 1/(\Gamma - 1)$ is used to classify polytropic fluid bodies.

When the polytropic EOS is used in WHISKY, the energy equation for $\hat{\tau}$ is not solved since the specific internal energy is fixed by (3.118).

The ideal-fluid or Γ-law EOS is a variant of the polytropic EOS that does not restrict the specific internal energy and is obtained through rewriting (3.118):

$$p = (\Gamma - 1)\rho\epsilon . \tag{3.119}$$

For purely adiabatic flow, this is consistent with (3.117).

Hybrid EOS

The above polytropic and ideal fluid equations of state in their standard incarnations are inadequate even for the simplest physical models of stellar iron core collapse. While the collapse phase itself is approximately adiabatic (see, e.g., [3, 36]) and can be modelled by a polytropic EOS with a Γ close to $4/3$, the nuclear equation of state stiffens at nuclear density, leading to core bounce and shock formation. Hence, it is necessary to (a) consistently approximate the stiffening of the EOS at nuclear density and (b) provide for the possibility of thermal, non-adiabatic contributions to the EOS to adequately capture the postbounce dynamics and shock propagation. Both (a) and (b) can be realized by assuming a hybrid polytropic–ideal-fluid EOS of the form [430]

$$p = p_{\mathrm{p}} + p_{\mathrm{th}} , \tag{3.120}$$

with a polytropic p_{p} and a thermal component p_{th} [12, 18, 30, 160–162]. The initial precollapse polytrope is set up with $\Gamma_{\mathrm{initial}} = 4/3$. To initiate collapse, $\Gamma_{\mathrm{initial}}$ is lowered to $\Gamma = \Gamma_1$ which is typically close to $4/3$. At nuclear density (usually assumed, $\rho_{\mathrm{nuc}} \simeq 2.0 \times 10^{14}$ g cm^{-3}), the adiabatic index Γ jumps from Γ_1 to Γ_2. Before core bounce, $p_{\mathrm{th}} \approx 0$. At core bounce, a shock forms and propagates out, shock-heating the infalling outer core material. This is reflected by a nonzero

$$p_{\mathrm{th}} = (\Gamma_{\mathrm{th}} - 1)\rho\epsilon_{\mathrm{th}} \tag{3.121}$$

where $\epsilon_{\rm th} = \epsilon - \epsilon_{\rm p}$ and $\epsilon_{\rm p} = p_{\rm p}/[\rho(\Gamma - 1)]$. Typically, $\Gamma_{\rm th} = 1.5$ to model a mixture of relativistic ($\Gamma = 4/3$) and nonrelativistic ($\Gamma = 5/3$) components of an ideal fluid. Γ_2 is set to 2.5 to approximate the adiabatic index of cold nuclear matter.

By demanding that p and ϵ be continuous at the transition density $\rho_{\rm nuc}$ and including the discussed thermal contributions, one arrives at the following relation that holds during all stages of the simulation:

$$P = \frac{\Gamma - \Gamma_{\rm th}}{\Gamma - 1} K \rho_{\rm nuc}^{\Gamma_1 - \Gamma} \rho^{\Gamma} - \frac{(\Gamma_{\rm th} - 1)(\Gamma - \Gamma_1)}{(\Gamma_1 - 1)(\Gamma_2 - 1)} K \rho_{\rm nuc}^{\Gamma_1 - 1} \rho + (\Gamma_{\rm th} - 1)\rho\epsilon \ . \tag{3.122}$$

This EOS is used in all collapse simulations that employ polytropic initial models. For completeness, I state explicit expressions for the polytropic specific internal energy below and above $\rho_{\rm nuc}$:

$$\epsilon_{\rm p} = \begin{cases} \dfrac{K}{\Gamma_1 - 1} \rho^{\Gamma_1 - 1} & \text{for } \rho \leq \rho_{\rm nuc} \, , \\ \dfrac{K}{\Gamma_2 - 1} \rho^{\Gamma_2 - 1} \rho_{\rm nuc}^{\Gamma_1 - \Gamma_2} + \dfrac{(\Gamma_2 - \Gamma_1) K}{(\Gamma_2 - 1)(\Gamma_1 - 1)} \rho_{\rm nuc}^{\Gamma_1 - 1} & \text{for } \rho > \rho_{\rm nuc} \, . \end{cases} \tag{3.123}$$

The relativistic speed of sound [18, 156, 166] is given by

$$c_s^2 = \frac{1}{h} \frac{dp}{d\rho}\bigg|_s = \frac{1}{h} \left(\frac{\partial p}{\partial \rho}\bigg|_\epsilon + \frac{p}{\rho^2} \frac{\partial p}{\epsilon}\bigg|_\rho \right) = \frac{1}{\rho h} \Big(\Gamma p_{\rm p} + \Gamma_{\rm th} p_{\rm th} \Big) \ , \tag{3.124}$$

where $h = 1 + \epsilon + p/\rho$ is the relativistic enthalpy.

3.5.6 Atmosphere Treatment

WHISKY was originally designed for the study of compact objects that have a sharply defined surface beyond which is vacuum. Although no astrophysical object will have such a sharp transition to vacuum, it is realized by finite resolution and limited floating-point precision in numerical simulations. In vacuum, the speed of sound is zero and the conservation equations describing the fluid dynamics break down. What makes things worse is that when evolving a strong-field compact object (e.g., a neutron star), with current formulations of {3+1} numerical relativity and constraint violating boundary conditions, it is necessary to place the outer boundaries many stellar radii away from the stellar surface. The largest fraction of the computational volume is vacuum in such simulations; in particular on Cartesian grids. The problem even arises for the case of extended low-density $n = 3$ polytropes, the initial models used in the core collapse simulations discussed in Chapter 5 of this dissertation. Similar to numerical neutron star models they also exhibit a sharp edge and require a special treatment in the vacuum region. In WHISKY, the vacuum problem is solved by the introduction of a very low-density atmosphere typically at 7 to 8 orders of magnitude below the initial maximum rest-mass density on the grid. This ensures that the solution of the GR hydrodynamics equations remains physical and stable in regions outside the fluid body of interest, while the density is so low that even a large atmospheric volume does not lead to significant contributions to rest mass and energy. WHISKY makes use of a mask grid function (a bit field provided by the CACTUS thorn SPACEMASK [431]) to keep track of all grid cells that are part of the atmosphere. This atmosphere mask is updated after each time integration step to account for variations in atmosphere extent.

The initial atmosphere setup is performed on the initial data slice by the CACTUS thorn that provides the initial data. During evolution, the atmosphere cells are considered to obey a polytropic EOS and are treated in a special way by two routines:

- **Computation of the update terms**: Before updating the right-hand side of equation (3.45), for each cell is checked whether $\hat{D}$ or $\hat{\tau}$ are below some minimum value or whether the update step might push them below such a value. If this is the case, the update terms are zeroed for the relevant cell and the hydrodynamical variables in the cell are reset to preset atmosphere values.
- **Conversion from conserved to primitive variables**: For all grid cells, an attempt is made to convert back to primitive variables. If the EOS is polytropic and if the iterative procedure

returns a negative value for ρ, then ρ is reset to the atmospheric value and the velocities are zeroed. Then p, ϵ, $\hat{S}^i$, and $\hat{\tau}$ are reset to be consistent with ρ. $\hat{D}$, however, is not reset to be consistent with ρ. This is only for a practical reason: If the values of the cell variables were set such that they lie precisely on the atmosphere, then small errors would move certain cells above the atmosphere values which could lead to the excitation of high-frequency noise and waves of low-density matter hitting the edge of the neutron star / iron core. This is – typically – not a severe problem, but will, for example, result in unwanted and unphysical visible secondary overtones in neutron star pulsations [123, 410].

If the EOS is more general, then ϵ is checked after the conversion. If it is less than a specified minimum, then the relevant grid cell is considered to be part of the atmosphere and the conserved–to–primitive routine for the polytropic EOS is called.

3.5.7 The WHISKY Flow Chart

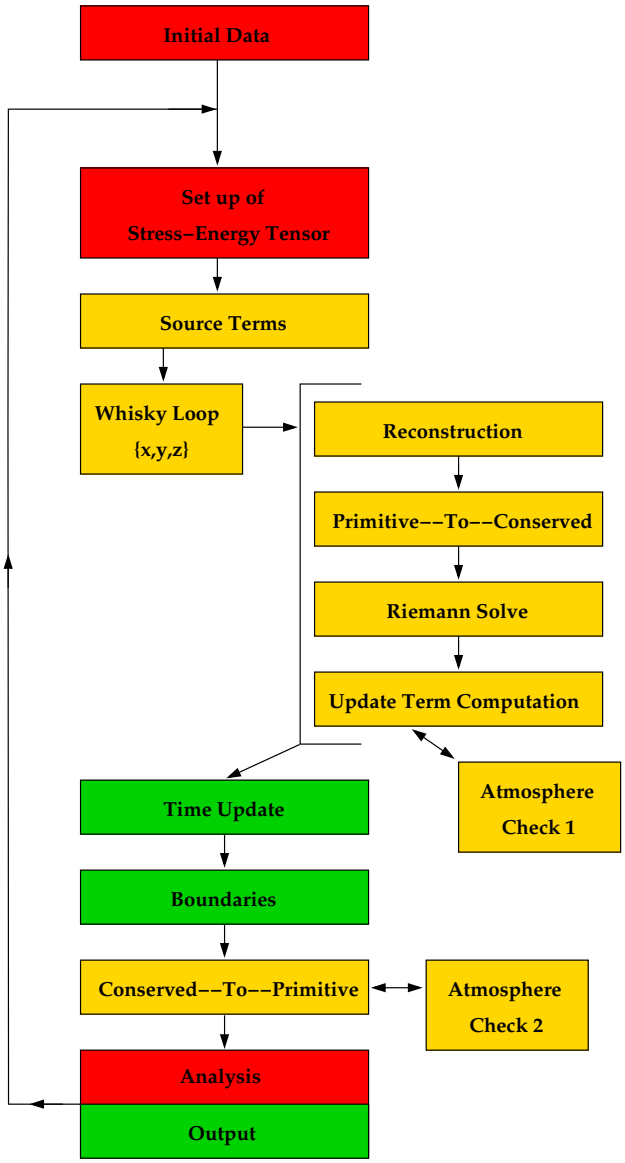

Figure 3.5: Schematic view of the WHISKY code and flow. Red boxes denote procedures implemented by physics thorns other than WHISKY. Green boxes mark procedures of the CACTUS/CARPET infrastructure and yellow boxes correspond to procedures implemented by WHISKY proper.

3.6 Astrophysics Add-Ons

One central goal of this work is to go beyond the commonly in GR studies used very simplified descriptions of the thermodynamical and microphysical details of the astrophysical objects under consideration. To date, all multi-D studies of stellar iron core collapse in general relativity [12, 13, 18, 160, 161, 204, 264, 267] have employed polytropic initial models and modelled collapse adiabatically using some sort of hybrid/Γ-law equation of state. Realistic precollapse iron cores, however, have a thermodynamical structure and chemical composition quite different from that of simple polytropes[16] (see, e.g., [3, 35, 36, 38, 64, 432]).

In the following sections I outline the additional routines that I have added to endow CACTUS/CARPET/WHISKY (CCW) with the capability of studying rotating stellar core collapse for the first time in {3+1} GR with presupernova models from stellar evolutionary calculations, a finite-temperature nuclear EOS, and a simplified, yet very effective deleptonization treatment in the collapse phase.

3.6.1 Advection of Composition

In precollapse stellar iron cores, strong force interactions are in near equilibrium, nuclear statistical equilibrium (NSE) prevails, and the EOS and all thermodynamic observables including the chemical abundances depend solely on density, temperature and on Y_e, the electron fraction per baryon [3, 36, 433]. Initial Y_e data are provided from stellar evolutionary calculations (see § 6.1 for example precollapse Y_e profiles). Y_e must be consistently advected with the fluid. This leads to an additional equation of advection / continuity nature that is added to the system of GR hydrodynamic equations (2.66):

$$\frac{1}{\sqrt{-g}}\left((\sqrt{\gamma} DY_e)_{,t} + (\sqrt{-g}(\alpha v^i - \beta^i) DY_e)_{,i} \right) = Q_{Y_e} \ , \tag{3.125}$$

with DY_e being the "conserved" variable in the flux-conservative sense. Q_{Y_e} is a source/sink term that is zero if the collapse is treated adiabatically and goes along with an energy source/sink in non-adiabatic collapse (see below in § 3.6.3). The conversion from conserved to primitive variable is analytic for Y_e. The above equation is implemented in identical fashion to the continuity equation for D. The source/sink term is treated in simple operator-split fashion as detailed below in § 3.6.3. In the reconstruction step, it is possible to choose between reconstruction of (ρY_e) or Y_e itself. Both approaches yield very similar results, while the former performs better in PPM near contact discontinuities in Y_e since contact steepening may be applied [434].

The routines added to WHISKY are set up to handle any number of compositional fractions for future use in more complicated applications requiring the advection of a large set of chemical species. Currently, normalization of each compositional set is not enforced as would be necessary in a multi-species non-NSE calculation [86, 434]. For a single compositional variable, the nature of the Valencia GR hydrodynamics scheme guarantees conservation.

3.6.2 Finite-Temperature Nuclear Equation of State

The EOS of core-collapse supernova matter has been under intense investigation for a number of decades. The basics of the EOS have been derived by Lamb et al. [435, 436], Bethe et al. [437], and Lattimer et al. [438], and a comprehensive review can be found in Hans Bethe's 1990 article [3].

The core-collapse supernova matter consists of a nuclear (nucleons and nuclei), an electron and a photonic component. Photons contribute significantly only at very low densities and high temperatures. Electrons are the dominant component at densities up to nuclear saturation density at ρ_s $\sim 2.67\times10^{14}$ g cm^{-3}. In fact, even at ρ_s, $p_{e^-}/p_{nuc} \sim 20$ [3]. Around $\rho_s/2$, a phase transition sets in between the phase with nuclei and a uniform bulk nuclear matter phase [439]. This phase transition was originally determined to be of first order since it is accompanied with a small energy change. Later studies [3, 436, 439, 440] indicate that the abrupt transition may be smoothed by a series of

[16] In fact, the supernova explosion mechanism can be sensitive to the precollapse structure. In early considerations of prompt explosion mechanisms the precollapse entropy and density stratification played an important role (see [3] and references therein).

smaller intermediate transitions to nuclear matter during which nuclei assume a variety of energetically favorable shapes (i.e., "bubbles", "spaghetti", "lasagna", "swiss cheese" etc.) [3, 439–441]. After the phase transition, the nuclear EOS quickly stiffens due to nuclear repulsive forces and the nuclear component dominates over the electrons.

There is no complete theory for nuclear matter and interactions that is able to explain all experimental results at low and high energies and momenta from first principles[3]. Hence, all models of the core-collapse supernova EOS are semi-phenomenological and depend on parameters extrapolated from experimental data on nuclear stability and interactions that are mostly obtained in conditions very different from those prevailing in a stellar iron core or in a PNS[17].

The EOSs worked out for practical application in core-collapse supernova calculations are based on a variety of approaches. The quite phenomenological compressible liquid-drop model for nuclei assuming a Skyrme-type [442] effective nuclear interaction has been successfully employed to procure an EOS for supernova simulations [438, 439, 443–445]. Most highlighted should be the effort of Lattimer & Swesty [439] who made their EOS routines freely available to the community. Their LSEOS — mostly in tabulated form — has been used in a large number of core-collapse supernova simulations. Other groups have employed more complicated nuclear Skyrme-Hartree-Fock (SHF) mean field calculations[18] [447–450] or nuclear Thomas-Fermi theory[19] [452–456] to derive a finite-temperature EOS for supernova matter. Since the early 1990s, relativistic mean field theory (RMF) [457–460], based on relativistic Brückner-Hartree-Fock theory [461, 462], has emerged as a variation on previous SHF approaches. RMF with the parameter set TM1 [458, 463, 464] has been quite successful in theoretically predicting properties of the ground states of heavy stable and unstable nuclei.

The EOS chosen for the general relativistic calculations presented in this work is the *Shen EOS* created by Shen et al. [464, 465]. The Shen EOS employs the full RMF Lagrangian for homogeneous nuclear matter at densities above $\sim \rho_s/3$ and switches to a statistical RMF-based Thomas-Fermi approach [466] for inhomogeneous nuclear matter consisting of a mixture of free neutrons, free protons, alpha particles, and a representative species of heavy nuclei. At low densities, the nuclear matter is treated as an ideal Boltzmann gas. Shen et al. provide a freely downloadable EOS table [464] to which the user must add the electron, and photon components. Variants of the original Shen table have been used in a number of studies comparing the LSEOS and the Shen EOS [467–469]. These studies did not reveal significant quantitative or qualitative differences in the collapse and bounce dynamics for the two EOSs. It rather showed that the Shen EOS leads to non-negligible differences in the general composition of the PNS and the postshock matter, and in particular to a consistently larger abundance of alpha particles during the postbounce stage.

The variant of the Shen EOS used in this work is provided by A. Marek of the Garching group and is similar to the one used in Marek et al. [469]. The original Shen table data are thermodynamically consistently (see, e.g., [470, 471]) interpolated onto a table of 180, 120, and 50 equidistant points in $\log_{10}\rho$, $\log_{10} T$, and Y_e, respectively. The table ranges are

$$6.31 \times 10^5 \text{ g cm}^{-3} < \rho < 1.12 \times 10^{15} \text{ g cm}^{-3} ,$$

$$0.1 \text{ MeV} < T < 200 \text{ MeV} ,$$

$$0.015 < Y_e < 0.56 .$$

The above ranges in ρ, T, and Y_e mark the clear technical advantage of the Shen EOS over the LSEOS: The Shen table reaches down to significantly lower values of density and temperature than the LSEOS (by two orders of magnitude in density) and is more readily applicable to stellar core collapse, where the density at the edge of the iron core can be lower than $\sim 10^6$ g cm^{-3}. The Shen treatment of low-density nuclear matter makes it also more easily extendable to even lower densities [16, 72, 472].

[17] Many heavy ion collision experiments from several hundred MeV up to GeVs have been performed with the hope of obtaining a nuclear EOS at high density [3]. Yet, it is important to keep in mind that the temperature in a PNS is on the order of $\sim$10 Mev and the entropy of order unity (in units of k_B/baryon).

[18] In Hartree-Fock calculations many-body effects are self-consistently approximated by an effective interaction potential that is derived iteratively. The method was first applied to electron orbit configurations in molecules. It is the basis of the nuclear shell model and details of its application in combination with the Skyrme force to nuclear theory can be found, for example, in [446].

[19] The statistical mean-field Thomas-Fermi theory, like the Hartree-Fock approach, was first introduced into atomic physics and later adopted by nuclear theorists. See [451] for a review.

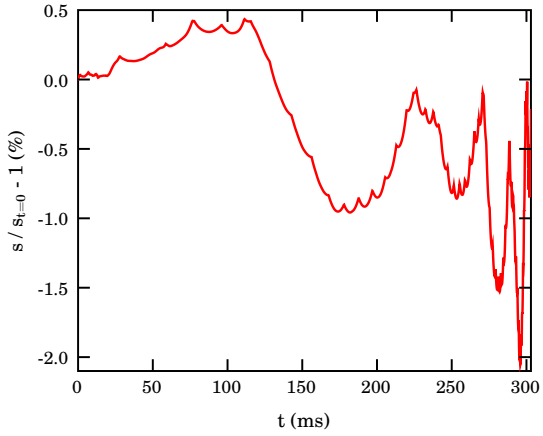

Figure 3.6: Relative deviation of the central entropy per baryon from its start value during adiabatic core collapse until core bounce using the Shen EOS table and routines as implemented in CACTUS/CARPET/WHISKY. The largest deviation is ∼2% and occurs shortly before core bounce.

At densities above 10^9 g cm^{-3} and temperatures above ∼1 MeV, the electron/positron contributions are added in the approximation of relativistic degeneracy and pair equilibrium. In this approximation, simple analytic expressions for the electron/positron chemical potential, number density, pressure, entropy and internal energy are obtained [36, 439, 473, 474]. For lower densities and temperatures, the full Fermi integrals (see, e.g., [36, 473]) are numerically integrated, using the code provided by version 2.7 of the LSEOS [439][20]. Neutrino contributions are not included in the EOS table and the photonic contribution is handled as a standard Planck photon gas.

The Shen EOS table used in this work contains entries at each point in (ρ,T,Y_e) for the total pressure, the specific internal energy ϵ, the entropy per baryon, and the quantity $\mu_e - \mu_n + \mu_p$, which is, in β-equilibrium, identical to μ_{ν_e}, the electron neutrino chemical potential. I have added entries for the effective adiabatic index Γ, the Newtonian speed of sound, and the derivatives $dp/d\epsilon|_\rho$ and $dp/d\rho|_\epsilon$ (see appendix B for details on the expressions used).

In the original Shen table, the internal energy is given in terms of the internal energy per baryon and is offset by the energy of one atomic mass unit, accounting for the baryon rest mass energy. In Newtonian gravity, such a zero-point shift of the internal energy can be neglected since only derivatives of ϵ are dynamically important. In general relativity, however, ϵ contributes directly to the right-hand-side of the Einstein equations. The rest mass density appears explicitly in the ADM and GR hydrodynamic equations and is not assumed to be part of the internal energy. Hence, it is necessary to correct for the offset in the internal energy table.

The Shen EOS is integrated with CACTUS/CARPET/WHISKY by means of an independent CACTUS thorn whose routines are callable through a generalized EOS interface. Since WHISKY operates on (ρ, ϵ, Y_e), a table lookup consists of two steps. First, the corresponding temperature T to (ρ, ϵ, Y_e) is found via a Newton-Raphson type iteration, then a trilinear interpolation is performed to obtain the desired quantity at (ρ, T, Y_e). Since the table is equidistant in $\log_{10}\rho$, $\log_{10} T$, and Y_e, the nearest table points to (ρ, T, Y_e) are found by integer arithmetic. It has been stated in the literature [470, 471] that the simple trilinear interpolation scheme used here is not sufficient to ensure thermodynamical consistency. One standard test of the latter is adiabatic core collapse during which the entropy must stay constant [3, 439, 475]. Figure 3.6 depicts the relative variation of the central entropy from its start value at the beginning of collapse to core bounce as calculated with a simple 1D Eulerian Newtonian hydrodynamics code to which the Shen EOS in the present form is coupled. The maximal deviation from adiabaticity is ∼2% which is not much worse than the ∼1% found for direct (non-tabulated) application of the LSEOS by [439]. The quite good conservation of adiabaticity despite trilinear interpolation is most likely due to the large number of (ρ, T, Y_e) points in the table. Hence, one can safely consider trilinear interpolation to be sufficient for all practical hydrodynamic purposes considered in this work, yet for precise studies of supernova mechanisms and energetics in the realm of

[20] Note that the original version of the LSEOS included only relativisticly degenerate electrons and positrons. From version 2.5 on the LSEOS routines allow arbitrary degeneracy.

radiation hydrodynamics, a thermodynamically more consistent interpolation scheme is advisable (though computationally much more expensive) due to the strong temperature dependence of the weak interaction physics (see, e.g., [3, 64] and references therein).

3.6.3 Deleptonization Treatment

As pointed out in §2.3.2, the capture of electrons on free protons and on protons bound in nuclei leads to a reduction of the iron core's electron fraction Y_e during collapse:

$$\begin{aligned} e^-\text{capture by nuclei:} \quad & e^- + (Z, A) \overset{(W)}{\rightarrow} \nu_e + (Z-1, A) \\ e^-\text{capture by free protons:} \quad & e^- + p \overset{(W)}{\rightarrow} \nu_e + n \ . \end{aligned} \tag{3.126}$$

Both reactions are charged-current weak interactions and the produced electron neutrinos either (1) directly escape at low densities, (2) thermalize and eventually escape, or (3) are trapped for longer than the dynamical timescale. Since in cases (1) and (2) the core actually loses leptons, one refers to electron capture during collapse as *deleptonization*. Case (3) is encountered at densities above $\sim 2\times10^{12}$ g cm^{-2} when the neutrino scattering opacities become so large that the timescale for neutrinos to leave the core becomes larger than the dynamical timescale [3, 36, 64]. The electron capture rates scale roughly $\propto \mu_e^5$ (see, e.g., [3, 36, 64]), where μ_e is the electron chemical potential that in turn scales $\propto \rho^{1/3}$, where ρ is the baryonic density. Hence, electron capture becomes more and more likely and Y_e is reduced more quickly as collapse proceeds and higher densities are reached. In the trapping regime, the total lepton fraction, $Y_l = Y_e + Y_\nu$, is conserved, and electrons and neutrinos are in β-equilibrium. μ and τ neutrinos and anti-neutrinos do not appear during collapse and are only created at postbounce times when the shock-heated material has temperatures sufficiently high for pair-creation processes [3].

The degenerate electron gas provides the dominant contribution to the fluid pressure at densities below nuclear matter density. A reduction in Y_e thus leads to a reduction of pressure support. Deleptonization accelerates collapse and, as first pointed out by [66], *decreases* the mass of the homologous inner core that coherently rebounds and that determines the mass coordinate of shock formation and the initial energy that is imparted to the shock. Core-collapse calculations that do not include deleptonization almost always yield prompt explosions, while calculations that do take into account deleptonization almost never produce explosions [64].

In fast rotating core collapse, the strongest gravitational wave signal is expected from the matter dynamics at core bounce. For reliable estimates of the gravitational wave signature of rotating iron core collapse it is essential to fully capture the bounce dynamics and include deleptonization which – in combination with the EOS and centrifugal effects – controls the mass of the inner core. Unfortunately,

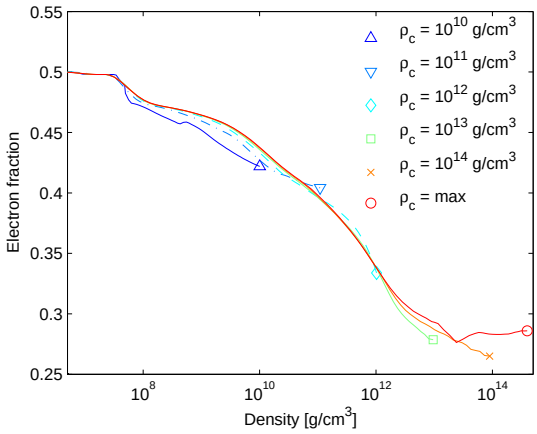

Figure 3.7: Electron fraction (Y_e) profiles in density at varying central densities during collapse in model G15 of Liebendörfer et al. [83]. As shown, $Y_e(\rho, t)$ is only a weak function of time. Figure taken from [476].

multi-dimensional neutrino radiation transfer calculations (e.g., [26, 73, 78, 86, 87, 477, 478] and references therein) and even simplified leakage/trapping schemes (e.g., [11, 68, 263, 272, 479–483]) are still too computationally (and in part conceptually) demanding to be incorporated into the {3+1} GR hydrodynamics calculations performed here. Alternatively, I follow an approach that has first been employed in early work by Müller & Hillebrandt [260, 261] and that has recently been revived by Liebendörfer [476]. It is based on the observation (figure 3.7; taken from [476]) that the function $Y_e(\rho, t)$ is only very weakly dependent on time. Moreover, a microphysically consistent Y_e during collapse in a hydrodynamics calculation can be obtained with high precision from a parametrization $Y_e(\rho) = Y_e(\rho, t = t_{\rm bounce})$ that is based on the results of a spherically symmetric detailed radiation hydrodynamics calculation. The bounce-$Y_e(\rho)$ profile is chosen to obtain a good approximation of the real $Y_e(\rho)$ at the time of core bounce. Liebendörfer [476] has shown that in spherical symmetry such a parametrization yields microphysical and (thermo)dynamical conditions at core bounce to within a few percent to those obtained with a detailed radiation-hydrodynamic calculation. The parametrization of deleptonization during collapse relies much more on the local density evolution than on the global geometry. Hence, using the same $Y_e(\rho)$ also for rotating models is likely to be almost as accurate as for the spherically symmetric model [476].

Following [476], I implement a source term for the Y_e advection equation (3.125) given by

$$\frac{\delta Y_e}{\delta t} = \frac{\min\left[0, \bar{Y}_e(\rho(t+\delta t)) - Y_e(t)\right]}{\delta t} \,, \tag{3.127}$$

where $\delta/\delta t$ denotes a Lagrangian change in a fixed mass element and where $\bar{Y}_e(\rho(t+\delta t))$ is the parametrized Y_e interpolated in $\log_{10}\rho$ to the updated density at $t+\delta t$. $Y_e(t)$ is the electron fraction at time t. The minimum function guarantees that Y_e decreases monotonically even if transient instances occur in which the parametrized $\bar{Y}_e$ is larger than $Y_e(t)$. This happens, for example, as seen in figure 3.7, at the beginning of Liebendörfer's calculation and the deleptonization described by equation (3.127) sets in slowly after a short time of adiabatic compression. During this the original Y_e profile moves to the right in the $\rho - Y_e$ plane to join the bounce profile, $\bar{Y}_e$.

I apply equation (3.127) first-order in time and operator-split[21] from the Eulerian hydrodynamics. The present deleptonization scheme manifest in equation (3.127) cannot capture the slight increase in Y_e around nuclear density seen in Liebendörfer's calculation (figure 3.7) which is due to increasing neutron degeneracy at these densities. In the neutrino trapping regime where β-equilibrium prevails, Y_l is constant and Y_e must – in principle – be obtained by means of a detailed weak equilibrium calculation. A parametrization of Y_l instead of Y_e would allow for a more consistent Y_e at nuclear density, but would lead to a significant increase in computational complexity of the scheme [476]. The most important limitation of the Y_e parametrization is, however, its inability to capture any post-core bounce neutrino effects such as the rapid postbounce deleptonization in the region immediately behind the supernova shock associated with the neutrino break-out burst when the shock reaches the electron-neutrino neutrinosphere (see, e.g., [70]). Following [476], I deactivate deleptonization once core bounce is reached. The immediate bounce and early postbounce dynamics remain unaffected by above limitation, but beginning a few milliseconds after core bounce, the PNSs in the calculations presented here exhibit artificially high Y_es and cannot cool via neutrino emission. This leads to significant differences in the PNS structure and thermodynamics on a timescale of $\sim$100 ms.

For the calculations presented in this work I employ a parametrization $\bar{Y}_e$ obtained from results of detailed spherically-symmetric Boltzmann neutrino radiation-hydrodynamics core-collapse simulations. These calculations were carried out by R. Buras and A. Marek of the Garching group with the VERTEX code [73, 86, 469]. VERTEX includes an approximate treatment of general relativistic gravity and is described in detail in [85] and was run with the same Shen EOS table that I use in my calculations. For electron capture on protons the rates derived by Burrows & Sawyer [484] were used. Capture on heavy nuclei is dominated by the Gamow-Teller transition from the single-particle $1f_{7/2}$ level to the single-particle $1f_{5/2}$ unless the reaction is blocked by the absence of neutron holes, which, in the standard picture [3, 475], occurs for $N \geq 40$. Hence, the standard rates [475, 485] for electron capture (that employed in [73, 86]) do not include electron capture on nuclei with $N \geq 40$. I point out that recent results by Langanke et al. [486], obtained via nuclear shell model calculations,

[21] Owing to the ad-hoc nature of the Y_e parameterization and to the fact that the stability of the numerical evolution is not affected by the always small δY_e. Test calculations in which I have included equation (3.127) at every intermediate time integration step show that the first-order operator-split approach is sufficient.

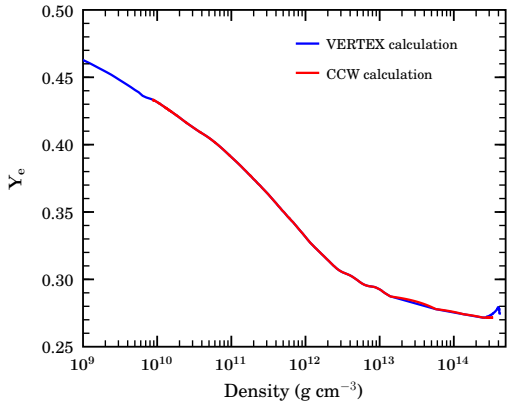

Figure 3.8: Electron fraction (Y_e) as a function of density for the spherically symmetric collapse of presupernova model s20 from [38]. Blue graph: $Y_e(\rho)$ profile at core bounce of the 1D radiation-hydrodynamics calculation carried out with VERTEX [85, 469]. Red graph: $Y_e(\rho)$ evolution at the stellar center as obtained with CACTUS/CARPET/WHISKY (CCW) and Y_e-parametrization based on the VERTEX calculation. The slightly higher Y_e in the CCW calculation between 2 and 6×10^{13} g cm^{-3} is due to interpolation in $\log_{10}\rho$ in between the only two datapoints present in the VERTEX output at these densities.

show that thermal unblocking and other effects lead to significant electron capture even on nuclei with $N \geq 40$. As a consequence [64, 106], electron capture on nuclei dominates the one on free protons throughout collapse and ∼5–10% lower Y_e at core bounce – and correspondingly smaller inner core masses – are obtained than with the electron capture rates employed by [73, 86].

For all baseline calculations with the Shen EOS (see §3.7.3 and §6.1 for a discussion of initial models and simulation parameters) I make use of the 20 $M_\odot$ (at zero-age main sequence [ZAMS] and solar metallicity) presupernova model of [38]. For maximum consistency, I obtain the employed $\bar{Y}_e(\rho)$ from a VERTEX collapse calculation for the same initial model. Liebendörfer has, however, demonstrated [476] that $Y_e(\rho)$ does not vary much with progenitor model since the evolution of Y_e during collapse depends most strongly on the local density evolution which varies only slightly with progenitor model. Hence, for simplicity, I employ the same $\bar{Y}_e(\rho)$ also in calculations with different presupernova models.

Figure 3.8 depicts the $Y_e(\rho)$ profile of model s20 [38] at the time of core bounce in the 1D VERTEX calculation. To demonstrate the consistent implementation of the scheme, I plot $Y_e(\rho)$ at the stellar center as obtained in a nonrotating CCW calculation in which I use a parametrization $\bar{Y}_e(\rho)$ based on the VERTEX bounce-Y_e profile. As expected, the slight increase of Y_e at nuclear density is not captured by the scheme. In addition, $\bar{Y}_e$ yields slightly larger values than the VERTEX Y_e between 2 and 6×10^{13} g cm^{-3}. This is due to the fact that there are no additional supporting points for the linear interpolation in $\log_{10}\rho$ between those values of ρ. Otherwise the original VERTEX bounce Y_e profile is very well approximated by my implementation of Liebendörfer's scheme (3.127).

Entropy and Energy Changes During Collapse

Electron capture during collapse not only reduces Y_e but also results in a change of the matter entropy and internal energy [3, 36]. The baryons are in NSE and the electrons are in thermal equilibrium. Changes of the entropy per baryon (δs) are then determined by the chemical potentials μ_n, μ_p, and μ_e of neutrons, protons, and electrons, respectively. The resulting energy transfer between matter and neutrinos (δq) has to be taken into account. One obtains [64, 475]

$$T\delta s = -\delta Y_e\left(\mu_e - \mu_n + \mu_p\right) + \delta q \ , \tag{3.128}$$

where T is the fluid temperature. As pointed out earlier, depending on the density of the matter and the energy of the produced neutrinos, a produced neutrino can either (1) escape directly without further interactions, (2) thermalize and escape, or (3) be trapped for longer than the dynamical time scale. In regime (1) which prevails at densities below $\sim2\times10^{11}$ g cm^{-3}, $\delta q \approx \delta Y_e E_\nu^{\rm escape}$ and $E_\nu^{\rm escape} > \mu_e - \mu_n + \mu_p$ [64]. Hence, the entropy of the fluid effectively decreases in regime (1). Since the escape

energy of the neutrinos ($E_\nu^{\rm escape}$) is only slightly larger than ($\mu_e - \mu_n + \mu_p$), the resulting entropy change is small and — following Liebendörfer [476] — is neglected here. In regime (2), between $\sim 2\times10^{11}$ g cm^{-3} and the onset of trapping around 2×10^{12} g cm^{-3}, the neutrino mean free path is reduced by increasing scattering off heavy nuclei. The increasing matter density causes the electron chemical potential to rise, resulting in the production of neutrinos at higher energies. As the neutrino mean free path scales $\propto E_\nu^{-2}$, thermalization to low energies provides the fastest way of escape. This thermalization process leads to a mean final escape energy on the order of $\sim$10 MeV [64]. I follow again Liebendörfer [476] and implement the entropy change via

$$\frac{\delta s}{\delta t} = -\frac{\delta Y_e}{\delta t}\frac{\mu_e - \mu_n + \mu_p - E_\nu^{\rm escape}}{T} \tag{3.129}$$

where $\delta Y_e/\delta t$ is given by equation (3.127). Here I choose $E_\nu^{\rm escape} = 10$ MeV and only evaluate (3.129) when $(\mu_e - \mu_n + \mu_p - E_\nu^{\rm escape}) > 0$ (when net energy is deposited and the entropy increases), and otherwise assume $\delta s = 0$. The sum $\mu_e - \mu_n + \mu_p$, which in β-equilibrium equals the electron neutrino chemical potential, is contained in the Shen EOS table employed and the change in the specific internal energy (ϵ) corresponding to δs is obtained via numerical iteration of the EOS. I point out that even in the case of $\delta s = 0$, a change in Y_e will result in a net change of ϵ and the consistent ϵ that is locally consistent with $\delta s = 0$ must be found using the EOS. Above trapping density ($\sim 2.0\times10^{12}$ g cm^{-3}; [64, 476]), in regime (3), the neutrinos are not able to escape before the postbounce neutrino break-out burst and β-equilibrium prevails. δq in equation (3.128) is determined by the neutrino chemical potential, $\delta q = \delta Y_e \mu_\nu$ [476]. Since $\mu_e + \mu_p = \mu_n + \mu_\nu$ in β-equilibrium, $\delta s = 0$ follows and $\delta\epsilon$ is obtained via the EOS. All changes of entropy and specific internal energy are applied in the same first-order operator-split fashion as the Y_e change described by equation (3.127).

3.6.4 Neutrino Pressure and Energy Contributions

In the optically thick regime, the neutrinos are trapped within the protoneutron star and their diffusion timescale is larger than the hydrodynamic timescale (e.g., [36, 64, 83]). Transport processes can be neglected and the neutrinos may be treated as an ideal Fermi gas in thermal equilibrium with the fluid. Including only electron and anti-electron neutrinos and using the electron-neutrino chemical potential[22] (μ_ν, with β equilibrium, $\mu_\nu = \mu_e - \mu_n + \mu_p$), the neutrino Fermi pressure in the optically-thick regime is given by

$$p_\nu = \frac{4\pi}{3(hc)^3}(kT)^4\Big[F_3(\eta_\nu) + F_3(-\eta_\nu)\Big] \ , \tag{3.130}$$

where $\eta_\nu = \mu_\nu/kT$ and F_n is the Fermi-Dirac function of order n, $F_n(\eta) = \int_0^\infty x^n(e^{x-\eta}+1)^{-1}dx$ [488]. For $[F_3(\eta_\nu) + F_3(-\eta_\nu)]$ I use the expression derived by van Riper and Bludman [487]:

$$F_3(\eta) + F_3(-\eta) = \frac{7\pi^4}{60} + \frac{1}{2}\eta^2(\pi^2 + \frac{1}{2}\eta^2) \ . \tag{3.131}$$

The specific neutrino energy is given by $\epsilon_\nu = 3p_\nu/\rho$.

The transition between trapping and free-streaming occurs in the semi-transparent region that spans in optical depth from $\sim$1 to $\sim 2/3$, the location of the neutrinosphere at which free-streaming sets in (see, e.g., [70] and references therein). The position (in space, mass, or density) of the neutrinosphere and the beginning of the semi-transparent region are very neutrino-energy and neutrino-flavor dependent. For the ad-hoc approach used in this work, I follow [476] and assume a transition density of 2×10^{12} g cm^{-3} from optically-thick to semi-transparent and set $p_\nu = 0$, $\epsilon_\nu = 0$ below this density[23]. This approach is justified by the fact that neutrino pressure and energy contributions are already small at the transition density ($\lesssim 5\%$ of the fluid pressure/internal energy) and, hence, for the collapse and bounce dynamics practically irrelevant. Postbounce neutrino energy and momentum depositions are likely to be important in the semi-transparent regime for any delayed-type explosion mechanism, but cannot be captured by the present scheme.

[22] In β-equilibrium, electron and anti-electron neutrinos have equal and opposite chemical potentials [487].

[23] Liebendöerfer [83] proposed a computationally intensive scheme (not implemented here) that allows the estimation of the neutrino pressure in optically semi-transparent regions.

Above trapping density, I include the neutrino pressure and energy contributions as additional contributions in the coupling to curvature (see §3.5). For this I construct a fluid stress energy tensor[24],

$$T^{\alpha\beta} = \left[\rho + \rho(\epsilon + \epsilon_\nu) + (p + p_\nu)\right] u^\alpha u^\beta + (p + p_\nu) g^{\alpha\beta} \ . \tag{3.132}$$

The neutrino-fluid interaction in the optically-thick regime is most consistently handled via momentum and energy source terms for the GR hydrodynamics equations. This emphasizes the fact that baryonic/electronic matter and neutrinos are separate, though coupled fluids. Alternatively, neutrino energy and pressure could simply be added to the corresponding fluid quantities. This would allow an inclusion of the neutrino pressure in the solution of the local Riemann problems, but, at the same time, introduce inconsistencies in the EOS and the solution of the Riemann problems at the transition density. I hence follow the more consistent source term approach which is commonly employed for coupling the neutrino radiation field to matter in radiation-hydrodynamics calculations (e.g.,[85, 86, 489]).

The stress exerted by the neutrino gas on the fluid is determined by the gradient of the neutrino pressure. In analogy with Newtonian fluid dynamics (e.g., [86, 149, 476]) and in terms of the Valencia GR hydrodynamics formulation [156, 157], I write the source term for spatial direction i in the GR momentum equation (see §2.5) as an additional pressure contribution pulled out of the flux term,

$$s_i^{\text{momentum}} = -(\alpha\sqrt{\gamma}p_\nu)_{,i} \ . \tag{3.133}$$

The source term in the energy equation is then simply

$$s^{\text{energy}} = v^i s_i^{\text{momentum}} = -v^i(\alpha\sqrt{\gamma}p_\nu)_{,i} \ . \tag{3.134}$$

Both source terms are applied as additional right-hand side contributions to the GR hydrodynamics equations within the Method of Lines time integration scheme (see §3.2). This provides numerically stable and consistent coupling with the hydrodynamics. The physical effects of the neutrino pressure and energy contributions are discussed in Chapter 6.

[24] I point out that this stress-energy tensor is only used in the coupling to the BSSN_MoL curvature evolution. The direct hydrodynamic effects of neutrino pressure gradients are handled via source terms in the GR hydrodynamics equations.

3.7 Initial Data for Core-Collapse Simulations

The minimal set of initial data that must be specified for a {3+1} GR hydrodynamics calculation are (1) the six 3-metric components γ_{ij}, the six components of the extrinsic curvature K_{ij}, (2) the basic matter variables density ρ, specific internal energy ϵ and 3-velocity v^i, and (3), an EOS relating ρ and ϵ to the fluid pressure p. The initial data should be physical and must satisfy the ADM momentum and Hamiltonian constraints. The York-Lichnerowicz procedure [119, 147, 148] delineated in §2.4.4 is one way of generating constraint satisfying initial metric and extrinsic curvature data for an arbitrary matter/energy distribution.

In this work I employ two distinct classes of initial data for my GR core collapse calculations. The first class are equilibrium solutions of general relativistic stellar structure equations. While intrinsically constraint satisfying (to numerical accuracy), such solutions provide approximations of limited quality to realistic precollapse stellar iron cores since they generally assume a simplistic isentropic thermodynamic structure. The second class of initial data that I consider are precollapse stellar models from spherically symmetric Newtonian stellar evolutionary calculations. These data provide much more realistic compositional and thermodynamic initial conditions for core collapse simulations, but have the disadvantage of being Newtonian and — in the rotating case — not being in axisymmetric rotational equilibrium.

In the following both classes of initial data are discussed in detail.

3.7.1 Tolman-Oppenheimer-Volkoff Polytropes

The simplest progenitor models for stellar collapse simulations are spherically symmetric polytropes in hydrostatic equilibrium. Polytropes are stellar models that obey the polytropic EOS specified by equations (3.117) and (3.118) on page 71. In Newtonian gravity, the Lame-Emden equation (see, e.g., [36]) is used to construct stellar models parametrized by central density ρ_c, K and adiabatic index Γ.

As discussed in §2.4.4, specifying fluid initial data alone is not sufficient. Initial data for the 3-metric, the extrinsic curvature and initial gauge choices (lapse and shift vector) are required for the Cauchy evolution of the Einstein field equations. Tolman [490] and Oppenheimer & Volkhoff [491] have found the equations of stellar structure for isentropic stars in general relativity (the *TOV* equations):

$$\frac{dp}{dr} = -(\rho(1+\epsilon)+p)\frac{m+4\pi r^3 p}{r(r-2m)} \ , \tag{3.135}$$

$$\frac{dm}{dr} = 4\pi r^2 \rho(1+\epsilon) \ , \tag{3.136}$$

$$\frac{d\ln\alpha}{dr} = \frac{m+4\pi r^3 p}{r(r-2m)} \ . \tag{3.137}$$

Here ρ, p, and ϵ have their usual meaning in the fluid context and α is the lapse. r is the *areal radius* defined by demanding that a 2-sphere of radius r have the proper area $4\pi r^2$ and proper circumference $2\pi r$. $m(r)$ is the mass inside the areal radius r including internal energy and gravitational potential energy contributions[25]. The line element in the interior of the star is then given by

$$ds^2 = -\alpha(r)^2 dt^2 + \left(1-\frac{2m(r)}{r}\right)^{-1} dr^2 + r^2(d\theta^2 + sin^2\theta d\varphi^2) \ . \tag{3.138}$$

Equations (3.135–3.137) are integrated numerically from $r=0$ to the stellar surface at radius R with inner boundary conditions $m(r=0)=0$, $\rho(r=0)=\rho_c$, $\ln\alpha(r=0)=0$. The central pressure p_c and the central specific internal energy ϵ_c are derived from the central density through the polytropic equation of state; $P_c = K\rho_c^\Gamma$ and $\epsilon_c = p_c/[(\Gamma-1]\rho_c)$. At the outer boundary the solution of equations

[25] See [36] for a discussion why this is the case given the simplicity of equation (3.136).

(3.135–3.137) is matched to an exterior Schwarzschild spacetime, fixing

$$P(r = R) = 0 \tag{3.139}$$
$$m(r = R) = M \tag{3.140}$$
$$\alpha(r = R) = \sqrt{1 - \frac{2M}{R}}, \tag{3.141}$$

where M is the total gravitational mass of the star. If one is interested in the solution of equations (3.135–3.137) for an isotropic radial coordinate $\bar{R}$ (as, for example, used for Cartesian grids: $\bar{r}^2 = x^2 + y^2 + z^2$), the additional equation [492]

$$\frac{dln(\bar{r}/r)}{dr} = \frac{\sqrt{r} - \sqrt{(r - 2/m(r))}}{\sqrt{r(r - 2m)}} \tag{3.142}$$

must be solved with $\bar{r}(r = 0) = 0$ and $\bar{r}(r \geq R) = \frac{1}{2}(\sqrt{r(r - 2M)} + r - M)$.

The TOV solution is static (hence, time symmetric), spherically symmetric and asymptotically flat. The extrinsic curvature and the shift vanish.

Choice of Γ and K

The TOV equations do not a priori fix the choice of ρ_c and the EOS parameters Γ and K, yet a stable equilibrium solution can only be found for a limited parameter space in ρ_c, Γ and K (see, e. g., [36, 63]).

Precollapse stellar iron cores have a central density of $\sim 10^{10}$ g cm^{-3} and are stabilized mainly by the pressure of extremely relativisticly degenerate Fermi gas of electrons [36]. This motivates a choice of

$$\begin{aligned} \rho_c &= 1 \times 10^{10} \mathrm{g\,cm^{-3}}\,, \\ \Gamma &= \frac{4}{3}\,, \\ K &= \frac{3}{4}\left(\frac{\pi}{3}\right)^{2/3} \hbar c \left(\frac{Y_e}{m_B}\right)^{4/3} \overset{\text{Iron}}{=} 1.2435 \times 10^{15}\,(0.5)^{4/3}\,[\mathrm{cgs}]\,, \end{aligned} \tag{3.143}$$

where Y_e is the electron fraction per baryon and m_B is the mean baryon rest mass defined as

$$m_B \equiv \frac{\sum_i n_i m_i}{\sum_i n_i A_i}\,, \tag{3.144}$$

with n_i and m_i being the number density and the mass of ion species i, respectively. A_i is the corresponding integer atomic weight. m_B may be approximated by the atomic mass unit m_u (see appendix A).

Parameter choice (3.143) yields a precollapse iron core TOV solution $M \sim 1.42$ M$_\odot$ with an isotropic coordinate radius of $\bar{R} \sim 1545$ km. $\Gamma = 4/3$ polytropes are stable to radial perturbations in Newtonian gravity, but, as Chandrasekhar [63] has demonstrated, not in general relativity. Once mapped onto the CCW grid, numerical truncation errors drive the TOV star dynamically unstable to collapse in finite time. However, depending on the grid resolution, the time until dynamical collapse can be rather long. Hence, I choose to lower the adiabatic index to a value below but close to $4/3$ to instigate collapse. This is in the tradition of all previous studies that have investigated the collapse of polytropic iron core models (see, e.g., [12, 13, 18, 30, 160, 161, 204, 267]) and leads to a sudden loss of pressure support, entailing a small initial violation of the Hamiltonian and momentum constraints. Since the initial data are spherically symmetric and time symmetric despite the pressure reduction, a solution of

$$\bar{\nabla}^2 \Psi = -2\pi \Psi^5 (\rho + \rho\epsilon)\,, \tag{3.145}$$
$$\gamma_{ij} = \Psi^4 \eta_i j\,, \tag{3.146}$$
$$K_{ij} = 0\,, \tag{3.147}$$

where η_{ij} is the flat space metric, is sufficient to satisfy the constraints on the initial data slice [127]. I implement this via a standard shooting technique (see, e.g., [493]) and the LSODA ODE solver [494].

See §4.2 for results of collapse calculations employing TOV initial data.

3.7.2 Polytropes in Rotational Equilibrium

Rotation breaks spherical symmetry and initial models in *rotational equilibrium* are oblate spheroids, or in the case of extreme differential rotation, oblate quasi-toroids[26]. I compute rotational-equilibrium polytropes using the CACTUS thorn WHISKY_RNSID written by N. Stergioulas. It is an extended version of his original RNS code [312, 495–497] which is based on the Komatsu-Eriguchi-Hachisu scheme [498, 499] and modifications of the former introduced by Cook et. al. [500]. For a review of rotating stars in general relativity and the computation of rotational equilibrium models, the interested reader is referred to the Living Reviews in Relativity article by N. Stergioulas [312]. Here I shall only delineate the most basic and salient aspects of WHISKY_RNSID and the Komatsu-Eriguchi-Hachisu scheme. Additional information and numerical details can be found in above references.

The three basic assumptions are that the considered spacetime is axisymmetric, stationary and asymptotically flat. Stationarity implies that there exists a timelike Killing vector (see, e.g., [116]) field t^α. Axisymmetry implies that there exists a spacelike Killing vector field φ^α in the symmetry direction. Asymptotic flatness guarantees that $t_\alpha t^\alpha \to -1$, $\varphi^\alpha \varphi_\alpha \to +\infty$ and $t_\alpha \varphi^\alpha \to 0$ at spatial infinity. The two Killing vectors commute [501] and it is possible and convenient to choose coordinates in which t^α and φ^α are basis vectors. If, in addition, the rotating flow is strictly circular, all 2-surfaces orthogonal to the two Killing vector fields can be described by the remaining two coordinates x^1 and x^2 [502]. In isotropic coordinates, the 2-surfaces spanned by $x^1 = r$ and $x^2 = \theta$ are conformally flat and the line element can be written as

$$ds^2 = -e^{2\nu}dt^2 + e^{2\psi}(d\varphi - \omega dt)^2 + e^{2\mu}(dr^2 + r^2 d\theta^2) \ , \tag{3.148}$$

with the metric potentials ν, ψ, μ and ω and with

$$\begin{aligned} g_{tt} &= t^\alpha t_\alpha = -e^{2\nu} + \omega^2 e^{2\psi} \\ g_{t\varphi} &= t^\alpha \varphi_\alpha = -\omega e^{2\psi} \\ g_{\varphi\varphi} &= \varphi^\alpha \varphi_\alpha = w^{2\psi} \ . \end{aligned} \tag{3.149}$$

The rotating matter is assumed to be a non-magnetic neutral perfect fluid with a stress-energy tensor as defined by equation (2.59) on page 22. The angular velocity of the fluid surface as seen by an observer at rest at infinity is in terms of the fluid 4-velocity given by

$$\Omega \equiv \frac{u^\varphi}{u^t} = \frac{\frac{d\varphi}{ds}}{\frac{dt}{ds}} = \frac{d\varphi}{dt} \ . \tag{3.150}$$

The normalization $u^\alpha u_\alpha = -1$ fixes u^t globally to

$$u^t = \frac{e^{-\nu}}{\sqrt{1 - (\Omega - \omega)^2 e^{2(\psi - \nu)}}} \ . \tag{3.151}$$

The fluid 3-velocity, as measured by an Eulerian observer (who has zero angular momentum locally and is hence called zero-angular momentum observer [ZAMO]) is

$$v = (\Omega - \omega) e^{\psi - \nu} \ . \tag{3.152}$$

In terms of v, the 4-velocity can then be written

$$u^\alpha = \frac{e^{-\nu}}{\sqrt{1 - v^2}} [1, 0, 0, \Omega]^T \ . \tag{3.153}$$

From equation (3.152) one figures that a ZAMO has angular velocity ω with respect to an observer at rest at infinity. This is related to the widely known *frame dragging* effect (e.g., [116, 312]).

[26] I use the "quasi" prefix to acknowledge the fact that true toroids have vanishing density outside the toroid body while the rotating stars considered here only have an off-center density maximum, yet a finite density at the center.

With the above choice of coordinates and symmetry assumptions, the Einstein equations reduce to [312, 503]

$$\nabla(B\nabla\nu) = \frac{1}{2}r^2\sin^2\theta B^3 e^{-4\nu}\nabla\omega\nabla\omega + 4\pi B e^{2\zeta-2\nu}\left[\frac{(\rho(1+\epsilon)+p)(1+v^2)}{1-v^2}+2p\right], \tag{3.154}$$

$$\nabla(r^2\sin^2\theta B^3 e^{-4\nu}\nabla\omega) = -16\pi r\sin\theta B^2 e^{2\zeta-4\nu}\frac{(\rho(1+\epsilon)+p)v}{1-v^2}, \tag{3.155}$$

$$\nabla(r\sin\theta\nabla B) = 16\pi r\sin\theta B e^{2\zeta-2\nu}p\ , \tag{3.156}$$

and a first-order, though lengthy, differential equation for ζ, relating only metric functions and given by Butterworth and Ipser [503]. In above equations, $B = e^{\psi+\nu}/(r\sin\theta)$, $\zeta = \mu+\nu$, and ∇ is the 3-dimensional flat-space derivative operator in spherical coordinates. The equation of hydrostationary equilibrium is given by

$$\frac{\nabla P}{\rho h} + \nabla\nu - \frac{v}{1-v^2}\nabla v + j\nabla\Omega = 0\ , \tag{3.157}$$

where j is the specific angular momentum

$$j = u^0 u_\varphi = \frac{v^2}{(1-v^2)(\Omega-\omega)}\,. \tag{3.158}$$

For barotropes where p depends on ρ only – which is the case for the polytropes considered here – the integrability of equation (3.157) allows j to be a specifiable function of Ω only. The most popular simple choice is [160, 312, 498, 499]

$$j(\Omega) = A^2(\Omega_c - \Omega)\ , \tag{3.159}$$

where Ω_c is the central angular velocity and A is a positive constant of dimension length parametrizing differential rotation. In the Newtonian limit the rotation law (3.159) reduces to

$$\Omega = \Omega_c\frac{A^2}{A^2+d^2} = \begin{cases}\Omega_c & \text{for } A\to\infty \\ \Omega_c\frac{A^2}{d^2} & \text{for } A\to 0\end{cases}\ , \tag{3.160}$$

where $d = r\sin\theta$ is the distance from the rotation axis. For $A\to\infty$, the rotation becomes uniform and for $A\to 0$, the rotation law becomes a j-constant rotation law. According to (3.160), the angular velocity is constant on cylinders. This accords with the Poincaré-Wavre theorem that states that the specific angular momentum in barotropes is constant on cylinders in Newtonian gravity (see, e.g., [504]).

WHISKY_RNSID computes equilibrium polytropes by iteratively solving the Einstein equations and the equations of hydrostationary equilibrium until convergence is reached [496, 498–500]. After that, lapse, shift and metric are appropriately transformed and mapped onto the CCW grid and the extrinsic curvature is computed from the 3-metric via (2.26). Model parameters are the central density ρ_c, the coordinate axis ratio r_p/r_e and a normalized rotation parameter $\hat{A} = A/r_e$ as well as the EOS parameters Γ and K. For $r_p/r_e = 1$ the TOV solution is recovered. As for TOV initial models, Γ is reduced to instigate collapse. Since no 2D/3D elliptic solver is available in CCW, I do not re-solve the constraint equations after the pressure reduction. This leads to a small initial constraint violation that is, however, dwarfed by the constraint violations induced by numerical truncation errors during the collapse evolution.

See §4.3 and chapter 5 for results from core collapse simulations employing polytropes in rotational equilibrium.

3.7.3 Presupernova Stellar Models

As pointed out in Section 2.3.2, massive stars above $\sim$8 $M_\odot$ form an onion-skin like compositional structure at the end of their nuclear burning lives. The massive 1–2 $M_\odot$ core composed of iron-group nuclei is surrounded by progressively lighter elements. Details on the evolution of massive stars can, e.g., be found in the textbooks of Clayton [505] and Kippenhahn & Weigert [432] and in the recent review article by Woosley et al. [38]. All to-date available presupernova stellar models are end products of Newtonian spherically symmetric (1D) stellar evolutionary calculations from hydrogen burning on the main sequence to the onset of core collapse by photo-dissociation of heavy nuclei and electron captures [38, 506–511]. Recently, the first presupernova models that include rotation in an approximate 1D fashion have become available [509–511]. In this work I employ nonrotating presupernova models of Woosley et al. [38] that I set into rotation assuming constant angular velocity on cylindrical shells and the rotation law specified by equation (3.160). In addition, I perform calculations with a number of "rotating" presupernova models from [509] and [511]. I point out that due to their 1D nature, none of the considered models are in rotational equilibrium. Model calculation details along with astrophysical considerations are laid out in §6.1.

At the time of mapping from 1D onto the 3D CCW grid, the presupernova models already exhibit negative velocities and nothing artificial is done to initiate or accelerate collapse. The actual mapping is performed via linear interpolation of the fluid data. Consistent specific internal energies are obtained by calling the Shen EOS with density, temperature and electron fraction as inputs. The typical precollapse iron core is less compact than the TOV stars and rotating polytropes considered in the previous section. Initial curvature data are obtained in the Newtonian metric approximation [115] by means of the Newtonian gravitational potential. The latter is obtained via a simple 1D integration of the Poisson equation

$$\Delta\phi = 4\pi\rho \ . \tag{3.161}$$

Using the "Newtonian" line element [115]

$$ds^2 = -(1+2\phi)dt + (1-2\phi)(dx^2+dy^2+dz^2) \ , \tag{3.162}$$

I set up the initial curvature and gauge data according to

$$\begin{aligned} \alpha &= \sqrt{1+2\phi} \ , \\ \beta^i &= 0 \ , \\ \gamma_{ij} &= (1-2\phi)\,\mathrm{diag}(1,1,1) \ , \\ K_{ij} &= 0 \ . \end{aligned} \tag{3.163}$$

The above choice yields a good approximation to the true GR initial data since (a) the precollapse cores are essentially Newtonian objects with $M/R \lesssim 0.1\%$ and (b) because the initial collapse radial velocity is small ($\lesssim 0.003\,c$). For a rapidly rotating initial setup, the maximum Hamiltonian constraint violation on the initial data slice is on the order of 10^{-7} and is located at the origin. The maximum momentum constraint violation is on the order of 10^{-9} and is located slightly off-origin corresponding to the steep rise in the initial collapse velocity. Both values are multiple orders of magnitude smaller than the constraint violations that are induced by the finite differencing of the NOK-BSSN equations during the evolution. Comparisons with conformally-flat axisymmetric calculations (presented in §6.3.8) carried out with the CoCoNuT code [18, 160, 161] by H. Dimmelmeier corroborate the quality of the Newtonian metric approximation for the precollapse iron cores considered here.

3.8 Gravitational Wave Extraction

In section 2.6 I have introduced and discussed the basics of gravitational wave theory. As mentioned in that section, I extract gravitational wave information via the quadrupole approximation (equations [2.96] through [2.101]) from the hydrodynamic matter motions in my simulations. The quadrupole formalism yields a direct estimate for the gravitational waves emitted by an accelerated aspherical mass distribution as seen by an asymptotic observer. For the relatively weak-field ($\frac{G}{c^2}\frac{M}{R} \sim 0.1$), relatively slow-motion ($v \sim 0.1 - 0.2c$) situation encountered in stellar core collapse, wave estimates by the quadrupole approximation may actually be more reliable than conceptually and technically more involved methods for wave extraction directly from curvature variables (see the discussion in section 2.6.5).

Throughout this section I will use standard cgs units, hence carry along all factors of c and G. The numerical code used to extract gravitational waves from my simulation data based on the formulae presented in this section was written by myself.

3.8.1 Quadrupole Waves

I start with the reduced mass quadrupole tensor defined by

$$I_{jk} = \int \rho \left(x^i x^j - \frac{1}{3}\delta^{ij} x_i x^i \right) d^3x \,. \tag{3.164}$$

Note that I assume the weak-field, slow-motion linear limit and thus raise and lower indices with $\eta_{ij} = \mathrm{diag}(1,1,1)$ making the difference between "upper" and "lower" index irrelevant. As motivated by Dimmelmeier [12, 18] and Shibata and Sekiguchi [174], I replace the Newtonian rest-mass density ρ with $\bar{D} = \sqrt{\gamma}\rho W$. Here W is the Lorentz factor and ρW is densitized, because (1) the actual hydrodynamically evolved variable is $\sqrt{\gamma}\rho W$ (see equation 2.66) and (2) because the volume element in above integral becomes an approximate natural volume element (see, e.g., [116]) with this choice.

The standard quadrupole formula (SQF), introduced in section 3.8.1, recapitulated in slightly different form reads

$$h_{jk}^{TT}(t,\vec{x}) = \frac{2}{c^4}\frac{G}{R}\left[\frac{d^2}{dt^2} I_{jk}(t - R/c)\right]^{TT} , \tag{3.165}$$

where R is the distance from the source to the observer and TT stands for transverse-traceless. Following Finn and Evans [178] and Blanchet et al. [171], I now make use of the continuity equation,

$$\hat{D}_{,t} + (\hat{D}v^i)_{,i} = 0 \,, \tag{3.166}$$

to eliminate one of the time derivatives from (3.165), arriving at the *first moment of momentum density* formula for the first time derivative of the mass quadrupole tensor:

$$\frac{d}{dt} I_{ij} = \int \hat{D}\left[v^i x^j + v^j x^i - \frac{2}{3}\delta^{ij}(v^l x^l) \right] d^3x \,. \tag{3.167}$$

Again, note that the choice of position of the indicies (upper/lower) is arbitrary. I use upper indices on the right-hand side since all primitive vector variables in WHISKY are contravariant.

For writing out the gravitational wave amplitudes in terms of the two possible polarizations of gravitational waves, h_+ and $h_\times$, I choose a source-local spherical coordinate frame (r,θ,ϕ) with normalized basis vectors. The unit polarization tensors (2.91) in this basis read [512, 513]

$$\begin{aligned} \boldsymbol{e}_+ &= \vec{e}_\theta \otimes \vec{e}_\theta - \vec{e}_\phi \otimes \vec{e}_\phi \,, \\ \boldsymbol{e}_\times &= \vec{e}_\theta \otimes \vec{e}_\phi + \vec{e}_\phi \otimes \vec{e}_\theta \,, \end{aligned} \tag{3.168}$$

and the two dimensionless gravitational wave strains have the particularly simple form

$$\begin{aligned} h_+ &= \frac{G}{c^4}\frac{1}{D}\left(\ddot{I}_{\theta\theta} - \ddot{I}_{\phi\phi} \right) \,, \\ h_\times &= \frac{G}{c^4}\frac{2}{D}\,\ddot{I}_{\theta\phi} \,, \end{aligned} \tag{3.169}$$

where I use the dot convention for time derivatives for simplicity of notation. The relevant components $\ddot{I}_{\theta\theta}$, $\ddot{I}_{\phi\phi}$, $\ddot{I}_{\theta\phi}$ expressed in terms of their Cartesian counterparts computed in the code, read

$$\begin{aligned}
\ddot{I}_{\theta\theta} &= (\ddot{I}_{xx}\cos^2\phi + \ddot{I}_{yy}\sin^2\phi + \ddot{I}_{xy}\sin 2\phi)\cos^2\theta + \ddot{I}_{zz}\sin^2\theta - (\ddot{I}_{xz}\cos\phi\ddot{I}_{yz}\sin\phi)\sin 2\theta \ , \\
\ddot{I}_{\phi\phi} &= \ddot{I}_{xx}\sin^2\phi + \ddot{I}_{yy}\cos^2\phi - \ddot{I}_{xy}\sin 2\phi \ , \\
\ddot{I}_{\theta\phi} &= -\frac{1}{2}(\ddot{I}_{xx} - \ddot{I}_{yy})\cos\theta\sin 2\phi + \ddot{I}_{xy}\cos\theta\cos 2\phi + (\ddot{I}_{xz}\sin\phi - \ddot{I}_{yz}\cos\phi)\sin\theta \ .
\end{aligned} \tag{3.170}$$

An observer located on the polar axis of the source ($\theta = 0$, $\phi = 0$) then sees

$$\begin{aligned}
h^p_+ &= \frac{G}{c^4}\frac{1}{D}(\ddot{I}_{xx} - \ddot{I}_{yy}) \\
h^p_\times &= \frac{G}{c^4}\frac{2}{D}\ddot{I}_{xy}
\end{aligned} \tag{3.171}$$

and an observer in the equatorial plane ($\theta = \pi/2$, $\phi = 0$) sees

$$\begin{aligned}
h^e_+ &= \frac{G}{c^4}\frac{1}{D}(\ddot{I}_{zz} - \ddot{I}_{yy}) \\
h^e_\times &= -\frac{G}{c^4}\frac{2}{D}\ddot{I}_{yz} \ .
\end{aligned} \tag{3.172}$$

In axisymmetry, h^p_+, $h^p_\times$, and $h^e_\times$ all vanish, leaving only $h_+ = h^e_+$.

The first moment of momentum density (3.167) recast of the SQF greatly reduces the numerical noise in the extracted wave signal (see, e.g., [170] or [18]). I compute the single remaining time derivative via finite differences in a postprocessing step. Finn and Evans [178] and Blanchet et al. [171] went a step further and additionally apply the Newtonian equation of momentum conservation which led to the *stress formula* variant of the SQF that does not contain any time derivatives, but terms involving derivatives of the Newtonian gravitational potential Φ:

$$\ddot{I}_{ij} = \int \hat{D}\left[2v^iv^j - x^i\Phi_{,j} - x^j\Phi_{,i} - \frac{2}{3}\delta^{ij}(v^lv^l - x^l\Phi_{,l})\right] d^3x \ . \tag{3.173}$$

The stress formula is widely used in Newtonian source simulations, but also in the work of Dimmelmeier and collaborators [12, 18, 161, 162] in conformally-flat spacetimes. Because of the ambiguities concerning the definition of a Newtonian potential in terms of GR field variables, I have decided not to use the stress formula in my GR simulations[27].

3.8.2 Total Energy Emission and Spectral Energy Density

The total energy emitted in quadrupole gravitational waves is given by the expression [116]

$$E_{\rm GW} = \frac{1}{5}\frac{G}{c^5}\int_{-\infty}^{\infty} \dddot{I}_{ij}\,\dddot{I}_{ij}\,dt = \frac{1}{5}\frac{G}{c^5}\int_{-\infty}^{\infty}\left[\dddot{I}^2_{xx} + \dddot{I}^2_{yy} + \dddot{I}^2_{zz} + 2(\dddot{I}^2_{xy} + \dddot{I}^2_{xz} + \dddot{I}^2_{yz})\right] dt \ . \tag{3.174}$$

This expression is straightforwardly implemented in the postprocessing code, but, due to the additional numerical time derivative required, not very accurate. It is thus numerically more reliable to evaluate the emitted energy in the frequency domain:

I introduce the Fourier transform of the second time derivative of the reduced mass quadrupole tensor,

$$\tilde{\ddot{I}}_{ij}(f) = \int_{-\infty}^{\infty} \ddot{I}_{ij}(t)e^{-2\pi ift}dt \ , \tag{3.175}$$

and the reverse transform,

$$\ddot{I}_{ij}(t) = \int_{-\infty}^{\infty} \tilde{\ddot{I}}_{ij}(t)e^{2\pi ift}df \ . \tag{3.176}$$

[27] See also the discussion in [12].

Using (3.175) and (3.176), I rewrite (3.174) in terms of $\ddot{I}$'s Fourier transform $\tilde{\ddot{I}}$

$$E_{\rm GW} = \frac{1}{5}\frac{G}{c^5}\int_{-\infty}^{\infty}(2\pi f)^2|\tilde{\ddot{I}}_{ij}|^2 df \ . \tag{3.177}$$

Hence, the spectral energy density of the emitted quadrupole gravitational waves reads

$$\frac{dE_{\rm GW}}{df} = \frac{1}{5}\frac{G}{c^5}(2\pi f)^2|\tilde{\ddot{I}}_{ij}|^2 \ , \tag{3.178}$$

where $|\tilde{\ddot{I}}_{ij}|^2 = \tilde{\ddot{I}}_{ij}\tilde{\ddot{I}}^*_{ij}$ and * denotes complex conjugation.

3.8.3 Characteristic Strain

Flanagan & Hughes [514] define a dimensionless *characteristic gravitational wave strain* as a function of frequency f in terms of the spectral gravitational wave energy density to better assess the detectability of gravitational waves:

$$h_{\rm char}(f) = \sqrt{\frac{2}{\pi^2}\frac{G}{c^3}\frac{1}{D^2}\frac{dE_{\rm GW}(f)}{df}} \ . \tag{3.179}$$

This is a sensible choice since the detectability of gravitational waves of a fixed frequency f scales with the square root of the number of wave cycles n emitted at this frequency. In terms of $h_{\rm char}$ Flanagan & Hughes [514] write the signal-to-noise ratio for an optimally oriented detector as

$$({\rm SNR}_{\rm optimal})^2 = \int d(lnf)\frac{h_{\rm char}(f)^2}{h_{\rm rms}(f)^2} \ , \tag{3.180}$$

with the (single) detector rms noise strain $h_{rms}(f)$ in an interval $\Delta f \approx f$ around f being defined as the square root of frequency times the detector noise power spectral density:

$$h_{rms}(f) = \sqrt{f\,S(f)} \ . \tag{3.181}$$

For two gravitational wave observatories, averaging over all angles, and demanding a SNR of 5, the detector *burst sensitivity* is considered to be $h_{\rm SB} \simeq 11\,h_{\rm rms}$[221, 515].

For the first time ever in the core-collapse supernova context, I have used (3.179) to compare theoretical gravitational wave estimates to the LIGO sensitivity [515] in the work done towards my diploma thesis [9, 170]. Since then, a similar approach has been taken by Müller et al. [95] and in my publication on gravitational waves from protoneutron star core oscillations [15].

3.9 Additional Analysis Tools

3.9.1 Total Energy, Linear Momentum, and Angular Momentum

For an asymptotically flat spacetime[28], it is possible to define a total energy and a total angular momentum vector in terms of surface integrals on a closed 2-surface at infinity (or, in a relaxed sense, at a very large distance from the gravitating object(s), where curvature is minute and no strong gravitational waves are present) [116, 117, 125, 126]. The *ADM mass* describes the total energy of spacetime, including energy carried by gravitational waves [126]. In Cartesian coordinates and in the usual ADM variables at spatial infinity (where $\alpha = 1$) it is

$$M^{\rm ADM} = \frac{1}{16\pi} \oint \sqrt{\gamma}\gamma^{ij}\gamma^{kl}(\gamma_{ik,j} - \gamma_{ij,k}) d^2S_i \ , \tag{3.182}$$

where d^2S_i is the surface element on a sphere with coordinate radius approaching infinity and normal n^i. Using Gauss's law, the surface integral (3.182) can be converted into a volume integral [126]:

$$M^{\rm ADM} = \frac{1}{16\pi} \int \left[\alpha\sqrt{\gamma}\gamma^{ij}\gamma^{kl}(\gamma_{ik,j} - \gamma_{ij,k})\right]_{,l} d^3x \ . \tag{3.183}$$

Using the Hamiltonian constraint equation (2.30) and the NOK-BSSN conformal-traceless formulation (see section 3.3) of the ADM equations, (3.183) can be rewritten [516] as

$$M^{\rm ADM} = \frac{1}{16\pi} \int \left[\Psi^5\left(16\pi\rho_{\rm ADM} + \tilde{A}_{ij}\tilde{A}^{ij} - \frac{2}{3}K^2\right) - \tilde{\Gamma}^{ijk}\tilde{\Gamma}_{jik} + (1-\Psi)\tilde{R}\right] d^3x \tag{3.184}$$

where $\rho_{\rm ADM} = n_\nu n_\mu T^{\mu\nu} = \rho h W^2 - P$ (see section 2.5).

The *ADM linear momentum* [125, 517] is

$$P_i^{\rm ADM} = \frac{1}{8\pi} \oint (K_{ki} - K\delta_{ki}) d^2S^i \ , \tag{3.185}$$

and the total angular momentum, including the angular momentum carried by gravitational waves, is described by the *ADM angular momentum* [116, 125, 517] (here in Cartesian coordinates),

$$J_i^{\rm ADM} = \frac{1}{8\pi}\epsilon_{ijk} \oint x^j K^{kl} d^2S_l \ . \tag{3.186}$$

In an fashion analogous to $M^{\rm ADM}$, volume-integral expressions for P_i^{ADM} and J_i^{ADM} can be found (see, e.g., [516]).

In my core-collapse simulations, the total ADM linear momentum should be zero[29] and $M^{\rm ADM}$ and $J_i^{\rm ADM}$ should remain constant unless gravitational waves (or matter) leave the computational domain.

Equations (3.182), (3.183), and (3.184) are directly implemented in the analysis routines. Equation (3.185) is indirectly implemented by (a) monitoring the center of mass position on my numerical grid[30] and (b) by evaluating

$$\mathcal{S}_i = \int \sqrt{\gamma} S_i d^3x \ , \tag{3.187}$$

where the S_i are the fluid momentum densities from section 2.5. I implement equation (3.186) in a volume-integral form introduced by Shibata [519] that utilizes the NOK-BSSN variables directly and is equivalent to the formula of Yo et al. [516].

[28] In an asymptotically flat spacetime curvature vanishes at large distances from some (central) regions, so that at large distances, the geometry becomes essentially that of a Minkowski spacetime. All spacetimes considered in this dissertation are assumed to be asymptotically flat.

[29] No "center of mass" motion unless gravitational waves carry away linear momentum [518].

[30] This is – in principle – gauge dependent. If one assumes symmetric shift behavior and imposes vanishing shift at the coordinate origin, the coordinate position of the center of mass should not change.

3.9.2 Indicative Matter Integrals

I now define a number of indicative integral observables for the matter variables. The definition of the total *rest mass* is straightforward considering the rest-mass conservation equation (2.66):

$$M_0 = \int \rho W dV = \int \rho W \sqrt{\gamma} d^3x \ . \tag{3.188}$$

Following Friedman et al. [520] and Saijo et al. [304], I further define the *proper mass*

$$M_p = \int \rho W (1+\epsilon) \sqrt{\gamma} d^3x \ . \tag{3.189}$$

The ratio of rotational kinetic to gravitational binding energy,

$$\beta = \frac{T}{|W|} \ , \tag{3.190}$$

is an important analysis quantity for the dynamics of rotating fluid bodies (see, e.g., the seminal work by Chandrasekhar [285]). In order to find an expression for β in terms of the evolved variables in my simulations, I again follow Saijo et al. [304] and define an approximate *fluid gravitational mass*

$$M_{\rm grav} = \int (\rho h W^2 - P) \Psi^5 d^3x \, . \tag{3.191}$$

thisis equivalent to equation (3.184) up to pure-curvature terms which I neglect here since I am only interested in matter contributions.

For the definition of the *rotational kinetic energy* T, an expression for the angular momentum must be given which is not so straightforward. Since I am interested in the fluid angular momentum, a choice $J_z = J_z^{\rm ADM}$ does not seem appropriate, since $J_z^{\rm ADM}$ (3.186) contains angular-momentum contributions that are pure curvature (in the case of the presence of a rotating black hole) and contributions from gravitational waves. An alternative is to make the assumption of axisymmetry and exploit the then existing space-like Killing vector field (see, e.g. [116]) which allows a straightforward definition of the fluid angular momentum with respect to the axis of symmetry [304, 520, 521],

$$J_z = \int T^t_\phi \, \alpha \sqrt{\gamma} d^3x = \int (x \, j_y - y \, j_x) \Psi^6 d^3x \ , \tag{3.192}$$

where the j_i are given by $j_i = -T^{\mu\nu} n_\mu \gamma_{\nu i} = \rho W h u_i$ [519]. I find that J_z and $J_z^{\rm ADM}$ agree to within one percent at all times in my simulations. Also note that (3.192) is identical to equation (2.26) of [519].

The rotational kinetic energy is then given by [304, 520, 521]

$$T = \frac{1}{2} \int \Omega (x \, j_y - y \, j_x) \Psi^6 d^3x \tag{3.193}$$

where I use

$$\Omega = \frac{x(\alpha v^y - \beta^y) - y(\alpha v^x - \beta^x)}{x^2 + y^2} \tag{3.194}$$

based on $\Omega = \frac{u^\phi}{u^0} = \alpha v^\phi - \beta^\phi$ and the Cartesian $\vec{\Omega} = \frac{\vec{r} \times \vec{v}}{r^2}$.

The *gravitational binding energy* is then defined as [304, 520, 521]

$$W = M_{\rm grav} - M_p - T \ , \tag{3.195}$$

and β becomes

$$\beta = \frac{T}{|W|} = \frac{T}{|M_{\rm grav} - M_p - T|} = \frac{1}{\left| \frac{M_{\rm grav} - M_p}{T} - 1 \right|} \, . \tag{3.196}$$

Note that equation (3.196) is just one way of defining β in dynamical general relativity. Shibata and collaborators, for example, use the ADM mass and angular momentum for the gravitational mass and the fluid angular momentum, respectively [204]. Fortunately, in the stellar core-collapse context, such differing definitions of β lead – by experience – only to relative differences of the results on the order of a few percent.

3.9.3 Analysis of Nonaxisymmetric Structure

The possibility for development of nonaxisymmetric structures and dynamics during stellar core collapse and/or in the protoneutron star at postbounce times has recently received much attention. In fact, time varying nonaxisymmetric flow caused by rotational fluid instabilities is likely to lead to copious emission of gravitational radiation (see, e.g., [240] and the discussions in §2.7.3 and §6.4).

To diagnose and monitor the development of nonaxisymmetric structure in my calculations of rotating collapse I employ three different methods.

Gravitational Wave Emission

In axisymmetry, no gravitational waves are emitted along the symmetry axis and only waves with $+$ polarization can be emitted in off-axis directions. Hence, monitoring the magnitudes of h^p_+, $h^p_\times$, and $h^e_\times$ as defined by equations (3.171) and (3.172) in the previous section and comparing them to the axisymmetric h^e_+ may be used as a diagnosis tool for time-changing nonaxisymmetric structure of quadrupole character. A prime example for such structure is the $\ell = m = 2$ f-mode deformation of rotating stars, known as the *bar mode* (see, e.g, [286]). A bar/cylinder spinning around an axis perpendicular to its symmetry axis emits gravitational waves along the rotation axis at twice its spin frequency and with a $\pi/2$ phase shift between $+$ and $\times$ gravitational wave polarizations [115, 116].

Azimuthal Fourier Analysis

A way to measure the growth of nonaxisymmetric structure is to examine various Fourier components in the density distribution [306, 522]. In cylindrical coordinates the density in a ring at fixed cylindrical radius ϖ from the rotation axis and fixed z can be written using the complex azimuthal Fourier decomposition

$$\rho(\varpi, z, \varphi) = \sum_{m=-\infty}^{+\infty} C_m(\varpi, z) e^{im\varphi} \; , \tag{3.197}$$

where the Fourier components C_m correspond to the azimuthal modes m and are defined by

$$C_m(\varpi, z) = \frac{1}{2\pi} \int_0^{2\pi} \rho(\varpi, z, \varphi) e^{-im\varphi} d\varphi \; . \tag{3.198}$$

In addition, it is useful to define normalized amplitudes

$$A_m = |C_m|/|C_0| \; , \tag{3.199}$$

where

$$|C_m| = \sqrt{\mathrm{Re}\{C_m\}^2 + \mathrm{Im}\{C_m\}^2} \; , \tag{3.200}$$

and where $C_0(\varpi, z) = \bar{\rho}(\varpi, z)$ is the mean density in the ring. At any point in time, the mode phase angle,

$$\Phi_m(\varpi, z) = \tan^{-1}(\mathrm{Im}\{C_m\}/\mathrm{Re}\{C_m\}) \; , \tag{3.201}$$

provides information about the azimuthal structure of each mode m. If a given mode m is globally dominant this is reflected in a radial variation of the phase angle that corresponds to the global structure of the mode. For a spiral-type mode, Φ_m should exhibit a spiral structure while a pure bar mode should result in a bar-like structure [22, 24]. In addition and also in the situation when a mode m becomes global, one can write the phase angle as

$$\Phi_m = \sigma_m t \; , \tag{3.202}$$

where σ_m is the eigenfrequency of the mth mode. The mode pattern speed is then

$$\sigma_p(\varpi, z) = \frac{1}{m} \frac{d\Phi}{dt} = \frac{\sigma_m}{m} \; . \tag{3.203}$$

In practice, I implement equation (3.198) by interpolating the density on discrete rings in the equatorial plane and then performing the Fourier analysis for $m \in \{1, 2, 3, 4\}$. I typically use 180 angular zones for 2π radians and perform the analysis at 30 radii between 5 and 100 km from the rotation axis. The confinement of the analysis to the equatorial plane is motivated by the assumption that globally unstable modes are likely to have only a weak z dependence inside the protoneutron star (see [23] and references therein).

Global Dipole, Quadrupole, and Sextupole Diagnostics

In order to obtain a more global measure for nonaxisymmetric structure, Saijo et al. [20] have proposed multipole diagnostics abutted to Cartesian representations of $\ell = m$ spherical harmonics decompositions of the density. Concretely, [20] define total mass-normalized dipole,

$$D = \langle e^{im\varphi} \rangle_{m=1} = \frac{1}{M} \int_{\rho \geq \rho_{\rm cut}} \rho \frac{x + iy}{\sqrt{x^2 + y^2}} d^3x \ , \tag{3.204}$$

and quadrupole,

$$Q = \langle e^{im\varphi} \rangle_{m=2} = \frac{1}{M} \int_{\rho \geq \rho_{\rm cut}} \rho \frac{x^2 - y^2 + i(2xy)}{x^2 + y^2} d^3x \ , \tag{3.205}$$

diagnostics, to which I add a sextupole,

$$S = \langle e^{im\varphi} \rangle_{m=4} = \frac{1}{M} \int_{\rho \geq \rho_{\rm cut}} \rho \frac{x^4 + y^4 - 6x^2y^2 + i(4x^3y - 4xy^3)}{(x^2 + y^2)^2} d^3x \ , \tag{3.206}$$

diagnostic to enable capture of the m=4 Cartesian grid mode dynamics. M is the total mass of material with density ρ greater than $\rho_{\rm cut}$. Note that the powers of $\sqrt{x^2 + y^2}$ in the integrands' denominators are not part of the Cartesian spherical harmonics representation, but are employed to accentuate the relevance of the highly compact matter distribution at small cylindrical radii. I typically choose $\rho_{\rm cut} = 10^9$ g cm^{-3}, again to put emphasis on the strongly condensed regions on the computational grid.

Chapter 4

GR Core-Collapse Simulations: Code Tests

This chapter is devoted to tests of the CACTUS/CARPET/WHISKY (CCW) code. Basic and more advanced code tests of WHISKY without mesh refinement, including relativistic 3D shock tube tests, rotating stationary, and collapsing neutron stars with and without curvature evolution via BSSN_MOL have already been published [123, 163]. In the following, I focus on tests of CCW in the context of the {3+1} GR mesh-refined stellar core-collapse calculations performed in this work. In §4.1 I present relativistic shock tube calculations and investigate the effects of a mesh refinement boundary on shock propagation. In §4.2 I investigate the convergence and consistency of the CCW approach in spherically-symmetric stellar core-collapse spacetimes and in §4.3 I perform an extensive set of code-verification calculations with rotating iron core collapse models, including resolution tests, a set of test calculations for progressive mesh refinement and tests with various spacetime gauge choices, hydrodynamic cell-interface reconstruction methods, flux-formulae/Riemann solvers and time-integrators.

4.1 Relativistic Shock Tubes with Mesh Refinement

Shock tube tests are conceptually simple, yet very effective and rigorous tests for the ability of a numerical hydrodynamics code to resolve and track strong shocks in one dimension. In addition, shock tube tests probe the handling of smooth flow by HRSC schemes based on Riemann solvers.

Two initially constant states are separated by a discontinuous jump in density and/or pressure. The exact solution of the full time-dependent Riemann problem is known and the quality of the numerical time evolution can be easily assessed by a comparison with the exact solution.

Relativistic shock tube test results obtained with WHISKY were published in [123, 163]. Here I present test calculations that investigate the effects of CARPET mesh refinement boundaries on shocks. A much more thorough and detailed discussion of shock passage through mesh refinement boundaries has been presented by Quirk [402].

I consider the two standard one-dimensional special relativistic shock tube problems analyzed by Martí & Müller [165]. The initially constant left and right states are listed in table 4.1. An ideal-fluid EOS with $\Gamma = 5/3$ is used and both test problems are computed in a flat one-dimensional Minkowski spacetime using Cartesian coordinates in the interval $x \in [0, 1]$. The initial discontinuity is placed

Table 4.1: Density ρ, pressure p, and velocity v^x. Initial values for the left and right states of the relativistic shock tube problems 1 and 2 of Martí & Müller [165].

	Problem 1		Problem 2	
	left state	right state	left state	right state
ρ	10.0	10^{-6}	1.0	1.0
p	13.333	1.0	10^3	10^{-2}
v^x	0.0	0.0	0.0	0.0

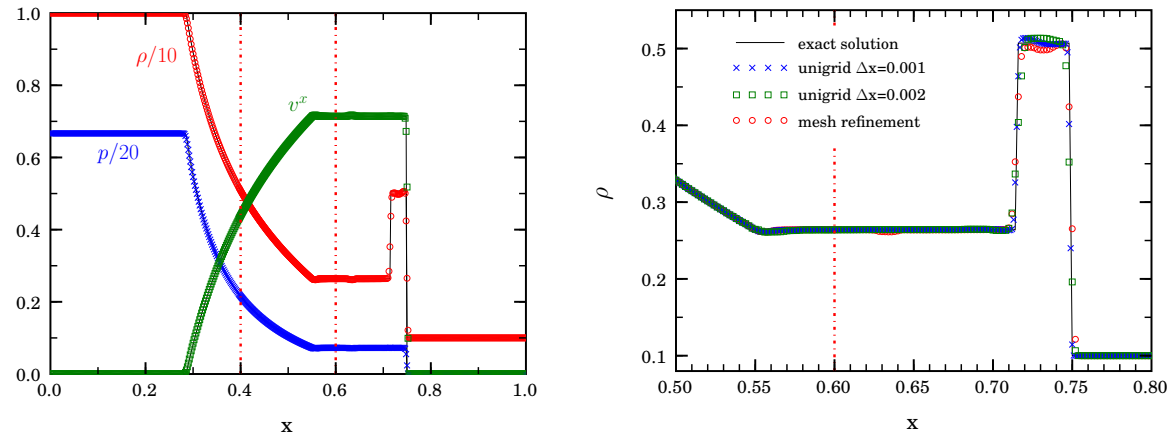

Figure 4.1: Relativistic shock tube problem 1. Left panel: Comparison of the results of the calculation with mesh refinement (symbols) with the exact solution (solid lines). Shown are profiles of the (rescaled) density ρ, pressure p and velocity v^x at time $t = 0.3$. The vertical red dash-dotted lines indicate mesh refinement boundaries. Right panel: Zoomed-in view of the Riemann solution for the density ρ at time $t = 0.3$. Shown are the exact solution (solid line) and the solutions obtained with the unigrid and mesh refinement calculations.

at $x = 0.5$. The Marquina flux formula and PPM reconstruction are employed. Each calculation is performed once without mesh refinement and 1000 equidistant zones (unigrid $\Delta x = 0.001$), once without mesh refinement and 500 equidistant zones (unigrid $\Delta x = 0.002$) and once with mesh refinement. In the calculation with mesh refinement, the base grid covers the entire interval with 500 zones ($\Delta x = 0.002$) and the fine grid covers the region $x \in [0.4, 0.6]$ with 200 zones ($\Delta x = 0.001$). In this way I can test the effect of shock passage through a mesh refinement boundary onto a coarser grid.

Figure 4.1 contrasts the numerical representation of problem 1 with its exact solution at time $t = 0.3$. Despite the mesh refinement boundaries at $x = 0.4$ and $x = 0.6$, the numerical solution with mesh refinement reproduces the exact solution extremely well. Only in the zoomed-in view of the density shown in the right panel, small errors are noticeable. The ρ profile obtained with mesh refinement shows a small dent at $x \simeq 0.63$ and the density in the shell between shock and contact discontinuity is slightly underestimated, but the contact discontinuity at the density shell and the shock front are as well resolved as by the lower-resolution unigrid calculation.

The results of the more demanding relativistic blast wave test problem 2 are portrayed by figure 4.2. With the exception of a density underestimation in the thin density shell behind the shock, the exact

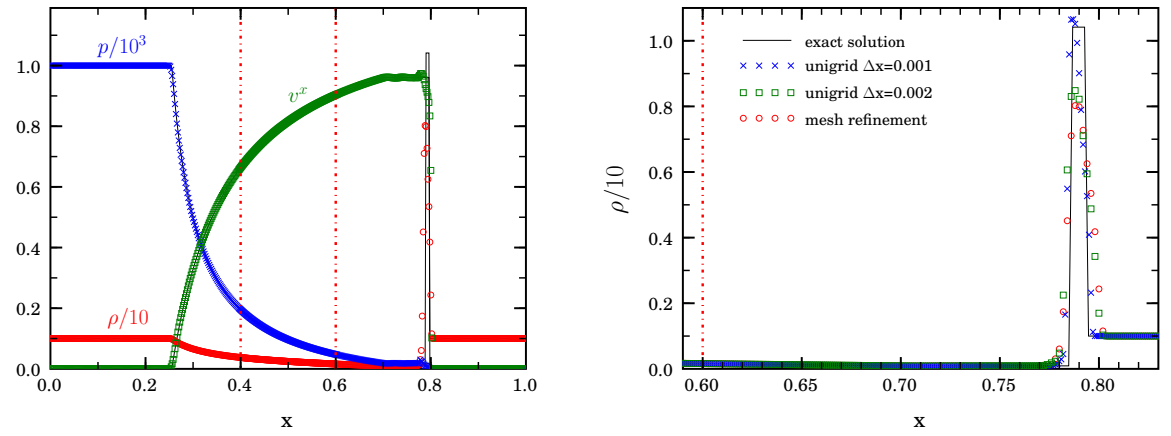

Figure 4.2: Relativistic shock tube problem 2. Left panel: Comparison of the results of the calculation with mesh refinement (symbols) with the exact solution (solid lines). Shown are profiles of the (rescaled) density ρ, pressure p and velocity v^x at time $t = 0.3$. The vertical red dash-dotted lines indicate mesh refinement boundaries. Right panel: Zoomed-in view of the Riemann solution for the density at time $t = 0.3$. Shown are the exact solution (solid line) and the solutions obtained with the unigrid and mesh refinement calculations.

solution is well reproduced despite shock passage through a mesh refinement boundary. However, note that not even the high-resolution unigrid calculation exactly resolves the thin density shell, and both the lower-resolution unigrid calculation and the calculation with mesh refinement underresolve the density shell. The WHISKY results for problem 2 are comparable to those presented in [18] for the COCONUT code.

Based on the results of the shock tube test problems presented here, I conclude that only small errors are introduced on shock passage through a mesh refinement boundary while the overall flow remains largely unaffected as long as both the fine and the coarse grid resolution are sufficient to adequately resolve the dynamics. However, the test problems considered here are idealized and one dimensional. The systematic problems at CARPET mesh refinement boundaries (e.g., reflections, flux-mismatches; see §3.4) can lead to significant distortions of the flow in a full {3+1} GR hydrodynamics calculation. See the discussion in §4.2 and §5.2.3.

4.2 Spherical Iron Core Collapse; Convergence and Consistency

In order to lend credibility and authority to results from numerical calculations, it is necessary to demonstrate convergence of the numerical scheme. In other words, as the resolution is increased, the numerical solution should get more accurate and approach the continuum solution. More precisely, for a scheme that is nominally nth-order accurate in space, a decrease in grid zone size by a factor of m should lead to a decrease of the deviation of the numerical solution from the continuum solution by a factor m^n. An analogous consideration is valid for temporal convergence.

If the continuum solution is not known, convergence can still be tested, given the availability of numerical results f_i of three computations with different grid zones sizes. In particular, let h_1 be the finest resolution and h_2 and h_3 be coarser resolutions. Assuming second-order accuracy one can expand the solutions to

$$\begin{aligned} f_{h_1}(x) &\approx f_0 + e_2 h_1^2 + \dots , \\ f_{h_2}(x) &\approx f_0 + e_2 h_2^2 + \dots , \\ f_{h_3}(x) &\approx f_0 + e_2 h_3^2 + \dots . \end{aligned} \tag{4.1}$$

were f_0 is the continuum solution and e_2 is an *resolution independent* error function *à la* Richardson [523, 524]. Using (4.1) one can spell out the convergence factor Q as

$$Q = \frac{f_{h_3} - f_{h_2}}{f_{h_2} - f_{h_1}} = \frac{h_3^2 - h_2^2}{h_2^2 - h_1^2} , \tag{4.2}$$

and for a general convergence order n:

$$Q = \frac{h_3^n - h_2^n}{h_2^n - h_1^n} . \tag{4.3}$$

In vacuum numerical relativity, the standard convergence test is based on the Hamiltonian constraint (2.30) which is 0 at the continuum level. Performing a convergence test in 3D with mesh refinement is a challenging task even in vacuum relativity. For the stellar core-collapse spacetimes considered in this dissertation, convergence testing becomes a problem of significant difficulty, both conceptually and computationally:

- The three resolutions must be chosen in such a way that none of them underresolve the curvature and matter dynamics. This is complicated by the fact that at early stages of collapse the resolutions required by BSSN_MOL and WHISKY are different: The hydrodynamic part must adequately resolve the development of the infall velocity profile while the curvature of spacetime exhibits only small gradients until collapse becomes very dynamic a few milliseconds before core bounce.
- The three resolutions must be chosen in such a way that none of them "overresolve" the curvature and matter dynamics. A convergence test can fail if the resolution-dependent variation

of a variable in question is dominated by numerical round-off error. An example for this is a convergence test on a Minkowski spacetime. For a typical pre-collapse stellar iron core, the magnitude of the γ_{xx} component of the 3-metric has a maximum of $\sim$1.01 and varies only by $\sim$1% over the *entire* grid while the rest-mass density varies by 6 orders of magnitude. This exemplifies the different resolution requirements of the curvature and matter components at early times.

Considering for a moment equations (2.28) and recalling that the Ricci tensor is quadratic in the first derivative of the metric and linear in its second derivative, some algebra reveals that variations in the metric on the order of $e_2 h^2 \approx 10^{-7} - 10^{-8}$ will after a few timesteps be buried at least partially in floating point round-off error of double-precision floating point numbers. At this point, the convergence decreases and only quadruple-precision floating point numbers would allow an improvement. Quadruple precision is currently not fully supported in CCW.

- Small errors in the early infall velocity profile lead to a time shift in the collapse evolution (see §4.3.2). Lower-resolution simulations tend to reach the plunge phase of collapse and core bounce slightly later than higher-resolution simulations. Hence, the direct comparison of time-dependent integral quantities such as the $L2$ norm of the Hamiltonian constraint becomes difficult and loses explanatory and predictive power.

- Near physical discontinuities, the accuracy of the hydrodynamics scheme – and thus the accuracy of the entire simulation code – is reduced to first order (see §3.5). In addition, local extrema are also handled with first-order accuracy to avoid spurious oscillations. On a Cartesian 3D grid, all fluid variables have a local extremum at the origin, and if the configuration is near spherical symmetry, also along the coordinate axes.

- The order of accuracy attainable in the curvature evolution will break down near discontinuities of the fluid variables. This is due to the coupling of matter with curvature and can be understood by considering a simple 1D variant of the Hamiltonian constraint as given in equation (2.52) on page 20. The second spatial derivative of the metric becomes discontinuous at jumps in the ADM matter energy density [390]. The implementation of the ADM/NOK-BSSN equations in BSSN_MoL has no shock-capturing capabilities. Hence, the appearance of discontinuities will lead to a not necessarily convergent constraint blow-up along with high-frequency oscillations at least in the first derivatives of the metric.

- A full-blown convergence test of a production-style core-collapse simulation with the standard choice of resolutions $\{h, 2h, 4h\}$ for convergence testing is firstly prohibitively computationally expensive and secondly, the factor-of-four interval in resolution makes it difficult to avoid under- and overresolution at the same instance.

The three main components of the simulation code used in this dissertation, WHISKY, CARPET, and BSSN_MoL have individually (and in part jointly) been tested for convergence in [123, 163], [391], and [144, 146], respectively. In particular, second-order convergence of WHISKY, CARPET and BSSN_MoL for the highly-relativistic case of neutron-star collapse to a black hole has been demonstrated in [123].

As explained above, strict convergence testing of a standard 3D core-collapse simulation is hardly feasible owing to the computational demands and the time-varying resolution requirements for curvature and matter evolution. Yet, it is absolutely necessary to demonstrate convergence in a situation in which a convergence test is not hampered by the aforementioned systematic limitations. In addition and despite the fact that strict second-order convergence cannot be expected globally for stellar core-collapse simulations, I must still demonstrate global consistency and stability of the numerical scheme for an entire collapse simulation. This includes checks of mass conservation. In §4.3 this check is repeated for rotating collapse.

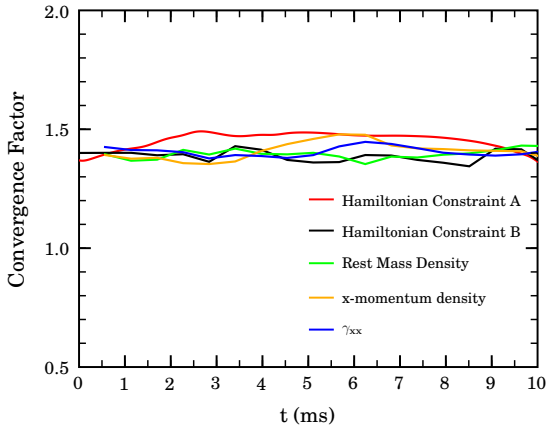

Figure 4.3: Convergence factor as obtained from the convergence study with resolution stepping $h, 1.5h, 2h$. For second-order convergence one expects a convergence factor of 1.4. Hamiltonian constraint A denotes the direct convergence test on the $L2$-norm of the Hamiltonian constraint. All other convergence graphs show the $L2$-norm of the pointwise convergence factors in the associated quantities. At t=0, γ_{xx}, ρ and S^x are identical in the three calculations.

Second-Order Convergence

To demonstrate second-order convergence of the coupled WHISKY, CARPET, BSSN_MOL thorns, I set up an equilibrium TOV $n = 3$ polytrope with a central density of 5×10^{10} g cm^{-3}. This is 5 times higher than the canonical iron core central density used in standard simulations, though it may be typical for accretion-induced collapse progenitors (see [16] and references therein). This slightly unphysical precollapse star has a coordinate radius of $\sim$900 km. This allows for a considerably smaller-than-regular extent of the computational grid and provides for (a) fast collapse, since the configuration is much more compact than the standard iron core and (b) initially larger gradients in the curvature variables, reducing the danger of overresolution. Collapse is triggered by a reduction of the adiabatic index to 1.28 after which the Hamiltonian constraint is solved in 1D via equation (2.52) on page 20. Initially $K_{ij} = 0$. The collapsing star is then evolved in octant symmetry with a 3-level refinement hierarchy and a finest fine-grid spacing of $h_1 = 6.6$ km. Additional runs are performed with $h_2 = 1.5h_1$ and $h_3 = 2h_1$. The equation of state is polytropic, $1 + \log$ slicing and zero shift are used. I stop the calculations at $\sim$10 ms evolution time, at which the central density has increased 10-fold and shortly before the matter dynamics becomes underresolved on the coarsest grid.

Figure 4.3 depicts the evolution of the convergence factors (4.2) for various quantities as obtained from the test calculations. The convergence factor for the Hamiltonian is computed in two independent ways. (A) by direct comparison of the $L2$-norms of the Hamiltonian constraint from each simulation and (B) by computing 3D pointwise convergence factors and computing the $L2$-norm of these pointwise factors. The convergence factors of the rest mass density, the x-momentum density and of the representative metric component γ_{xx} are all computed according to method (B). If global pointwise convergence prevails, (A) and (B) must agree. This is — as expected — not the case, yet all considered quantities show convergence on average to second order: a convergence factor $Q = 1.4$ is expected for second-order convergence in the resolution stepping employed here.

Global Consistency and Stability

In order to demonstrate the overall consistency and stability of all code components and their coupling through the Method of Lines (see §3.2), I perform three full scale collapse simulations with a spherically symmetric TOV $n = 3$ initial iron core model with a 9-level refinement hierarchy and finest grid spacings $\sim$180 m, $\sim$260 m, and $\sim$350 m. These simulations were originally planned to serve as convergence tests, but as discussed below, turn out to be systematically flawed and show first-order convergence at best. Nevertheless, their results still demonstrate overall consistency and

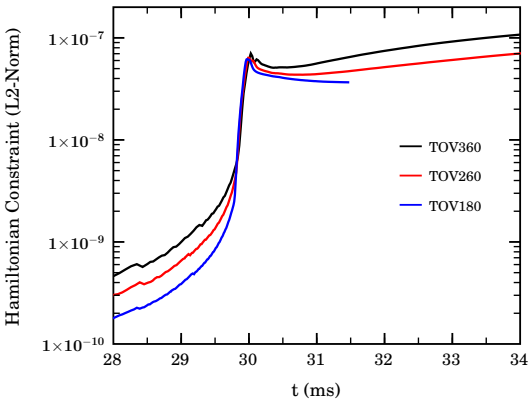

Figure 4.4: L2 norm of the Hamiltonian constraint shortly before and after core bounce.

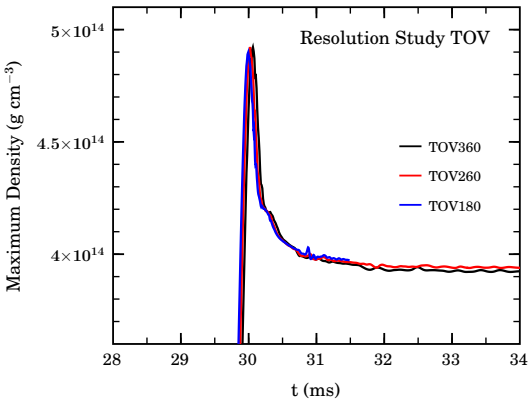

Figure 4.5: Evolution of the maximum density on the grid before and shortly after core bounce.

stability of the scheme from the initial data slice to times well after core bounce.

The spherically symmetric initial model is mapped onto the 3D grid and only reflection symmetry with respect to the equator is assumed. I name the runs corresponding to the resolutions, TOV180, TOV260, and TOV360. Progressive mesh refinement (§3.4 and §4.3.2) is used and 4 refinement levels are activated initially. I make use of refinement hierarchies RH8IV, RH8III, and RH8II, for TOV180, TOV260, and TOV360, respectively (see appendix E). Note that calculation TOV180 requires 8 times more memory than TOV360 and, due to a factor of two decrease in the time step, is overall 16 times more computationally expensive. Evolving it to 1.5 ms after core bounce requires one week of computation on 64 Intel Itanium 2 cpus. Hence, I do not evolve this model to later postbounce times.

I perform all runs with $1 + \log$ slicing, the Γ-driver shift specified in equation (3.37) and the iterated Crank-Nicholson time integrator (§3.2.1) with 3 intermediate steps. Collapse is triggered by lowering the adiabatic index to 1.28. The constraint equations are not solved after the pressure depletion[1] and the particular initial data used here are only first-order convergent, while the initial constraint violation is largest in the highest-resolution model. This situation is reversed after a few thousand timesteps. Yet, at no time convergence to better than first order is achieved. This is due to (a) high-frequency noise present in the curvature initial data, (b) the inconsistencies introduced by the initial pressure reduction, and (c) small differences in the refinement hierarchy setups leading to errors introduced by refinement boundaries at different locations. In particular, a detailed analysis indicates that (a) leads to qualitatively and quantitatively different early-time behavior of the Γ-driver shift which is sensitive to noise in first and second derivatives of the metric.

Figure 4.4 depicts the evolution of the L2-norm of the Hamiltonian constraint from shortly before to a few ms after core bounce. Given the resolution stepping $\sim$ 1:1.5:2, one notices approximate first order convergence a few milliseconds before core bounce. The high-resolution and intermediate-resolution simulations reach core bounce slightly earlier than the low-resolution simulation, hence their evolutions of the Hamiltonian constraint violations which peak at core bounce, cross during the plunge phase. At and after core bounce the constraint violations converge and the highest resolution simulation yields the smallest peak constraint violation. At postbounce times the high-resolution simulation again yields the smallest error. Due to the presence of the bounce shock, convergence should not be better than first order locally, yet it is artificially enhanced by a slight underresolution of the strong curvature in and around the neutron star on the coarsest grid. At this point it is important to emphasize that the violation of the Hamiltonian and momentum (not shown here, but of the same magnitude as the Hamiltonian constraint) constraints is on average very small compared to the total energy of the system ($\sim$1.4 $M_\odot$) and exhibits a point maximum of $\sim$0.2% in the coarsest-resolution simulation at the time of core bounce, while otherwise being much smaller.

Figure 4.5 demonstrates that the hydrodynamics is very well converged. In particular, the factor of 2 in resolution between TOV180 and TOV360 leads only to a shift of the time of core bounce by $\sim$0.3% and a change of the bounce density of $\sim$0.8%. The convergence of the maximum density is

[1] At the time these simulations were performed, the initial data routines were not capable of re-solving the constraints after pressure reduction.

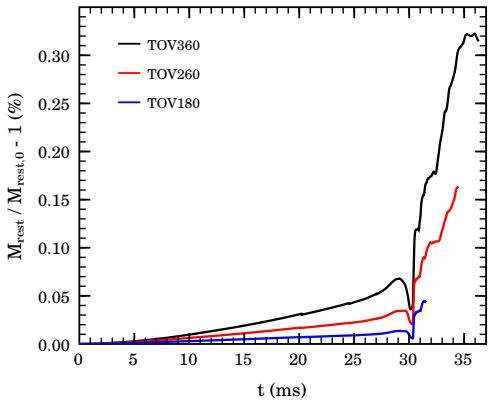

Figure 4.6: Relative error in the conservation of total rest mass.

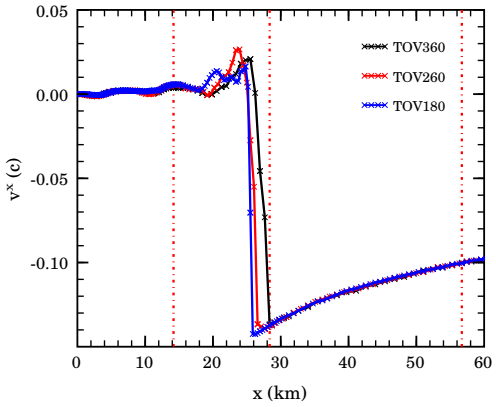

Figure 4.7: Velocity profile along the x-axis at $\sim$1 ms after core bounce.

approximately first order as should be expected for high-resolution shock-capturing methods at a (local or global) extremum. It is interesting to point out that the time of core bounce exhibits almost second-order convergence. This is due to the fact that the shift in bounce time is primarily related to the resolution of the initial infall velocity profile that forms during the first few milliseconds of the simulation. During that time the convergence is primarily determined by the hydrodynamics part and is hence less hampered by inaccuracies in the initial curvature data.

Figure 4.6 depicts the relative error in total rest mass conservation as a function of time. Until the time of core bounce, the error converges to approximately second order (given the resolution stepping, one expects a convergence factor of $\sim$1.4 from equation (4.2)) and stays well below 0.1% even in the coarsest-resolution simulation. After core bounce and shock formation, the error increases to $\sim$0.32% in TOV360 and levels off there while it stays much smaller in the higher-resolution simulations.

In figure 4.7, I compare velocity profiles along the x-axis from the three simulations at $\sim$1 ms after core bounce. Refinement boundaries are marked by red dash-dotted lines. The figure shows clear convergence of the shock position, inside the protoneutron star and at radii that have not yet been reached by the shock. In the immediate postshock region, convergence is less obvious. The differences observable there are caused by systematic flux mismatches and grid-scattering effects at the refinement boundaries that lead to high-frequency noise directly behind the shock. Given the good shock tube test results presented in §4.1, one would not have expected such large effects of mesh refinement boundaries. Also see the discussion in §5.2.3.

Discussion

I have performed a set of test calculations to verify the overall consistency, stability, and convergence of the numerical implementations of the coupled ADM/NOK-BSSN and GR hydrodynamics equations. As previously elaborated, global pointwise convergence is not expected and I have demonstrated second-order convergence on average for the numerical schemes in a collapse simulation. In addition, I have furthermore carried out a set of three calculations from the onset of collapse through bounce and the early postbounce epoch. I find that the numerical methods behave stably and consistently and that the matter dynamics are in the numerically converged regime, with maximum constraint violations on the order of $\sim 10^{-7}$ (considering the $L2$-norm) and mass conservation errors with a maximum of $\sim$3 parts in 10^3 for the coarsest resolution considered.

4.3 Rotating Iron Core Collapse

This section is devoted to the presentation of a variety of test calculations of rotating iron core collapse. All tests are performed with model A1B3G5 of the Zwerger & Müller / Dimmelmeier, Font & Müller (ZM/DFM) model suite [12, 30]. This model suite is discussed extensively in §5.1, §5.2.2, and §5.2.4. I choose model A1B3G5 because it contains a considerable amount of angular momentum / rotational energy (initial ratio of rotational kinetic to gravitational energy, β_{initial}, $\sim$0.9%) while still collapsing quickly (core bounce is reached within $\sim$30 ms) and reaching supernuclear densities at core bounce. It hence poses a rigorous stress test to the code while the relatively short collapse time allows for quick resource-sparing test calculations. In addition, tests with the axisymmetric CoCoNuT code show that A1B3G5 is among the most resolution-sensitive models of the entire ZM/DFM model suite [525].

The initial model data are in 2D rotational equilibrium computed with Whisky_RNSID (described in §3.7.2) and mapped onto the Cactus/Carpet/Whisky (CCW) 3D grid. On the initial data slice, the adiabatic index Γ is lowered from 4/3 to 1.28. The resulting pressure reduction initiates collapse. The specific internal energy ϵ is reset to be consistent with the reduced pressure. The Hamiltonian and momentum constraints are *not* re-solved after the pressure reduction[2]. As pointed out in §4.2 and in [123, 202] (for neutron star collapse), the initial constraint violations due to the pressure reduction are dwarfed by those building up by finite-difference errors during collapse. While convergence of the constraints cannot be guaranteed, the physical results appear unaffected by the initial constraint violation [123, 202, 404]. Unfortunately, Whisky_RNSID's solution of the rotational equilibrium stellar structure equations contains high-frequency noise that is related to the Gibbs phenomenon [526, 527] at the initial data resolutions required for the extended precollapse $n = 3$ polytropes. These high-frequency oscillations are amplified when the data are interpolated from Whisky_RNSID onto the 3D CCW grid and in consequence render a rigorous convergence test with Whisky_RNSID-based initial data impossible [528].

In the following, I present a resolution study by which I demonstrate that the standard grid hierarchy and set of resolutions used for the physics production calculations presented in chapters 5 and 6 yields results that are in the numerically converged regime. The resolution study is followed by a test of progressive mesh refinement (PMR) in §4.3.2 in which I investigate the dependence of the results on PMR parameters. Subsequently, I present test calculations investigating the effects of various choices of gauge conditions (§4.3.3), Riemann solvers / flux formulae and reconstruction methods (§4.3.4), and ODE integrators and the spatial order of accuracy in BSSN_MoL (§4.3.5).

4.3.1 Resolution Study

I perform four calculations (RES1–RES4) with initial model A1B3G5 covering a factor of four in grid resolution. All calculations are set up to use a maximum of 9 refinement levels and the bitant mode[3] refinement hierarchies RHI–RHIV are used with finest grid resolutions of 0.48 ($\sim$710 m), 0.24 ($\sim$355 m), 0.18 ($\sim$266 m), and 0.12 ($\sim$177 m) for RES1, RES2, RES3, and RES4, respectively. The refinement hierarchies are detailed in appendix E. With the exception of grid resolution / refinement hierarchy, all calculations are performed with a standardized simulation setup: $1 + \log$ slicing and Γ_S shift, second-order finite differencing in BSSN_MoL without artificial dissipation[4], iterative Crank-Nicholson time integration with a courant factor of 0.375, PPM cell-interface reconstruction and the Marquina approximate Riemann solver in Whisky and the standard PMR settings discussed in §4.3.2. In addition to the four resolution study calculations, I perform a fifth calculation in which I remove the restriction to bitant mode in order to demonstrate that the dynamics remain unaltered when equatorial symmetry is not enforced for the simple polytropic models considered here. I call this calculation RES2full and employ RHII in full mode. All calculations are summarized in table 4.2.

[2] Solving the Hamiltonian and momentum constraints in 2D/3D is currently not supported by CCW.

[3] Bitant mode refers to the upper half of the 3D box, that is, the northern hemisphere. Reflection symmetry with respect to the equatorial plane is enforced.

[4] The calculations presented here were performed before the artificial dissipation operator described in §3.3.4 became a standard component of code.

Table 4.2: Summary of the resolution study calculations for the rotating test model A1B3G5. RH denotes the refinement hierarchy employed and Δt is the time each calculation was continued for after core bounce. The numbers given for the computational costs should be considered with caution. They do not only depend on the scalability of CACTUS/CARPET/WHISKY, but also on I/O performance (checkpoint/recovery; output) and CPU speed as the machine on which they were obtained is not heterogeneous in CPU clock speed.

Run Name	RH[a]	Central Resolution	Δt	Computational Cost[b]
RES1	RHI	∼710 m	2.4 ms	4 IA-64-2 CPUs × 12 h — 48 CPU hours
RES2	RHII	∼355 m	5.0 ms	8 IA-64-2 CPUs × 48 h — 384 CPU hours
RES2full	RHII[c]	∼355 m	4.3 ms	16 IA-64-2 CPUss × 52 h — 832 CPU hours
RES3	RHIII	∼266 m	4.6 ms	24 IA-64-2 CPUs × 72 h — 1728 CPU hours
RES4	RHIV	∼177 m	3.5 ms	64 IA-64-2 CPUs × 168 h — 10752 CPU hours

[a] Refinement Hierarchy. See Appendix E.
[b] The numbers were obtained from calculations on the Itanium 2 Cluster Mercury at the U.S. National Center for Supercomputing Applications (NCSA).
[c] This calculation is performed in full mode. No assumed symmetries.

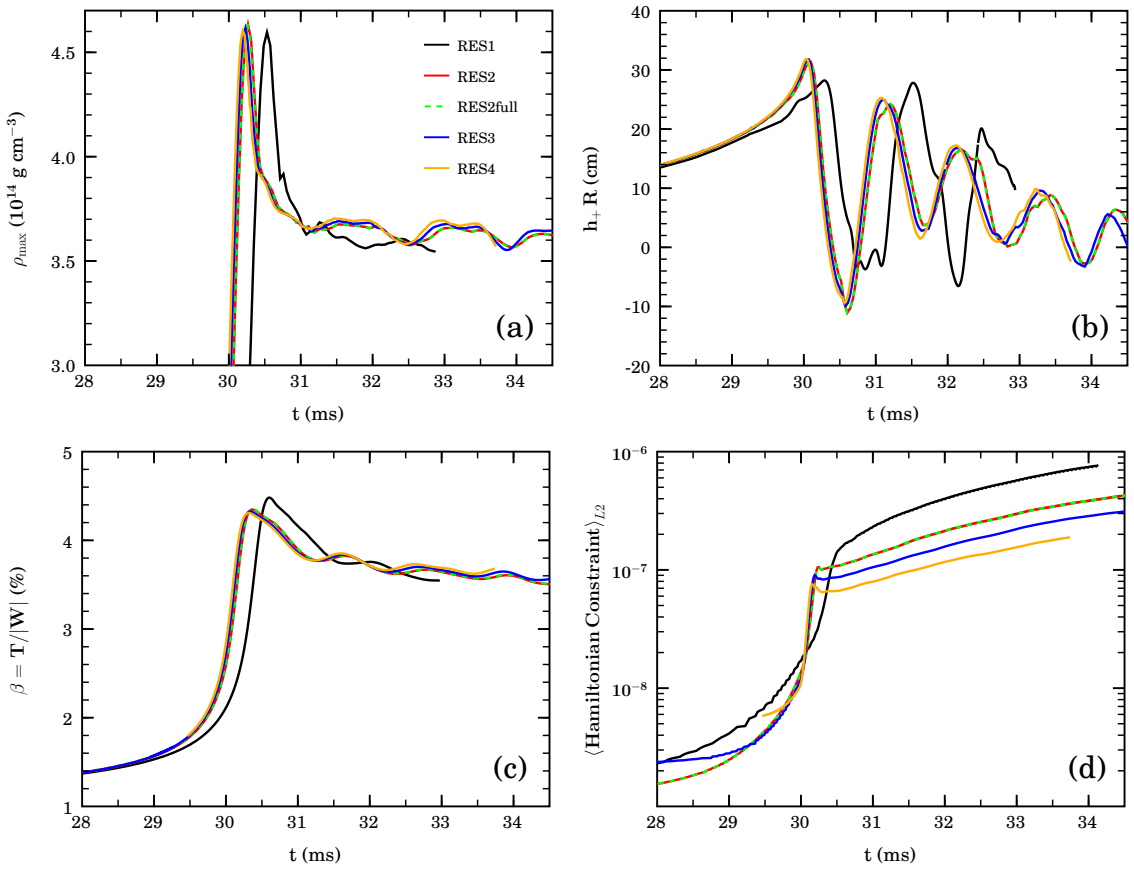

Figure 4.8: Resolution study for model A1B3G5. Panel (a): Evolution of the maximum density (ρ_{max}) from ∼2 ms before to ∼4 ms after bounce. Panel (b): Gravitational wave signal h_+ as seen by an observer at the equator; scaled by distance to the source R. Panel (c): Rotation parameter $\beta = T/|W|$ as defined in §3.9.2. Panel (d): $L2$-norm of the Hamiltonian constraint. A large fraction of the prebounce evolution data of the highest-resolution calculation RES4 was lost. Note that the lowest-resolution calculation RES1 clearly underresolves the matter dynamics and leads to the largest constraint violation. Also note that the prebounce constraint violation is actually larger for finer resolution. This is due to high-frequency noise in the initial data. Dissipation on curvature variables is not used in the calculations presented here.

Axisymmetric rotating collapse — at least for moderate initial rotation rates — proceeds largely in the same manner as the canonical spherically symmetric core collapse discussed in the introduction (§2.3.2). Collapse can be divided up into a long infall phase, plunge and core bounce at supernuclear densities and subsequent ring-down of the protoneutron star. More details are discussed in §5.

Panel (a) of figure 4.8 depicts the evolution of the maximum density ($\rho_{\max}$) from shortly before to shortly after core bounce in all five test calculations. First of all, one notes that the equatorial-symmetry calculation RES2 and its full-mode counterpart RES2full yield identical results in the evolution of $\rho_{\max}$. This and the other panels of figure 4.8 confirm that indeed equatorial symmetry yields excellent results for A1B3G5[5] while saving a factor of two in computer memory and CPU hours. In fact, using so-called "rotation symmetry" in octant mode which is realized by imposing a periodic boundary condition on the y–z and x–z-faces, it would be possible to cut down by another factor of four in resource needs. Yet, rotation symmetry in octant mode would suppress any azimuthal mode that is not an integer multiple of four, thus limiting the code's ability to track the possible formation of nonaxisymmetric structures.

As clearly visible in panel (a) of figure 4.8, there is convergence towards the $\rho_{\max}(t)$ of the highest-resolution calculation. RES1 is underresolved and reaches bounce $\sim$0.5 ms later than RES2, RES3 and RES4 which are all in the numerically converged regime. Among the latter three calculations, higher resolution yields slightly earlier core bounce at slightly lower densities (with variation on the 0.5% level), but more small-scale postbounce features are captured and the core settles at minutely higher postbounce densities. Panel (b) of the same figure proves that the gravitational wave signal of model A1B3G5 is more sensitive to the resolution than the $\rho_{\max}$ evolution. RES1 yields a wave signal that departs quantitatively and qualitatively from that obtained in the higher-resolution calculations. Even though there is obvious convergence towards the graph of the highest-resolution calculation (RES4), even RES3 exhibits non-negligible small quantitative and qualitative variations. Qualitative deviations become significant beginning at the second postbounce maximum in the wave signal when RES2 (in particular) develops substructure not present in RES3 and RES4. Also, from that point on, RES2–RES4 appear slightly out of phase. A detailed analysis shows that these variations are related to spurious numerical errors introduced in the density and velocity fields when the bounce shock traverses a refinement boundary. They become smaller with increased resolution and can influence the wave signal at high frequencies and at an ambient level of $\sim$10 cm in h_+R. Since model A1B3G5's wave signal is of rather low amplitude, the errors produce a significant effect. Models with larger signal amplitudes should be less affected.

The resolution dependence of the rotation parameter β, the ratio of rotational to gravitational energy (see §3.9.2), is similar to that of $\rho_{\max}$ (panel (c) of figure 4.8). RES1 underresolves the dynamics, while RES2–RES4 agree very well — except for the already discussed slight mismatch in the time of bounce. Panel (d) of figure 4.8 depicts how the evolution of the $L2$-norm of the Hamiltonian constraint varies with resolution. Since the calculations presented here are not run with dissipation (see §3.3.4) the high-frequency noise in the initial data leads to a larger constraint violation with increased resolution at prebounce (or, rather, preplunge) times. During the plunge and bounce phase and at postbounce times however, the picture is consistent: higher resolution yields smaller constraint violations. I find similar behavior for the momentum constraints (not shown here). Interestingly, RES1, which clearly underresolves the matter dynamics, does not lead to an unstable curvature evolution during the postbounce times covered here. This is most likely connected to the fact that in these matter dominated core-collapse spacetimes, the matter dynamics require a higher spatial resolution than the curvature dynamics (§4.2).

The two top panels (a) and (b) of figure 4.9 show snapshots at 3 ms postbounce of the velocity and density profiles along the x-axis, respectively. Most notable is that although RES1 reaches core bounce later than RES2–RES4, RES1's bounce shock has travelled to $\sim$15% greater distances. This indicates a grossly incorrect shock speed in this low-resolution simulation. All other calculations converge well on the shock position and exhibit similar postshock structure, while small-scale variations are due to numerical errors introduced by the shock passage through refinement boundaries. This is discussed in detail for velocity profiles in §5.2.3.

[5] It is safe to assume that equatorial symmetry will be an excellent choice for any model in which no significantly strong convection or shock instability develops. Note that even rotationally nonaxisymmetrically unstable stars may be described well with the assumption of equatorial symmetry since in such instabilities, equatorial symmetry is typically not broken and the dependence on position along the rotation axis is weak [23].

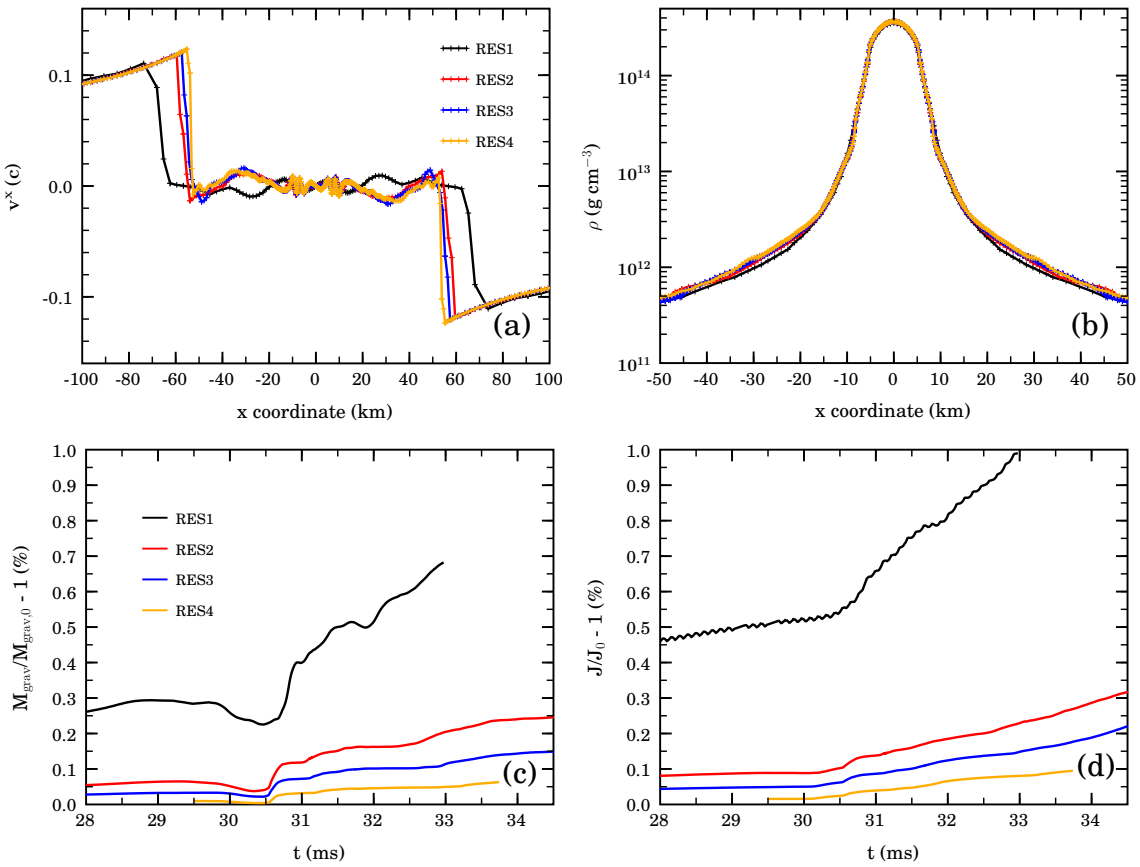

Figure 4.9: Resolution study for model A1B3G5. Panel (a): x-velocity profile along the x axis at 3 ms after core bounce. The shock is clearly visible at ∼55 km and the calculations converge on the shock position. RES1 is clearly underresolved. Panel (b): Profile of the rest-mass density along the x axis. Panel (c): Relative error in percent in the gravitational mass, a measure of the total energy of the system (see §3.9.2). Panel (d): Relative error in percent in the axisymmetric total angular momentum as defined in §3.9.2. A1B3G5's spacetime is nearly axisymmetric. In axisymmetry, gravitational waves cannot carry angular momentum. Hence, it should be conserved.

In Newtonian astrophysical hydrodynamics it is common and straightforward to test a numerical scheme for mass, energy, momentum and angular momentum conservation. In GR, particularly with a {3+1} free-evolution approach, finding conserved quantities and testing their conservation in a numerical simulation is usually much more complicated. Here I make the assumptions that (a) core-collapse spacetimes are asymptotically flat (i.e., that there is some radius r at which the metric tends to the Minkowski metric) and (b) that the gravitational wave content is very small. Assumption (a) is valid because the Schwarzschild/Kerr solutions can be matched to core-collapse spacetimes at sufficiently large radii where there is little matter and assumption (b) is valid since simple back-of-the-envelope calculations show that the energy emitted by gravitational waves during collapse and bounce should even in extreme cases be not much larger than 10^{-6} $M_\odot$ while the total energy of the system is on the order of ~ 1 $M_\odot$. Panel (c) of figure 4.9 shows the relative error in the gravitational mass[6] that accumulates during the numerical evolution in calculations RES1 to RES4. As expected, the violation of energy conservation is largest in the lowest-resolution calculation RES1 and RES2–RES4 show clearly convergent behavior. Despite their small relative energy errors, none of the considered resolutions would suffice to study the details of supernova explosion energetics, since a ∼0.05% error in the total energy (including the rest mass!) is of the same order of magnitude as a typical supernova explosion energy ($\sim 10^{51}$ erg = 1 foe). Since the details of the supernova explosion mechanism are not studied, the present degree of energy conservation by the code is acceptable.

[6] See §3.9.2. Defined as the total energy.

Angular momentum should be conserved in axisymmetric spacetimes. A1B3G5 stays axisymmetric and panel (d) of figure 4.9 portrays the relative error in the angular momentum (§3.9.2). At post-bounce times, RES1's angular momentum has increased by about 1% from its value at $t = 0$, while the finer resolutions again show clear convergence towards much better conservation of angular momentum. A check of linear momentum conservation yields numbers that are similar to those of energy and angular momentum conservation.

Discussion

I have performed a resolution study on model A1B3G5 of the ZM/DFM [30, 160] model set and find that three of the four resolutions considered yield results that are in the numerically convergent regime. A cost-benefit analysis based on the numerical results presented in this section and the computational costs of the calculations listed in table 4.2 brings me to the decision to employ the lowest grid resolution that yields convergent results as the standard resolution for production calculations. Stepping up to the next higher resolution would imply at least a five-fold increase in the computational costs which cannot be justified by an improvement on the order of 5–10% in the results for the gravitational wave signal. I find that conservation of the total energy and angular momentum becomes significantly better (by factors of 2 and more) with increased resolution, yet none of the considered resolutions conserves energy to a precision needed in calculations that are concerned with the details of supernova explosion mechanisms and energetics. Since the study of the latter phenomena is not the objective of this work, I consider the 0.2-0.3% violation of energy and angular momentum conservation at the standard resolution level as acceptable.

In addition to the four resolution-study calculations, I have performed one calculation in which I have relaxed the assumption of equatorial symmetry (i.e. bitant mode/symmetry) to investigate possible impacts on the dynamics and the gravitational wave signal. For model A1B3G5 considered here, I find that equatorial symmetry is well maintained even when not enforced by the grid setup / boundary conditions. It can hence be considered safe to employ equatorial symmetry for all models in which genuine 3D processes occur that do not exhibit equatorial symmetry. In the supernova context, convection and instabilities of the standing accretion shock are examples of such processes. Rotational instabilities of the protoneutron star are usually most pronounced in the equatorial plane and typically equatorially symmetric (e.g., [23]).

4.3.2 Progressive Mesh Refinement

As discussed in §3.4, I use a simplified adaptive mesh refinement scheme in my simulations. It was developed in collaboration with Erik Schnetter, Ian Hawke and Burkhard Zink (see also [202, 404]). *Progressive mesh refinement* (PMR) is based on the fact that there is some *a priori* knowledge of the physically required resolution. In the stellar core collapse problem, a numerical resolution of $\sim$500 m (the exact number depending on model parameters, formulation of the governing equations, and implementation details, see, e.g., [18]) has empirically been determined to be necessary for adequate capture of the dynamics of rotational/nonrotational core bounce and protoneutron star formation. A similar (but possibly slightly higher) resolution is needed to keep a protoneutron star in hydrostationary quasi-equilibrium[7]. Again, from experience and basic considerations, the highest resolution will only be needed in the central-most regions and only from times shortly before the plunge phase of collapse and core bounce. At earlier stages of collapse, it is only necessary to (a) adequately resolve the radial dynamics of the inner homologous core out to and slightly beyond the sonic point where the collapse velocity becomes equal to the local speed of sound (see, e.g., [3, 65]) and (b) sufficiently resolve stellar rotation and rotational spin up (due to angular momentum conservation) during collapse. Which resolution is needed for (a) and (b) is *not* known in advance and may vary from model to model. I have found it most practical to use the maximum density on the grid as the observable governing the activation of additional refinement levels. This is a natural choice because initially the collapse velocities are small and the maximum density increases only slowly and additional resolution is only needed at a small time rate. As the collapse progresses and becomes more dynamic, higher resolution is needed in shorter time intervals, and the maximum density increases more rapidly.

In the following, I present tests that I have conducted in order to investigate the quality of PMR and to empirically determine on a cost-benefit basis the best PMR parameters for the stellar core-collapse problem. Finding a general and unambiguous definition of "numerical convergence" in the AMR/PMR context is not straightforward since the globally lowest and highest resolutions are not modified and only the times at which resolution is added during the course of a simulation vary. In this study of PMR I focus on the PMR-dependent behavior of the physical observables I aim at extracting from my simulation data, that is, first and foremost, on the gravitational wave signal.

For all tests I use the grid hierarchy given in table 4.3. This bitant-mode refinement hierarchy with reflection symmetry on the equatorial plane is also used in production runs, hence it is optimized with particularly large refinement levels 4 and 5 to resolve the postbounce evolution and the shock propagation well out to several hundred kilometers.

Table 4.3: Refinement hierarchy for PMR tests. This is RHII. For further refinement hierarchies, see appendix E.

level	lower			upper			Δx^a	grid points
	x	y	z	x	y	z		
0	-1966.08	-1966.08	0	1966.08	1966.08	1966.08	61.44	(65x65x33)
1	-1228.80	-1228.80	0	1228.80	1228.80	1228.8	30.72	(81x81x41)
2	-614.40	-614.40	0	614.40	614.40	614.40	15.36	(81x81x41)
3	-307.20	-307.20	0	307.20	307.20	307.20	7.68	(81x81x41)
4	-184.32	-184.32	0	184.32	184.32	184.32	3.84	(97x97x49)
5	-92.16	-92.16	0	92.16	92.16	92.16	1.92	(97x97x49)
6	-38.40	-38.40	0	38.40	38.40	38.40	0.96	(81x81x41)
7	-19.20	-19.20	0	19.20	19.20	19.20	0.48	(81x81x41)
8	-9.60	-9.60	0	9.60	9.60	9.60	0.24	(81x81x41)

[a] Δx: grid spacing
Note that all units are in $c = G = M_\odot = 1$.
A length of 0.24 in these units corresponds to 354.43 meters in cgs (see appendix A for details). Levels 4 and 5 are enlarged to allow for a better-resolved shock traversal out to large radii.

The tests are performed with the standard set of simulation parameters and only for model A1B3G5, my standard polytropic test model, combining moderate rigid initial rotation with fast collapse. Ideally, PMR should be tested for a large variety of models, but time and computational constraints do

[7] The protoneutron star quasi-statically contracts as it deleptonizes and cools.

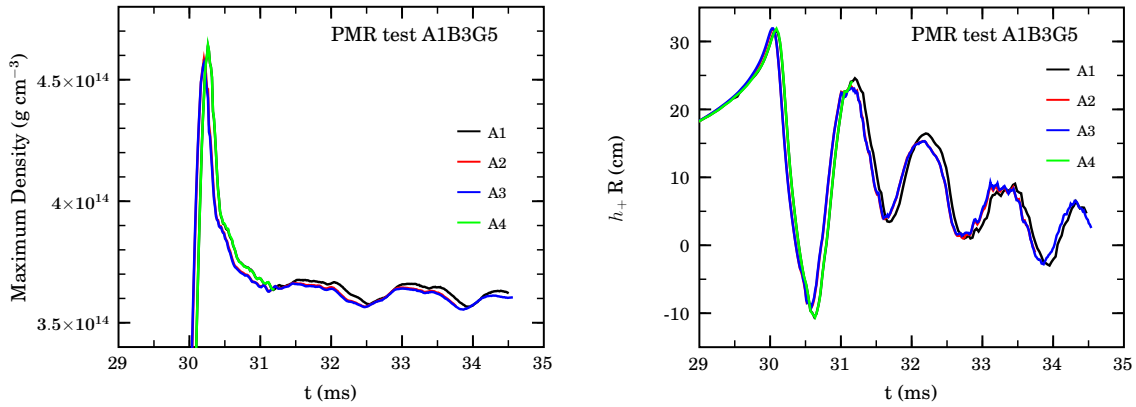

Figure 4.10: Comparisons of the evolutions of the maximum density (left panel) and of the axisymmetric gravitational-wave strains (right panel) of models PMR A1 through PMR A4. Shown is the time interval from ∼1 ms before bounce to the time I stop the test simulations. The oscillations in the wave strains that appear a few ms after core bounce are purely numerical and caused by spurious numerical errors introduced in the density and velocity fields when the bounce shock traverses a refinement boundary. They influence the extracted signal at high frequencies and at an ambient level of ∼10 cm. The PMR test calculations were among the first carried out in the work towards this dissertation. An improved numerical implementation of the quadrupole gravitational wave extraction employed in later calculations significantly improves the smoothness of the extracted waveforms.

not allow me to carry out such a study. Hence, the test results presented in the following should be taken with care and may not apply fully to all models studied[8].

Table 4.4: Summary of PMR test calculations performed. The number of initially active refinement levels and the values of the maximum density on the grid at which additional refinement levels are activated ($\rho_{\rm activate}$) are varied.

Run name	Active Levels at t=0	$\rho_{\rm activate}$ (g cm^{-3}) Level 5	Level 6	Level 7	Level 8	Level 9
PMR A1	4	5.00×10^{10}	2.00×11^{10}	8.00×10^{11}	3.20×10^{12}	1.28×10^{13}
PMR A2	5	—	5.00×10^{10}	2.00×11^{10}	8.00×10^{11}	3.20×10^{12}
PMR A3	6	—	—	5.00×10^{10}	2.00×11^{10}	8.00×10^{11}
PMR A4	4	5.00×10^{10}	2.00×11^{10}	8.00×10^{11}	3.20×10^{12}	6.40×10^{12}
PMR A5	5	—	2.00×11^{10}	8.00×10^{11}	3.20×10^{12}	1.28×10^{12}

Table 4.4 lists the set of PMR test runs that I perform. Most runs are carried out to ∼4 ms after core bounce. Run PMR A1 starts out with four refinement levels (see table 4.3) and the first additional level is added once the maximum density reaches 5×10^{10} g cm^{-3}. This is five times its initial value. From there on, additional levels are added whenever the maximum density reaches four times the value of the time at which the previous level was added. PMR A1 is the reference run. Its maximum density evolution and its waveform are plotted in black in figure 4.10. In order to test the sensitivity of the results on when additional refinement levels are added, I perform the test runs PMR A2 and PMR A3 (plotted in red and blue color in figure 4.10, respectively) that start out with 5 and 6 refinement levels, respectively, while using the same regridding[9] parameters as for run PMR A1. The left panel of figure 4.10 displays the evolution of the maximum density (a one-zone value). Runs PMR A2 and PMR A3 yield almost identical maximum density evolutions and reach core bounce (defined here by the time the global density maximum is reached) 0.06 ms earlier than run PMR A1 (0.02% relative difference) at a slightly lower (4.64×10^{14} g cm^{-3} vs. 4.59×10^{14} g cm^{-3}; ∼1% relative difference) maximum density. Hence, the quantitative evolutions are nearly identical, while the qual-

[8]Especially for models in which centrifugal effects significantly change the dynamics I find it necessary to adjust the PMR settings to provide increased resolution at earlier times of the collapse and out to larger coordinate radii.

[9]In the PMR context I use the verb *to regrid* to mean the addition of a refinement level.

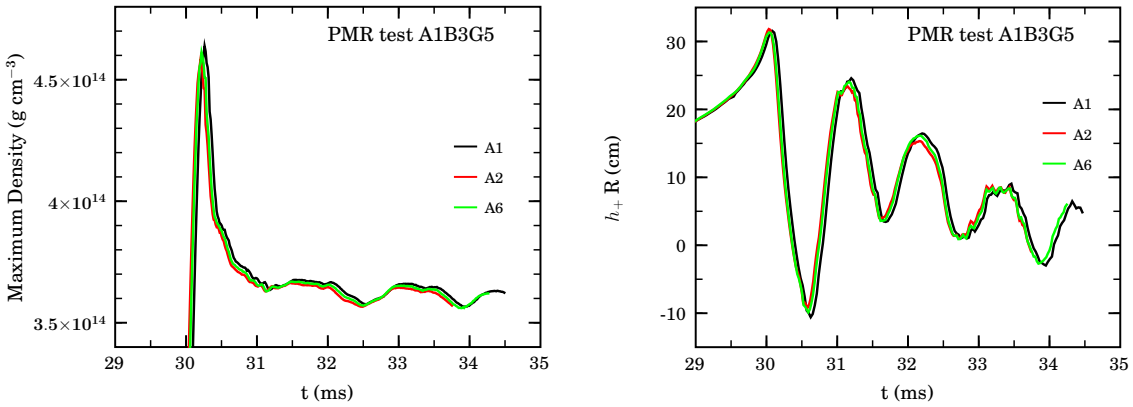

Figure 4.11: Comparisons of the evolutions of the maximum density (left panel) and of the axisymmetric gravitational-wave strains (right panel) of models PMR A1, PMR A2 and PMR A5. Shown is the time interval from ∼1 ms before bounce to the time I stop the test simulations.

itative evolution of the maximum density is identical among models PMR A1, PMR A2 and PMR A3. In the right panel of figure 4.10, I superpose the late prebounce and early postbounce gravitational wave strains of the test simulations. Again, all test runs agree very well qualitatively, while interestingly PMR A2 and PMR A3 reach lower maximum strains (but with total discrepancy not more than ∼10% at any point and much less on average), while exhibiting idential wave modulation and phase as seen for model PMR A1.

Tests PMR A1, PMR A2 and PMR A3 indicate that for model A1B3G5 the PMR set up used in test PMR A1 is adequate to fully capture the qualitative shape of A1B3G5's wave signature. On the quantitative side, PMR A1 appears to overestimate the peak amplitudes by ∼10% at most, but less on average. Given the uncertainties associated with the initial conditions, equation of state and microphysics treatment, the partial overestimate of the strain amplitudes is acceptable. However, it is interesting to investigate its cause.

Both panels of figure 4.10 show excellent agreement between test runs PMR A2 and PMR A3 and I assert that they are in the "converged" regime. There are three potential reasons for the differences with PMR A1. (a) The addition of the last refinement level(s) happens too late before core bounce in PMR A1 and hence the bounce and postbounce dynamics are affected, (b) the resolution available in PMR A1 at the early stages of collapse is not sufficient to accurately capture the early collapse phase, and (c) the resolution provided by PMR A1 is not high enough at some intermediate phase of collapse.

To test possibility (a), I perform test run PMR A4 which is very similar to PMR A1, but the final refinement level is added at 6.4×10^{12} g cm^{-3} instead of at 1.28×10^{13} g cm^{-3}. A glance at figure 4.10 reveals that the maximum density evolutions and the gravitational wave strains of PMR A1 and PMR A4 superpose perfectly. If (a) were the case, there should be at least minor disagreement between PMR A1 and PMR A4. Hence, I rule out possiblity (a).

To test possibilities (b) and (c), I perform run PMR A5, which, similarly to PMR A2, starts out with five active refinement levels, but the sixth and subsequent levels are only added starting at 2×10^{11} g cm^{-3} (see table 4.4). In this way I can test the sensitivity of the bounce and postbounce dynamics on the resolution at early and intermediate phases of collapse. Figure 4.11 displays the maximum density evolution (left panel) and the axisymmetric waveform (right panel) of PMR A5 compared with PMR A1 and PMR A2. The increased initial resolution of model PMR A5 over PMR A1 leads to a maximum density and waveform evolution closer to those of PMR A2. This indicates that there is in fact a dependence of the numerical results at bounce and during the postbounce phase on the resolution (i.e., the number of active refinement levels) at the early stages of collapse. Due to the box-in-box structure of the refinement hierarchy I use here, additional refinement levels increase the resolution in the central-most regions of the iron core only. Given this, the slight dependence of the bounce and postbounce results on the number of active refinement levels during early and

intermediate phases of collapse can be linked directly to how well the dynamics of the central core regions is resolved during early and intermediate stages of collapse. Too little (or slightly too little) resolution will result in a slightly incorrect collapse velocity profile and dynamics. The dynamics of the inner core during collapse is the most important discriminant for the bounce and postbounce dynamics and the resulting gravitational waveform. This explains the bounce and postbounce differences observed.

Discussion

I have performed five test computations for which I have varied the number of initially active refinement levels and the threshold densities at which additional refinement levels are activated. I find that the PMR method with the standard refinement hierarchy (table 4.3) and the PMR A1 parameter set (table 4.4; 4 active levels at the beginning of the calculation) yields results for the evolution of the maximum density and the gravitational waveform that differ only on the percent level from results of test computations which use more than 4 initially active levels, but that are computationally much more expensive[10]. Given that small variations of the input physics, the equation of state and the microphysics treatment (completely missing for the polytropic models considered here) may easily lead to variations on the order of $\sim$10% and more, I find that the standard PMR setup A1 has the best cost-benefit ratio and I will continue to use it for most of the model calculations presented in this dissertation. Finally, I must again point out that I have performed the above PMR tests only for one particular model. Models with different initial conditions, in particular strongly differentially rotating ones, may well require additional resolution at earlier times and out to larger radii. However, I expect above results to hold for models in a relatively large parameter space from rigid to moderate differential rotation and initial T/|W| up to $\sim$1%.

4.3.3 Gauge Conditions

Most observables that I consider in the analysis of my stellar core collapse simulations are not gauge invariant. The prime example is the gravitational wave signal which is computed via the Newtonian quadrupole formalism (see § 3.8.1), but any standard grid function, e.g., the rest mass density ρ, is in general dependent on the spatial and temporal gauge. Hence, it is useful to study how changes in shift and lapse prescription affect the coordinate dependent observables.

All test calculations are carried out with model A1B3G5, the standard fast-collapse test model. Because of the high computational costs that are required for {3+1} GR hydrodynamics calculations, I limit myself to comparing three lapse and three shift prescriptions. I choose the widely used hyperbolic $1 + \log$ slicing

$$\alpha_{,t} = -2\alpha(K - K_0) \ , \tag{4.4}$$

harmonic slicing

$$\alpha_{,t} = -\alpha^2(K - K_0) \ , \tag{4.5}$$

and constant slicing $\alpha(t) = \alpha(t = 0)$, using the $\alpha(t = 0)$ set by the initial data code. I do not include maximal slicing ($K = $ const.), since it requires the solution of an elliptic equation, which is (a) computationally very expensive and (b) currently not implemented on refined CCW grids[11]. The considered shift conditions include Γ_S (see §3.3.2), given by

$$\beta^i{}_{,t} = (\tilde{\Gamma}^i + \Delta t\, \tilde{\Gamma}^i{}_{,t}) \ , \tag{4.6}$$

Γ2 (see §3.3.2),

$$\frac{\partial^2}{\partial t^2}\beta^i = F\, \tilde{\Gamma}^i{}_{,t} - \eta \beta^i{}_{,t} \ , \tag{4.7}$$

where I choose $F = 3/4$, η =0.001, and zero shift ($\beta^i = 0 = $ const.). Table 4.5 summarizes the test calculations performed.

[10] A factor of 2 and more until all levels are active.

[11] However, $1 + \log$ and maximal slicing yield very similar results. See Section 5.2.3 for a comparison.

Table 4.5: Test calculations with various gauge conditions. See text and §3.3.2 for details on the employed gauge conditions. All simulations are carried out with refinement hierarchy RHII (see appendix E)

Run Name	Lapse Condition	Shift Condition
A1B3G5ref	1+log	Γ_S
A1B3G5geo	constant	Γ_S
A1B3G5harm	harmonic	Γ_S
A1B3G5zs	1+log	0
A1B3G5g2	1+log	$\Gamma 2$

On the continuum level any combination of any coordinate and slicing conditions will satisfy the Einstein equations[12]. As pointed out in §2.4.3 and §3.3.2, this is not generally true on the discretized level, and the quality of the numerical evolution can depend sensitively on the choice of gauge conditions. A "good" gauge condition is defined as a one that allows long term stable evolution in numerical relativity.

Figure 4.12 portrays the lapse evolution at the origin as given by the three considered slicings. The $\alpha =$ const. condition is very close to geodesic slicing, and as the inlay plot of Figure 4.12 reveals, harmonic and $1 + \log$ slicing yield practically identical lapse evolutions for model A1B3G5. Although harmonic and $1 + \log$ slicings have been found to lead to differing lapse evolutions and long-term stability in black hole spacetimes[13], it is not entirely surprising to find the close match of harmonic and $1 + \log$ slicing in the weak-field regime. It is likely that the two conditions will lead to differing evolutions both at later postbounce times and for more massive / compact PNSs which are not considered here. The $\alpha =$ const. calculation fails before core bounce is reached. A glance at figure 4.13 reveals why. The ∞-norm of the Hamiltonian constraint in the $\alpha =$ const. calculation at 10 ms before bounce is already three orders of magnitude larger than in the $1 + \log$ and harmonic slicing calculations. A few ms before bounce, strong exponential constraint growth sets in and the calculation crashes. Constant/geodesic slicing is clearly a bad choice of gauge, while both $1 + \log$ and harmonic slicing give stable long-term evolutions with maximum Hamiltonian and momentum constraint (not shown here) violations on the sub-one-percent level.

[12] But may not properly foliate spacetime [384].

[13] This is mostly due to the fact that $1 + \log$ is genuinely singularity avoiding while harmonic slicing is only marginally singularity avoiding [120].

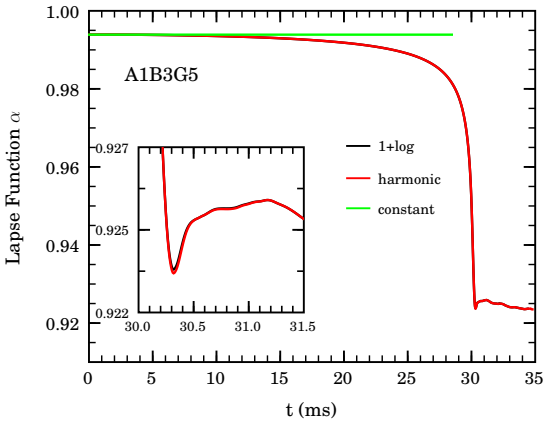

Figure 4.12: Lapse evolution at the origin as obtained with $1 + \log$, harmonic and constant slicing. Harmonic and $1 + \log$ yield practically identical results, while the simulation with $\alpha =$ const. crashes before core bounce is reached.

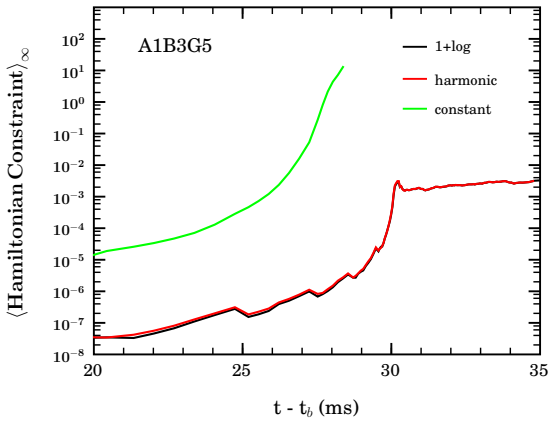

Figure 4.13: Evolution of the ∞-norm of the Hamiltonian constraint of the $1 + \log$, harmonic and constant slicing calculations from $\sim$10 ms before to $\sim$5 ms after bounce. The $\alpha =$ const. calculations becomes unstable $\sim$2 ms before bounce. The jumps visible throughout the prebounce phase are connected to the addition of finer levels by progressive mesh refinement.

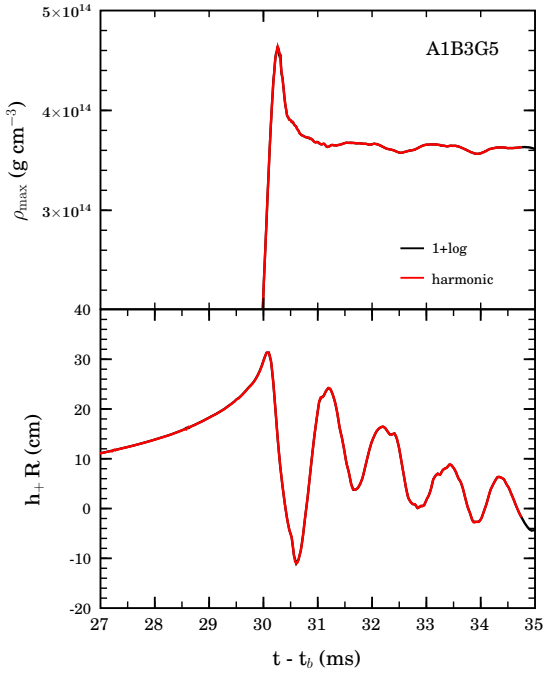

Figure 4.14: Evolution of the maximum rest-mass density on the grid (top) and of the gravitational wave signal (bottom) of model A1B3G5 computed with $1+\log$ and harmonic slicing. The two different gauge conditions lead to practically identical behavior of these coordinate dependent dynamical observables.

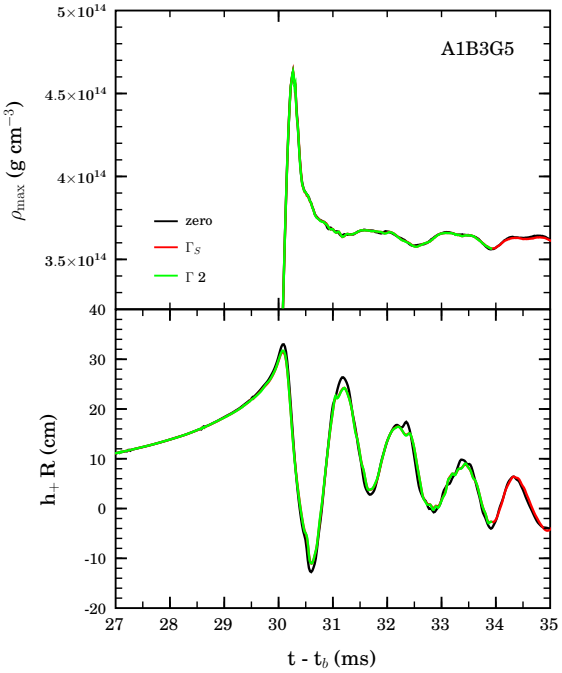

Figure 4.15: Comparison of the maximum density (ρ_{max}; top) and gravitational wave signal evolution of model A1B3G5 calculated with zero shift, Γ_S shift and $\Gamma 2$ shift. While the ρ_{max} evolutions agree quite well for all shift conditions, the maximum gravitational wave amplitudes obtained with zero shift are consistently ∼5–10% larger than those obtained with the Γ_S and $\Gamma 2$ calculations. See text for details.

The close similarity of the central lapse evolutions obtained with $1+\log$ and harmonic slicing lets one believe that the time evolution of coordinate dependent dynamical observables may be very similar as well. That this is indeed the case is shown by figure 4.14. The evolutions of the maximum density (ρ_{max}) and the quadrupole gravitational wave signal ($h_+ R$) agree almost perfectly with slight discrepancies only on the sub-one-percent level.

Figure 4.15 compares the ρ_{max} and quadrupole wave signal evolutions as obtained with $1+\log$ slicing and three different shift conditions. The two gamma-driver type shift conditions (see §3.3.2) lead to practically identical ρ_{max} and $h_+ R$ behavior. This is not surprising given their close relationship through the Γ-freezing / minimal distortion coordinate gauges [389]. The zero-shift calculation yields a very similar $\rho_{max}(t)$ to those of the Γ drivers, yet its wave signal exhibits about ∼5–10% larger maximum amplitudes while staying perfectly in phase with the wave signals found with Γ_S and $\Gamma 2$. This is remarkable and can be understood by recalling that the variant of the quadrupole formula used in this work and given by equation (3.167) makes direct use of the Eulerian 3-velocity, which, in turn, is constructed (equation 2.22) from the spatial components of the 4-velocity and the shift. A non-zero shift will hence always contribute to the quadrupole wave signal, and since in the case of the Γ drivers the shift components typically have the opposite sign of the fluid velocity in matter dominated spacetimes[14], it is obvious that *with* non-zero shift one should expect slightly smaller wave amplitudes, but preservation of phase. This is an important finding about the gauge dependence of the gravitational wave signal extracted with the quadrupole formula in the first-moment of momentum density formulation (FMOD), and it agrees well with what Shibata & Sekiguchi [174] have found when comparing FMOD waveforms with waveforms obtained via a gauge-invariant formalism. Importantly, my results corroborate Shibata & Sekiguchi's finding that the FMOD wave signal adequately captures the important phase and frequency information of the physical waveform.

[14] This follows from the time evolution equation for the $\tilde{\Gamma}^i$; equation (3.29).

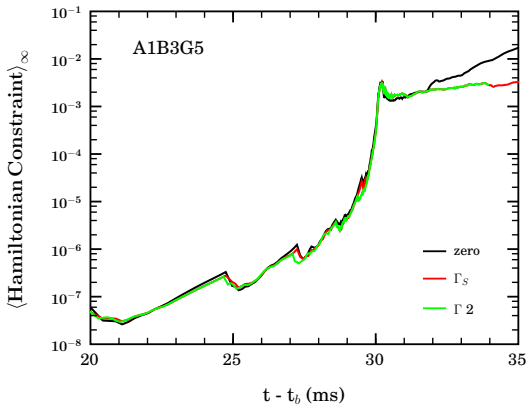

Figure 4.16: ∞-norm of the Hamiltonian constraint for the zero shift, Γ_S and $\Gamma 2$ calculations. Core bounce occurs at $\sim$30.3 ms. The discontinuities in the prebounce phase are connected to the addition of finer refinement levels by progressive mesh refinement.

Figure 4.16 displays the ∞-norm of the Hamiltonian constraint for the three shift test calculations. While both Γ_S and $\Gamma 2$ lead to very similar almost constant postbounce constraint violations, the zero-shift calculation exhibits continued constraint growth after bounce. During collapse however, all three shift conditions yield very similar Hamiltonian constraint evolutions. This is to be attributed to the fact that both Γ_S and $\Gamma 2$ shifts stay very small throughout collapse and have to counteract significant coordinate distortion due to the quickly spinning collapsing core and the protoneutron star only at and after bounce. In the zero-shift calculation, coordinate distortion is not corrected and it becomes increasingly difficult for the numerical scheme to accurately evolve the spacetime. This is reflected in the postbounce constraint growth that eventually leads to the termination of the zero-shift calculation.

Discussion

I have performed a set of test calculations in order to estimate how much key coordinate-dependent observables such as the quadrupole-formula gravitational wave signal and the evolution of $\rho_{\max}$ vary with choice of temporal and spatial gauge conditions. I find that $1 + \log$ and harmonic slicing yield identical results for $\rho_{\max}$ and for the wave signal, while geodesic/constant slicing may lead to an early crash of the calculation. For the shift dependence, I find that non-zero shifts lead to slightly lower maximum gravitational wave amplitudes than those obtained with zero shift, but that the phase of the wave signal is shift independent – at least for the non-pathological shift conditions considered here. This is an important finding and confirms previous findings on the coordinate dependence of quadrupole-formula waveform estimates [174]. In addition, I find that both Γ-driver [381, 389] type shift conditions yield good postbounce stability and virtually identical results for $\rho_{\max}$ and waveform.

The fact that all "good" gauge conditions considered here lead to practically identical qualitative and quantitative evolutions of coordinate-dependent observables leads one to the conjecture that any set of temporal and spatial gauge conditions that allow for long-term stable evolutions of core collapse spacetimes with the methods and discretization schemes employed here will yield essentially the same results. This conjecture does not imply that the coordinate-dependent observables can be taken as physically valid, rather it highlights the coordinate dependence of the numerical stability of the spacetime evolution scheme.

4.3.4 Riemann Solvers / Flux Formulae and Reconstruction Methods

It is very common in computational fluid dynamics to test schemes for the solution of the Euler equations on a number of well defined test problems for which analytic solutions are known. Perhaps the most common of these tests is the 1D shock tube problem (see, e.g., [165]). The reconstruction methods and approximate Riemann solvers in WHISKY have been thoroughly tested with the shock tube in 3D on the diagonal [123, 163] and in 1D with mesh refinement in §4.1. In this section I take a somewhat different approach and compare the performance of various reconstruction methods and approximate Riemann solvers in a full rotating core collapse simulation. From the tests in [18, 123, 157], one knows that the combination of PPM reconstruction with the Marquina flux formula produces the best results with WHISKY in the shock tube problem. However, both PPM and the Marquina flux formula are computationally quite expensive and it is important and useful to know how simpler and computationally cheaper methods compare in the core collapse context. As for most other tests presented in this chapter, I choose model A1B3G5 and evolve it with refinement hierarchy RHII (see appendix E) and the standard set of parameters used for production-type runs (see §5.2.2). In the following, I compare results obtained with PPM and Marquina, TVD MC/minmod and Marquina, PPM and HLLE, and TVD MC and HLLE. Details on the Riemann solvers and reconstruction methods can be found in §3.5 and table 4.6 summarizes the set of test calculations.

The top panel of figure 4.17 portrays the evolution of the maximum density ($\rho_{\max}$) on the grid from $\sim$3 ms before to $\sim$5 ms after core bounce. All test calculations agree very well in the time of core bounce and $\rho_{\max}$ at core bounce and the largest deviation is exhibited by the calculation employing the simple and diffusive minmod limiter. The latter is also the single calculation in which the compact remnant does not assume a postbounce equilibrium but rather gradually diffuses/dissolves away. At $\sim$3 ms after bounce, Marquina-TVD-minmod's $\rho_{\max}$ is 15% below that of all other calculations.

Otherwise the picture is quite clear and as expected: The Marquina-PPM calculation resolves the smallest features and settles at the highest postbounce density. It is closely followed by the slightly more diffusive HLLE-PPM and Marquina-TVD-MC combinations, but even the HLLE-TVD-MC combination still resolves most features well and settles at an only $\sim$1% lower $\rho_{\max}$ than the Marquina-PPM calculation. A more detailed look reveals that the HLLE-PPM run in fact follows all minute features in Marquina-PPM's $\rho_{\max}$ evolution, just offset by a constant $\sim$0.5%. Both HLLE and Marquina-TVD-MC runs, however, tend to smear out small features that are captured by the -PPM calculations.

The lower panel of figure 4.17 displays the gravitational wave signal of model A1B3G5 as computed with the various combinations of reconstruction methods and Riemann solvers / flux formulae. The picture is similar to the $\rho_{\max}$ evolution. TVD with the minmod limiter is unable to resolve the postbounce dynamics and leads to a grossly deviating wave signal that is out of phase with that obtained with the PPM calculations, interestingly even the TVD-MC wave signals are slightly out of phase with the PPM results. The overall agreement is quite good until $\sim$2.5–3 ms after core bounce when the shock travels onto a grid that may be too coarse for TVD-MC to accurately resolve the shock. Hence, I attribute the deviations in the wave signal that begin to appear between the second and third postbounce maxima to lack of resolution in the TVD-MC calculations.

Figure 4.18 displays density and velocity profiles along the x-axis at 3 ms after bounce. It is clear that the TVD-minmod calculation leads to a more diffused, more spread out and lower maximum

Table 4.6: Test calculations carried out with Marquina and HLLE approximate Riemann solvers / flux formulae and PPM and TVD reconstruction methods. Tests with ENO reconstruction and with the Roe Riemann solver are omitted. A comparison of reconstruction methods and tests with the Roe solver in WHISKY can be found in [123, 163]. For details see §3.5. All calculations are carried out with refinement hierarchy RHII (see appendix E).

Run Name	Riemann Solver / Flux Formula	Reconstruction
Marquina-PPM	Marquina	PPM
HLLE-PPM	HLLE	PPM
Marquina-TVD-MC	Marquina	TVD MC Limiter
Marquina-TVD-minmod	Marquina	TVD minmod Limiter
HLLE-TVD-MC	HLLE	TVD MC Limiter

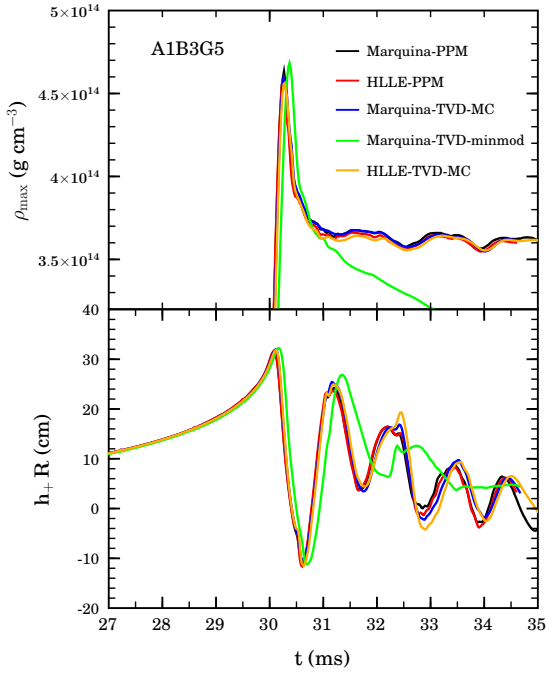

Figure 4.17: Evolution of the maximum density (top) and the gravitational wave signal (bottom) of model A1B3G5 as calculated with the various combinations of reconstruction methods and approximate Riemann solvers / flux formulae listed in the legend and in table 4.6.

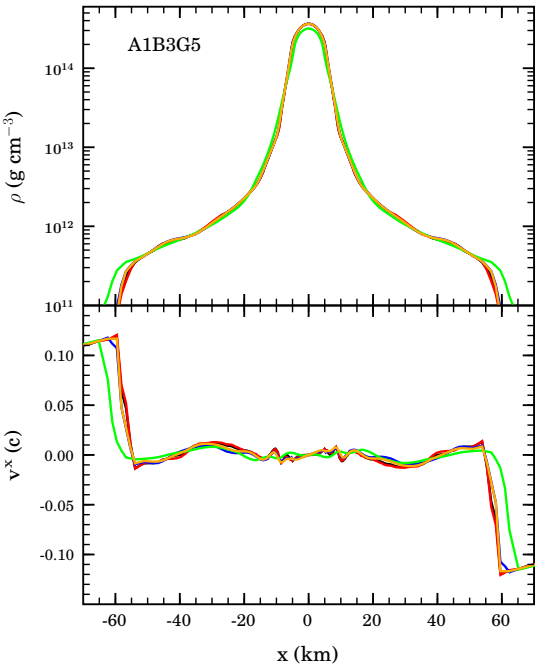

Figure 4.18: Comparison of reconstruction methods and Riemann solvers / flux formulae. Top: Profile of the rest mass density along the x-axis at 3 ms after core bounce in model A1B3G5. Bottom: Profile of the x-velocity component on the x-axis at the same time. The color coding is the same as in figure 4.17.

density remnant. In addition, the velocity profile reveals that at the same postbounce time the shock is smeared out over more zones and has covered a greater distance. All other combinations of reconstruction methods and Riemann solvers / flux formulae yield much better results for the density and velocity profiles that lie practically on top of each other (though beware of the log-scale in the top panel of figure 4.18).

Discussion

I have performed a small set of exploratory collapse calculations with the standard test model A1B3G5 for which I varied the reconstruction methods and the choice of approximate Riemann solver / flux formula. I find that both the Marquina flux formula and the HLLE Riemann solver yield very good results when used in combination with PPM reconstruction. The quality of TVD reconstruction with the monotonized centered (MC) slope limiter is acceptable when used in combination with the Marquina flux formula and marginally acceptable when used with HLLE. In both combinations, higher resolution than with PPM may be required. TVD reconstruction with the minmod slope limiter is an inappropriate reconstruction method and leads to gross underresolution of the dynamics and of the gravitational wave signal.

The above results for the stellar core collapse problem confirm the results obtained from simple shock tubes: PPM reconstruction in combination with the Marquina flux formula yields the best results at the resolutions considered here. However, I point out that I have considered only model A1B3G5 in this technical comparison. It is possible that the TVD-MC/minmod may perform marginally better for other models that collapse and bounce more slowly. For differentially rotating models I expect TVD-MC/minmod to perform worse than in the initially rigidly rotating model A1B3G5.

4.3.5 ODE Integrators and BSSN_MoL Spatial Order

So far I have investigated the dependence of results from core collapse simulations with CACTUS/-CARPET/WHISKY on resolution, progressive mesh refinement, gauge choices, Riemann solvers and cell-interface reconstruction methods. In this section I cover two additional aspects: (a) the variation of the results when the ODE time integrator in MoL (which jointly handles the time integration of the curvature and hydrodynamics equations; §3.2) is exchanged and (b) the dependence of the simulation outcomes on the order of spatial discretization in BSSN_MoL.

Again, I choose model A1B3G5 for the test calculations and compare its maximum density evolution and gravitational wave signal as obtained with the 2nd-order iterative Crank-Nicholson (ICN) time integrator (3 steps as suggested in [377]) and the 3rd order Runge-Kutta method (RK3) with second and fourth order spatial finite differencing in BSSN_MoL. For second spatial order in BSSN_MoL, ICN yields a stable evolution with a Courant factor of 0.375[15] while RK3 tends to have a smaller stability radius than ICN and requires a somewhat smaller time step / Courant number[16]. I set the latter to 0.25, which is the value commonly used for RK3 in second and fourth order vacuum calculations with BSSN_MoL.

Figure 4.19 reveals that all five test calculations yield results for the gravitational wave signal and $\rho_{\max}$ evolution identical by all sensible measures. The largest deviations are on the sub-one-percent level and hardly visible even in the highly zoomed-in view of the maximum density evolution. Key single-value observables like the maximum density at core bounce, the time of core bounce, the maximum gravitational wave signal amplitude and the peak of the gravitational wave frequency spectrum coincide to better than one part in 10^3. This suggests that the overall accuracy of the CAC-

[15] The time step Δt has to obey the Courant-Friedrichs-Lewy (CFL) criterion [375]. The Courant factor is the factor by which Δt is reduced from the maximum allowed by the CFL criterion. It depends on the stability properties of the evolved equations and the discretization scheme chosen. See also §3.2.1.

[16] This finding is entirely empirical in nature and may only be relevant for the particular type of physical problem that I am considering.

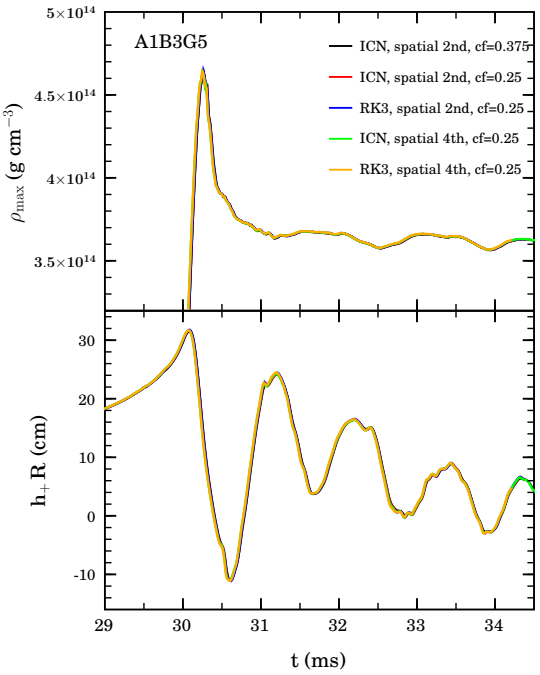

Figure 4.19: Comparison of numerical evolutions of model A1B3G5 with varying ODE integrators and spatial discretization orders in BSSN_MoL. Top: Maximum density evolution from shortly before to shortly after core bounce. Bottom: Gravitational wave signal during the same interval. All considered methods agree perfectly.

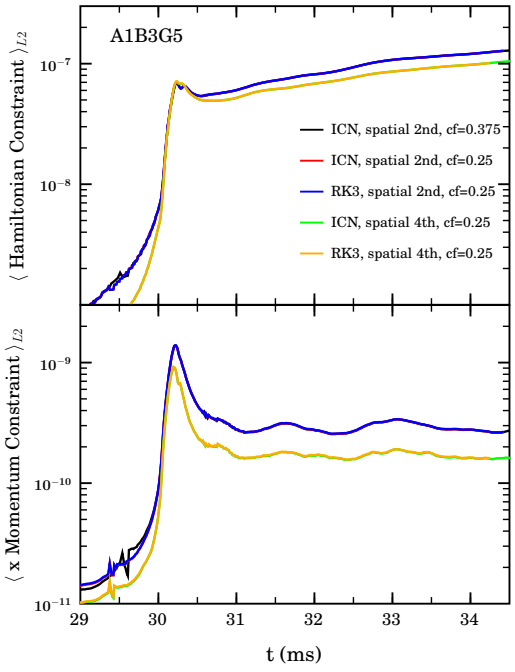

Figure 4.20: Model A1B3G5. Comparison of the $L2$-norm of the Hamiltonian (top) and x-momentum constraints (bottom) for the same set of calculations considered in figure 4.19. The spikes appearing in both constraints about 1 ms before bounce are artefacts introduced by the addition of an additional refinement level. They are quickly smoothed out.

TUS/CARPET/WHISKY code package depends most strongly on the spatial accuracy of the hydrodynamics discretization in WHISKY. Variations in the accuracy of the time integration, in the spatial discretization of the NOK-BSSN system and even in time step size (that certainly influences global stability) only lead to miniscule changes in the matter dynamics. This may seem surprising at first glance, but again realizing that stellar core collapse spacetimes are both of weak-field nature and matter dominated renders the above finding plausible.

A slightly different picture originates from figure 4.20 that portrays the evolution of the $L2$-norms of the Hamiltonian and x-momentum constraints. Again, a change of the ODE integrator leads to no noticeable alteration of the result, yet going from second to fourth order spatial differencing in BSSN_MOL leads — as one would expected — to overall smaller constraint violations, with the exception of the Hamiltonian constraint at bounce and shock formation. The hydrodynamic bounce shock goes along with a discontinuity in the rest-mass density which in turns leads to a discontinuity in the second derivative of the metric (see [390], this is also apparent from equation (2.52) in §2.4.4). Since the Hamiltonian constraint contains second derivatives of the metric, one cannot expect convergence in the presence of strong discontinuities. After its formation, the shock propagates downward on the stellar density slope and carries a gradually smaller jump in density. Hence, one sees the expected postbounce behavior in the Hamiltonian constraint. The momentum constraint on the other hand contains only first derivatives of the metric and is formally first-order convergent in the presence of discontinuities. This is reflected in the fact that the x-momentum constraint violation of the fourth-order BSSN_MOL calculation stays always considerably below that of the second-order calculations[17].

Discussion

The performed test calculations with the standard test initial model A1B3G5 indicate that the choice of (stable and TVD; see §3.2) ODE time integrator in the method of lines and variations in the spatial finite differencing accuracy in BSSN_MOL have little impact on the matter dynamics and the gravitational wave signal in rotating iron core collapse. The accuracy appears to be dominated by the overall second-order accurate spatial finite differencing of the GR hydrodynamics equations by WHISKY. Fourth-order finite differencing for the curvature evolution does, however, lead to smaller constraint violations and may be preferable for very long evolutions.

For standard production calculations, I find iterative Crank-Nicholson time integration and second-order spatial finite differencing in BSSN_MOL to be sufficiently accurate.

[17] Clearly, one cannot expect "true" convergence here — BSSN_MOL is only one component of the code and, importantly, is coupled to WHISKY whose spatial order is not varied in the present set of test calculations.

Chapter 5

GR Core-Collapse Simulations: Polytropes

In this chapter I present results from the first fully self-consistent {3+1} general-relativistic simulations of stellar core collapse. Although still employing $n = 3$ polytropic initial models and a simple analytic EOS, the simulations presented in this chapter mark an immense advancement over previous studies: From $t = 0$ through the entire collapse, bounce, and postbounce phases all models are evolved in a single computer code on a single mesh-refinded grid in 3D and full general relativity. The only previous study in 3D general relativity is the one performed by Shibata & Sekiguchi [204] who carried out the collapse simulations for the longest part in 2D and mapped to 3D only shortly before core bounce.

Pioneering studies in the field of 3D stellar core collapse in the gravitational wave emission context were carried out by Bonazzola and Marck [264] who computed only the collapse phase in 3D Newtonian gravity. A post-Newtonian extension of that work was carried out by Seidel, Bonazolla and Marck, but was never published [529]. Rampp, Müller, and Ruffert [267] investigated the possibility of dynamical nonaxisymmetric instability in one of the axisymmetric Zwerger & Müller [30] models. They as well relied on Newtonian gravity and mapped from 2D to 3D only shortly before core bounce. The only fully consistent 3D study in Newtonian gravity is the one by Fryer & Warren [89] with a smooth-particle hydrodynamics code. The gravitational wave emission in their models was analyzed by Fryer, Holz, and Hughes [271].

The present study of stellar core collapse is the first to take advantage of recent developments in numerical relativity for stable long-term and mesh-refined numerical evolution of coupled curvature and matter fields in full {3+1} GR [144, 146, 158, 163, 387, 391]. In this chapter I discuss the application of these recently developed methods to the collapse of $n = 3$ polytropes initially in rotational equilibrium. At large, my discussion is devoted to a detailed comparison with the axisymmetric study in conformally-flat general relativity by Dimmelmeier, Font and Müller [12]. The discussion of genuine 3D effects is postponed to chapter 6 where physicially more realistic models are studied.

In the following, I refer to the technical approach followed in this dissertation as CACTUS/CARPET/WHISKY (CCW). It has been discussed at length in chapter 3 and tested thoroughly in chapter 4.

5.1 A Morphology of Collapse Types and Waveforms

As delineated in §2.7.1, the extensive parameter studies of rotating core collapse in axisymmetry performed by Zwerger & Müller (ZM) [30] (in Newtonian gravity; using a hybrid EOS, see §3.5.5) and by Dimmelmeier, Font & Müller (DFM) [12] (in conformally-flat GR; using the same hybrid EOS) have identified three distinct characteristic types of collapse dynamics — types I, II, and III[1]. Their classification is primarily based on the qualitative shape of the gravitational waveforms. However, as the latter reflect from the matter dynamics, the classification may be employed to describe the collapse dynamics as well.

[1] In a recent Newtonian magneto-hydrodynamic study, Obergaulinger et al. [276, 277] have identified an additional type of dynamics that is governed by magnetic field effects and which they call type IV, but which only occurs for very large precollapse field strengths on the order of 10^{12}–10^{13} G.

Ott et al. [9] (OBLW) performed an extensive parameter study in the initial degree of differential rotation and the initial rotation rate and employed realistic presupernova models and a finite-temperature EOS in Newtonian gravity. They found type I, type II, and mixed type I/II dynamics, but did not observe type III dynamics. The absence of type III models in their study is most likely due to their more realistic EOS treatment as I shall discuss below (see also [11, 14]).

5.1.1 Type I Dynamics and Waveforms

Iron core collapse models of type I rotate so slowly that they undergo collapse largely unimpeded by centrifugal effects. They experience core bounce due to the stiffening of the EOS at nuclear density ($\sim 2\times 10^{14}$ g cm^{-3}). Type I dynamics is very similar to that of nonrotating collapse and can similarly be divided into three phases (see, e.g., [9, 11, 12, 30, 530, 531]:

Infall Phase – The infall phase encompasses the longest part of collapse from its onset until a few milliseconds before core bounce. As for nonrotating collapse (see §2.3.2, an inner, homologously ($v \propto r$) collapsing core develops which interfaces with the supersonically collapsing outer core at the *sonic point* where the local speed of sound matches the infall velocity. For very slow rotators, the standard homology relation $v \propto r$ of nonrotating collapse holds well, while faster models that experience some rotational flattening show quasi-homologous behavior with $v \simeq \alpha(t,\theta)r$, where the magnitude of α decreases with increasing polar angle θ [30].

Since centrifugal effects are small, the mass M_{ic} of the inner core of type I models (which varies during collapse) is predominantly determined by the EOS and gravity, and at core bounce – in realistic models that treat EOS and neutrino microphysics / transfer adequately – is in the range $0.5\,M_\odot \lesssim M_{ic} \lesssim 0.8$ [3, 64, 530]. General relativity typically leads to $\sim$20% smaller inner core masses than Newtonian gravity. In the simple hybrid polytropic–ideal-gas EOS considered by ZM, DFM, and in this Chapter of this dissertation, the evolution of M_{ic} of type I models is determined by the adiabatic Γ chosen for the collapse evolution: the larger the initial pressure reduction (i.e. the smaller the evolution-Γ with respect to $\Gamma_{initial} = 4/3$), the smaller the inner core mass at core bounce [30, 66]. But, as pointed out by van Riper [67], also the greater the initial (relative) bounce shock kinetic energy in these simple models.

Plunge and Bounce Phase — The plunge phase precedes core bounce and sets in when the central core density reaches a few times 10^{12} g cm^{-3} and when neutrinos become trapped in the inner core from which point on M_{ic} stays roughly constant [11, 64, 530]. At that time, the core has been in collapse for several tens and up to hundreds of milliseconds and the radial infall velocity peak has reached $\sim 0.1c$. The inner core now *plunges* quickly due to the increasingly strong gravitational pull and reaches nuclear density within 2–3 ms where nuclear repulsive forces lead to a sudden stiffening of the EOS, initiating the rebound of the inner core, and sending out a pressure wave that steepens to a bounce shock at the edge of the inner core and propagates out into the still infalling outer core. In the calculations of ZM and DFM, the bounce shock never stalls, since energy losses due to photodissociation of heavy nuclei and neutrino emission are not taken into account.

Ring-Down Phase —At bounce, the inner core overshoots its postbounce equilibrium configuration and, after the launch of the bounce shock due to its rebound, oscillates in various radial and nonradial eigenmodes [9, 12, 30] that are damped on timescales of milliseconds by the emission of strong sound waves into the postshock region. The newborn protoneutron star (PNS) *rings* down.

Figure 5.1 depicts the maximum density (ρ_{max}) and gravitational waveform evolutions for the typical type I model A1B3G3 of the ZM/DFM model suite. The computation has been carried out with CCW. The three phases are clearly distinguishable in both observables: During infall, ρ_{max} slowly increases. At plunge and core bounce, ρ_{max} overshoots to $\sim 2\rho_{nuc}$, after which the core slightly re-expands and settles at a ρ_{max} of $\sim 1.5\rho_{nuc}$, exhibiting only weak, low-amplitude variations in ρ_{max}.

In order to understand the qualitative evolution of the gravitational waveform it is useful to recall (a) that in axisymmetry, no gravitational waves are emitted along the axis of symmetry, and that in other directions only gravitational waves of the $+$ polarization are emitted, and (b) that, in axisymmetry and in a coordinate system in which the symmetry axis coincides with the z-axis, the mass-quadrupole moment reduces [178] to $\ddot{I}_{xx} = \ddot{I}_{yy} = -\frac{1}{2}\ddot{I}_{zz}$. Along the equator, the quadrupole

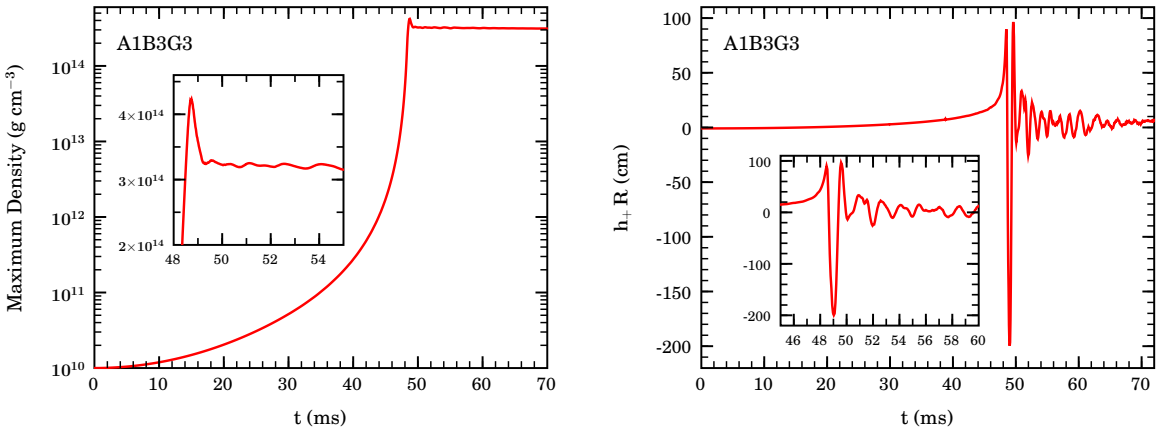

Figure 5.1: Model A1B3G3 of the ZM/DFM model set evolved with CCW as an example for type I dynamics. Inset zoom-ed in view of $\rho_{\max}$ at and shortly after bounce. Left panel: Evolution of the maximum density. Right panel: Gravitational wave signal amplitude $h_+ R$, where R is the distance to the source.

wave amplitude is then given by

$$h_+^e = \frac{3}{2}\frac{G}{c^4}\frac{1}{\mathrm{R}}\ddot{I}_{zz}\,. \tag{5.1}$$

Hence, it is sufficient to consider the evolution of I_{zz} and its time derivatives to understand the way the collapse, bounce, and ring-down dynamics imprints itself onto the waveform. From its definition (equation (3.164)) it follows that I_{zz} is negative for oblate configurations. As one would expect, I_{zz} becomes increasingly negative during some fraction of the infall phase as conservation of specific angular momentum forces the core to deviate more and more from spherical symmetry — even in a slowly rotating type I model[2]. This behavior is reflected by the initially slightly negative gravitational wave amplitude in figure 5.1. However, as the collapse progresses, the core becomes more and more centrally condensed. Since the density of the inner core roughly increases $\propto r^{-3}$ while I_{zz} has an r^4 dependence (taking the volume element into account), the contraction of the core eventually reverses the increase of $|I_{zz}|$. In model A1B3G3 this happens already $\sim$4 ms into the collapse and is marked by I_{zz}'s second time derivative reaching positive values. As figure 5.2 portrays, a few milliseconds later, I_{zz}'s first time derivative reaches positive values as well, leading to a decrease of I_{zz} in absolute value. At core bounce, when the infall velocities of the inner core are dramatically reversed within a fraction of a millisecond, the largest accelerations occur and lead to the prominent negative peak in the waveform at $\sim$49 ms, roughly 0.2 ms after the global maximum in the central density is reached. I'_{zz}s second time derivative becomes negative when the core begins to decelerate in a fraction of a millisecond before bounce. A detailed analysis shows that in type I models, the global maximum of the density is reached on the left flank of the bounce spike of the waveform. Note, however, that the point at which the density reaches its global maximum is not necessarily a good indicator for core bounce[3]. The maximum density is a one-zone value that only roughly describes the inner core dynamics. A somewhat better definition of the time of core bounce in the context of gravitational wave emission is the time at which the radial velocities of the bulk of the inner core cross zero and become positive.

During the inner core's rebound, the wave signal becomes positive again (as the rebound velocities decrease) and is followed by the ring-down wave signature, which is dominated by the radial and non-radial oscillations of the newly formed protoneutron star, but with no one-to-one correspondence of the maximum density evolution and the features in the waveform. During the ring-down phase, the gravitational wave signal settles down to very small values, while I_{zz}'s first time derivative remains positive and $|I_{zz}|$ decreases throughout the postbounce evolution of model A1B3G3 as portrayed by figure 5.2).

[2]If the initial model is not in rotational equilibrium it will relax to a more oblate configuration during collapse leading to a prolonged period of increasing $|I_{zz}|$ [11].

[3]In the literature on core-collapse supernova theory, core bounce is frequently defined by shock formation when the entropy increases beyond $\sim 3\,k_B$ per baryon (see, e.g., [73])

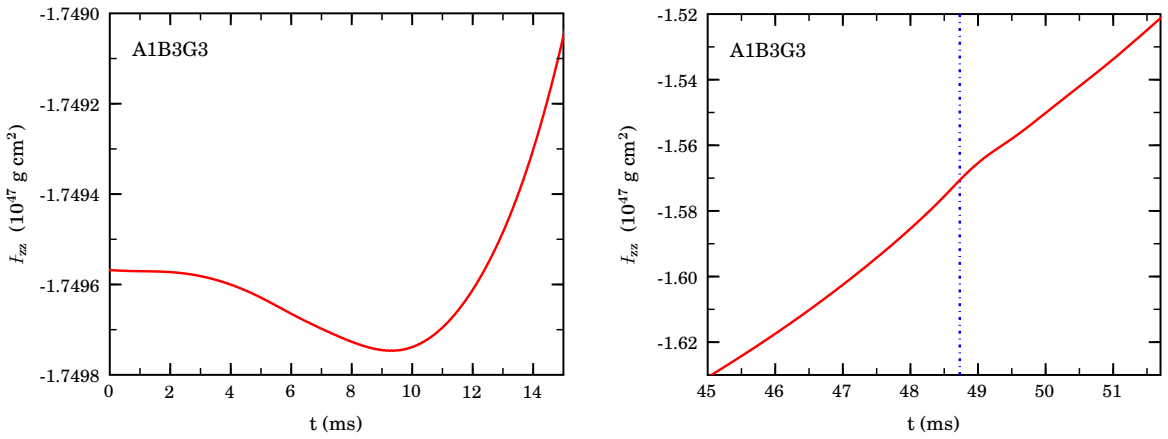

Figure 5.2: Evolution of I_{zz} in model A1B3G3 during the first 15 milliseconds (left panel) and around core bounce (right panel). The time of core bounce is marked by a blue dash-dotted line. I_{zz} stays negative and decreases in absolute value throughout the tracked postbounce evolution.

ZM and DFM characterize their initial polytropic rotational-equilibrium models according to their degree of differential rotation (governed by the parameter A in the rotation law), the initial rotation parameter $\beta_{\rm initial} = T/|W|$ (see §3.9.2) and the value of the adiabatic exponent used during collapse in their hybrid EOS. The initial $n = 3$ polytropes are essentially Newtonian objects and it is sensible to consider the rotation law (3.159) in its Newtonian limit:

$$\Omega(d) = \Omega_{\rm c}\frac{A^2}{A^2+d^2} = \begin{cases} \Omega_{\rm c} & \text{for } A \to \infty \\ \Omega_{\rm c}\frac{A^2}{d^2} & \text{for } A \to 0 \end{cases}, \tag{5.2}$$

where d is the distance from the rotation axis. A and the central angular velocity $\Omega_{\rm c}$ are free parameters that determine the rotational speed/energy and the distribution of angular momentum. The larger A, the more solid-body like is the rotation.

A ZM/DFM model name is constructed by choosing A from {A1, A2, A3, A4} which correspond to {50000 km, 1000 km, 500 km, 100 km}, choosing $\beta_{\rm initial}$ from {B1, B2, B3, B4, B5}, corresponding to {0.25%, 0.5%, 0.9%, 1.8%, 4%}, and choosing Γ from {G1, G2, G3, G4, G5} that correspond to {1.325, 1.320, 1.310, 1.300, 1.280}. Hence, the above discussed model A1B3G3 is constructed with A =50000 km, $\beta_{\rm initial}$ =0.9% and evolved with Γ= 1.30.

OBLW who used a finite-temperature nuclear equation of state and realistic presupernova models, named their models according to the following convention: [initial presupernova model name]A[in km]β_i[in %]. For example, s11A1000β0.3 corresponds to an 11 $M_\odot$ presupernova model with A = 1000 km and $\beta_{\rm initial}$ of 0.3%.

5.1.2 Type II Dynamics and Waveforms

OBLW found that for fixed A, centrifugal effects become more relevant to the collapse and bounce dynamics with increasing $\beta_{\rm initial}$: The larger $\beta_{\rm initial}$, the slower is the collapse and the lower is the maximum density reached at core bounce. On the other hand, for fixed $\beta_{\rm initial}$, the influence of rotation becomes greater for decreasing A which leads to a more centrally-concentrated angular momentum distribution in the precollapse core. ZM/DFM found a similar relationship in their models with $\Gamma \gtrsim 1.30$. Figure 5.3, which I have drawn from OBLW, depicts systematically the transition in collapse, bounce, and postbounce dynamics as the angular momentum (i.e., the rotation parameter $\beta_{\rm initial}$) of the precollapse core is increased at a fixed degree of differential rotation.

In the ZM/DFM classification, type II comprises models that experience significant centrifugal support and undergo core bounce at subnuclear densities and/or under the strong influence of centrifugal forces. They assume postbounce rotationally supported equilibrium configurations at densities below nuclear density. The possibility of such subnuclear-density equilibria was first pointed out by

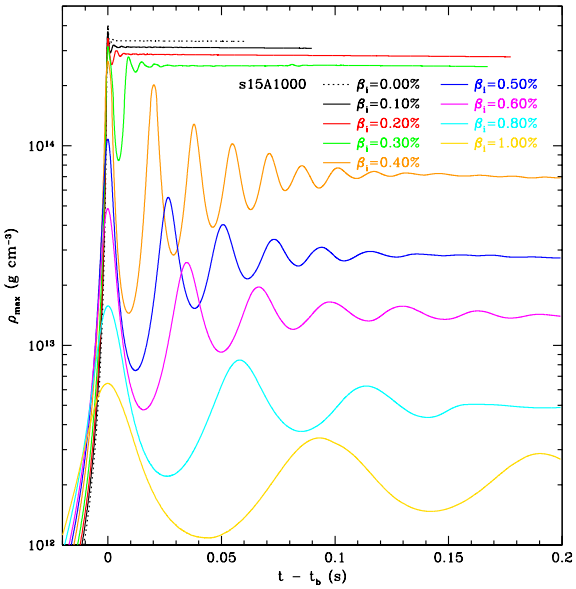

Figure 5.3: Evolution of the maximum density of OBLW's [9] s15A1000 model series parametrized by initial $\beta = T/|W|$ as a function of time after core bounce. With increasing $\beta_{\rm initial}$, centrifugal forces become more relevant, eventually leading to a transition of collapse dynamics from type I to type II.

Shapiro & Lightman [314] and for the first time studied systematically by Tohline [313]. They may be understood by considering that for slow and rigid rotation in Newtonian gravity, for a given $\Gamma < 4/3$, there is a critical $\beta_{\rm c}$,

$$\beta_{\rm c} = \frac{1}{2}\frac{(4-3\Gamma)}{(5-3\Gamma)} \,, \tag{5.3}$$

beyond which rotation stabilizes self-gravitating fluid bodies against pseudo-radial modes [11, 30, 313, 314, 504, 532]. In GR, this simple expression can only be regarded as a lower bound for β_c [12, 63, 504] and the critical β for stabilization must be larger than the above defined Newtonian $\beta_c + k\,(GM)/(Rc^2)$, where k depends on the stellar structure and angular momentum distribution [63]. In the limit of a $n = 3$ polytrope and zero β, $k \approx 6.75$.

Equation (5.3) is a necessary condition for a core bounce at subnuclear densities. It does, however, not determine the maximum β reached during collapse, since rotation acts approximately like a gas with a Γ of $5/3$ [11, 504] and hence only slowly decelerates the inner core (compared with nuclear repulsive forces with $\Gamma \gtrsim 2$), allowing it to overshoot β_c significantly [9, 30].

Similarly to type I, the dynamics can be divided into three phases:

Infall Phase — As in type I collapse, the collapsing core splits into a quasi-homologously collapsing inner core and a supersonically collapsing outer core. The homology relation for the inner core is $v \simeq \alpha(t,\theta)r$, where α decreases strongly from pole to equator, and where centrifugal support is strongest. $v \simeq \alpha(t,\theta)r$ holds until bounce along the equator, but breaks down along the symmetry axis shortly before the plunge phase sets in which happens slightly earlier along the polar axis than on the equator [9, 30].

The rapid rotation of type II models leads to a significant increase of the inner core mass. ZM, who studied this systematically, found that for fixed EOS Γ and approximately rigid rotation ($A \geq$ 1000 km), the mass of the inner core scales roughly according to

$$\frac{M_{\rm ic}}{M_{\rm ic,0}} = (1-2\beta)^{-3/2} \,, \tag{5.4}$$

which follows from the viral theorem (for a white dwarf in rotational equilibrium; see, e. g., [36]) and where $M_{\rm ic,0}$ is the mass of a corresponding nonrotating inner core.

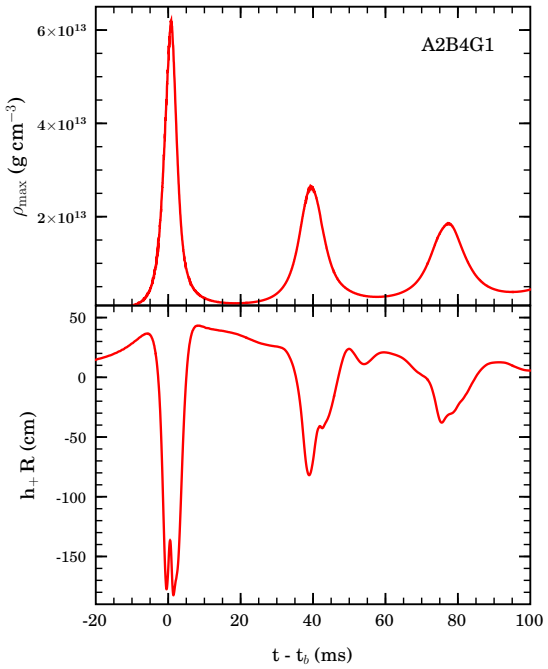

Figure 5.4: Type II model A2B4G1 of [12] evolved with CoCoNuT. Top panel: Evolution of the maximum density. Bottom panel: Evolution of the gravitational wave signal.

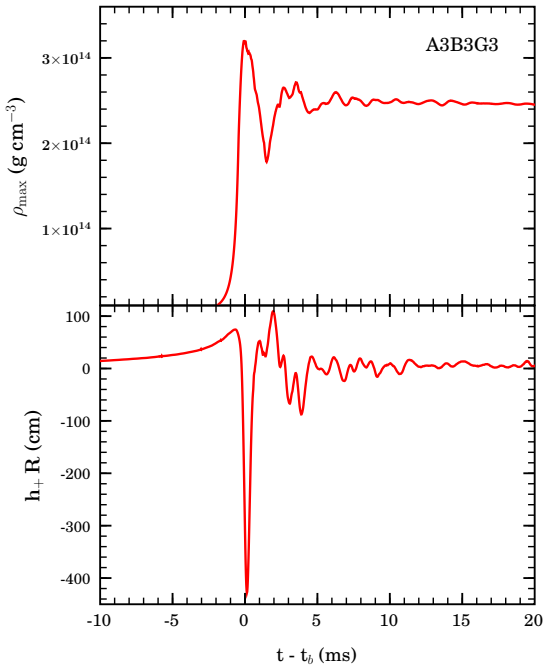

Figure 5.5: Transitional type I/II model A3B3G3 evolved in CCW. Top panel: Maximum density evolution. Bottom panel: Evolution of the gravitational wave signal.

Bounce Phase — Type II models experience no coherent extremely dynamic plunge phase before core bounce. Rather, once centrifugal forces become dominant over gravitational attraction, the core is smoothly decelerated over a timescale of multiple milliseconds at large latitudes while along the polar axis, plunge and bounce proceed with little influence of centrifugal forces. The rotation-dominated, highly-aspherical bounce of type II models leads to shock formation at larger radii on the equator than on the poles and creates, since it is much less abrupt, less entropy and much weaker bounce shocks than in type I models [9].

Re-Expansion-Collapse-Bounce Cycles — After core bounce, the inner core of type II models expands coherently in a single volume mode, leading typically to an almost order-of-magnitude drop in the central density. This expansion is reversed when gravitational forces again begin to dominate over centrifugal forces and pressure gradients. In this way, the quickly spinning postbounce core undergoes several damped re-expansion-collapse-bounce cycles until it settles into an equilibrium configuration. As pointed out by Mönchmeyer et al. [11], it acts much like a harmonic oscillator with a Hamiltonian consisting of radial kinetic, rotational, internal, and gravitational energies that is damped by the emission of strong sound waves emitted at each bounce [9, 12]. Figure 5.3 depicts the type II dynamics apparent in OBWL's s15A1000 model series for $\beta_{\text{initial}} \gtrsim 0.4\%$. Because of the presence of the re-expansion-collapse-bounce cycles in type II models, they are frequently referred to as *multiple-bounce* models in the literature [9, 12, 14, 30].

In figure 5.4 I show the evolution of the maximum density and the gravitational wave signal in model A2B4G1 from DFM[4] which exhibits prototypical type II dynamics. In type II models, the initial evolution of I_{zz} and its time derivatives is similar to that of type I, but the deceleration of the core, marked by negative values in the wave signal begins earlier before bounce and the entire bounce dynamics is less abrupt. The latter is reflected in the much wider bounce spike in A2B4G1's waveform when compared with that of A1B3G3 (figure 5.1). A close look at the bounce spike in A2B4G1 reveals an interesting substructure in the form of a small upward oriented subspike with whose peak the global maximum in the density coincides. A2B4G1's inner core is large ($\gtrsim 1\ M_\odot$) and its radial motion is not entirely coherent during bounce. Some parts of the inner core reach

[4]Note that the data presented here are not the original data from the DFM paper, but stem from more recent calculations [161].

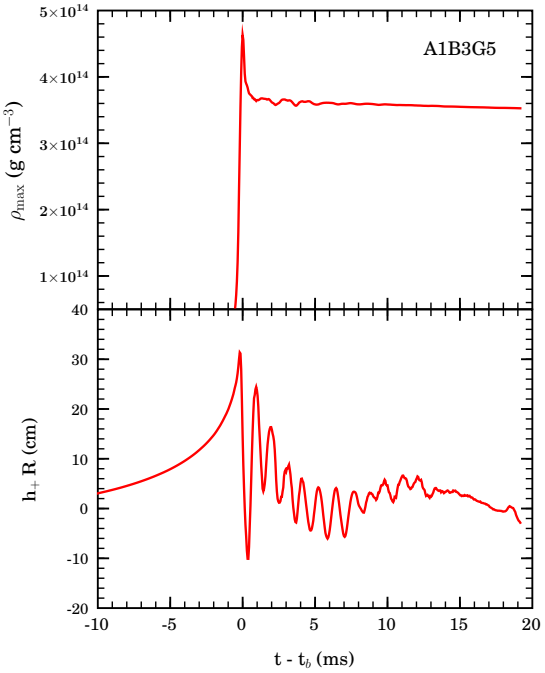

Figure 5.6: Model A1B3G5 of the ZM/DFM model set evolved with CCW as an example for type III dynamics and wave signature. A1B3G5 has a very small inner core mass $\lesssim 0.15 M_\odot$. Top panel: Evolution of the maximum density; similar to type I dynamics. Bottom panel: Type III gravitational waveform.

positive velocities earlier than other parts and the innermost region experiences a somewhat slower deceleration in the final phase of collapse than the bulk. A slower deceleration corresponds to a smaller (in magnitude) second time derivative of I_{zz} which is reflected in the small subspike within the bounce spike[5].

After the initial core bounce, the ring-down of type I models is replaced by the signature of the core's coherent damped re-expansion-collapse-bounce cycles, manifest by wide peaks in the wave signal. Model A2B4G1 (Figure 5.4) shows weak imprints of shorter-period substructure that originates from additional nonspherical pulsation modes. These are present in all type II models but become increasingly less pronounced with increasing β_{initial} [9].

As figure 5.3 indicates, the transition from type I to type II dynamics is not abrupt, but happens gradually with increasing angular momentum in the inner core. There exists a range of type I/II transitional models that exhibit a mixture of type I/II features. Model A3B3G3 is such a transitional model. As can be seen in Figure 5.5, bounce occurs at supernuclear density, but centrifugal forces are strong enough to lead to one pronounced postbounce minimum in the maximum density. In the waveform, the type I ring-down signal is dominant, but a low-frequency modulation of the waveform akin type II models is discernible during the first few milliseconds after bounce.

DFM found that a large fraction of those models classified by ZM as type II exhibit type I/II dynamics in GR. DFM attribute this to the more realistic and *stronger* gravity in their study, leading smaller homologous cores, collapse to higher densities and increasing the influence of the stiff nuclear EOS on the bounce dynamics.

5.1.3 Type III Dynamics and Waveforms

For models in which the adiabatic Γ during evolution is considerably smaller than 4/3, ZM and DFM found similar collapse, bounce and postbounce dynamics as in type I models, but large qualitative and quantitative differences in the wave signature to both type I and type II models. Figure 5.6

[5]ZM, DFM, and OBLW found such a small feature in a number of models, some of which where of type I in which it appeared on the left flank of the bounce spike but is in most models less pronounced than in A2B4G1.

depicts the maximum density and wave signal evolutions of model A1B3G5. In this model, Γ is reduced from $4/3$ to 1.28 which, at an initial central density of $\sim 10^{10}$ g cm^{-3}, corresponds to a central pressure reduction by $\sim$70%. As pointed out by ZM and DFM, type III dynamics is very similar to type I, the most important difference being the very small inner core ($M_{ic} \lesssim 0.15 M_\odot$) of type III models. Due to the large pressure reduction, type III models reach core bounce very rapidly and overshoot to larger bounce densities than type I models, yet, because of the small amount of mass involved in the inner core dynamics, the gravitational wave amplitudes at and after core bounce remain small — about an order of magnitude smaller than those of typical type I models. In addition, the maximum (in absolute value) signal amplitude in type II models is assigned to the first positive (and prebounce) peak in the waveform and not to the negative bounce spike. This is most likely due to the very small inner core, to the fact that the bounce shock develops at very small radii (at $\sim$5 km), and to the correspondingly large amount of mass of the outer core that is still infalling and has already reached small radii and large velocities when the inner core rebounds. Hence, the deceleration of the inner core has a smaller effect on the overall wave signature than in type I models.

Type III models are not observed in studies in which finite-temperature nuclear EOS come to use [9, 11, 14], since the effective Γ of such EOSs is typically very close to $4/3$ during the infall phase of collapse (see, e.g., [64, 530]). Type III dynamics and waveforms are unlikely to occur generically in nature, except, perhaps in the accretion induced collapse of O-Ne-Mg white dwarfs to neutron stars (see, e.g., [16] and §7.3 in this dissertation).

To conclude my discussion of collapse dynamics and waveform types observed in previous studies, I point out that in the recent Newtonian magneto-hydrodynamic simulations of Obergaulinger, Aloy, and Müller [276, 277] and of Kotake et al. [274] magnetic fields have not been found to alter the collapse dynamics significantly unless extremely large initial magnetic field strengths $\gtrsim 10^{12}$ G are assumed.

5.2 Comparison to CFC Approach

The work presented in this dissertation was originally motivated by the need for a verification study in full general relativity for the gravitational waveform estimates obtained by Dimmelmeier, Font & Müller [12, 18, 160] (DFM) in conformally-flat (CFC)[6] general relativity using the CoCoNuT [18, 160, 161] code. In 2004, Shibata & Sekiguchi published [13] simulations of rotating collapse of polytropes in axisymmetric general relativity using initial models similar to those of DFM. They found good qualitative agreement in the waveforms, but quantitative differences on the order of ∼20% that they attributed to differences in gauge conditions, grid setup / resolution and wave extraction methods. Recently, Cerdá-Durán et al. [162] have presented an extension to CFC that they call CFC+ and that is exact to the second post-Newtonian order. Their simulations yield practically identical results to those of DFM.

In this section, I introduce the CFC approximation and present results of 3D fully general relativistic simulations that I have carried out using the methods described in Chapter 3 of this dissertation. First, I present a detailed comparison of a spherically symmetric collapse calculated in CoCoNuT and with the Cactus/Carpet/Whisky (CCW) approach. Since CFC is exact in spherical symmetry, this allows me to identify discrepancies brought about systematically by differences in the numerical implementations and gauge choices. Subsequently, I compare axisymmetric simulations, with initial rotational-equilibrium polytropic models that are drawn directly from the DFM model set, allowing me to compare directly with DFM results and assess the quality of CFC in the stellar core-collapse problem.

5.2.1 Conformally-Flat General Relativity

In the CFC approximation to GR introduced by Isenberg [533] and first used by Wilson et al. [534], the ADM spatial 3-metric is replaced by the conformally flat 3-metric:

$$\gamma_{ij} = \phi^4 \eta_{ij} \,, \tag{5.5}$$

where η_{ij} is the flat-space metric, hence $\eta_{ij} = \delta_{ij}$ in Cartesian coordinates and $\eta_{ij} = \mathrm{diag}(1, r^2, r^2 \sin\theta)$ in spherical coordinates. ϕ is the conformal factor and its appearance in its fourth power in equation (5.5) is pure convention that simplifies the ADM equations (introduced in section 2.4.3). In maximal slicing ($K = 0$; see section 3.3.2) the Hamiltonian and the momentum constraints decouple and the ADM equations in the CFC approximation reduce to the following set of elliptic equations:

$$\begin{aligned}
\hat{\Delta}\phi &= -2\pi\phi^5 \left(\rho h W^2 - p + \frac{K_{ij}K^{ij}}{16\pi} \right) , \\
\hat{\Delta}(\alpha\phi) &= 2\pi\alpha\phi^5 \left(\rho h (3W^2 - 2) + 5 + \frac{7K_{ij}K^{ij}}{16\pi} \right) , \\
\hat{\Delta}\beta^i &= 16\pi\alpha\phi^4 S^i + 2\phi^{10} K^{ij} \hat{\nabla}_j \left(\frac{\alpha}{\phi^6} \right) - \frac{1}{3} \hat{\nabla}^i \hat{\nabla}_k \beta^k \,,
\end{aligned} \tag{5.6}$$

where $\hat{\nabla}$ and $\hat{\Delta}$ are the flat-space Nabla and Laplace operators, respectively. Approximating GR with CFC implies a special choice of coordinates. In particular, the coordinate basis is always orthogonal. Hence the equation for the shift vector in (5.6). The extrinsic curvature tensor components are specified by

$$K_{ij} = \frac{1}{2\alpha} \left(\nabla_i \beta_j + \nabla_j \beta_i - \frac{2}{3} \gamma_{ij} \nabla_k \beta^k \right) , \tag{5.7}$$

where ∇ is the covariant derivative with respect to γ_{ij}.

The CFC approximation is exact in spherical symmetry. In 2 and 3 dimensions a CFC spacetime may be regarded as general relativistic minus the dynamical degrees of freedom of the gravitational field that correspond to the gravitational wave content[7] [147]. Yet this statement is not sufficient to

[6] CFC is an acronym for *conformal-flatness condition* and is interchangeably used with *conformally flat*.

[7] In axisymmetry, the gravitational field has one dynamical degree of freedom corresponding to gravitational waves. In 3D it has two. York [118, 147] has shown that the dynamical degrees of freedom of the gravitational field can be identified with parts of the conformally related spatial metric and the transverse-traceless part of the conformally-related extrinsic curvature.

describe CFC in general: even stationary spacetimes that do not contain gravitational waves can be non-conformally flat. Prime examples are Kerr black holes [535] and rotating neutron stars [536] in equilibrium.

The CFC ADM equations do not contain explicit time derivatives, and thus the CFC spacetime fields are calculated in a fully constrained approach and at each timestep anew.

5.2.2 Model Suite and Simulation Parameters

Dimmelmeier, Font and Müller [12] have performed calculations involving 26 distinct models in the Zwerger & Müller [30] parameter space introduced in §5.1.1. Due to the extreme demands in main memory and CPU time of the 3D CCW simulations, it is necessary to limit the comparison calculations carried out with CCW to a representative subset of DFM's models that encompasses all collapse/waveform types discussed in Section 5.1. The development of nonaxisymmetric 3D structures would be an encumbrance to the comparison of CFC to full GR. Hence, in addition, only such models should be included that remain essentially axisymmetric during collapse, bounce, and postbounce phases for which the comparison to 2D CFC is carried out.

Table 5.1 lists the two spherically symmetric and the 6 axisymmetric $n = 3$ polytropic initial models that Harald Dimmelmeier and I have chosen for this comparison. Model TOVG1 and TOVG5 are employed for the code and coordinate comparison in spherical symmetry where CFC is exact. All rotating axisymmetric initial models are in rotational equilibrium and are computed with WHISKY_RNSID, written by Nikolaos Stergioulas and discussed in Section 3.7.2. Models A1B3G3 and A3B2G4 exhibit type I dynamics [12], while A1B3G3 is initially in solid body rotation and A3B3G2 rotates differentially[8]. Models A3B3G2 and A3B3G3 are of transitional type I/II character and it is interesting to investigate in how far full GR leads to qualitative and quantitative differences in their dynamics and waveforms. Model A2B4G1 is one of the few models identified as being of type II by DFM and A1B3G5 is a prototypical type III model and is used as a standard test case throughout this dissertation.

All CCW calculations are carried out with PPM reconstruction and the Marquina flux formula (see §3.5). $1 + \log$ slicing and the Γ-driver shift (3.37) are employed in BSSN_MOL which is run in second-order accurate mode (see §3.3). For the time integration in MOL, the iterative Crank-Nicholson time integrator with three intermediate steps is used (see §3.2). Gravitational waves are extracted via the quadrupole formula in the first-moment of momentum-density formulation given by equation (3.167). The resolution and grid setup choices (Table 5.1) are motivated as follows: Type I and type III models have little rotational support and experience bounce and shock formation at small radii, typically $\lesssim 20$ km. Type II and transitional type I/II models, on the other hand, experience considerable centrifugal effects that lead to more extended inner cores and shock formation at greater radii. In A2B4G1, for example, the shock develops at $\sim$60 km. Since shock formation must be well resolved, type II and type I/II models require high resolution out to much larger radii than standard type I and type III models. In order to accommodate these different resolution requirements, I use more extended fine grids in the refinement hierarchies of type I/II and type II models. Model A2B4G1 is the most computationally intensive model of all considered here. It is evolved in an octant with a reflection symmetry boundary condition on the equatorial plane and periodic rotation symmetry boundary conditions on the x–z and y–z-faces[9]. All other models are evolved in bitant mode with reflection symmetry on the equatorial plane. All model calculations are carried out to $\sim$20 ms after bounce.

All COCONUT calculations are performed with the most recent version of the code using a spectral metric solver [161], 200–250 logarithmically-spaced and centrally-condensed radial zones (central zone size $\sim$350 m), 30 angular zones covering 90° and an outer grid radius of $\sim$3000 km. Gravitational waves are also extracted via the quadrupole formula with the first-moment of momentum-density formulation as discussed in §3.8.1.

[8] See figure 6.3 in §6.1 for a visualization of the rotation law for various values of the parameter A.

[9] Note that octant mode with with periodic boundary conditions on the x-z and y-z faces suppresses azimuthal modes $\propto \exp(im\varphi)$ whose m is not a multiple of 4.

Table 5.1: Model set for CFC/full GR comparison. RH is the refinement hierarchy used (see Appendix E). A is the differential rotation parameter of the rotation law defined in §3.7.2. β_{initial} is the initial ratio of rotational kinetic to gravitational potential energy. Γ_1 is the value to which the adiabatic index is lowered to instigate collapse. Type specifies the collapse dynamics type according to the Zwerger-Müller scheme [30] as outlined in §5.1. All models are evolved with the hybrid EOS discussed in §3.5.5 with $\Gamma_{\text{th}} = 1.5$ and supranuclear $\Gamma_2 = 2.5$. Further model details can be found in Appendix D.

Model	RH	A (10^8 cm)	β_{initial} (%)	Γ_1	Type
TOVG1	RHII	—	—	1.325	nonrotating
TOVG5	RHII	—	—	1.280	nonrotating
TOVG5HR	RHIII	—	—	1.280	nonrotating
A1B3G3	RH8II	∞	0.9	1.310	I
A1B3G5	RH8II	∞	0.9	1.280	III
A2B4G1	ORHIIIe	1.0	1.8	1.325	II
A3B2G4	RH8II	0.5	0.5	1.300	I
A3B3G2	RH8IIe	0.5	0.9	1.320	I/II
A3B3G3	RH8IIe	0.5	0.9	1.310	I/II

5.2.3 TOV core collapse – Comparison of Codes and Coordinates

In order to set the stage for the subsequent detailed comparison of rotating core-collapse simulation results obtained with CCW and CoCoNuT, it is necessary to first consider spherically symmetric core collapse. CFC is exact in spherical symmetry, hence CoCoNuT and CCW should yield identical physical results. This allows me to identify discrepancies brought about systematically by differences in the numerical implementations.

When comparing results from simulations carried out in general relativity one faces the dilemma that, while general relativity certainly provides a more realistic handling of gravity than the Newtonian approximation, its coordinate freedom makes it very difficult to compare results from simulations that did not start from identical initial data and/or did not employ exactly the same gauge conditions.

As an example, consider two hypothetical numerical simulations of the collapse of a spherically-symmetric TOV $n = 3$ polytrope. Initially, the configuration is time symmetric and the initial lapse is fixed by $K = K^i_i = 0$. The initial shift is set to 0. Simulation A runs in quasi-isotropic spherical coordinates and initiates collapse, re-solves the constraint equations and then evolves with maximal slicing (and enforcing $K = 0$). Simulation B on the other hand runs in Cartesian coordinates, initiates collapse, but does not re-solve the constraint equations and evolves with geodesic slicing ($\alpha = 1$ everywhere). When trying to compare results of the two simulations, one faces several problems.

(1) The actual initial data are different. After the pressure reduction that is performed to initiate collapse and before the first timestep, the initial-data equations (see §2.4.4) are solved again in simulation A, but not in simulation B. The data are still formally (though not physically) time symmetric, since all velocities are zero on the initial slice[10]. Depending quantitatively on how dramatic the pressure reduction is, A's metric components are different from B's. The dynamics during A's evolution will be more correct than in B's evolution since B has a greater initial constraint violation.

(2) Simulation A uses an isotropic radial coordinate. This implies a radial shift (see [120]). Simulation B on the other hand uses Cartesian coordinates with no additional demands on the shape of the coordinates. The shift can be freely specified and is kept at zero in simulation B. Hence, the initial simple relationship between A's spherical and B's Cartesian spatial coordinates vanishes. In addition, A's shift terms may affect A's slicing of spacetime.

(3) Simulation A uses maximal slicing, simulation B geodesic slicing. This is the most dramatic difference. Consider an observer at the origin of the coordinate system. Their proper time evolves with $d\tau = \alpha dt$. $d\tau$ is invariant. A different choice of lapse always implies a different

[10] This situation is frequently called *Moment of Time Symmetry*.

coordinate time. This is commensurate with the picture of coordinate time as the (arbitrary monotonic) parameter that is used to label the slices Σ_t of spacetime.

While (1) is mostly an accuracy issue, items (2) and (3) pose a serious problem when trying to compare results of simulations A and B, since they lead to different spatial and temporal coordinates. In addition, A's and B's coordinates are changing differently. In general, it is not meaningful to compare physical observables at a given coordinate location $(t,\vec{x})$, since the same coordinate labels indicate different physical positions in time and space. One must compare points of equal proper time and identical physical position for a physically meaningful comparison. For general non-spherically symmetric spacetimes a comparison becomes quickly very complicated.

Now, the above example is somewhat extreme and, fortunately, even when comparing a simulation carried out with CoCoNuT in CFC with one carried out with Cactus/Carpet/Whisky (CCW) in full Cauchy free-evolution, the time and coordinate conditions turn out to be considerably more similar than in the above discussed example:

- CoCoNuT uses maximal slicing, while I use the hyperbolic $1+\log$ lapse prescription, which is similar but not identical to maximal slicing. Maximal slicing assumes $K = 0$ (which is enforced in CoCoNuT) while $1+\log$ slicing (see equation (3.31)) only attenuates the change in K and in practice, $K = K(t = 0)$ is not obtained. One way to measure the difference between CoCoNuT's maximal slicing and $1+\log$ is to monitor the evolution of K at the origin where in spherical symmetry the shift must vanish. Note that $1+\log$ slicing was explicitly designed as an approximate algebraic version of maximal slicing. It has been thoroughly studied and compared to maximal slicing in vacuum numerical relativity (see, e.g., [120, 385, 386, 389]).
- CoCoNuT uses the CFC Einstein equations and quasi-isotropic coordinates. This leads to the elliptic shift condition in (5.6), which happens to be equivalent to the minimal distortion shift condition up to second derivatives of the shift [188] (see also equation (5.32) of [120]). The Γ-driver-like shift condition (3.37) that I use in CCW is also related to minimal distortion.

In the following I compare results of two spherically symmetric collapse models that are numerically evolved with both CoCoNuT and CCW. The initial data are $n = 3$ polytropic solutions of the TOV equations. In model TOVG5 I initiate collapse by lowering the Γ to 1.28 and in model TOVG1, Γ is lowered to 1.325. I choose these models to have examples for slow and fast collapse, corresponding to small and large initial pressure reduction, correspondingly. The initial-data equations are not resolved after pressure reduction on CCW's 3D grid. This leads to an initial constraint violation which is, however, too small to affect the dynamics (see §4.2).

I perform the CCW simulations with the standard refinement hierarchy RHII described in §4.3. Its minimal central diagonal cell size is ∼600 m. Model TOVG5 is also evolved with refinement hierarchy RHIII with a central diagonal cell size of ∼450 m. The CoCoNuT simulations are carried out on a 1D grid with logarithmic spacing and a central effective radial zone size of ∼500 m.

The left panel of figure 5.7 displays the evolution of the lapse function in the center of model TOVG5. Core bounce occurs at ∼30 ms coordinate time. There are only minute differences between the CFC maximal-slicing lapse evolution and the $1+\log$ slicing that I use in my full GR simulations. In addition, the deviations become smaller with increased resolution. The time of core bounce and the local minimum of the lapse at core bounce are closer to the maximal-slicing CFC lapse in the higher-resolution full GR simulation. This is consistent with the findings of my resolution study in §4.3 where increased resolution leads to slightly earlier core bounce at lower maximum densities. The right panel of figure 5.7 depicts the relative differences in the proper time at the origin. Increased resolution leads to a smaller deviation of $1+\log$ from maximal slicing, yet even for the lower-resolution run *the proper times at the origin do not differ by more than ∼0.1% at most*. The similarity of the slicings is furthermore substantiated by the evolution of the trace of the extrinsic curvature shown in figure 5.8 for the standard-resolution full GR simulation. K stays orders of magnitude below unity even during the most dynamic phases of collapse and core bounce. Unfortunately, no K output from the high-resolution full GR simulation is available; yet the trend seen in figure 5.8 should apply to K as well and I expect an even better agreement with the CoCoNuT simulation.

The next interesting and easily obtained observable for this comparison is the proper time measured by Eulerian observers that stay at rest with respect to the coordinate locations labeled by x^i. They

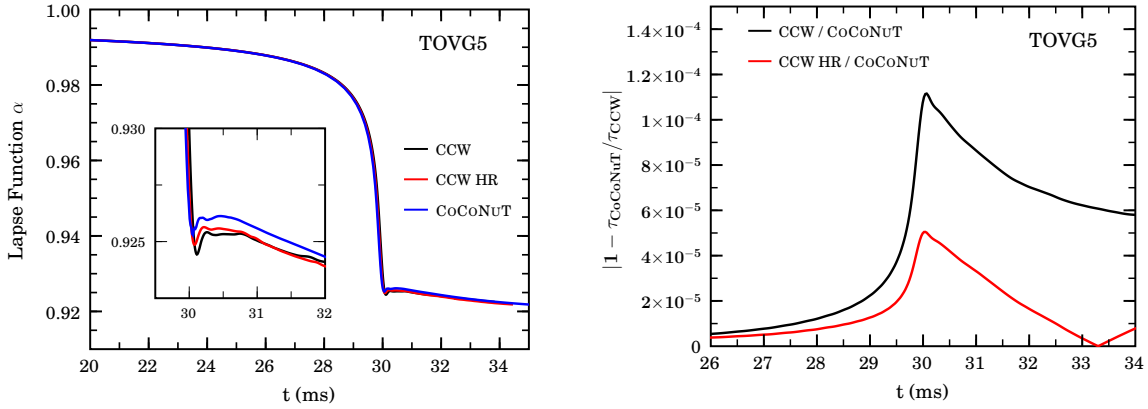

Figure 5.7: Left panel: Evolution of the lapse function at the origin for model TOVG5 evolved in CFC, full GR and full GR in high resolution. The inlay plot displays the same quantity but zoomes in on a few milliseconds around core bounce. Right panel: Relative difference in the proper time of the full GR runs and CFC runs as a function of the coordinate time of the CACTUS/CARPET/WHISKY run.

have $d\tau = \sqrt{\alpha^2 - \beta_i \beta^i} dt$. Note that these Eulerian observers are physically moving outward as the star collapses and the curvature becomes stronger. In other words, their physical distance from the star's center $R = \int_0^r \sqrt{\gamma_{rr}}\, dr$ increases with time. Figure 5.9 displays the proper time of Eulerian observers as a function of coordinate radius at 30 ms (top panel; at bounce) and at 32 ms (bottom panel; shortly after bounce) for the CoCoNuT and the standard-resolution CCW simulation. The gravitational time-dilation effect is nicely illustrated. The difference in proper time of Eulerian observers located at different coordinate radii increases with time, but maximal-slicing CoCoNuT and CCW with $1 + \log$ slicing and the Γ-driver shift condition (3.37) yield a very similar evolution of proper time as a function of coordinate radius and coordinate time. In fact, the apparent slight faster-ticking of the observer clocks in the CCW simulation is likely due to the fact that core bounce is reached about a tenth of a millisecond (in coordinate time) later than in the CoCoNuT simulation. This is supported by the graphs in the right panel of figure 5.7 that indicate that the relative difference in proper time between the CoCoNuT and CCW simulations decreases after bounce. Also, the slicing in the CCW simulation becomes more similar to maximal slicing at postbounce times (figure 5.8).

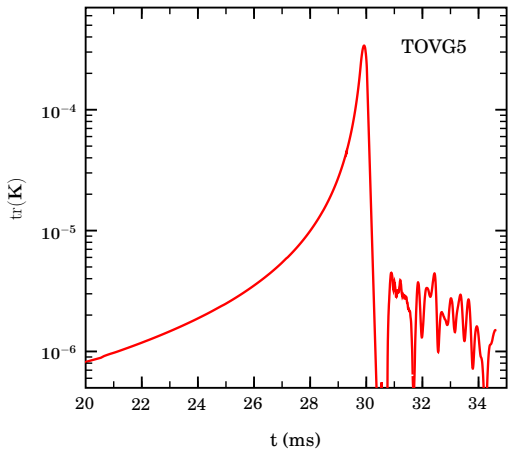

Figure 5.8: Trace of the extrinsic curvature K at the origin for model TOVG5 with standard resolution and $1 + \log$ slicing. In maximally-sliced CFC GR, the trace of the extrinsic curvature vanishes. Shortly after core bounce, K drops to values below zero, but becomes positive again shortly after.

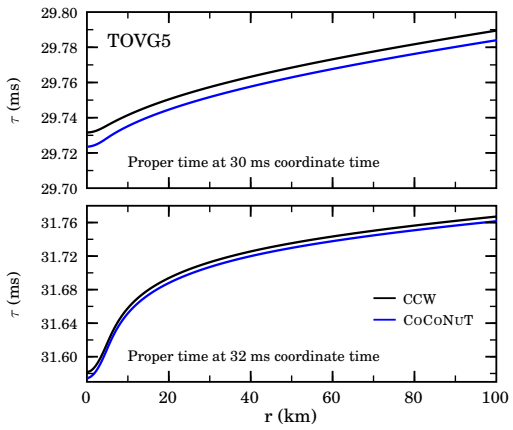

Figure 5.9: Top: Proper time measured by Eulerian observers as a function of coordinate radius at 30 ms coordinate time. Bottom: The same at 32 ms. Note that the interval in τ shown is larger in the bottom panel. Unfortunately, proper time output from the HR simulation is not available.

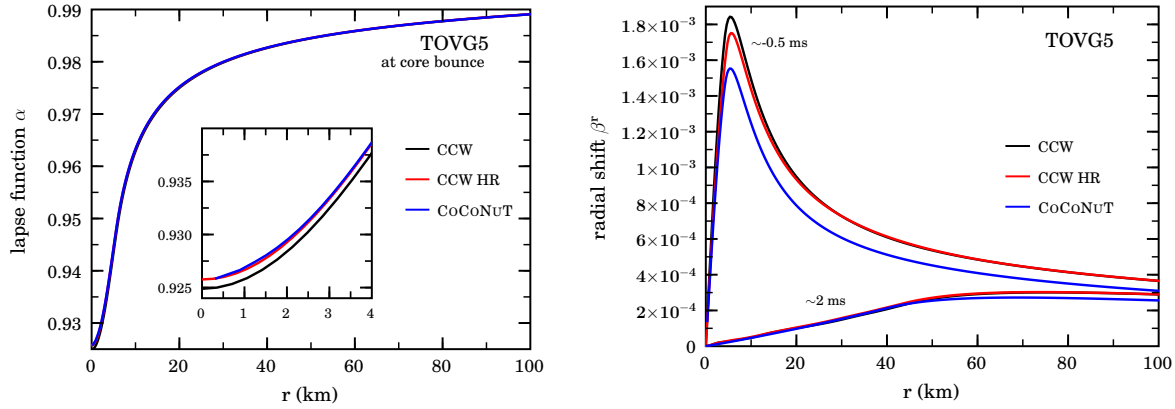

Figure 5.10: Left panel: Lapse vs. coordinate radius at core bounce. The inlay zoomed-in plot reveals only minute differences between CoCoNuT and Cactus/Carpet/Whisky. Right panel: Radial shift vs. coordinate radius at shortly before bounce when β_r reaches its maximum and at $\sim$2 ms after core bounce.

Having demonstrated the match to better than $\sim$0.1% of the proper time evolution at the origin and of Eulerian observers at $r > 0$, I can safely assume that the time and spatial coordinates have a very similar or rather, – for all practical purposes – the same, meaning in CoCoNuT and CCW with the discussed coordinate and slicing conditions. Furthermore, I can use coordinate-dependent quantities to compare simulations carried out with CoCoNuT and CCW. This significantly smoothes out the difficulties mentioned and concerns raised at the beginning of this section. One must keep in mind that the spacetime considered here is spherically symmetric and that in spacetimes that deviate from spherical symmetry, the evolution of lapse and shift may become different in the two approaches. However, keeping the Newtonian analog in mind, deviations from spherical symmetry will appear as higher-order corrections to the gravitational field, and, as long they stay on the percent level, are thus unlikely to dramatically affect the evolution of the temporal and spatial coordinates. Furthermore, one may expect that rotation, the agent that breaks spherical symmetry, will be handled similarly to radial infall by the CFC shift and the dynamical Γ-driver shift used in CCW. Both shift conditions do not exhibit directional preference and both are related to the minimal distortion condition (see §3.3.2). To conclude the comparison of coordinates, I show in figure 5.10 radial profiles of the lapse function and the shift at times at which they reach their global maximum and minimum, respectively. The agreement in the lapse is marvelous and close to perfect for the high-resolution CCW simulation even in the central-most region. The coordinate shifts match very well in the central region while exhibiting significant, though not dramatic, differences at larger intermediate radii.

In the now following comparison of coordinate-dependent fluid variables I limit myself for conciseness to comparing central rest-mass density evolutions, and radial velocity as well as density profiles. Figure 5.11 shows the evolution of the density at the origin (ρ_c) for the fast collapse model TOVG5. The comparison with CoCoNuT is hampered by the fact that CoCoNuT's discretization approach leads to purely numerical oscillations in the density in the central-most grid zones at core bounce. Despite this, it is clear from figure 5.11 that the ρ_c evolutions agree exceptionally well on average. The CCW standard-resolution simulation reaches core bounce less than 0.1 ms later than the CoCoNuT run and the high-resolution variant reduces this difference to 0.05 ms. Averaging out the oscillations in the CoCoNuT data, the bounce densities agree to less than 2%. Importantly, the postbounce ρ_c of all three simulations settle at $\sim 3.9\times10^{14}$ g cm^{-3}.

In order to investigate the influence of long-term numerical evolution on the comparability of results from CoCoNuT and CCW, I consider the ρ_c evolution of the slow-collapse model TOVG1 which reaches core bounce only at $\sim$95 ms after the onset of collapse (figure 5.12). The absolute difference in the times of core bounce is larger than for the fast-collapse model TOVG5, yet the relative difference to the CoCoNuT results – given the relatively late bounce time – is still only 0.2%. Similarly to TOVG5, the comparison is complicated by the numerical high-frequency oscillations in the CoCoNuT data. However, when correcting for the difference in the time of bounce and averaging out the oscillations, the CoCoNuT and CCW profiles match very well. I do not perform a

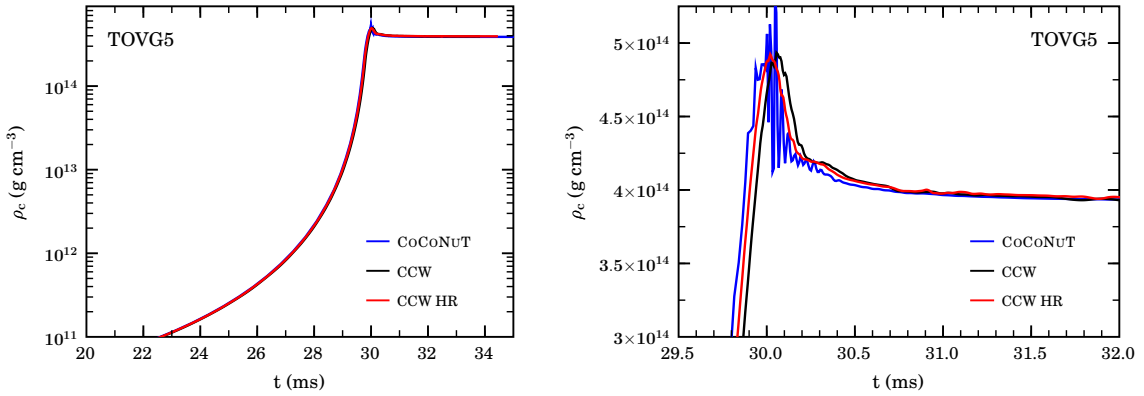

Figure 5.11: Left panel: Evolution of the rest-mass density vs. coordinate time at the origin for model TOVG5. Right panel: Zoomed-in view. The oscillations in the CoCoNuT data are purely numerical and related to discretization difficulties near the origin. In rotating models these oscillations are smoothed out.

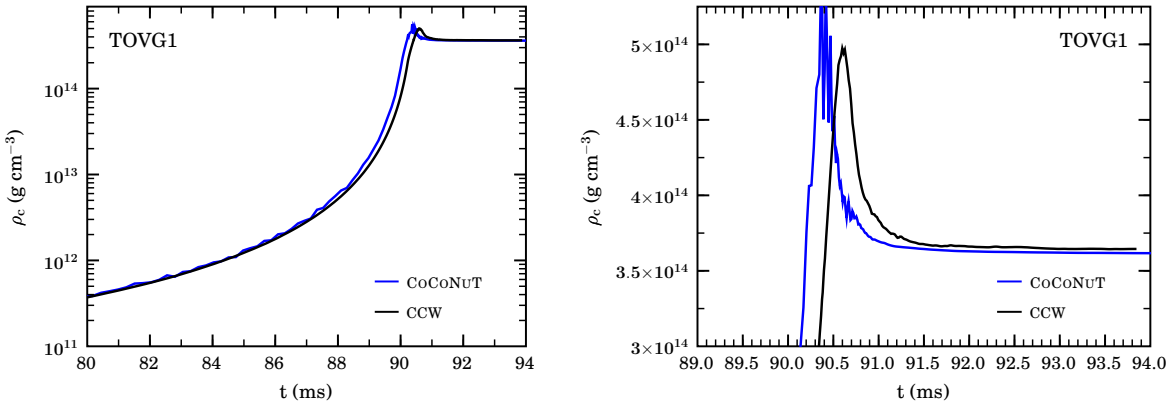

Figure 5.12: Left panel: Evolution of the rest-mass density vs. coordinate time at the origin for model TOVG1. Right panel: Zoomed-in view. The oscillations in the CoCoNuT data are purely numerical and related to discretization difficulties near the origin. In rotating models these oscillations are smoothed out.

high-resolution CCW simulation for model TOVG1, but the results for TOVG5 indicate that a higher-resolution variant will exhibit a slightly earlier time of core bounce, matching the CoCoNuT results to even higher precision.

The left panel of figure 5.13 shows radial velocity profiles from before and after core bounce in model TOVG5. At 0.5 ms before bounce, the CoCoNuT and CCW profiles match perfectly. At postbounce times, however, the agreement is much less perfect for the shock position and in the post-shock region. In the CCW results, the shock speed appears to be higher, the shock is spread out over a larger radial interval and post-shock oscillations are present. Extensive tests have revealed the following causes for the observed differences: (a) at postbounce times, the CCW grid refinement hierarchy is fixed and the shock is not tracked by mesh refinement. Whenever the shock crosses a refinement boundary the sudden drop in resolution results in it being smeared out over a larger radial interval. (b) The error in the shock location which is $\sim$1 grid zone at 1 ms after bounce and $\sim$3–4 at 4 ms after bounce. Given the number of numerical timesteps involved and the fact that at 4 ms the shock has already passed 3 refinement boundaries, the error in the shock speed of $\sim$8% is within the boundaries of what must be expected. In addition, the shock resolution and the shock position are closer to the CoCoNuT results in the higher-resolution CCW simulation (figure 5.13). (c) The post-shock oscillations, visible strongest in the velocity profiles, appear to not converge away with higher resolution. They are a systematic error introduced by the resolution jump and flux mismatches between fine and coarse grid at the refinement boundaries when the shock crosses (see,

e.g., [394, 402]). At the refinement boundary, the shock is partly and spuriously reflected. This leads to the visible spikes in the velocity profiles and the post-shock oscillations. As mentioned in §3.4, this problem could be alleviated by introducing flux corrections on the coarse grid, so-called *refluxing* [394]. Yet, the jump in resolution at the refinement boundaries would even with refluxing still lead to spurious, though converging, reflections (*grid scattering*) of the shock, hence the benefit from refluxing is debatable.

Given the above discussed postshock oscillations, the question must arise whether they can have a significant effect on the global dynamics and in this way alter the gravitational waveform estimates derived from the fluid dynamics in non-spherically symmetric models. The answer is 'No, not significantly': First, the oscillations are relatively small in amplitude ($\sim$0.005–0.01 c). Second, they involve little mass, appear to be confined to the post-shock region outside the protoneutron star and cause only small variations (a few percent) of the post-shock density profile. Third, and most importantly, by their very nature as reflections of the shock at resolution jumps they are comprised of high-frequency variations ($\sim 10^4$ Hz) in the fluid variables, significantly higher than the variations ($\sim 10^3$ Hz) in the large scale aspherical fluid motions dominantly emitting gravitational waves.

To conclude this extensive code comparison, I recapitulate my main findings:

(1) The choice of coordinate and slicing conditions in CACTUS/CARPET/WHISKY leads to a very similar evolution of the slicing and the spatial coordinates to those of COCONUT. The differences in the proper time of Eulerian coordinate observers as a function of coordinate radius and coordinate time in the test cases considered are below $\sim$1%. This finding greatly facilitates subsequent simulation comparisons since it is possible to directly compare coordinate-dependent quantities to within a 1% error. Deviations from spherical symmetry should be expected to lead to somewhat larger deviations. However, the gauge conditions of both codes do not exhibit any directional preference, hence the deviations should remain small.

(2) The collapse, bounce, and postbounce dynamics computed with CACTUS/CARPET/WHISKY and COCONUT agree very well for both models considered here. The times of core bounce and the maximum densities match to within 1% and show convergence with increased resolution of the CACTUS/CARPET/WHISKY simulation. The radial density and velocity evolution is nearly identical before core bounce. After shock formation the accuracy of the Cartesian-grid CACTUS/CARPET/WHISKY approach is somewhat worse than that of COCONUT since radial motion can only be perfectly tracked on a Cartesian mesh-refined grid in the limit of infinite resolution. In addition, the centered mesh refinement leads to poor shock resolution at radii larger than $\sim$50 km. This can be corrected by enlarging the extent of the fine grids.

(3) COCONUT's CFC approach is exact in spherical symmetry. The comparison that I have performed is thus not obstructed by fundamental systematic differences of the equations solved.

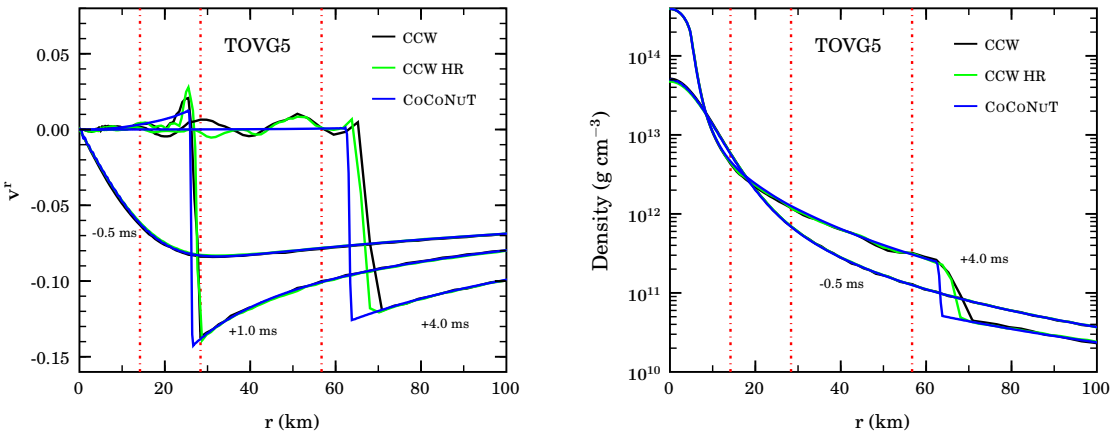

Figure 5.13: Left panel: Radial velocity profiles at 0.5 ms before, 1 ms, and 4 ms after core bounce. The red dash-dotted lines indicate mesh refinement boundaries. Right panel: Radial density profiles at 0.5 ms before and 4 ms after core bounce. I omit the profile from 1 ms after core bounce for clarity of presentation.

In addition and as demonstrated in §4.3, the initial constraint violation introduced in the CCW simulations by the pressure reduction is on the 10^{-7} level and is quickly dwarfed by the constraint violation due to inaccuracies during evolution. Yet, even at postbounce times the constraint violation stays on the percent level.

Hence, above points (1) and (2) lead to the assessment that deviations from conformal flatness in rotating core collapse are detectable down to the few-percent level by comparing simulations carried out with CoCoNuT and Cactus/Carpet/Whisky. This statement is true at least for the collapse and the very early prebounce phases before the shock has propagated out to distances greater than ∼25 km, and the major prerequisite is numerical convergence of the relevant simulation results from both codes for each individual model considered. Care must be taken to differentiate between numerical inaccuracies and real physical differences brought about by the CFC approximation.

5.2.4 Axisymmetric Rotating Polytropes

Since I am comparing 3D fully general relativistic simulations with simulations in conformally-flat general relativity that were carried out on a 2D computational grid assuming axisymmetry, the presence of 3D structure and dynamics would significantly affect and possibly spoil the comparison. In axisymmetry, no gravitational waves are emitted along the axis of symmetry and only waves of the $+$ polarization are emitted at off-axis angles (see, e.g., [116, 178]). Hence, the magnitudes of the wave emission in the $\times$ polarization and along the polar axis can serve as indicators for dynamically relevant 3D structure. In table 5.2, I list the maximum gravitational wave amplitudes for both polarizations as observed along the equator and along the poles. Though not being identical to zero and hence indicating the presence of some nonaxisymmetric structure and dynamics, the maximum amplitudes of the $\times$ polarization and the maximum amplitude of the $+$ polarization along the poles are in all models by at least one to two orders of magnitude smaller than the axisymmetric $+$ amplitudes. It is thus safe to consider the dynamics to be dominated by axisymmetric fluid motion. The largest nonaxisymmetric amplitudes appear in in the transitional type I/II models A3B3G3 and A3B3G2. I do not investigate the development of nonaxisymmetric structures in the calculations with polytropic initial models presented here. See §6.4 for a discussion in the context of the more astrophysically realistic models considered in chapter 6.

Another caveat that needs highlighting before I may go on to comparing results from CCW and CoCoNuT is the fact, that Dimmelmeier et al. [12, 161] use physical velocities (equation 2.25 in §2.4) in CoCoNuT for the quadrupole formula, while CCW uses standard Eulerian 3-velocities[11]. This difference was noticed only after all simulations had been performed. Differences between physical and Eulerian velocities will be on the percent level ($\propto \sqrt{|\gamma_{ij}|}$; $|\gamma_{ij}|_{\max} \simeq 1.3$ at postbounce times in CCW and CoCoNuT) and largest deep inside the core where curvature is strongest. Due to the integral nature of the quadrupole formula, the differences in wave signals derived from Eulerian and physical velocities will hence stay on the percent level. This is confirmed by a short test calculation in

[11] Since there is no unique definition of the mass quadrupole moment in general relativity [116], it is not clear what the "right" velocities to use are.

Table 5.2: Maxima (in absolute value) of the gravitational wave amplitudes (multiplied by distance R) for waves of $+$ and $\times$ polarization emitted in the equatorial plane (superscript e) and along the poles (superscript p). All model calculations are carried out to ∼20 ms after bounce.

Model	$\lvert h^e_{+,\max}R\rvert$ (cm)	$\lvert h^e_{\times,\max}R\rvert$ (cm)	$\lvert h^p_{+,\max}R\rvert$ (cm)	$\lvert h^p_{\times,\max}R\rvert$ (cm)
A1B3G3	199.85	0.0052	1.1510	1.0331
A1B3G5	31.50	0.0022	0.1375	0.1506
A2B4G1	160.00	0.0130	0.3453	0.2401
A3B2G4	159.91	0.0570	0.8784	1.1611
A3B3G2	596.29	0.5680	4.3682	4.6390
A3B3G3	428.53	0.2125	9.4200	10.0660

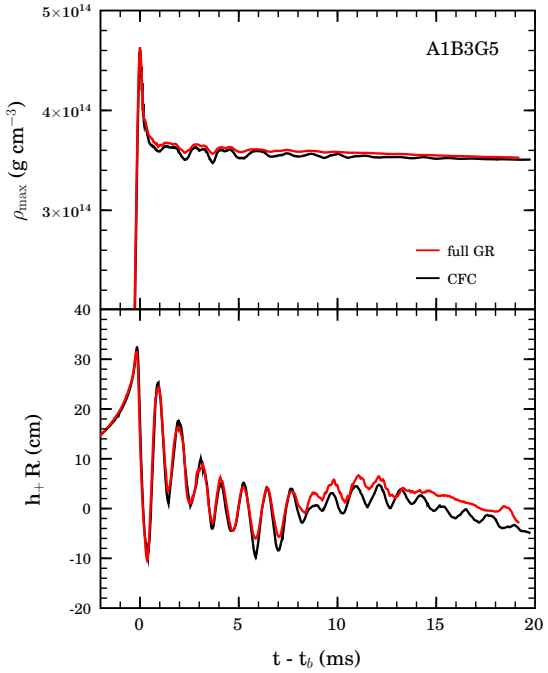

Figure 5.14: Type III model A1B3G5. Top: Comparison of the maximum density evolution CFC/full GR. Bottom: Gravitational wave signal. CFC/full GR agree perfectly in the bounce signature and deviate at late times most likely due to larger damping of the ring-down oscillations on CCW's Cartesian grid.

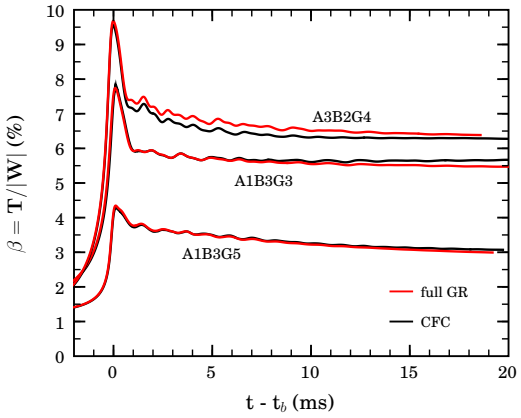

Figure 5.15: Evolution of the rotation parameter $\beta = T/|W|$ in type I models A1B3G3 and A3B2G4 and in the type III model A1B3G5.

CCW covering the bounce phase of model A1B3G5. The maximum signal amplitudes derived with physical and Eulerian velocities agree to within ∼3% for the bounce spike of this model.

In figure 5.14 I contrast the evolutions of the maximum density (ρ_{max}) and of the gravitational wave signal for model A1B3G5 (type III) as computed in CFC and in full GR. The ρ_{max} and waveform evolutions agree very well: as listed in table 5.3, the times of core bounce and the maximum densities at bounce differ by less than 1% and the maximum wave amplitudes by less than ∼1.5%. Importantly, even at postbounce times of several milliseconds the waveforms and ρ_{max} evolutions match very well and are in phase. In CCW, A1B3G5 settles at slightly higher postbounce densities (∼0.9%), while small features of the ring-down motions are considerably less well resolved as in the CoCoNuT simulation. This is most likely a pure grid and resolution effect and should not be considered as a significant qualitative/quantitative difference between CFC and full GR. The poorer resolution of the ring-down dynamics of the postbounce core in the CCW simulation is reflected in its wave signal as well: the waveform appears to damp earlier and small variations on the few-cm scale are not resolved at postbounce times greater than ∼10 ms. The resolution study presented in §4.3 indicates that increased resolution (though not affordable for production simulations on present supercomputers) would lead to an improved capture of such small variations by CCW.

Figure 5.15 contrasts the CFC and full GR results for the evolution of the rotation parameter $\beta = T/|W|$ in models A1B3G5 (type III), A1B3G3 (type I), and A3B2G4 (also type I). β is computed in CCW according to the prescription given in §3.9.2 which is only correct in stationary spacetimes but can be used as a reasonably good approximation to β in the dynamical (and predominantly axisymmetric) case. β is an important variable, capturing the global dynamics of the rotating fluid. The remarkable agreement of CFC and full GR simulations in β hence indicates close congruence of the dynamics in CFC and full GR; in particular for model A1B3G5, but also for the type I models A1B3G3 and A3B2G4. In all three models CFC and full GR agree in the maximum β and in the β at ∼20 ms postbounce to better than ∼5% (table 5.3) while the differences appear to be non-systematic and must most likely be attributed to differences in resolution and grid geometry.

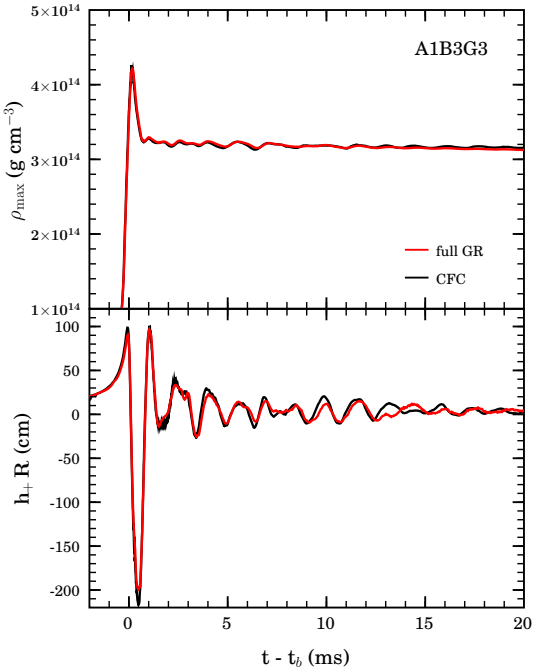

Figure 5.16: Type I model A1B3G3, CFC contrasted with full GR. Top: Evolution of the maximum density. Bottom: Gravitational wave signal.

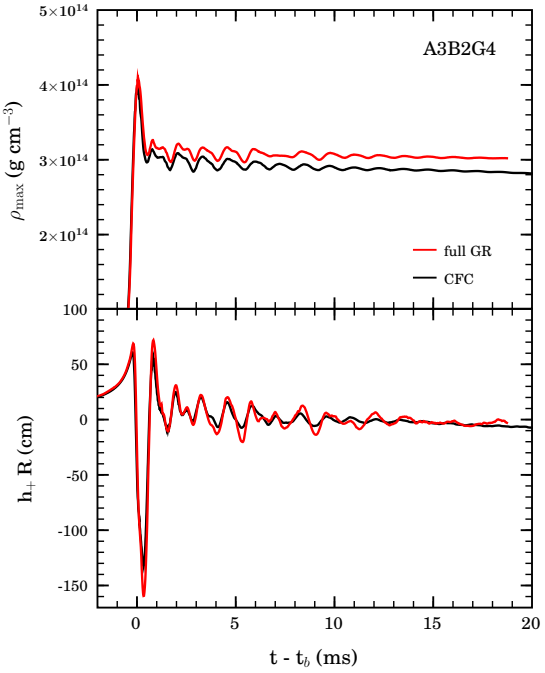

Figure 5.17: Same as figure 5.16, but showing data of the type I model A3B2G4. The fact that that CCW yields higher postbounce densities and resolves finer features than CoCoNuT is most likely due to slightly better resolution in CCW for model A3B2G4.

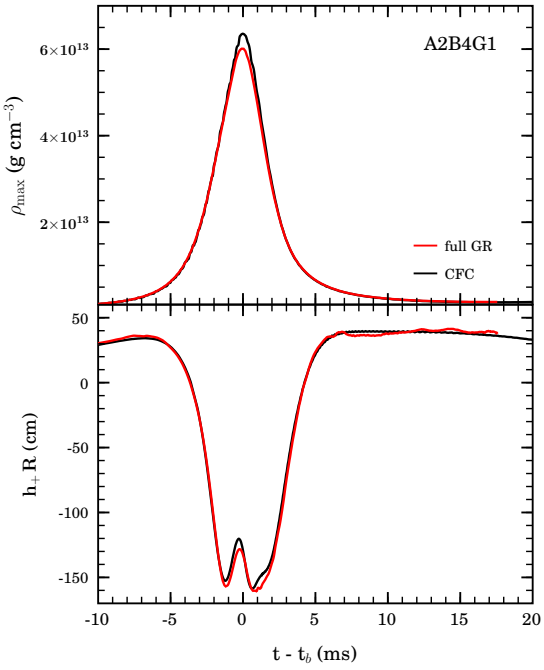

Figure 5.18: Type II model A2B4G1 followed to ∼20 ms after core bounce with CCW and CoCoNuT. Top: Evolution of the maximum density. Bottom: Gravitational wave signal. Although the global ρ_{max} is underestimated by CCW, the gravitational waveforms match well since the bounce dynamics are governed by centrifugal forces that are insensitive to small variations in ρ_{max}.

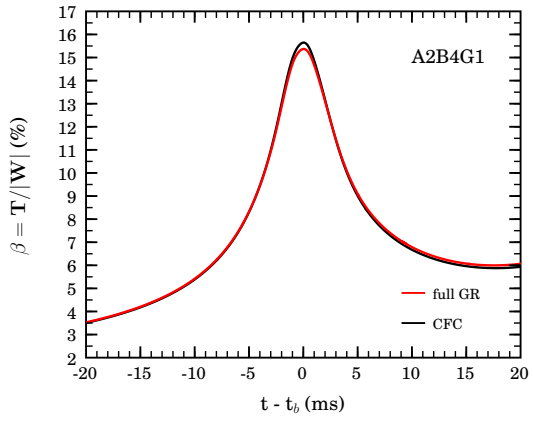

Figure 5.19: Model A2B4G1. Comparison of the evolution of the rotation parameter $\beta = T/|W|$ from 20 ms before to 20 ms after core bounce. There is very good agreement in pre- and postbounce β of the CFC and full GR results, despite differences at bounce that are likely due to slight underresolution of the dynamics by CCW.

Model	$\frac{t_{b,\mathrm{CFC}}}{t_{b,\mathrm{GR}}}$ - 1 (%)	$\frac{\rho_{b,\mathrm{CFC}}}{\rho_{b,\mathrm{GR}}}$ - 1 (%)	$\frac{\beta_{b,\mathrm{CFC}}}{\beta_{b,\mathrm{GR}}}$ - 1 (%)	$\frac{\rho_{f,\mathrm{CFC}}}{\rho_{f,\mathrm{GR}}}$ - 1 (%)	$\frac{\beta_{f,\mathrm{CFC}}}{\beta_{f,\mathrm{GR}}}$ - 1 (%)	$\frac{\lvert h_+ R\rvert_{\mathrm{max,CFC}}}{\lvert h_+ R\rvert_{\mathrm{max,GR}}}$ - 1 (%)	$\frac{E_{\mathrm{GW,CFC}}}{E_{\mathrm{GW,GR}}}$ -1 (%)	$\frac{f_{\mathrm{max,CFC}}}{f_{\mathrm{max,GR}}}$ -1 (%)
A1B3G3	+0.05	-0.09	+0.59	0.64	-4.19	+8.79	+57.05	−2.50
A1B3G5	−0.19	−0.68	−1.40	−0.85	+2.06	+2.84	+51.43	−1.57
A2B4G1	0.51	5.82	4.10	2.42	0.17	−2.56	−29.82	−8.51
A3B2G4	−0.13	−2.61	−1.14	−6.95	−1.72	−13.70	−14.43	−0.49
A3B3G2	−0.25	−0.95	2.98	−2.11	−0.08	−17.58	−42.91	1.42
A3B3G3	−0.14	−1.88	1.25	−6.30	0.33	−13.30	−13.25	0.92

Table 5.3: Summary of relative differences in key single-value observables of CoCoNuT CFC simulations and simulations carried out in full GR with CCW. t_b, ρ_b, and β_b are the time of core bounce, the maximum density reached at core bounce and the maximum rotation parameter β reached at core bounce, respectively. ρ_f is the maximum density and β_f is the rotation parameter at ∼20 ms after bounce. $|h_+ R|_{\mathrm{max}}$ is the maximum gravitational wave amplitude at distance R. E_{GW} is the energy in gravitational waves emitted until ∼20 ms after bounce. f_{max} is the frequency at which the gravitational wave spectral energy density peaks. Note that the large relative differences observed in E_{GW} are due to the fact that in CCW the Fourier-transformed $\ddot{I}_{ij}$ is used for the energy calculation, while in CoCoNuT $\dddot{I}_{ij}$ is employed, the latter running greater risk of picking up unphysical high-frequency variations. Note that the numbers stated in this table are relative differences that depend on the simulation and grid setups in CoCoNuT and CCW and are subject to variation under changes in the resolution / grid setup. They should be taken with caution and understood as being only of indicative, not of definite nature.

Figures 5.16 and 5.17 show the ρ_{max} and wave signal evolutions of the type I models A1B3G3 and A3B2G4, respectively. As in A1B3G5, there is nearly perfect agreement of the results from the CFC and full GR calculations in ρ_{max} at bounce, in the maximum gravitational wave amplitude and, in particular, in the shape of the first and largest peak in the wave signal. Throughout the postbounce evolution the dynamics remain in phase. In A1B3G3, small features in ρ_{max} and h_+ are less well resolved by CCW while in A3B2G4 the opposite appears to be the case. In addition, the overall largest differences in the postbounce maximum density evolution of all models are observed in model A3B2G4. The maximum densities at ∼20 ms after bounce differ by ∼7%. Given the excellent agreement in models A1B3G3 and A1B3G5, the cause of the differences in A3B2G4 is not obvious. The good overall qualitative agreement, however, lets me surmise that the differences are caused by slightly insufficient resolution, this time on the part of the CoCoNuT simulation.

Model A2B4G1 has the largest precollapse β of all models in the comparison set. It collapses slowly and rebounds ∼100 ms after the onset of collapse under the strong influence of centrifugal forces at only $\sim 6\times10^{13}$ g cm^{-3} (see table 5.4). Its homologously collapsing inner core is large (∼1 $M_\odot$) and the bounce shock forms at about 60 km radius. Since the CCW approach does currently not provide true adaptive mesh refinement, this model is among the most computationally expensive, because here fine grids must be extended out to large radii to fully capture the bounce dynamics. Figures 5.18 and 5.19 depict that this — — even in the highest computationally feasible resolution[12] — is not entirely possible. The maximum density at core bounce and the maximum β are underestimated by CCW, while while the gravitational wave signature matches well with the CoCoNuT result. Belonging to the class of type II models, A2B4G1 exhibits several postbounce coherent and damped re-expansion-collapse-bounce cycles over an interval of tens of milliseconds (see figure 5.4). Unfortunately, it is computationally too expensive to carry out A2B4G1 to such late postbounce times in 3D.

The comparison results for the transitional type I/II models A3B3G2 and A3B3G3 are shown in figure 5.20 and 5.21, respectively. A3B3G2 reaches supernuclear densities, but, due to strong centrifugal support, exhibits large scale postbounce oscillations in ρ_{max} that are reflected by the shape of the gravitational waveform. While the general qualitative agreement of the maximum density and wave signal evolutions is good, there are two things to note: (1) the CCW simulation yields a ∼18% larger amplitude for the bounce spike than the CoCoNuT simulation and small postbounce features in the waveform are slightly better resolved by CCW than by CoCoNuT. (2) Starting from the first postbounce maximum in ρ_{max}, the CCW ρ_{max} and waveform evolutions appear slightly phase and frequency shifted. A more detailed analysis shows that the coherent re-expansion after bounce encompasses material out to radii of ∼100 km that crosses at least two, if not three, mesh refine-

[12] Using refinement hierarchy ORHIIe (see Appendix E). Tests with lower resolutions indicate that A2B4G1 with ORHIIe is almost, but not completely numerically converged.

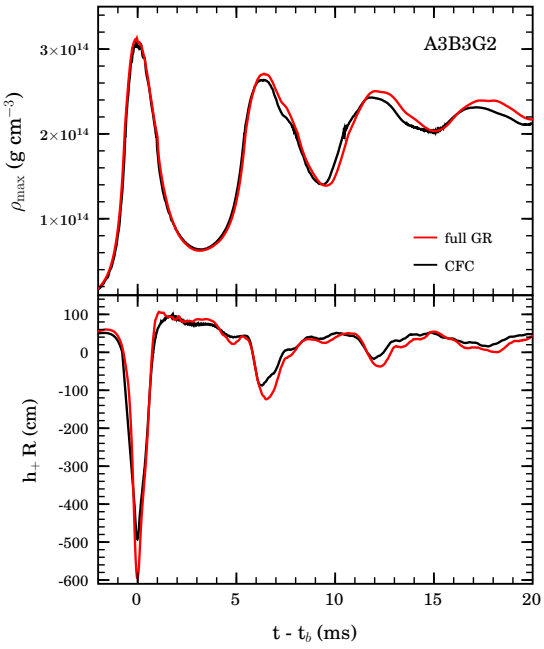

Figure 5.20: Type I/II transitional model A3B3G2. Maximum density (top) and gravitational wave signal (bottom) evolution as calculated in CFC and full GR. A3B3G2 reaches core bounce at supernuclear densities, but exhibits several coherent large-scale postbounce oscillations in ρ_{max}. The full GR/CCW results show a shift of phase and frequency. See text for details.

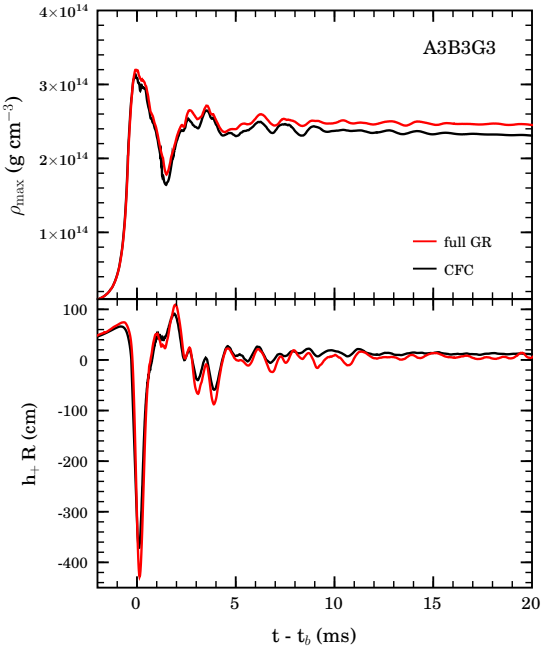

Figure 5.21: Same as figure 5.20, but for model A3B3G3 which is a type I/II transitional model.

ment boundaries during expansion and re-contraction. I hence attribute the observed phase shift at least in part to numerical inaccuracies in the handling of flux through mesh refinement boundaries (as discussed in §3.4 and §5.2.3). Despite the observable phase/frequency shift, the gravitational wave energy spectra of the full GR and CFC variants of A3B3G2 agree in peak frequency to better than ∼2%. Model A3B3G3 is a transitional type I/II model which is closer to type I than to type II

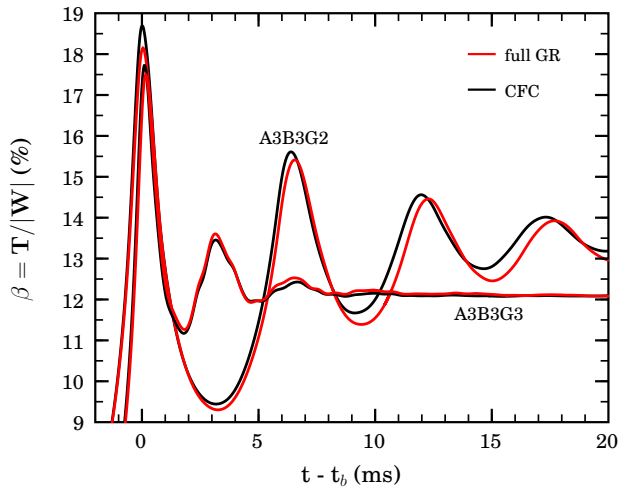

Figure 5.22: Evolution of the rotation parameter $\beta = T/|W|$ shown for the transitional type I/II models A3B3G2 and A3B3G3. The full GR/CCW results exhibit a shift in postbounce oscillation frequency and phase for model A3B3G2. See text for details.

Model	t_b (ms)	Δt (ms)	ρ_b (10^{14} g cm^{-3})	ρ_f	β_b (%)	β_f (%)	$\lvert h_+ R\rvert_{\max}$ (cm)	$E_{\rm GW}$ (10^{-8} M$_\odot$ c^2)	$f_{\max}$ (Hz)
A1B3G3	48.73	23	4.23	3.13	7.75	5.43	199.85	1.490	680
A1B3G5	30.26	19	4.64	3.53	4.34	3.01	31.50	0.035	890
A2B4G1	99.60	18	0.60	1.46	15.17	5.86	160.00	0.112	94
A3B2G4	39.36	19	4.08	3.02	9.67	6.39	159.91	0.949	810
A3B3G2	71.32	24	3.13	2.18	18.15	13.30	596.29	4.039	494
A3B3G3	49.73	19	3.20	2.46	17.50	12.05	428.53	3.539	757

Table 5.4: Summary of key single-value observables for all axisymmetric comparison models. CCW data. t_b is the time of core bounce (defined as the time at which the global maximum of the density is reached), Δt is the interval in time after bounce through which each individual calculation is carried out. ρ_b and ρ_f are the maximum density at bounce and at the end of the simulation, respectively. β_b is the value of $T/|W|$ at bounce at β_f is the value of $T/|W|$ at the end of the simulation. $|h_+ R|_{\max}$ is the maximum (in absolute value) of the gravitational amplitude, $E_{\rm GW}$ is the total energy emitted in gravitational waves, and $f_{\max}$ is the frequency at which the spectral energy density peaks.

dynamics. As visible in its gravitational waveform and $\rho_{\max}$ evolution, it exhibits only one large postbounce re-expansion and then recovers type I ring-down dynamics. As in model A3B3G2, CCW yields a larger maximum gravitational wave amplitude, most likely related to a slight insufficiency in grid resolution in the CoCoNuT simulation [525].

Finally, I contrast β evolutions obtained in CFC and in full GR for A3B3G2 and A3B3G3 in figure 5.22. The CFC variant of A3B3G2 reaches a $\sim$3% higher β at bounce than the full GR simulation. The higher β at bounce in combination with the slightly lower bounce density ($\sim$1%) and the considerably lower maximum gravitational wave amplitude ($\sim$18%) gives rise to the suspicion that the CFC and full GR simulations started out with slightly different initial conditions. This could also in part explain the observed postbounce differences in phase/frequency between CFC and full GR results. The initial configurations in CCW and CoCoNuT differ in β by 0.5% (on the entire grid and — given that the grid geometry and sizes differ – in the central regions of the core most likely less than that). Harald Dimmelmeier, by experience from a large number of simulations carried out with CoCoNuT, points out that especially type I/II transitional and type II models are very sensitive to small changes in the initial conditions [18, 525] while type I and type III models typically are not. In the context of the harmonic-oscillator-like postbounce re-expansion-collapse-bounce phases, slightly different initial conditions may lead to slightly different inner core masses, resulting in different eigenfrequency of the volume mode dominant in type II and transitional models.

5.2.5 Summary and Discussion

In this section I have presented the first detailed comparison of stellar core-collapse simulations carried out with two entirely distinct computer codes, one treating numerical relativity in a constrained-evolution sense in the conformal-flatness approximation in 2D spherical coordinates, the other one freely evolving the ADM/NOK-BSSN field equations on a refined 3D Cartesian grid. I have demonstrated that in spherical symmetry the slicing and spatial coordinate choices implied by the CFC approximation in maximal slicing are compatible with standard $1 + \log$ slicings and Γ-driver shift conditions used in BSSN_MoL. The spacetimes considered here are matter dominated, i.e. the terms directly related to matter, being without directional preference, dominate gauge prescriptions. Hence, I conclude that even when spherical symmetry is relaxed to axisymmetry or full 3D, time and spatial coordinates will have the same meaning or at least very similar (to a few percent) meaning in CoCoNuT and CCW. This allows a direct one-to-one comparison of gauge-dependent quantities from simulations carried out in CFC and full GR. Previous comparison studies either used more similar codes (CFC+ vs. CFC within the CoCoNuT code; [162]) or did not clarify how the spatial and temporal coordinates compared [13].

I have performed *en detail* comparisons of the matter dynamics and quadrupole gravitational wave signals up to $\sim$20 ms after core bounce for six models of the Zwerger & Müller [30] / Dimmelmeier, Font & Müller [12] model suite evolved in CFC by CoCoNuT and full GR by CCW. All models stay axisymmetric throughout the time covered in this comparison and in all models CFC/CoCoNuT

and full GR/CCW agree on the maximum density reached at bounce within $\lesssim$6%, on the maximum $\beta = T/|W|$ within $\lesssim$4%, on the maximum gravitational wave amplitude to within $\lesssim$18%, and on the peak frequency of the gravitational wave energy spectrum to within $\lesssim$ 8.5%. Based on knowledge of the various systematic and numerical resolution-caused shortcomings and advantages of both codes, I attribute the observed differences to (a) slight differences in the wave extraction methods, (b) slightly insufficient resolution either on the CoCoNuT or the CCW side, (c) mesh-refinement-caused inaccuracies in CCW, and (d) to small variations in the initial data that influence the bounce and postbounce dynamics. I do not find any indication of significant (i.e., above the error margins) quantitative differences that could be attributed to differences between CFC and full free-evolution numerical relativity. In addition, and most importantly: there are no indications of any qualitative differences that could be considered as being systematically caused by an inadequacy of the CFC approximation for the stellar core-collapse problem. All qualitative features present in the full GR results are present as well in the CFC data. Given the fact that CCW and CoCoNuT are two very different codes (in grid coordinates; spacetime evolution and discretization etc.), the level of agreement that I find is surprising and encouraging.

I conclude that the CFC approximation in the incarnation and implementation presented and employed in [12, 18, 160, 161] is an excellent approximation to full general relativity for tracking the collapse, bounce, and early postbounce phases of rotating stellar iron core collapse to a neutron star. This supports the findings of previous comparison studies in CFC+ [162] and axisymmetric general relativity [13]. In addition, Cook et al. [536] compared CFC and full GR for rapidly rotating equilibrium neutron stars and found deviations of CFC from the exact solution to be at most $\sim$5% for extreme models and much smaller otherwise. Kley & Schäfer [537] compared CFC and full GR solutions for relativistic dust disks and found CFC to be equivalent in accuracy to first-order post-Newtonian approximations.

The good agreement of the CFC approach with full GR in the stellar iron core collapse models considered here and the estimates on the energy emitted in gravitational waves during collapse, bounce, and early postbounce phases ($\lesssim 10^{-7}$ M$_\odot$; [9, 11, 30, 95, 160]) may motivate the assertion that the stellar core collapse spacetimes considered here are *essentially* conformally flat, with the meaning of *essentially* being defined as 'not yielding dynamics notably different from CFC'. That this indeed appears to be the case can be shown more strictly by considering the 3-Bach and Cotton-York tensors [538]. York [147] has pointed out that the 3-Bach tensor, defined by [539, 540]

$$B_{ijk} \equiv R_{ij;k} - R_{ik;j} + \frac{1}{4}\left(\gamma_{ik}R_{;j} - \gamma_{ij}R_{;k}\right) , \tag{5.8}$$

where R_{lm} is the 3-Ricci tensor and R the 3-Ricci scalar, vanishes on any conformally-flat 3-hypersurface. It is the 3-geometry analogon to the Weyl tensor in higher dimensions [116, 189]. The 3-Bach tensor has 5 independent components and it is algebraically equivalent to the Cotton-York tensor [147, 541]

$$Y^{ij} \equiv \epsilon^{ilm}\left(R_m{}^j - \frac{1}{4}\delta^k_j R\right)_{;l} = -\frac{1}{2}\epsilon^{ilm}\gamma^{jn}B_{nlm} , \tag{5.9}$$

where ϵ^{ilm} is the standard completely antisymmetric tensor density of weight $+1$ (the Levi-Civita symbol), with $\epsilon^{123} = +1$. In the literature, $\tilde{Y}^{ij} = \gamma^{1/3}Y^{ij}$ can be found, which is invariant under conformal transformations [147]. Y^{ij} is symmetric, traceless, and transverse ($Y^{ij}{}_{;j} = 0$) [147]. The Cotton-York tensor has been used by Garat & Price to show that there are no conformally flat slices of Kerr spacetime [535]. Miller et al. [542] have employed the Cotton-York tensor to assess the deviations from conformal flatness in simulations of binary neutron star coalescence. In addition, Miller et al. defined a scalar H as the matrix norm[13] of the Cotton-York tensor, normalized by the size of the covariant derivative of the 3-Ricci tensor:

$$H = \frac{\|Y_{ij}\|}{\sqrt{R_{jk;i}R^{jk;i}}} . \tag{5.10}$$

The normalization provides a local measure for determining how much the spatial slice considered is deviating from conformal flatness. For a global measure in matter spacetimes, Miller et al. [542]

[13]The matrix norm of a real matrix A_{ij} is defined as $\|A_{ij}\| = \sqrt{\lambda_{\max}}$, where $\lambda_{\max}$ is the maximum eigenvalue of the matrix $A_{ij}A^j{}_k$.

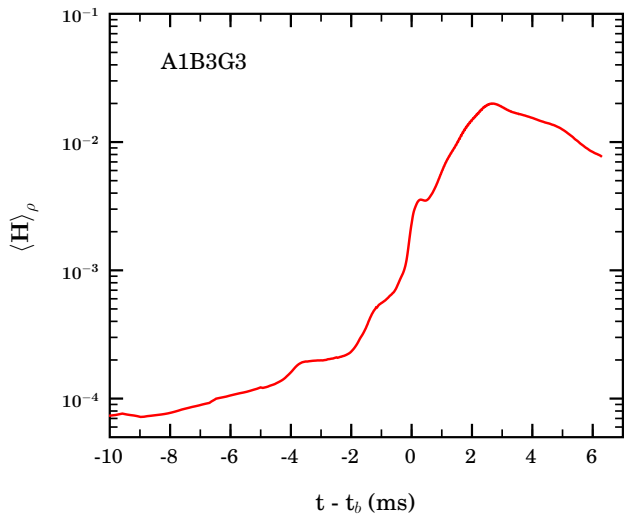

Figure 5.23: Evolution of the density-weighted mean Ricci-normalized matrix norm of the Cotton-York tensor as specified in equations (5.10–5.11) in model A1B3G3 (type I) at times shortly before and after core bounce. $\langle H \rangle_\rho$ peaks at $\sim$2% which is at the same order of magnitude, but a factor of two smaller than the maximum $\langle H \rangle_\rho$ found by [542] for binary neutron stars at orbital separations nearly double that of their innermost stable circular orbit.

introduced a baryonic density weighted norm

$$\langle H \rangle_\rho = \frac{\int d^3x H \sqrt{\gamma} \rho W}{\int d^3x \sqrt{\gamma} \rho W} \ . \tag{5.11}$$

In close collaboration with Erik Schnetter, I have implemented equations (5.9–5.11) in CCW, using second-order accurate symmetric finite differences. Since Y^{ij} contains third spatial derivatives of the 3-metric, it is very sensitive to high-frequency content in the metric variables. Tests with a spherically symmetric TOV matter spacetime showed convergence to zero for (5.11) on the initial data slice, but exhibited large finite-difference errors on the 10^{-7} level for $\langle H \rangle_\rho$ during evolution. I have performed a test simulation for model A1B3G3 of the ZM/DFM model series (see table 5.1) using BSSN_MoL in fourth-order accurate mode and tracked $\langle H \rangle_\rho$ until a few ms after bounce. The results are shown in figure 5.23. While the details of qualitative $\langle H \rangle_\rho$ evolution require a detailed analysis in future work, the overall picture is quite clear: $\langle H \rangle_\rho$ peaks at and stays below the percent level even at early postbounce times in model A1B3G3. If one considers model A1B3G3 as a representative model and trusts the normalization of H by the magnitude of the covariant derivative of the 3-Ricci tensor, then one may state that stellar core collapse spacetimes differ from CFC by not more than $\sim$1% during collapse and the early postbounce phase. The later postbounce evolution of $\langle H \rangle_\rho$ is unknown. For the promptly exploding polytropic progenitors considered here, it will most likely stay around or below the percent level. More realistic models whose protoneutron star experiences a prolonged period of accretion of outer core material or models that become close to or undergo black hole formation will significantly deviate from conformal flatness and a full GR treatment becomes indispensable.

Chapter 6

GR Core-Collapse Simulations: Realistic Progenitors

The work presented in this chapter has been carried out in collaboration with Harald Dimmelmeier, who has performed axisymmetric counterpart simulations in conformally-flat general relativity with the CoCoNuT code. A short report on the results has been submitted to a scientific journal [10].

In this chapter, I present results that are obtained by means of the first simulations of rotating stellar iron core collapse in {3+1} GR with a finite-temperature equation of state (EOS), an approximate treatment of deleptonization during collapse, and supernova progenitor models from state-of-the-art stellar evolutionary calculations.

In direct continuation of the simulations discussed in the previous chapter, all results are obtained with the Cactus/Carpet/Whisky (CCW) method introduced in Chapter 3. The Hybrid EOS (§ 3.5.5) is replaced by the finite-temperature Shen EOS ([464, 465] and § 3.6.2) and advection of the electron fraction Y_e, deleptonization, and neutrino pressure effects are taken into account as described in §3.6.

I begin with an overview on the employed supernova progenitor data and discuss model ingredients and parameters in detail. In §6.2, I present results from calculations starting out with spherically symmetric data and systematically lay out the effects of GR, electron capture, and neutrino radiation pressure during collapse and core bounce. I shall demonstrate that the changes brought about by including the approximate electron capture treatment are tremendous, and that GR significantly alters the dynamics from the Newtonian case and should not be neglected in core-collapse supernova calculations.

In §6.3 I discuss the axisymmetric collapse, bounce, and postbounce dynamics and present new estimates for the axisymmetric gravitational wave signature of these phases. I investigate the effects of variations in the degree of differential rotation, initial rotation rate, and progenitor structure on the gravitational wave signature of rotating core collapse, bounce, and early postbounce phases. In addition, I compare calculations with and without neutrino pressure contributions, with various degrees of deleptonization during collapse and also present comparisons to results obtained with the CoCoNuT code.

§6.4 discusses the development of genuinely 3D spatial structure and dynamics that develop in a number of models over several tens of milliseconds after core bounce and are most likely related to a dynamical low-$T/|W|$ rotational instability of the protoneutron star (PNS). This instability goes along with prolonged narrow-band gravitational wave emission from its quadrupole components.

The prospects for detection of the gravitational waves emitted in the models considered here by current and future gravitational wave observatories are assessed in §6.5 and in §6.6 I summarize my conclusions concerning the generic features of the gravitational wave signature of rotating iron core collapse and postbounce nonaxisymmetric dynamics.

6.1 Astrophysical Considerations, Model Suite, Simulation Parameters

In spherical symmetry, the GR field equations have zero dynamical degrees of freedom. No gravitational waves can be emitted (e.g., [116]). The same is true for static and even stationary configurations in axisymmetry. On the other hand, gravitational waves will be emitted by any mass (or curvature) configuration with a non-vanishing time-varying quadrupole moment[1].

Fortunately, as astronomical observations have shown (e.g., [543–547]), most massive stars on the main sequence rotate with typical equatorial surface velocities $\sim$200 km s^{-1} [543] which corresponds to $\sim$10% of their Keplerian breakup speed. Hence, there is hope that at the end of the nuclear-fuel burning stellar life the precollapse iron core might contain sufficient angular momentum to yield a significant deviation from spherical symmetry during collapse and core bounce and emit gravitational waves of sizable amplitudes during these highly dynamic phases. However, while observations can procure information about the surface rotational velocities, we have currently no means for studying empirically the internal rotational structure of evolving massive stars in any detail. Furthermore, all to-date available theoretical predictions of presupernova structure are based on spherically symmetric calculations. These have either neglected rotation completely or included rotational effects and angular momentum redistribution in a semi-phenomenological and parametrized way (see §3.7.3, and [38, 273, 506–511, 548]). Until multi-D stellar evolutionary calculations from zero-age main sequence (ZAMS) to the onset of core collapse become technically and computationally feasible, all predictions of the precollapse iron core rotation rate and angular momentum distribution should be considered with caution.

Given the uncertainties associated with the rotational configuration of precollapse iron cores, it is common practice to perform parameter studies, prescribing a rotation law and working in a parameter space spanned by the degree of initial differential rotation and initial rotation parameter[2] $\beta = T/|W|$ [9, 11–14, 30, 162, 260, 276, 277]. With the exception of [9] none of these studies have investigated the impact of variations in presupernova structure on the gravitational wave signal.

In this study I follow a two-fold approach and use two sets of supernova progenitor models. The first set encompasses model s11.2, s15, s20, and s40 (ZAMS mass of 11.2, 15, 20, and 20 $M_\odot$, respectively; at solar metallicity) of Woosley, Heger, and Weaver [38]. These models were evolved without rotation. In figure 6.1 I compare the matter density and electron fraction profiles of the presupernova models. Also shown are models of the second progenitor set discussed below and data for a standard $n = 3$ polytrope used in numerous previous studies [12, 13, 30, 162, 264, 266, 276, 277, 549]. Note that model s11.2 has the most compact iron core of all models considered in this study. Also note that model s20 is more compact and has a smaller iron core mass than model s15 that is smaller in ZAMS mass (table 6.1). The polytrope density profile exhibits the overall largest densities at radii between $\sim$400 and $\sim$600 km while dropping off to unphysically low densities shortly after. That realistic iron cores are not simple polytropes is also vividly displayed by the electron fraction plot in figure 6.1: While electron capture during silicon burning has neutronized the inner regions of the iron cores, the polytrope assumes a constant Y_e at 0.5. Figure 6.2 portrays the initial radial entropy distribution in the presupernova models. Note that all models have their global entropy minima at small radii and that higher ZAMS mass models have higher central entropies than lower mass models. This is due to the highly compact state of matter at the densities prevailing in the central-most iron core regions and to the fact that more massive models tend to be slightly less centrally condensed than lower mass models at the precollapse stage [509, 511].

Initial curvature data are generated in the Newtonian metric approximation [115], according to what is stated in §3.7.3. All considered progenitor models are unstable and exhibit initial infall velocities on the order of 10^7 cm s^{-1}. Nothing artificial need be done to initiate collapse. Rotation is introduced using the standard rotation law [9, 12, 30]

$$\Omega(\varpi) = \Omega_c \frac{A^2}{A^2 + \varpi^2} \,, \tag{6.1}$$

where ϖ is the distance from the rotation axis, and A governs the degree of differential rotation

[1] The time variation must be non-constant, i.e., change with time as well.

[2] β_{initial} denotes the initial (precollapse) value. β and $T/|W|$ are used interchangeably throughout this work.

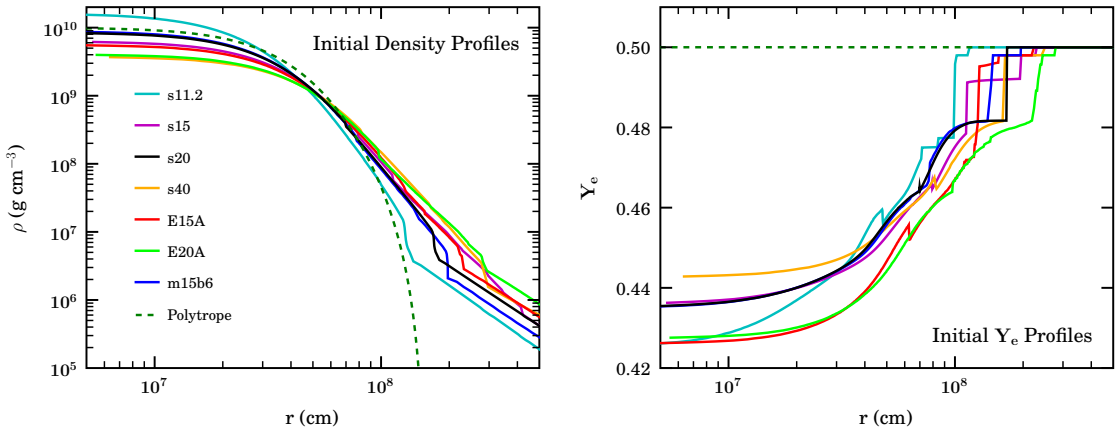

Figure 6.1: Left Panel: Initial baryonic rest mass density as a function of radius of the s11.2, s15, s20, s40 presupernova models of [38], of the "rotating" progenitors E15A and E20A of [509] and of the "magnetic rotating" model m15b6 of [511]. In addition, the density profile of an $n = 3$ polytrope with $Y_e = 0.5$ and a central density of 1.0×10^{10} g cm^{-3} is plotted. Model s20 is used most extensively throughout this work. See text for details. Right Panel: Initial electron number fraction per baryon Y_e vs. radius for the same set of presupernova models.

(for $\varpi < A$ the initial rotation is roughly solid body, and at $\varpi = A$, $\Omega = \Omega_c/2$). Ω_c is determined by setting $\beta_{\rm initial}$. This rotation law enforces constant angular velocity on cylinders according to the Pointcaré-Wavre theorem. It states that rotating Newtonian fluid bodies supported by degeneracy pressure tend to assume constant specific angular momentum on cylinders [504]. It is important to point out that rotation is introduced in an ad hoc fashion and the initial models are *not* in rotational equilibrium, since such equilibrium configurations can only be found consistently for isentropic models with constant electron fraction [550]. Despite the emphasis various studies have put on the importance of initial models in rotational equilibrium [12, 30], it is unlikely that the non-rotational-equilibrium nature of the initial models considered here will alter the dynamics in the plunge, bounce, and early postbounce phases in any significant way. Collapse proceeds slowly enough to allow for the adjustment of the core to the appropriate angular density stratification for its rate of rotation. [11, 30] point out that the use of non-rotational-equilibrium models is justified in this case. I name the models according to the following convention which I adopt from my previous work [9]: [progenitor name]A[A in km]β[$\beta_{\rm initial}$ in %].

I choose model s20 to be the representative baseline model and consider moderately differential rotation with A set to 1000 km. This is motivated by the supposition that angular momentum gradients are smoothed out in convective nuclear burning regions [88, 509] and that hence the entire central iron core region is likely to be in approximate solid-body rotation. To investigate the effect of more rigid and more differential rotation, I perform calculations with A set to 50000 km and $A = 500$ km.

Table 6.1: Suite of supernova progenitor models used in this study. The ZAMS mass is the stellar model mass at zero-age main sequence in solar masses. ρ_c is the precollapse central core density. $R_{\rm Fe}$ and $M_{\rm Fe}$ are the radius and the mass of the iron core (determined by the discontinuity in the electron fraction Y_e at the outer edge of the iron core where $Y_e \sim 0.5$), respectively. For models that were evolved with a 1D prescription of rotational effects and angular momentum redistribution, the initial ratio of rotational kinetic to gravitational energy, $\beta_{\rm initial}$, is given. Note that for such models, $\beta_{\rm initial}$ also depends on the physical extent of the computational domain.

Model Name	References	ZAMS Mass ($M_\odot$)	ρ_c (10^9 g cm^{-3})	$R_{\rm Fe}$ (10^8 cm)	$M_{\rm Fe}$ ($M_\odot$)	$\beta_{\rm initial}$ (%)
s11.2	[38]	11.2	15.75	1.16	1.28	—
s15	[38]	15.0	6.16	2.29	1.62	—
s20	[38]	20.0	8.42	1.70	1.46	—
s40	[38]	40.0	3.65	2.50	1.79	—
E15A	[509]	15.0	5.43	2.22	1.62	0.58
E20A	[509]	20.0	3.97	2.78	1.84	0.37
m15b6	[511]	15.0	8.78	1.95	1.47	9.60×10^{-4}

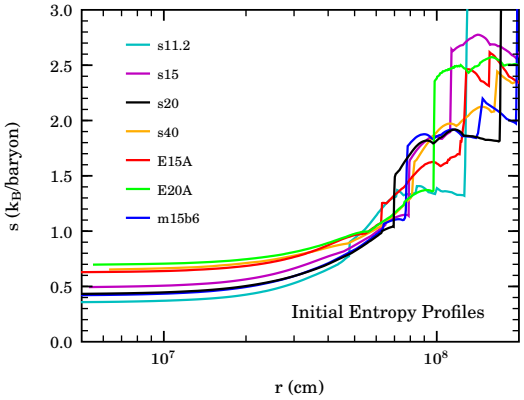

Figure 6.2: Initial entropy radial profile of all models considered in this study. The entropy is given in units of the Boltzmann constant per baryon. Note that models with greater ZAMS mass have higher central entropies, that is, are hotter than less massive models. Also note that despite the high temperatures all models exhibit global entropy minima in the central-most regions of their iron cores. This is due to the highly ordered state of matter at the densities prevailing deep inside the core.

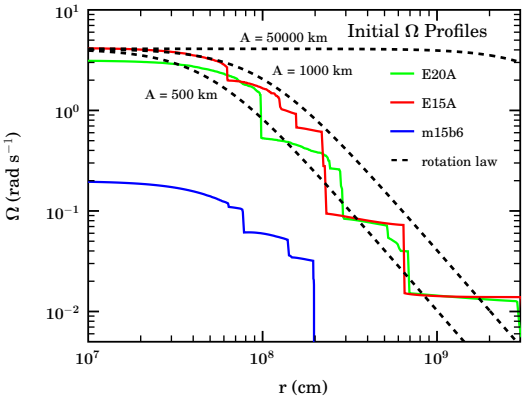

Figure 6.3: Initial angular velocity profiles of the rotating 15 and 20 $M_\odot$ (ZAMS) presupernova models of [509] and the 15 $M_\odot$ magnetic and rotating presupernova model of [511]. In addition, the initial angular velocity profile of models that are set into rotation according the rotation law of equation (6.1) with A set to 500, 1000, and 50000 km is shown and with Ω_c set to the value of that of model E15A to illustrate the qualitative behavior of the rotation law.

Due to the high computational cost associated with these 3D calculations, I perform only a single calculation each for models s11.2, s15, and s40 in order to investigate the effect of progenitor structure on the gravitational wave signal.

For $\beta_{\rm initial}$ I choose values in the range from 0.25% to 4.00%. While even $\beta_{\rm initial}$ = 0.25% will lead to a PNS spinning too fast to explain observed pulsar birth spin rates (unless there exists a currently unknown, efficient spin-down mechanism; see [273]), they fall in the range of what has been considered in previous studies [9, 11, 12, 30] and are consistent with theoretical predictions for progenitor stars in which angular momentum redistribution by magnetic fields is not present or ineffective [113, 114, 509–511]. In table 6.2, I summarize important model parameters.

The second set of presupernova models (in the following *Heger models*) that I consider consists of models E15A, E20A [509], and m15b6 [511]. These progenitors were evolved to the onset of core collapse with the approximate treatment of rotation described by [509], but centrifugal forces were included only until the end of core carbon burning. Models E15A and E20A are relatively fast rotators with initial β of 0.37% and 0.58%, respectively. In model m15b6, angular momentum redistribution by magnetic torques was included which led to slow and slightly more rigid rotation of its iron core as can be inferred from figure 6.3 in which I contrast the precollapse angular velocity profiles of the three Heger models and the rotation law (6.1) for various choices of A. In the left panel of figure 6.1 I compare the precollapse density profiles of the Heger models with those of the nonrotating progenitors of [38]. The slowly rotating m15b6 has a density structure very similar to that of the nonrotating s20 model, while model E15A comes close to s15 and E20A matches with the nonrotating s40 model.

The Heger models are incorporated into the CCW simulation in the same manner as the first set of models and their 1D angular velocity is mapped to 3D under the assumption of constant angular velocity on cylinders.

All calculations are performed with the standard set of simulation and code parameters previously used for the polytropic initial models of Chapter 5. In WHISKY, PPM reconstruction and the Marquina flux formula or the HLLE solver are employed. BSSN_MOL is run in second-order accurate mode with $1 + \log$ slicing and the Γ_S shift. Time integration is carried out by MoL using the iterative Crank-Nicholson ODE integrator with 3 steps and a Courant factor of 0.375. A significant number of calculations with the s20 and E20A models are performed in bitant mode assuming only discrete symmetry with respect to the equatorial plane. All calculations involving the s11.2, s15, s40, E15A,

and m15b6 progenitors are carried out in octant[3] mode with periodic "rotating" boundary conditions on the x-z and y-z faces. In these calculations all non-axisymmetric azimuthal models whose m is not an integer multiple of 4 are suppressed.

In all model calculations I employ the Shen EOS (see §3.6.2) and advect Y_e with the fluid. Since nuclear statistical equilibrium (NSE) prevails, Y_e is the single most important compositional variable [36]. Deleptonization is treated during collapse as described in §3.6.3; it is active by default. I call all models including it *non-adiabatic* since matter energy corrections due to thermalizing neutrinos in the neutrino semi-transparent regime are taken into account during collapse. The deleptonization data $Y_e(\rho)$ are derived from detailed 1D calculations with Boltzmann radiative transfer and an approximate treatment of GR effects in the VERTEX code [85, 86, 551] carried out by A. Marek [469]. These calculations are performed with the Shen EOS and include standard rates for electron capture on protons and heavy nuclei.

Deleptonization is deactivated at core bounce which (in this context) is defined by the moment when the entropy on the edge of the inner core reaches 3 k_B/baryon and nuclei start to dissociate [3]. After bounce no further deleptonization is taken into account while the electron fraction continues to be advected with the fluid. The neglect of postbounce neutrino losses limits the quality of my models, but is unlikely to significantly alter the bulk dynamics of matter during the early postbounce phases considered in this study. However, it clearly diminishes any capability of the present approach to answer more general questions on the supernova mechanism.

Neutrino radiation pressure effects are taken into account in the neutrino optically-thick regime only where β-equilibrium (e.g., [3]) prevails and electron neutrinos and antineutrinos can be treated as a two-component Fermi gas according to the prescription presented in §3.6.4. Neutrino pressure and energy effects are considered as additional source terms for the momentum and energy equations and appear as additional pressure and energy contributions in the stress-energy tensor. In the semi-transparent and optically-thin regimes, the Fermi gas approximation does not hold and neutrino radiation pressure contributions are neglected[4].

[3] Bitant mode saves a factor of 2 in computational resources to full mode. Octant mode saves a factor of 8, but restricts the growth of genuine 3D structures. In §4.3 I compare bitant to full mode and find that for models in which no convection develops equatorial symmetry is maintained. In the models considered here, convection will develop and equatorial symmetry is unlikely to remain preserved. Due to the factor of 2 in computational costs it has been impossible to carry out a calculation in full mode.

[4] This is a reasonable approximation since neutrino (radiation) pressure effects are small outside the trapped region and certainly cannot significantly influence the dynamics of the dense inner core.

Table 6.2: List of models and their parameters considered in this study. Test calculations are not listed. RH denotes the employed refinement hierarchy (see Appendix E), A is the rotation parameter governing the degree of differential rotation and Ω_c is the initial central angular velocity. J is the total angular momentum on the grid and $\beta_{\rm initial}$ is the initial ratio of rotational kinetic energy T to gravitational energy $|W|$. Note that both J and T also depend on the extent of the computational domain, that is, how much of the progenitor star is covered by the latter. This is of particular relevance for almost uniformly rotating models. See §3.9.2 for the expressions used to compute J and $\beta_{\rm initial}$.

Model Name	RH	A (10^8 cm)	Ω_c (rad s^{-1})	J (10^{49} erg s)	$\beta_{\rm initial}$ (%)	Notes
s20nonrot	RHII	—	—	—		
s20A500β0.50	ORHIIe	500	6.179	0.59	0.50	(1)
s20A500β0.90	ORHIIeHR	500	8.291	0.77	0.90	(1)
s20A500β1.80	ORHIIeHR	500	11.733	1.09	1.80	(1)
s20A50000β0.25	RHII	50000	0.654	2.55	0.25	
s20A50000β4.00	RHII	50000	4.239	9.90	4.00	
s20A1000β0.25	RHII	1000	2.497	1.99	0.25	
s20A1000β0.50	RHII	1000	3.526	2.81	0.50	
s20A1000β0.90	RHIIe2	1000	4.730	3.76	0.90	
s20A1000β1.80	RHIIe2	1000	6.679	5.54	1.80	
s11.2A1000β0.5	ORHIIe2	1000	4.182	1.95	0.50	(1)
s15A1000β0.5	ORHIIe	1000	3.187	3.51	0.50	(1)
s40A1000β0.5	ORHIIe2	1000	2.974	4.70	0.50	(1)
E20A	RHIIe	—	3.128	3.15	0.37	
E15A	ORHIIeHR	—	4.176	3.18	0.59	(1)
m15b6	ORHIIe	—	0.198	0.10	9.60×10^{-4}	(1)

Notes. — (1) Simulation performed in octant mode with reflection symmetry on the equatorial plane and rotating periodic boundary conditions on the x-z and y-z faces. (2) Simulation performed without neutrino pressure contributions. (3) Adiabatic: Simulation performed without deleptonization and neutrino pressure contribution.

6.2 Spherically Symmetric Collapse

Before indulging into the discussion of the axisymmetric collapse and bounce dynamics and its reflection in the core-collapse supernova gravitational wave signature, it is pertinent to first consider the collapse of spherically symmetric initial data to clearly separate the various effects of the new physics ingredients in the absence of angular momentum and due centrifugal effects.

I perform three calculations with model s20 in 3D CCW. My baseline calculation s20nonrot is run with deleptonization during collapse and neutrino radiation pressure effects in the neutrino optically-thick regime above $\sim 2\times 10^{12}$ g cm^{-2}. s20nonrot is the first calculation ever that tracks stellar core collapse in full {3+1} GR at this level of astrophysical and microphysical detail. Despite the limitation to zero angular momentum and in contrast to the simplicity typically attributed to spherically symmetric calculations, s20nonrot marks a great advance in bringing together numerical relativity with supernova theory in particular and astrophysical relativity in general. The baseline calculation is complemented by s20nonrot-nnp in which I include deleptonization but neglect any neutrino pressure contributions, and by s20nonrot-ad in which neither deleptonization nor neutrino pressure is included and in which collapse proceeds adiabatically. In the following, I dub s20nonrot and s20nonrot-nnp "non-adiabatic", while s20nonrot-ad is the "adiabatic"[5] model. To assess the differences brought about by GR in iron core collapse, I include data from a 1D Newtonian calculation carried out by H. Dimmelmeier with the CoCoNuT code in Newtonian mode. This calculation employs all deleptonization/neutrino pressure effects and, of course, makes use of the Shen EOS. I call this calculation "Newtonian". With the exception of the adiabatic model, all model calculations are carried out to postbounce times of at least 10 ms.

Panel (a) of figure 6.4 depicts the evolution of the central (= maximum) rest mass density in the four calculations. I first focus on the differences seen when comparing the adiabatic to the non-adiabatic calculation. The non-adiabatic models reach core bounce some 28 ms earlier and overshoot to ∼30% lower maximum densities than the adiabatic model in which the central electron fraction stays practically constant throughout collapse (figure 6.4 (b)). As has been first pointed out explicitly in the article [68] by van Riper and Lattimer, these effects are entirely due to the reduction of the electron fraction during collapse and can be understood in more detail by considering an *effective* adiabatic index calculated along a collapse trajectory of a Lagrangian mass element M:

$$\Gamma_{\text{effective}} = \left.\frac{D\ln p}{D\ln\rho}\right|_M = \left.\frac{\partial\ln p}{\partial\ln\rho}\right|_{s,Y_e} + \left.\frac{\partial\ln p}{\partial\ln Y_e}\right|_{\rho,S}\left.\frac{\delta\ln Y_e}{\delta\ln\rho}\right|_M + \left.\frac{\partial\ln p}{\partial\ln Y_\nu}\right|_{\rho,S}\left.\frac{\delta\ln Y_\nu}{\delta\ln\rho}\right|_M + \left.\frac{\partial\ln p}{\partial S}\right|_{\rho,Y_e}\left.\frac{\delta S}{\delta\ln\rho}\right|_M , \tag{6.2}$$

where Y_ν is the number of electron neutrinos per baryon. The first term is the standard adiabatic Γ as obtained from the EOS (Γ_{EOS}). Since core collapse goes along only with small entropy changes [3, 68, 530], the last term in equation (6.2) is small. In the optically thin regime, neutrinos can stream out with little scattering and momentum/energy transfer to the surrounding matter; thus the third term remains small until neutrinos become trapped. The second term, however, is large throughout infall, and, importantly, negative due to electron capture. The EOS below nuclear density is dominated by relativisticly degenerate electrons and if one assumes free escape for the created neutrinos, one obtains a simple expression for the effective adiabatic index [68, 530]

$$\Gamma_{\text{effective}} = \left.\frac{\partial\ln p}{\partial\ln\rho}\right|_{s,Y_e} + \frac{4}{3}\frac{1}{Y_e}\frac{\delta Y_e}{\delta\ln\rho} , \tag{6.3}$$

hence $\Gamma_{\text{effective}} < \Gamma_{\text{EOS}}$ if $\delta Y_e < 0$. A lower effective adiabatic Γ relates to lower pressure support, hence this demonstrates that the density-dependent deleptonization reduces the effective adiabatic index and thus leads to a destabilization of the collapsing core, while $\Gamma_{\text{effective}}$ remains very close to 4/3 in the adiabatic calculation. This explains the shorter time to core bounce in the non-adiabatic models. Another direct consequence of electron capture (and the resulting lower $\Gamma_{\text{effective}}$) is a reduction in the size of the *inner core*. As pointed out before (see §2.3.2 and §5.1), during iron core

[5] Strictly speaking, "adiabatic" implies only "zero entropy change". I use it interchangeably with "no deleptonization". This is common practice in the literature. See, e.g., [3, 64, 530].

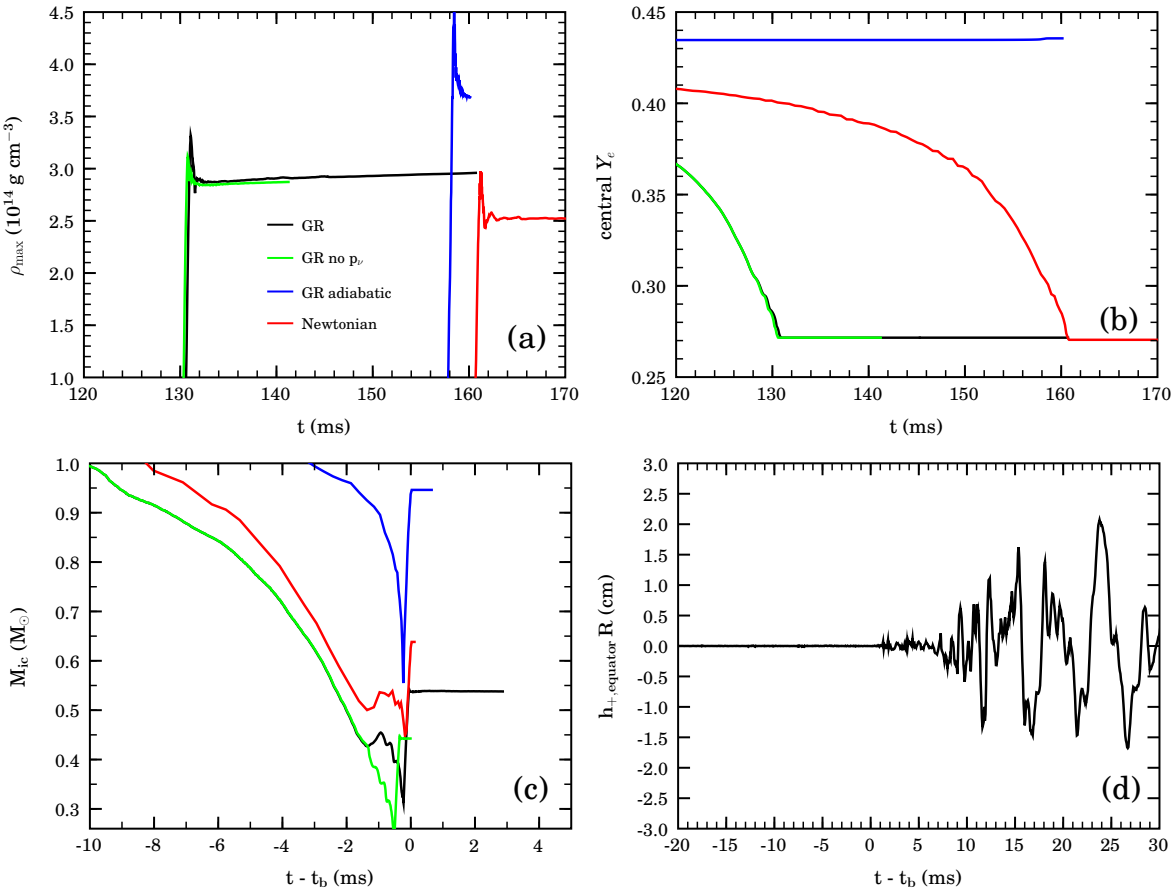

Figure 6.4: s20 model calculations with spherically symmetric initial data. Comparison of calculations in GR with all neutrino/deleptonization effects, in GR without neutrino pressure contributions, in GR, but purely adiabatic, and in Newtonian gravity with all neutrino/deleptonization effects. The Newtonian calculation was run in 1D with the CoCoNuT code [160, 161] and the data were kindly provided by H. Dimmelmeier. Panel (a): Evolution of the maximum density on the grid as a function of time. Note that the non-adiabatic Newtonian run reaches core bounce tens of milliseconds later and bounces at lower ρ_{max} than the non-adiabatic GR calculations. This is expected due to the decreased stability of the precollapse structures in GR [63, 67] and is in accord with what was found by [552]. The adiabatic GR calculation reaches core bounce $\sim$28 ms later and at $\sim$50% larger ρ_{max} than the non-adiabatic GR calculations. This is owing to the stronger pressure support during infall without deleptonization and to the resulting large quasi-homologous core in the adiabatic calculation. Panel (b): Evolution of the electron fraction (Y_e) at the stellar center. According with the Liebendörfer prescription [476], deleptonization is deactivated at core bounce. All non-adiabatic calculations exhibit similar behavior while the adiabatic GR calculation sees a slight increase of the central Y_e during collapse due to advection effects. Panel (c): Evolution of the mass of the homologous inner core (M_{ic}) at times relative to the time of core bounce. M_{ic} is measured according to equation (6.4) and encompasses all material that is in sonic contact and unshocked, i.e., with specific entropy $s < 3$. This is the mass of the inner core at core bounce typically referred to in the literature. Note the very large M_{ic} of the adiabatic calculation. The non-adiabatic calculation without neutrino pressure contributions exhibits the smallest M_{ic} while the non-adiabatic Newtonian calculations yields a M_{ic} that is roughly 20% larger than in both GR calculations. This is in accord with standard estimates [3, 64] and with what was found by [81, 83, 552]. Note that the "no p_ν" graph is shifted back by $\sim$0.3 ms to allow a better appreciation of the neutrino pressure effects. Panel (d): Gravitational wave signal of the non-adiabatic baseline GR run. It is zero until $\sim$1 ms after core bounce and then exhibits gravitational wave emission at amplitudes $\sim$1 order of magnitude smaller than fiducial rotating models. The graph is representative for all three 3D calculations in CCW and proves that spherical symmetry (of course, only up to $\ell = 4, m = 4$ grid contributions) is maintained to high precision until postbounce times when convective motions in the Ledoux-unstable regions behind the shock set in quickly due to the large Cartesian grid seeds ($m = 4$ on the $\sim$0.5–1% level).

collapse an inner subsonically collapsing core develops (dubbed homologous core[6] collapsing, due to the self-similarity represented by $v \propto r$) that is joined with the supersonically collapsing outer core at the sonic point. It is the material of the inner core that coherently experiences core bounce and launches the bounce shock into the still infalling out-of-sonic-contact outer core. The size of the inner core does not only determine the mass of the infalling material that remains to be dissociated by the shock, but additionally, it determines (in a rotating model) the amount of angular momentum that may become dynamically relevant during the final phases of collapse and, perhaps most importantly, it determines the initial kinetic energy imparted to the bounce shock (see, e.g., [64] and references therein). In my calculations, I define $M_{\rm ic}$ as

$$M_{\rm ic} = \int\limits_{\substack{0 \\ \text{where } s<3\,k_{\rm B}}}^{r_{\rm sonic}} W\rho\sqrt{\gamma}d^3x \ , \tag{6.4}$$

where $r_{\rm sonic}$ is the radius of the sonic point in the equatorial plane that separates inner core and outer core and the specific entropy criterion $s < 3$ ensures that only unshocked material is counted as part of the inner core.

In their analytic work, Goldreich & Weber [65] and Yahil [66] have shown that the mass of the inner core ($M_{\rm ic}$) is well approximated by

$$M_{\rm ic} \simeq (K/K_0)^{3/2} M_0 \ , \tag{6.5}$$

where K is the coefficient in the polytropic EOS, $p = K\rho^\Gamma$ with $\Gamma \approx 4/3$, and where the index 0 denotes the values of the corresponding quantities at the point where collapse sets in. Considering the polytropic coefficient for the degenerate ultra-relativistic electron Fermi gas [36],

$$K = \frac{\hbar c}{4}(3\pi^2)^{1/3}\left(\frac{Y_e}{m_B}\right)^{4/3} , \tag{6.6}$$

it is straightforward to realize the strong Y_e^2 dependence of the inner core mass while keeping in mind that both equation (6.5) and equation (6.6) are simple estimates and are only precise if the EOS is polytropic.

During collapse, the central Y_e in the non-adiabatic models drops from $\sim$0.435 at the onset of collapse to $\sim$0.27 at core bounce (figure 6.4 (b)). The adiabatic model, on the other hand, has a constant central Y_e. In panel (c) of figure 6.4, I compare the inner core masses shortly before and at core bounce. As expected, the non-adiabatic baseline GR model yields an inner core mass at core bounce of $\sim$0.54 $M_\odot$ which is almost a factor of 2 smaller than that of the adiabatic model ($\sim$0.94 $M_\odot$). Hence, while the non-adiabatic models reach core bounce sooner than their adiabatic counterpart, the amount of inertial mass whose momentum is coherently reversed during bounce is much larger in the latter calculation, leading to the observed overshoot to much larger supernuclear densities (figure 6.4 (a)). Although I do not follow the adiabatic model to significant postbounce times, it is clear from above considerations that its bounce shock is quite energetic and has much less outer core material to dissociate than in the non-adiabatic models. It is hence unlikely to stall[7] and will prompt-explode the star. On the other hand — and as depicted by figure 6.5 for the baseline calculation — the shock *does stall* in the non-adiabatic models and no prompt explosion occurs. This is due to (1) the lower initial energy that is imparted to the shock and (2) to continued energy losses to dissociation[8] of infalling iron-group nuclei into protons (at a cost of 8.8 MeV per nucleon) [3]. If weak-interaction physics were included at postbounce times, energy losses due to neutrinos would further decrease the shock energy (see, e.g., [3]). Note that in calculations that neglect deleptonization, but include a detailed finite-temperature EOS, (2) is accounted for and can in extreme cases lead to shock stall by itself [9].

[6] Dimmelmeier [18] who studied homologous collapse in 1D GR pointed out that due to GR effects, perfect homology is not obtained/preserved in the plunge phase for the central regions of the inner core. While the Newtonian collapse solutions [65, 66] yield self-similar solutions, any realistic stellar collapse will exhibit slight local deviations from homology because of local density/temperature/compositional variations.

[7] Note that shock stall — though at large radii and only for the most massive iron cores — has been observed by Ott et al. [9] to occur even in adiabatic models.

[8] The adiabatic calculation as well loses energy to dissociation of infalling material, but its higher shock kinetic energy allows a prompt explosion in most cases.

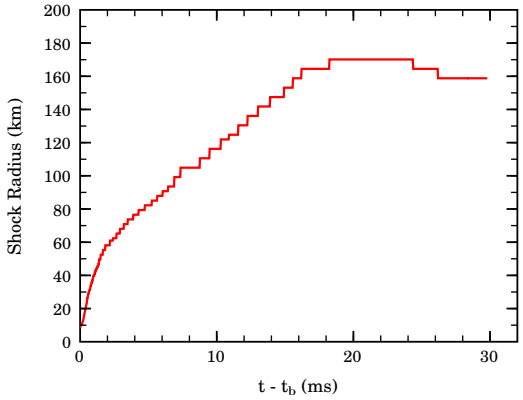

Figure 6.5: Radial shock position in the baseline calculation s20nonrot as a function of postbounce time. After formation the shock loses energy quickly to dissociation of infalling outer core nuclei and stalls eventually at a radius of ∼170 km and even slightly recedes towards the end of the simulation. The stair-like behavior of the shock radius is due to increasingly coarse resolution at large radii and to the postprocessing technique that is used to compute the shock position.

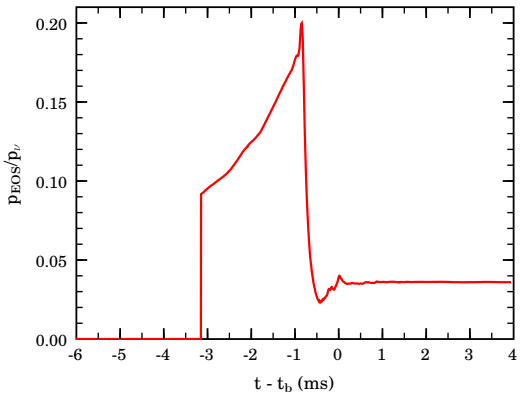

Figure 6.6: Relative magnitude of the neutrino pressure contribution with respect to the pressure given by the Shen EOS at the center of the collapsing core at times shortly before and shortly after core bounce. Once neutrino trapping is achieved at densities above $\sim 2\times10^{12}$ g cm^{-3} the neutrino part becomes increasingly relevant and reaches ∼20% just before the stiffening of the nuclear EOS that initiates core bounce. After bounce its relative importance at the PNS center drops to a few percent.

I turn now to the discussion of the impact of neutrino pressure contributions on the dynamics in the plunge phase of collapse. Model s20nonrot-nnp does not include neutrino pressure contributions but is otherwise identical to the baseline calculation. As can be inferred from figure 6.4 (a)[9] , this model reaches core bounce about 0.3 ms earlier than s20nonrot and overshoots to a ∼5% smaller maximum density. In addition, it does not show the small (barely visible in figure 6.4 (a)) postbounce minimum in $\rho_{\max}$ that is found in s20nonrot and in the Newtonian calculation. These differences can be understood by considering the stabilizing effect the neutrino pressure has on the inner core. Figure 6.6 shows the relative magnitude of the neutrino pressure compared with the fluid pressure returned by the Shen EOS at the center of the collapsing core. Before the neutrinos become trapped their pressure contribution is neglected. Above trapping and during the final phase of collapse, the neutrino contribution becomes increasingly large and reaches ∼20% of the electron/baryon pressure at about 1 ms before bounce. After that it quickly drops to ∼4% when the nuclear EOS stiffens and initiates core bounce. Hence, there is significant additional pressure support in model s20nonrot that is not present in s20nonrot-nnp. This leads to a slight slow-down of the plunge phase and, as panel (c) of figure 6.4 proves, to an increase in the size of the inner core in the last 2 ms before and at core bounce. This more massive inner core leads to the greater overshoot in $\rho_{\max}$ in s20nonrot compared with s20nonrot-nnp. Finally, it is worth noting that the influence of the neutrino-related contributions to the stress energy tensor is dynamically subdominant and the increased pressure support of the matter greatly outweighs the slightly stronger pull of gravity brought about by the inclusion of neutrino pressure and energy in the stress-energy tensor from the plunge phase on.

Comparing my baseline GR calculation results with the 1D Newtonian data, I find that s20nonrot reaches core bounce 23% (or ∼30 ms) earlier than its Newtonian counterpart. This accords with what other studies have found when comparing Newtonian and GR core collapse (e.g., [67–69, 83, 552] and references therein) and is caused by the decreased stability of the collapsing core in GR [12, 63, 67]. Collapse proceeds faster in GR and, importantly, GR's stronger gravitational pull leads to a decrease in the mass of the inner core at bounce.[10] (0.54 $M_\odot$ vs. 0.68 $M_\odot$ in the Newtonian calculation) while still leading to higher $\rho_{\max}$ at bounce and postbounce times.

[9] Note that the data of the model without neutrino pressure have been shifted in time by 0.3 ms in figure 6.4.

[10] Note that the M_{ic} that I find for s20nonrot at core bounce is slightly larger than what has been reported by [106] for the most recent electron capture rates on heavy nuclei by Langanke et al. [486]. The electron capture rates incorporated in the version of VERTEX [78, 85, 86] used for the $Y_e(\rho)$ parametrization employed here are based on [475, 485] and slightly underestimate the captures on heavy nuclei. See §3.6.3.

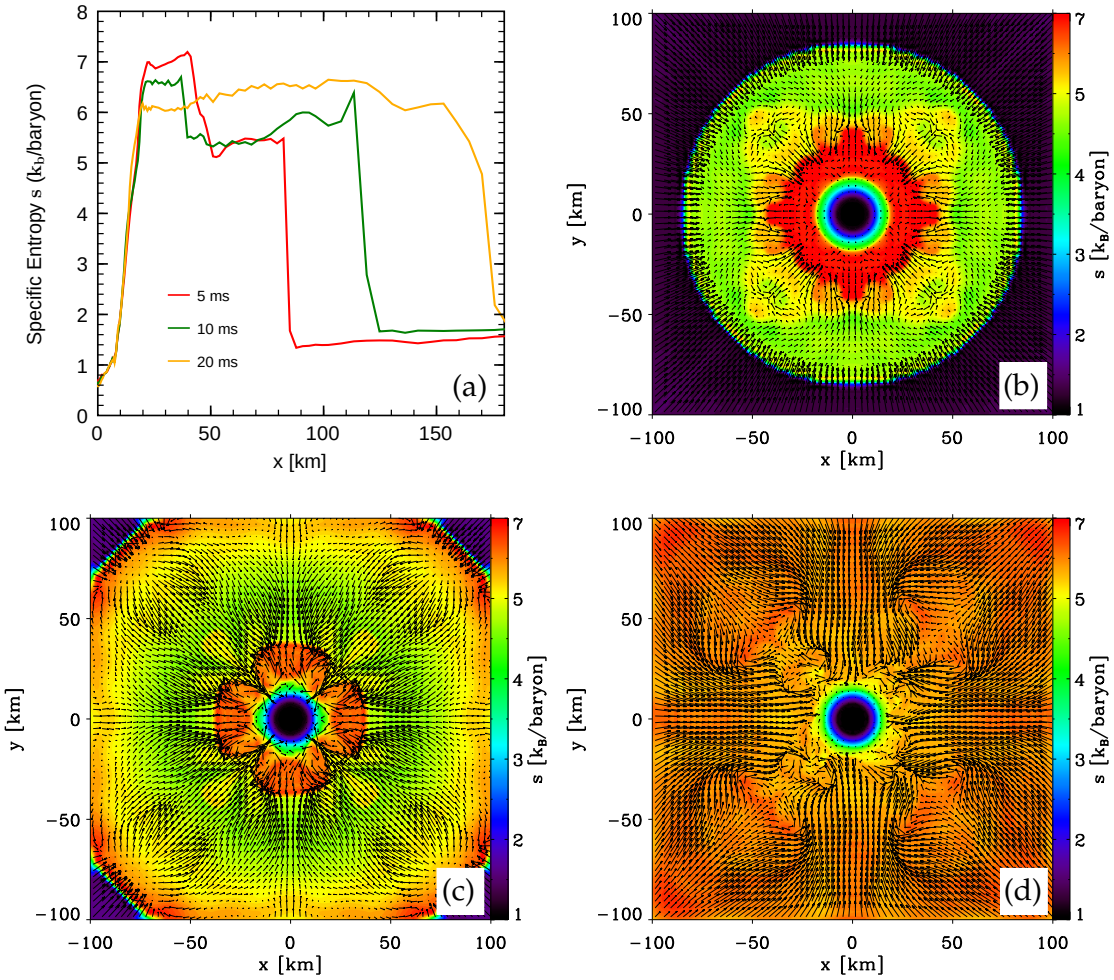

Figure 6.7: Panel (a): Specific entropy along the x-axis in model s20nonrot at 5, 10, and 20 ms after core bounce. The shock leaves behind a negative entropy gradient that dominates over the monotonically positive, but small gradient in Y_e and drives convective instability. It is smoothed out over a period of tens of ms. Panels (b-d): Slices of the specific entropy on the equatorial plane at 5, 10, and 20 ms after core bounce in panel b, c, and d, respectively. Shown are the inner 100 x 100 km^2 and velocity vectors are superposed. Overturn is seeded by the strong $m = 4$ (and higher integer multiples of 4) imprint of the Cartesian mesh. Initially, vortical motions are restricted to small radii close to the entropy drop but gradually spread through the entire area covered in the panels.

Panel (d) of figure 6.4 depicts the + gravitational wave amplitude in the baseline calculation as seen by an observer positioned at the equator. It is shown rescaled by the distance to the source and given in units of cm. It is important to note that there is no gravitational wave signal associated with core bounce. This proves that no artificial quadrupole moment is introduced by CCW in the entire collapse phase and speaks for the quality of the numerical methods employed.

A few ms after core bounce, aspherical fluid motions set in and lead to a growth of the gravitational wave amplitudes to non-negligible values (yet about an order of magnitude smaller than those observed for a weakly emitting type III rotating polytrope; §5.1.3). These non-radial fluid motions are messengers of the convective instability that develops behind the stalling supernova shock. The general condition for convection to occur in the realm of stellar/supernova interiors is given by the Ledoux criterion (e.g., [3, 282, 553–555] and references therein),

$$C_{\rm L} \equiv \left(\frac{\partial\rho}{\partial s}\right)\Big|_{Y,p} \frac{{\rm d}s}{{\rm d}r} + \left(\frac{\partial\rho}{\partial Y}\right)\Big|_{s,p} \frac{{\rm d}Y}{{\rm d}r} \ . \tag{6.7}$$

In the present context, most generally, $s = s + s_\nu$, where s is the fluid specific entropy per baryon

and s_ν is the specific neutrino entropy per baryon, and $Y = Y_l = Y_e + Y_\nu$. A region is unstable to convection if $C_\mathrm{L} > 0$. Since, generally [3, 282],

$$\left(\frac{\partial\rho}{\partial s}\right)\Big|_{Y,p} < 0 \ , \qquad \left(\frac{\partial\rho}{\partial Y}\right)\Big|_{s,p} < 0 \ , \tag{6.8}$$

negative radial gradients in Y and s favor convective instability. In fact, the outward propagating and weakening bounce shock leaves behind a large negative radial entropy gradient in model s20nonrot. This is apparent from figure 6.7 (a) and in combination with the seed perturbations introduced by the numerics and the Cartesian $m = 4$ grid mode[11], leads to the fast growth of vortical overturn motions that start at the large drop in entropy right behind the shock (Panel (b) in figure 6.7) and spread from there throughout the postshock region, equilibrating the entropy gradient and washing out the initial $l = 4, m = 0$ and $m = 4$ (and higher integer multiples of 4) structures over time (Panels (a), (c-d)).

Convection in the postshock region is a well known and extensively studied phenomenon in supernova theory [3, 72, 73, 77–80, 86, 279, 280, 282, 284, 555–563] and typically goes along with negative entropy and/or lepton gradients, the latter being a consequence of the burst of neutrinos being emitted from the immediate postshock region when the shock reaches the neutrinosphere, defined as the radius at which the optical depth τ of the matter to neutrinos is 2/3 and at which the neutrinos begin to decouple from the matter and free-stream (e.g., [70] and references therein). Since I neglect postbounce neutrino effects, there is in fact a slight positive gradient in Y_e present in the postshock region of s20nonrot. According to equation (6.7), it has a stabilizing effect on convection, but is dominated by the strong negative entropy gradient, resulting in the observed convective flow.

I point out that in the absence of significant rotation, convective overturn in combination with late-time SASI-type[12] instabilities of the stalled shock and, possibly, PNS core g-mode oscillations [15, 26, 343] is likely to be the major gravitational-wave emitting process in core-collapse supernovae [15, 95, 284]. The late-postbounce-time supernova gravitational wave signature is discussed in §7.2.

[11] I point out that for vanishing seed perturbations, the growth time to noticeable strength for convective instability would tend to infinity.

[12] SASI: Standing Accretion Shock Instability; see [26, 73, 86, 90, 92, 97–101].

6.3 Axisymmetric Dynamics and Gravitational Wave Emission

6.3.1 The s20A1000 Model Series

The moment rotation is added, spherical symmetry is broken and a symmetry axis, the rotation axis, is set. During collapse, angular momentum conservation leads to an increase of the angular velocity $\Omega \propto \varpi^{-2}$, where ϖ is the distance of a given mass element from the rotation axis[13]. At the same time, the specific centrifugal force is proportional to $\Omega^2\varpi$, hence increases with ϖ^{-3} during collapse. Depending on the precollapse angular momentum distribution, centrifugal support (a) may lead to significant oblate deformation of the collapsing core, and (b) may considerably slow down collapse and lead to core bounce at lower, possibly subnuclear, densities. In this section I focus on the axisymmetric collapse and bounce dynamics and the resulting gravitational wave signal. I postpone the discussion of nonaxisymmetric structure and dynamics to § 6.4.

I have discussed the dynamics of adiabatic rotating collapse in §5.1 and more detail can be found in [9, 11, 30]. For the present context it will be useful to recall that in Newtonian gravity for an effective adiabatic index $\Gamma_{\rm effective}$ (equation (6.2) on page 149) a critical value of $\beta = T/|W|$ exists beyond which rotation will stabilize a self-gravitating *rigidly-rotating* fluid body in equilibrium against pseudo-radial linear isentropic perturbations [9, 11, 30, 313, 504]. $\beta > \beta_c$ is a necessary condition for rotation to halt collapse in Newtonian gravity. This β_c is given by

$$\beta_c = \frac{1}{2}\frac{(4 - 3\Gamma_{\rm effective})}{(5 - 3\Gamma_{\rm effective})} \ . \tag{6.9}$$

In GR, this simple expression is as a lower bound for β_c [12, 63, 504] and the critical β for stabilization must be larger than above defined Newtonian $\beta_c + k\,(GM)/(Rc^2)$, where k depends on the stellar structure and angular momentum distribution [63]. In the limit of a $n = 3$ polytrope and zero β, $k \approx 6.75$. Note that differential rotation which shifts angular momentum and rotational energy to smaller radii generally leads to smaller β_c for collapse stabilization by centrifugal support[14] [9, 30, 313].

I begin my discussion of non-adiabatic rotating collapse with the s20A1000 model series. Models of that series are in approximate solid-body rotation throughout their iron cores (see figure 6.3 on

[13] For the sake of simplicity, I keep this argument Newtonian, setting coordinate distance equal to physical distance.

[14] Note that equation (6.9), even with GR corrections, can only be regarded as an approximate measure for β_c in fully dynamical collapse since it is derived for equilibrium configurations.

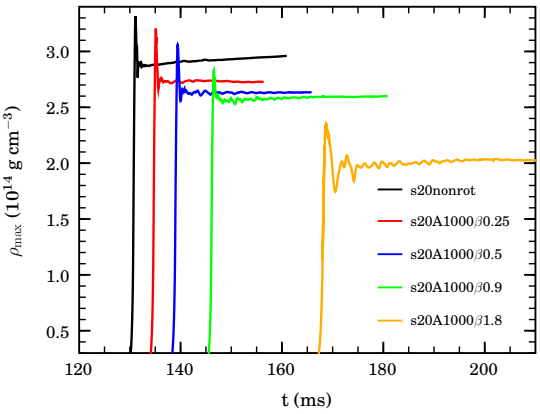

Figure 6.8: Maximum density ($\rho_{\rm max}$) of the s20A1000 model series, including the nonrotating baseline calculation. Rotation leads to an increase in the time to core bounce that scales $\propto \beta^2_{\rm initial}$ while the decrease in $\rho_{\rm max}$ at bounce is roughly linear. This indicates that although decelerating collapse, rotation does not govern the dynamics in the plunge and bounce phase.

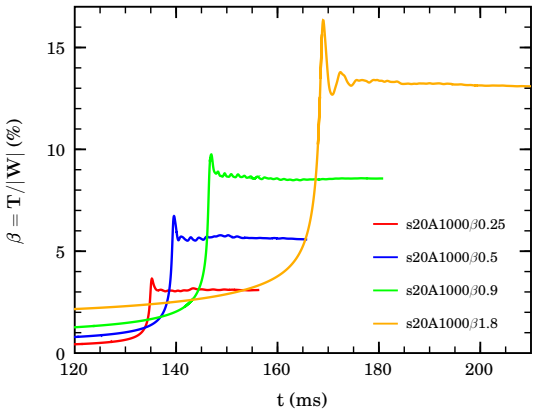

Figure 6.9: Evolution of the rotation parameter $\beta = T/|W|$ — a global integral quantity — for the s20A1000 model series. The times of the maxima in β correspond to the times of core bounce. Note that the increase in β at core bounce is approximately linear in $\beta_{\rm initial}$ for $\beta_{\rm initial} \lesssim 0.5\%$ and becomes sublinear for larger $\beta_{\rm initial}$. Model s20A1000β1.8 settles at a postbounce β of $\sim$13%, very close to the limit for classical secular nonaxisymmetric rotational instability [285] at 14%. See §6.4.

page 146). I perform four model calculations with initial βs of 0.25%, 0.5%, 0.9% and 1.8% to investigate the effect of increased angular momentum and rotational energy at a fixed degree of differential rotation.

Figure 6.8 shows the evolution of the maximum rest-mass density ($\rho_{\rm max}$) from the plunge phase of collapse through bounce and the postbounce phase for the s20A1000 model series. For comparison, I also plot $\rho_{\rm max}$ of the nonrotating baseline model. As can be seen, an increase in initial rotation rate maps to gradually later core bounce at lower maximum density. For small and moderate initial β, centrifugal effects during collapse are small and $\rho_{\rm max}$ and the time to core bounce exhibit a linear dependence on $\beta_{\rm initial}$. For large $\beta_{\rm initial}$, centrifugal support during infall becomes significant leading to a roughly $\beta^2_{\rm initial}$ dependence for the shift in core bounce time caused by rotation during the infall phase, while $\rho_{\rm max}$ at bounce still scales approximately inversely linear with increasing $\beta_{\rm initial}$. In combination with the fact that even in the fastest rotating model core bounce occurs at nuclear densities, this indicates that the plunge and bounce dynamics are even for $\beta_{\rm initial} = 1.8\%$ only affected, but not dominated by centrifugal forces.

In figure 6.9 I compare the evolution of β during collapse and bounce in the s20A1000 model series. β mirrors qualitatively the evolution of $\rho_{\rm max}$. In the infall phase, it gradually increases on a steepening slope towards the plunge phase and reaches its global maximum at core bounce from which it relaxes to a lower postbounce equilibrium value. With increasing $\beta_{\rm initial}$ and all else kept fixed, β at bounce $\propto \beta^{1/a}_{\rm initial}$, with $a \approx 1$ (linear) for models with $\beta_{\rm initial} \lesssim 0.5\%$ and $a > 1$ for models with larger $\beta_{\rm initial}$. This scaling of β is related to the stabilizing effects of rotation that become non-negligible at $\beta_{\rm initial} \gtrsim 0.9\%$ in the s20A1000 models. As a consequence, fast rotating collapsing cores reach lower maximum densities and overall lower compactness and, in general, for a given configuration of progenitor star model and degree of differential rotation, an "optimal" $\beta_{\rm initial}$ can be found that yields the largest β at bounce [9]. $\beta_{\rm initial}$ larger than this optimal value lead to decreasing β at bounce. Although I do not attempt to find such an optimal $\beta_{\rm initial}$ for the s20A1000 model series, model s20A1000β1.80's β at bounce may be close to the maximum possible β at bounce in this model series.

More visually manifest and appreciable are the rotational effects portrayed by figure 6.10 that contains snapshot z–x-slices of density and specific entropy taken at 2 ms after core bounce from models s20A1000β0.25, s20A1000β0.5, and s20A1000β1.80. As is expected, increased initial rotation leads to more pronounced flattening of the PNS and to increasing ratios of polar to equatorial elongation (axis ratios). Drawing a density cut at $\sim 1.0\times10^{12}$ g cm^3, I infer at 2 ms after bounce a moderate axis ratio of 1:1.15 for s20A1000β0.25, while I find 1:1.40 and 1:1.92 for models s20A1000β0.50 and s20A1000β1.80, respectively. These numbers will change during the continued postbounce evolution when the PNS accretes more high-angular momentum material and eventually settles to quasi-hydrostatic and rotational equilibrium. It is important to note that there is an apparent shift from oblate morphology at small radii to *prolate* morphology at intermediate radii seen both in the density and entropy distributions. During collapse and spin-up owing to angular momentum conservation, the iron core becomes increasingly oblate. Since centrifugal forces are strongest in equatorial regions, collapse proceeds more slowly on the equator than along the poles where the collapsing core experiences little centrifugal support. Net effects of this are that (a) the polar regions become thinned out as centrifugal force components accelerate the collapsing material towards greater ϖ and (b) that core bounce occurs earlier and without centrifugal support along the poles. The earlier and stronger bounce along the poles causes the apparent prolateness and is most manifest in the entropy distributions that become more polar peaked with increasing rotation. It shows jet-like features in the fastest model that grows most oblate during collapse and in which the density along the poles is about an order of magnitude smaller at small to intermediate radii than in the equatorial regions, leading to the more extreme jump in entropy at the shock.

A close look at the innermost regions shown in figure 6.10 reveals interesting substructure in the density and entropy distributions of the PNSs. This substructure becomes more pronounced with increased $\beta_{\rm initial}$ and is most manifest in s20A1000β1.80. It is the imprint left by non-radial pulsations of the PNS whose entire pulsational spectrum is excited in the solid-wall-like bounce at nuclear density. In 3D, all possible ℓ, m modes are present and appear with increased power for greater prebounce deviations from spherical symmetry while on Cartesian meshes $\ell = m = 4$ can be expected to be next in amplitude to the dominant $\ell = 2, m = 0$ quadrupole mode.

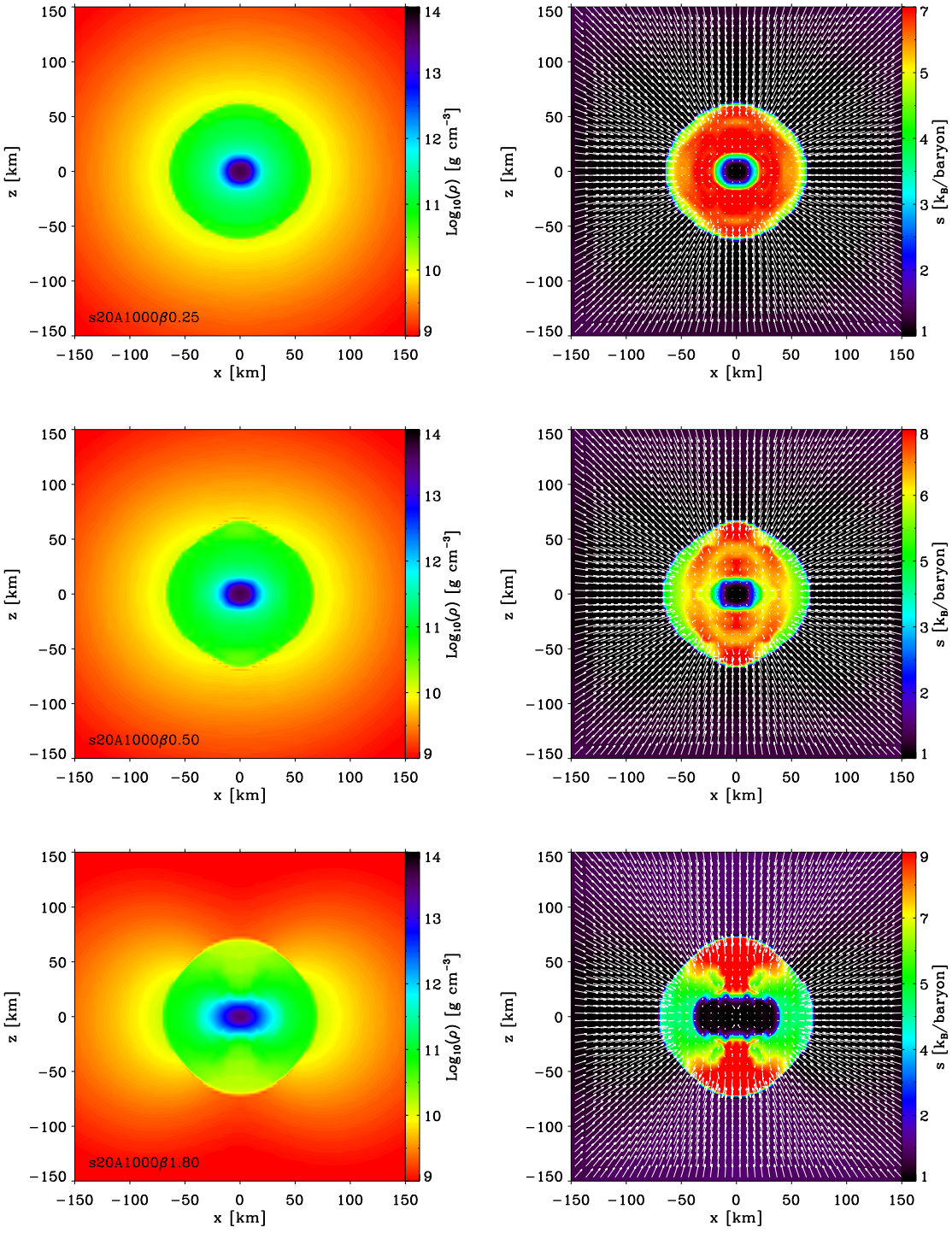

Figure 6.10: Snapshot slices of the density distribution (left-hand side) and the entropy distribution (right-hand side) on the x–z-plane at 2 ms after core bounce in models s20A1000β0.25 (top), s20A1000β0.50 (center), and s20A1000β1.80 (bottom). Shown are the inner 150x150 km^2 and the z-axis coincides with the axis of rotation. I superpose fluid velocity vectors on the entropy slices. The vector length scale is saturated at 0.075 c. With increasing $\beta_{\rm initial}$, the resulting PNS becomes more equatorially elongated, while the shock forms progressively earlier and more energetically at the poles than on the equator, leading to the observed oblate (PNS) / prolate (shock) morphology with higher entropies and almost jet-like features along the polar axis. Note that due to the change in color map ranges in the entropy slices, the extent of the lowest-entropy inner PNS region appears disproportionally enlarged in the fastest rotator.

Gravitational Wave Signal

Having solidified the general features and systematics with increasing $\beta_{\rm initial}$ of the rotating collapse and bounce of stellar iron cores, I now focus on the gravitational wave signature of the models under consideration. The gravitational wave signal is estimated based on time-changing quadrupole mass motions via the quadrupole formalism (see §3.8). Higher multipole-order mass and mass-current contributions are suppressed by powers of v/c, have been shown to be much smaller than the standard mass quadrupole wave emission in the core collapse context [11, 260], and are not considered here.

During infall, the gravitational wave signal is small and initially negative, marking an increase in magnitude of the mass quadrupole moment as the collapsing core assumes an oblate configuration[15]. This increase is reversed during progressing infall when smaller radii dominate over increasing oblateness. The global mass quadrupole moment decreases[16] and the wave signal becomes

[15]The zz-component of the mass quadrupole tensor relevant here is negative for oblate configurations. See §5.1 and [11].

[16]The "global mass quadrupole" moment in GR may not be a good measure as its definition in GR is ambiguous [116, 173, 174]. I use it here to facilitate the presentation, accepting systematic errors on the order M/R and v/c.

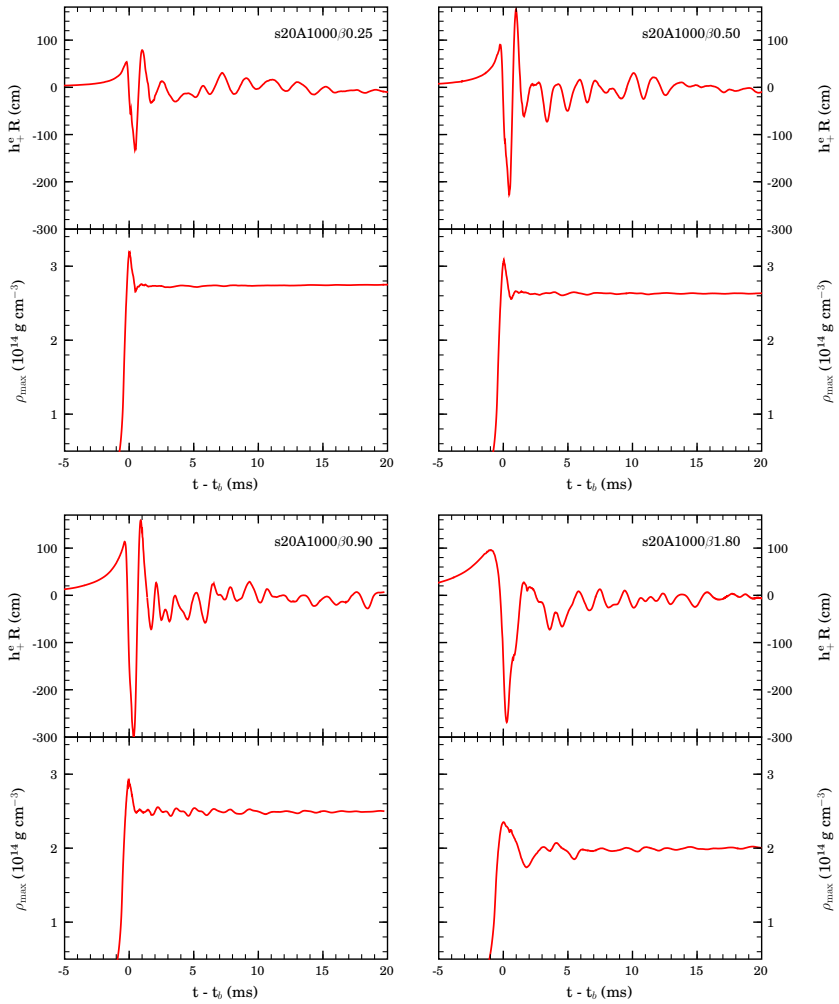

Figure 6.11: h^e_+ gravitational waveforms plotted in time-correlated fashion with the evolution of the maximum density for each model in the s20A1000 model series. Shown is an interval from 5 ms before to 20 ms after core bounce and the times are given relative to the time of bounce (t_b). The ordinate range is fixed to facilitate comparison of the waveforms and $\rho_{\rm max}$ evolutions. With increasing initial rotation parameter ($\beta_{\rm initial}$) the peak gravitational wave amplitudes first increase (from $\beta_{\rm initial} = 0.25$ to $\beta_{\rm initial} = 0.9$). For larger $\beta_{\rm initial}$, the peak amplitudes stagnate while the waveform morphology changes as rotation becomes dynamically more influential.

positive some tens of ms after the onset of collapse. In the plunge phase of collapse (setting in when central densities on the order of 10^{12} g cm^3 are reached; roughly $\sim$5–2 ms before bounce) radial infall velocities between 0.1–0.3c are reached and the wave signal becomes increasingly positive. This behavior is exhibited by all models in the s20A1000 model series. I plot their gravitational waveforms time-correlated with their $\rho_{\rm max}$ evolutions in figure 6.11. At core bounce, when the infall velocities of the inner core are reversed within a fraction of a millisecond, the largest accelerations occur and lead to the first and most prominent negative spike in the waveforms. The newborn PNS overshoots its equilibrium configuration at bounce, quickly re-expands and then settles down to a postbounce equilibrium by dissipating away in the form of strong sound waves its remaining pulsational energy from core bounce. This "ring-down" phase consists of a radial "ringing", accompanied by higher-order non-radial oscillations whose $\ell = 2$ components are imprinted on the gravitational waveform and visible in all panels of figure 6.11.

Model s20A1000β0.25, the slowest rotator in the model series, exhibits a maximum gravitational wave amplitude[17] $h^e_+ R$ of $\sim$130 cm (corresponding to a dimensionless strain of 4.21×10^{-21} at a distance of 10 kiloparsecs (kpc)). The next faster model, s20A1000β0.50, yields a significantly larger maximum gravitational wave amplitude of $\sim$230 cm ($\sim7.5\times10^{-21}$ cm at 10 kpc), a more pronounced positive peak after the negative bounce spike and a considerably enhanced postbounce ringing in the waveform. The further increase of $\beta_{\rm initial}$ from 0.5% to 0.9% in s20A1000β0.90 leads to no qualitative change in the waveform, yet to a larger bounce-spike amplitude ($\sim$302 cm; $\sim9.8\times10^{-21}$ at 10 kpc) and more pronounced and greater-amplitude postbounce oscillations in $\rho_{\rm max}$.

Before discussing the quite significant changes observable in the waveform and $\rho_{\rm max}$ evolutions brought about by the increase of $\beta_{\rm initial}$ from 0.9% to 1.8%, it is interesting to more closely consider the postbounce ring-down wave signature. As stated above and documented in [9, 11, 12, 30], these waveform features are associated with quadrupole pulsational modes that become excited during core bounce. As shown in figure 6.11, the model sequence from s20A1000β0.25 – s20A1000β0.90 exhibit such pulsations that become more regular and increase in frequency with increasing $\beta_{\rm initial}$. I infer a frequency of $\sim$500 Hz for the $\beta_{\rm initial} = 0.25\%$ model and $\sim$640 Hz and $\sim$790 Hz for models s20A1000β0.50 and s20A1000β0.90, respectively. The frequencies of the preferred pulsational modes (*eigenmodes*; in the linear regime) depend in general on the EOS and the PNS structure. Compactness, measured in terms of $(GM)/(Rc^2)$, plays a crucial role (see, e.g., [564]). In their recent study, Dimmelmeier, Stergioulas, & Font [323] have computed series of equilibrium neutron star models and analyzed their linear pulsational eigenstructure. They find that for approximately fixed $(GM)/(Rc^2)$, increased β leads to an increase in the eigenfrequencies. This is qualitatively consistent with what I find here for the $\ell = 2$ modes of the hot, ringing close-to-equilibrium PNS whose compactness (gauged by the postbounce quasi-equilibrium densities) varies only slightly in the $\beta_{\rm initial}$ range of 0.25–0.90%.

The increase in $\beta_{\rm initial}$ by a factor of two from model s20A1000β0.90 to model s20A1000β1.80 results in a much stronger influence of centrifugal support on the dynamics which is reflected in the latter model's gravitational waveform and $\rho_{\rm max}$ evolution shown in figure 6.11. Collapse is considerably slowed down and core bounce occurs at densities just below nuclear saturation density ($\rho_s \approx 2.67\times10^{14}$ g cm^3), but above the onset of the phase transition from nuclei to homogeneous nuclear matter at $\sim 1/3\,\rho_s$. While in the three slower models, the waveform bounce peak width at half maximum is roughly constant at $\sim$0.5 ms, the increased centrifugal influence in model s20A1000β1.80 leads to a less abrupt bounce reflected in the widening of the bounce feature in the waveform. This is also clearly discernible from this model's $\rho_{\rm max}$ evolution which exhibits a much wider bounce peak with a subsequent rotation-induced large undershoot of the equilibrium during the rebound. This dynamics enters the waveform but is modulated by the postbounce non-radial pulsational ringing of the PNS. Compared with s20A1000β0.90, s20A1000β1.80 exhibits a smaller maximum gravitational wave amplitude of $\sim$270 cm (8.75×10^{-21} at 10 kpc). This, again, is due to the centrifugally slowed bounce.

Figure 6.12 depicts the energy spectra of the gravitational wave emissions from axisymmetric collapse, core bounce and PNS ring-down in the models of the s20A1000 model series. As discussed above, s20A1000 models with $\beta_{\rm initial}$ in the broad range of 0.25%–0.90% experience core bounce vastly dominated by nuclear repulsive forces. They emit most of their gravitational radiation at frequen-

[17] In axisymmetry, $h_\times$ is zero everywhere and h_+ is zero along the polar axis [116]; nonaxisymmetric gravitational wave emission is considered in §6.4)

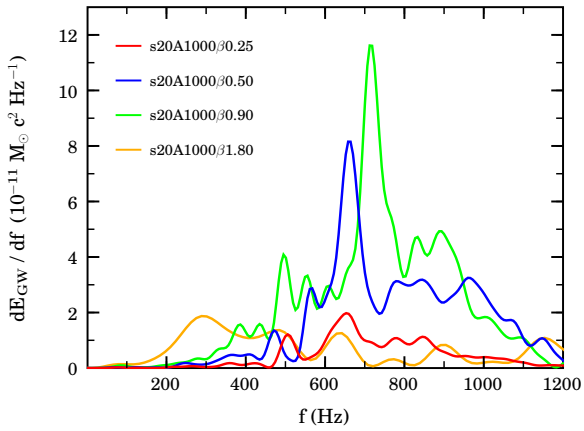

Figure 6.12: Energy frequency spectra of the gravitational waves emitted by axisymmetric core bounce and PNS ring-down in the models of the s20A1000 model series. Note the prominent maxima of the spectral energy density distributions $dE_{\rm GW}/df$ (see equation (3.178) on page 89) between 600–800 Hz in models with $\beta_{\rm initial}$ 0.25–0.90%. I compute dE_{GW}/df for model s20A1000β1.80 based on the axisymmetric gravitational wave signal up to 10 ms after core bounce to emphasize the gravitational wave emission from core bounce and the very early postbounce phase. This model is significantly affected by rotational effects and its core-bounce gravitational wave emission peaks in the frequency domain at around 300 Hz with strong secondary peaks at ∼500 and ∼650 Hz.

cies between ∼600 – 1000 Hz, corresponding to the rebound timescale at nuclear density of ∼1.0–1.6 ms. Model s20A1000β1.80, on the other hand, experiences non-negligible rotational effects that slow down its plunge and core bounce, leading to gravitational wave emission with a spectral peak frequency of ∼290 Hz. Note, however, that rotation does not dominate model s20A1000β1.80's dynamics. It still reaches densities near nuclear saturation density and a not insignificant fraction of the total energy radiated in gravitational waves is emitted in the frequency range of 500-1000 Hz as indicated by the secondary peaks in its gravitational wave energy spectrum.[18]

Intermission — General Features of the Dynamics and Waveforms, Comparison with Previous Studies — First Conclusions

Figures 6.8–6.12 indicate that while rotation certainly affects the axisymmetric dynamics and the resulting gravitational wave signal of the s20A1000 model series, it does not become the dominating component of the dynamics in collapse, plunge, and core bounce for the broad range of $\beta_{\rm initial}$ from 0.25% to 1.80% considered here. All models undergo core bounce at nuclear densities and only the fastest model, s20A1000β1.80, is significantly affected by centrifugal support. Correspondingly qualitatively similar are the gravitational waveforms of this model series.

These findings are in contrast to what has been found in previous less detailed and/or Newtonian studies. Zwerger & Müller [30] (ZM in the following) have performed Newtonian axisymmetric (2D) simulations of the adiabatic collapse of rotating polytropes and found three characteristic types of collapse dynamics and correlated waveforms — type I, II, III. Their dynamics and waveform morphology is discussed in Section 5.1 of this dissertation. Here I shall mention only the features most salient to the present discussion: Type I dynamics is characterized by little influence of centrifugal effects during collapse and bounce. Type I models overshoot to supernuclear densities and settle quickly to a postbounce equilibrium. Their waveforms exhibit one pronounced large spike at bounce while showing a gradually damped ring-down wave signal at postbounce times. Type II models, on the other hand, are rotation dominated and undergo core bounce at densities below nuclear under the influence of centrifugal forces (so-called "centrifugal bounces"). Their waveforms exhibit many harmonic-oscillator like re-expansion–collapse–bounce cycles and are dominated by much lower frequencies than the waveforms of type I models. Type III dynamics goes along with fast collapse, extremely small inner core masses, and low amplitude gravitational wave emission. It does not occur

[18]Note that the high-frequency (∼450–600 Hz) postbounce PNS ring-down pulsations in model s20A1000β1.80 that last for ∼20 ms after bounce actually emit more energy than is emitted at core bounce in this model.

in the models considered here and shall not be discussed (however, see §7.3).

In this classification scheme, models s20A1000β0.25, s20A1000β0.50, and s20A1000β0.90 show type I dynamics and waveforms, while the fastest model, s20A1000β1.80 exhibits type I/II transitional behavior (see §5.1 and [9, 12, 30]).

Dimmelmeier, Font & Müller [12] (DFM in the following) have performed a follow-up study to ZM in conformally-flat GR and found that the $\beta_{\rm initial}$ at which the transition to type II dynamics begins is shifted to higher $\beta_{\rm initial}$ in GR. Their findings have been verified by Shibata & Sekiguchi [13] and in this work (Chapter 5). They however still find characteristic type II dynamics and waveform for their A2B4 polytropic model[19] which corresponds to the A1000β1.80 rotational setup considered here.

In Ott et al. [9] I have performed a comprehensive parameter study of the effects of rotation on the adiabatic core collapse dynamics and the resulting gravitational wave emission. The study was carried out in Newtonian gravity but employed the finite-temperature Lattimer-Swesty EOS [439] and progenitor data from stellar evolutionary calculations, but deleptonization during collapse was not taken into account. In accord with the Newtonian work of ZM and the GR study of DFM I found type I and type II dynamics and waveforms. In figure 5.3 in Section 5.1 of this dissertation I display results for the $\rho_{\rm max}$ evolution of a model series of [9] similar to the s20A1000 models considered here. The differences to my new results are striking: For as low $\beta_{\rm initial}$ as 0.3%, the Ott et al. models begin to show strong effects of rotation and overshoot to subsequently much lower $\rho_{\rm max}$ at core bounce than even my quite extreme $\beta_{\rm initial}$ = 1.80% model. In addition, Ott et al. models begin to show typical type II dynamics (multiple large-scale coherent core re-expansion–collapse–bounce cycles; "multiple bounces") at $\beta_{\rm initial} \gtrsim 0.4\%$ for A = 1000 km and at progressively lower $\beta_{\rm initial}$ with decreasing A (more differential rotation). *On the other hand, clear type II behavior is not even obtained in the present s20A1000 $\beta_{initial}$ = 1.80% model*.

Müller [260, 261] performed a pioneering set of 2D Newtonian calculations of rotating core collapse with a predecessor of the Wolff EOS [447, 448] and parametrized deleptonization during collapse from more microphysically detailed 1D calculations in a similar fashion as done here, but did not include neutrino pressure contributions. In their four model calculations they did not observe type II behavior, but their strongly differentially rotating model B2 could be classified as type I/II transitional. Mönchmeyer & Müller [11] performed Newtonian 2D calculations with the Wolff EOS [448] and included deleptonization during collapse and neutrino pressure contributions. They observed clear type II dynamics and waveforms for their very differentially rotating model C ($\beta_{\rm initial}$ = 0.7%; A = 100 km) and for their model D ($\beta_{\rm initial}$ = 1.0%, A $\sim$1000 km). While the type II morphology of their model C can be explained by the extremely differential initial rotational setup, their model D's initial setup is similar to that of s20A1000β0.90 considered here. Yet, s20A1000β0.90 behaves quite differently and exhibits type I dynamics and waveform.

Recently, Kotake, Yamada, & Sato [14, 272] have performed 2D Newtonian calculations with the Shen EOS [464, 465] and with a more elaborate neutrino leakage / deleptonization scheme than used by [11]. Their results confirm the earlier findings of Mönchmeyer & Müller [11]. However, they found clear type II dynamics and waveforms only in models with strong differential rotation (A $\sim$100 km) while their more rigidly rotating models (A $\sim$1000 km) exhibit type I and type I/II transitional dynamics.

To summarize all the above:

- All models of the s20A1000 model series considered here with $\beta_{\rm initial}$ in the range from 0.25% to 1.80% and calculated with the CACTUS/CARPET/WHISKY code exhibit qualitatively similar dynamics and a generic type I waveform. Only the dynamics and waveform of the fastest rotating model show significant effects of rotation. *Importantly, no type II multiple-bounce dynamics and waveform are observed*.

- In Newtonian adiabatic collapse[20], type II models obtain for moderate differential rotation starting at $\beta_{\rm initial}$ $\sim$0.5% and the transition $\beta_{\rm initial}$ become larger and smaller, for decreased and increased differential rotation, respectively [9, 30].

[19] With $\Gamma_1 = 1.325$ in the hybrid EOS [12].

[20] Assuming a finite-temperature nuclear EOS that yields Γ very close to 4/3 or a hybrid polytropic/ideal fluid EOS with Γ very close to 4/3.

- In GR, the transition $\beta_{\rm initial}$ do generally increase and from DFM it can be inferred that the transition for A = 1000 km polytropes becomes gradually manifest from $\beta_{\rm initial}$ $\sim$0.9% and earlier for more differential rotation.
- In Newtonian non-adiabatic collapse with deleptonization, the results of [11, 14, 260] differ pointwise but clearly converge into the direction that type II dynamics and resulting waveforms appear for moderate differential rotation at $\beta_{\rm initial} \gtrsim 1\%$ and at lower $\beta_{\rm initial}$ for strong differential rotation, largely independent of progenitor model or employed (finite-temperature, microphysical) EOS.

In the context of the previous work discussed above, it is now enlightening to take a step back and recall that *the plunge, bounce, and very early postbounce dynamics and waveform are determined by the dynamics of the inner core*, that is by the material that is in sonic contact throughout these phases [11, 30, 67–69, 83]. *Material that is out of sonic contact cannot immediately affect the dynamics in the plunge phase and at core bounce.* More massive inner cores extend to larger radii and in rotating collapse, comprise more angular momentum, and experience stronger centrifugal support. Rotation itself tends to slightly increase the inner core mass ($M_{\rm ic}$ see §5.1 and [11, 30, 36]) while deleptonization during collapse and GR strongly decrease the inner core mass at bounce (see §6.2, and, e.g., [3, 64, 530]) and hence the enclosed angular momentum for a fixed degree of differential rotation. Increased differential rotation leads to increased angular momentum in the inner core and a larger $M_{\rm ic}$ [30]. This correlation is important; it allows a single-parameter discussion based on $M_{\rm ic}$.

The appearance of type II model in adiabatic calculations is readily explained by the large inner core masses found in such calculations [9, 30], owing to the absence of deleptonization. The shift to higher $\beta_{\rm initial}$ at fixed degree of differential rotation in GR is consistent with the decrease of the inner core mass at core bounce (at fixed $\beta_{\rm initial}$ and degree of differential rotation) in GR [12].

It is less straightforward to understand why clear type II dynamics and waveform morphology is observed in previous Newtonian calculations that did include deleptonization during collapse [11, 14] in models similar to the s20A1000 series considered here. For their type II models, Mönchmeyer & Müller and Kotake et al. give inner core masses of $\sim$1.0 $M_\odot$ and 0.9–1.1 $M_\odot$, respectively. For the fastest rotating model considered here, s20A1000β1.80%, I find an inner core mass of only $\sim$0.76 $M_\odot$ (see table 6.3). The calculations presented here differ in two important aspects from those of Mönchmeyer & Müller and Kotake et al.:

(1) The calculations presented here are general relativistic while the previous work of Mönchmeyer & Müller and Kotake et al. was carried out in Newtonian gravity. As pointed out (6.2), GR reduces $M_{\rm ic}$ and shifts the transition from type I to type II morphology to higher $\beta_{\rm initial}$.

(2) Mönchmeyer & Müller considered only electron captures on free protons and neglected capture processes on protons bound in heavy nuclei. Kotake et al. included electron captures on free protons and heavy nuclei, but employed [272] a relatively crude approximation for the capture rates derived by Epstein & Pethick [481] that yields $Y_e\sim$0.33 in the inner core at core bounce [272]. The $Y_e(\rho)$ prescription employed here (see §3.6.3) is derived from detailed 1D radiation-hydrodynamics calculations that incorporate more modern electron capture rates [73, 86, 475, 485] and yield $Y_e\sim$0.27 at core bounce in the inner core. Given the approximate Y_e^2 dependence of $M_{\rm ic}$, the inner core masses in the calculations presented here are systematically smaller than found by Mönchmeyer & Müller and Kotake et al.

Based on (1) and (2), I surmise that the smaller inner core masses, and consequently, the absence of type II dynamics in the s20A1000 model series are owing to combination of GR effects and more efficient and greater deleptonization during collapse than considered by previous studies.

I point out that above findings do not rule out completely the possibility for rotationally-dominated core bounce and type II waveform morphology. Larger $\beta_{\rm initial}$ and more differentially rotating initial models are likely to lead to stronger centrifugal support of the inner core and larger $M_{\rm ic}$. However, when recalling that the currently best estimates on the precollapse rotation rate of iron cores suggest $\beta_{\rm initial}$ in the range from 10^{-4}% to $\sim$3% (with a strong bias towards the lower end) [113, 273, 509–511] it seems very unlikely that the garden-variety iron core contains enough angular momentum or rotates sufficiently differentially to have a large enough rotationally-supported inner core to reach $\beta > \beta_c$ (cf. equation (6.9)) and undergo rotation-dominated core bounce, yielding a type II waveform.

In the following sections, I present case studies detailing the effects of deleptonization (§6.3.2), neutrino pressure (§6.3.6), increased and decreased degree of differential rotation (§6.3.4), and variations in progenitor structure (§6.3.5). In addition, I carry out a model calculation with an identical precollapse rotational setup to that employed by Mönchmeyer & Müller in one of their type II models (§6.3.3). The effects of GR on the (adiabatic) rotating collapse dynamics have already been substantiated by DFM [12] and since CACTUS/CARPET/WHISKY is not capable of performing simulations in Newtonian gravity, I do not investigate GR's impact on the collapse dynamics in further detail than done for the calculations presented in §6.2. A comparison with results obtained with the COCONUT code in conformally-flat GR is presented in §6.3.8.

Table 6.3: Summary of results of all collapse simulations carried out with the standard set of parameters, deleptonization, and neutrino pressure contributions. t_b is the time of core bounce. $\Delta t = t_f - t_b$ denotes the interval in time a simulation is continued after bounce and t_f is the last simulated time. ρ_b is the maximum density reached at core bounce, $M_{\mathrm{ic},b}$ is the mass of the inner core at core bounce, and β_b is the rotation parameter $\beta = T/|W|$ at core bounce. ρ_f and β_f denote the maximum density and the value of β at the last simulated time, respectively. $|h^{e/p}_{+,e,\mathrm{max}}|R$ and $|h^{e/p}_{\times,\mathrm{max}}|R$ are the peak gravitational wave strains observed by an equatorial/polar observer, rescaled by the observer distance R. The superscripts e and p stand for observer position on the equator at $\varphi = 0$ or along the polar axis ($\theta = 0$), respectively. $h_{\mathrm{char,max}}$ is the maximum characteristic gravitational wave strain as defined by equation (3.179) and f_{peak} is the frequency at which $h_{\mathrm{char,max}}$ is located. E_{GW} is the total emitted energy in gravitational waves (equation (3.174)).

Model	t_{b} (ms)	Δt (ms)	ρ_{b} (10^{14} g cm^{-3})	$M_{\mathrm{ic,b}}$ ($\mathrm{M}_\odot$)	β_{b} (%)	ρ_{f} (10^{14} g cm^{-3})	β_{f} (%)	$\lvert h^{e}_{+,\mathrm{max}}\rvert R$ (cm)	$\lvert h^{p}_{+,\mathrm{max}}\rvert R$ (cm)	$\lvert h^{e}_{\times,\mathrm{max}}\rvert R$ (cm)	$\lvert h^{p}_{\times,\mathrm{max}}\rvert R$ (cm)	$h_{\mathrm{char,max}}$ (10^{-21})	f_{peak} (Hz)	E_{GW} ($\mathrm{M}_\odot\, c^2$)	Notes
s20nonrot	131.1	29.5	3.32	0.54	—	2.96	—	2.0	1.7	4.0	1.6	0.20	952	2.43×10^{-11}	
s20A500β0.50	142.8	24.6	2.80	0.69	11.62	2.40	9.21	352.5	—	—	—	11.21	759	3.69×10^{-8}	(1)
s20A500β0.90	154.5	23.4	2.33	0.82	16.57	1.95	12.92	315.0	—	—	—	5.58	292	1.24×10^{-8}	(1)
s20A500β1.80	191.1	25.2	0.84	0.92	19.78	0.47	16.68	189.4	—	—	—	3.91	148	1.96×10^{-9}	(1)
s20A1000β0.25	135.1	21.3	3.20	0.57	3.65	2.75	3.10	132.0	1.6	2.4	2.5	4.32	653	6.34×10^{-9}	
s20A1000β0.50	138.3	26.4	3.07	0.61	6.72	2.63	5.58	226.7	7.5	6.2	5.8	8.77	658	2.20×10^{-8}	
s20A1000β0.90	145.9	35.0	2.89	0.67	10.60	2.50	8.97	302.4	2.2	5.4	2.7	10.46	713	3.04×10^{-8}	
s20A1000β1.80	167.6	90.4	2.36	0.76	16.33	2.10	12.83	269.1	142.6	14.5	148.4	64.23	918	1.69×10^{-7}	
s20A1000β1.80 (axi)	167.6	20.0	2.36	0.76	16.33	1.99	13.22	269.1	0.7	0.2	0.8	4.52	289	9.41×10^{-9}	(2)
s20A50000β0.25	132.2	45.0	3.29	0.57	0.90	2.97	0.90	35.3	1.9	1.7	1.8	1.47	667	5.40×10^{-10}	
s20A50000β4.00	151.8	20.8	2.91	0.67	10.52	2.55	8.86	271.8	0.6	2.0	1.7	9.68	691	2.69×10^{-8}	
s11.2A1000β0.50	98.7	20.3	3.17	0.60	4.79	2.74	4.15	153.5	—	—	—	5.72	672	1.01×10^{-8}	(1)
s15A1000β0.50	168.3	22.3	3.03	0.66	7.57	2.61	6.41	252.1	—	—	—	10.69	677	2.79×10^{-8}	(1)
s40A1000β0.50	200.5	22.0	2.85	0.72	11.31	2.44	9.29	334.4	—	—	—	12.46	715	3.82×10^{-8}	(1)
E20A	217.6	71.1	2.79	0.73	11.31	2.54	8.47	346.7	83.2	22.6	81.3	24.23	928	7.54×10^{-8}	
E20A (axi)	217.6	20.0	2.79	0.73	11.31	2.46	9.15	346.7	1.70	0.90	1.62	12.19	722	3.28×10^{-8}	(2)
E15A	184.2	23.2	2.65	0.76	12.67	2.32	10.07	351.7	—	—	—	10.54	719	2.99×10^{-8}	(1)
m15b6	127.1	22.3	3.31	0.55	0.02	2.89	0.04	10.2	—	—	—	0.39	643	5.41×10^{-11}	(1)

(1) Model was run in octant mode. In octant mode only h^e_+ is evaluated.
(2) Results from the axisymmetric collapse, bounce and early postbounce phases.

6.3.2 Deleptonization and Collapse/Bounce Dynamics

A central result discussed in the previous section is that none of the initial rotation rates / initial values of β considered there lead to core bounce caused or strongly influenced by centrifugal support. This is in rather strong contrast to previous studies that either did not take electron captures into account, assumed Newtonian gravity and/or used outdated electron capture prescriptions that lead to central Y_e's at core bounce that are 10–30% larger than obtained in the up-to-date calculations from which the Y_e parametrization used here is obtained [106, 486, 551].

In order to investigate further the relevance of the degree of deleptonization in rotating core collapse, I carry out a set of test calculations in which I limit the deleptonization systematically to consecutively higher minimum Y_e's.

Until nuclear repulsive forces become significant at densities close to nuclear matter density, electron degeneracy pressure is the vastly dominant component of the fluid pressure (e.g., [3]). Capture of electrons on free protons and heavy nuclei during collapse reduces the number of electrons per baryon (Y_e) and hence effectively reduces the overall pressure support, leading to faster collapse of the iron core and, importantly, to a smaller quasi-homologous inner core. In the neutrino-trapped regime (above $\sim 2\times10^{12}$ g cm^{-3}; varying with neutrino energy and flavor), the total lepton fraction $Y_l = Y_e + Y_\nu$ is conserved, while Y_e and Y_ν may individually, but in correlated fashion, vary. In fact, Y_e typically decreases slightly from trapping to core bounce (see figure 3.8 and, e.g., [3, 64])[21].

I choose model s20A1000β1.80 as a prototype for models that may be spinning fast enough to yield type II multiple-bounce dynamics/waveforms without deleptonization [12] and/or in Newtonian gravity, yet are only marginally affected by centrifugal forces when evolved with deleptonization in GR. Using the standard parametrization described in §3.6.3, with the deleptonization data from [469],

[21] Note that I use the term *deleptonization* to denote *reduction of* Y_e. While this is correct at densities below neutrino trapping, it is strictly incorrect above trapping where the lepton number is conserved.

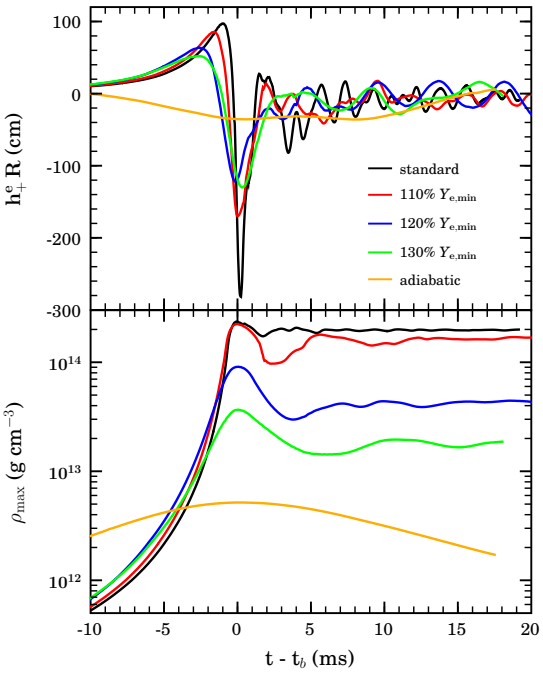

Figure 6.13: Comparison of the gravitational waveforms (top) and ρ_{max} evolutions (bottom) of the deleptonization test model series. The time is given relative to the time of core bounce (t_b) in each calculation. The "standard" model is s20A1000β1.80 (black graphs). The red, blue, and green graphs correspond to calculation in which the minimum value of Y_e is increased to 110%, 120% and 130%, respectively. The adiabatic calculation does not include any deleptonization. Note the clear trend from type I towards type II dynamics with decreased deleptonization.

model s20A1000β1.80 has a minimum Y_e at core bounce of 0.277. I perform three calculations in which I limit deleptonization to 110%, 120% and 130% of this value — corresponding to minimum Y_e's at core bounce of $\sim$0.305, $\sim$0.330, $\sim$0.360, respectively. In addition, I carry out a calculation without any deleptonization. I call the latter calculation "adiabatic". It has a central Y_e at core bounce of $\sim$0.43.

Figure 6.13 contrast the waveform and $\rho_{\rm max}$ evolutions of the four test calculations with the results obtained for s20A1000β1.80 with standard deleptonization. The 110% $Y_{e,\rm min}$ calculation reaches core bounce only $\sim$0.5 ms later than the standard calculation and at about the same $\rho_{\rm max}$. However, its $\rho_{\rm max}(t)$ possess a strongly enhanced first postbounce minimum in which $\rho_{\rm max}$ drops by a factor of 2 from its bounce value. In comparison with the standard calculation, the waveform of the 110% $Y_{e,\rm min}$ model exhibits a wider bounce peak with a $\sim$40% smaller maximum amplitude (in magnitude). The postbounce waveform exhibits less pronounced peaks and overall slower variations with time than in the standard calculation. With increasing minimum Y_e, the collapse times to core bounce increase, the $\rho_{\rm max}$ at core bounce decrease, while the gravitational wave bounce peaks become wider and the maximum amplitudes decrease (though not necessarily monotonically, as figure 6.13 portrays). The 130% $Y_{e,\rm min}$ calculation already exhibits what is clear type II behavior in its $\rho_{\rm max}$ and waveform evolutions. The purely adiabatic model is rotation dominated and undergoes centrifugal bounce at $\sim 5\times10^{12}$ g cm$^{-3} \ll \rho_{\rm nuc}$. Table 6.4 summarizes important results from the test calculations.

The systematics of the changes in collapse/bounce dynamics and waveforms with increased minimum Y_e observed here are in exact qualitative agreement with what is found in adiabatic studies when the rotation rate is increased at fixed initial structure, degree of differential rotation, and EOS Γ [9, 12, 30] (also: figure 5.3)[22]. This correspondence is readily explained by equations (6.2–6.3) and (6.9): The value of β during collapse at which centrifugal forces become dynamically dominant is a function of the effective adiabatic index $\Gamma_{\rm effective}$ (defined along a mass trajectory; equation (6.3)). With increasing $\Gamma_{\rm effective}$ the critical value β_c decreases[23] — and vice versa. On the other hand, $\Gamma_{\rm effective}$ decreases with increased deleptonization — and vice versa. *Hence, models that deleptonize less, experience more rotational support at lower values of β than others that deleptonize more.*

In the light of the discussions in the previous sections §6.2-§6.3 it is expedient to consider the inner core masses ($M_{\rm ic}$'s) at core bounce in the calculations presented here. The mass of the inner core at bounce has a $\sim Y_e^2$ dependence, but also increases like $\beta^{3/2}$ (strictly, this holds only for a white dwarf in rotational equilibrium, see, e.g., [36]). As pointed out before, more massive inner cores generally extend to larger radii. In rotating collapse, more massive inner cores comprise more angular

[22]The same systematics would obtain in the present non-adiabatic calculations; though at much higher $\beta_{\rm initial}$ and over a much larger interval in $\beta_{\rm initial}$.

[23]Note that this is a *qualitative* statement. The actual value of β at which collapse is halted by centrifugal forces depends in non-linear fashion on the initial rotational configuration, on the mass and deleptonization of the inner core. The simple $\Gamma_{\rm effective}$–β_c relationship described by equations (6.2–6.3) and (6.9) holds strictly only for equilibrium configurations.

Table 6.4: Overview of deleptonization test calculations performed based on model s20A1000β1.80 with standard deleptonization. t_b is the time of core bounce. $\Delta t = t_e - t_b$ denotes the interval in time a simulation is continued after bounce and t_e is the last simulated time. ρ_b is the maximum density reached at core bounce and β_b is the rotation parameter $\beta = T/|W|$ at core bounce. $M_{\rm ic,b}$ is the mass of the inner core at core bounce. $|h^e_{+,e,\rm max}|R$ is the axisymmetric peak gravitational wave strain as seen by an observer in the equatorial plane; rescaled by observer distance R. $h_{\rm char,max}$ is the maximum characteristic gravitational wave strain as defined by equation (3.179) and $f_{\rm b}$ is the dominant frequency in the gravitational wave burst from core bounce. Note that in models that experience centrifugal bounce, $f_{\rm b}$ is not necessarily the frequency at which $h_{\rm char,max}$ is located. $E_{\rm GW}$ is the total emitted energy in gravitational waves (equation (3.174)). Note that model s20A1000β1.80 is followed to 90 ms postbounce. The data shown here are based on its infall, bounce, and first 20 ms after core bounce.

Calculation	$t_{\rm b}$ (ms)	Δt (ms)	$\rho_{\rm b}$ (10^{14} g cm^{-3})	$\beta_{\rm b}$ (%)	$M_{\rm ic,b}$ (M$_\odot$)	$\lvert h^e_{+,\rm max}\rvert R$ (cm)	$h_{\rm char,max}$ (10^{-21})	$f_{\rm b}$ (Hz)	$E_{\rm GW}$ (M$_\odot$ c^2)
standard	167.6	20.0	2.36	16.33	0.76	269.1	4.62	289	9.41×10^{-9}
110% $Y_{e,\rm min}$	168.1	20.5	2.24	15.68	0.80	169.8	3.36	218	2.78×10^{-9}
120% $Y_{e,\rm min}$	168.9	22.5	0.91	13.01	0.89	121.6	3.10	190	1.08×10^{-9}
130% $Y_{e,\rm min}$	169.1	18.0	0.37	11.49	0.94	130.1	2.34	105	8.42×10^{-10}
adiabatic	238.8	17.4	0.05	9.63	1.39	35.9	1.16	88	8.92×10^{-11}

momentum and experience stronger centrifugal support for a given initial rotational configuration. For the standard model s20A1000β1.80, I find an inner core mass at core bounce of $\sim$0.76 $M_\odot$, while the 110% $Y_{e,\mathrm{minimum}}$, the 120% $Y_{e,\mathrm{minimum}}$, and the 130% $Y_{e,\mathrm{minimum}}$ yield inner core masses at bounce of 0.80, 0.87, and 0.93$M_\odot$, respectively. The purely adiabatic model has a very large inner core of $\sim$1.37 $M_\odot$ at core bounce. As expected, the mass of the inner core increases strongly with decreased degree of deleptonization. Note, however, that due to the interplay of deleptonization and centrifugal support, no clear power-law dependence of M_{ic} on Y_e can be established[24].

The above findings corroborate what I have stated in §6.3. They demonstrate the importance of an as exact as possible deleptonization treatment during collapse. In combination with GR's stronger effective gravitational pull, it also explains straightforwardly why previous Newtonian studies that included deleptonization have observed type II like dynamics and waveforms [11, 14] (but not: [260]!) for initial rotational configurations similar to the s20A1000 model series presented here: The deleptonization treatments in [11, 14] were based on outdated electron capture prescriptions that significantly underestimate the degree of deleptonization of the collapsing core. Concretely, [14] obtained core-bounce Y_e of $\sim$0.33 in their fiducial 15 $M_\odot$ model [272]. This value of Y_e corresponds to the one employed here in the 120% $Y_{e,\mathrm{min}}$ calculation. [11] did not publish their inner core Y_e at bounce, yet, since they completely ignored electron captures on heavy nuclei, core-bounce Y_e similar to or larger than those obtained by [14] are likely.

It is now straightforward to conclude that the observation of type II multiple-bounce dynamics and waveforms by [11, 14] in models with moderately differential rotation is primarily related to their weaker deleptonization and higher central Y_e at core bounce and secondarily to their Newtonian treatment of gravity [12]. For models that are extremely differentially rotating (e.g., in terms of the rotation law employed here, $A \lesssim 500$ km), type II morphology may occur even with more up-to-date electron capture treatment employed here (§6.3.4).

6.3.3 Comparison with Mönchmeyer & Müller (1991)

In the light of the results obtained in §6.3.2 and in order to substantiate the preliminary conclusions drawn in §6.3.1, I perform a calculation employing the 20 $M_\odot$ progenitor model of [38] and with the same initial setup used in model D of Mönchmeyer & Müller (1991; MM) [11]. MM observed type II dynamics and waveform for this moderately fast and rather rigidly rotating initial model. They used a presupernova model computed by [565] and forced it to rotate according to

$$\Omega(\varpi, z) = \Omega_{\mathrm{c}} \frac{A_\varpi^2}{\varpi^2 + A_\varpi^2} \frac{A_z^4}{z^4 + A_z^4} \,, \tag{6.10}$$

with the choice of $\Omega_{\mathrm{c}} = 5.5$ rad s^{-1}, $A_\varpi = 1000$ km, and $A_z = 1000$ km. With these parameters, MM give $\beta_{\mathrm{initial}} = 1\%$ which is identical[25] to β_{initial} found for this rotational setup with CACTUS/CARPET/WHISKY (CCW). Table 6.5 compares key observables of MM's model D with the results obtained for this model in CCW. Note that MM employed the Wolff-EOS [448] while CCW uses the Shen EOS. A recent study [566] compared the Wolff, Shen, and Lattimer-Swesty [439] EOSs and did not find significant EOS-related variations in the dynamics of plunge and core bounce.

Figure 6.14 depicts the maximum rest-mass evolution (bottom panel) and the axisymmetric quadrupole gravitational wave signal (top panel) of MM's model D as obtained with CCW. In CCW, model D experiences core bounce dominated by the stiff nuclear EOS at $\rho_{\mathrm{max}} \sim 2.3\times10^{14}$ g cm^{-3} while MM found a ρ_{max} at core bounce of only $\sim 1.5\times10^{14}$ g cm^{-3}. In the CCW calculation, model D's dynamics and waveform morphology is of type I. It is largely unaffected by centrifugal support and its gravitational wave energy spectrum peaks at a frequency of $\sim$720 Hz. On the other hand, the original MM evolution of model D resulted in type II dynamics and gravitational wave emission at much lower frequencies around 100–400 Hz (see table 6.5).

Along the lines of the discussion of the deleptonization test calculations in §6.3.2, the key to the understanding of the differences between MM's results for model D and those obtained here may

[24] Also note that (1) the findings of [65–69] were obtained in spherical symmetry and (2) that in a multi-dimensional simulation, the mass of the inner core is less well defined and more difficult to measure than in 1D. The values given here are approximate.

[25] Note that this indicates very similar stellar structure in the 20$M_\odot$ progenitors of [565] and [38].

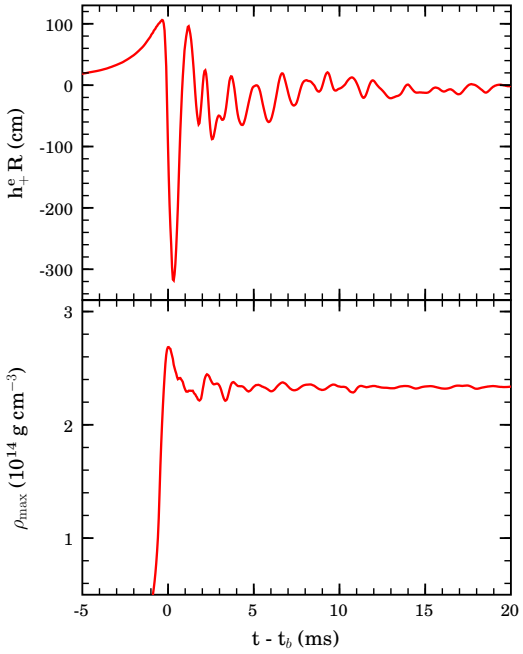

Figure 6.14: Gravitational wave signal (top) and maximum rest-mass density evolution in a CCW model calculation which is setup with the same rotation law, initial degree of differential rotation and rotation parameter β as the Newtonian model D of Mönchmeyer & Müller (MM)[11]. The CCW variant of MM's model D shows clear type I characteristics while [11] found type II waveform/dynamics.

be found in the inner core masses ($M_{\rm ic}$). MM give an $M_{\rm ic}$ at core bounce of 1.02 $M_\odot$ for their model D while I find $M_{\rm ic} \sim 0.73\,M_\odot$. For a given initial model and rotational set up, $M_{\rm ic}$ depends most strongly on the degree of deleptonization the collapsing core experiences and to a lesser, though still significant, extent on the description of gravity used.

Since MM considered only electron capture on free protons and neglected captures by heavy nuclei [263], the core Y_es in model D's late infall, plunge, and bounce phases are most likely[26] significantly higher than obtained with the more realistic $Y_e(\rho)$ prescription that I employ here. From the work of Kotake et al. [272], who included an approximate treatment of electron captures on free protons similar to MM, but also included captures on heavy nuclei, I infer a lower bound $\gtrsim$0.35 for the Y_e at core bounce in MM's Newtonian calculation of model D. As surmised in §6.3.1 and demonstrated in §6.3.2, such a relatively high Y_e does lead[27] to core masses $\gtrsim 0.90\,M_\odot$ in GR. In (effectively "weaker") Newtonian gravity, $M_{\rm ic}$ will be larger by ∼10%. This explains the large $M_{\rm ic}$ and, in turn (§6.3.2), the different dynamics/waveform morphology observed by MM.

[26] As pointed out before, MM's actual Y_e's were not published.

[27] In a model with moderately differential rotation and $\beta_{\rm initial}$∼1–2%.

Table 6.5: Comparison of model MM with model D of Mönchmeyer & Müller [11]. t_b is the time of core bounce. $\Delta t = t_e - t_b$ denotes the interval in time a simulation is continued after bounce and t_e is the last simulated time. ρ_b is the maximum density reached at core bounce and β_b is the rotation parameter $\beta = T/|W|$ at core bounce. $M_{\rm ic,b}$ is the mass of the inner core at core bounce. $|h^e_{+,\rm max}|R$ is the axisymmetric peak gravitational wave strain as seen by an observer in the equatorial plan; rescaled by observer distance R. $h_{\rm char,max}$ is the maximum characteristic gravitational wave strain as defined by equation (3.179) and $f_{\rm peak}$ is the frequency at which $h_{\rm char,max}$ is located. $E_{\rm GW}$ is the total emitted energy in gravitational waves.

Calculation	$t_{\rm b}$ (ms)	Δt (ms)	$\rho_{\rm b}$ (10^{14} g cm^{-3})	$\beta_{\rm b}$ (%)	$M_{\rm ic,b}$ ($M_\odot$)	$\lvert h^e_{+,\rm max}\rvert R$ (cm)	$h_{\rm char,max}$ (10^{-21})	$f_{\rm peak}$ (Hz)	$E_{\rm GW}$ ($M_\odot\,c^2$)
CCW	151.9	20.9	2.34	12.95	0.73	321.8	9.22	718	2.50×10^{-8}
MM [11]	221.0	20.0	1.51	(—)[a]	1.02	409.7	(—)[a]	100–400[b]	1.10×10^{-8}

[a] Information not given by [11] [b] Visually inferred from figure 5 of [11].

6.3.4 Differential Rotation

In order to investigate the effects of variations in the degree of differential rotation, I perform calculations with three different values of the differential rotation parameter A in the rotation law defined by equation (6.1). To achieve rigid rotation throughout the entire precollapse core, I set A to 50000 km, and to explore moderately differential rotation, I use $A = 1000$ km (the "preferred" standard setting, see §6.1) and $A = 500$ km. Note that according to the rotation law, A is the distance ϖ from the rotation axis at which the angular velocity Ω equals $1/2$ its central value. Figure 6.3 shows a sample of initial angular velocity profiles for different values of A. Key model observables are documented in table 6.3.

In figure 6.15 I present selected results for models s20A50000β4.00, s20A1000β0.90, s20A1000β1.80, s20A500β0.90 and s20A500β1.80. From all panels, close qualitative and quantitative correspondence between models s20A50000β4.00 and s20A1000β0.90 and between models s20A500β0.90 and s20A1000β1.80 is obvious. This at first consideration unexpected agreement of models with different A and $\beta_{\rm initial}$ is a simple consequence of their rotational setup: Because of the increased degree of differential rotation, to achieve a given global $\beta_{\rm initial}$, models with smaller A have to be set up with larger central angular velocities (Ω_c) than models with larger A. As pointed out before (see, e.g., §5.1), the rotational configuration and the mass of the material that forms the inner core determine the plunge, bounce, and early postbounce dynamics and the resulting gravitational wave signal.

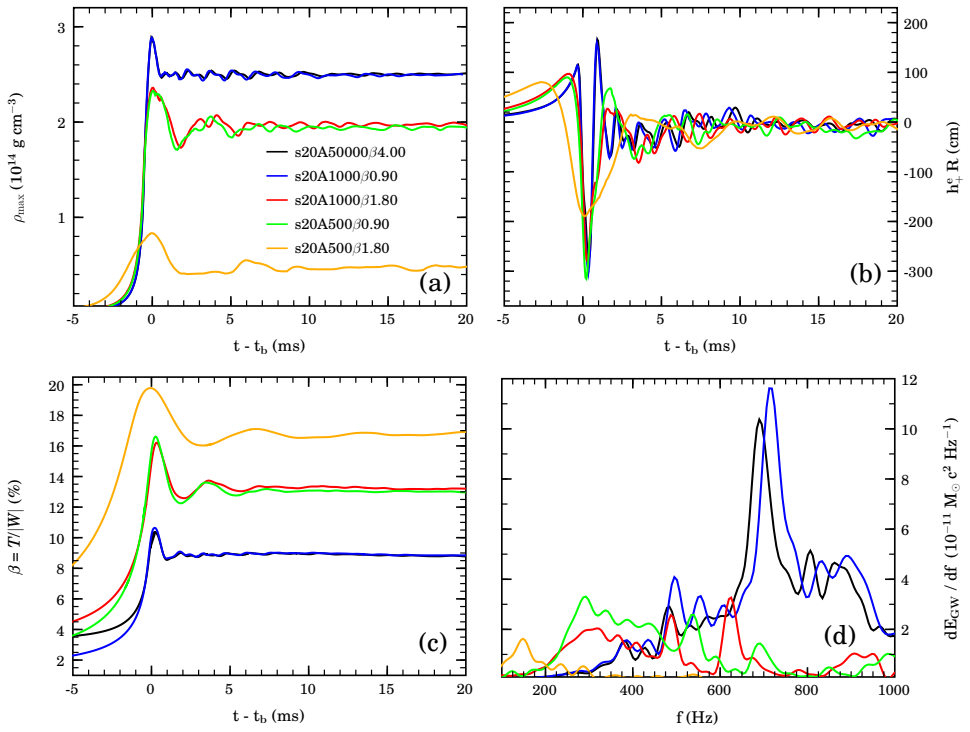

Figure 6.15: Comparison of model calculations with varying degree of differential rotation and $\beta_{\rm initial}$. Panel (a): Time evolution of the maximum rest-mass density at bounce and postbounce times in models s20A500β4.00, s20A1000β0.90, s20A1000β1.80, s20A500β0.90, and s20A500β1.80. All times are given relative to the individual model bounce times (see table 6.3). For a given initial rotation parameter β, rotational effects become increasingly relevant with decreasing A for fixed $\beta_{\rm initial}$. Note the close correspondence in the $\rho_{\rm max}$ evolutions of models s20A50000β4.00 and s20A1000β9.0 and in models s20A1000β1.80 and s20A500β0.90. Only model s20A500β1.80 is sufficiently centrifugally supported to experience core bounce at subnuclear densities not significantly influenced by nuclear repulsive forces. Panel (b): Axisymmetric mass-quadrupole gravitational wave amplitudes of the models considered. Despite the considerable variations in the degree of differential rotation, all models produce qualitatively similar gravitational waveforms. Panel (c): Evolution of the rotation parameter β. Models with smaller A have at fixed $\beta_{\rm initial}$ more angular momentum in their inner cores and, hence, have greater rotational energies and are more strongly influenced by centrifugal forces. Panel (d): Gravitational wave energy spectra. The peak frequencies shift to lower values with increasing degree of differential rotation at fixed $\beta_{\rm initial}$.

Since the degrees of differential rotation considered here are moderate and most of the material that forms the inner core is located at small radii,[28] *similar initial Ω_c lead to similar dynamics and waveforms*. This may be different for extremely differentially rotating initial configurations.

By coincidence, and as documented in table 6.2, models s20A50000β4.00 and s20A1000β0.90 both have $\Omega_c \approx$4–5 rad s^{-1}. This explains the close agreement of these two models. By another coincidence, models s20A1000β1.80 and s20A500β0.90 start out with similar Ω_c in the range of 6.5–8.5 rad s^{-1}.

In general, as A is lowered, more angular momentum and rotational energy is (for fixed $\beta_{\rm initial}$) moved interior to A. Hence, the influence of rotation on the collapsing and plunging central regions is larger in models with smaller A. This is most clearly demonstrated by model s20A500β1.80 that experiences a rotationally-induced bounce at subnuclear densities while its more rigidly rotating counterpart s20A1000β1.80 goes through core bounce induced by nuclear repulsive forces and subdominant centrifugal support. In terms of the classification scheme discussed in §5.1, model s20A500β1.80 comes closer to type II dynamics than any other model considered in this work. This is also reflected in the gravitational wave signals (panel (b) of figure 6.15) and their energy spectra (panel (d) of figure 6.15) and confirms the overall qualitative picture drawn in my previous adiabatic Newtonian study [9, 170].

Owing to the nature of stellar iron core collapse whose plunge phase is governed by the inner core mass and rotational configuration which is largely degenerate in moderate degrees of differential rotation, it is likely to be extremely difficult to determine the precollapse rotational configuration of an iron core from its observed collapse and bounce gravitational wave signature. However, very strong differential rotation, although physically not well motivated [509, 511], may lead to quasi-toroidal configurations during collapse and gravitational waveforms distinct from the generic shape obtained with moderate initial differential rotation.

Concerning the evolution of the rotation parameter β which is displayed in panel (c) of figure 6.15, it is important to note that the fastest model with $A = 500$ km, s20A500β1.80, reaches the overall largest β at core bounce. Yet, s20A500β1.80 reaches core bounce at $\sim 8.5\times10^{13}$ g cm^{-3}. A further increase of $\beta_{\rm initial}$ would lead to an even lower bounce density, compactness at core bounce, and, beyond some threshold $\beta_{\rm initial}$, to decreasing maximum values of β [9, 313]. This imposes a natural and *physical* limit on the values of β that are *attainable* in stellar iron core collapse before a *centrifugal barrier* is hit. This fact is relevant to the discussion of rotational nonaxisymmetric instabilities in §6.4.

6.3.5 Progenitor Comparison

All iron cores are alike, but not all iron cores are identical — with increasing ZAMS mass, the precollapse iron cores generally become more massive and less centrally condensed with shallower density gradients and higher central temperatures and entropies (see figures 6.1 and 6.2). Naturally, one would expect a variation of the collapse, bounce and early postbounce dynamics, and the associated gravitational wave signatures with progenitor model. In the course of my diploma thesis [9, 170], I have carried out the first study that included a variety of supernova progenitor models and investigated the impact of variations in progenitor structure on the rotating core collapse gravitational waveform. This previous work of mine was limited to Newtonian gravity and adiabatic collapse and I shall now reconsider the progenitor dependence in GR with the deleptonization and neutrino radiation/degeneracy pressure treatment discussed in §3.6, §6.3.2, and §6.3.6.

I choose A1000β0.50 (see §6.1 for a description of the rotational parameters) as my baseline comparison rotational configuration. This corresponds to moderately differential rotation with $\beta_{\rm initial} = T_{\rm initial}/|W|_{\rm initial} = 0.50\%$. Note that owing to differences in precollapse stellar structure, fixing of $\beta_{\rm initial}$ leads to variations in the initial central angular velocity from model to model. Table 6.2 summarizes all initial model parameters.

In a first step, I perform progenitor test calculations with the s11.2, s15, s20, and s40 progenitors of [38], corresponding to ZAMS masses of 11.2 M$_\odot$, 15 M$_\odot$, 20 M$_\odot$, and 40 M$_\odot$, respectively. I focus on the axisymmetric dynamics and waveforms. The presupernova stellar structure of these models

[28] In the 20 M$_\odot$ presupernova model employed here, 0.72 M$_\odot$ are located within the inner 500 km and 1.24 M$_\odot$ within 1000 km.

is portrayed by figures 6.1 and 6.2 and summarized in table 6.1 in §6.1. The results are summarized in table 6.3 on page 164.

A striking effect of variations in progenitor structure (all else kept fixed) is the change in the time it takes the iron core to reach nuclear densities and bounce. The s20A1000β0.50 baseline model reaches core bounce after 138.3 ms, while s11.2, s15, and s40 need 98.7, 168.3, and 200.5 ms, respectively. The differing times to core bounce can be understood by — for a moment — considering collapse as free fall. The Newtonian free-fall timescale (see, e.g., [36]) is set by

$$\tau_{\rm ff} = \frac{1}{4}\sqrt{\frac{3\pi}{2G\rho}} \ . \tag{6.11}$$

Hence, the infall phase of collapse will be faster for progenitors that have evolved to higher central densities. As figure 6.1 shows, lower-ZAMS-mass progenitors tend to evolve to higher central densities and have more compact iron cores [38]. At the onset of collapse, the s11.2 progenitor has a central density ($\rho_{\rm c}$) of $\sim 1.6\times10^{10}$ g cm^{-3}. Model s15's precollapse $\rho_{\rm c}$ is $\sim 6.1\times10^{9}$ g cm^{-3}. Model s20 has a greater ZAMS mass than s15, yet [38] predict a higher $\rho_{\rm c}$ of $\sim 8.3\times10^{9}$ g cm^{-3} at the onset of collapse. This non-monotonicity in the ZAMS-mass–precollapse $\rho_{\rm c}$ relationship is due to details in the nuclear burning history of stellar models in the ZAMS mass range of $\sim$12–20 M$_\odot$ [38]. s40's precollapse $\rho_{\rm c}$ is $\sim 3.7\times10^{9}$ g cm^{-3}, the lowest in the progenitor test calculation series. The sequence of times to core bounce is fully consistent with equation (6.11) and the sequence of precollapse $\rho_{\rm c}$ exhibited by s11.2, s15, s20, and s40.

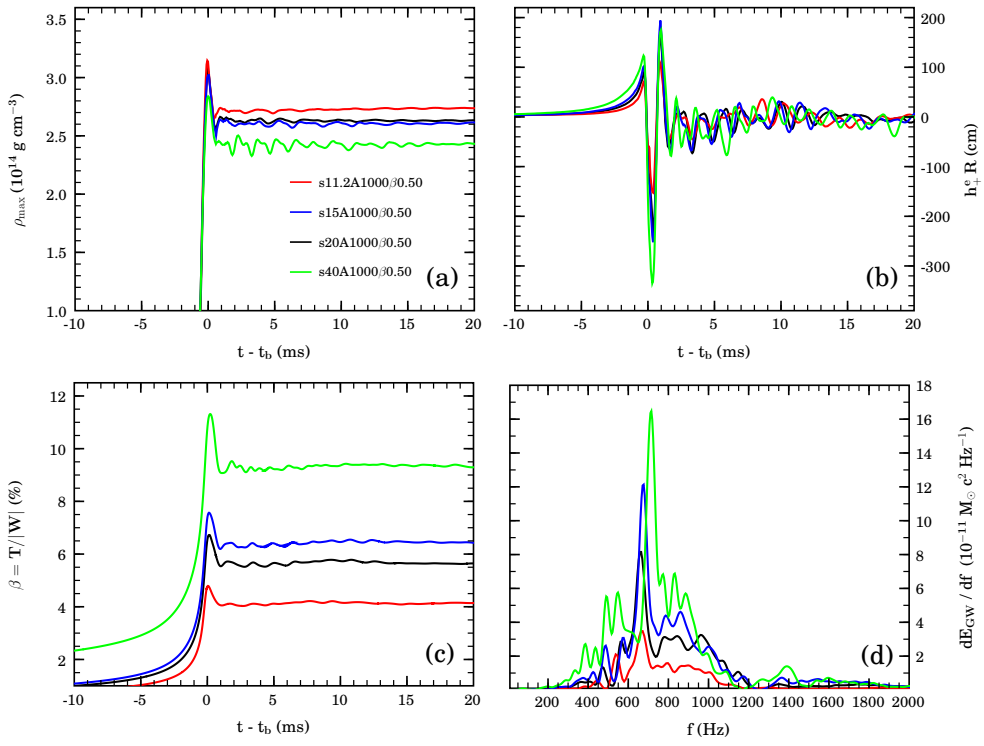

Figure 6.16: Comparison of models employing the s11.2, s15, s20, and s40 progenitors, corresponding to 11.2, 15, 20, and 40 M$_\odot$ at ZAMS, of [38] at fixed rotational configuration A1000β0.50. Panel (a): Evolution of $\rho_{\rm max}$ as a function of postbounce time. Note that all models undergo core bounce at nuclear densities and that with increased progenitor ZAMS mass the densities at and after core bounce decrease slightly. Panel (b): Gravitational waveforms h^e_+ as seen by an observer in the equatorial plane and rescaled by observer distance R. All models exhibit generic type I morphology. The maximum strain amplitudes in the bounce spike increase with progenitor ZAMS mass, with the exception of model s20A1000β0.50 that yields a slightly smaller maximum amplitude than its s15 counterpart. Panel (c): Rotation parameter β as a function of postbounce time. β increases with increasing progenitor ZAMS mass, though non-monotonically, since s20A1000β0.50 yields smaller β than s15A1000β0.50. This is due to the latter model's slightly larger iron core and shallower density profile. Panel (d): Gravitational wave energy spectra of the four models considered here. All spectra peak at $\sim$650–710 Hz and are dominated by the energy emission in the strong bounce peak of the waveforms.

In panel (a) of figure 6.16, I compare the evolutions of the maximum rest-mass density ($\rho_{\rm max}$) in the progenitor test models. The time coordinate of each model is normalized to the time of bounce to accommodate comparison. The collapse and plunge phases are qualitatively very similar in all models. s11.2, the model with the highest precollapse $\rho_{\rm c}$ and the fastest collapse, overshoots to the highest $\rho_{\rm max}$ at core bounce. With decreasing precollapse central density, $\rho_{\rm max}$ at core bounce decreases, the inner core masses ($M_{\rm ic}$) and angular momenta increase (see table 6.3) and the postbounce oscillatory variations in $\rho_{\rm max}$ become more pronounced. These general systematics are in agreement with what was found in the previous (Newtonian, adiabatic) progenitor study [9, 170]; but note that the models considered there showed rotation-dominated type II collapse dynamics and bounce while all present models undergo core bounce dominated by nuclear repulsive forces at nuclear densities.

Panel (b) of figure 6.16 portrays the axisymmetric gravitational waveforms $h_{+,\ell}R$ (rescaled by observer distance R) associated with the four progenitors. All models exhibit a clear type I waveform morphology and show qualitatively virtually identical bounce waveform peaks, while differing in maximum positive and negative signal amplitudes. Here the scaling with initial central density and iron core extent is inverse to that for the bounce density. s40, the progenitor model with the initially lowest $\rho_{\rm c}$ and largest iron core, yields the largest amplitudes, followed (in that order) by the s15, s20, and s11.2 progenitors. This systematic amplitude increase with decreasing precollapse $\rho_{\rm c}$ (and increasing shallowness of the precollapse density profile) is readily explained by the fact that $M_{\rm ic}$ and centrifugal support increase systematically with decreasing precollapse $\rho_{\rm c}$ (table 6.3). While still reaching high compactness at bounce owing to deleptonization, the more massive and more rotationally-deformed inner core leads to greater bounce gravitational wave amplitudes and more pronounced postbounce non-radial ringing of the PNS. Note, however, that none of the models experiences core bounce significantly influenced by centrifugal forces, hence the gravitational wave energy spectra of all models (shown in panel (d) of figure 6.16) peak in a narrow frequency range of $\sim$650-710 Hz. The integrated energy emission in gravitational waves is dominated by model s40 that emits a total of $\sim 3.8\times10^{-8}\ {\rm M}_\odot c^2$ until $\sim$20 ms after core bounce, followed by s15, s20, and s11.2 (in that order), all emitting on the order of $10^{-8}\ {\rm M}_\odot c^2$ (table 6.3).

In panel (c) of figure 6.16, I compare the evolution of the rotation parameter β in the A1000β0.50 models s11.2, s15, s20, and s40. Note the clear inverse relationship of β at bounce and postbounce times with precollapse $\rho_{\rm c}$ and iron core extent/mass: At core bounce, model s40 reaches a maximum β of $\sim$11.3% and settles at a postbounce β $\sim$9.3%. This value may be sufficiently large for this model to experience a low-$T/|W|$ rotational instability (see §6.4). However, the s40 model calculation considered here is carried out in octant mode to minimize computational costs. Consequently, all azimuthal modes $\propto \exp(im\varphi)$ whose m is not a an integer multiple of 4 are suppressed. The less massive iron (and inner) cores of progenitors s15, s20, and s11.2 reach systematically lower bounce and postbounce β for the same initial A1000β0.50 setup. This behavior is directly related to the fact that more extended, smaller prebounce-$\rho_{\rm c}$ iron cores (1) have more total angular momentum in the A1000β0.50 rotational setup than more compact, higher-density cores (see table 6.2) and hence spin up to higher rotational energies and (2) have to contract and spin-up more during collapse than cores that start out at higher $\rho_{\rm c}$. This is in agreement with [9, 170] and with what was found by [273] who, among other things, studied the PNS birth-spin dependence on progenitor structure in Newtonian gravity, but with neutrino radiation transport in the multi-group flux-limited diffusion approximation.

I point out that my results confirm the overall systematics described by [9, 170] of the effects of changes in the presupernova stellar structure on the collapse dynamics and the resulting gravitational wave signatures. The most striking difference is that all models considered here undergo core bounce at nuclear densities with little influence of centrifugal effects and exhibit type I waveform morphology with gravitational wave amplitudes and energy emissions that vary only in a narrow range from progenitor to progenitor. This makes it very difficult — if not impossible — to establish a clear one-to-one waveform–progenitor relationship for a given observed waveform even if the precollapse rotational configuration should be known (which is unlikely).

The Heger Models

As a second set of supernova progenitor models, I consider models E15A (15 $M_\odot$ at ZAMS), E20A (20 $M_\odot$ at ZAMS) of [509] and m15b6 (15 $M_\odot$ at ZAMS) of [511]. In contrast to the s progenitor series of [38], these models were evolved with a 1D treatment of rotation and angular momentum redistribution. In addition, m15b6 was evolved with magnetic field effects that lead to enhanced angular momentum redistribution [511, 548, 567] and has a very slowly rotating precollapse iron core with $\beta_{\rm initial} \sim 0.001\%$ (see table 6.2). Figure 6.3 displays the precollapse angular velocity profiles of the Heger models and contrasts them with rotation-law (equation (6.1)) angular velocity profiles with various A. Note that a value of $A \approx 1000$ km yields a reasonable approximation to the angular velocity profiles of the Heger models in the inner $\sim$1000 km. Tables 6.1 and 6.2 list key initial model parameters and table 6.3 summarizes the calculation results.

In the following I present results from collapse calculations employing the Heger models and compare them with models s20A1000β0.50 and s20A1000β0.90 of my baseline model series which exhibit values of $\beta_{\rm initial}$, β_b and β_f in the same range as those of the Heger models. I have performed a similar comparison in Newtonian gravity for adiabatic collapse in [9, 170].

Panel (a) of figure 6.17 compares the $\rho_{\rm max}$ evolutions of the Heger and the two s20A1000 models at times shortly before and shortly after core bounce. Model m15b6, which is largely unaffected by rotational effects, reaches the highest densities at core bounce and settles at the overall highest $\rho_{\rm max}$ at

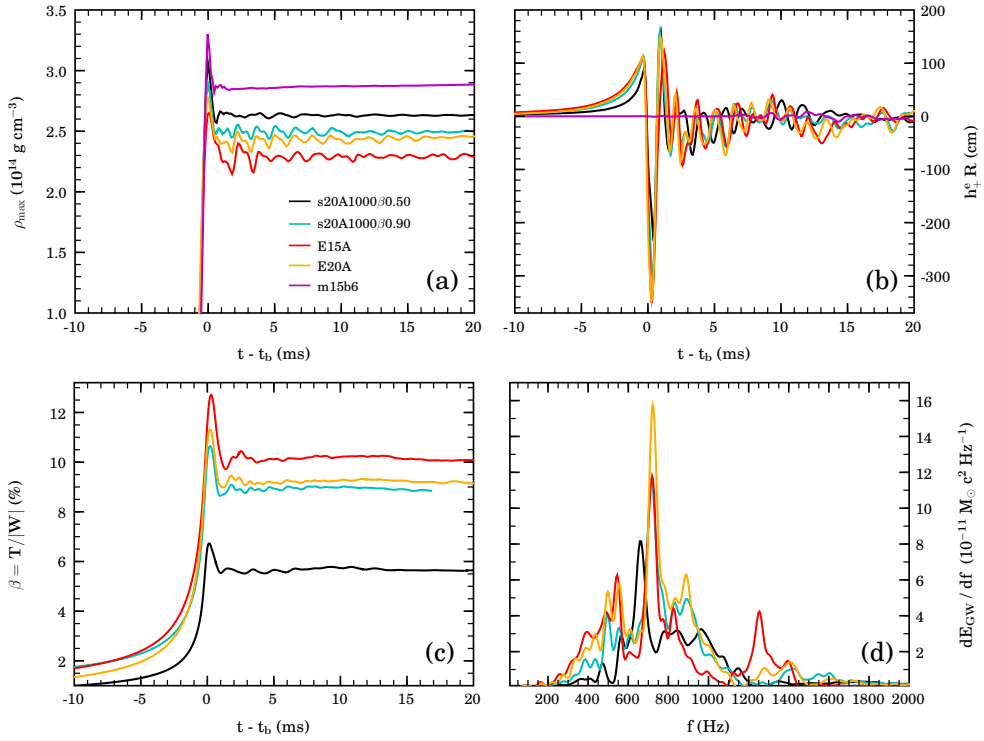

Figure 6.17: Comparison of the *Heger models* E15A, E20A, and m15b6 that were evolved with 1D rotation with models s20A1000β0.50 and s20A1000β0.90. Panel (a): Evolution of $\rho_{\rm max}$ as a function of postbounce time. Note that the slowest of all rotators, m15b6, yields the largest $\rho_{\rm max}$. Also note that E20A, while having a smaller $\beta_{\rm initial}$ than both s20A1000β0.90 and s20A1000β0.50, exhibits smaller $\rho_{\rm max}$ than the latter two models. Panel (b): Gravitational waveforms $h_{+,e}$ as seen by an observer in the equatorial plane and rescaled by observer distance R. All models — even the fastest rotators — exhibit clear type I morphology. Model m15b6 is rotating so slowly that no waveform feature associated with bounce is notable. Models E20A and E15A reach comparable maximum amplitudes in the bounce feature of their waveforms. Panel (c): Evolution of the rotation parameter β. E15A yields the largest bounce and postbounce β, closely followed by E20A. m15b6 reaches a maximum β of$\sim$0.89% a few milliseconds after bounce and is not covered by the present plot range. Panel (d): Gravitational wave energy spectra. All model spectra peak in the frequency range of 600–800 Hz. Note that for E20A only the gravitational wave emission in the first 20 ms postbounce is used to compute its spectrum. Due to its late-time rotational instability, the complete spectrum of E20A peaks at $\sim$930 Hz.

postbounce times. Its ρ_{max} evolution closely resembles that of the nonrotating s20 model presented in §6.2. This is not surprising, given m15b6's extremely small $\beta_{initial}$, and its s20-like precollapse density profile (see figure 6.1). The two fast Heger models and the two s20A1000 comparison models show ρ_{max} evolutions that are consistent with what has been observed above in the ZAMS-mass comparison of the s progenitor series: E15A has a lower precollapse ρ_c and a more extended iron core than the s20 progenitor. Hence, it spins up more (cf. panel (c) of figure 6.17), has a larger inner core mass and undergoes core bounce at lower ρ_{max} than s20A1000β0.90 which starts out with a significantly higher $\beta_{initial}$ (table 6.2). The higher-ZAMS-mass E20A progenitor has a by $\sim$40% smaller $\beta_{initial}$ than E15A, but, owing to its more extended iron core and lower precollapse ρ_c, reaches core bounce at densities only slightly higher than E15A. I emphasize that all Heger models considered here undergo core bounce at nuclear densities, largely unaffected by centrifugal forces. This is in support of [88, 273], but in contrast to adiabatic collapse without deleptonization in which E15A and E20A have exhibited centrifugally supported bounces (in Newtonian gravity, [9, 170]).

In panel (b) of figure 6.17 I contrast Heger model and s20A1000 gravitational waveforms. First, note that there is virtually no gravitational wave signal from core bounce in model m15b6. This is a direct result of its very slow precollapse rotation and, consequently, small angular momentum. Only convective overturn, setting in $\sim$10 ms after core bounce, leads to non-zero gravitational wave amplitudes in this model[29]. All other models show prototypical type I waveforms. E20A and E15A yield the largest amplitudes of all models considered in this work (table 6.3), and, quite surprisingly, almost identical postbounce waveforms, despite their variations in precollapse ρ_c and $\beta_{initial}$. In absolute value, maximum amplitudes of 351.7 cm and 346.7 cm are reached in models E15A and E20A, respectively. For an observer located at 10 kpc distance, these numbers translate to dimensionless strains of $\sim 1.14\times10^{-20}$. This is a factor of $\sim$4 larger than what I estimated in my previous adiabatic calculations [9] in which the absence of deleptonization and Newtonian gravity increased the relevance of centrifugal support and led to type II dynamics and waveforms, and hence lower maximum gravitational wave amplitudes, for model E15A and E20A.

The type I nature of the (fast) Heger models' collapse dynamics/waveforms in the more realistic calculations presented here is emphasized by the gravitational wave energy spectra portrayed by panel (d) of figure 6.17 The spectra of all models considered peak in the narrow frequency interval of $\sim$660–720 Hz — a direct consequence of the extremely rapid rebound initiated and dominated by the stiffening of the nuclear EOS. For comparison, E20A and E15A gravitational wave energy spectra obtained in my previous Newtonian adiabatic study had global maxima at 193 and 90 Hz, respectively.

Panel (c) of figure 6.17 portrays the evolution of the rotation parameter β in the two fast Heger models and the s20A1000 comparison models. E15A and E20A reach higher β at bounce and settle at higher postbounce β than the s20A1000 comparison models. This is expected, since (1) both E20A and E15A have smaller precollapse ρ_c (table 6.1) and (2) have larger inner core masses, encompass more angular momentum, and spin up to higher rotational kinetic energies. E15A reaches a maximum β of 12.7% at bounce and settles at a postbounce value of $\sim$10%. E20A's β peaks at 11.3% and settles at a postbounce value of $\sim$8.5%. Note that all Heger and s20 comparison models considered here may have sufficiently large β and may be rotating differentially enough to be subject to a low-$T/|W|$ corotation type rotational instability [19, 21–24]. In §6.4 I discuss the development of nonaxisymmetric structures in a subset (including E20A) of all models considered in this work.

Discussion

To summarize and conclude this progenitor comparison, I point out that all models of the s series (s11.2/s15/s20/s40,[38]) and the fast Heger models E15A and E20A [509] show very similar collapse and bounce dynamics and consequently have qualitatively very similar gravitational wave signatures. The differences found are mainly of quantitative nature and indicate that more massive precollapse cores tend to yield larger maximum gravitational wave amplitudes for a given initial rotational setup (in terms of degree of differential rotation and $\beta_{initial}$). They also show a more pronounced postbounce PNS ringing in ρ_{max} that is also reflected in the gravitational waveforms. How-

[29] Note that the late postbounce gravitational wave signature of m15b6 (along with nonrotating 15 $M_\odot$ and 25 $M_\odot$ progenitor models of [508]) has been considered in the long-term 2D Newtonian radiation-hydrodynamics study discussed in §7.2.

ever, these changes in the dynamics and waveforms cannot only be caused by changes in progenitor structure (i.e., variation in precollapse ρ_c; extent/mass of the iron core), but similarly by changes in the precollapse rotational configuration. Given this multi-dimensional parameter space spanned by progenitor structure parameters and rotational configuration, it will be highly difficult for gravitational wave astronomy to extract physically valuable information about the progenitor star from an observed core-collapse supernova waveform. Additional input from optical and, if the supernova occurs in the Milky Way, neutrino astronomy will most likely be necessary.

Given pulsar birth spin estimates [273, 511], it is not unlikely that massive presupernova iron cores that make garden-variety core-collapse supernovae and leave behind neutron stars, rotate with precollapse rates similar to that of model m15b6. In this case, no significant gravitational wave emission can be expected from collapse and bounce and only postbounce convection, the standing accretion shock instability (SASI) (see, e.g., [26, 101] and references therein) and/or PNS core oscillations may lead to significant gravitational wave emission (see §7.2).

6.3.6 Influence of Neutrino Pressure Contributions

The calculations presented here include a simple Fermi-gas approximation of neutrino radiation/degeneracy pressure in the neutrino optically thick regime above the neutrino trapping density (set to 2×10^{12} g cm^{-3}). Details are discussed in §3.6.4.

In §6.2 I have discussed the effects of neutrino pressure in the spherically symmetric case. Here I present results from two rotating test calculations in order to gauge the effect of the neutrino pressure on the plunge, bounce, and early postbounce phases and the related gravitational waveforms of rotating collapse and core bounce. I consider initial setups corresponding to s20A1000β0.25 and s20A1000β0.5 and simply deactivate neutrino pressure contributions. The no-neutrino-pressure calculations carry a "nnp" suffix in their model names. Table 6.6 summarizes the key results of the nnp calculations. For comparison, the corresponding results from the standard calculations are listed too.

Figure 6.18 compares the standard and nnp variants of model s20A1000β0.25 in $\rho_{\max}$ and gravitational waveform. The nnp calculation reaches core bounce $\sim$0.3 ms earlier and and at $\sim$5% lower $\rho_{\max}$ than the standard calculation. In addition, the slight postbounce undershoot in $\rho_{\max}$ exhibited by the standard calculation is not present in the nnp run. As already pointed out for the spherically-symmetric case, the inclusion of neutrino pressure is responsible for the slight slow-down of collapse and leads to a marginally larger inner core region in sonic contact. On the other hand and counter-intuitively, the inclusion of neutrino pressure effects leads to a greater overshoot in $\rho_{\max}$ at core bounce. This is due to the fact that the fractional contribution of the neutrino pressure to the total fluid pressure is initially small and gradually grows with increasing density to a maximum of 20% at the core's center at $\sim$1 ms before core bounce (see figure 6.6 on page 152) after which it is quickly overwhelmed by the nuclear component. Hence, since the neutrino pressure contribution is too small to decelerate the coherent contraction of the inner core sufficiently, the increase in mass and inertia of the inner core leads to the observed greater overshoot in $\rho_{\max}$ (cf. §6.2).

Table 6.6: Overview of test calculations performed without neutrino pressure (nnp model name suffix) and comparison with counterpart standard calculations. t_b is the time of core bounce. $\Delta t = t_f - t_b$ denotes the interval in time a simulation is continued after bounce and t_f is the last simulated time. ρ_b is the maximum density reached at core bounce and β_b is the rotation parameter $\beta = T/|W|$ at core bounce. $|h^e_{+,\max}|R$ is the axisymmetric peak gravitational wave strain as seen by an observer in the equatorial plane (at $\varphi = 0$); rescaled by observer distance R. $h_{\mathrm{char,max}}$ is the maximum characteristic gravitational wave strain as defined by equation (3.179) and f_{peak} is the frequency at which $h_{\mathrm{char,max}}$ is located. E_{GW} is the total emitted energy in gravitational waves (equation (3.174)).

Model	t_{b} (ms)	Δt (ms)	ρ_{b} (10^{14} g cm^{-3})	β_{b} (%)	$\lvert h^e_{+,\max}\rvert R$ (cm)	$h_{\mathrm{char,max}}$ (10^{-21})	f_{peak} (Hz)	E_{GW} ($\mathrm{M}_\odot\, c^2$)
s20A1000β0.25	135.1	21.3	3.20	3.65	132.0	4.32	653	6.34×10^{-9}
s20A1000β0.25nnp	134.8	26.4	3.03	3.20	73.0	4.84	745	3.28×10^{-9}
s20A1000β0.50	139.4	26.4	3.07	6.72	226.7	8.77	658	2.20×10^{-8}
s20A1000β0.50nnp	139.2	20.6	3.01	6.22	103.5	6.24	676	6.02×10^{-9}

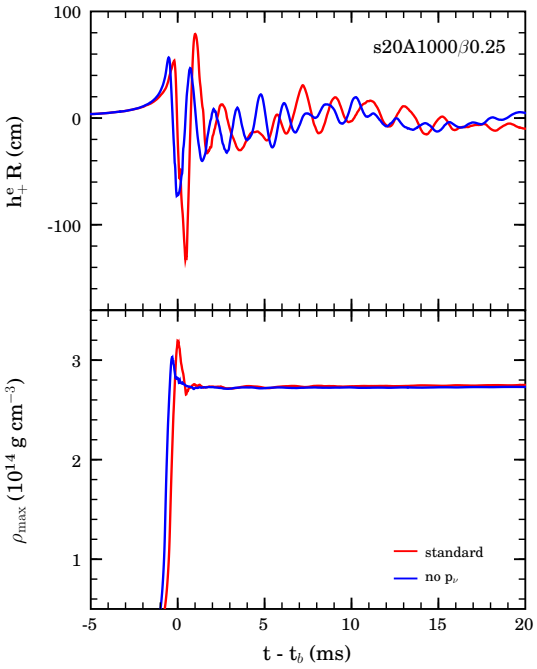

Figure 6.18: Comparison of gravitational waveforms (top) and ρ_{max} evolutions (bottom) for variants of model s20A1000β0.25 with and without neutrino pressure contributions. The times are given relative to the time of core bounce of the standard calculation that includes neutrino pressure effects. Note that the variant without neutrino pressure reaches core bounce slightly early, but at lower densities and shows weaker gravitational wave emission.

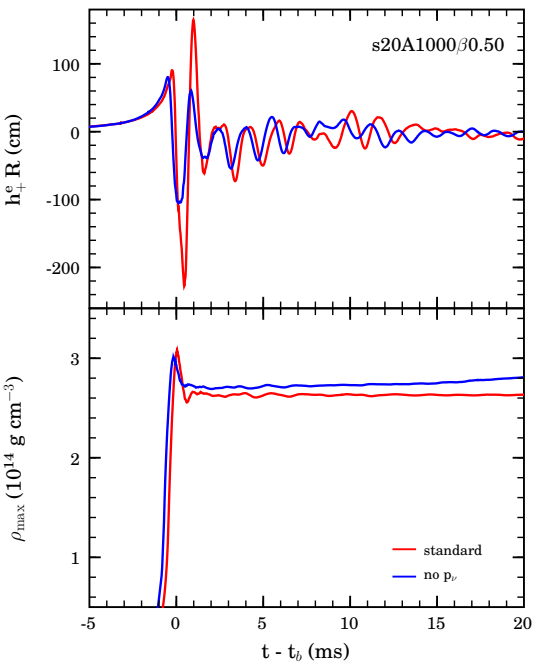

Figure 6.19: Same as figure 6.18, but for model s20A1000β0.50.

The standard variant of s20A1000β0.25 exhibits a factor of almost two larger peak gravitational wave amplitudes and total emitted energies than its nnp counterpart. This is due to (a) the greater inner core mass in the standard calculation in combination with (b) the higher bounce densities and more energetic rebound in the standard calculation with neutrino pressure.

In figure 6.19 I compare the gravitational waveforms and ρ_{max} evolutions of model s20A1000β0.50 with its nnp counterpart. The systematic differences brought about by the inclusion/neglect of neutrino pressure contributions are essentially identical to what I have described above for the slower rotator s20A1000β0.25. However, it is interesting to point out that for model s20A1000β0.50 the nnp runs settles at significantly higher postbounce ρ_{max} than the standard calculation. This is intuitively expected and in agreement with the decreased pressure support of the PNS core when neutrino pressure is neglected. Curiously, this behavior of ρ_{max} is not exhibited by s20A1000β0.25 and the nonrotating calculation (§6.2). The explanation for this may be the somewhat greater compactness of the PNS in the latter models and the consequently greater dominance of the nuclear pressure component at postbounce times. In this picture, the neutrino pressure is too weak to significantly lower ρ_{max}. In s20A1000β0.50, on the other hand, the PNS is less compact due to stronger centrifugal support and has more material at densities at which the neutrino pressure contributes significantly. This in turn leads to an altered density stratification and lower postbounce densities when neutrino pressure is included. More detailed tests would be necessary to strengthen this assumption.

Mönchmeyer & Müller [11, 263] (MM) employed a very similar scheme for including neutrino pressure in their Newtonian axisymmetric calculations. These authors pointed out that their incorporation of neutrino pressure is at least in part responsible for their observation of type II dynamics and waveforms. Furthermore, they surmised that the neglect of neutrino pressure effects may be the reason why Müller & Hillebrandt [260, 261] found (according to MM) very small $\Gamma_{effective}$ (equation (6.2)) and did not observe type II morphology for their models.

All models of the s20A1000 model series that I present in §6.3, do include neutrino pressure contributions and cover the parameter space in $\beta_{\rm initial}$ that was covered by MM. In addition, I perform a model calculation with an identical rotational setup as used in MM's type II model D (see §6.3.3). Yet, type II morphology does neither appear in the s20A1000 model series *nor* do I observe it in the calculation of MM's model D carried out with CCW. MM's surmise may be questionable, especially, if one keeps in mind that: (a) Centrifugal support (which may be regarded as an additional effective pressure component [11]) and neutrino pressure cannot be compared on equal footing. The latter does not have a clear radial dependence, is centrally peaked and a function of rest-mass density, while the former increases with cylindrical radius and is no function of density. (b) Neutrino pressure contributes significantly only above trapping density, hence cannot affect the collapse dynamics before the plunge phase of collapse — at which point it may already be too late for a strong impact on the bounce dynamics for physically sensible values of the neutrino pressure contribution. (c) As demonstrated in §6.3.2, the degree of deleptonization during collapse in combination with GR is most relevant for the type of collapse dynamics/waveform for a given initial rotational configuration.

Given (a), (b), and (c) and the results presented in this section, it is quite unlikely that the inclusion/neglect of neutrino pressure can be decisive on the qualitative collapse/bounce dynamics and overall waveform morphology. However, as shown here, it does have a significant quantitative impact on the amplitudes of the gravitational wave signal associated with core bounce and thus should be included. Finally, I point out that in the models presented here the transition from neutrino trapping to free streaming is abrupt and occurs at a fixed density of 2×10^{12} g cm^{-3} below which I set the neutrino pressure to zero. In a realistic collapsing core or PNS, the transition is smoother. An improved, though considerably more computationally expensive treatment has been proposed by Liebendörfer [476], but is not implemented in CCW.

6.3.7 Resolution Tests

In §4 I have investigated and discussed the general stability and consistency of the CCW approach in the context of rotating stellar core collapse. In order to investigate the resolution dependence of the results from the model calculations that include the Shen EOS, deleptonization, and neutrino pressure effects, I perform test calculations with 20% increased resolution for a representative subset of the models considered here. Note that in {3+1} GR hydrodynamics calculations a resolution increase by 20% results in an increase of the computational costs by a factor of two, since the number of zones increases by a factor of $(1.2)^3$ and the numerical timestep decreases by a factor of 1.2.

In Panels (a)–(c) of figure 6.20 I contrast the maximum rest-mass density ($\rho_{\rm max}$) evolutions and the quadrupole gravitational wave signal amplitudes ($h^e_+ R$) of standard-resolution and higher-resolution variants of models s20A1000β1.80, s20A500β0.90 and E20A. Both $\rho_{\rm max}$ and $h^e_+ R$ are shifted in time to facilitate comparison of standard and higher-resolution results. Note, however, that the differences in the time to of core bounce caused by resolution are small and for all models considered here on the order of 0.1 ms, corresponding to relative changes on the order of $\sim$0.1%. The near perfect agreement of the standard-resolution and higher-resolution calculations in both $\rho_{\rm max}$ and h^e_+ indicates that the calculations are already very well numerically converged at the standard resolution.

Panel (d) of figure 6.20 depicts the relative errors[30] in angular momentum (J) and gravitational mass ($M_{\rm grav}$) and their consistent variation with increased resolution in model s20A500β0.90. At 20 ms after bounce, the relative errors in J and $M_{\rm grav}$ in the standard resolution calculation amount to $\sim$3.4% and $\sim$0.4%, respectively. The higher resolution calculation which I carry out to only $\sim$12.5 ms after core bounce shows consistently smaller errors. Since WHISKY uses a flux-conservative scheme, the non-conservation of J and $M_{\rm grav}$ is owing to flux mismatches and reflections at mesh-refinement boundaries, the curvature–matter coupling, and to outer boundary effects. The errors in J and $M_{\rm grav}$ are qualitatively and quantitatively similar in E20A and s20A1000β1.80 and are not shown here.

Figure 6.21 compares the L2-norms of x-momentum and Hamiltonian constraint violations in the standard-resolution and higher-resolution calculations of models s20A500β0.90 (panel (a)) and E20A (panel (b)). The constraint violations grow exponentially during the plunge and bounce phase of

[30] Note that in a {3+1} GR calculation, gravitational mass and angular momentum should only be conserved up to gravitational wave losses/gains (which should be small, given that most models emit energies $\lesssim 10^{-7} M_\odot c^2$ and stay essentially axisymmetric). Moreover, the expressions used to compute $M_{\rm grav}$ and J are approximate. See §3.9.2.

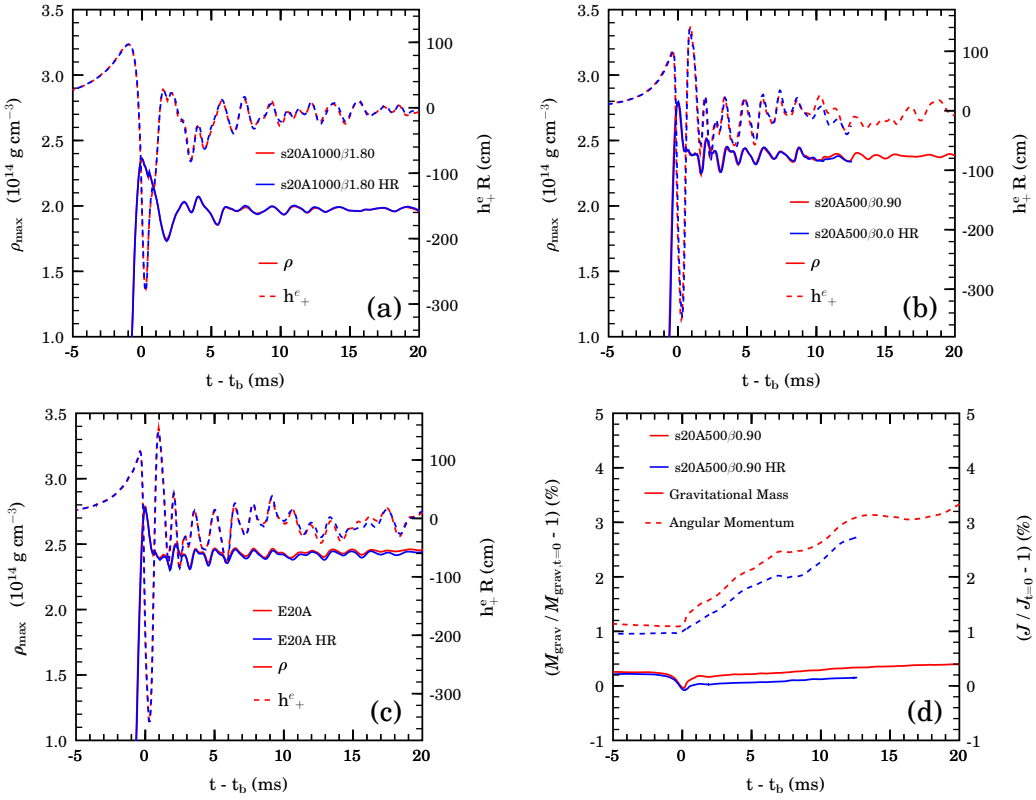

Figure 6.20: Results of resolution comparison calculations. The red colored graphs in panels (a)–(c) portray the axisymmetric gravitational waveforms and the maximum rest-mass density evolutions in models s20A1000β1.80, s20A500β0.90 and E20A. Overplotted in blue color are the results of calculations with 20% higher resolution. The higher-resolution variant of model s20A500β0.90 is evolved to only 12 ms after core bounce while all other models are calculated to 20 ms postbounce time. Panel (d) shows the relative error in the total angular momentum and in the gravitational mass accumulating during the numerical evolution of model s20A500β0.90 and in its higher-resolution counterpart. It is qualitatively and quantitatively representative for all model calculations. The expressions used to compute angular momentum and gravitational mass are discussed in §3.9.2.

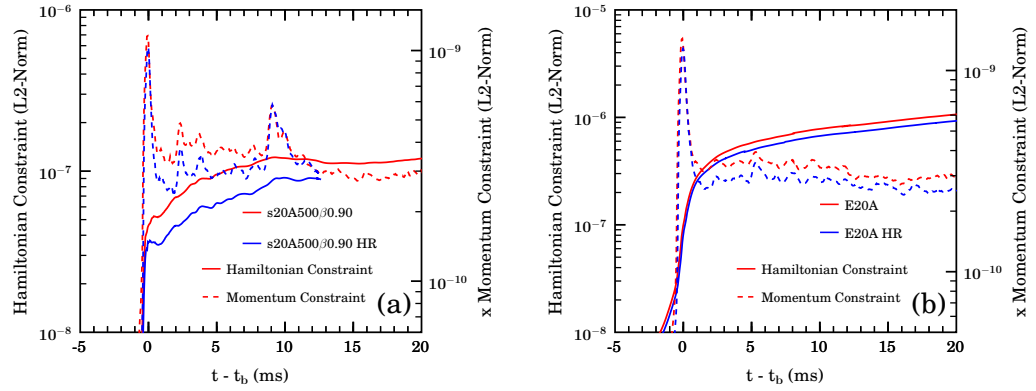

Figure 6.21: L2-norms of the Hamiltonian and x-momentum constraint violations in standard and higher-resolution calculations of model s20A500β0.90 (panel (a)) and E20A (panel (b)). The Hamiltonian and x-momentum constraints show consistency with resolution up to a glitch around $\sim$10 ms after bounce in model s20A500β0.90's momentum constraint leading to momentarily larger violation in the higher-resolution calculation. I attribute this to a shock–mesh-refinement boundary crossing that can lead to non-convergent errors (see §3.4). Note that model E20A's Hamiltonian constraint violation is of larger absolute magnitude than that of model s20A500β0.90. This is in part owing to differences in the physical model dynamics and correspondingly different resolution demands and in part to the use of improved hydrodynamics/EOS routines in model s20A500β0.90's numerical evolution.

collapse. In these phases the large curvature and matter gradients lead to significant errors in the curvature–matter coupling. After bounce the constraint violations level off to stable non-exponential growth. Increased resolution leads to smaller constraint violations — apart from an inconsistency in the x-momentum constraint of model s20A500β0.90 around 10 ms after bounce. This I attribute to errors associated with the shock passage through a mesh refinement boundary which can generally lead to non-convergent errors and high-frequency reflections (see §3.4).

6.3.8 Comparison with CFC

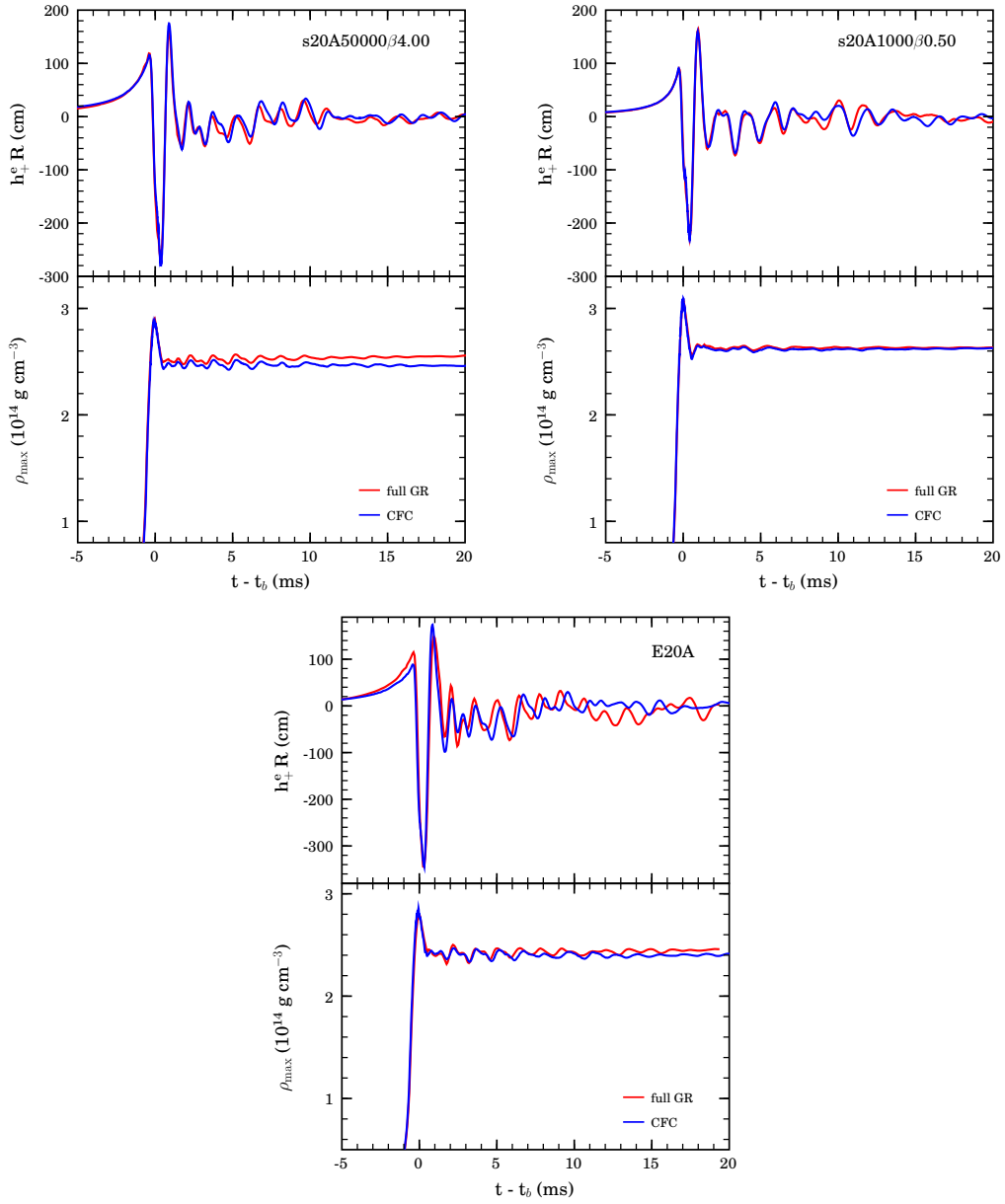

Figure 6.22: Comparison of the {3+1} GR calculations performed with CACTUS/CARPET/WHISKY with conformally-flat GR counterpart calculations performed by H. Dimmelmeier with the COCONUT code. Shown are the (axisymmetric) gravitational wave signal (top panel) and the maximum rest-mass density evolution (bottom panel) for models s20A50000β4.00, s20A1000β0.50, and E20A (from left to right). The time in each panel is given relative to the time of core bounce in the individual calculations to facilitate comparison. Note that – as in the calculations involving the polytropic initial models – the times to core bounce in the CCW and COCONUT calculations differ by less than 1%.

In §5.2 I have presented a comprehensive comparison between collapse calculations of polytropic initial models carried out with CACTUS/CARPET/WHISKY (CCW) in full {3+1} GR and with the COCONUT code [18, 160, 161] in conformally-flat GR (CFC) and axisymmetry. The results of the comparison indicate that the CFC approximation is excellent for calculations of stellar iron core collapse to neutron stars. H. Dimmelmeier has independently implemented in COCONUT the deleptonization scheme and the neutrino pressure formalism discussed in §3.6. He has carried out 2D-CFC counterpart simulations for most models considered in this work. It stands to reason to compare results obtained with CCW and COCONUT for the more microphysically detailed models. Given the good agreement of CFC with full GR for the polytropic models, the comparison presented here will serve mainly as a verification of the independent implementations of the deleptonization/neutrino pressure/EOS routines and of the quasi-Newtonian initial data approximation used in CCW.

In the following, I compare CFC and full GR results from a representative subset of the models considered in this work. The subset encompasses the rigidly rotating model s20A50000β4.00, the moderately differentially rotating model s20A1000β0.50 and model E20A which uses the rotating Heger progenitor model of the same name [509]. The full GR CCW calculations are carried out with the refinement hierarchies listed in table 6.2. The COCONUT calculations of models s20A50000β4.00, and s20A1000β0.50 are carried out with 250 logarithmically-spaced radial zones (central zone size $\sim$250 m) and 45 angular zones covering a 90° wedge. Model E20A is numerically evolved with 200 logarithmically-spaced radial zones (central zone size $\sim$400 m) and 30 angular zones covering 90°.

Figure 6.22 compares the gravitational wave signals ($h^e_+ R$) and the maximum rest-mass evolution ($\rho_{\max}$) of the CFC (blue graphs) and full GR calculations (red graphs). Both $h^e_+ R$ and $\rho_{\max}$ show near perfect qualitative and quantitative agreement of full GR CCW and CFC COCONUT. In all three models the agreement is best at core bounce and in the first few postbounce milliseconds after which the COCONUT and CCW calculations begin to diverge slightly. As pointed out in §5.2, this is most likely owing to the different grid geometries (Cartesian vs. spherical) and correspondingly slightly different artificial numerical damping of the PNS postbounce ringing and onset of vortical motions near negative radial entropy gradients (see §6.2). Note that the CFC/full GR results match slightly less well for model E20A. I attribute this to the relatively low spatial resolution of the E20A model calculation carried out with COCONUT.

6.4 Nonaxisymmetric Dynamics and Gravitational Wave Emission

Most studies concerned with nonaxisymmetric rotational instabilities in compact stars start their investigations with initial isolated stellar models in rotational equilibrium. See, e.g., the recent review by N. Andersson [286], the recent studies [20, 21, 23, 24, 268, 300–302, 304–310], and references therein.

Of particular interest to supernova theorists and gravitational wave observers alike is the question whether significant rotationally-induced nonaxisymmetric structure may develop during collapse, bounce, and postbounce phases of core collapse supernovae and in the subsequent evolution of the slowly cooling and deleptonizing PNS. Before presenting the new results obtained from my {3+1} GR simulations, I give a short introduction to nonaxisymmetric rotational instabilities in the core-collapse supernova context with an emphasis on the early postbounce evolution of the PNS and briefly, but critically summarize previous work that has been done on this topic.

The dynamical/rotational situation in a collapsing realistic stellar iron core and in the resultant protoneutron star is quite different from an isolated neutron star in rotational equilibrium:

- Small perturbations in the stellar structure introduced during carbon, oxygen, and silicon burning are essentially frozen in during infall and may grow during the plunge phase of collapse [568–571]. At core bounce and at postbounce times, these perturbations are likely to have white-noise character, hence feed power into the entire nonaxisymmetric mode spectrum.

- Rotational equilibrium models are characterized by vanishing radial motion. During collapse, bounce, and in the mixture of radial and nonradial ring-down pulsations after core bounce an iron core/PNS is out of hydrostationary equilibrium. In addition — and as pointed out in [267] — nonaxisymmetric dynamics with a global structure can only develop in the part of the collapsing core / of the PNS that is in sonic contact. The amount of matter in sonic contact varies significantly throughout the plunge, bounce and early postbounce phases.

- After the ring-down pulsations have damped, the PNS has settled into hydrostationary and rotational quasi-equilibrium. However, it does constantly accrete matter through the stalled supernova shock at a rate of $\gtrsim$0.5–1.0 $M_\odot$[31] in the first few 100 ms after core bounce. Attached to this matter is angular momentum. Hence, a realistic PNS is by no means isolated and has no well defined "edge" beyond which dynamics could be neglected. It has been pointed out that accretion processes and PNS – shock interactions may have an important impact on the development of dynamical and secular rotational instabilities in PNSs [23, 291, 297].

- The nascent neutron star cannot be well described by a polytropic EOS with a single adiabatic Γ. Instead, the PNS has a complicated thermodynamic and compositional structure and cools and deleptonizes on a timescale of seconds to minutes to its late-time cold structure [445, 572].

To date there are four studies[32] that have addressed the development of nonaxisymmetric structure in rotating PNSs in a hydrodynamical context. Most of these studies were concerned with the classical rotational instability at *high* $\beta = T/|W|$ (see, e. g. [240, 241, 286] for reviews). The instability thresholds for $\ell = m$ f-modes with azimuthal structure $\propto \exp(im\varphi)$ derived for incompressible rigidly-rotating Newtonian MacLaurin spheroids (e.g.,[285, 504]) are $\beta_{\rm dyn} \simeq 0.27$ for the purely dynamical instability and $\beta_{\rm sec} \simeq 0.14$ for the secular instability[33], driven by viscosity [24, 287, 288, 291, 297, 310] or gravitational radiation reaction [289, 290]. Interestingly, $\beta_{\rm sec}$ and $\beta_{\rm dyn}$ do not change significantly when compressible matter, GR, and (moderate) differential rotation are included (e.g., [291, 297, 300, 302–304, 306, 307] and references therein). The $m = 2$ bar-mode is expected to be the fastest growing mode in the classical picture [286].

[31] Depending on the progenitor density profile and the amount of rotational support.

[32] There are in total six previous studies that have considered 3D rotating core collapse and postbounce evolution at least in part [22, 89, 204, 264, 267, 268]. Of these only [89, 264] were not concerned with nonaxisymmetric rotational instabilities. Although claimed otherwise [300], the study by Saijo [303] *cannot* be considered a study on rotating iron core collapse. He considered the collapse of compact $n = 2.5$–1.5 polytropes.

[33] The growth timescales of gravitational radiation-reaction / viscosity driven instabilities in rotating PNS are estimated to be on the order of *seconds* (e.g., [291, 297]) and hence not relevant for the hot, newborn PNSs considered here.

Rampp, Müller & Ruffert (RMR) [267] performed Newtonian collapse calculations with the hybrid EOS (§3.5.5) of the extremely differentially and quickly spinning quasi-toroidal[34] model A4B5G5 of Zwerger & Müller [30]. The A4B5 configuration is the most extreme considered in [30, 160] and is set up in precollapse rotational equilibrium with a differential rotation parameter A of only 100 km (see the rotation law given by equation (6.1); compare with the much higher values of A considered here: §6.1 and table 6.2)[35] and an initial β of 4%. Due to the high degree of differential rotation, most of the angular momentum is stored in the central regions of this model. RMR initiated collapse by lowering the hybrid-EOS Γ from 4/3 to 1.28, which corresponds to a pressure reduction of $\sim$70% at an initial maximum rest-mass density of $\sim 10^{10}$ g cm^{-3}. This pressure reduction is unusually large and unlikely to obtain via electron capture in canonical iron cores (but, perhaps in accretion-induced collapse, see §7.3).

RMR evolved A4B5G5 through the infall phase of collapse *in 2D* and mapped to Cartesian 3D (using CARPET-like box-in-box mesh refinement and a maximum linear resolution of $\sim$1 km) only a few milliseconds before core bounce during the plunge phase when β reached 10%. At the time of mapping RMR introduced random density perturbations on the 10%-level and, in one model, an additional 5% azimuthal density perturbation with $m = 3$ spatial character. At core bounce the RMR cores reached $\beta \sim$35%, but stayed for only 1.5 ms above $\beta_{\rm dyn}$ after which they settled around or slightly above $\beta_{\rm sec}$ with maximum densities below $\rho_{\rm nuc}$. RMR carried out their simulations to $\sim$15 ms after core bounce and observed the growth of large-scale nonaxisymmetric structures in their models of mixed $m = \{1, 2, 3\}$ character[36] within $\sim$5 ms after core bounce. Yet they did not observe a significant enhancement of the gravitational wave emission in 3D over the 2D calculation, since their cores had already re-expanded to subnuclear densities due to centrifugal forces when the nonaxisymmetric deformations became large.

Brown [268] carried out collapse and postbounce simulations with an approach in many ways similar to that used by RMR. He as well considered model A4B5G5 of [30] and, in addition, performed model calculations with two more rigidly rotating iron cores that yield centrally-condensed PNSs while exceeding $\beta_{\rm dyn}$ at core bounce and postbounce times (Brown's models Ω20 and Ω24). Infall was followed in 2D and on mapping to 3D, Brown introduced 1% random density perturbations. In contrast to RMR, Brown found no significant $m = \{1, 3\}$ structures, but the growth of a dominant $m = 2$ bar mode, beginning at $\sim$15 ms after core bounce, in model A4B5G5. Despite the high postbounce β in models Ω20 and Ω24, Brown did not observe the development of nonaxisymmetric structures until $\sim$100 ms after core bounce in model Ω24. At this time a bar-like $m = 2$ structure formed in the central (but sub-$\rho_{\rm nuc}$) region of this model and persisted for about 100 ms. In model Ω20 Brown did not find any sign for the development of nonaxisymmetric structures and dynamics. The late-time development of the bar-mode instability in model Ω24 may be explained by the low compactness of this model, while it is not clear why Brown's Ω20 did not show any nonaxisymmetric structures. Brown computed postbounce βs for the central regions ($\rho > 10^{10}$ g cm^{-3}) of his model calculations and found values of 15%, 19%, and 19%, for models Ω20, Ω24, and A4B5G5, respectively. These inner-core βs are for the Ω models up to 50% lower than the corresponding global βs. Brown argued that both model Ω24 and model A4B5G5 were less stable than model Ω20, but did not elaborate on why Ω20 did not go bar-unstable.

The work of RMR and, in particular, that of Brown showed that (a) the classical dynamical instability threshold $\beta_{\rm dyn}$ may not hold in the non-equilibrium situation during collapse, bounce, and early postbounce supernova evolution, and, related to that, (b) that the global value of β alone may not be a good indicator for a models stability or instability to nonaxisymmetric perturbations if rotation is strongly differential. RMR pointed out that only regions that are in sonic contact can develop large-scale nonaxisymmetric structures.

Almost five years after Brown and seven years after RMR, Shibata & Sekiguchi (S&S) revisited the problem and performed simulations in full GR. Similar to RMR and Brown, they used polytropic initial models in rotational equilibrium, the hybrid EOS with Γ = 1.28 or 1.30, and followed the infall phase in 2D and mapped to 3D only shortly before core bounce. All models were perturbed with $m = 2$ seeds, with spatially varying relative magnitude on the 1%–10% level. S&S performed 3D

[34] I denote models that exhibit off-center density maxima as quasi-toroidal.

[35] Note that all astrophysical considerations indicate that precollapse stars are in solid-body rotation throughout the greatest part of their iron core [509–511].

[36] RMR did not carry out a detailed mode analysis and inferred the mode structure from isodensity contour plots.

calculations only for models that reached $\beta_{\rm dyn}$. They followed the 3D postbounce evolutions of their models to $\lesssim$15 ms postbounce.

In order to investigate the effect of more massive iron cores, S&S increased the size of the constant K in the polytropic initial model EOS (see §3.5.5) with the argument that more massive iron cores had additional radiation pressure support. Unfortunately, this approach is inappropriate in two ways: (1) Photon radiation pressure plays no role at the densities and temperatures prevailing in a precollapse iron core (see, e.g., [36]). (2) What increases with iron core size/progenitor ZAMS mass is the non-degenerate Maxwell-Boltzmann thermal pressure component that is due to the iron-group nuclei. This cannot be modelled as a component in a polytropic EOS. Their iron core models with K other than that predicted and well tested by nuclear/statistical physics for standard electron degeneracy [36] are strictly speaking unphysical. In addition, in nature, more massive iron cores will have significantly varying density/temperature/compositional stratifications while different choices of K just quantitatively scale a generic profile. The results of their calculations involving the scaled progenitors (7 out of their 10 models evolved in 3D) should be considered while keeping this in mind.

In their models that developed non-negligible nonaxisymmetric structures and dynamics, S&S found a dominant and fastest growing $m = 2$ component, and an $m = 1$ component subdominant at early times, but more strong and eventually dominating over the $m = 2$ mode at late times when the bar mode loses strength[37]. In agreement with RMR and Brown, S&S conclude that nonaxisymmetric rotational instabilities (at high β) develop only if (i) the precollapse $\beta > 1\%$, (ii) the initial degree of differential rotation is large (A is small), and (iii) the EOS Γ in the infall phase is sufficiently small to lead to rapid collapse.

In recent studies [19–21, 23–25, 308, 309] dynamical rotational instabilities of $m = 2$ and/or $m = 1$ character were found in strongly differentially rotating equilibrium neutron star models at *low* $T/|W|$ in the range of 1–20%. In contrast to the classical high-$T/|W|$ instability, this new kind of dynamical instability at low-$T/|W|$ appears to be related with resonant amplification of azimuthal modes at corotation points where the pattern speed of the mode coincides with the local angular velocity [19, 23]. Motivated by these new results, I together with J. Tohline, S. Ou, and A. Burrows performed 3D calculations of the postbounce phase of a stellar core collapse event [22]. The 3D calculations were carried out with the Louisiana State University hydrodynamics code FLOWER [573] using a hybrid polytropic/ideal-fluid EOS (see §3.5.5). They started out with an early-postbounce snapshot of model s20A500β0.2 of [9]. s20A500β0.2 is based on the 20-$M_\odot$ (at ZAMS) presupernova model of [508], was put into rotation with the standard rotation law (equation (5.2)) with $A = 500$ km and $\beta_{\rm initial}$ = 0.2% and then purely hydrodynamically collapsed in axisymmetry with the VULCAN/2D (see §7 and [9, 574]) code and the finite-temperature nuclear Lattimer-Swesty EOS [439]. At core bounce, s20A500β0.2 reached a maximum β of 8.96% and settled at a postbounce value near 8%. This model had a centrally-condensed structure at all times. We performed two 3D calculations. Model Q15 started out at 15 ms after core bounce. On mapping to 3D we perturbed the density with 0.1% relative amplitude, bar-like $m = 2$ seeds. Model W5 started out at 5 ms after core bounce and we added random noise on the 0.02% level to the density. The models were evolved in 3D to $\sim$130 ms postbounce.

Interestingly, model W5 and Q15 (despite its initial $m = 2$ perturbation) developed dominant $m = 1$ structure with an $m = 2$ harmonic at the same pattern frequency, but lower mode amplitude. We determined the angular eigenfrequency of the $m = 1$ mode to be $\sigma_1 \sim 2.5\times10^3$ rad s^{-1}. The PNS's angular velocity profile showed corotation points with σ_i. Hence, we identified this with the corotation-type low-$T/|W|$ instabilities observed in isolated equilibrium models [19–21, 23–25, 308, 309].

Important downsides of this study are (i) the purely adiabatic treatment of collapse (this is in common with RMR, Brown and S&S) , and (ii) the inconsistent switch from the detailed LS-EOS used in VULCAN/2D during collapse and bounce to the hybrid EOS in FLOWER. In addition, about 25% of the total mass of s20A500β0.2's had to be discarded in order for the PNS to fit on the FLOWER grid that extended out in radius to only $\sim$140 km.

To conclude this discussion of previous work on the development of rotational instabilities in the collapse, bounce, and in the early postbounce epochs of core-collapse supernovae, I reiterate that none

[37] Note that a qualitatively similar behavior to that has recently been observed by [300].

of the previous studies have consistently followed collapse, bounce, and postbounce evolution in a single 3D hydrodynamics code. All studies treated the infall phase of collapse in axisymmetry and mapped only shortly before or shortly after core bounce to 3D. In addition, all studies completely neglected deleptonization/neutrino effects and performed the 3D calculations with the simple hybrid EOS. S&S, RMR, and Brown employed an unphysically low Γ at subnuclear densities and used initial models with degrees of differential rotation incompatible with the predictions of nuclear astrophysics and stellar evolutionary calculation. Only S&S carried out simulations in GR and only Ott et al. used initial presupernova models from stellar evolutionary calculations and a finite-temperature nuclear EOS through infall, plunge, and core bounce.

6.4.1 Candidate Models and the Absence of High-$T/|W|$ Dynamical Instability

Many authors have considered stellar iron core collapse, bounce, and early postbounce evolution as a site for dynamical rotational instabilities at high-$T/|W|$ (e.g., [30, 169, 204, 240, 267, 268, 298, 299, 307, 308, 313, 351, 575–577] and references therein). As discussed in the previous section, it is indeed possible to *construct* models that reach maximum $\beta \gtrsim \beta_{\rm dyn}$ [30, 160, 204, 267, 268] in the plunge phase of collapse and at core bounce. While such models may be used as numerical toys to study processes generally allowed by the laws of (GR) hydrodynamics, it is from an astrophysical point of view important to ask whether such precollapse configurations are possible when nuclear physics and stellar evolution theory are taken into account:

(1) *The degree of differential rotation of the iron core*. RMR, Brown, and S&S found that strongly differential rotation ($A \lesssim 100$ km in the rotation law (6.1)) is a necessary condition for reaching high βs. More rigidly rotating cores have much less angular momentum in their inner cores and more angular momentum in outer core regions. They generally spin up less during collapse and produce lower-β PNSs (§6.3.4 and [9, 30, 160]). From first principles [578], it is clear that solid-body rotation is the lowest rotational energy state for a fluid body of fixed angular momentum and any rotating fluid will tend towards rigid rotation if a mechanism for angular momentum redistribution is present. Nuclear astrophysics and stellar evolution theory predict that massive stars go through multiple convective nuclear burning stages. Convection can redistribute angular momentum [38, 509, 511, 579] and, in combination with magnetic torques and microscopical turbulent viscosity is likely to smooth out angular velocity gradients, leading to almost rigidly rotating iron cores [509, 511] (see figure 6.3). *Unless the current theory of massive star evolution is significantly flawed, it is unlikely that precollapse iron cores will show the extreme degree of differential rotation invoked by RMR, Brown, and S&S*. Note that the progenitors of accretion-induced collapse (AIC) may be significantly differentially rotating, however, owing to accretion of angular momentum, in the opposite sense, with Ω increasing with radial distance from the rotation axis (e.g., [16, 114, 580] and §7.3).

(2) *The equation of state of a collapsing stellar core and the pressure reduction due to electron capture and photodissociation of iron-group nuclei*. Given their models' rotational configuration (degree of differential rotation / initial rotation rate), RMR, Brown, and S&S found it necessary to choose an adiabatic Γ in the hybrid EOS (§3.5.5) of $\sim$1.28–1.30 in the subnuclear regime to obtain $\beta \gtrsim \beta_{\rm dyn}$. The EOS in a collapsing stellar iron core at subnuclear density is however quite precisely known. The dominant pressure component is due to relativisticly degenerate electrons obeying a well known Fermi-gas EOS [3]. Thermal pressure of the heavy nuclei and photon radiation pressure contribute little to the total pressure (see, e.g., **??**). Hence, the adiabatic Γ of the iron core EOS is very close to $4/3$, typically between 1.32–1.325 [3, 439]. However, most relevant for the collapse dynamics is $\Gamma_{\rm effective}$ (equations (6.2–6.3)) which *depends sensitively on the rate of electron capture during collapse and varies with time. The results presented in §6.2–6.3 show, however, that $\Gamma_{effective}$ is on average well above the values of Γ considered by RMR, Brown, and S&S*. This is most apparent when considering the times to core bounce and the inner core masses. Constant $\Gamma = 1.28$ during collapse leads to fast collapse and core bounce after $\sim$30–50 ms [12, 13, 30] and yields an inner core mass at core bounce much smaller than that resulting from much slower collapse with a microphysical EOS and electron capture [30]. This may be different in AIC in which electron capture can be extremely efficient (§7.3 and [16]).

(3) *Precollapse rotation rate of the iron core*. RMR used a model with precollapse $\beta_{\rm initial} = 4\%$, while S&S chose $\beta \gtrsim 1\%$ and Brown's model Ω24 (rotating less differentially than the RMR and S&S models) required an initial β of 24% to reach $\beta_{\rm dyn}$ during collapse. Unfortunately, little is known

about the precollapse iron core rotation rate. The only observational constraint is the period at which young pulsars are "injected" into the $P/\dot{P}$ space. This constraint suggests a neutron star birth spin period of $\sim$10–50 ms [273, 511]. Unless there are yet undiscovered efficient postbounce spin-down mechanisms, precollapse iron cores have to rotate with central periods of tens of seconds and $\beta_{\rm initial}$ $\sim 10^{-3}$% [273, 511] to match with observations. On the other hand, the progenitor cores of collapsar-type gamma-ray bursts (GRBs) are likely to be spinning quickly with precollapse $\beta_{\rm initial} \gtrsim 1$% [113, 114, 509]. Hence, the $\beta_{\rm initial}$ assumed by RMR and S&S are not totally out of the range of what may be possible. However, recall that, owing to the extremely differential rotation, most of the angular momentum in their models is located at small radii. The inner cores of such models experience extraordinarily strong centrifugal support and undergo rotational core bounce at subnuclear density when a microphysical EOS in conjunction with an electron capture treatment is employed (see §6.3.4). They evolve to so-called *Fizzlers* [313, 314, 581] that are centrifugally hung-up at subnuclear densities and have β too low for a classical high-$T/|W|$ rotational instability [9, 294]. Fizzlers may, however, on a secular timescale contract and become dynamically or secularly rotationally unstable (see, e.g., [294–296] and references therein). Given what I have said in (2) concerning the degree of differential rotation that is to be expected in realistic precollapse iron cores, fizzlers may occur only very rarely.

Given items (1), (2), and (3) it is unlikely that the average iron core is spinning fast and differentially enough to reach $\beta_{\rm dyn}$ during collapse. Even more exotic, quickly spinning cores of evolved low-metallicity (at ZAMS) progenitors that carry sufficient specific angular momentum to support massive accretion disks around a GRB central engine may not be spinning differentially enough to reach $\beta_{\rm dyn}$ [113, 114, 509]. On the other hand, progenitor white dwarfs of AIC may be spun up to very high precollapse β, collapse quickly owing to extremely efficient electron capture, and could reach $\beta_{\rm dyn}$ at early postbounce times (§7.3).

In panel (a) of figure 6.23 I plot the evolution of β shortly before and shortly after core bounce for the six fasted models considered in this study. Model s20A500β1.80 is more differentially and more quickly spinning than predicted by the fast Heger models [509] and is likely to be on the more extreme side of possible/likely iron core precollapse rotational configurations. This models reaches the overall highest $\beta_{\rm bounce}$ of $\sim$19.8% — a value that is far from $\beta_{\rm dyn}$ of the classical high-$T/|W|$ instability — and settles at a postbounce β $\sim$16.8% which is above the instability threshold of the gravitational-radiation or viscosity driven secular rotational instability which may grow on a $\sim$1 s timescale [297]. Models that are initially more rigidly or more slowly rotating reach lower $\beta_{\rm bounce}$ and settle at lower postbounce β. Importantly, none of the initially moderately-fast rotating Heger models E20A ($\beta_{\rm initial}$ = 0.37%) and E15A ($\beta_{\rm initial}$ = 0.59%) reaches β near $\beta_{\rm sec}$ or $\beta_{\rm dyn}$ during core bounce or the first 20 ms postbounce. The rigidly rotating model s20A50000β4.00 is already rotating beyond the mass-shedding limit and loses a fair fraction of its outer angular momentum during the infall phase. Despite its large $\beta_{\rm initial}$ it only reaches $\beta_{\rm bounce}$ $\sim$10% and its PNS settles at a postbounce β of $\sim$9%.

Based on the maximum β collected in table 6.3 and the β systematics shown in figure 6.23, I conclude that none of the models considered in this study are likely to undergo a classical high-$T/|W|$ rotational instability during their collapse, bounce and early postbounce phases. The model set considered here (and summarized in table 6.2 on page 148) is representative for the faster-rotating part of possible and plausible iron core models. The average, garden-variety iron core may be rotating much more slowly [273, 511] than most models considered here. Hence, realistic iron cores of $\sim$solar metallicity stars are unlikely to reach high enough β during collapse and at the early postbounce stage to become unstable to the classical dynamical instability at high-$T/|W|$. The situation may be different for the late postbounce evolution which is not tracked here. If the supernova is successful, the PNS will cool and contract on a timescale of $\sim$1–100 s. If no process removes or significantly redistributes angular momentum during the cooling phase, most of the models considered here will exceed $\beta_{\rm sec}$ and, perhaps, $\beta_{\rm dyn}$, at some point in their cooling history [273].

Panel (b) of figure 6.23 depicts the angular velocity along the positive x-axis at 5 ms after core bounce in the six fastest models considered in this study. The core of all PNSs is roughly in solid body rotation out to $\sim$10 km. This is a direct consequence of the homologous collapse of the inner core and the conservation of angular momentum [273]. The outer regions of the PNS between $\sim$10–100 km show generically a factor-of-ten drop in Ω. This drop leads to a significant kink in the specific angular momentum slope. While j increases by a factor of $\sim$50–100 from 1 to 10 km, it increases only by a factor of $\sim$5–10 from 10 to $\sim$70 km and is roughly constant in the range $\sim$70–300 km.

In the light of recent results on dynamical rotational instabilities in compact stars occurring at low-$T/|W|$ and always in combination with strongly differential rotation [19–24, 308, 309], it is reasonable to suspect that at least some of the models considered here may be subject to such a low-$T/|W|$ rotational instability. In order to investigate this possibility, I have a performed calculations of a total of seven models (see table 6.2) without imposing any symmetry constraints[38] on azimuthal flow, hence allowing the entire spectrum of azimuthal modes spatially varying with $\propto \exp(im\varphi)$. I do not add any additional seed perturbation on top of the finite-differencing noise and the systematic $m = 4$ Cartesian grid seed. Since all of the above mentioned studies on low-$T/|W|$ rotational instabilities found $m = 2$ spatial contributions (see, in particular, [22, 24]), the nonaxisymmetric quadrupole gravitational wave strains $h^e_\times$, $h^p_\times$, and h^p_+ (where p and e stand for observer position along the positive polar axis and in the equatorial plane at $\varpi = 0$, respectively) may be used as first indicators for the development of nonaxisymmetric structures. In axisymmetry they are identically zero.

Note the complication that nonaxisymmetric structures and dynamics in PNS could not only develop via rotational instabilities but also as a consequence of convective instability. In fact, all models considered here are to some extent unstable to convective overturn at postbounce times (see §6.2). Overturn is likely to be more pronounced in more slowly rotating PNSs, since rotation tends to stabilize convection in regions with strong positive radial specific angular momentum gradients [88, 273, 553]. The nonaxisymmetric convective dynamics are most prominently of $m = 4$ character (§6.2, figures 6.4 and 6.7), but have a non-vanishing quadrupole component.

Figure 6.24 depicts the quadrupole gravitational wave strain h^p_+ (polar observer) in model calculations whose grid setup permits the entire m spectrum. Shown are the last 5 ms before and the first 40 ms after core bounce. Due to the extreme computational costs[39] for these calculations I can not evolve all models to postbounce times beyond ∼20 ms. Note that h^p_+ vanishes before core bounce in all models. In the first ∼5–10 ms after core bounce h^p_+ remains small ($h^p_+ R \lesssim 1$ cm, 2 orders of magnitude smaller than the typical axisymmetric bounce amplitude of h^e_+) and evolves qualitatively and quantitatively similarly in all models. About 15 ms after core bounce, most prominently model E20A's h^e_+ strain amplitudes begin to grow quickly and assume a clear and systematic, almost single-frequency time variation. Such a signal is not to be expected from convection in which short-period

[38] I assume discrete reflection symmetry with respect to the equatorial plane. This does not affect azimuthal flow. Bitant mode is twice as computationally expensive than rotational π-symmetry (suppressing all modes with uneven m) and a factor of 4 more computationally expensive than rotational $\pi/2$-symmetry (suppressing all modes with m not a multiple of 4).

[39] A typical calculation requires 32 Intel Xeon 3.4 GHz CPUs or AMD Opteron CPUs (model 246) and ∼32 GB of RAM for 24 hours in order to progress by 1 ms in physical postbounce evolution time. The aggregate computation cost to evolve 7 bitant-mode calculations to ∼20 ms postbounce amounts to $\gtrsim 10^5$ CPU hours and more than 2 TB of 3D output data (stored in single floating point precision). Including two long-term postbounce calculations and high-resolution test calculations, I estimate that this work consumed a total of well over 5×10^5 CPU hours.

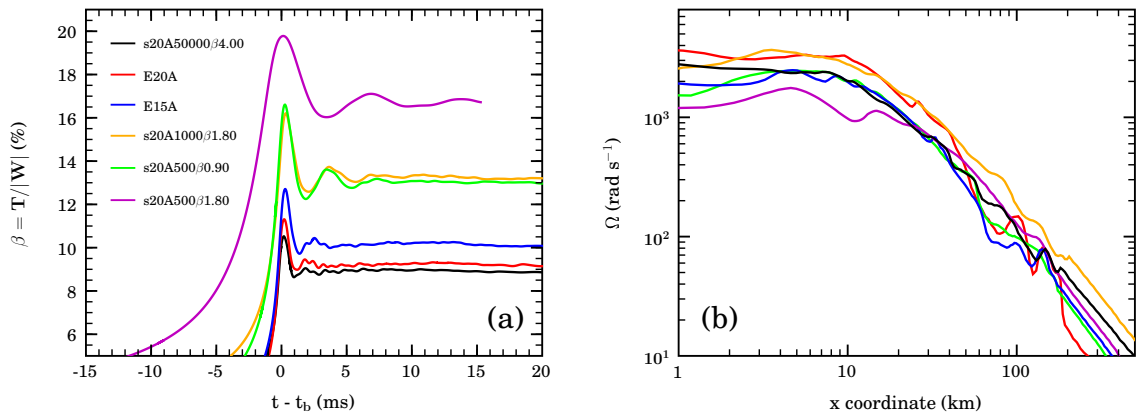

Figure 6.23: Panel (a): Evolution of the rotation parameter β as a function of postbounce time for the six fastest rotating models considered in this study. Panel (b): Equatorial profiles of the angular velocity (see §3.9.2) taken along the x-axis at ∼5 ms after core bounce in each model. Note the region of approximate solid body rotation inside ∼10 km. Also note that while model s20A500β1.80 exhibits the highest β in panel (a), it has the lowest central angular velocity of all models. This is a consequence of the low compactness of this model. It is the only model that experiences rotationally-induced core bounce at subnuclear densities.

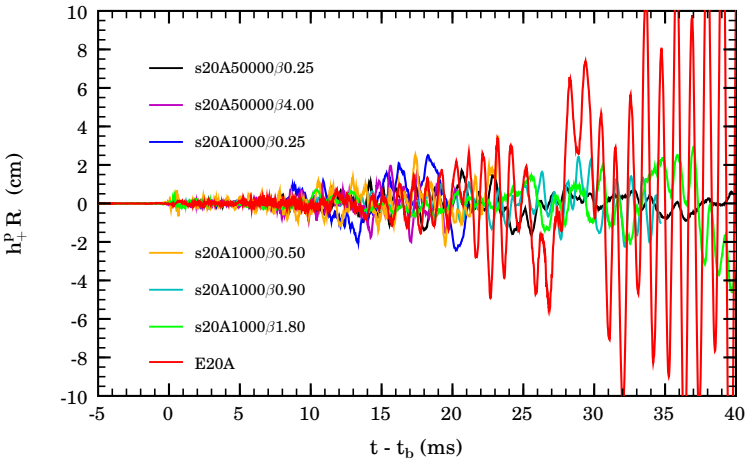

Figure 6.24: Quadrupole gravitational wave strain h_+ as seen by an observer located along the polar axis rescaled by observer distance R in model calculations without symmetry constraints on azimuthal flow. h_+ along the polar axis is identically zero in axisymmetry. Note that nonaxisymmetric (quadrupole) dynamics can be induced by convective and rotational instabilities while only the latter should lead to quasi-periodic gravitational wave emission at the frequency of the quadrupole spatial components of the nonaxisymmetric structures.

small-scale and long-period large-scale aspherical mass motions lead to a relatively broad-spectrum gravitational wave emission [9, 15, 95]. On the other hand, one would expect such a characteristic emission from a global nonaxisymmetric rotating quadrupole structure such as a spinning bar (e.g., [115, 116, 306]).

h_+^p in models s20A1000β0.90 and s20A1000β1.80 begins to exhibit a similar systematic time variation at postbounce times $\gtrsim$20 ms, but does not show fast amplitude growth in these models in the time interval covered by figure 6.24.

Model s20A50000β0.25 is the slowest rotator (postbounce $\beta \approx 0.9\%$) whose h_+^p is included in figure 6.24. It is evolved to $\sim$45 ms after core bounce and does not exhibit any significant growth or systematics in its nonaxisymmetric wave signature. Hence, its h_+^p does not convey evidence for rotation-induced nonaxisymmetric structures. The remaining three models, s20A50000β4.00, s20A1000β0.25, and s20A1000β0.50 are, unfortunately, not evolved to sufficiently late postbounce times to make a clear judgement whether their h_+^p show the imprint of a global rotational instability. At least for s20A50000β4.00, one can make out a more systematic variation in its h_+^p starting around 15 ms after bounce. s20A1000β0.25 and s20A1000β0.50, on the other hand, show relatively large h_+^p amplitudes, yet not with a clear systematic time variation.

Based on h_+^p in figure 6.24, I summarize:

(1) At least for model E20A there is strong evidence for the postbounce development and exponential growth of nonaxisymmetric structures and dynamics with a systematically time-varying mass quadrupole moment. This *suggests* that model E20A (postbounce $\beta \approx 8.5\%$) may experience a nonaxisymmetric rotational instability at low-$T/|W|$.

(2) At least 2, if not 3, additional models with postbounce β in the range of $\sim$8–13% exhibit systematically varying h_+^p amplitudes qualitatively similar to those in model E20A. However, no significant growth is observed in these models in the time interval covered by figure 6.24.

(3) At least one model, possibly 3, with postbounce β in the range of $\sim$1–6% does not/do not exhibit sufficiently systematic time variation and growth in h_+^p for their nonaxisymmetric gravitational wave emission to be related with global rotation-induced time-changing nonaxisymmetric structures. Convective overturn most likely dominates the nonaxisymmetric dynamics and postbounce gravitational wave emission in this/these model(s).

I identify models E20A, s20A1000β1.80, s20A1000β0.90, and s20A50000β4.00 as candidates whose PNSs may become unstable to a nonaxisymmetric rotational instability at β much lower than in any

model considered by RMR, Brown, and S&S who investigated only models that reached $\beta \gtrsim \beta_{\rm dyn}$. Hence, the instability at work here must be of different nature than the classical high-$T/|W|$ rotational instabilities and may be related to the low-$T/|W|$ instabilities observed in [20–24]. Model s20A50000β0.25 appears to have too low β (or degree of differential rotation) to become rotationally unstable. For the two intermediately fast models, s20A1000β0.50 and s20A1000β0.25 no clear statement on stability/instability can be made.

In the following, I present results of late-time postbounce calculations with model E20A and model s20A1000β1.80 and investigate from various perspectives the growth of rotationally-induced nonaxisymmetric structures in these models.

6.4.2 Rotational Instability at Low-$T/|W|$: Model E20A

In order to investigate the growth of nonaxisymmetric structures and dynamics at late postbounce times, I carry the simulation of model E20A out to 71 ms after core bounce[40]. The computational cost of this calculation amounts to $\sim$36000 Intel Xeon 3.4 Ghz CPU hours which correspond to a computation time of $\sim$80 days on 20 CPUs. In addition to model E20A, I also evolve model s20A1000β1.80 to late postbounce times. This model's evolution terminates at 90 ms after core bounce because of the accidental deletion of crucial restart files. I discuss it in §6.4.3.

For verification purposes, I perform a second calculation for model E20A with by $\sim$20% increased grid resolution which I carry out to $\sim$50 ms after core bounce[41]. Long-term postbounce calculations with even higher resolutions are impossible with currently available computational hardware and parallel scaling of the CARPET mesh refinement driver.

Before discussing their results, it is important to remember that the calculations presented in this section are the first ever long-term postbounce evolutions of protoneutron stars carried out in {3+1} full GR. They are also the first calculations (1) to be carried out in 3D from the onset of collapse to the late postbounce times in one computational code, (2) to start out with presupernova models from stellar evolutionary calculations, and (3) to include a finite-temperature nuclear EOS and an approximate treatment of deleptonization during collapse. The generality and validity of the results presented here are limited by (1) uncertainties in precollapse structure and rotational configuration, (2) by the neglect of postbounce deleptonization and neutrino radiation transport and (3) by the impossibility of performing a rigorous resolution study.

In the following I will characterize nonaxisymmetric structure and dynamics in terms of azimuthal modes $\propto \exp(i(m\varphi + \sigma_m t))$ with integer m and mode eigenfrequency σ_m. The mode analysis techniques that I employ are discussed in §3.9.3.

Hydrodynamics and Mode Evolution

Model E20A employs a recent "Heger" presupernova model that was evolved with a 1D prescription for rotational effects [509]. The precollapse structure and rotational configuration shown in figures 6.1, 6.2, and 6.3 may be representative for a class of massive solar-metallicity stars with weak core-envelope coupling and consequently quickly spinning precollapse iron cores. Such stars may be spinning fast enough to be related with the progenitors of collapsar-type GRBs [38, 108, 109, 113][42].

The axisymmetric collapse dynamics and gravitational wave emission of model E20A is discussed in §6.3.5 and summarized by figure 6.17. At core bounce, model E20A reaches a maximum β of $\sim$11.3% and settles at an early postbounce β of $\sim$9% (see figure 6.23). More initial model properties and quantitative results can be inferred from tables 6.1, 6.2, and 6.3.

I do not add any kind of nonaxisymmetric seed perturbations during model E20A's axisymmetric collapse. Nevertheless, nonaxisymmetric perturbations build up during collapse owing to finite-difference noise (concentrated mostly in the $m = 4$ Cartesian grid mode) and random noise intro-

[40] The simulation ultimately terminates because of lack of convergence in the temperature-finding routine in the EOS.

[41] The high-resolution simulation is stopped at $\sim$50 ms after core bounce in order to save computational resources.

[42] Note that GRB progenitor stars are likely more massive than model E20A considered here. They must lose a considerable fraction of their hydrogen and helium envelopes to allow for the supernova type Ib/c signatures in the GRB afterglows.

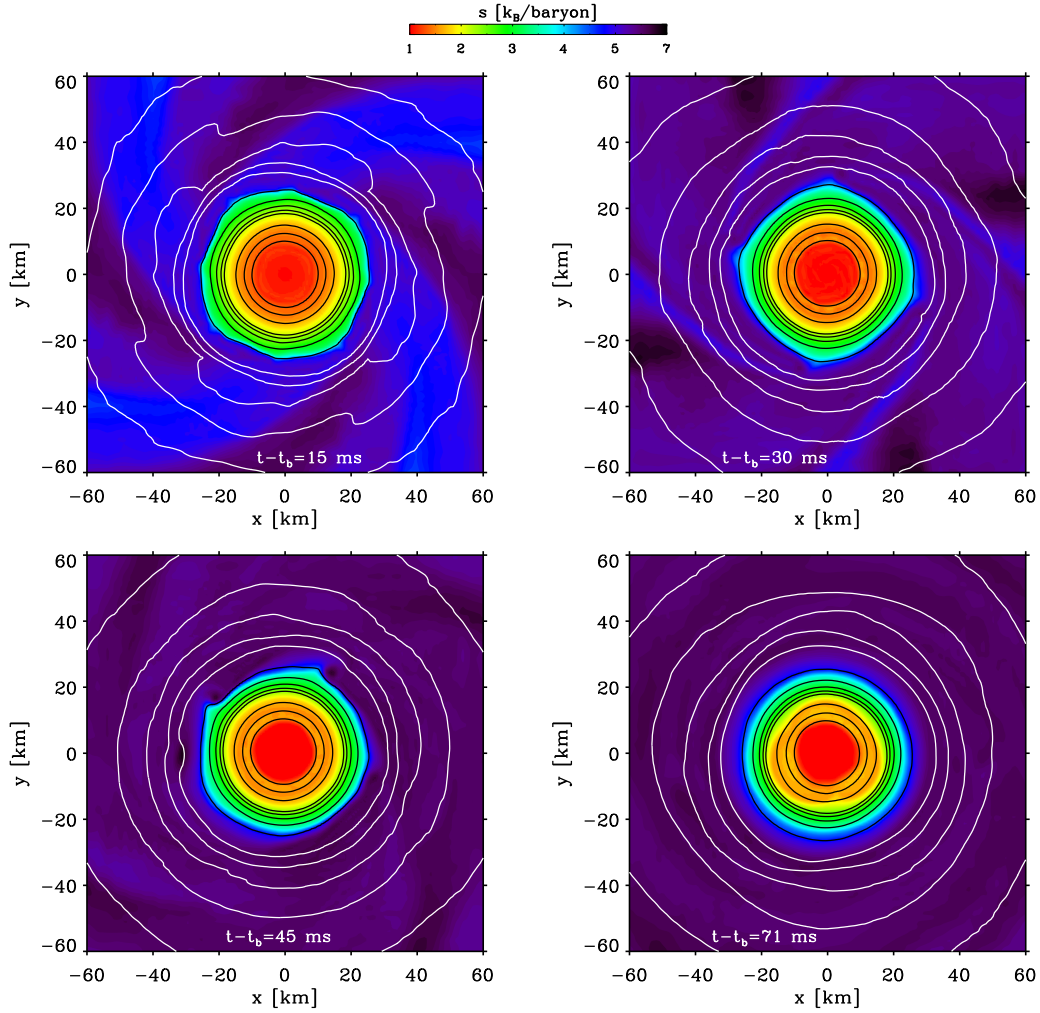

Figure 6.25: Equatorial plane snapshot slices of the specific entropy (per baryon) in model E20A at postbounce times of 15, 30, 45, and 71 ms. Shown are the inner 60×60 km^2. The 71 ms slice corresponds to the last simulated timestep. Overplotted are isodensity contours at $\{2,4,6,8\}\times10^{11}$ g cm^3, $\{1,2,4,6,8\}\times10^{12}$ g cm^3, $\{1,2.5,5\}\times10^{13}$ g cm^3, and 1×10^{14} g cm^3. The 2×10^{12} g cm^3 isocontour is the first that is plotted in black color. Note the steep radial density slope between 1×10^{13} g cm^{-3} and $\sim4\times10^{12}$ g cm^{-3} present at all times. This marks the edge of the PNS core. At 15 ms after core bounce the equatorial entropy and density distributions exhibit signs of the initially dominant $m = 4$ Cartesian grid mode that is imprinted at core bounce and shock formation and apparent in the immediate postbounce flow's characteristic 4-armed spiral structures. As the evolution proceeds, the $m = 4$ structures become gradually washed out by rotation and turbulent (large-eddy) overturn operating on entropy gradients. By $\sim$30 ms after core bounce they have practically disappeared from the density distribution in the equatorial plane, but remain faintly visible in the entropy. The snapshot from 45 ms after core bounce shows two prominent lumps in the 2×10^{12} g cm^3 isocontour and a bulge in its lower left region. At 71 ms after core bounce, both density and entropy distributions exhibit pear-like shapes, caused by a superposition of $m = \{1,2,3\}$ modes with radially varying dominance.

duced by (1) fluctuations near the lower density boundary of the EOS table ($\sim6.5\times10^5$ g cm^3), below which a polytropic EOS with $\Gamma = 4/3$ is used, (2) the finite precision of the Newton-Raphson/bisection search routine in the EOS module employed to find $T(\rho, Y_e, \epsilon)$ in every call to the EOS, and (3) the finite precision of the Newton-Raphson scheme in WHISKY that is required for the conversion from conserved to primitive hydrodynamical variables (§3.5.3).

Figure 6.25 shows equatorial-plane snapshots of the entropy distribution in model E20A's PNS at various postbounce times. Density isocontours are overplotted. As already pointed out in §6.2, core bounce and shock formation leave behind a negative entropy gradient with a strong imprint of the

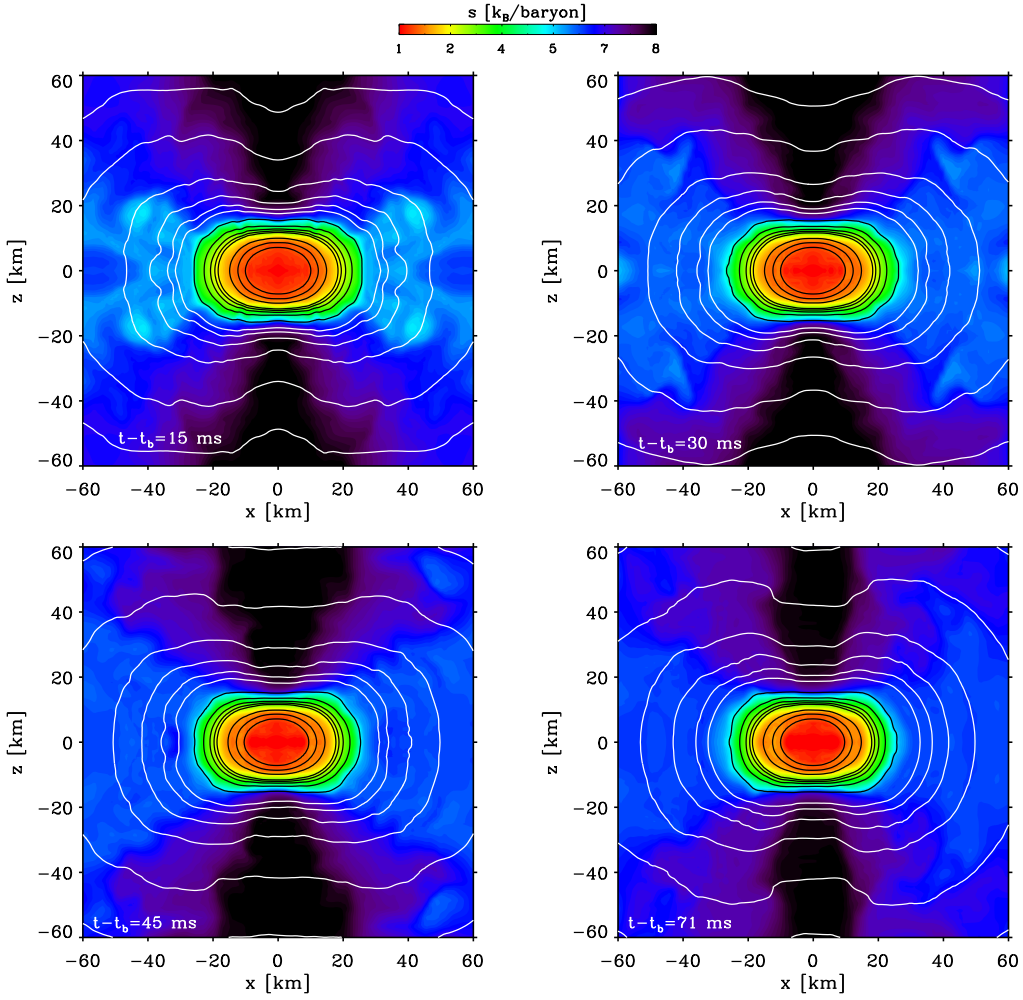

Figure 6.26: Polar slices of model E20A's specific entropy distribution at various postbounce times with isodensity contours superposed in the same fashion as in figure 6.25. Shown are the inner 60×60 km^2 on the x–z-plane. The z-axis is the rotation axis. In axisymmetry, polar slices have discrete reflection symmetry with respect to the z-axis. Top-bottom symmetry is assumed and only the upper hemisphere is numerically evolved. Note that this symmetry does not inhibit the growth of nonaxisymmetric structure, but inhibits the growth of axisymmetric modes of uneven ℓ. While differing in detail, the entropy/density isocontour snapshots exhibit a similar global morphology of the PNS. As expected for rotating collapse and bounce (§6.3), the highest entropy regions are located near the poles, where core bounce occurs earliest and strongest. The core of the PNS is strongly oblate with steeper density gradients in the polar than in the equatorial direction. With increasing radius the PNS becomes less oblate. At 15 ms after core bounce the entropy distribution still reflects the strong Cartesian grid imprint from shock formation. This imprint disappears as entropy gradients are smoothed out during the postbounce evolution. Note that starting at $\sim1\times10^{12}$ g cm^{-3} and with decreasing density, the PNS becomes thick-disk-like with a prominent polar dent in the density isocontours. Even in the final snapshot, taken at at 71 ms after core bounce, both entropy and density distributions/isocontours are almost symmetric with respect to the z-axis. The mild asymmetry / lopsidedness is not larger than a few percent.

Cartesian $m = 4$ mode. Rotation quickly disperses out the $m = 4$ grid pattern on the equatorial plane into a 4-armed spiral structure that is still prominently visible in density and entropy at 15 ms after core bounce, but is gradually washed out as the postbounce evolution progresses and is only barely visible at $\sim$30 ms after core bounce. In the snapshot taken at 45 ms after bounce one notes two relatively prominent dents in the 2×10^{12} g cm^3 isodensity contour in the upper half of the equatorial plane. A much less pronounced third dent may be made out in the middle right of the 2×10^{12} g cm^3 density contour. Interestingly, the core of the PNS is mildly lopsided with a slightly farther extending 2×10^{12} g cm^3 isocontour towards the lower left of the PNS core. The nonaxisymmetric structure at

45 ms after core bounce does not exhibit a strong signature of a single globally dominant mode, but rather suggests an interplay of multiple modes. At 71 ms after core bounce the PNS has become significantly nonaxisymmetric. It is slightly lopsided with pear-like deformed isosurfaces, varying in phase and slightly in shape with equatorial radius. The pear shaped structure, which is particularly strong in the outer regions of the PNS ($\varpi \gtrsim 25$ km), indicates a strong $m = 3$ mode while the slight lopsidedness is (weak) evidence for $m = 1$ azimuthal structure.

Figure 6.26 shows polar slices (x–z-plane) of model E20A's central 60×60 km^2 specific entropy distribution at 15, 30, 45 and 71 ms after core bounce. As in figure 6.25, density isocontours are superposed. Note that top-bottom symmetry, i.e. reflection symmetry with respect to the x-axis, has been assumed. The strong rotational flattening of the PNS is a striking feature in all panels. With increasing radius and decreasing density, the density isocontours become more disk-like with prominent dents in the polar region and prominent bulges at lower latitudes. The central region of the PNS remains spheroidal throughout model E20A's postbounce evolution. As expected for rotating core bounce (§6.3 and figure 6.10), a high-entropy region is present along the rotation axis where shock formation occurs first and most strongly. The region of high entropy gradually becomes smaller in angular extent as the postbounce evolution progresses, most likely owing to convective mixing with lower-entropy regions at its edges. At 15 ms strong relatively low-entropy Cartesian relics of shock formation are visible in entropy and density at latitudes below $\sim45^\circ$. These are gradually smoothed out and have vanished by ~30 ms after bounce.

In axisymmetry, the PNS polar slices shown in figure 6.26 should exhibit reflection symmetry with respect to the z-axis.[43] In the 15 ms postbounce polar slice virtually no deviations from axisymmetry are visible. The 30 ms slice shows minute deviations from axisymmetry in the $\sim2\times10^{12}$ g cm^{-3} isocontour (the last black isocontour in the panels of figure 6.26), but at larger radii and lower densities, the PNS is almost perfectly axisymmetric. At 45 ms and certainly at 71 ms after bounce, deviations from axisymmetry are obvious in both density isocontours and entropy distribution, yet – by visual judgement – are relatively small and do not dramatically alter the PNS structure.

For a more quantitative analysis of the nonaxisymmetric structure, I perform a Fourier mode analysis of the form discussed in §3.9.3 in which I decompose the rest-mass density ρ in rings of constant equatorial coordinate radius ϖ in the equatorial plane into complex Fourier components [306, 522]

$$C_m(\varpi, z = 0) = \frac{1}{2\pi} \int_0^{2\pi} \rho(\varpi, z = 0, \varphi) e^{-im\varphi} d\varphi \ , \tag{6.12}$$

whose normalized absolute values,

$$A_m = \frac{1}{|C_0|} \sqrt{\mathrm{Re}\{C_m\}^2 + \mathrm{Im}\{C_m\}^2} \ , \tag{6.13}$$

where $C_0(\varpi, z = 0) = \bar{\rho}(\varpi, z = 0)$ is the mean density in a given ring, are considered as indicators for relative mode strengths.

Figure 6.27 depicts the $m = \{1, 2, 3, 4\}$ mode evolutions as a function of postbounce time for various equatorial radii in the range 10 km $< \varpi <$ 100 km, covering the entire PNS. At the end of the calculation, ~1.37 M$_\odot$ are contained within a 100 km radius from the origin and the accretion rate is ~1.7 M$_\odot$/s; the core of the PNS, material with $\rho \gtrsim 10^{12}$ g cm^{-3}, extends to ~30 km.

Shortly before core bounce, the $m = \{1, 2, 3\}$ mode amplitudes have grown to $\sim10^{-6}$, while the $m = 4$ grid mode is at a prebounce 10^{-4} level in the central finely resolved region. In the final ms of collapse, when the shock begins to form at the boundary of the subsonically collapsing inner core with the supersonically collapsing outer core, all mode amplitudes increase by at least one order of magnitude. This mode amplification is most likely connected to the highly-dynamical event of shock formation in which the almost solid-wall like reflection of the outer core off the inner core's outer edge which injects power into the entire mode spectrum.[44]. The mode amplification is strongest near the radius of shock formation ($\sim$10–20 km) and is somewhat delayed at larger radii.

[43] Note that a purely ($m = 2$) bar-deformed PNS spinning around the z-axis will show reflection symmetry on the x–z plane at times when its bar is in alignment with the x-axis. Due to the strongly differential rotation of the PNS, such a global alignment is highly unlikely. A perfectly wound $m = 2$ spiral pattern may also appear as axisymmetric on a polar slice.

[44] This is most likely due to the amplification of nonaxisymmetric perturbations already present in the prebounce flow by the strongly non-linear dynamics associated with core bounce and shock formation. In addition, discretization errors and mass loss owing to errors in the curvature-matter coupling may be involved.

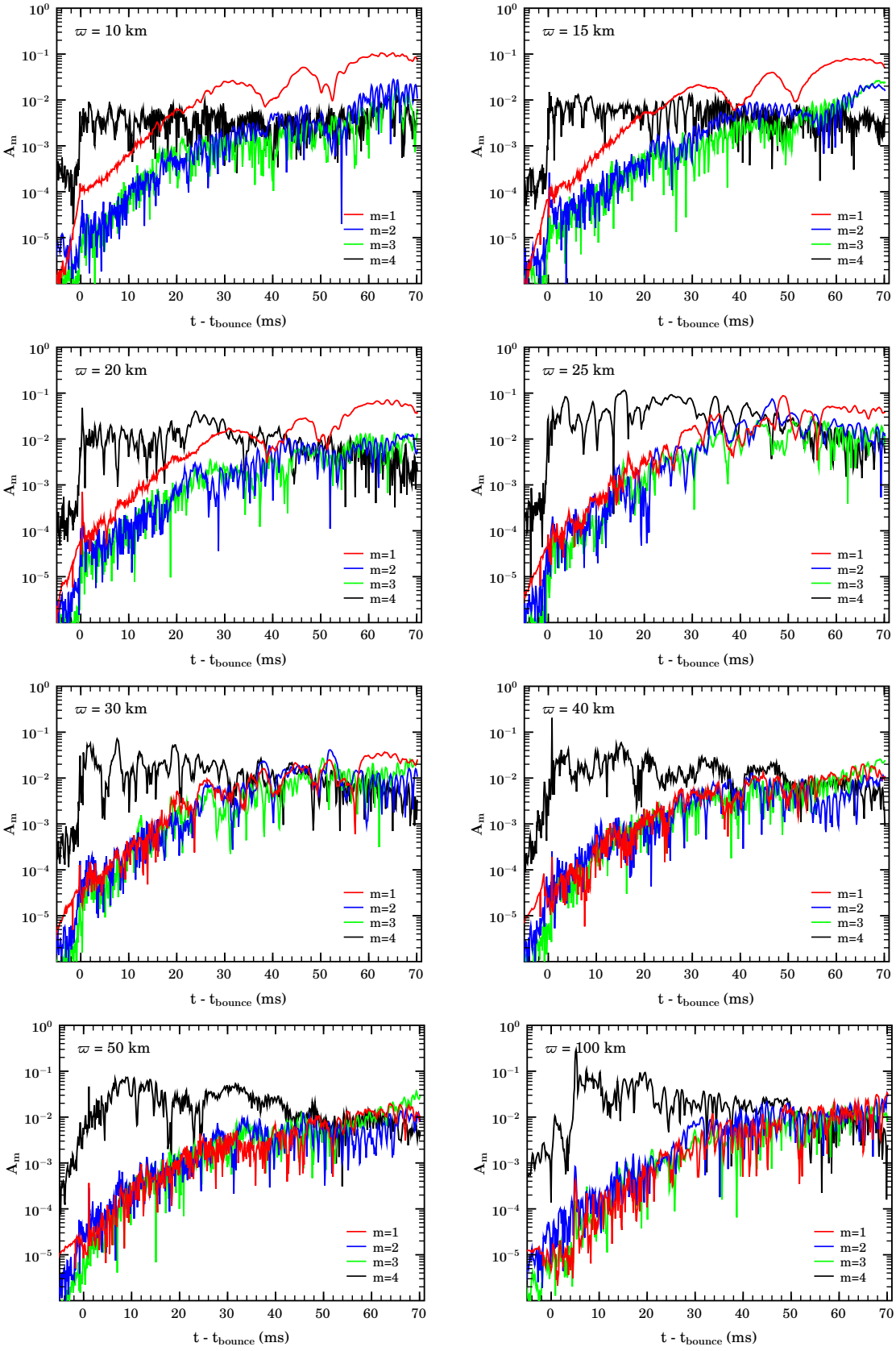

Figure 6.27: The growth of the normalized mode amplitudes A_m (§3.9.3), evaluated at various coordinate radii in the equatorial plane of model E20A. The time is given relative to the time of core bounce. Note that the $m = 1$ mode dominates at all times at equatorial radii $\varpi \lesssim 25$ km and blends in with the growth of $m = \{2, 3\}$ at larger radii. The PNS appears to be dynamically stable to the $m = 4$ grid mode which is dominant at early times, but whose amplitude does not grow with time. Note that a more global-type analysis, as proposed by [20, 300], would gloss over the important radial variation in the mode structure observed here.

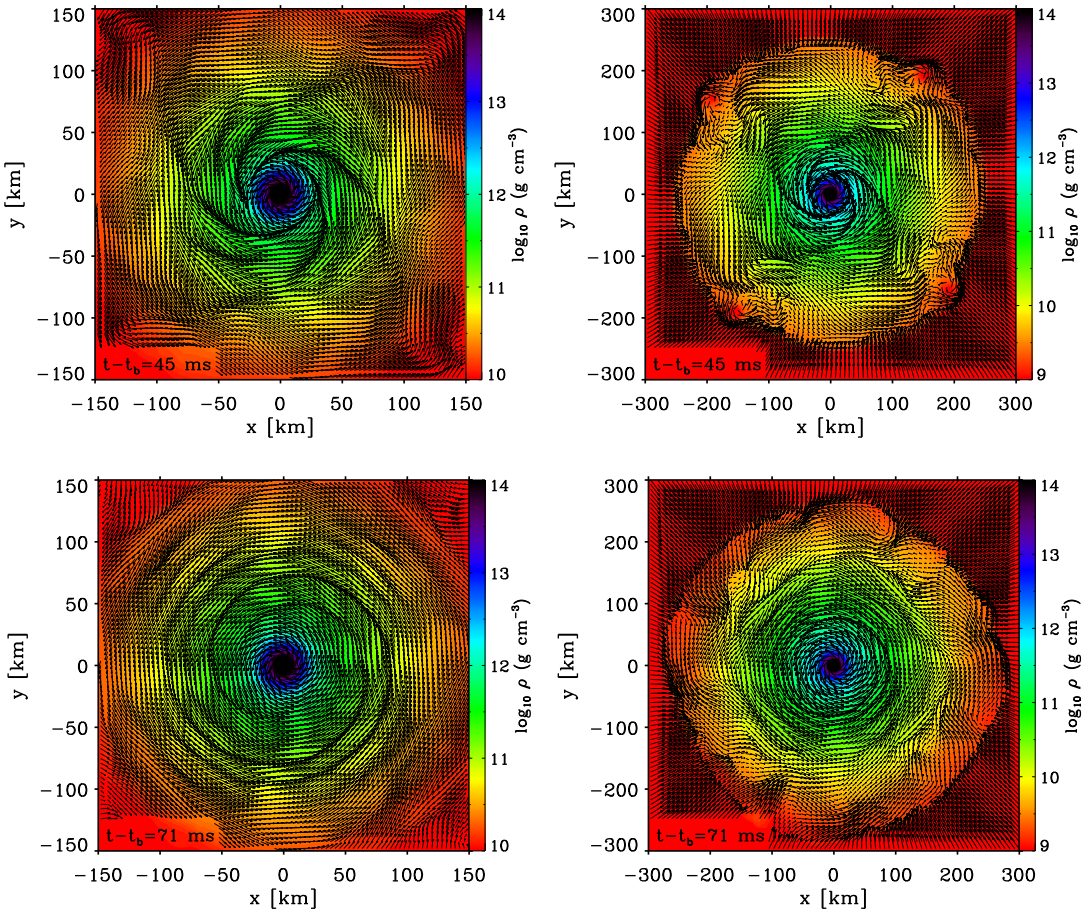

Figure 6.28: Equatorial density distribution with overplotted velocity vectors (vector length saturated at $0.04c$) in model E20A at 45 ms (top row) and 71 ms (bottom row) after core bounce. Left panels: Shown are the inner 150×150 km^2. At 45 ms after bounce strong $m = 4$ features are still visible in the flow at intermediate equatorial radii. This corresponds to the mode amplitude evolutions at these radii shown in figure 6.27 which show a dominant $m = 4$ component. At 71 ms, however, the $m = 4$ features have almost disappeared and two strong and one barely noticeable third spiral arm originate at $\sim$30 km radius, are relatively tightly wound and extend throughout the region shown, but are most prominent within $\sim$100 km radius. Right panel: Shown are the inner 300×300 km^2 including the shock position at 200–250 km equatorial radius. At 45 ms after core bounce the shock is strongly distorted by $m = 4$ features, most likely strongly emanating from a mesh-refinement boundary close to the shock front. At 71 ms the $m = 4$ features have mostly disappeared and the spiral pattern of the lower m nonaxisymmetric structures extends out to $\sim$200 km where it hits the immediate postshock region, distorts the shock and is distorted by accretion flows through the stalled shock.

The inner core that collapsed quasi-homologously and coherently experienced core bounce forms the core of the newborn PNS that extends out to $\sim$20 km after core bounce. In this core region, the $m = 1$ mode amplitude exhibits the fastest growth rate and becomes dominant over the also growing $m = 2$ and $m = 3$ mode amplitudes shortly after core bounce. The amplitude of the initially dominant $m = 4$ grid mode does not exhibit significant variations in magnitude in the PNS core throughout the simulated postbounce time. At 20–25 ms after core bounce, the $m = 1$ mode amplitude reaches the nonlinear regime ($\sim$1% amplitude) and passes the $m = 4$ amplitude level. It becomes the globally dominant mode in the central $\sim$20 km of the PNS and its growth begins to saturate shortly after, while the $m = \{2, 3\}$ mode amplitudes continue to grow.

From the mode analysis at $\varpi = 15$km, I infer an amplitude e-folding time τ_e of $\sim$4.5 ms for the $m = 1$ mode in the exponential growth regime and a total growth time $\tau_{\rm growth}$ to nonlinear amplitudes of $\sim$20 ms. A characteristic dynamical timescale $\tau_{\rm dyn}$ is frequently defined in terms of the Keplerian

angular velocity (e.g., [22, 24, 286])

$$\Omega_{\rm K} = \sqrt{\frac{4}{3}\pi G\bar{\rho}} \tag{6.14}$$

of a star with average density $\bar{\rho}$:

$$\tau_{\rm dyn} \approx \frac{2\pi}{\Omega_{\rm K}} = \frac{\sqrt{3}\pi}{\sqrt{\pi G\bar{\rho}}} \ . \tag{6.15}$$

The central 20 km (in coordinate radius) contain $\sim$0.68 $M_\odot$ at postbounce times in model E20A, hence $\bar{\rho} \sim 4\times10^{13}$ g cm^{-3} and $\tau_{\rm dyn} \sim$1.9 ms. Comparing $\tau_{\rm dyn}$ with τ_e and $\tau_{\rm growth}$ of the unstable $m = 1$ mode it is clear that the instability is dynamical: $\tau_e/\tau_{\rm dyn} \approx 2.4$ and $\tau_{\rm growth}/\tau_{\rm dyn} \approx 10.5$. The rotation period of the PNS core is around 2–3 ms at 5 ms after core bounce (see figure 6.23). Hence, the $m = 1$ mode grows within a few rotation periods of the PNS core. A secular instability, at least one driven by the theoretically known viscosity or gravitational-radiation reaction mechanisms, would require a much longer growth timescale, probably on the order of $\sim$1 s [286, 291, 297].

The $m = 1$ mode amplitude appears to saturate just below the 10^{-1} level. This and its at least partial confinement to the PNS core are why the $m = 1$ spatial structure, characterized by an offset of the local center of mass[45] of a certain region, typically in combination with a one-armed spiral-like pattern [20–22, 22, 23], is not obvious from the density and entropy distributions displayed in figures 6.25 and 6.26.

Figure 6.27 suggests that the instability originates in the PNS core and from there propagates outward through the postshock region while partly shifting in spatial structure to higher-order modes. This is corroborated by figure 6.28 that depicts the density and flow field within 150 km (left panels) and 300 km equatorial radius (right panels) at 45 ms (top panels) and 71 ms (bottom panels) after core bounce. At 45 ms the $m = 4$ mode is still dominant at radii $\gtrsim$40 km and the flow patterns show its strong imprint including a strong $m = 4$ disturbance of the standing accretion shock front, caused by the presence of a CARPET mesh refinement boundary close to the shock position. Fully adaptive mesh refinement would be needed to adequately resolve the shock at all postbounce times. At 71 ms after bounce the $m = 4$ features have practically vanished from the velocity field and the density distribution. The flow is now dominated by two strong and one weaker spiral waves that emerge at $\sim$30 km equatorial radius from the PNS center and reach out through almost the entire postshock region. They significantly distort the shock, but cannot propagate beyond the shock radius were outer core material is accreting with supersonic velocities.

Angular Momentum Redistribution

The spiral arms that develop in the equatorial plane of model E20A are very much reminiscent of spiral structures in disk galaxies or in thick self-gravitating accretion disks, formed by density waves that propagate through the disks and interact with the disk background flow. This interaction can lead to net outward angular momentum transport and increasingly rigid rotation. (Lin-Shu theory, see, e.g. [578, 582–586]). While the accretion-disk density-wave phenomenon occurs on a dynamical timescale, the resulting angular momentum redistribution happens more slowly. In principle, one can find the angular momentum flux associated with an individual density wave [583, 586]. In a less physical, though perhaps more practical way, angular momentum redistribution may be described by an effective kinematical viscosity [587, 588]. If H is the disk semi-thickness and R the disk radius, then in the case of a relatively thin disk ($H \ll R$), the effective local kinematic viscosity is

$$\nu_{\rm eff} = \frac{1}{Q^2} H^2 \Omega \ , \tag{6.16}$$

where Ω is the local angular velocity and Q is the Toomre parameter [584], describing the relevance of self-gravitation. For disks with significant self-gravitation $Q \lesssim 1$. With $\alpha \approx Q^{-2} > 1$, this

[45] Defining a center of mass position and observing momentum conservation is a difficult task in numerical relativity. Similar to the ADM mass one can define an ADM momentum via a surface integral in flat region far away from the gravitating source [126], but then has to account for ingoing and outgoing gravitational waves that may carry linear momentum. For simplicity, I define a coordinate-dependent center of mass coordinate $C^i = M^{-1}\int x^i \rho W \sqrt{\gamma} d^3x$ which should be conserved approximately. Conservation may be violated by outgoing gravitational waves, gauge and boundary effects, and discretization errors such as flux-mismatches at mesh-refinement boundaries. The approximate global center of mass stays within the central-most computational cell throughout the evolution of model E20A.

effective viscosity is equivalent to the standard α-viscosity [588]. The "viscous" timescale for angular momentum redistribution is approximately [587] given by

$$\tau_\nu \sim \frac{R^2}{\nu_{\rm eff}} \sim \left(\frac{M}{M_{\rm d}}\right)^2 \frac{1}{\Omega}\,, \tag{6.17}$$

where M and $M_{\rm d}$ are the total and the disk mass, respectively. The postbounce configuration of model E20A may indeed be regarded as a system with a central object (the PNS core) and an (non-Keplerian) accretion region/disk (the postshock accretion flow, which experiences strong rotational effects at low latitudes, but remains non-Keplerian) whose outer boundary is defined by the standing accretion shock in the equatorial plane. However, note the caveat that there is no well defined boundary between PNS and postshock flow. Figure 6.29 shows a polar slice snapshot of the entropy distribution with superposed density isocontours in the innermost 300×300 km^2 of the x–z-plane. The clearly visible standing accretion shock separates the high-entropy postshock region from the infalling low-entropy material of the outer core. At least the region encompassing material with density greater than $\sim 10^{11}$ g cm^{-3} is rotationally-flattened enough and has a sufficiently evacuated polar region to resemble (to some extent) a central object — thick accretion disk system. The PNS core is very oblate, but both density and entropy distributions show decreasing oblateness with increasing radius and decreasing density. The density isocontours outside the PNS have weakly quasi-toroidal shape with individual x–y-slices having off-center density maxima. In addition, considerable deviations from axisymmetry, possibly of dominant $m = 1$ character, are most obvious in the density isocontours that show considerable lopsidedness near the polar axis and at z-coordinates outside the PNS.

If the nonaxisymmetric instability in model E20A is of similar nature as the spiral waves in a galaxy or accretion disk, then angular momentum redistribution should occur on a timescale slower than

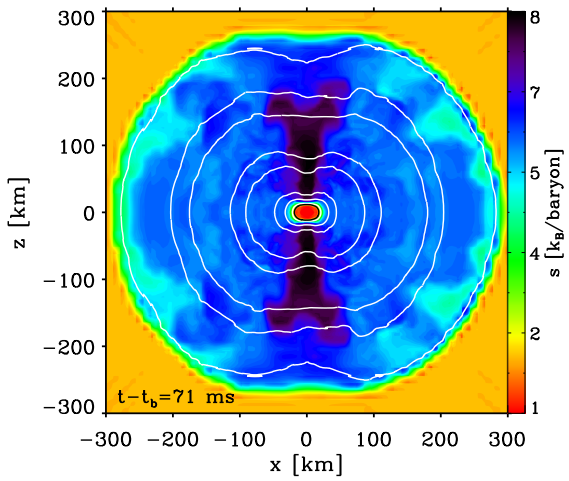

Figure 6.29: Polar x–z-slice of the entropy distribution at 71 ms after core bounce in model E20A. Shown are the innermost 300×300 km^2. Density isocontours are superposed at 1×10^9 g cm^{-3}, 5×10^9 g cm^{-3}, 1×10^{10} g cm^{-3}, 5×10^{10} g cm^{-3},1×10^{11} g cm^{-3}, 5×10^{11} g cm^{-3}, 1×10^{12} g cm^{-3}, 5×10^{12} g cm^{-3}, and 1×10^{13} g cm^{-3}. Note the polar dents in the isocontours, indicating off-center density maxima in the corresponding x–y-planes. See figures 6.32 and 6.33 for x–y-slices at various z-coordinates.

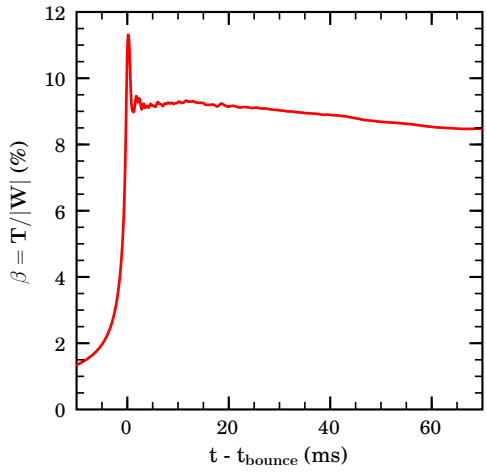

Figure 6.30: Postbounce evolution of the rotation parameter $\beta = T/|W|$ in model E20A. The slow but continuous decrease in β is caused by the postbounce accretion of relatively low angular momentum material (in particular along the polar axis) that results in a greater increase in compactness (and, hence, in $|W|$) than in rotational energy. A causal relationship with the rotational instability in model E20A is unlikely, given that the amount of angular momentum contained in the PNS core stays approximately fixed throughout the postbounce times covered by the simulation. In addition, any dynamical angular momentum redistribution effects should appear in β at late postbounce times when the instability gets strong. Yet, the evolution of β does not exhibit signs of rapid angular momentum redistribution.

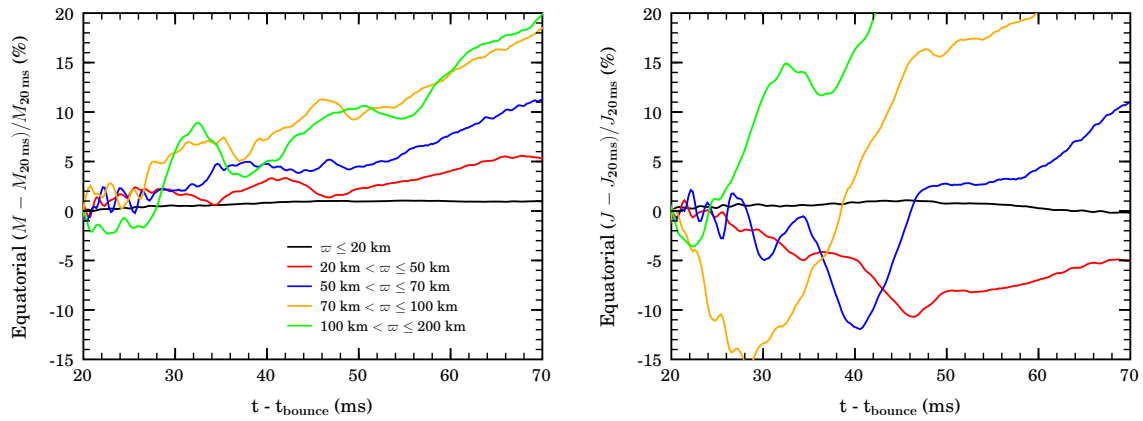

Figure 6.31: Left Panel: Evolution of the relative change in the mass contained in slabs within various equatorial radial intervals and $|z| \leq 10$ km. The changes are measured with respect to the values at 20 ms after bounce. Right panel: Same as the left panel but for the integral angular momentum. While there are significant temporal variations that do not show obvious systematics, it is important to note that the angular momentum contained within 20 km from the rotation axis does not and that contained in $20 < \varpi \leq 50$ km does slightly decrease while the mass contained in these regions increases slightly. This may be (weak) evidence for angular momentum transport by the equatorial spiral density waves seen in figure 6.28.

the dynamical. This would set the instability observed here significantly apart in nature from high-$T/|W|$ instabilities that lead to dynamical redistribution of angular momentum (e.g. [286]).

At $\sim$70 ms after core bounce, the PNS core ($\sim$ all material with densities $\gtrsim 10^{12}$ g cm^{-3}) has a mass of $\sim$0.8 M$_\odot$. If one considers all material with densities in between $\sim 10^{12}$ g cm^{-3} and $\sim 1\times 10^{10}$ g cm^{-3} to be part of the extended relatively thin (H/R is still < 1) "disk", then $M_{\mathrm{d}} \sim$0.4 M$_\odot$. With an angular velocity of $\sim$50 rad s^{-1} at 150 km equatorial radius, I estimate via equation (6.17) an approximate angular momentum redistribution timescale of $\sim$80 ms. Note, however, that the estimate assumes fixed total angular momentum in the accretion disk. This clearly does not hold for the PNS considered here whose postshock layers are continously fed with mass and angular momentum from the accreting outer core material. Rather, it is likely that the angular momentum accretion and redistribution timescales are comparable.[46] This would suggest that (a) the angular momentum of the PNS core should stay approximately constant while its mass increases and (b) that eventually and as a consequence of outward angular momentum transport, Keplerian angular velocities may be reached in the postshock region. The latter may – in combination with neutrino heating which is not included in this study – be beneficial towards the revival of the stalled supernova shock.

Figure 6.30 shows the evolution of the rotation parameter β in model E20A. Beginning at $\sim$10 ms after core bounce, β slowly and continuously decreases from 9.3% to 8.5%. This slight decrease is most likely not due to angular momentum redistribution by the nonaxisymmetric instability. It is rather a consequence of accretion of large-latitude, low angular momentum material onto the PNS. This can, for example, be inferred from the variations of the polar density isocontour positions in figure 6.26 and also from this model's ρ_{max} evolution plotted in panel (c) of figure 6.40 on page 205. The accreted low angular momentum material increases $|W|$ at a higher rate than T. Hence, with this explanation for the slow postbounce decrease of β in mind, no evidence for significant angular momentum redistribution can be inferred from the postbounce evolution of β.

In order to more directly capture the dynamics near the equatorial plane where the spiral structures are most pronounced and where most of the angular momentum is located, I compute mass and angular momentum integrals in volumes extending 10 km along the z axis on either side of the equatorial plane and bounded by various inner/outer equatorial radii ϖ. The results are shown in figure 6.31. The left panel depicts the almost monotonic increase in mass that is contained within all radii considered in this analysis. The PNS core (extending to $\sim$20 km) gains $\sim$1% in mass from 20 to 50 ms after bounce. Regions of greater ϖ show greater relative mass gains. The right panel of figure 6.31 displays the relative change in the angular momentum[47] J in the regions considered.

[46] Note that in a Keplerian disk the viscous timescale would *set* the accretion timescale.

[47] For simplicity, I compute the angular momentum integral based on the matter dynamics only and neglect curvature terms.

The regions with intermediate ϖ show significant variations in J at times earlier than $\sim$40 ms postbounce. These may be related to later currents owing to the postbounce convective instability not totally suppressed by centrifugal support at intermediate ϖ. By 70 ms after core bounce, the angular momentum in the regions with $\varpi \gtrsim 50$ km has significantly increased (as expected from the corresponding increase in mass). On the other hand, the region with 20 km $< \varpi <$ 50 km does – if one focusses for a moment on the first and last times displayed in figure 6.31 only – appear to *lose angular momentum while gaining mass*. However, this observation may be precipitate and more involved interpretation is necessary: The relative increase in mass in the region under consideration may in part be explained by low-J accretion along the polar axis. In addition, the 10% decrease in J from 20 to $\sim$45 ms after bounce is most likely due to lateral angular momentum transport in the early postbounce convection [273]. At $\sim$45 ms after bounce accretion of angular momentum begins to dominate over lateral redistribution and J in 20 km $< \varpi <$ 50 km begins to increase, but, interestingly, with a significantly shallower slope than the regions at greater ϖ. The mass accretion, on the other hand, happens at the same rate in all ϖ regions outside the PNS core.

It is only the slight discrepancy of mass and angular momentum accretion rates that provides hint of angular momentum redistribution in the equatorial regions of model E20A. The evidence is weak. Since the accretion is sub-Keplerian and angular momentum from the outer core is continuously fed into the postshock region, it is intrinsically difficult to measure angular momentum redistribution and much longer term calculations would be necessary to uncover its details and quantitative aspects.

However, based on the analysis that I have performed, I can rule out a dynamical large-scale gravitational torque driven angular momentum redistribution in model E20A. Such a redistribution would be manifest in the β and J evolutions and would require nonaxisymmetric mode amplitudes of order unity which I clearly do not observe in model E20A (see, e.g., the mode analysis results presented in figure 6.27).

z-Dependence of the Nonaxisymmetric Structure

The development of nonaxisymmetric structure and dynamics in simulations of disks, tori, and stars is frequently diagnosed on the equatorial plane only (see, e.g., [21, 24, 25, 306, 522, 589, 590]). While this approach may be reliable and sufficient for thin disks and tori, and for stars that deform in a globally coherent fashion, possibly important features of rotating and accreting PNS at nonzero z-coordinates may be missed by a restriction of the analysis to the equatorial plane. Various studies have tried to include off-equatorial plane information via global volume-integral type "diagnostics" (e.g., [20, 22, 23, 204, 300, 302–304, 308, 309]). This approach falls short of capturing qualitative and quantitative *changes* of the flow with increasing distance from the equatorial plane.

The polar x–z-slices displayed in figures 6.26 and 6.29 demonstrate considerable variations in the PNS and postshock entropy and density distributions along the z-axis: Beginning at a z-coordinate of $\pm$20 km and with increasing $|z|$, the outer layers of the PNS and the postshock region show off-axis density maxima in slices of constant z. Hence, a x–y slice at $|z| \gtrsim 20$ km would exhibit a density maximum located on a ring at some ϖ from the rotating axis. Such an off-center maximum indicates *quasi-toroidal* structure in the outer PNS regions. In addition, figure 6.29 shows a lopsidedness of the density isocontours, changing with z-coordinate and density suggestive of variations in nonaxisymmetric structure.

Figure 6.32 depicts x–y-slice snapshots of model E20A's density distribution at $z = \{10, 25, 50, 100\}$ km with superposed velocity vectors. The snapshots encompass the entire postshock region and are taken at the last simulated time. The slices at $z = 10$ and $z = 25$ km exhibit the same spiral structure as observed in the equatorial plane (see figure 6.28). At $z = 50$ km the flow appears less structured and the spirals are barely visible and appear washed out and, finally, at $z = 100$ km the low-m spirals have disappeared and the nonaxisymmetric structures in flow, shock front and density distribution are of dominant $m = 4$ character, which may be a consequence of the relatively low spatial resolution of $\sim$3 km at that z-position.

In figure 6.33, I show zoomed-in x–y-slices of the density distribution at the same z-positions and time as in figure 6.33. Here I have superposed density isocontours to visually emphasize the nonaxisymmetric structures. The $z = 10$ km slice bears very similar nonaxisymmetric features as the equa-

torial slice in figure 6.25, including the $m = 3$ pear-like deformation close to the PNS core boundary and a slight lopsidedness in the central regions. The density distribution is centrally condensed. At $z = 25$ km a prominent high-density region in a heavily distorted thick ring around the origin is visible. The density maximum is located in a single small region and the entire density distribution is significantly $m = 1$-like lopsided. At $z = 50$ km the picture is different again. There is a high-density region located in a lopsided ring around an almost bar-like deformed central lower-density region. The highest density material is located in a U-shaped region. At $z = 100$ km the U-shape has spread to greater ϖ (note the greater x–y extent of the $z = 100$ km panel and the small range in density covered by isocontours and color map) and at this z-position marks the high-density region. The density maximum is located in a single small and elongated region within the U.

For a more quantitative understanding of how the nonaxisymmetric structure varies with distance to the equatorial plane, I perform a mode analysis of the density distribution on x–y-planes of various z-coordinates. Figure 6.34 depicts the nonaxisymmetric $\propto \exp(im\varphi)$ mode amplitudes computed at 20 km from the rotation axis and at 10, 25, 50, and 100 km from the equatorial plane. In spite of the decreased spatial resolution at intermediate and large distance from the equatorial plane, the $m = 4$ mode amplitude does not vary much with the z-coordinate. Possibly, the decreased vorticity/circulation at large z-coordinate lowers the power in nonaxisymmetric modes and thus compensates for the lower resolution that would lead to larger $m = 4$ mode amplitudes. This explanation may be plausible since the $m = \{1, 2, 3\}$ mode amplitudes exhibit a drift to lower amplitudes with in-

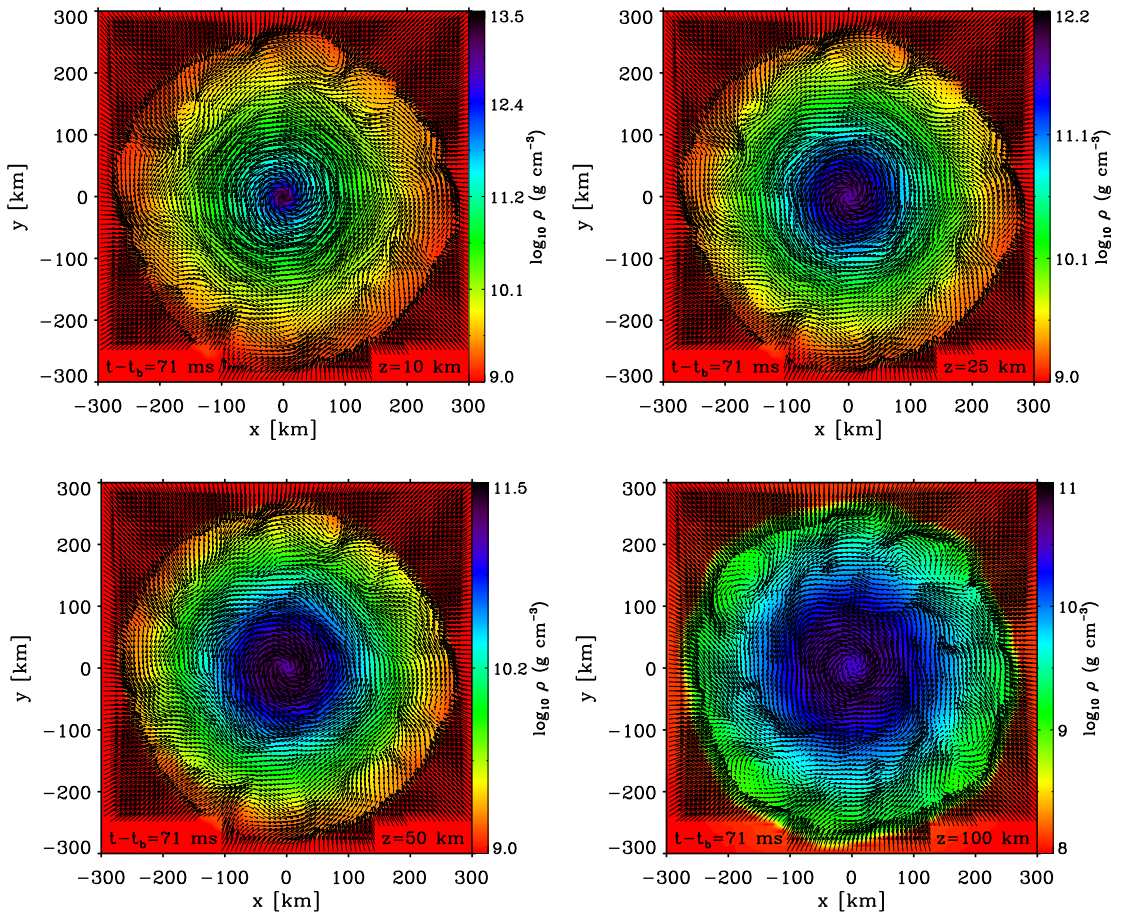

Figure 6.32: x–y-plane slices of the density distribution with overplotted velocity vectors (vector length saturated at $0.04c$) in model E20A at the last simulated time and at z-coordinates of 10, 25, 50, and 100 km. Shown are the inner 300×300 km^2. Note that the color map ranges vary from slice to slice. At z-locations of 10 and 25 km the spiral structure observed in the equatorial plane (figure 6.28) is marginally visible. At $z = 50$ km, the spirals are heavily distorted and barely discernible from the background flow. At $z = 100$ km the long-armed spiral pattern has vanished and $m = 4$ features dominate the flow.

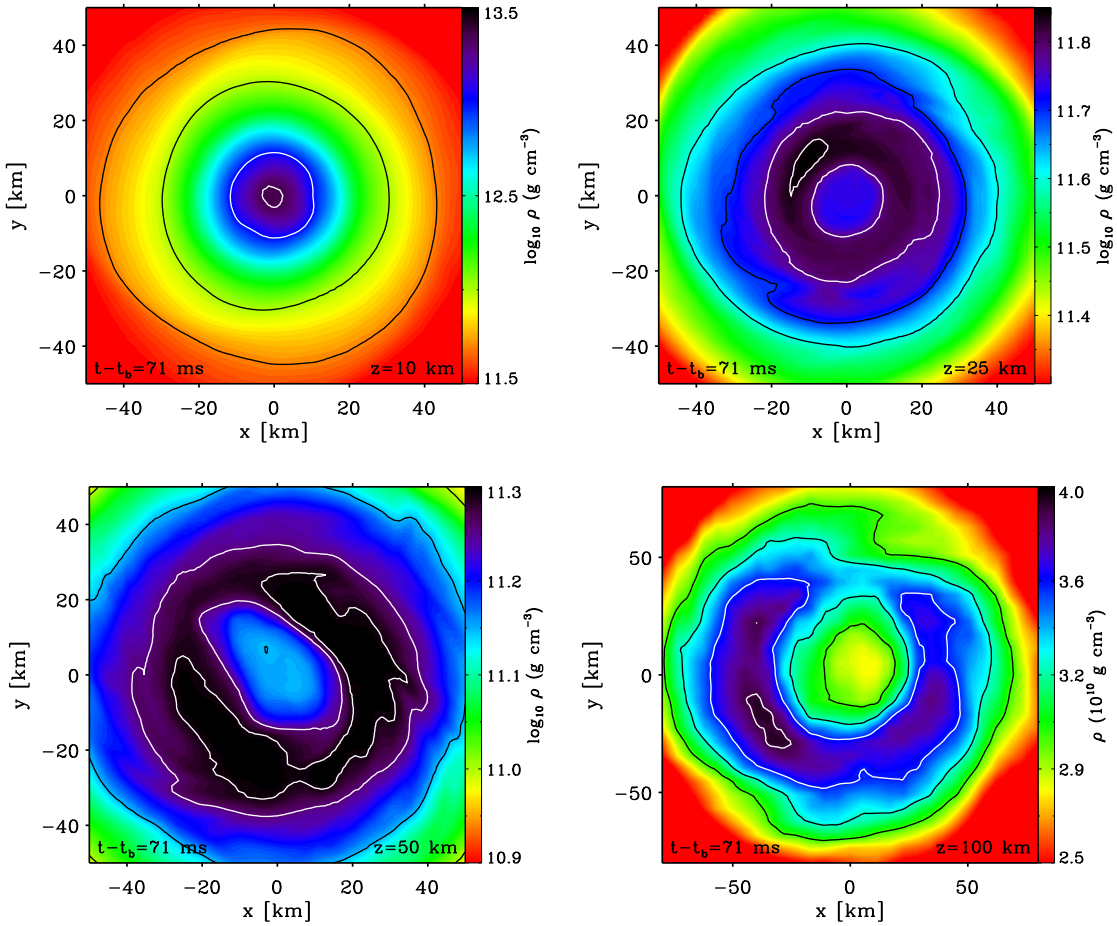

Figure 6.33: x–y-slices of the density distribution in model E20A at z-positions of 10, 25, 50, and 100 km. The snapshots are taken at 71 ms after core bounce and density isocontours are superposed. With increasing $|z|$ the range in ρ covered by the slices decreases. In contrast to figure 6.32, only the inner 50×50 km^2 (in the bottom left panel, the inner 100×100 km^2) are shown. Note that the $z = 100$ km slices uses a linear scale in the colormap. Top left: Isocontours at 5×10^{11}, 1×10^{12}, 1×10^{13}, and 2.2×10^{13} g cm^{-3}. Top right: Isocontours at 4×10^{11}, 5×10^{11}, 6×10^{11}, and 6.85×10^{11} g cm^{-3}. Bottom left: 1×10^{11}, 1.4×10^{11}, 1.8×10^{11}, and 1.95×10^{11} g cm^{-3}. Bottom right: 3×10^{10}, 3.3×10^{10}, 3.6×10^{11}, and 3.9×10^{11} g cm^{-3}.

creasing z-coordinate while maintaining the same overall growth behavior. At $z = 10$ km, the mode amplitude evolution is qualitatively similar to the corresponding equatorial plane mode evolution presented in figure 6.27. However, note that the $m = 3$ contribution at late times is considerably stronger than on the equatorial plane. With increasing z-distance from the equatorial plane, the $m = 2$ component becomes more relevant and even dominant at various times in E20A's postbounce evolution. It is particularly strong on the $z = 50$ km and $z = 100$ km planes where $m = 2$ features are readily observable in the density distribution (at 71 ms after core bounce in figure 6.33).

All the evidence collected and presented here indicates that there are significant variations in the nonaxisymmetric structures and dynamics with increasing distance from the equatorial plane. To my knowledge such variations have so far not been discussed in the literature on rotational non-axisymmetric instabilities. This is most likely because of the fact that the usual/classical rotational instabilities of fluid bodies that occur at high-$T/|W|$ and which are well studied in linear theory lead to globally coherent deformations. A bar mode is a bar mode is a bar mode — independent of z-coordinate. The instability studied here is of low-$T/|W|$ nature and occurs in and around a PNS that continously accretes matter and angular momentum. It is natural to expect complicated spatially and temporally varying nonaxisymmetric structure and dynamics. In particular, the variations in the z-direction are likely to be related to the change from centrally-condensed structure to a torus/ring-like density distribution with increasing z-coordinate. In the light of what has been found

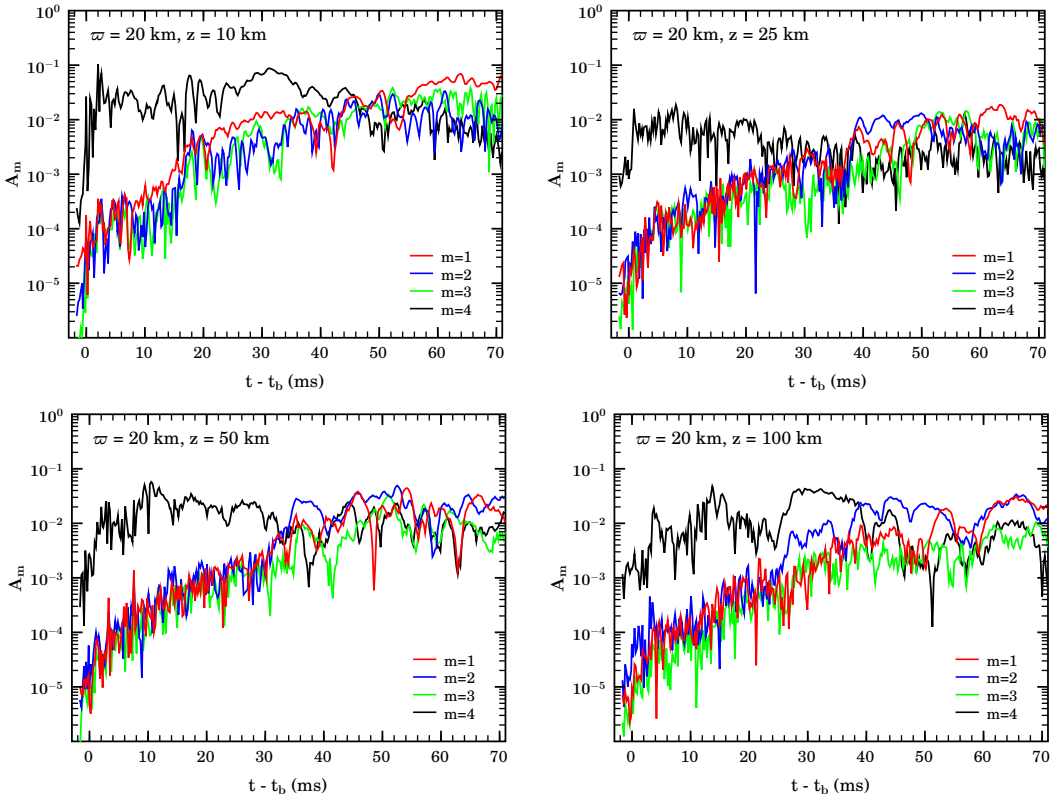

Figure 6.34: Evolution of the normalized mode amplitudes A_m (§3.9.3) evaluated on x–y-planes at 20 km distance from the z-axis and at various z-coordinates in model E20A. The time is given relative to the time of core bounce. The mode amplitudes at 71 ms are the quantitative counterpart to the qualitative picture obtained from figure 6.33.

in previous work on quasi-toroidal compact stars (e.g., [20, 21, 23, 25, 204, 267, 309, 404]) one may suspect that quasi-toroidal objects/regions tend to be more apt to develop large-scale nonaxisymmetric features than centrally-condensed objects/regions. The mixture of centrally-condensed and quasi-toroidal structure observed here has not been discussed before, but is likely to appear generically in rotating PNS. Unfortunately, this limits the predictive power of linear perturbation analyses of the stability of rotating compact stars that genererally assume constant mode structure in the z-direction (e.g., [19, 23]).

Nature of the Instability

As pointed out in §6.4, several recent numerical studies [20–25, 308, 309] have found that dynamical rotational instabilities that excite $m = 1$ as well as $m = 2$ azimuthal modes can arise in differentially rotating self-gravitating structures with β much smaller than the classical threshold $\beta_{\rm dyn} \simeq 27\%$ for dynamical rotational instability. Watts et al. [19] performed a linear analysis of the models considered in [308, 309] and were the first to point out a possible relationship of such low-$T/|W|$ instabilities to *corotation resonances* in the context of dynamical shear instabilities [591–594] at *corotation points* at which the local fluid angular velocity equals the pattern speed $\sigma_p = \sigma_m/m$, where m is the azimuthal mode number and σ_m is the mode eigenfrequency. The underlying physical idea is that a corotating nonaxisymmetric wave (or mode; $\propto \exp(i(m\varphi + \sigma_m t))$) is driven unstable by resonant energy transfer from the initially axisymmetric background flow in regions where the mode pattern speed is equal to the local fluid angular velocity. Corotation points have been identified in the low-$T/|W|$ unstable models of [22–25, 308, 309].

Corotation instabilities that lead to amplification of waves at corotation points are, for example, a key ingredient in the density wave models of spiral patterns in galaxies (e.g., [582, 585, 595, 596]). Dynamical nonaxisymmetric instabilities, associated with the presence of corotation points, are also

Table 6.7: Measurements of the mode logarithmic growth times $d \ln A_m / dt$, mode eigenfrequencies σ_m and pattern speeds σ_p. $\Delta t_{\rm extract}$ gives the interval of postbounce time over which σ_m is determined from the real/imaginary parts of C_m. $\varpi_{\rm extract}$ denotes the equatorial radius/radii at which σ_m is determined. At small equatorial radii the $m = 1$ mode amplitudes exhibit a low-frequency modulation at $\sim$50 Hz / 300 rad s^{-1} whose nature is unclear. For σ_m and σ_p estimates of the "measurement error" based on variations in the measurements at various times / radii are given. The nearly identical σ_p of the $m = \{1, 2, 3, 4\}$ modes indicates that these modes are related / non-linearly coupled at the times when their σ_m are measured. Note that prior to $t - t_{\rm bounce}$ $\sim$50 ms, the $m = 4$ mode shows no clear temporal structure despite its large amplitude.

Mode	$d \ln A_m / dt$ (ms^{-1})	σ_m (rad s^{-1})	σ_p (rad s^{-1})	$\Delta t_{\rm extract}$ (ms)	$\varpi_{\rm extract}$ (km)
$m = 1$	0.23	3100$\pm\sim$500	3100$\pm\sim$500	40–70	20,30,40
$m = 2$	0.21	5750$\pm\sim$300	2875$\pm\sim$150	62–70	20,30,40
$m = 3$	0.20	8550$\pm\sim$300	2850$\pm\sim$100	65–70	20,30,40
$m = 4$	—	11400$\pm\sim$300	2850$\pm$ $\sim$80	60–66	20,30,40
($m = 1$	0.23	300$\pm\sim$100	300$\pm\sim$100	40–70	15)[a]

[a] Low-frequency "precession" of the PNS-local "center of mass". Nature unclear.

known in various incarnations in accretion disk theory, including the Papaloizou-Pringle instability [597–600] and the Rossby-wave instability [601–603] in both of which the presence of a corotation point is a necessary, though not sufficient criterion for non-linear nonaxisymmetric mode growth. In addition, it appears [597, 601] that some sort of resonant cavity is also required to drive unstable modes to large amplitudes. In the case of the Papaloizou-Pringle instability, the inner and outer edges of the accretion disk (or torus) form a resonant cavity in which waves are reflected back and forth and can be greatly amplified by multiple passages through the corotation radius [24]. As pointed out by [601, 602], local minima in the radial vortensity (potential vorticity; $\vec{z}/|z|(\nabla \times \vec{v})/\Sigma$; were Σ is the surface density $\Sigma = \int_{-\infty}^{\infty} \rho dz$ of the disk/torus) and local maxima in the radial entropy distribution can also trap radially propagating waves in the vicinity of corotation points and, hence, can serve as resonant cavities. It is conceivable that such a resonant-cavity mechanism may work to amplify corotation resonances in stellar models. Recently, Ou & Tohline [24] found supporting evidence by identifying local vortensity minima near corotation points in their low-$T/|W|$ unstable models.

Since corotation points have been identified in previous studies of low-$T/|W|$ instabilities in compact stars and even in simplified PNS models [22], it may be reasonable to suppose that a similar corotation mechanism is at work in the model studied here. In the following, I will present circumstantial evidence for a corotation instability in model E20A. A detailed explanation of the mechanism behind the instability would require a much more complete understanding of corotation instabilities in the context of compact stars by means of linear theory and detailed, high-precision modelling of idealized systems. This would be beyond the scope of this work and must be left to future research.

Since I do not perform[48] a linear analysis of the pulsational eigenspectrum of model E20A's PNS, I am forced to measure the pattern speed σ_p of each mode based on the output data of my non-linear GR hydrodynamic calculations. With this approach it is, in general, possible to find σ_m only when/where the corresponding mode dominates the nonaxisymmetric evolution [24]. This is complicated by the spatial and temporal variations in mode dominance shown by model E20A (e.g., figure 6.27). One has $\sigma_p = \sigma_m / m = 1/m\, d\Phi/dt$, where Φ is the mode phase angle defined in §3.9.3 as

$$\Phi_m(\varpi, z) = \tan^{-1}(\mathrm{Im}\{C_m\}/\mathrm{Re}\{C_m\}) \ , \tag{6.18}$$

where C_m is the complex non-normalized amplitude of mode m. Unfortunately, the direct determination of Φ_m via equation (6.18) and, in particular, of its time derivative proves to be rather difficult numerically – not the least because of the coarse temporal resolution of the post-processing based analysis. An alternative way of obtaining σ_m suggests itself from the physical interpretation that the oscillation period of mode m, $P_m = 2\pi/\sigma_m$, is equivalent to the time it takes the real or imaginary parts of C_m to complete a full cycle from a positive to a negative value, then back to a positive value [24]. In this way, σ_m can be read-off directly from the mode amplitudes in time intervals during which they show clear temporal behavior.

[48] Such an analysis would – in principle – be possible, but would require the development of additional technology beyond the scope of this work.

In table 6.7, I present results for the logarithmic mode growth times, eigenfrequencies and pattern speeds. While the $m = 1$ mode clearly reaches the highest amplitudes in the PNS and out to intermediate ϖ in the postshock region (see, e.g., figure 6.27), its eigenfrequency is the hardest to determine since the $m = 1$ mode is strongly amplitude-modulated by a low-frequency ($\sim$50 Hz / $\sim$300 rad s^{-1}, $\sim$20 ms period) component at small ϖ. The nature of this low-frequency component is unclear. It may be related to a long-wavelength density/sound wave resonating in the postshock cavity[49]. It may also be an artificial low-frequency component in the PNS-local center-of-mass motion. However, note that the approximate global center of mass stays within one grid zone throughout the numerical evolution of model E20A. Such a low-frequency modulation of the $m = 1$ mode is also present in some of the models considered by [24]. I determine an eigenfrequency/pattern speed for the high-frequency component of the $m = 1$ mode of $\sim$3100 rad s^{-1} with a rather large uncertainty of $\pm$500 rad s^{-1}. The pattern speeds of all modes, even that of the "background" $m = 4$ mode, fall into a narrow range of angular frequencies. This suggests that the instability in its non-linear phase is dominated by a single mode with pattern speed $\sim$2800–3000 rad s^{-1} and that the other modes are non-linear harmonics of that mode. In the light of previous results [20–22] and because of its prominence in the PNS core it is conceivable that the $m = 1$ mode may be the unstable mode that drives the growth of the potential daughter modes $m = \{2, 3\}$. In this case, one would expect a growth rate of the $m = 1$ amplitude significantly faster than that of the $m = \{2, 3\}$ amplitudes [21]. However, the growth rates collected in table 6.7 and the panels of figure 6.27 indicate very similar growth rates of $m = 1$ and $m = \{2, 3\}$. The non-linear relationship of $m = 1$ and $m = \{2, 3\}$ and the details of the non-linear mode couplings in model E20A remain unclear.

Figure 6.35 depicts equatorial angular velocity profiles of model E20A at various postbounce times. In addition, σ_p is marked and exhibits corotation at an equatorial radius ϖ around 10–15 km. This is still within the PNS core but close to its edge where the radial density gradient is steep (ρ drops from $\sim 9\times10^{13}$ to $\sim 6\times10^{12}$ g cm^{-3} from 10 to 20 km radius on the equator; see figures 6.25 and 6.26). Along with the drop in density goes a strong increase in the specific entropy as apparent from figure 6.36 that separates the low-entropy PNS core from the high-entropy postshock region. I point out that this entropy gradient is physical and to be expected in any PNS (see, e.g., [3, 72, 73, 77, 86]). In the context of resonant wave amplification at corotation points, local vortensity minima and/or local specific entropy maxima have been deemed necessary to provide a cavity with "wave-reflecting" walls (e.g., [24, 601, 602]). The vortensity profiles of model E20A exhibit no significant local maxima/minima and the entropy profiles shown in figure 6.36 exhibit a small local specific entropy maximum near the corotation radius only at postbounce times greater than $\simeq$40 ms. On

[49] For a shock radius of $\sim$200 km and speed of sound of $0.1c$, the sound crossing time from the PNS to the shock would be $\sim$15 ms.

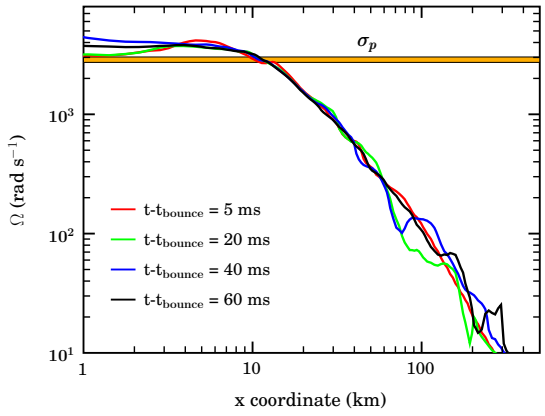

Figure 6.35: Angular velocity in model E20A at 5, 20, 40, and 60 ms after core bounce. Shown are profiles along the positive x-direction out to 500 km. The pattern speed σ_p of the rotational instability is marked by the horizontal bar. The unstable mode(s) is/are corotating at a coordinate radius of $\sim$10 km.

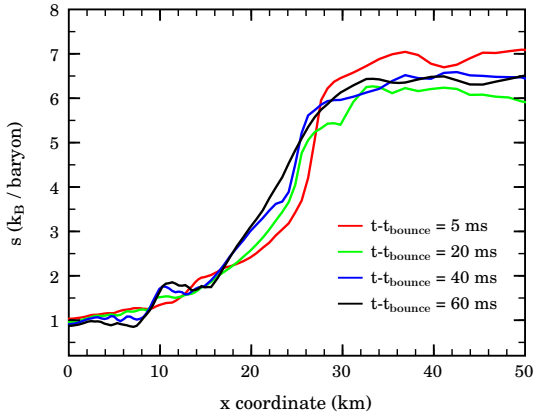

Figure 6.36: Radial equatorial specific entropy profiles of model E20A at 5, 20, 40, and 60 ms after core bounce. The PNS core has low entropy around 1–2 k_B/baryon. The increasing entropy around 10–30 km marks the transition from PNS core to postshock region.

the other hand, it is not inconceivable that the entire PNS core, bounded by the large density and entropy gradients between 15–30 km, acts as a resonant cavity for density/pressure waves that are reflected at the PNS core–postshock region boundary. A detailed investigation of this supposition with high-resolution equilibrium models mimicking various postbounce PNS configurations would be required to make better statements about corotation and resonant wave amplifications.

To conclude, I point out that the common pattern speed (evaluated at multiple radii) of all nonaxisymmetric modes considered here indicates that the rotational instability in model E20A is indeed of global nature (though with radially varying structure) and that the modes are non-linearly coupled. Owing to the complicated spatial and temporal mode structure of model E20A, I have been unable to unambiguously determine the driving unstable mode and the fundamental nature of the instability. Based on the mode pattern speeds (see table 6.7) and the mode amplitude plots presented in figure 6.27, one might surmise that $m = 1$ is the mode that is driven unstable by a corotation resonance early on in model E20A's postbounce evolution and non-linearly couples with $m = \{2, 3\}$. However, questions and significant doubts remain that cannot be answered here and require more detailed and higher-resolution longer-term postbounce investigations in the future.

Gravitational Wave Emission

Of key interest in the context of nonaxisymmetric rotational instabilities is their gravitational wave emission. Nonaxisymmetric PNS are expected to be strong emitters of gravitational waves (e.g., [169]) and could possibly enhance the gravitational wave emission of core-collapse supernovae to allow detection by Earth-based gravitational wave observatories out to megaparsec (Mpc) distances [240]. Figure 6.37 depicts the h_+ and $h_\times$ mass-quadrupole gravitational wave amplitudes in model E20A that are computed according to what is stated in §3.8. Higher order mass-multipole and mass-current emission is not computed, but may be relevant in the late postbounce emission. In axisymmetry, $h_\times$ is zero everywhere and h_+ vanishes on the polar axis. Hence – as confirmed by figure 6.37 – h^p_+, $h^e_\times$, and $h^p_\times$ are zero at core bounce and early postbounce times and the axisymmetric core-bounce and PNS ring-down wave signature is captured by h^e_+.

At ∼20 ms core bounce, nonaxisymmetric mass-quadrupole emission sets in and grows to amplitudes of up to 1/5 of the bounce spike. It is characterized by coherent high-frequency oscillations that appear strongest in h_+ and $h_\times$ for an observer along the polar axis, but are also visible in h_+ on the equator. $h^e_\times$ exhibits only small amplitudes with no coherent temporal structure.[50]

The gravitational waves are emitted by time-changing nonaxisymmetric quadrupole structures and are closely related to $\ell = 2, m = 2$ flow components and, hence, to the $m = 2$ azimuthal mode amplitude in the mode analysis presented earlier in this section. A pure $m = 2$ bar mode emits gravitational waves in the polar direction in the same fashion as a top over spinning rod [115, 116]. For such a system one expects a quarter-cycle phase shift between h^p_+ and $h^p_\times$. Figure 6.38 demonstrates that the quadrupole nonaxisymmetric structures in model E20A emit gravitational waves much like a spinning massive rod and at a single temporally constant frequency. This is also apparent from figure 6.39 which compares the spectral gravitational wave energy densities of the total gravitational wave emission and of the emission up to 20 ms after core bounce. The quadrupole components of the nonaxisymmetric dynamics in model E20A lead to narrow-band gravitational wave emission around ∼925 Hz over multiple tens of milliseconds. This long-term emission readily makes up for the relatively low gravitational wave amplitudes and leads to a ∼2 times larger total energy emitted in gravitational waves than from core bounce and PNS ring-down (see table 6.3).

The pattern speed of the unstable azimuthal mode(s) in model E20A is σ_p ∼2700–3200 rad s^{-1} and the pattern frequency, $f_p = \sigma_p/(2\pi)$, is ∼430–500 Hz. A top-over spinning bar emits at twice its pattern frequency, thus one would expect a quadrupole gravitational wave emitting from the $m = 2$ mode at f ∼860–1000 Hz which agrees well with the observed gravitational wave emission at f ∼925 Hz.

I point out that at the end of model E20A's numerical evolution the nonaxisymmetric mode amplitudes and the gravitational wave emission show no sign of decay.

[50] $h^e_\times \propto \ddot{I}_{yz}$, hence it is small for little temporal variation in the z-direction.

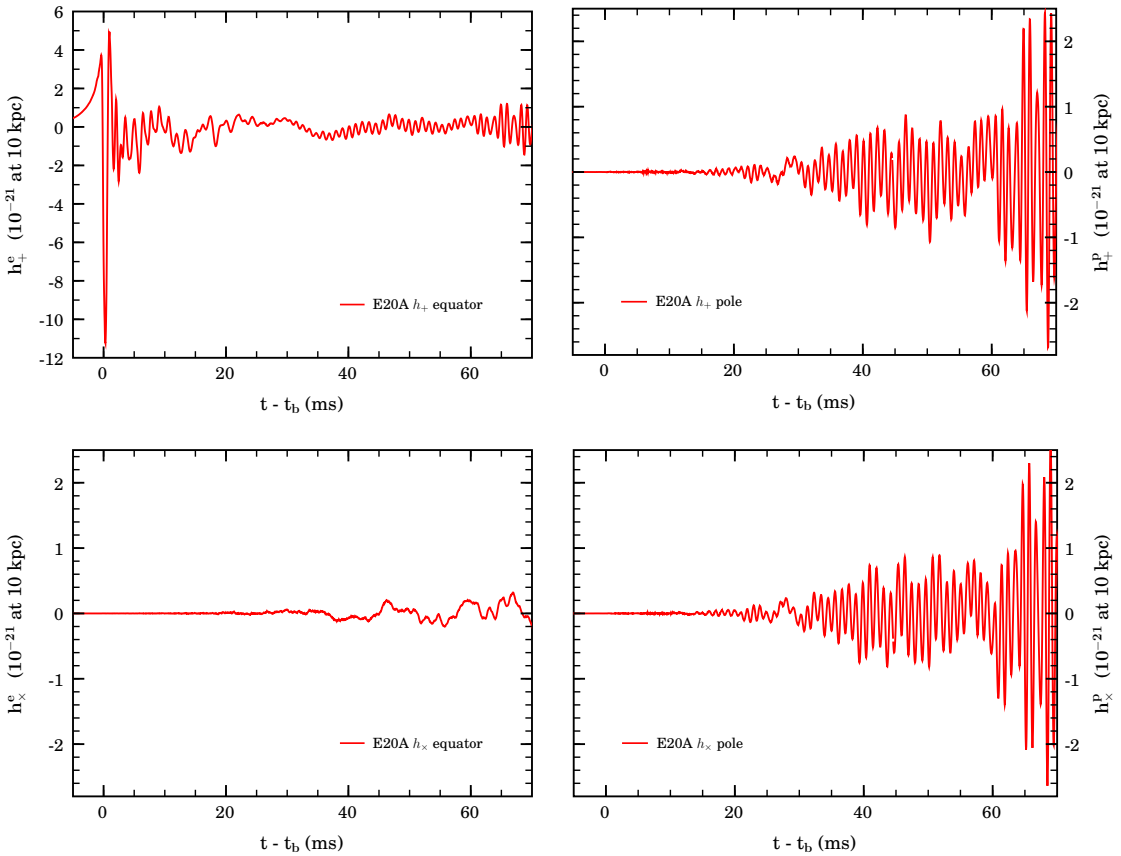

Figure 6.37: Quadrupole matter gravitational waveforms of model E20A. Top row: + polarization as seen by an observer situated on the positive x-axis on the equatorial plane (left panel, e superscript) and along the polar axis ($\theta = 0$/positive z; right panel, p superscript). Bottom row: $\times$ polarization on the equator (left) and along the polar axis (right). The waveforms are scaled to an observer distance of 10 kpc. Note that the top-left panel has a different ordinate range to accommodate the high-amplitude bounce spike in h^e_+. In axisymmetry, h^p_+, $h^p_\times$, and $h^e_\times$ vanish.

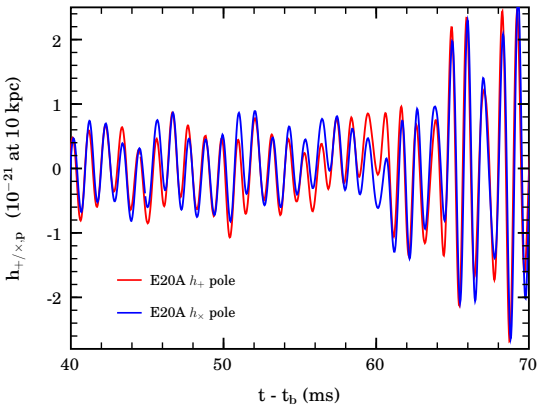

Figure 6.38: + and $\times$ gravitational wave amplitudes as seen by an observer located along the polar / rotation axis. The dominant emission frequency is ∼925 Hz. The polarizations are shifted in phase by a quarter cycle. For this figure I have artificially shifted the $\times$ waveform by ∼0.27 ms $\simeq (925Hz)^{-}1/4$ to demonstrate the coherence of + and $\times$ gravitational wave emissions.

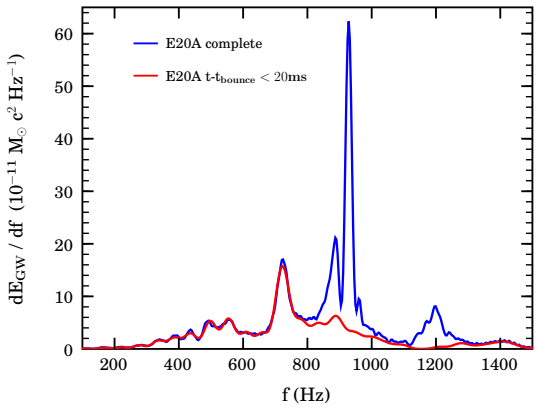

Figure 6.39: Energy spectra computed based on the gravitational wave emission in model E20A up to 20 ms after core bounce (red graph) and up to the last simulated time (blue graph). The broad local peak around 720 Hz is associated with core bounce. The narrow global maximum at ∼925 Hz and the two smaller peaks at ∼880 Hz and 1200 Hz are due to the nonaxisymmetric gravitational wave emission at postbounce times ≥20 ms.

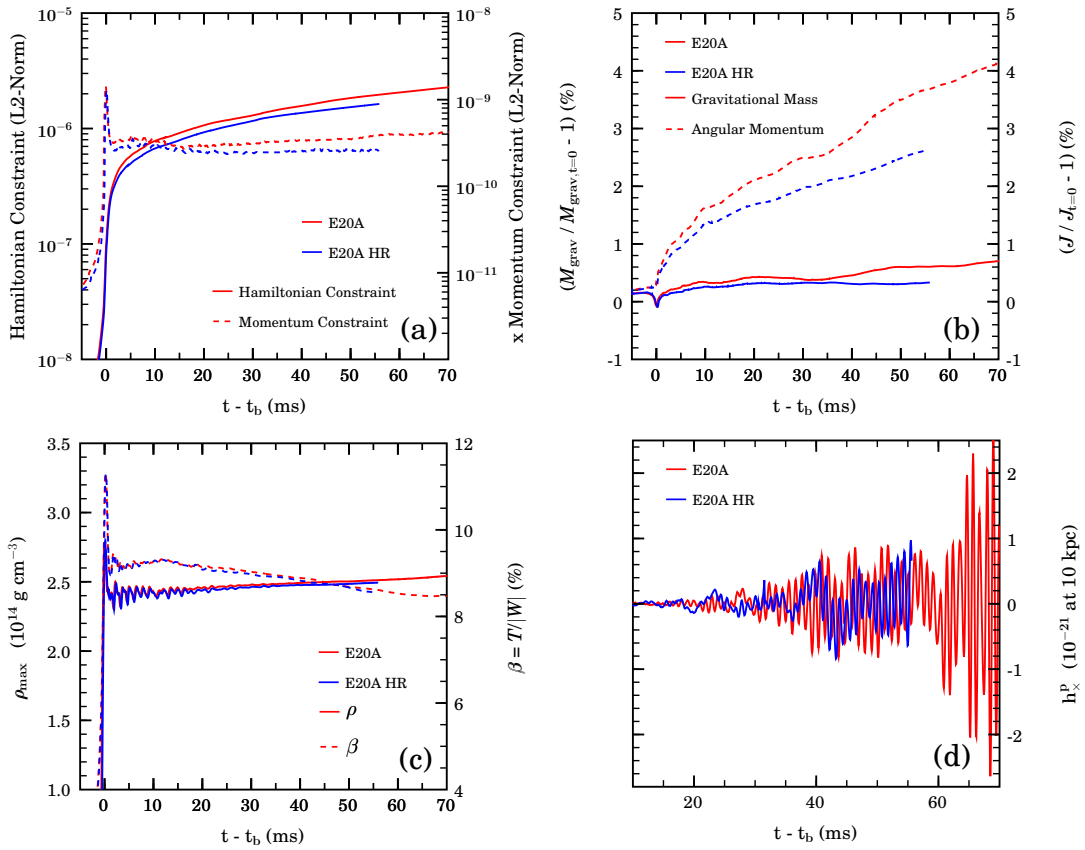

Figure 6.40: Comparison of models E20A and E20AHR by means of key quantities. Panel (a): $L2$-norms of the Hamiltonian and x-momentum constraint violations. Panel (b): Relative errors in the conservation of gravitational mass $M_{\rm grav}$ and angular momentum J. $M_{\rm grav}$ and J are computed according to the expressions in §3.9.2. Panel (c): Rest-mass density ρ and rotation parameter $\beta = T/|W|$. Panel (d): $h_\times$ gravitational wave strain as seen by an observer situated on the polar axis at 10 kpc distance.

Much longer calculations will be necessary to study the late postbounce behavior of the nonaxisymmetric instability. In principle, the nonaxisymmetric structures may persist as long as the driving phenomenon – the proposed corotation instability – persists, which in turn is likely to depend on differential rotation and angular momentum inflow. Black hole formation and/or the shock revival, turning accretion into explosion, may put an end to the nonaxisymmetric deformation of the PNS.

Comparison with a Higher-Resolution Calculation

I perform a second calculation with the E20A progenitor model in which I increase the resolution by ∼20% for verification purposes and in order to investigate the resolution dependence of the nonaxisymmetric dynamics. I point out that the small-scale turbulent postshock flow in the core-collapse models considered here does not permit a convergence test in the classical sense. However, while small spatial and temporal variations are to be expected, the overall qualitative and quantitative results should be unaffected by a 20% increase in resolution.

Model E20A uses refinement hierarchy RHIIe (2614821 grid points + ghost zones) and the high-resolution variant E20AHR is set up with RHIIeHR (4290744 grid points + ghost zones; see Appendix E). The smallest linear zone size decreases from 354.43 m in E20A to 295.36 m in E20AHR. I evolve E20AHR only as far as ∼50 ms after core bounce due to its extreme computational demands. The total computational cost of the higher-resolution E20A calculation amounts to ∼100000 Intel Xeon 3.4 GHz CPU hours which correspond to a computation time of ∼90 days on 48 CPUS.

In panels (a) and (b) of figure 6.40 I summarize the time evolution of key diagnostics. As is apparent, the Hamiltonian and momentum constraint violations decrease with increasing resolution and grow in a numerically stable fashion throughout the postbounce evolution. Hence, the calculations can be

considered stable and consistent. The errors in conservation of gravitational mass and angular momentum[51] in model E20A amount to $\sim$0.7% and $\sim$4%, respectively. They are considerably smaller in E20AHR which indicates that the late-time dynamics in model E20A may be slightly underresolved.

Panel (c) of figure 6.40 depicts the evolutions of maximum rest-mass density $\rho_{\max}$ and rotation parameter β in E20A and E20AHR. The qualitative and quantitative agreement of the two calculations is excellent and only at postbounce times $\gtrsim$20 ms do small differences in $\rho_{\max}$ and β become visible.

Panel (d) of the same figure compares the $h_\times$ gravitational wave amplitudes in E20AHR and E20A as seen by a polar observer at 10 kpc distance. As in E20A, time-changing nonaxisymmetric structures lead to growing gravitational wave amplitude beginning around $\sim$20 ms after core bounce in model E20AHR. Despite variations in signal modulations and the initially less coherent and smaller-amplitude emission in E20AHR, the overall qualitative shape of model E20A's waveform is confirmed by the higher-resolution calculation. A spectral analysis of the wave signal yields an emission frequency $f \simeq$930 Hz in E20AHR which is in very good agreement with model E20A. The qualitative and small quantitative differences in the early phase of the gravitational wave emission are most likely due to variations in the non-linear mode couplings, possibly owing to resolution-caused differences in the initial (essentially random-noise) perturbations and/or to different postshock turbulent flow in E20AHR.

In addition to numerical instabilities and inaccuracies arising from insufficient numerical resolution and/or systematic errors, the quality and reliability of long-term evolutions in numerical relativity may depend on the extent of the computational grid, that is, on the distance of the strong-field region from the generally constraint-violating (see §3.3.3) outer grid boundaries. However, for the matter-dominated spacetimes studied here, a multi light-crossing-times test calculation that I performed with twice the computational domain size than regularly used does not show any significant variations in the constraint violation growth.

[51] Note that in a GR calculation, gravitational mass and angular momentum should only be conserved up to gravitational wave losses/gains. Moreover, the expressions used to compute $M_{\rm grav}$ and J are approximate. See §3.9.2.

6.4.3 Rotational Instability at Low-$T/|W|$: Model s20A1000β1.80

Owing to limited time and computational resources, model s20A1000β1.80 is the only other model besides E20A that I could evolve to later times than $\sim$40 ms. The total computational costs for its numerical evolution to 90.4 ms after core bounce amounts to $\sim$46000 Intel Xeon 3.4 GHz CPU hours which corresponds to a computation wall clock time of $\sim$120 days on 16 CPUs. The calculation could not be carried on to later postbounce times because of the accidental deletion of restart files.

Model s20A1000β1.80 is among the models deemed to be candidates that might develop nonaxisymmetric structure and dynamics at low-$T/|W|$ (§6.4.1). In contrast to model E20A discussed in the previous section, model s20A1000β1.80 experiences relatively strong centrifugal support during the plunge phase of collapse. This results in a slower bounce and lower-frequency gravitational wave

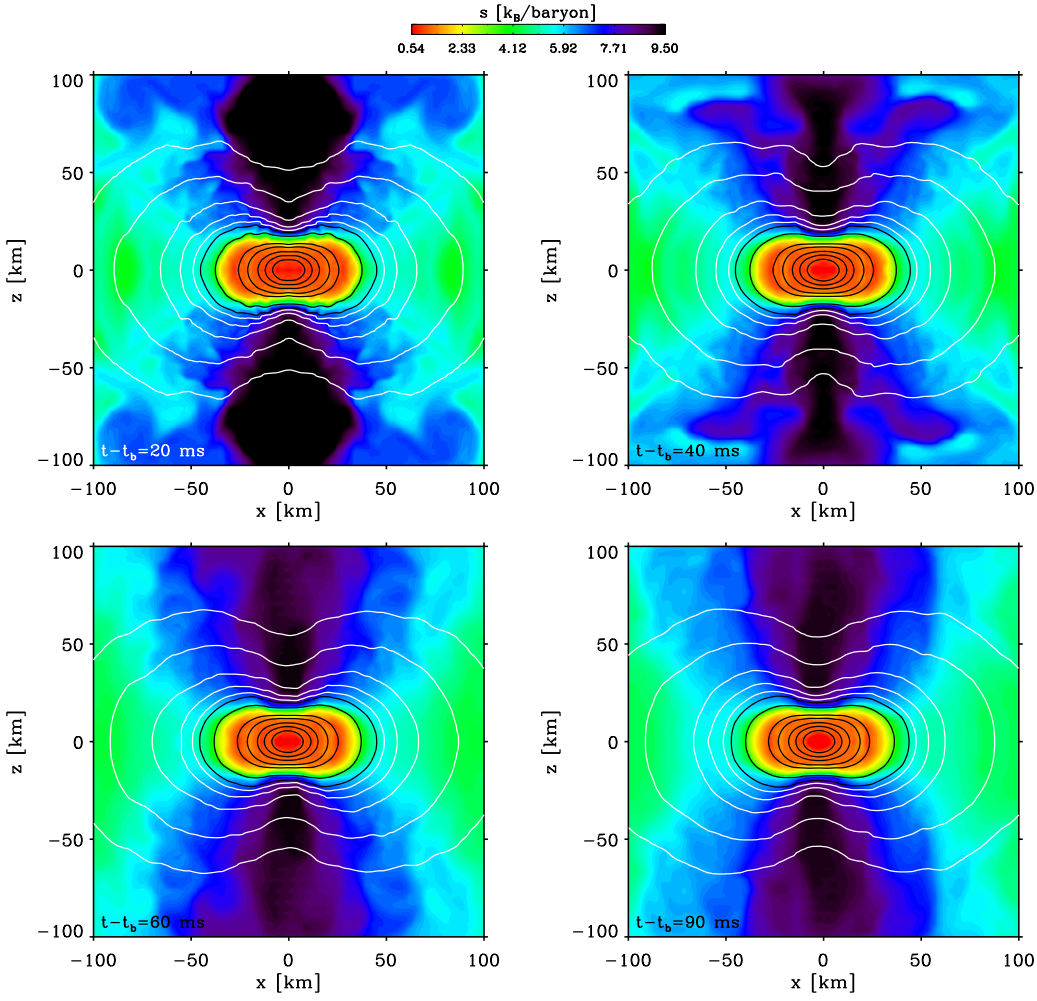

Figure 6.41: Polar x–z-plane snapshot slices of the specific entropy per baryon in model s20A1000β1.80 at postbounce times of 20, 40, 60, and 90 ms after core bounce. Shown are the inner 100×100 km^2 and density isocontours are superposed at 5×10^{10} g cm^3, $\{1,2,3,4,5\}\times10^{11}$ g cm^3, $\{1,5\}\times10^{12}$ g cm^3, $\{1,2.5,5\}\times10^{13}$ g cm^3, and 1×10^{14} g cm^3. Reflection symmetry with respect to the x–y-plane is assumed. At 20 ms after core bounce, strong jet-like features, remnants of shock formation and fast propagation, are clearly visible along the polar axis. The strongly rotationally-flattened PNS core exhibits high-ℓ axisymmetric substructure on its surface near the outermost isocontours drawn in black color. These density "ripples" are related to the vigorous early postbounce radial/non-radial ring-down pulsations discussed in §6.3.1. At 40 ms after bounce these small features have disappeared. Until the end of model s20A1000β1.80's calculation, the entropy and density distributions in x–z-plane vary only slightly and only small deviations from axisymmetry are apparent in the snapshots from 60 and 90 ms after core bounce.

emission from core bounce than in model E20A (see table 6.3). I follow model s20A1000β1.80 from the onset of collapse to $\sim$90 ms after core bounce in CACTUS/CARPET/WHISKY with the same refinement hierarchy used for model E20A. I do not add any kind of nonaxisymmetric seed perturbations during model s20A1000β1.80's axisymmetric collapse. Nevertheless, nonaxisymmetric perturbations build up during collapse for the reasons discussed in the context of model E20A. A slightly improved atmosphere treatment suppresses the artificial growth of the prebounce $m = 1$ mode amplitude by 1–2 orders of magnitude. However, owing to the non-linear mode amplification at core bounce and shock formation that affects the entire spatial mode spectrum, the immediate postbounce $m = 1$ amplitude is comparable to that in model E20A.

Nonaxisymmetric Dynamics

At core bounce, model s20A1000β1.80 reaches a maximum β of 16.3% (E20A: 11.3%) and settles at an early postbounce β of $\sim$13% (E20A: $\sim$9%). The fast rotation and the correspondingly strong rotational flattening of model s20A1000β1.80's PNS is also apparent from the postbounce snapshots of its specific entropy and density distribution on the polar x–z-plane that I show in figure 6.41 (compare with figure 6.26 that shows similar x–z-slices for model E20A). The snapshot taken at 20 ms after core bounce shows high-ℓ axisymmetric substructure on the PNS core surface near the 1×10^{12} g cm^{-3} density isocontour. These density "ripples" are related to the postbounce non-radial ring-down pulsations that are particularly strong in model s20A1000β1.80 and are discussed §6.3.1. By 40 ms after core bounce, the ripples on the PNS surface have disappeared and the high-entropy regions near the polar axis that bear jet-like features in the 20 ms slice have decreased in angular extent. Except for small nonaxisymmetric features visible in the isocontours, the PNS specific entropy and density distributions on the x–z-slice are essentially axisymmetric at 40 ms after core bounce. In the slice snapshot taken at 60 ms postbounce, a slight lopsidedness in the PNS core and postshock flow is visible and becomes more manifest in the x–z-slice from the last simulated timestep at $\sim$90 ms after core bounce.

Figure 6.42 depicts snapshots of the equatorial specific entropy distribution of model s20A1000β1.80 at postbounce times of 20, 40, 60, and 90 ms. The snapshot taken at 20 ms after bounce exhibits strong $m = 4$ features at equatorial radii $\varpi \gtrsim 50$ km. The PNS core is separated from the intermediate-entropy postshock flow by a region of high specific entropy (5–6 k_B/baryon) between 35–45 km (dark blue colors in figure 6.42). The low-specific-entropy PNS core exhibits entropy bumps close to its surface with $m = 16$ spatial frequency, but is practically axisymmetric in its central region. The localized $m = 16$ features are spatial-frequency harmonics of the $m = 4$ Cartesian grid mode and are artificially excited by the strong postbounce non-radial ring-down oscillations in model s20A1000β1.80. They are likely to be related to the high-ℓ features visible in the 20 ms polar x–z-slice snapshot shown in figure 6.41. I point out that while such high-m/ℓ features are clearly artefacts of the Cartesian meshes used in the simulations presented here and would converge away with increasing resolution, high spatial-frequency modes may be present in precollapse stellar cores [568] and could lead to similar features in nature.

The equatorial entropy snapshot, taken at 40 ms after bounce and shown in the top-right panel of figure 6.42, shows gradually washed out $m = \{4, 16\}$ features on an otherwise visually axisymmetric postbounce flow. At 60 ms after bounce, the $m = \{4, 16\}$ nonaxisymmetric features have almost disappeared and low-m structures deform the PNS core regions. The PNS central parts out to $\sim$10 km show significant lopsidedness which migrates in ϖ to an elongated structure that in turn changes to pear-like shape with increasing ϖ. At the location of the PNS core – postshock region boundary around a density of $\sim 1 \times 10^{12}$ g cm^{-3} and $\varpi \sim$35 km the flow is nearly axisymmetric with a barely noticeable $m = \{1, 3\}$ deformation. At 90 ms after core bounce the high-specific entropy region around the PNS core is strongly deformed and appears akin to a tightly wound trailing spiral dominated by one arm. The high-entropy spiral is separated from the PNS core by a region of intermediate specific entropy (2–3k_B/baryon) that is only marginally nonaxisymmetrically deformed. Inside that region appear strong central bar-like and pear-like features, corresponding to $m = 2$ and $m = 3$, respectively. The entire PNS core is lopsided and its local center of mass is located slightly off the grid origin.[52]

[52]Note that I monitor the approximate global center of mass position of model s20A1000β1.80 in the same fashion as discussed in context with model E20A in §6.4.2. Model s20A1000β1.80's approximate global center of mass shows a slight drift

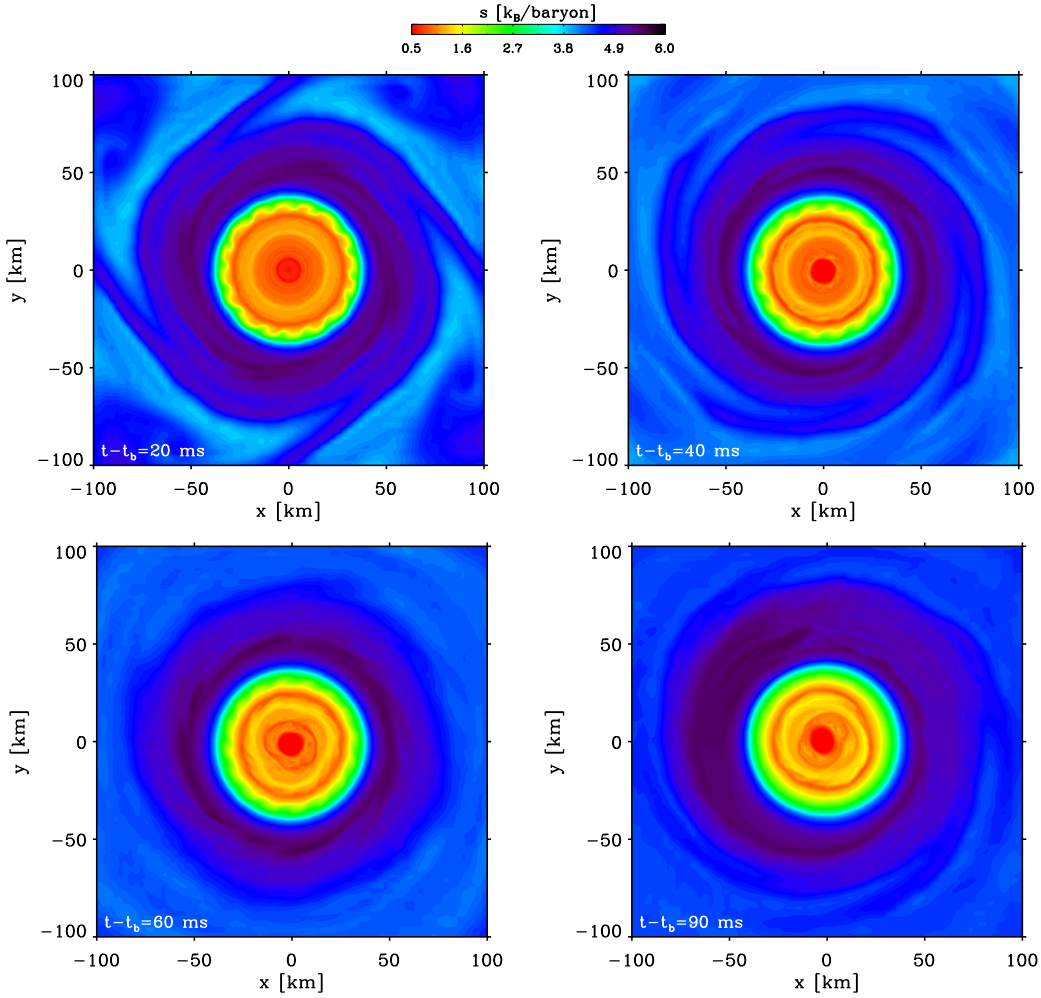

Figure 6.42: Equatorial plane snapshot slices of the specific entropy per baryon in model s20A1000β1.80 at post-bounce times of 20, 40, 60, and 90 ms after core bounce. Shown are the inner 100×100 km^2. At 20 ms after bounce, strong $m = 4$ features are apparent and strong regular 4-armed spiral structures are the most prominent features in the region between $\sim$40 and 100 km equatorial radius. The PNS core is separated from the postshock flow by a high-entropy region at 35–45 km and inside $\sim$30 km exhibits remarkable entropy bumps close to its surface with $m = 16$ spatial frequency, but is nearly axisymmetric in its central regions. At 40 ms after bounce, the $m = 4$ and $m = 16$ structures appear washed out and the innermost PNS region exhibits slight nonaxisymmetric deformation. By 60 ms after bounce, the PNS core regions exhibit a mixture of $m = \{1, 2, 3\}$ features while $m = \{4, 16\}$ features have practically vanished and the postshock region appears relatively smooth and almost axisymmetric. In the snapshot taken at the last simulated time (90 ms after core bounce) the entire PNS is rotationally deformed with a strong $m = 2$-like elongation of the inner PNS core and $m = 3$ deformation at intermediate PNS radii. The PNS is slightly offset from the origin and has one dominant high-entropy spiral arm extending through the postshock region.

A comparison of figures 6.41 and 6.42 with figures 6.26 and 6.25 indicates qualitative similarities in the development of the nonaxisymmetric structures in models s20A1000β1.80 and E20A. Both model calculations exhibit only marginally nonaxisymmetric structures and flow features in the polar x–z-plane while developing $m = \{1, 2, 3\}$ structures on equatorial and x–y-slices with spatially and temporally varying characteristics. The two models are set apart most prominently by the fact that, owing to strong centrifugal support during the plunge phase, model s20A1000β1.80 has a slightly

that sets in at core bounce and levels off at $\sim$1 km distance from the coordinate origin, hence at a $\sim$1–2 zone distance on the finest refinement level. This is slightly larger than what I observe in model E20A. The mode analysis presented in figure 6.43 is carried out with respect to the approximate global center of mass.

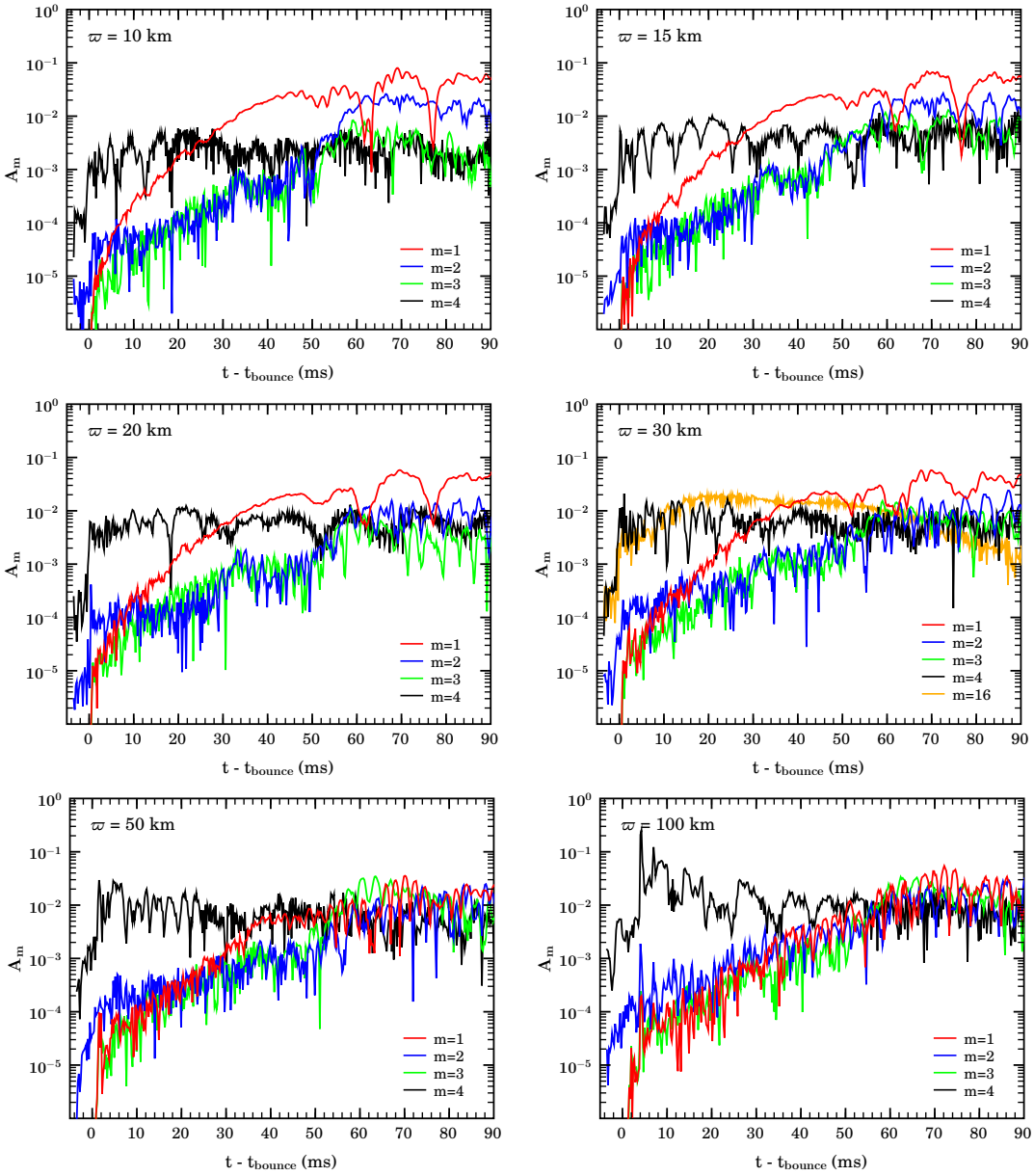

Figure 6.43: The growth of the normalized mode amplitudes A_m (see §3.9.3) evaluated at various coordinate radii in the equatorial plane of model s20A1000β1.80. The time is given relative to the time of core bounce. Note that the $m = 1$ mode exhibits the shortest growth times and dominates the postbounce nonaxisymmetric mode evolution for equatorial radii $\lesssim 50$ km and blends in with the growth of $m = \{2, 3\}$ at larger radii. The PNS appears to be dynamically stable to the $m = 4$ grid mode. Note the similarity of the mode amplitude evolution to that observed in model E20A (figure 6.27), but also note that the $m = 2$ bar-mode is considerably stronger in s20A1000β1.80 and particularly prominent at small equatorial radii inside the PNS core. In the center-right panel, showing the mode amplitude evolution at $\varpi = 30$ km, I have included the $m = 16$ mode amplitude that is related to the entropy ripples with $m = 16$ spatial frequency observed in the top panels of figure 6.42. One clearly notes the fast growth of the $m = 16$ contribution and its dominance over $m = \{4, 1, 2, 3\}$ at $\varpi = 30$ km from $\sim$15–35 ms postbounce.

larger inner core mass at core bounce (see table 6.3) and, consequently, a slightly more massive, but significantly more extended unshocked low-entropy PNS core that is more rotationally flattened than in model E20A. In addition, s20A1000β1.80's PNS core exhibits significantly more entropy substructure than that of model E20A.

In figure 6.43 I present the results of a quantitative Fourier mode analysis of the rest-mass density ρ in rings of constant equatorial radius ϖ in the equatorial plane of model s20A1000β1.80 (see §3.9.3). Like

for the mode evolution in model E20A, the nonaxisymmetric mode amplitude evolutions in model s20A1000β1.80 vary with ϖ. Core bounce and shock formation with their non-linear dynamics lead to mode amplification across the entire mode spectrum. Inside the PNS core at $\varpi \lesssim 50$ km, the $m = 1$ mode amplitude begins to grow exponentially at the moment of maximum compression and crosses the ambient $m = 4$ grid mode amplitude at $\sim$30 ms after core bounce. The $m = \{2, 3\}$ modes grow as well, though at a slower pace, and reach non-linear amplitudes ($\gtrsim$0.1%) around 40–50 ms after bounce which is about 5–10 ms later than in model E20A. Also, in comparison with model E20A, model s20A1000β1.80 shows a significantly stronger $m = 2$ contribution in the PNS core (top panels of figure 6.43 and bottom panels of figure 6.42). Outside the PNS core, both $m = 1$ and $m = 2$ amplitude evolutions blend in with the $m = 3$ mode and evolve almost concurrently to nearly identical amplitude levels at $\varpi \gtrsim$50 km in the postshock region.

In the center-right panel of figure 6.43, which shows the mode evolution at $\varpi = 30$ km, I include the $m = 16$ mode amplitude which dominates the mode spectrum at this ϖ from $\sim$15–35 ms after bounce. The $m = 16$ mode amplitude is related to the precisely 16 ripples visible on the PNS core surface at postbounce times $\lesssim$40 ms (see figure 6.42). As pointed out earlier, the $m = 16$ feature is very likely an artefact owing to non-linear mode coupling of the $m = 4$ Cartesian grid mode at core bounce and in the radial/non-radial ring-down phase of the PNS core.

Figure 6.44 shows an equatorial snapshot of the rest-mass density distribution at 70 ms after core bounce on which flow velocity vectors are superposed. Tightly wound long-armed spiral structures are apparent in the postshock flow outside the PNS core. These spiral features in the flow have (harder to observe) counterparts in the density distribution and are similar to what I observe in model E20A close to the end of that model's numerical evolution. In model s20A1000β1.80 they appear in the postshock flow around 50–60 ms when the $m = \{1, 2, 3\}$ amplitudes begin to dominate the $m = 4$ grid mode in the entire postshock region. The spiral features persist until the end of the s20A1000β1.80 model calculation and show temporal and spatial variations in strength and

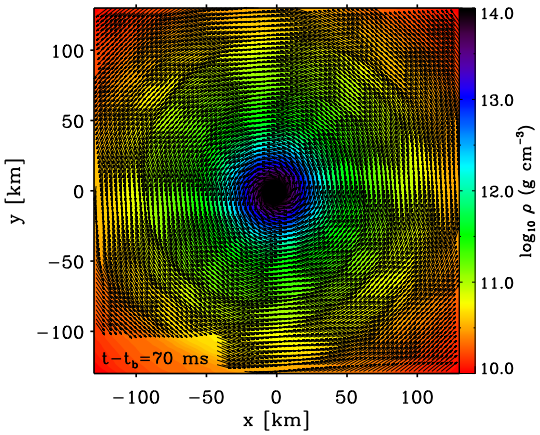

Figure 6.44: Equatorial rest-mass density distribution with overplotted velocity vectors (vector length saturated at 0.05c) in model s20A1000β1.80 at 70 ms after core bounce. Shown are the inner 130×130 km^2. A low-m spiral pattern with one strong arm, and 1–2 weaker arms extends out from the PNS core through the postshock region. The shock is not shown. Note that the emergence of spiral-like patterns in the flow corresponds temporally with the moment the $m = \{1, 2, 3\}$ mode amplitudes surpass the ambient $m = 4$ distortion globally. The postshock flow is sub-Keplerian throughout the simulated postbounce times.

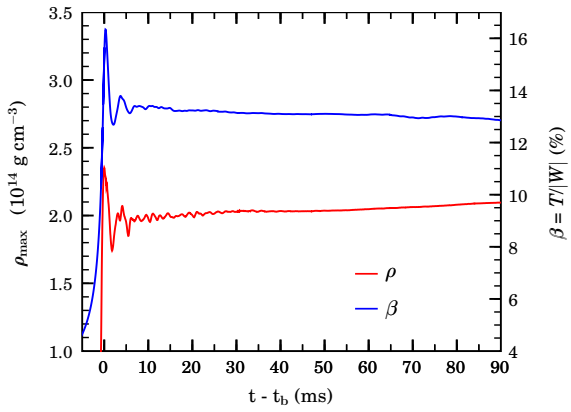

Figure 6.45: Postbounce evolution of the maximum rest-mass density ($\rho_{\max}$) and of the rotation parameter β in model s20A1000β1.80. After the initial postbounce phase dominated by radial and non-radial ring-down oscillations, $\rho_{\max}$ steadily but slowly increases as the PNS slowly gains mass through accretion and slowly contracts. β starts decreasing at $\sim$10 ms after core bounce by $\sim$0.4% until the end of the calculation. This decrease is similar to what I observe in model E20A and is most likely related to the sub-Keplerian accretion of low angular-momentum material from regions close to the polar axis. Neither $\rho_{\max}$ nor β show any indication for rapid angular momentum redistribution. Note that the calculation globally conserves z-axis angular momentum to 3.2% from the prebounce value to 90 ms after bounce.

Table 6.8: Measurements of the mode logarithmic growth times $d \ln A_m/dt$, mode eigenfrequencies σ_m, and pattern speeds σ_p in model s20A1000β1.80. $\Delta t_{\rm extract}$ gives the interval of postbounce time over which σ_m is determined from the real/imaginary parts of C_m. $\varpi_{\rm extract}$ denotes the equatorial radius/radii at which σ_m is determined. At small equatorial radii, the $m = 1$ mode amplitudes exhibit a low-frequency modulation at $\sim$60 Hz / 400 rad s^{-1} whose nature is unclear and which is also observed in model E20A. For σ_m and σ_p estimates of the "measurement error" based on variations in the measurements at various times / radii are given. The nearly identical σ_p of the $m = \{1, 2, 4\}$ modes indicates that these modes are related / non-linearly coupled at the times when their σ_m are measured. The $m = 3$ mode has a significantly different σ_p and appears unrelated to the other modes. Note that prior to $t - t_{\rm bounce}$ $\sim$50 ms, the $m = 4$ mode shows no clear temporal structure despite its large amplitude.

Mode	$d \ln A_m/dt$ (ms^{-1})	σ_m (rad s^{-1})	σ_p (rad s^{-1})	$\Delta t_{\rm extract}$ (ms)	$\varpi_{\rm extract}$ (km)
$m = 1$	$\sim$0.19	2980$\pm\sim$400	2970$\pm\sim$400	40–90	20,40,50
$m = 2$	$\sim$0.12	5970$\pm\sim$200	2985$\pm\sim$100	60–90	20,40,50
$m = 3$	$\sim$0.11	6905$\pm\sim$300	2300$\pm\sim$150	50–90	20,50,100
$m = 4$	—	11500$\pm\sim$500	2880$\pm\sim$250	50–90	20,40,50
($m = 1$		370$\pm\sim$10	370$\pm\sim$100	40–90	10)[a]

[a] Low-frequency "precession" of the PNS-local "center of mass". Nature unclear.

shape. In the context of central-object–Keplerian-disk systems, spiral density waves are theoretically known to transport angular momentum and lead to rigid rotation on a timescale larger than the dynamical timescale of the system under consideration (e. g., [586]). Like in model E20A, model s20A1000β1.80's postshock region and PNS core can in rough approximation be considered to be a central-object–disk system (see figure 6.41). However, note that despite the higher postshock angular velocities in model s20A1000β1.80 (figure 6.23), the accretion onto its PNS is still sub-Keplerian at all times. The evolution of the maximum rest-mass density and of the rotation parameter $\beta = T/|W|$ of model s20A1000β1.80 shown in figure 6.45 bear no sign of rapid (i.e. on a dynamical timescale) angular momentum redistribution by the nonaxisymmetric dynamics. This confirms my findings for model E20A in §6.4.2 and is in contrast to what was found in the idealized 3D postbounce study [22] that investigated the growth of nonaxisymmetric structure in a PNS largely isolated from accretion. One may surmise that the embeddedness of the PNS in the postshock region and the continuous accretion of matter and angular momentum is a key ingredient in the nonaxisymmetric instability observed in the models presented here.

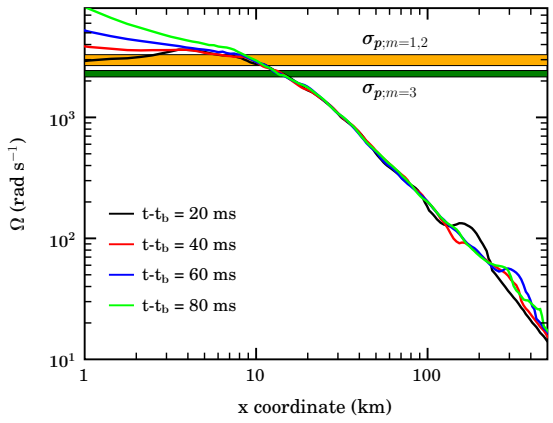

Figure 6.46: Angular velocity in model s20A1000β1.80 at 20, 40, 60, and 80 ms after core bounce. Shown are profiles along the positive x-direction out to 500 km. The pattern speeds σ_p of the unstable modes are marked by horizontal bars. The corotation points are situated at coordinate radii between $\sim$8 and $\sim$15 km. Note the increase of the angular velocity in the central PNS core regions with postbounce time.

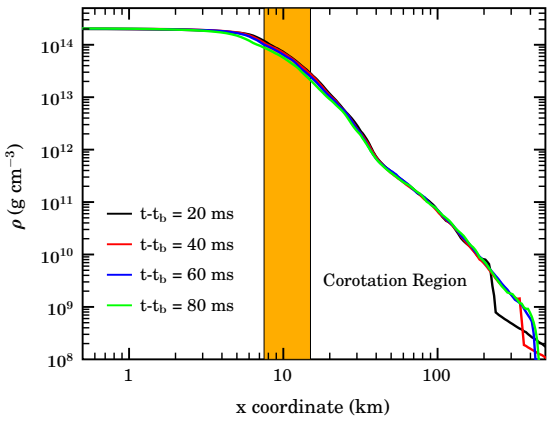

Figure 6.47: Rest-mass density profiles along the positive x-axis in model s20A1000β1.80 at 20, 40, 60, and 80 ms after core bounce. The region in which the unstable nonaxisymmetric modes have corotation points with model s20A1000β1.80's angular velocity profile is marked in orange color. Note the almost constant-ρ inner PNS core and the steep ρ gradient in the corotation region in the outer PNS core.

Table 6.8 summarizes the logarithmic amplitude growth times, mode eigenfrequencies, and pattern speeds, obtained in the same fashion as described for model E20A in §6.4.2. I point out that the determination of the eigenfrequency of a given mode from non-linear hydrodynamics data is in general only reliable when the mode is dominating the mode spectrum (e.g., [24, 25]). Since the $m = 1$ is globally dominant at small radii, the eigenfrequencies of the higher-m modes may not be very reliable. The eigenfrequency of the $m = 1$ mode proves to be difficult to extract at radii inside the PNS core since its mode amplitude is modulated by a low-frequency ($\sim$60 Hz / $\sim$400 rad s^{-1}) $m = 1$ contribution at small ϖ (see figure 6.43 and table 6.8). Since it appears in qualitatively and quantitatively similar fashion in model E20A, it cannot be excluded that it is an artefact related to a systematic error in the model calculations presented here.

I determine an eigenfrequency/pattern speed for the high-frequency component of the $m = 1$ mode of $\sim$3000 rad s^{-1} with a rather large uncertainty of $\pm$ $\sim$400 rad s^{-1}. The $m = 2$ mode has roughly the same pattern speed and thus is likely to be a non-linear harmonic of the dominant $m = 1$ mode. The initially lower amplitude and smaller growth rate of the $m = 2$ mode in the PNS core (see figure 6.43) is supportive of this view. Model s20A1000β1.80's PNS and postshock region are dynamically stable to the $m = 4$ grid mode. Nevertheless, the $m = 4$ mode adopts the temporal characteristics of the $m = \{1, 2\}$ modes. Interestingly, the $m = 3$ mode has a pattern speed of $\sim$2300 rad s^{-1} which differs significantly from the σ_p evaluated for $m = \{1, 2, 4\}$, thus does not suggest a direct non-linear coupling with the $m = 1$ mode. This is surprising, given the $m = 3$ mode amplitude's very similar growth time and qualitative behavior to that of the $m = 2$ mode (figure 6.43).

Figure 6.46 depicts equatorial angular velocity profiles of model s20A1000β1.80 at various post-bounce times. In addition, the pattern speed of the $m = \{1, 2, 4\}$ modes and that of the $m = 3$ mode are marked and exhibit corotation at equatorial radii between $\sim$8 and $\sim$12 km. The rest-mass density profiles presented in figure 6.47 demonstrate that the corotation region coincides radially with the transition region from the inner, almost constant-density PNS core and the outer PNS marked by a large radial density gradient. Note that model s20A1000β1.80 is centrally condensed on the equatorial plane at all times. This changes for density distributions on slices at $z \neq 0$.

Model s20A1000β1.80 becomes dynamically rotationally unstable to nonaxisymmetric modes at post-bounce values of $\beta\sim$13%. This value of β is too low for a classical dynamical instability. Considering the presence of corotation regions in model s20A1000β1.80, the overall qualitative agreement with model E20A suggests that model s20A1000β1.80 may be experiencing the same general type of corotation instability that operates via resonant amplification of nonaxisymmetric modes in regions of corotation with the background flow.

Gravitational Wave Emission

In figure 6.48 I plot the h_+ and $h_\times$ mass-quadrupole gravitational wave strain amplitudes in model s20A1000β1.80 as seen by observers at 10 kpc distance. Note that the ordinate ranges in the panels showing the nonaxisymmetric gravitational wave strains are larger by a factor of two than those in figure 6.37 for model E20A.

At $\sim$25–30 ms after core bounce, nonaxisymmetric gravitational wave emission picks up with initially slowly growing amplitudes. Between 40 and 60 ms after core bounce, the nonaxisymmetric wave amplitudes h^p_+ and $h^p_\times$ grow quickly in bar-like[53] correlated fashion as seen in model E20A and level off at amplitudes around 3–5$\times10^{-21}$ — less than a factor of two smaller in amplitude than the axisymmetric bounce signal in model s20A1000β1.80. h^e_+ shows similar late-time growth, though levels off at lower maximum amplitudes. As observed in model E20A, $h^e_\times$ shows little growth and only marginal temporal coherence.

The quasi-periodic gravitational wave emission from the quadrupole components of the nonaxisymmetric dynamics is tracked for almost 40 ms in model s20A1000β1.80 and shows no sign of decay in amplitude at the end of this model's numerical evolution. The total energy radiated in gravitational waves between 20 ms after bounce and the end of the calculation amounts to $\sim1.6\times10^{-7}\,M_\odot c^2$. This is about 20 times the energy emitted in gravitational waves during the axisymmetric core bounce and ring-down (see table 6.3). It is also a lower limit on the total energy emitted in gravitational waves

[53] See the discussion for model E20A in §6.4.2.

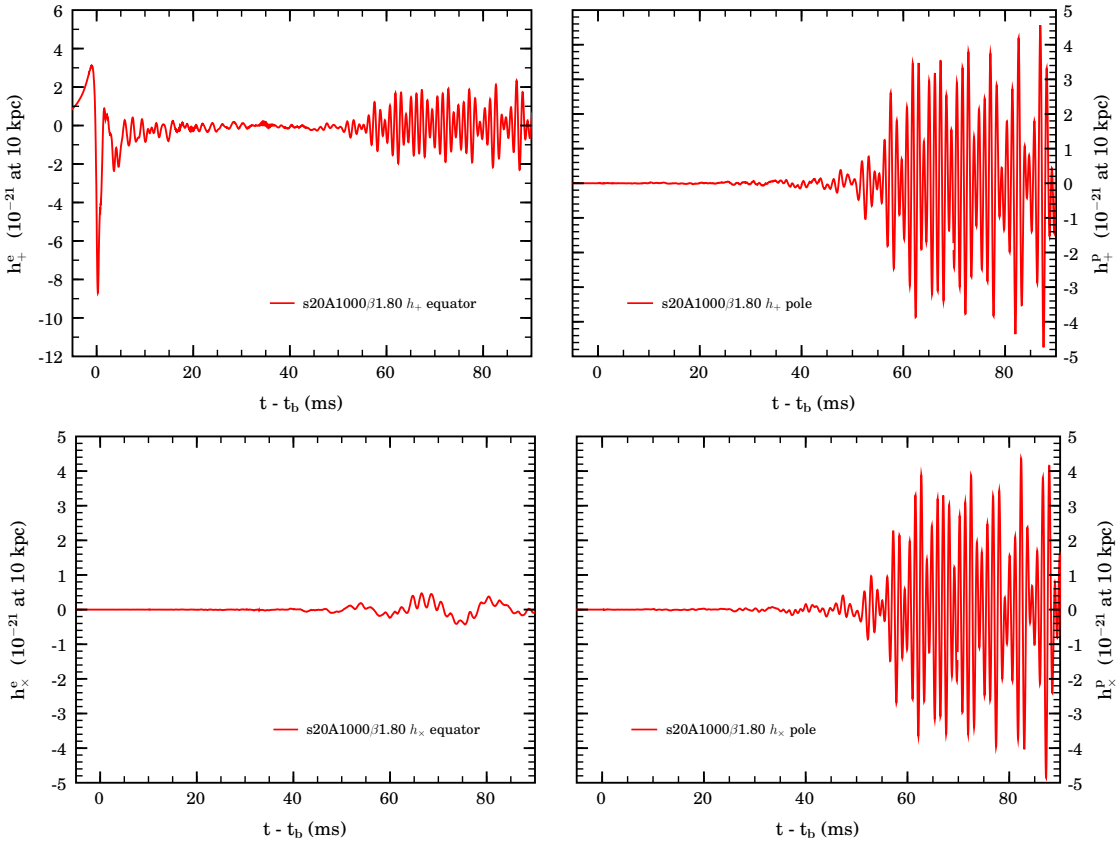

Figure 6.48: Mass-quadrupole gravitational waveforms of model s20A1000β1.80. Top row: $+$ polarization as seen by an observer situated on the positive x-axis in the equatorial plane (left panel, superscript e) and along the polar axis (positive z; right panel, superscript p). Bottom row: $\times$ polarization on the equator (left panel) and along the polar axis (right panel). The waveforms are scaled to an observer distance of 10 kpc. Note that the top-left panel has a different ordinate range to accomodate the high-amplitude bounce spike in h^e_+. In axisymmetry, h^p_+, $h^p_\times$, and $h^e_\times$ vanish.

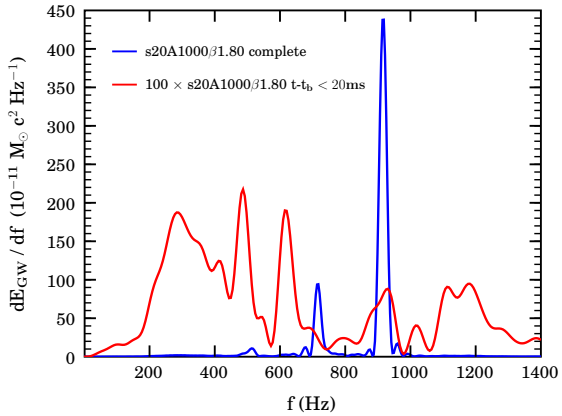

Figure 6.49: Gravitational wave energy spectra of model s20A1000β1.80 based on the emission up to 20 ms after core bounce (red graph; scaled by a factor 100) and up to the last simulated time (blue graph). The broad local maximum of the red graph at $\sim$300 Hz is related to the rotationally-slowed core bounce and the peaks at higher-frequency are related to various quadrupole pulsational modes in the PNS ring-down oscillations. The prominent maximum of the full spectrum (blue graph) at $\sim$915 Hz is directly related to the quadrupole components of the nonaxisymmetric dynamics. Its frequency corresponds closely to twice the pattern speed of the $m = 2$ bar-mode component. The smaller local maximum at $\sim$730 Hz may be related to a quadrupole daughter mode of the $m = 3$ mode whose doubled pattern speed corresponds to this frequency.

in model s20A1000β1.80 which could be much larger depending on how long the nonaxisymmetric structures and wave emission persist.

Figure 6.49 contrasts the spectral gravitational wave energy densities of the total gravitational wave emission in model s20A1000β1.80 and of the emission up to 20 ms after core bounce, encompassing only the core bounce and ring-down wave signal. The quadrupole components of the nonaxisymmetric dynamics at postbounce times $\gtrsim$20–30 ms in model s20A1000β1.80 lead to energetic narrow-band gravitational wave emission around a frequency of $\sim$920 Hz over multiple tens of milliseconds. In addition, a considerable fraction of the total energy is emitted at a frequencies around $\sim$730 Hz which is reflected in the second and smaller peak in the total gravitational wave energy spectrum of model s20A1000β1.80.

The pattern speeds of the unstable azimuthal modes(s) in model s20A1000β1.80 are σ_p $\sim$2600–3400 Hz ($m = \{1, 2\}$) and σ_p $\sim$2200–2400 Hz ($m = 3$). The corresponding pattern frequencies, $f_p = \sigma_p/(2\pi)$ are 420–540 Hz and 350–380 Hz. For a spinning bar one would expect quadrupole gravitational wave emission by $m = 2$ spatial components / daughter modes at frequencies in the ranges of 840–1080 Hz and 700–760 Hz. Figure 6.49 confirms that the nonaxisymmetric gravitational wave emission is strongly peaked in these two frequency intervals. I point out that the observed significant gravitational wave emission from a quadrupole-structure daughter mode of the independently unstable $m = 3$ mode is unexpected, though not improbable in the non-linear regime [604].

6.5 Prospects for Detection

In order to assess the detectability of the gravitational waves emitted by the core collapse models considered in this work, I follow Abramovici et al. [221] and Flanagan & Hughes [514]. For a given frequency f, [514] define the characteristic gravitational wave strain

$$h_{\rm char}(f) = \sqrt{\frac{2}{\pi^2}\frac{G}{c^3}\frac{1}{R^2}\frac{dE_{\rm GW}(f)}{df}}\ , \tag{6.19}$$

where R is the distance of the source from the detector (for galactic sources I set this to 10 kpc) and $dE_{\rm GW}(f)/df$ is the spectral energy density of the gravitational radiation defined by equation (3.178). The optimal (with respect to the relative orientation of source and detector) signal-to-noise (S/N) ratio obtained from matched filtering[54] is given [95, 514] by

$$\mathrm{S/N} = \int_0^\infty d(\ln f)\frac{h_{\rm char}}{h_{\rm rms}}\ , \tag{6.20}$$

with the (single) gravitational wave detector rms noise strain $h_{\rm rms}(f)$ in a bandwidth $\Delta f \approx f$ around f being defined as the square root of frequency times the detector noise power spectral density

$$h_{\rm rms}(f) = \sqrt{fS(f)}\ . \tag{6.21}$$

For two observatories, averaging over all angles and both gravitational wave polarizations, and demanding a S/N of 5, the detector *burst sensitivity* is considered to be $h_{\rm burst} \approx 11 h_{\rm rms}$ [221, 515].

For all models considered in this work, I find that collapse, core bounce, and the early postbounce ring-down oscillations of the PNS proceed essentially axisymmetric. The left panel of figure 6.50 contrasts the initial LIGO and advanced LIGO rms strain sensitivities with the characteristic strain

[54] Matched filtering refers to the matching of theoretical waveform estimates with detector data. I point out that matched filtering signal searches require a complete set of theoretical waveform estimates covering the entire possible space of physical parameters. For core-collapse supernovae it is unlikely that one will ever possess such a precise prediction of the gravitational waveform as the details are influenced by chaotic processes (i.e., turbulent convective flow)[95].

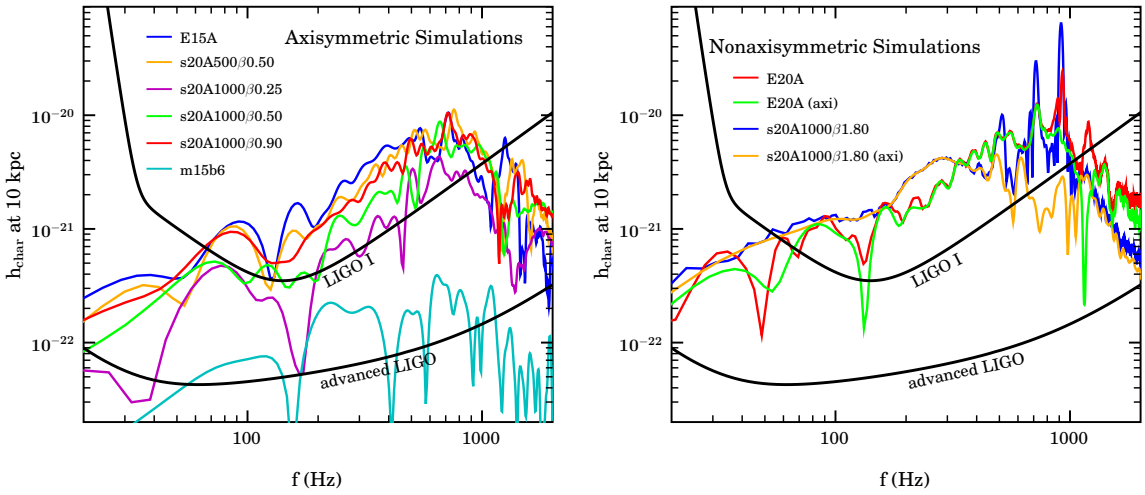

Figure 6.50: Ligo sensitivity plots showing the optimal rms noise strain amplitudes $h_{\rm rms}$ of the initial [515] and advanced LIGO [228] interferometer designs. Optimal means that the gravitational waves are incident at an optimal angle and optimal polarization for detection. For gravitational waves from burst sources incident at random times from a random direction and a signal to noise ratio (S/N) of 5, the rms noise level is approximately a factor of 11 above the one plotted here [221, 514]. Left panel: Characteristic gravitational wave strain spectra $h_{\rm char}(f)$ of the axisymmetric collapse, bounce, and ring-down gravitational wave emission in selected models. Right panel: Full $h_{\rm char}$ spectra of models E20A and s20A1000β1.80 that develop significant nonaxisymmetric dynamics and $h_{\rm char}$ spectra that include only the axisymmetric bounce and ring-down gravitational emission in these models.

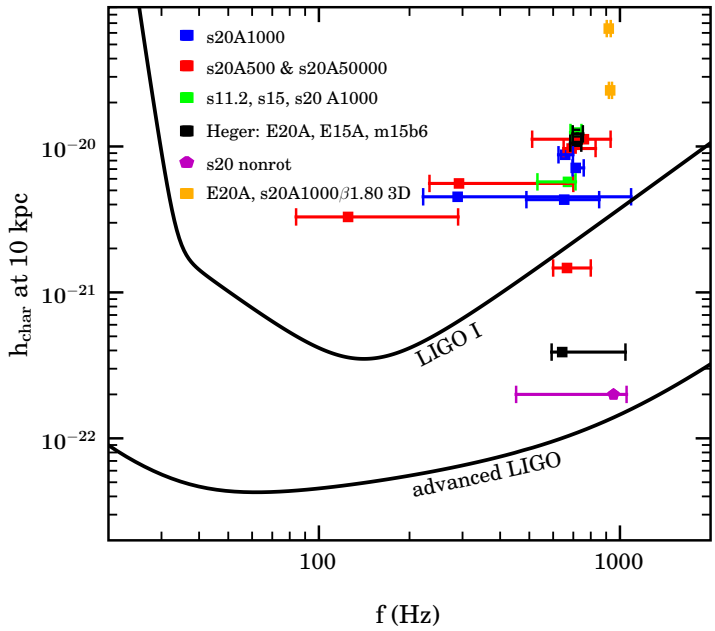

Figure 6.51: Ligo sensitivity plot as in figure 6.50. The maxima of the $h_{\rm char}$ spectra of all 18 model calculations listed in table 6.3 are marked. Note that the model markers are color coded according to model group. In particular, models E20A and s20A1000β1.80 that are evolved to late postbounce times and develop nonaxisymmetric dynamics are marked in orange. For all models the interval in frequency is marked inside which $h_{\rm char}$ is within 50% of its peak value.

spectra scaled to 10 kpc distance and computed from the axisymmetric gravitational wave emissions in a representative subset of models. The $h_{\rm char}$ spectra of the moderately fast rotating models E15A, s20A500β0.50, s20A1000β0.25, s20A1000β0.50, and s20A1000β0.90 shown in that panel peak in a narrow range of frequencies between 600 and 1000 Hz and have S/N greater than unity with respect to the initial and certainly with respect to the advanced LIGO design sensitivity if occurring within the Milky Way. The characteristic strain of the axisymmetric gravitational wave emission in the more rotationally affected model s20A1000β1.80 (shown in the right panel) peaks at significantly lower frequencies around $\sim$300 Hz, but, due to the greater sensitivity of the initial LIGO observatories at frequencies in the range of $\sim$80–150 Hz, has a S/N comparable to that of models with $h_{\rm char}$ maxima at higher frequencies.

Model m15b6 is the slowest rotating model considered in this work. Its $h_{\rm char}$ spectrum (based on the axisymmetric gravitational wave emission at core bounce and during its early postbounce PNS ring-down phase) peaks at a frequency of $\sim$650 Hz but at too low maximum $h_{\rm char}$ to be detectable by the initial LIGO-class detectors even when undergoing core collapse within the Milky Way. m15b6's low precollapse rotation rate is consistent with pulsar birth spin estimates [273, 511]. To current knowledge [273], it is likely that a large fraction of all core-collapse supernova progenitor stars have iron cores rotating as slowly as that of model m15b6. If that should be the case, advanced LIGO observatories would be required to detect the gravitational wave signature of the collapse, bounce, and very early postbounce phase in core-collapse supernovae. However, note that the gravitational wave emission from postbounce convection, from the standing-accretion shock instability (SASI, see, e.g., [26, 27, 73, 86]), and from PNS core oscillations may dwarf the gravitational wave emission from slowly rotating core bounce by multiple orders of magnitude in amplitudes and total emitted energies (see, [10, 95] and §7.2).

The right panel in figure 6.50 presents the total $h_{\rm char}$ spectra of models E20A and s20A1000β1.80 which I evolve to late postbounce times and which develop large-scale nonaxisymmetric dynamics. For comparison, the $h_{\rm char}$ spectra of the purely axisymmetric collapse, bounce, and early postbounce phases are shown as well. Owing to the prolonged narrow band gravitational wave emission from the quadrupole components of the nonaxisymmetric structures in model s20A1000β1.80, its total characteristic strain spectrums peaks at a frequency $f \sim 920$Hz and with a $h_{\rm char} \sim 6.4 \times 10^{-20}$, more than an order of magnitude larger than the maximum axisymmetric $h_{\rm char}$ in this model. Model

E20A's axisymmetric $h_{\rm char}$ peaks at 1.2×10^{-20} and at a frequency $\sim$720 Hz. The postbounce gravitational wave emission by the nonaxisymmetric instability shifts the peak of $h_{\rm char}$ to a frequency of $f \sim 930$ Hz and a magnitude of $\sim2.4\times10^{20}$.

In figure 6.51 the maximum $h_{\rm char}$ (scaled to 10 kpc distance) of all models considered in this work and listed in table 6.3 are marked at their corresponding frequencies. In addition, horizontal bars are attached to each data point, indicating the interval in frequency over which $h_{\rm char}(f)$ is within 50% of its peak value. The model marks are color coded according to model type (see tables 6.2 and 6.3). The models in which I track the development of nonaxisymmetric structures are marked with orange boxes and show the overall largest $h_{\rm char}$ with a narrow emission frequency band of $\sim$900–950 Hz. The characteristic strain from axisymmetric core bounce and PNS ring-down peaks in almost all models at frequencies between 600 and 1000 Hz, characteristic for core bounce and PNS ring-down dominated by nuclear repulsive forces. With increasing influence of centrifugal forces during infall and in the plunge phase of collapse, plunge and core bounce are slowed down, resulting in broader-band gravitational wave emission at lower frequencies. In this study, I find only three models, namely s20A500β0.90, s20A500β1.80, and s20A1000β1.80, that have sufficient angular momentum in their central regions to experience strong centrifugal support.

Previous studies that did not include deleptonization based on state-of-the-art electron capture prescriptions and/or neglected GR, found for a comparable set of initial model parameters a much broader distribution of $h_{\rm char}$ maxima in frequency and a considerable number of models that experienced core bounce at subnuclear densities under the strong influence of centrifugal forces and with $h_{\rm char}$ maxima at frequencies $\lesssim$100 Hz (see, e.g., [9, 11–14, 30]). As pointed out in §6.3, the absence of such dynamics and gravitational waveforms is a direct consequence of the improved treatment of the microphysical details in this work, and, though to a lesser degree, of GR.

The axisymmetric bounce and PNS ring-down gravitational wave signals of most models considered in this work are likely to be detectable by the initial LIGO-class detectors throughout the Milky Way. The only three models that have maximum $h_{\rm char}$ below initial LIGO $h_{\rm rms}$ are the extremely slowly rotating m15b6, the slow and rigid rotator s20A50000β0.25, and the nonrotating model s20nonrot. The major contribution to their gravitational wave signatures stems from postbounce convective overturn. Their immediate bounce and early postbounce wave emission may be detectable by advanced LIGO if occurring within the Milky Way.

It is *important to note* that the values of $h_{\rm char}$ that I find for the gravitational wave emission from the nonaxisymmetric rotational instabilities in models E20A and s20A1000β1.80 are *lower limits* on their total $h_{\rm char}$, since the nonaxisymmetric dynamics and the corresponding gravitational wave emission show no sign of decay at the end of the numerical calculations conducted here. If the nonaxisymmetric deformations of the PNSs persist until shock revival and explosion, or, alternatively, until black hole formation, one may expect gravitational wave emission for multiple hundreds of milliseconds after core bounce. Based on the results of my calculations, one may scale $h_{\rm char}$ to longer-term emission via the standard $\sqrt{n}$ (n being the number of emission cycles) scaling:

$$h_{\rm char,max} = \sqrt{\frac{\Delta t}{\Delta t_{\rm sim}}}\, h_{\rm char,sim} \ , \tag{6.22}$$

where Δt is the emission interval to which the simulation result $h_{\rm char,sim}$ is scaled and $\Delta t_{\rm sim}$ is the emission interval covered by the simulation. Assuming $\Delta t = 300$ ms and $\Delta t_{\rm sim} = 50$ ms, I find an approximate upper limit $h_{\rm char,max} \sim 6.4\times10^{-20}$ for model E20A and $h_{\rm char,max} \sim 1.7\times10^{-19}$ for model s20A1000β1.80. Comparing these numbers to the advanced LIGO $h_{\rm rms}$ sensitivity at $\sim$900–1000 Hz, model s20A1000β1.80 has a S/N > 1 out to $\sim$10 Mpc distance and model E20A may just be below the theoretical (and optimal) detectability threshold for advanced LIGO at 10 Mpc distance. Note that even LIGO I-class detectors may allow detection of these models throughout the Local Group of galaxies. However, current core-collapse supernova event rate estimates indicate (see §2.2) that the core-collapse supernova rate increases only slightly from that in the Milky Way neighborhood if the entire Local Group is considered. Sensitivity to core-collapse events out to the Virgo cluster ($\gtrsim$10–20 Mpc) would be necessary for a significantly higher observable event rate.

6.6 Summary and Discussion

In this chapter, I presented results from the first set of calculations of rotating stellar iron core collapse in {3+1} general relativity that employ state-of-the art precollapse stellar structure data from stellar evolutionary calculations, incorporated a finite-temperature nuclear EOS, included deleptonization during collapse and neutrino pressure effects.

I performed a total of 23 model calculations[55], investigating the gravitational wave signature of rotating iron core collapse and its dependence on the initial ratio of rotational energy to gravitational potential energy ($\beta_{\rm initial}$), the degree of deleptonization during collapse, the initial degree of differential rotation and progenitor structure. For this, I employed the 11.2, 15, 20 and 40 $M_\odot$ presupernova models of Woosley, Weaver & Heger [38] and put them into rotation via a rotation law that assumes constant rotation on cylinders. In addition, I performed GR collapse calculations with the progenitor models of Heger et al. [509, 511] that include a one-dimensional prescription for rotational evolution. I considered a range of precollapse rotation rates from $\beta_{\rm initial}$ that yield cold neutron star spin periods in accordance with pulsar birth spin observations to precollapse rotational configurations that permit the support of solar-mass accretion disks around a BH, required for the central engines of collapsar-type gamma-ray bursts. I systematically tested the consistency and stability of the CACTUS/CARPET/WHISKY simulation code and compared a subset of models with counterpart calculations carried out with the axisymmetric COCONUT code and found excellent agreement.

My findings indicate that *core-collapse supernova progenitor iron cores in the physically well-motivated range of initial rotational configurations considered here remain axisymmetric throughout their infall, plunge, core bounce and postbounce ring-down phases up to at least 20 ms after core bounce*. The most extreme model considered in this work yields a core-bounce β of $\sim$20% which is too low for a classical dynamical rotational instability requiring $\beta \gtrsim 27\%$. Hence, my results show that classical high-$T/|W|$ bar-mode instabilities are very unlikely to occur during collapse, bounce and the early postbounce phases in core-collapse supernovae with progenitor iron cores in the range of physically motivated precollapse rotation rates and degrees of differential rotation. This corroborate earlier findings by [9, 273, 318].

Previous axisymmetric studies of rotating iron core collapse (e.g, [9, 11–14, 30] and references therein) have identified and agreed upon at least two generic types of collapse/bounce dynamics and resulting gravitational waveforms. Models that show type I morphology, collapse largely unaffected by centrifugal forces and undergo core bounce dominated by nuclear repulsive forces. Type I gravitational waveforms exhibit a prominent negative amplitude associated with core bounce and show a characteristic high-frequency wave signal from PNS ring-down. The gravitational wave energy spectra of type I models peak typically at frequencies between $\sim$500 and 1000 Hz. Type II models, on the other hand, are strongly affected by centrifugal support. They experience centrifugal core bounce at subnuclear densities and largely unaffected by nuclear repulsive forces and typically undergo multiple postbounce harmonic-oscillator-like expansion-collapse-bounce cycles until they settle into an equilibrium configuration. Their gravitational wave signatures are dominated by low-frequency emission at $\sim$50–200 Hz. Models with type I/II transitional characteristics have been suggested.

In this work I find that *the gravitational wave signature of rotating stellar core collapse is much more generic than previously estimated*. The combined effects of general relativity, of a microphysical finite-temperature EOS and of electron capture on free protons and heavy nuclei during collapse lead to collapse dynamics and core bounce largely unaffected by centrifugal support for most initial model configurations and independent of progenitor iron core model. Importantly, *all models considered here show type I and type I/II transitional gravitational waveform morphology and not a single precollapse rotational/progenitor configuration yields a type II waveform*. In other words, *type II multiple centrifugal bounces at subnuclear densities do not occur if all known relevant physics is included*. This is exemplified by figure 6.52 in which I plot the maximum rest-mass density and the axisymmetric gravitational wave signal of representative moderately differentially rotating models with $\beta_{\rm initial} = 0.25\%$, 0.50% and 1.80%. For comparison, I include a corresponding model with $\beta_{\rm initial} = 0.40\%$ from a previous Newtonian study that neglected deleptonization [9]. All GR models with deleptonization during collapse reach den-

[55]Of the 23 models, 16 have initial model details listed in table 6.2 and results listed in table 6.3. The remaining 7 models include 5 deleptonization test calculations and 2 neutrino pressure test calculations. In addition, I presented resolution test calculations for 3 models.

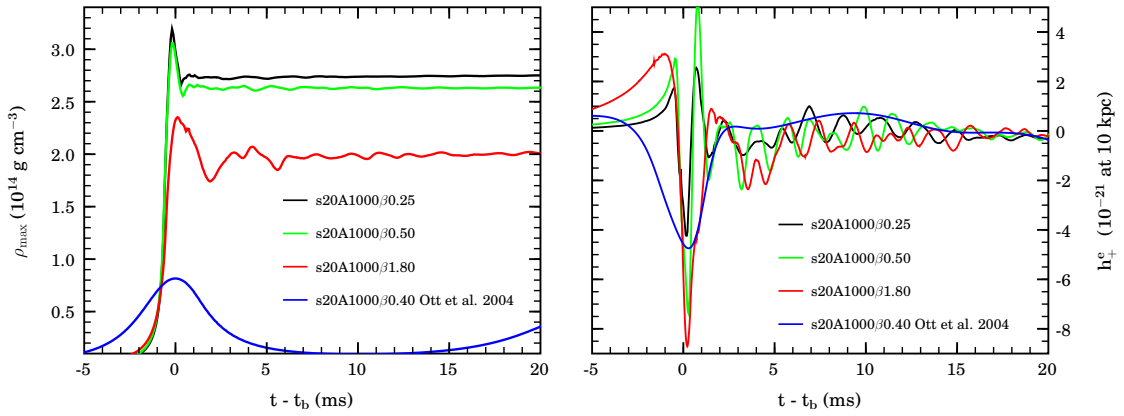

Figure 6.52: Maximum rest-mass density (left) and gravitational wave signal (right) at times relative to the time of core bounce for models s20A1000β0.25, s20A1000β0.50, and s20A1000β1.80 ($\beta_{\rm initial} = 0.25\%$, 0.5% and 1.8%, respectively) computed with the methods presented in this work. For comparison, model s20A1000β0.40 ($\beta_{\rm initial} = 0.4\%$) of the Newtonian adiabatic study of Ott et al. [9] is shown. The gravitational wave amplitudes are scaled to 10 kpc source distance. See §6.3 for details.

sities above nuclear ($\sim 2\times10^{14}$ g cm^{-3}) and show generic type I gravitational waveforms. Only the model with the largest $\beta_{\rm initial}$, s20A1000β1.80 bears evidence of rotationally-slowed core bounce. The adiabatic Newtonian model, on the other hand, shows multiple-bounce dynamics at subnuclear densities and a type II gravitational waveform at an initial β which is more than a factor of 4 smaller than the $\beta_{\rm initial}$ of the fastest GR model with deleptonization that yields a type I waveform. These results underline the importance of the inclusion of general relativity and microphysical aspects (progenitor models, EOS, weak interaction physics) in calculations that aim at providing reliable qualitative and quantitative estimates for the gravitational wave signature of rotating stellar iron core collapse.

The models considered in this work yield maximum dimensionless gravitational wave strains h from *axisymmetric* collapse, bounce and postbounce phases in the interval

$$6.5\times10^{-23}\left(\frac{R}{10\,\mathrm{kpc}}\right) \lesssim h_{\rm max} \lesssim 1.1\times10^{-20}\left(\frac{R}{10\,\mathrm{kpc}}\right) , \tag{6.23}$$

where R is the source distance. The total energy radiated ($E_{\rm GW}$) up to 20 ms after core bounce lies in the range

$$2.4\times10^{-11}\,\mathrm{M}_\odot c^2 \lesssim E_{\rm GW} \lesssim 3.82\times10^{-8}\,\mathrm{M}_\odot c^2 . \tag{6.24}$$

I have computed the characteristic gravitational wave strain spectra $h_{\rm char}(f)$ [514] for all models. $h_{\rm char}(f) \propto \sqrt{dE_{\rm GW}(f)/df}$ is a particularly useful measure, since it incorporates the amount of energy radiated in a spectral interval df around frequency f. I find maximum characteristic strains in the range

$$0.20\times10^{-21}\left(\frac{R}{10\,\mathrm{kpc}}\right) \lesssim h_{\rm char,max} \lesssim 12.46\times10^{-21}\left(\frac{R}{10\,\mathrm{kpc}}\right) , \tag{6.25}$$

which are located in the frequency interval

$$290\,\mathrm{Hz} \lesssim f_{\rm peak} \lesssim 950\,\mathrm{Hz} . \tag{6.26}$$

Based on the characteristic strain spectra, I surmise that the gravitational waves emitted in axisymmetric collapse, bounce and early postbounce phases of sufficiently quickly spinning stellar iron cores should be detectable by initial LIGO-class detectors if occurring within the Milky Way and by advanced LIGO detectors out to the Magellanic Clouds. I point out that *all models that yield sizable gravitational wave emission from core bounce have precollapse angular velocities too high to yield neutron star remnants in agreement with the observed periods of young pulsars without the need for yet unknown PNS/NS spin-down mechanisms* [273, 511]. Models that do not rotate and models that rotate sufficiently slowly to leave neutron stars with periods in the pulsar birth-spin range of ~10–60 ms do not deviate enough from spherical symmetry to produce a detectable gravitational wave signal during core bounce. Their gravitational wave emission is due to postbounce convective overturn, anisotropic

neutrino emission, and, possibly, to late time instabilities of the standing accretion shock (SASI) and PNS core pulsations which I discuss in §7.2.

One of the ultimate goals of gravitational wave astronomy is to solve the *inverse problem*, that is, to extract information about core-collapse supernova physics and the progenitor star and its precollapse rotational configuration from an observed gravitational wave signal. First theoretical attempts towards solving the inverse problem have been made by gravitational wave data analysts [605] based on the data of [9]. The results obtained here show that the quantitative aspects of the late collapse dynamics and core bounce and the resulting gravitational wave signal are primarily determined by the mass and the angular momentum of the subsonically collapsing inner core. My results show that different choices in the parameter space spanned by progenitor structure, initial rotation rate, degree of differential rotation and degree of deleptonization can lead to virtually identical gravitational waveforms. As a consequence, one must consider the gravitational wave signal of rotating core-collapse as *multi-degenerate* in above parameter space. This finding dramatically complicates the extraction of physically valuable information from an observed gravitational wave signal associated with a core-collapse event.

Recent studies based on polytropic rotational-equilibrium compact star models [20, 21, 23–25, 308, 309] and on a simplified PNS model [22] found evidence for dynamical rotationally-induced development of nonaxisymmetric structures at β below the classical threshold for dynamical rotational instability. Such low-$T/|W|$ instabilities have been identified [19, 23, 24] with resonant amplification of nonaxisymmetric disturbances at corotation points at which the local fluid angular velocity equals the pattern speed of a nonaxisymmetric eigenmode of a compact star.

In order to investigate the possibility of a low-$T/|W|$ corotation-type instability in the more realistic postbounce supernova cores considered in this work, I carried out the calculations of models E20A and s20A1000β1.80 to times later than 70 and 90 ms after bounce, respectively. Model E20A uses the progenitor model of the same name of [509] that includes a one-dimensional prescription for rotational evolution. It settles at an immediate postbounce β of $\sim$9%. Model s20A1000β1.80 has more rotational energy and an early postbounce β of $\sim$13%. Both models stay centrally condensed throughout their numerical evolutions and *in both models I observe the development of nonaxisymmetric structures with growth times comparable with the PNS dynamical timescale*. I have performed a Fourier mode analysis of the rest-mass density for nonaxisymmetric azimuthal structures $\propto \exp(im\varphi)$ and find that in both models the instability is originating from the PNS core with dominant $m = 1$ spatial structure. $m = 2$ and $m = 3$ components grow as well, but both models appear stable to the ambient $m = 4$ Cartesian grid mode. The nonaxisymmetric mode amplitudes level off on the multi-percent level. This is small compared with the classical high-$T/|W|$ bar-mode instability in which the relative deformation typically reaches order unity, but is in agreement with what has been found in other studies of low-$T/|W|$ unstable compact stars [21, 22, 24].

With progressing postbounce time, the instability spreads in the equatorial plane through the entire postshock region and becomes manifest as a spatially and temporally varying spiral wave pattern reminiscent of spiral density waves in a galaxy or in a Keplerian accretion disk. Such density waves are theoretically known to redistribute angular momentum on a timescale that is longer than the dynamical timescale of the system (e.g, [586, 587]). Neither in model E20A nor in model s20A1000β1.80 do I find evidence for rapid angular momentum redistribution. A detailed analysis of the angular momentum and mass contained in various radial intervals in the equatorial plane in model E20A indicates that the PNS core regions gain mass while keeping an approximately fixed amount of angular momentum, despite the fact that the accretion proceeds sub-Keplerian and thus does not require angular momentum redistribution to function. This may be circumstantial evidence for a slowly operating angular momentum redistribution mechanism. However, I point out that accretion onto the PNS occurs from all latitudes and at spatially and temporally varying rates. That and the limited amount of postbounce time over which I was able to track the PNS and the postshock angular momentum evolution make it impossible to draw robust conclusions about angular momentum redistribution by the rotational instability.

The embeddedness of the low-entropy PNS core in the high-entropy postshock region and the continuous inflow of matter and angular momentum through the stalled supernova shock make it extremely difficult to isolate the driving mechanism behind the rotational nonaxisymmetric instability in models s20A1000β1.80 and E20A. In addition and unlike nonaxisymmetric instabilities in simpler

isolated NS models, the instability found here exhibits temporally and radially varying spatial structure in the equatorial plane and also changes in structure with z-distance from the equator. I extract mode eigenfrequencies σ_m from the hydrodynamics data and find that all unstable nonaxisymmetric modes in model E20A have a common mode pattern speed $\sigma_p = \sigma_m/m \approx 2900$ rad s^{-1} which suggests their non-linear relationship. Model E20A's PNS is corotating with this σ_p throughout its postbounce evolution at a radius of $\sim$10 km. It is conceivable that the nonaxisymmetric dynamics in this model are driven by the $m = 1$ mode that experiences a corotation instability in the PNS core and injects power into higher-m modes through non-linear mode couplings. In model s20A1000β1.80 I find two distinct σ_p. One associated with the $m = 1$ and $m = 2$ modes at $\sim$2900 rad s^{-1} and a second, slower σ_p of $\sim$2300 rad s^{-1}, associated with $m = 3$ spatial structure. Both σ_p are in corotation with model s20A1000β1.80's equatorial angular velocity profile inside the PNS core at radii between 8–15 km. As for model E20A, it is not unfounded to surmise that a corotation resonance in combination with non-linear mode couplings may be driving the development of nonaxisymmetric structures with multi-m spatial character in model s20A1000β1.80.

One, if not *the* central motivation for {3+1} GR hydrodynamic calculations of stellar iron core collapse is the possibility of powerful and long-term gravitational wave emission from time-changing nonaxisymmetric structures. Despite the complicated nonaxisymmetric dynamics in models E20A and s20A1000β1.80, I find extremely coherent gravitational wave emission. In both models, nonaxisymmetric gravitational wave emission sets in and grows to amplitudes of the same order of magnitude as the signal from axisymmetric core bounce. *The emission is narrow band and h_+ and $h_\times$ as seen by an observer located on the rotation axis oscillate at the same frequency and are phase-shifted by a quarter cycle which is in remarkable agreement with expectations for a top-over spinning bar [115].* In both models, most energy is emitted in a narrow frequency band of $\sim$900–940 Hz, again in agreement with a simple bar-model, *corresponding exactly to twice the pattern speeds of their $m = 2$ modes*. Figure 6.53 compares the gravitational wave emission from axisymmetric core bounce and PNS ring-down in model s20A1000β1.80 with that from the late-postbounce emission from the quadrupole substructures of the nonaxisymmetric dynamics. The late postbounce emission is lower in amplitude, but at higher frequency, and occurs over a much greater interval in time than the axisymmetric bounce and ring-down emission. In model s20A1000β1.80 the quadrupole gravitational wave energy emitted by the nonaxisymmetric structures alone amounts to 1.7×10^{-7} M$_\odot c^2$ which is a factor of $\sim$18 larger than the energy in axisymmetric core bounce and PNS ring-down in this model. Model E20A, which I track to only 70 ms after core bounce and whose late-time emission reaches lower amplitudes than that of model s20A1000β1.80, emits a total of 7.5×10^{-8} M$_\odot c^2$ in gravitational waves which is twice the amount of energy emitted during its axisymmetric bounce and PNS ring-down.

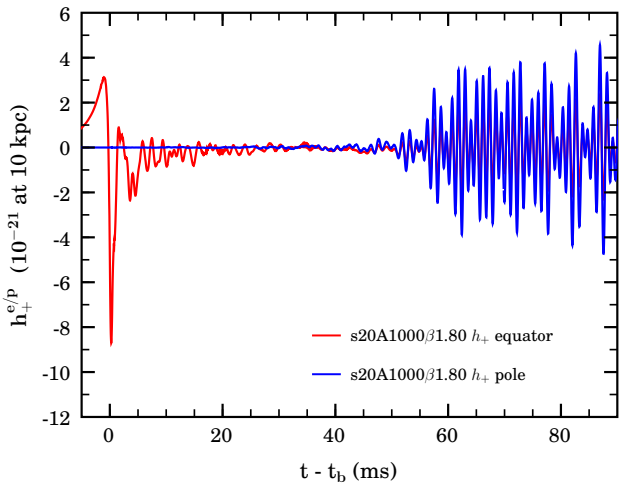

Figure 6.53: Gravitational wave signal in model s20A1000β1.80. The time is given relative to the time of core bounce. Shown in red color is the h_+ gravitational wave strain as seen by an observer located at 10 kpc distance in the equatorial plane along the positive x-axis ($\varphi = 0$) and in blue color the same polarization is plotted, but as seen by an observer located at 10 kpc distance along the positive polar axis ($\theta = 0$). See §6.4.2 for details.

It is important to point out that neither model E20A nor model s20A1000β1.80 shows any sign of decay in their nonaxisymmetric structures and dynamics, and, correspondingly in their gravitational wave emissions. If the driving instability is functioning via a corotation resonance, it is likely to persist as long as the unstable mode(s) has/have corotation points with the PNS. Since accretion of mass and angular momentum through the stalled shock essentially inhibits net large-scale redistribution of angular momentum, the instability may not cease to exist until after successful shock revival has turned accretion into explosion, or, alternatively, until a black hole has formed and a gamma-ray burst jet disrupts the outer core and the stellar envelope. When $\sqrt{n}$-extrapolating the nonaxisymmetric gravitational wave emissions of model E20A and model s20A1000β1.80 to an emission interval of 300 ms, I find conservative upper limits on the characteristic gravitational wave strains of 6.4×10^{-20} and 1.7×10^{-19} for model E20A and model s20A1000β1.80, respectively. Based on these numbers, model s20A1000β1.80 could be marginally detectable by advanced LIGO-class detectors out to Virgo Cluster distances ($\sim$10–30 Mpc), which would lead to a significantly increased observable event rate, if the development of nonaxisymmetric rotational instabilities as observed in the calculations presented here were a generic process occuring in a large fraction of all core-collapse events.

Based on the calculations carried out in this work, I can make no judgement on the generic nature of the instability observed in model E20A and s20A1000β1.80. Due to the extreme computational and data analysis demands of long-term postbounce {3+1} GR hydrodynamic calculations, I was able to follow only two models to late postbounce times and track the growth of nonaxisymmetric structures and dynamics. While I find that slowly rotating models with $\beta_{\rm initial} \lesssim 0.25\%$ and postbounce $\beta \lesssim 6\%$ show no significant rotationally-induced growth of nonaxisymmetric modes up to $\sim$20–25 ms after core bounce, it is not clear if such models are stable and remain axisymmetric or if the instability is present, but has a much longer growth time. In the case of a corotation resonance mechanism, the instability would not be present in models that rotate too slowly (and/or too rigidly) to have corotation points or in models that rotate too fast so that the corotation radius would be located in regions of low density and correspondingly low rotational energy.

A much larger set of calculations than considered here would be necessary to uncover the details of the mechanism behind the instability. I was able to perform only a single resolution test calculation for the late postbounce evolution in model E20A. It shows results consistent with those of the standard-resolution calculation, yet additional and higher-resolution calculations are needed to more deeply understand the resolution dependence of the nonaxisymmetric dynamics. In particular, it is necessary to perform counterpart calculations on different grid geometries to understand and exclude artificial effects of the strong Cartesian $m = 4$ grid mode.

The calculations presented in this chapter are the first attempt to unite core-collapse supernova theory and numerical relativity in a multi-dimensional context. They mark an important step towards future fully general relativistic calculations of core-collapse supernovae and of collapsar-type gamma-ray bursts, yet they are still severely limited in many ways. Importantly, the prescription used for deleptonization approximates full neutrino radiation transport only during the collapse phase. Postbounce deleptonization of the PNS, the neutrino break-out burst and neutrino heating and cooling in the postshock region are completely neglected. This significantly decreases the physical quality of the models that I evolve to late postbounce times and makes it impossible to address more general questions such as the supernova explosion mechanism to any degree. Further technical and computational limitations that may impinge on the quality and robustness of the results presented here include (1) the assumption of reflection symmetry with respect to the equatorial plane that inhibits the growth of odd-ℓ fluid modes, (2) the use of fixed mesh refinement in the present form that leads to flux-mismatches and reflections at mesh-refinement boundaries and to the partial underresolution of the standing accretion shock and (3) the neglect of magnetic fields which makes it impossible to consider potentially important MHD effects. In particular, the magneto-rotational instability (MRI; see, e.g., [276–278, 606–609]) that operates on the shear energy stored in differential rotation and that may lead to rapid angular momentum redistribution, cannot be investigated with the present approach.

Future work will be directed towards higher-precision calculations with fully adaptive mesh refinement, improved treatment of postbounce deleptonization and, at a later point, towards magnetohydrodynamics on generalized multi-block grid hierarchies [610].

Chapter 7

Studies in Newtonian Gravity

In collaboration with the Arizona supernova group I have performed axisymmetric radiation-hydrodynamics supernova calculations in Newtonian gravity using the VULCAN/2D code, originally developed by E. Livne [477, 574]. I have co-authored studies of a possible new explosion mechanism of core-collapse supernovae based on energy and momentum transfer from PNS core g-mode oscillations to the stalled shock by means of acoustic waves [26, 27]. I have also been involved in studies of rotation-induced anisotropic neutrino radiation fields [87], PNS convection [72], and accretion-induced collapse (AIC) of white dwarfs [16]. I have authored articles on PNS birth spin estimates [273] and on the gravitational wave emission from the strong PNS core g-mode oscillations [15], first observed in the calculations of Burrows et al. [26].

Since this dissertation is primarily concerned with the gravitational wave signature of core-collapse supernovae, I will in the following — after a brief description of VULCAN/2D based on [27, 72, 477, 574] — focus on theoretical estimates of the gravitational wave emission from PNS core g-mode oscillations [15, 26, 27] and from AIC events [16].

7.1 The VULCAN/2D Code

VULCAN/2D's axisymmetric hydrodynamics implementation is based on an Arbitrary-Lagrangian-Eulerian (ALE) scheme which implements the Lagrangian formulation (see, e.g., [149]) of the Newtonian hydrodynamic equations in second-order finite-difference artificial-viscosity von Neumann–Richtmyer fashion [611] in combination with a remap of the updated fluid quantities to the Eulerian grid. The code has been developed and is actively maintained by E. Livne. The original hydrodynamic scheme dates back to 1992 and is described and tested in [574]. VULCAN/2D was first employed in the core-collapse supernova context in the purely hydrodynamic study of rotating iron core collapse in the course of my diploma thesis [9, 170]. It has subsequently been used in numerous radiation-hydrodynamics calculations [15, 16, 26, 27, 72, 87, 477]. The discussion of VULCAN/2D in this Section is based primarily on the text in [27, 72].

In contrast to most other multi-dimensional, grid-based astrophysical hydrodynamics codes (e.g., WHISKY, see §3.5), VULCAN/2D does *not* use dimensional splitting. Instead, and by virtue of the ALE approach and similar to finite-element approaches, the grid cells are treated as *elements*. Each element has four *nodes*, defining the corners of the quadrilateral cells/elements. Scalar quantities are defined at cell centers, while vector quantities are located at the nodes. The Lagrangian update is performed on an element-by-element basis by computing the relevant fluxes through the cell interfaces and between nodes with each neighbor. The Eulerian remap step is performed for each element after the Lagrangian sweep by a linear slope-limited TVD interpolation scheme[1]. VULCAN/2D can be run in implicit or explicit time integration mode. For the core-collapse supernova calculations presented here, the explicit mode is used. All calculations are performed with the EOS of Shen et al. [464, 465] in the implementation of the Arizona group (see §3.6.2 and [26, 27]).

Because of its element/nodes structure, VULCAN/2D is able to to deal with arbitrarily shaped grids while internally assigning cylindrical coordinates (ϖ, z) to each node. This key feature of VUL-

[1] See §3.2.1 and §3.5.1 for a definition of the TVD property and the application of slope limiters in the cell-interface reconstruction of finite-volume high-resolution shock-capturing schemes.

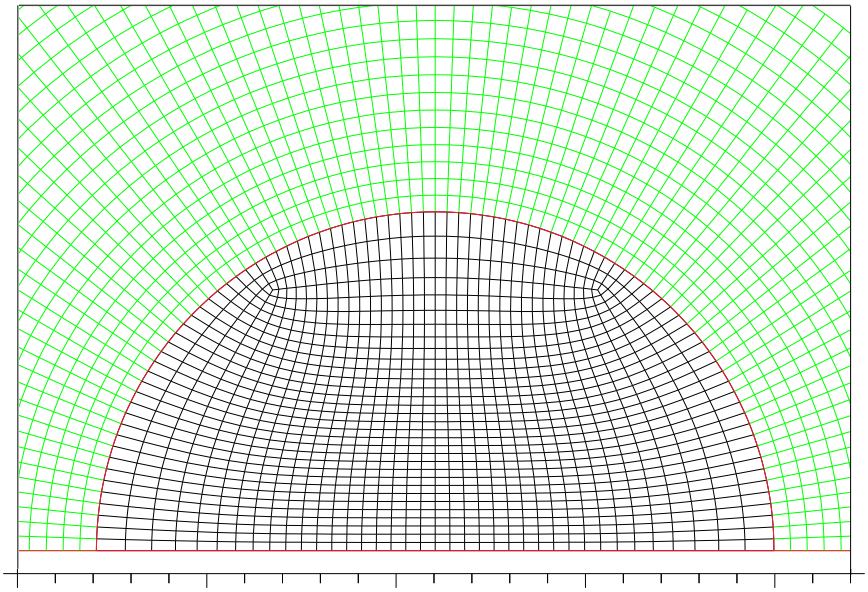

Figure 7.1: Central region of the VULCAN/2D computational grid. Shown in black is the inner pseudo-Cartesian region that typically extends out to ∼20–30 km where it transitions to the outer spherical grid.

CAN/2D is exploited in core-collapse supernova calculations. The grid is typically set up in such a way that the inner ∼20–30 km are covered by a Cartesian grid with essentially uniform resolution that transitions smoothly to an outer spherical-polar, logarithmically-space grid. Figure 7.1 displays an example grid structure. Such a grid setup has three important advantages over the spherical-polar grids typically used in other supernova codes: (1) The inner Cartesian grid allows for much larger timesteps than possible with a regular spherical-polar grid that suffers from severe timestep constraints imposed in the angular direction close to the origin, and, more importantly, (2) the VULCAN/2D grid covers the entire PNS, not excising the central-most part and completely liberating the PNS core and thus allowing core translational motion, and (3) no coordinate singularity (in the angular direction) at the origin is present. Other groups treat the core of the PNS in 1D out to a few kilometers (e.g., [73, 79, 86, 478]) and in this way inhibit core translation/oscillatory (ℓ=1) motion.

Typical VULCAN/2D simulation grids cover the full 180° and extend out to ∼5000 km with 120 angular and 160 logarithmically spaced, centrally refined radial zones. At this resolution, VULCAN/2D conserves energy to better than ∼0.7% near bounce and to ∼0.4% on average in terms of $\Delta E/E_g$. A high resolution calculation with 180 angular and 300 radial zones, carried out in the course of the preparation of [26, 27], revealed no large qualitative or quantitative differences during the collapse, bounce, and early postbounce phase. However, due to the chaotic/turbulent nature of the postshock flow at later postbounce times, the high-resolution simulation diverges quantitatively from the one carried out with standard resolution. The deviation is, however, not dramatic and all qualitative features, including the Standing Accretion Shock Instability (SASI), PNS core g-mode oscillations, and the explosions seen in the models of [26, 27] are present.

7.1.1 2D Multi-Group Flux-Limited Diffusion of Neutrinos

The radiation transport module in VULCAN/2D is capable of performing axisymmetric multi-energy-group, multi-species full Boltzmann neutrino radiation transport calculations using the discrete-ordinates (S_n) method [477]. However, due to the extreme computational demands of full Boltzmann transport even in 2D, the calculations presented here are performed in the multi-group multi-species flux-limited diffusion (MGFLD) approximation (see, e.g., [27, 87, 475]) which is computationally very efficient and allows exploratory studies involving long-term evolutions of a large set of models. However, MGFLD is only an approximation to full Boltzmann transport and differences with the more exact treatment will emerge in the neutrino semi-transparent and transparent regimes

above the protoneutron star surface. Nevertheless, inside the neutrinospheres the two-dimensional MGFLD approach provides a very reasonable representation of the multi-species, multi-group neutrino radiation fields.

The evolution of the neutrino radiation field is described in the flux-limited diffusion approximation (see, e.g., [475]) by a single (group-dependent) equation for the average intensity J_g of energy/species group g with neutrino energy ε_ν^g:

$$\frac{1}{c}\frac{\partial J_g}{\partial t} - \nabla(D_g \nabla J_g) + \sigma_g^a J_g = S_g \,, \tag{7.1}$$

where the diffusion coefficient is given by $D_g = 1/(3\sigma_g)$ (and then is flux-limited according to the recipe below), the total inverse mean-free-path ("cross section") is σ_g, and the inverse absorption mean-free-path (absorption "cross section") is σ_g^a. The source term on the right-hand side of equation (7.1) is the emission rate of neutrinos of group g. Note that equation (7.1) neglects inelastic scattering between energy groups. This may affect the size of the homologous core at bounce by up to $\sim$10%, but is otherwise subdominant [273].

The finite-difference representation of equation (7.1) consists of cell-centered discretization of J_g. It is important to use cell-centered discretization because the radiation field is strongly coupled to matter and the thermodynamic matter variables are cell-centered in the hydrodynamical scheme. The finite-difference approximation of equation (7.1) is obtained by integrating the equation over a cell. Omitting group indices and cell indices, one obtains

$$V\left[\frac{1}{c\Delta t}(J^{n+1} - J^n) + \sigma^a J^{n+1}\right] + \Sigma_i d\vec{S}_i \cdot \vec{F}_i^{n+1} = VS \,. \tag{7.2}$$

Here V is the volume of the cell, $d\vec{S}_i$ is the face-centered vector "area$_i$ $\vec{n}_i$," $\vec{n}_i$ being the outer normal to face i. The fluxes $\vec{F}_i$ at interfaces are the face-centered discretization of

$$\vec{F}_i = -D_i \nabla J^{n+1} \,, \tag{7.3}$$

where

$$D_i = \left(\frac{1}{3\sigma_i}\right) \mathrm{FL}_i \,. \tag{7.4}$$

The employed flux limiter, following Bruenn [475], is

$$\mathrm{FL}_i = \frac{1}{1 + D_i|\nabla J|/J} \,. \tag{7.5}$$

It approaches free streaming when D_i exceeds the intensity scale height $J/|\nabla J|$. The fluxes on the outer boundary of the system are defined by free streaming outflow and not by the gradient of J. Note that in equation (7.3) the fluxes are defined as face quantities, so that they have exactly the same value for the two cells on both sides of that face. The resulting scheme is, therefore, conservative by construction. In order to have a stable scheme in semi-transparent regions (large D_g) the variables in equation (7.2) are centered implicitly. The fluxes, defined by the intensity at the end of the time step, couple adjacent cells and the final result is a set of linear equations. The matrix of this system has the standard band structure and direct LU decomposition [612] is used to solve the linear system.

VULCAN/2D is parallelized according to energy and neutrino species groups. Each CPU computes one to a few groups (usually one) and transfers the needed information to the other processors using standard Message-Passing Interface (MPI) [398–400] routines. For typical supernova calculations, 16 energy groups per neutrino species are employed, logarithmically spaced from 1 or 2.5 MeV to 250 or 320 MeV. Electron neutrinos (ν_e) and anti-electron neutrinos ($\bar{\nu}_e$) are followed separately, while the remaining four known neutrino species are bundled in "ν_μ" bins in the standard fashion. Since VULCAN/2D does not decompose its computational domain, the parallelization is very simple. In fact, each processor performs the hydrodynamics step on the entire grid. In order to avoid divergent evolution between different CPUs due to accumulation of machine round-off errors, VULCAN/2D copies the grid variables of one chosen CPU (CPU 0) into those of the other CPUs, typically every thousand timesteps.

The neutrino-matter interaction physics is taken directly from [70] and employed in tabulated fashion parametrized by $(T, \rho, Y_e,$ neutrino species and energy$)$, incorporating all relevant scattering, absorption, and emission processes discussed, e.g., in [64, 613].

7.1.2 Gravity and Poisson Solvers

Currently, there are two Poisson solvers in VULCAN/2D — a *multipole solver* and a *grid solver*. The multipole solver performs a standard axisymmetric Legendre expansion of the Newtonian gravitational potential of the form [614]

$$\Phi(r,\theta) = -G\sum_{l=0}^{\infty} P_l(\cos\theta)\int dr' r'^2 d\cos\theta' \rho(r',\theta')\frac{r_<^l}{r_>^{l+1}}P_l(\cos\theta')\ , \tag{7.6}$$

where $P_l(\cos\theta)$ is the Legendre polynomial of order l and $r_<$ ($r_>$) is the smaller (larger) of the two radii r and r'. Typically 20 to 33 terms are employed. For the potential calculations, one generally needs a special auxiliary grid, which is not identical with VULCAN/2D's complex computational grid. This leads to a number of interpolations between the grids, which can introduce significant numerical errors. Most importantly, with the multipole solver, conservation of total energy is poor through bounce and later. Conservation of total energy is much better with the grid solver, and the numerical noise in the core region is significantly reduced when it is employed.

The grid solver uses a standard finite-element method (FEM) which is adequate for unstructured grids, to obtain the potential at grid nodes. In axial symmetry and cylindrical coordinates Poisson's equation takes the form

$$\Delta\Phi = \frac{1}{\varpi}\frac{\partial}{\partial\varpi}\left(\varpi\frac{\partial\Phi}{\partial\varpi}\right) + \frac{\partial^2\Phi}{\partial z^2} = -4\pi G\rho\,. \tag{7.7}$$

Let $\{\alpha_i(\varpi,z)\}$ be a set of interpolation functions which span the FEM approximation. Multiplying equation (7.7) by α_i, and integrating by parts over the entire domain, one obtains

$$\begin{aligned} -\iint \nabla\Phi\nabla\alpha_i\varpi\, d\varpi\, dz + \{\text{surface-integral}\} \\ = -4\pi G\int\int \rho\alpha_i\varpi\, d\varpi\, dz\,. \end{aligned} \tag{7.8}$$

In particular, if Φ is expanded using the set $\{\alpha_i\}$, specifically

$$\Phi(\varpi,z) = \Sigma_j\Phi_j\alpha_j(\varpi,z)\,, \tag{7.9}$$

where Φ_j is the value of Φ at node j, one obtains a linear system of the form

$$A\mathbf{\Phi} = \mathbf{B}\,, \tag{7.10}$$

where

$$A_{ij} = -\iint \nabla\alpha_i\nabla\alpha_j\varpi\, d\varpi\, dz \tag{7.11}$$

and

$$B_i = -4\pi G\iint \rho\alpha_i\varpi\, d\varpi\, dz\,. \tag{7.12}$$

The matrix A has good qualities, i.e. is easy to invert, if one chooses $\{\alpha_i\}$ to be continuous, positive, and local, with the following specifications: $\alpha_i(\varpi_j,z_j) = \delta_{ij}$ at the nodes of the grid, $\alpha_i = 0$ in any zone not containing node i, and $\Sigma_i\alpha_i(\varpi,z) = 1$ everywhere. In practice, bilinear interpolation functions are employed in each zone. The integrals (7.11) are computed once and the integrals (7.12) are computed at each timestep.

Note, however, that the grid solver needs boundary values, and for this the zeroth moment $\Phi_b = -GM/R_b$ is employed, where R_b here is the distance between a boundary point and the center of mass (which is usually very close to the center of the grid). This approximation is good for large outer radii, where the potential drops by orders of magnitude compared with that at the center.

The gravitational forces in the ϖ and z directions are computed as suggested by Shu [585] via the divergence

$$\vec{f}_g = \mathrm{div}S_{ij} \tag{7.13}$$

of the gravitational stress tensor

$$S_{ij} = -\frac{1}{4\pi G}\left(g_ig_j - \frac{1}{2}|\vec{g}|^2\delta_{ij}\right), \tag{7.14}$$

where $\vec{g} = \nabla\Phi$. In cylindrical coordinates, the force components then read

$$f_\varpi = -\frac{1}{4\pi G}\left(\frac{1}{2\varpi}\frac{\partial[\varpi(g_\varpi^2 - g_z^2)]}{\partial\varpi} + \frac{\partial(g_\varpi g_z)}{\partial z} + \frac{1}{2\varpi}(g_\varpi^2 + g_z^2)\right) , \tag{7.15}$$

$$f_z = -\frac{1}{4\pi G}\left(\frac{1}{\varpi}\frac{\partial(\varpi g_\varpi g_z)}{\partial\varpi} + \frac{1}{2}\frac{\partial(g_z^2 - g_\varpi^2)}{\partial z}\right) . \tag{7.16}$$

7.1.3 Gravitational Wave Emission by Aspherical Mass Motions

The gravitational wave extraction routine within VULCAN/2D has been implemented in the course of my diploma thesis [9, 170]. It is based on the mass quadrupole formalism (see §2.6.4 and §3.8) in the *stress formula* fashion introduced by Blanchet et al. [171] who write the transverse-traceless gravitational wave strain as

$$\ddot{I}_{ij} = \frac{2G}{Dc^4} P_{ijkl}(\vec{N}) \int \rho \left[2v^i v^j - x^i\Phi_{,j} - x^j\Phi_{,i} - \frac{2}{3}\delta^{ij}(v^l v^l - x^l\Phi_{,l})\right] d^3x \; . \tag{7.17}$$

Here D is the distance to the source and $P_{ijkl}(\vec{N})$ (with $\vec{N} = \vec{D}/D$) is the transverse-traceless projection operator onto the plane orthogonal to the outgoing wave direction $\vec{N}$ and is of the form

$$P_{ijkl}(\vec{N}) = (\delta_{ik} - N_i N_k)(\delta_{jl} - N_j N_l) - \frac{1}{2}(\delta_{ij} - N_i N_j)(\delta_{kl} - N_k N_l) \, . \tag{7.18}$$

I follow Mönchmeyer et al. [11] and rewrite equation (7.17) in spherical coordinates and in terms of pure spin tensor harmonics $T_{ij}^{E2,lm}$ and $T_{ij}^{B2,lm}$ [168]:

$$h_{ij}^{TT}(\vec{D}, t) = \frac{1}{D}\sum_{l=2}^{\infty}\sum_{m=-l}^{l}\left[\, A_{lm}^{\mathrm{E2}}(t - \frac{D}{c})T_{ij}^{E2,lm}(\theta,\phi) + A_{lm}^{\mathrm{M2}}(t - \frac{D}{c})T_{ij}^{M2,lm}(\theta,\phi)\right] . \tag{7.19}$$

The coefficients A_{lm}^{E2} and A_{lm}^{M2} represent the mass quadrupole and the mass-current quadrupole contributions, respectively. In the quadrupole approximation, higher-order as well as mass-current contributions are neglected. Due to the assumption of axisymmetry, only one non-vanishing term remains in equation (7.19), namely A_{20}^{E2}. By comparing equation (7.17) with the lowest-order term of equation (7.19), Mönchmeyer et al. [11] write A_{20}^{E2} in terms of the hydrodynamic variables:

$$\begin{aligned} A_{20}^{\mathrm{E2}} = {} & \frac{16\,\pi^{3/2}}{\sqrt{15}}\frac{G}{c^4}\int_{-1}^{1}\int_0^{\infty} r^2 d\mu\, dr \cdot \rho \\ & \cdot\Big[v_r^2(3\mu^2 - 1) + v_\theta^2(2 - 3\mu^2) - v_\phi^2 - 6\, v_r v_\theta \mu\sqrt{1-\mu^2} \\ & -r\,\partial_r\Phi\,(3\mu^2 - 1) + 3\,\partial_\theta\Phi\,\mu\sqrt{1-\mu^2}\Big] , \end{aligned} \tag{7.20}$$

where $\mu = \cos\theta$ and v_r, v_θ, and v_ϕ are the components of the velocity vector in the r, θ, and ϕ directions. Furthermore, $\partial_r = \partial/\partial r$ and $\partial_\theta = \partial/\partial\theta$.

The components of the quadrupole gravitational wave field h^{TT} are then given by [11, 168]:

$$h_{\theta\theta}^{TT} = \frac{1}{8}\sqrt{\frac{15}{\pi}}\sin^2\alpha\;\frac{A_{20}^{\mathrm{E2}}}{D} \equiv h_+ , \tag{7.21}$$

where α is the angle between the symmetry axis and the line of sight of the observer. The only other nonzero component is $h_{\phi\phi}^{TT} = -h_{\theta\theta}^{TT} = -h_+$. Due to the assumption of axisymmetry, $h_\times$ equals zero.

As an alternative to the stress formula, I have implemented the *first order of momentum divergence* formula (see §3.8.1 and [178]). In its axisymmetric incarnation it is given by

$$\frac{dI_{zz}}{dt} \;=\; \frac{4\pi}{3}\int_{-1}^{1} d\mu \int_0^{\infty} dr\; r^3\,\rho\left[P_2(\mu)v_r + \frac{1}{2}\frac{\partial P_2(\mu)}{\partial\theta}v_\theta\right] , \tag{7.22}$$

where $P_2(\mu)$ is the second Legendre polynomial in μ and I_{zz} the zz-component of the reduced mass-quadrupole moment tensor. The gravitational wave strain is then obtained as

$$h_{\theta\theta}^{TT} = \frac{6G}{Dc^4}\;\sin^2\alpha\frac{d^2}{dt^2}I_{zz} \; . \tag{7.23}$$

7.1.4 Gravitational Wave Emission by Anisotropic Neutrino Radiation

Not only aspherical fluid motion, but in more general terms, any accelerated transport of energy with a non-zero quadrupole (and/or higher order) component will emit gravitational waves. For the case of anisotropic radiation of neutrinos from a hot protoneutron star this has been first realized in linear theory via the solution of the inhomogeneous wave equation (2.96) for a distant anisotropic point source by Epstein [281] (but, see also [615] for a derivation in the zero-frequency limit). Burrows & Hayes [265] and Müller & Janka [284] were the first authors to implement the formalism. It has since been used in a number of other studies [94, 95, 241]. I have implemented the scheme and have used it for the post-processing of VULCAN/2D radiation-hydrodynamics data.

For axial symmetry, [265, 284] write the dimensionless gravitational wave strain for an observer positioned in the equatorial plane as

$$h^{TT}_{+,e}(t) = \frac{2G}{c^4 D}\int_{-\infty}^{t-D/c} \alpha(t')L_\nu(t')dt' \;, \tag{7.24}$$

where $L_\nu(t)$ is the total neutrino luminosity and $\alpha(t)$ is the instantaneous neutrino radiation anisotropy that includes the transverse-traceless projections [284]. It is defined as

$$\alpha(t) = \frac{1}{L_\nu(t)}\int_{4\pi} \Psi(\vartheta',\varphi')\frac{dL_\nu(\vec{\Omega}',t)}{d\Omega'}d\Omega' \;, \tag{7.25}$$

where $dL_\nu(\vec{\Omega},t)/d\Omega$ is the energy radiated at time t per unit of time and per unit of solid angle into direction $\vec{\Omega}$ with

$$L_\nu(t) = \int_{4\pi} \frac{dL_\nu(\vec{\Omega}',t)}{d\Omega'}d\Omega' \;. \tag{7.26}$$

$\Psi(\vartheta,\varphi)$ represents the angle dependent factors in terms of source coordinate system angles ϑ and φ and depends on the particular gravitational wave polarization and the observer position relative to the source. In axisymmetry, $h^{TT}_{\times} = 0$ and $h^{TT}_{+} = 0$ along the axis of symmetry. For an observer located in the equatorial plane, observing the $+$ gravitational wave polarization, $\Psi(\vartheta,\varphi)$ is given [241, 284] by

$$\Psi(\vartheta,\varphi) = -(1+\sin\vartheta\cos\varphi)\frac{\cos^2\vartheta - \sin^2\vartheta\sin^2\varphi}{\cos^2\vartheta + \sin^2\vartheta\sin^2\varphi} \;. \tag{7.27}$$

Note that the neutrino gravitational waveform observed at time $t + D/c$ contains contributions from anisotropies in the neutrino radiation field at all times before t. This leads to a memory effect in the gravitational waveform, leaving behind a constant ("DC") offset after the anisotropic neutrino emission subsides. The implications and detectability of such memory gravitational wave bursts is discussed in [276, 277, 283].

7.2 Gravitational Wave Emission from PNS g-modes

The work presented in this section appeared in a shortened version in Ott, Burrows, Dessart, and Livne, *A New Mechanism for Gravitational Wave Emission in Core Collapse Supernovae*, Physical Review Letters 96, 201102 (2006) [15]. I shall in the following assume first person plural to emphasize its collaborative nature.

In recent simulations, Burrows et al. [26, 27] have observed that protoneutron star (PNS) core g-modes are excited by turbulence and by accretion downstreams through the unstable and highly-deformed stalled supernova shock (undergoing the Standing-Accretion-Shock Instability [SASI] [26, 73, 90, 92, 98, 101]) at postbounce times of many hundreds of milliseconds. The oscillations damp by the emission of strong sound waves and do not ebb until accretion subsides. In this way the core g-modes act as transducers for the conversion of accretion gravitational energy into acoustic power that is deposited in the supernova mantle and, as proposed by Burrows et al. [26, 27], may be sufficient to drive an explosion. Most easily excited is the fundamental ℓ=1 core g-mode, but higher-order eigenmodes and, through nonlinear effects, harmonics of eigenmodes with complicated spatial structures, emerge at later times.

In this work, we consider the intriguing possibility of the emission of strong gravitational waves from the quadrupole spatial components of the PNS core oscillations. We obtain new estimates for the gravitational wave signature of core-collapse supernovae. With three different presupernova stellar models, we have performed the longest 2D Newtonian radiation-hydrodynamics supernova simulations to date. We find that the gravitational waves from the quadrupole components of the core oscillations dominate the total wave signature in duration, maximum strain, and total energy emission by one to several orders of magnitude. We have also discovered an approximate progenitor dependence: more massive iron cores may experience higher frequency, higher amplitude oscillations, and, hence, more energetic gravitational wave emission.

7.2.1 Method and Initial Models

We carry out our axisymmetric calculations with the VULCAN/2D code in the multi-group, flux-limited diffusion approximation [26, 27, 72, 87, 477], with 16 neutrino energy groups and ν_e, $\bar{\nu}_e$, and "ν_μ" flavors as discussed in §7.1.

We explore three models in this study. Model s11WW is the 11-$M_\odot$ (Zero-Age Main Sequence [ZAMS] and solar metallicity) presupernova model of Woosley & Weaver [508] without rotation. Model s25WW is nonrotating as well, but is the 25-$M_\odot$ progenitor from the same study. Model m15b6 corresponds to the 15-$M_\odot$ progenitor model of Heger et al. [511] which was evolved with a 1D prescription for rotation and magnetic-field-driven angular momentum redistribution. We map this model onto our 2D grid under the assumption of constant rotation on cylinders. It has a pre-collapse ratio of rotational kinetic energy to gravitational potential energy, $\beta = T/|W|$, of $\sim 10^{-5}$. This value is up to three orders of magnitude smaller than typically assumed in studies that investigate the gravitational wave signature of rotating collapse and bounce (e.g., Chapters 5 and 6 in this dissertation and [9, 11, 12, 14, 30]), but yields a PNS spin consistent with neutron star birth spin estimates [273, 511].

7.2.2 Results

Figure 7.2 depicts the quadrupole gravitational wave strain h_+, as emitted by mass motions scaled to a source distance of 10 kiloparsecs (kpc). In the top panel, we superpose the waveforms of models s11WW and m15b6. Despite the presence of some rotation in the latter and its greater ZAMS mass, the two models have very similar precollapse stellar structures [273, 508, 511]. This is reflected in the very similar shapes of their waveforms. Even though s11WW is not rotating, a bounce burst strain of $\sim 1.3 \times 10^{-21}$ (at 10 kpc) is present in our numerical model. The first one to two milliseconds of this burst are the imprint of the transition in grid geometry from the outer polar to the inner Cartesian grids (figure 7.1) which generates a non-negligible time-varying quadrupole moment at core bounce. It also induces initial perturbations for vortical motions in the Ledoux-unstable regions

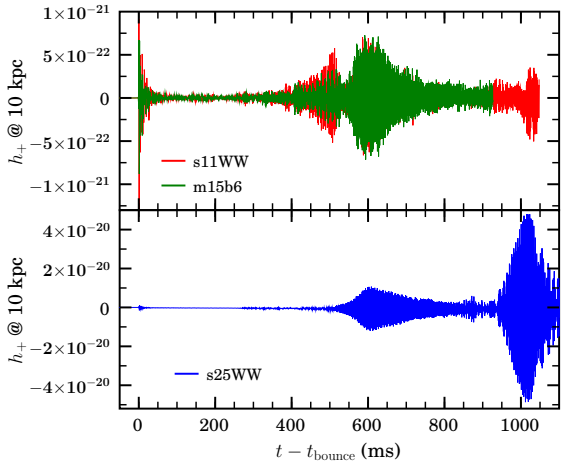

Figure 7.2: Dimensionless gravitational wave strain h_+ along the equator at a distance of 10 kpc derived from aspherical fluid flow. Upper panel: h_+ of the nonrotating s11WW and the slowly rotating m15b6. Both models have similar precollapse structures which is reflected in the similarity of their waveforms. Lower panel: h_+ of model s25WW. Note that the range of h_+ in the lower panel is almost 50 times larger than that of the top panel.

behind the expanding shock that set in almost immediately and with an initial growth rate after core bounce that is, perhaps, too fast. Test calculations with different transition radii and varied resolutions show the artificial bounce feature in the waveform of the nonrotating models to converge away with decreasing grid transition radius. Further numerical test calculations indicate that it is important to cover the entire region that experiences the late-time core oscillations with the finely spaced Cartesian grid. We choose a transition radius of 30 km and accept the artificial wave emission induced by the grid transition at core bounce.

The amount of rotational energy in m15b6's core (at bounce, $\beta \lesssim 2\times10^{-4}$ and at the end, $\beta\sim8\times10^{-4}$) is too small to have a large influence on the core dynamics and, thus, on the waveform, except to slightly stabilize the aspherical fluid motion at and shortly after bounce. In both models, until about $\sim$250 ms after bounce, the physical waveform is dominated by convective motions in the PNS and in the postshock region. As the SASI becomes vigorous and leads to global deformation of the standing shock (see, e.g., [26]) the wave emission from the postshock flow increases.

As described in Burrows et al. [26], the fundamental core g-mode (ℓ=1, with a frequency $f\sim$330 Hz in s11WW and m15b6) is excited by turbulence and accretion. As shown in figure 7.3, it grows strong around $\sim$400 ms after bounce and starts transferring energy to the harmonic at $2f$ through nonlinear effects. This is reflected in the rise of s11WW's gravitational wave strain around that time visible in figure 7.2. h_+ reaches a local maximum, then quickly decays to about one-third that amplitude, only to pick up again after some tens of milliseconds, rising to even higher amplitudes (a maximum of $\sim7\times10^{-22}$ [at 10 kpc]), followed by a quasi-exponential decay with a $\sim$100 ms e-folding time. We attribute the gravitational wave emission in these two 'humps' to the quadrupole spatial component of the $2f$ harmonic of the fundamental ℓ=1 core g-mode. Model s11WW's gravitational-wave energy spectrum exhibits prominent emission in a band around $\sim$650 Hz. Interestingly, we do not observe significant gravitational wave emission at the frequency of the fundamental core g-mode. This mode must thus have been of clean ℓ=1 mode structure and the non-linear energy transfer to its harmonic introduces additional structure of different spatial character. We note in passing that this behavior is unexpected and that harmonics of stellar pulsation modes tend to have the same spatial character as their parent mode [528] (and see, e.g., [323]).

The frequency analysis displayed in figure 7.3 shows that the $2f$ harmonic appears first at a frequency of $\sim$590 Hz, which increases over 200 ms to a maximum of about 680 Hz, and then continuously decreases to $\sim$500 Hz at the end of the simulation. In this way, the gravitational wave emitting component exactly mirrors the behavior of the ℓ=1 g-mode which goes through the same phases [26, 27]. Ferrari et al. [343] have studied the PNS quasi-normal mode frequency evolution in general relativity. Their prediction for the frequency evolution of the fundamental PNS core g-mode is in

qualitative agreement with above the behavior while, owing to their GR treatment, they obtain more compact PNSs with higher-frequency modes. Interestingly, we find that the time of the first lull in the wave emission (at ∼530 ms; figure 7.2) coincides with the point in time at which the core-oscillation mode reaches its maximum frequency and its frequency derivative is zero (figure 7.3). Although model s11WW begins to explode around 550 ms, its core oscillation does not subside immediately and persists as long as accretion continues [26, 27].

The lower panel of figure 7.2 displays model s25WW's waveform. s25WW's precollapse stellar structure is significantly different from those of s11WW and m15b6. Most importantly, its iron core is more massive (∼1.92 $M_\odot$ vs. ∼1.37 $M_\odot$ and ∼1.47 $M_\odot$, respectively) and more extended. These differences in progenitor structure lead to a different postbounce evolution for model s25WW. Its initial shock radius is significantly smaller and the SASI becomes vigorous some 100 ms later than in the two other models. Figure 7.4 shows a frequency-time plot of s25WW's gravitational wave energy spectrum starting at 400 ms after bounce. The first burst of gravitational waves, starting at about 500 ms and slowly fading afterwards (Fig. 7.2), is centered about ∼800 Hz. In this model, the ℓ=1 fluid mode, which dominates the dynamics at that time, is centered at ∼400 Hz and as for models s11WW and m15b6, we identify the wave emitting component as part of the harmonic at $2f$ of the former. At ∼900 ms after bounce, much stronger waves begin to be emitted through the excitation of an ℓ=2 core eigenmode (figure 7.4; at that time f ∼950 Hz). It reaches a maximum strain of $\sim 5\times10^{-20}$ (at 10 kpc) and lasts for at least 200 ms, emitting a total of $8.2\times10^{-5}\ M_\odot c^2$ ($\simeq 1.5\times10^{50}$ erg!) in gravitational waves (figure 7.5). Given usual type-II supernova energetics (e.g., [38]), s25WW emits about 15% of the total kinetic explosion energy and more than ten times more energy than the supernova optical emission. Clearly, gravitational radiation reaction effects may be relevant in this model. However, since we did not expect such strong emission, the VULCAN/2D calculations do not include radiation reaction force terms. Nevertheless, it is important to obtain quantitative insight on the importance of radiation reaction effects. This is most straightforwardly done by comparing the quadrupole gravitational wave luminosity,

$$L_{\rm GW} = \frac{dE_{\rm GW}}{dt} = \frac{1}{5}\frac{G}{c^5}\langle \dddot{I}_{jk}\dddot{I}_{jk}\rangle = \frac{c^3}{32\pi G}\left\langle \left|\frac{dA^{E2}_{20}}{dt}\right|^2\right\rangle , \tag{7.28}$$

with the acoustic power ($L_{\rm acoustic}$) emitted by the core oscillations. It is a lower bound on the total gravitational wave luminosity since higher multipole emission is not taken into account. By comparing $L_{\rm GW}$ with $L_{\rm acoustic}$ it is possible to estimate the relevance of radiation reaction as an additional

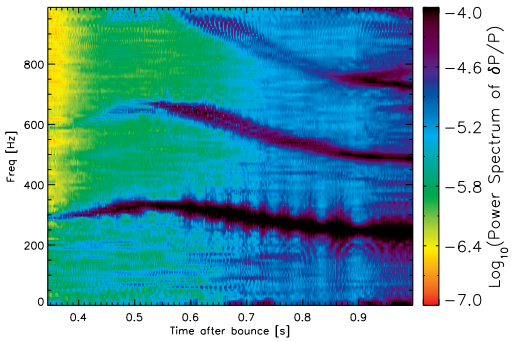

Figure 7.3: Power spectrum of the fractional pressure variation $\langle p(r,\theta) - p(r,\theta)\rangle_\theta / \langle p(r,\theta)\rangle_\theta$ at a radius r = 30 km, as a function of time after core bounce and frequency in model s11WW. For each time t, a power spectrum is calculated from a sample of time snapshots covering $t \pm 50$ ms, at a resolution of 0.5 ms. Note the emergence of power in the 330 Hz g-mode, as well as the strengthening of its harmonic at $2f$ at later times. Towards the end of the numerical evolution, higher-frequency modes become strong as well.

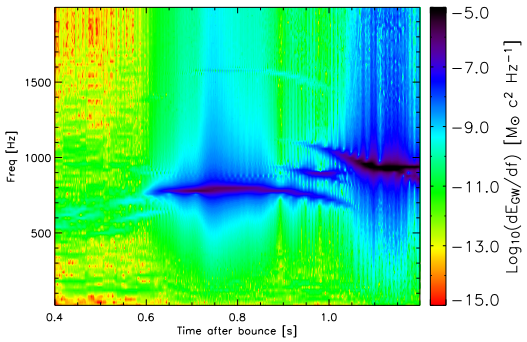

Figure 7.4: Frequency-time evolution of model s25WW's gravitational wave energy spectrum ($dE_{\rm GW}/df$, see §3.8.2) computed with a 50 ms sampling interval. Clearly visible is the prominent emission at ∼800 Hz setting in when the quadrupole component of the $2f$ harmonic of the $\ell = 1$ PNS g-mode becomes energetic at ∼600 ms after bounce. At late times the emission is dominated by an ℓ=2 eigenmode at ∼950 Hz. This figure appeared on the front cover of Physical Review Letters, Volume 96, 26 May 2006.

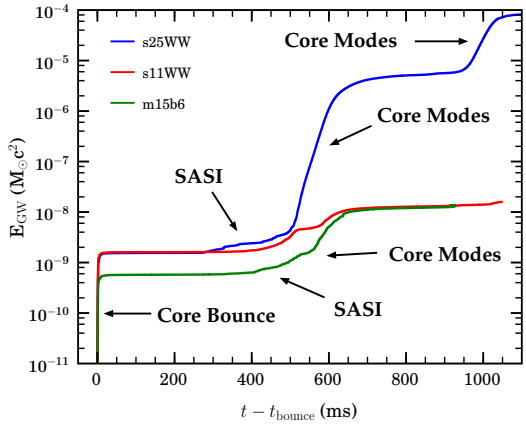

Figure 7.5: Integrated energy emitted in gravitational waves in the three considered models. The core bounce gravitational wave emission is overestimated by our models. In all models the emitted energy increases when the SASI becomes strong a few hundred milliseconds after bounce. The core oscillations lead to an order-of-magnitude and for s25WW to a many-orders-of-magnitude increase in the emitted energy.

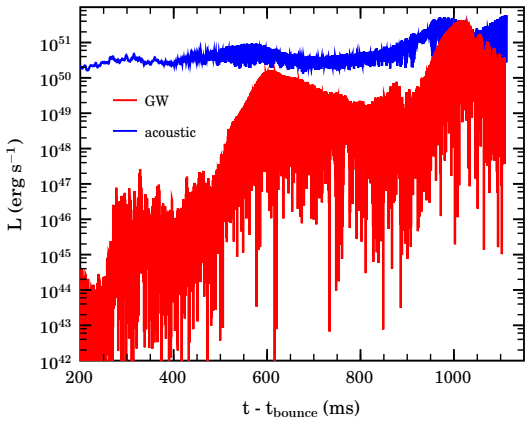

Figure 7.6: Comparison of the quadrupole gravitational wave and acoustic luminosity of the PNS core g-modes in model s25WW. The gravitational wave luminosity (L_{GW}) is given by equation (7.28), but no temporal averaging is carried out, leading to the high-frequency oscillations in L_{GW}. The acoustic luminosity (L_{GW}) is roughly estimated via equation (7.29). L_{GW} is at early and intermediate times subdominant, but becomes relevant at late times and for a short interval of time dominant due to the strong burst of gravitational waves occurring at $\sim$1 s after bounce.

damping mechanism for the core oscillations. This is done in figure 7.6, for which we estimate the acoustic power output by

$$L_{\text{acoustic}} \approx \frac{E_{\text{g-mode}}}{\tau_{\text{g-mode}}} \tag{7.29}$$

where $E_{\text{g-mode}}$ is the total g-mode kinetic energy of material with densities $\gtrsim 10^{10}$ g cm^{-3} and $\tau_{\text{g-mode}}$ is the acoustic damping e-folding time of the core pulsations which is taken to be $\sim$100 ms based on our simulation data[2]. However, due in part to the very complicated flow patterns and sonic refraction and reflection, it is difficult to determine precisely $L_{\text{accoustic}}$. We estimate a $\pm$50% ambiguity associated with our current estimate of L_{acoustic}, plotted in figure 7.6. Despite the uncertainties associated with the exact magnitude of L_{acoustic}, it is obvious from figure 7.6 that radiation reaction can play a significant role in model s25WW and should be taken into account as an additional damping agent in future calculations.

Gravitational Wave Emission from Anisotropic Neutrino Radiation

We extract the gravitational wave contribution that is due to anisotropic neutrino emission by means of the formalism discussed in §7.1.4. In reality, any angular anisotropy present in the neutrino radiation field at the point of decoupling from matter on the surface of the neutrinospheres will be preserved to infinity. Unfortunately, this is not the case in our calculations since our 2D MGFLD approach[3] has a too strong tendency to smooth out lateral gradients. At about 100 km above the neutrinospheres, angular variations are already smoothed out to a large, though not straightforwardly inferable degree. With an (energy/species) upper neutrinosphere radius of $\sim$30–50 km (see, e.g., [72, 73, 86]), we extract the total neutrino luminosity and its angular variation at an radius of 100 km[4], assuming the latter to be a lower limit for the true anisotropy of the neutrino radiation field and thus for the gravitational wave emission by neutrinos. More realistic and definite statements

[2]One can use the FWHM of the power spectrum of the core pressure fluctuations around the fundamental mode or the early growth rate of the core oscillation kinetic energy to get a handle on this quantity.

[3]Note that VULCAN/2D implements full 2D MGFLD; not MGFLD along radial rays as used in, e.g., [77].

[4]Note that the published version of this work assumed an extraction radius of 200 km. Our current understanding however favors a smaller extraction radius to avoid the too much artificially smoothed radiation field at 200 km.

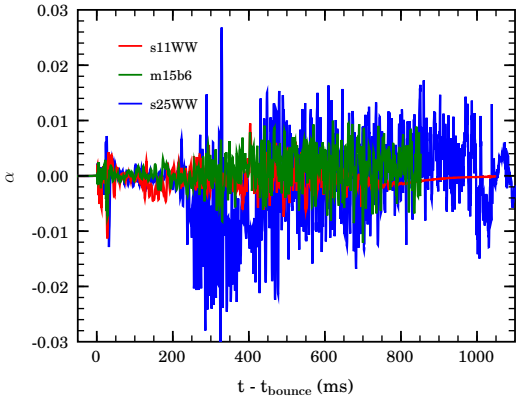

Figure 7.7: Neutrino radiation field anisotropy parameter (α) as defined by equation (7.25) for the three considered models as a function of postbounce time. α determines the magnitude of the time derivative of the neutrino gravitational wave emission. While $|\alpha|$ increases with postbounce time there is no direct one-to-one correspondence with bursts in the mass-quadrupole gravitational wave emission.

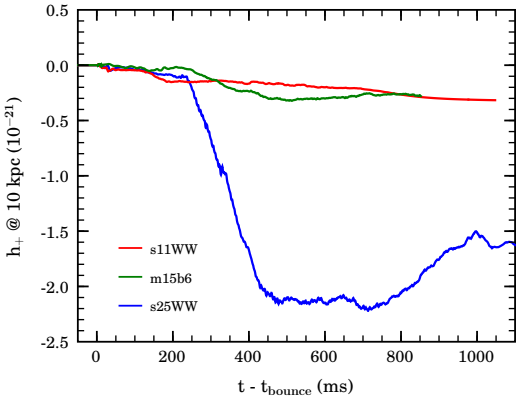

Figure 7.8: Gravitational wave dimensionless strain amplitudes originating from anisotropic neutrino emission and scaled to a distance of 10 kpc. In s11WW and m15b5 the neutrino gravitational wave strain is on the same order of magnitude as the mass-quadrupole emission, yet exhibits much smaller temporal variation and is hence much less energetic. In model s25WW the neutrino gravitational wave strain amplitudes are from factors of a few to one order of magnitude smaller than those of the mass motions.

will only be possible with full 2D multi-angle transport [477], currently too computationally expensive for long-term postbounce calculations. A new, fast and more accurate scheme than MGFLD, currently under development [616], may lead to improved results in the intermediate term.

In figure 7.7 we display the neutrino anisotropy parameter α as defined by equation (7.25), extracted at an observer radius of 100 km. The parameter α, in combination with the total neutrino luminosity L_ν, sets the magnitude and the temporal variation of the gravitational wave emission by neutrinos (equation (7.24)). While α is a somewhat normalized quantity it is observer-position dependent and not necessarily a good measure for the magnitude of the anisotropic part of L_ν in the source coordinate system, i.e. on the computational grid. As apparent from figure 7.7, there is some neutrino radiation anisotropy associated with core bounce. This bounce feature is related to the neutrino break-out burst and results from the vortical mass motions in the neutrino-matter decoupling region that are present and likely too rapidly growing because of the grid transition in our VULCAN/2D calculation at $\sim$30 km. As can be inferred from the matter gravitational waveforms (figure 7.2), the asphericities smooth out quickly in the early postbounce phase, and correspondingly the magnitude of α becomes small again until the physical PNS convection (see, e.g., [72, 73]) becomes strong, resulting in an overall increase of $|\alpha|$ in all models. Since α quite subtly depends on fluid asphericities in the neutrino energy and species dependent decoupling region, it varies with time and progenitor in a way that is not straightforwardly related to short-term global fluid features. The PNS core oscillations that become strong several hundred milliseconds after core bounce certainly do not leave any strong qualitative or quantitative imprint on α. We surmise that interaction with overlying relatively dense outer core material before decoupling smoothes the angular neutrino distribution sufficiently to wash out the core oscillation imprint on the neutrino radiation field.

Figure 7.8 depicts the gravitational wave strains at 10 kpc distance related to anisotropic neutrino emission in the three considered models. As expected from Model s25WW's large α magnitudes this model calculation yields the largest neutrino-caused gravitational wave strain. The large negative contribution/offset is due to the burst in anisotropy between $\sim$200–400 ms after core bounce during which α stays almost exclusively negative in this model. After that, α varies around zero and becomes only at late times predominantly positive, leading to the observed decrease in magnitude of s25WW's h_+. s25WW dominates over the other two models because of its more massive PNS, significantly higher late-time accretion rates and associated smaller shock radii, and more vigorous turbulent convective overturn in the neutrino-matter decoupling region. A comparison with the matter gravitational wave emission presented in figure 7.2 shows that in s11WW and m15b6 the neutrino

Table 7.1: Model summary

Model	Δt^a	$\lvert h_{+,\max}\rvert^b$	$h^{b,c}_{\mathrm{char,max}}$	f($(h_{\mathrm{char,max}})$	E^d_{GW}
	(ms)	(10^{-21})	(10^{-21})	(Hz)	(10^{-7} $M_\odot$ c^2)
s11WW	1045	1.3	22.8	654	0.16
s25WW	1110	50.0	2514.3	937	824.28
m15b6	927.2	1.2	19.3	660	0.14

[a] time between bounce and the end of the simulation
[b] at 10 kpc [c] see §3.8.3 [d] see §3.8.2

induced gravitational wave strain is almost of the same order of magnitude as the baryonic matter contribution. In s25WW the peak neutrino gravitational wave strain is an order of magnitude lower than the maximum amplitude of the baryonic matter component. It is important to keep in mind that despite the comparability in the maximum wave strains, the total emitted gravitational wave energies are very different between baryonic matter and neutrino components. *The low-frequency, almost 'DC' character (due to the described memory effect) of the neutrino-caused gravitational wave emission leads to lower emitted energies by many orders of magnitude*. We find total integrated neutrino gravitational wave energies of 1.76×10^{-12} $M_\odot$ c^2, 3.51×10^{-14} $M_\odot$ c^2, and 7.62×10^{-14} $M_\odot$ c^2 for models s25WW, s11WW, and m15b6, respectively. By comparing these numbers to the total energy emission by quadrupole fluid motions summarized in Table 7.1, one realizes that the neutrino-caused gravitational wave emission is energy-wise completely negligible when compared with the gravitational wave emission from quadrupole fluid motions.

In comparison with the recent work of Müller et al. [95], the neutrino-induced gravitational wave strains in our models fall into the same orders of magnitude[5]. Note, however, that our results *as well as those obtained by Müller et al.* are tentative. While our flux-limited diffusion approach tends to smooth out anisotropies, the ray-by-ray approach of the Müller et al. work tends to emphasize them.

The gravitational wave energy spectra (dE_{GW}/df) of the neutrino gravitational wave emissions peak at low frequencies between 1 and 10 Hz, hence in the worst possible window between the LIGOs' low-frequency limit and the upper frequency limit of LISA. However, cosmological (red-shifted) supernova neutrino gravitational wave signals might be detectable by LISA and/or by second generation space-based gravitational wave antennas [617].

7.2.3 Summary and Discussion

We have analyzed the gravitational wave emissions in long-term Newtonian 2D radiation-hydrodynamics supernova calculations for three different progenitors, one of which includes angular momentum consistent with the inferred rotation period of young pulsars. We find that the gravitational wave emissions of all models are dominated by the quadrupolar components of the core g-mode oscillations first discovered by Burrows et al. [26, 27]. If the core oscillations seen in our simulations do obtain, their gravitational wave emission will exceed the emission from all previously considered emission processes, including rotational core bounce, convection, and anisotropic neutrino emission. Importantly, *we point out that the excitation of the core g-modes does not depend on the particular explosion mechanism proposed by Burrows et al. [26, 27], but is likely to be a generic phenomenon induced by turbulence and accretion downstreams in any suitably delayed explosion mechanism*.

The recent study of Müller et al. [95] suggests a total energy emission of 3×10^{-9} $M_\odot c^2$ for a rotating model (initially about 3 times as fast as our m15b6). For our nonrotating, low-mass model s11WW we find about 5 times as much energy emission: 1.6×10^{-8} $M_\odot c^2$. For the slowly rotating, but otherwise very similar model m15b6, we calculate a total gravitational wave energy emitted in gravitational waves of 1.4×10^{-8} $M_\odot c^2$ (Fig. 7.5 and Table 7.1). For the initial rotation rate and angular momentum distribution present in the m15b6 progenitor, we do not find significant qualitative or quantitative differences caused by such slow rotation. Model s25WW, due to its more massive iron core, higher postbounce accretion rates, and higher pulsation frequencies and amplitudes, emits an amazing 8.2×10^{-5} $M_\odot c^2$, almost one tenth of a typical supernova explosion energy. We estimate that

[5]Note that in the published version of this work our estimates were about a factor of 5 smaller. This is due to the too large extraction radius assumed in the published version.

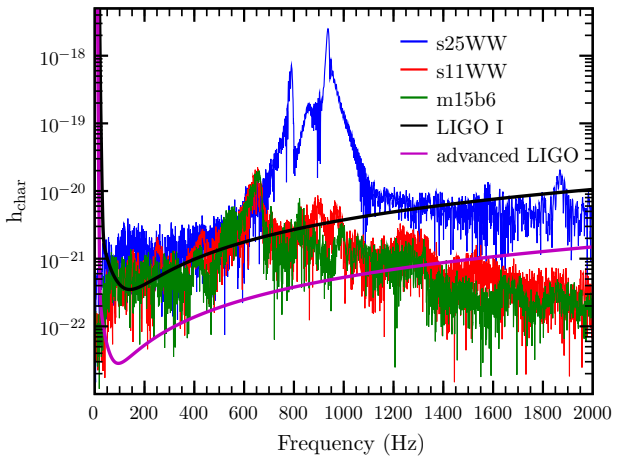

Figure 7.9: Characteristic strain spectra at 10 kpc contrasted with initial and advanced LIGO (optimal) rms noise curves.

gravitational radiation reaction effects are likely to provide additional damping in this model and ought to be included in future work.

We have studied the gravitational wave emission from anisotropic neutrino radiation fields and found maximum wave strains in rough order-of-magnitude agreement with Müller et al. [95], but conclude that improved methods [616], and perhaps full angular-dependent neutrino radiation transport [477] will be needed for reliable estimates. The time-integral nature of the neutrino gravitational wave strain will, however, always lead to emission at low frequency (∼1–10 Hz) and correspondingly low total emitted energies.

In Fig. 7.9, we show the characteristic gravitational wave strain spectra ($h_{\rm char}$) of the three models, if located at 10 kpc. $h_{\rm char}$ is defined by [514] (and discussed in §3.8.3) as

$$h_{\rm char}(f) = \frac{1}{D}\sqrt{\frac{2}{\pi^2}\frac{G}{c^3}\frac{dE_{\rm GW}(f)}{df}}\,, \tag{7.30}$$

where D is the distance to the source. This is a particularly useful measure, since it incorporates the amount of energy radiated in a spectral interval df around f. In addition, we show the optimal rms noise strain ($h_{\rm rms} = \sqrt{fS(f)}$, $S(f)$ being the spectral strain sensitivity) of both LIGO I and advanced LIGO [515]. All $h_{\rm char}$ spectra peak strongly at the frequencies identified with the quadrupole components of the core oscillations (Fig. 7.4, between 600 and 1000 Hz, likely to be higher when general relativity is included), corroborating the narrow-band nature of the emission process. Given our results, we conclude that, if the core oscillations observed in our simulations are generically excited in core-collapse supernovae, even nonrotating supernovae of small to intermediate progenitor mass should be observable by LIGO throughout the Milky Way and beyond. Massive progenitors could be detectable out to ∼100 times greater distances and their prolonged and extremely energetic core-oscillation wave signature might be the generic precursor of stellar-mass black-hole formation.

We point out that the work presented here is based on simulations in 2D Newtonian gravity and only quadrupole wave emission has been considered. General relativity is likely to increase the frequency of the PNS eigenmodes, but is unlikely to lead to qualitative differences. Fast rotation might lead to the partial stabilization of the postshock convection, may affect the growth of core oscillations, and will likely lead to nonaxisymmetric rotational instabilities for $\beta \gtrsim 8\%$ ([22] and §6.4). In 3D, the temporal and spatial mode and SASI structures may change.

7.3 Gravitational Waves from Rotating Accretion-Induced Collapse of White Dwarfs to Neutron Stars

The results presented in this section have been summarized and published as part of Dessart, Burrows, Ott, Livne, Yoon, and Langer, *Multidimensional Simulations of the Accretion-Induced Collapse of White Dwarfs to Neutron Stars*, Astrophysical Journal, 644, 1063 (2006) [16]. The focus of the work presented here is the analysis of the gravitational wave emission in the models considered in the former study.

Electron-degenerate C/O and O/Ne/Mg white dwarfs mark the end stage of low-mass ($\lesssim 8 M_\odot$) stellar evolution. If located in a close binary system, a white dwarf may accrete matter and angular momentum from its companion star, and, in the usual picture, eventually experience explosive nuclear burning, leading to total disruption and a Type Ia supernova [1, 432, 505]. Theoretically, white dwarfs with O/Ne/Mg cores, due to their high central density ($\gtrsim 10^{10}$ g cm^{-3}), may experience rapid electron capture. This leads to core collapse, rather than to thermonuclear explosion, when the white dwarf is pushed over its effective Chandrasekhar mass[6] by accretion. This is accretion-induced collapse (AIC) [618]. It is currently unclear what fraction of all white dwarfs lead to AICs, but of those white dwarfs that evolve to form a Chandrasekhar-mass O/Ne/Mg core, all will necessarily undergo collapse [16]. Binary star population synthesis studies predict the occurrence of AICs with a galactic rate of 8×10^{-7} yr^{-1} to 8×10^{-5} yr^{-1}, depending, among other things, on the treatment of the common-envelope phase and the mass transfer history in the binary system [619]. This is equivalent to 1 AIC per $\sim$50–100 standard Type Ia events [16].

Previously, only one study had addressed the gravitational wave emission in AICs: Fryer, Holz, and Hughes (FHH) [270] analyzed the single rotating AIC model of [42], who performed 2D axisymmetric smooth particle hydrodynamics / gray flux-limited diffusion calculations of AIC. The model's initial configuration was rigid rotation with a total angular momentum of 10^{49} erg s and an initial surface period of $\sim$10 s, which is in the ball park of the shortest observed periods of cataclysmic accreting white dwarf variables [620]. The model was forced into rotation and had no precollapse rotational equilibrium configuration. FHH give a maximum mass-quadrupole wave strain (they neglect the neutrinos) from rotating core bounce of 5.9×10^{-20} at 10 kpc. Note that this value given by FHH is exceptionally large, almost one order of magnitude larger than, for example, obtained in any rotating model considered in Chapters 5 and 6 of this dissertation. Despite the fact that the Fryer et al. model exhibited a postbounce $\beta = T/|W|$ of only $\sim$0.06 and was mildly differentially rotating, its PNS showed quasi-toroidal structure with a density maximum located at $\sim$15 km despite only moderate differential rotation and a spin period of $\sim$1 s. Given the rotation rates / degrees of differential rotation required for quasi-toroidal structure as derived by other studies (e.g., [9, 12, 30, 308, 309] and references therein), these numbers are difficult to understand.

In this work we present gravitational wave estimates for AIC, based on results from the first 2D multi-group flux-limited diffusion (MGFLD) Newtonian radiation-hydrodynamic calculations of rotating AIC with initial white dwarf models in rotational equilibrium [16]. We compute and analyze the gravitational wave emissions from quadrupole mass motions and, for the first time in the AIC context, of anisotropic neutrino emission. In our more self-consistent calculations, we find by one to two orders of magnitude smaller maximum gravitational wave strains. We also find that the neutrino component dominates over matter emission in amplitude, but owing to its low-frequency nature, not in the integrated energy emission.

7.3.1 Method and Initial Models

The numerical calculations on which this work is based are performed with the 2D Newtonian radiation-hydrodynamics code VULCAN/2D in MGFLD mode with 16 neutrino energy groups and ν_e, $\bar{\nu}_e$, and "ν_μ" flavors. The code features and the gravitational wave extraction methods are delineated in §7.1. Note that in this work, the multipole gravity solver is employed.

We draw our AIC progenitor white dwarf data from the study of Yoon & Langer (YL) [61]. YL computed Newtonian 2D rotational equilibrium barotropes ($p = p(\rho)$; usually a good approximation

[6] Depending on structure, composition, and rotational support [36].

Table 7.2: Properties of selected AIC progenitors. M is the baryonic mass, R_p and R_e are the polar and equatorial radii, respectively. J is the total angular momentum and $\beta = T/|W|$ is the ratio of rotational kinetic to gravitational energy.

M	$R_{\rm p}$	$R_{\rm eq}$	J	$\beta = T/\|W\|$	
($M_\odot$)	(km)	(km)	(10^{49} erg s)	Initial	Final
1.46	800	1130	1.60	0.0076	0.059
1.92	660	2350	5.45	0.0833	0.262

for degeneracy-pressure dominated objects) in rotational equilibrium for prescribed angular velocity distributions $\Omega(\varpi)$ via the self-consistent-field method [550, 621] (see also §3.7.2 for a general relativistic variant). For this work, we select models computed with the methods described in YL with masses of 1.46 and 1.92 $M_\odot$. Both models have a relatively high initial central density ρ_c equal to 5×10^{10} g cm^{-3}. Note that at such high densities electron capture sets in quite strongly at the very beginning of the calculation. It is very likely that collapse in a real O/Ne/Mg white dwarf starts already at lower ρ_c [618]. We nevertheless adopt the high ρ_c to ensure fast collapse and to avoid EOS problems encountered with models of lower initial ρ_c.

A shortcoming of the present white dwarf progenitor models is their unknown initial thermal structure that cannot be derived by the methods of YL. Given the additional EOS difficulty in handling low temperatures ($T \lesssim 0.5 \times 10^{10}$ K) at high densities ($\rho \gtrsim 10^{10}$ g cm^{-3}), we resort to parametrizing the temperature as a function of the local density, that is,

$$T(\varpi, z) = T_c \big(\rho_c/\rho(\varpi, z)\big)^{0.35} , \tag{7.31}$$

with $T_c = 10^{10}$ K in the 1.46-$M_\odot$ model and $T_c = 1.3\times10^{10}$ K in the 1.92-$M_\odot$ model. Note that, similarly, Woosley & Baron [622] adopted a T parametrization with $T_c = 1.2\times10^{10}$ K in their 1D AIC calculations. We point out that, since electron degeneracy pressure is the dominant pressure component, the precollapse temperature distribution is of minor importance to the hydrodynamics. The initial Y_e is set to 0.50 throughout the white dwarf.

The 1.46-$M_\odot$ model is evolved on the full hemisphere (180°), a Cartesian–spherical-polar transition at 20 km and a maximum grid radius of 5000 km. The maximum resolution in the Cartesian inner region is 0.56 km, while the minimum resolution is 150 km close to the outer boundary. 121 regularly spaced zones are used to cover 180°. Since we find that this model maintains almost perfect top–bottom symmetry during its entire evolution, we evolve the 1.92-$M_\odot$ model on a 90° wedge, but increase the maximum resolution to 0.48 km and the minimum resolution at the outer boundary of 4000 km to 100 km. 71 regularly spaced angular zones are used to cover 90°.

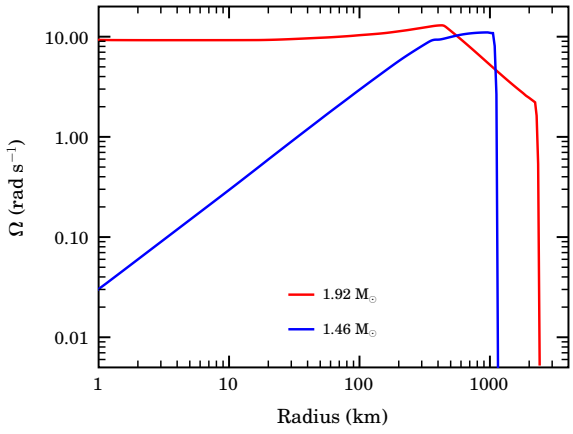

Figure 7.10: Equatorial angular velocity profiles of the 1.46-$M_\odot$ (blue) and the 1.92-$M_\odot$ (red) models at 5 ms into the calculations. While exhibiting similar surface angular velocities, the 1.92-$M_\odot$ model is in approximate solid-body rotation and, because of this and its greater mass, carries more than three times greater total angular momentum than the 1.46-$M_\odot$ model (Table 7.2). See [16, 61] and text for details on the employed rotation law.

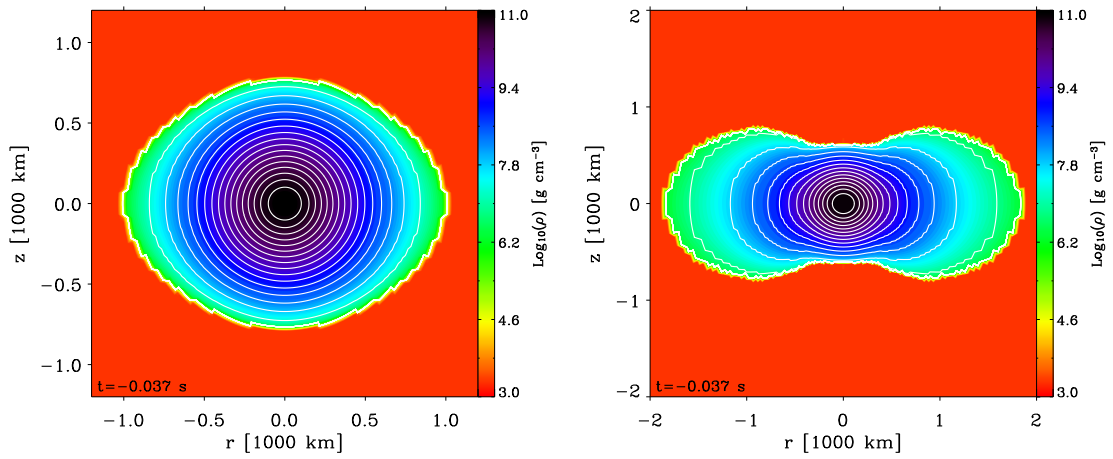

Figure 7.11: Initial density $\rho(\varpi, z)$ for the 1.46-$M_\odot$ model (left) and the 1.92-$M_\odot$ model (right). We overplot the equipotentials corresponding to the equilibrium configurations whereby the density $\rho(\varpi, z)$ is solely a function of the effective potential $\Psi(\varpi, z)$ given as the sum of the gravitational potential, i.e., $\Phi(\varpi, z) = -G \int \rho(\varpi, z)/|\vec{R} - \vec{R}'|d^3R'$, and the centrifugal potential, i.e., $\Theta(\varpi) = -\int \Omega^2(\varpi')\varpi' d\varpi'$ [16, 61]. A low-density 1000 g cm^{-3} atmosphere surrounds the white dwarf. This figure corresponds to figure 1 of [16] and was prepared by L. Dessart.

We follow the postbounce evolutions of the 1.46-$M_\odot$ and 1.92-$M_\odot$ models for 550 ms and 780 ms, respectively. Table 7.2 summarizes important model parameters.

Figure 7.10 depicts the initial angular velocity profiles of the two progenitor models. Rotation is constant on cylindrical shells, hence $\Omega = \Omega(\varpi)$ only. The rotation laws employed by YL are so-called *accreting white dwarf rotation* laws, that typically exhibit positive Ω gradients throughout most of the white dwarf. They were derived and discussed by YL [61, 580]. The models employed here differ only in initial central angular velocity Ω_c and use otherwise identical rotation law parameters[7]. The 1.48 $M_\odot$ model's angular velocity increases rapidly with cylindrical radius from 0 rad s^{-1} at its center to a peak at the model's surface of a value of $\sim$11 rad s^{-1}, corresponding to a period $P \sim 0.57$ s. The 1.92-$M_\odot$ model is much less differentially rotating. It has an initial central angular velocity of $\sim$17.62 rad s^{-1} and its angular velocity peaks at a radius of $\sim$425 km at a value of $\sim$13 rad s^{-1} (P $\sim$0.5 s) and drops to $\sim$2.2 rad s^{-1} (P $\sim$2.9 s) at the surface. The 1.92-$M_\odot$ model has a total angular momentum of $\sim 5.5\times10^{49}$ erg s and an initial $\beta = T/|W|$ of 0.0833, while the 1.46-$M_\odot$ model carries 1.6×10^{49} erg s and has an initial $\beta = T/|W|$ of 0.0076. The 1.46-$M_\odot$ model hence serves as a reference for a precollapse white dwarf with moderate initial rotational energy[8]. As figure 7.11 depicts, the 1.46-$M_\odot$ model has spheroidal structure with an axis ratio of $\sim$0.7. The 1.92-$M_\odot$ model, on the other hand, has a very large precollapse angular momentum / rotational energy, allowing for its by $\sim$0.5 $M_\odot$ greater mass and leading to an almost toroidal, but still centrally condensed precollapse structure.

7.3.2 Results

In this section, we focus on those aspects of the Dessart et al. [16] calculations that are relevant for the gravitational wave signature of AIC events. For a more detailed discussion of the radiation-hydrodynamics and the explosion physics, the reader is referred to the original article [16].

[7] In the notation of YL these parameters are: $f_K = 0.95$, $f_{sh} = 1.0$, a=1.2. f_K is the ratio of surface velocity to Keplerian velocity. f_{sh} is a shear parameter, and a is constant governing the rotation in the outer white dwarf layers. Note that the rotation law is not in closed analytic form. See YL for details.

[8] Note that what is *moderate* in the white dwarf context is *high* in the massive star / iron core context. See §6.1.

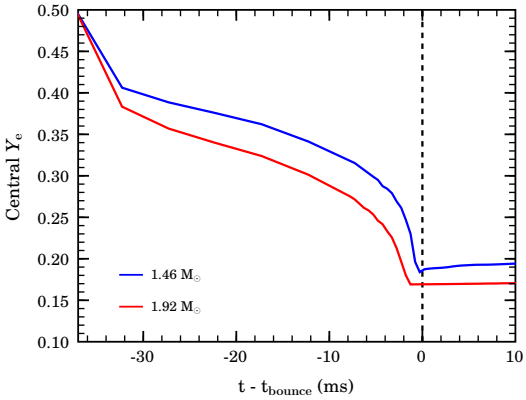

Figure 7.12: Collapse evolution of the electron fraction Y_e at the stellar centers of both considered models. The calculations start with $Y_e = 0.5$ throughout the white dwarf. Note that the data output interval is 5 ms until ∼3 ms prior to bounce, leading to the "roughness" in $Y_e(t)$. Note that the Y_es reached at core bounce are 30–40% lower than what is expected for standard iron core collapse.

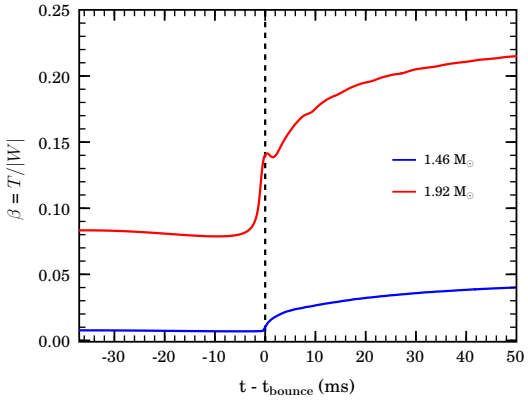

Figure 7.13: Evolution of the rotation parameter $\beta = T/|W|$ for the 1.46-$M_\odot$ (blue) and the 1.92-$M_\odot$ (red) models from the onset of collapse to 50 ms after core bounce. Note that, owing to its initial rotational set up (figure 7.10), the 1.46-$M_\odot$ model's β does not increase significantly during collapse and reaches a value of only ∼0.01 at core bounce.

Gravitational Wave Emission from Rotating Collapse and Core Bounce

Both models start out with a central density of 5×10^{10} g cm^{-3} and, due to their rotational equilibrium configuration, 0.74 $M_\odot$ in the 1.46-$M_\odot$ model and 0.68 $M_\odot$ in the 1.92-$M_\odot$ model have densities above 10^{10} g cm^{-3} already at the onset of collapse. Owing to their high initial central densities, electron capture sets in strongly as soon as the calculations are started. Figure 7.12 depicts the evolution of the electron fraction Y_e at the stellar centers of both models. In both models Y_e plummets from 0.5 to ∼0.4 within the first 5 ms of the calculations. Invoking a simplified picture with a polytropic EOS for a relativistically degenerate Fermi gas of electrons, the pressure p equals

$$p = 1.2435 \times 10^{15} \frac{\mathrm{cm}^2}{\mathrm{s}^2} (Y_e)^{4/3} \rho^{4/3} \; . \tag{7.32}$$

This Y_e reduction corresponds to a central pressure reduction of ∼25%. This large initial pressure drop leads to a fast onset of dynamical collapse with continued strong deleptonization. The 1.92-$M_\odot$ deleptonizes somewhat more quickly and to lower central Y_e than the 1.46-$M_\odot$ model. This is most likely due to the different initial thermodynamic conditions and angular/radial density stratifications. At core bounce, Y_es of ∼0.19 and ∼0.17 are reached in the 1.46-$M_\odot$ and 1.92-$M_\odot$ model, respectively. These values are remarkably low. A standard iron core collapse of massive stars typically ends with $Y_e \approx 0.25$–0.30 (depending on the electron capture prescription; see, e.g., [64]). As pointed out by [3, 64–66, 68, 69] (and references therein) and in §6.2–6.3 of this dissertation, the mass of the inner core (M_{ic}) at core bounce exclusively determines the core dynamics during that phase. M_{ic} sets the mass of the outer infalling material that remains to be dissociated by the bounce shock, it determines the initial kinetic energy imparted to the shock, and sets the amount of angular momentum that may become dynamically relevant during bounce. M_{ic} decreases with decreasing Y_e and increases with increasing rotational support of the inner core (increasing β; see §5.1). In the following, we determine M_{ic} via

$$M_{\mathrm{ic}} = \int_{|v_r|<c_s;\, v_r<0;\, r<100\ \mathrm{km}} \rho dx^3 \; , \tag{7.33}$$

where v_r is the local radial velocity, c_s is the local speed of sound, and r is the radius $r = \sqrt{\varpi^2 + z^2}$.

Figure 7.13 depicts the evolution of the rotation parameter $\beta = T/|W|$ from the beginning of the calculations to 50 ms postbounce as a function of postbounce time. The 1.46-$M_\odot$ model reaches core bounce after only 37 ms, and, owing to its initial angular momentum distribution (figure 7.10), spins up from its precollapse value β ∼0.0076 to only β ∼0.01 (and an asymptotic value — due to accretion of higher angular momentum material — of ∼0.06 at the end of the calculation). Hence, rotational

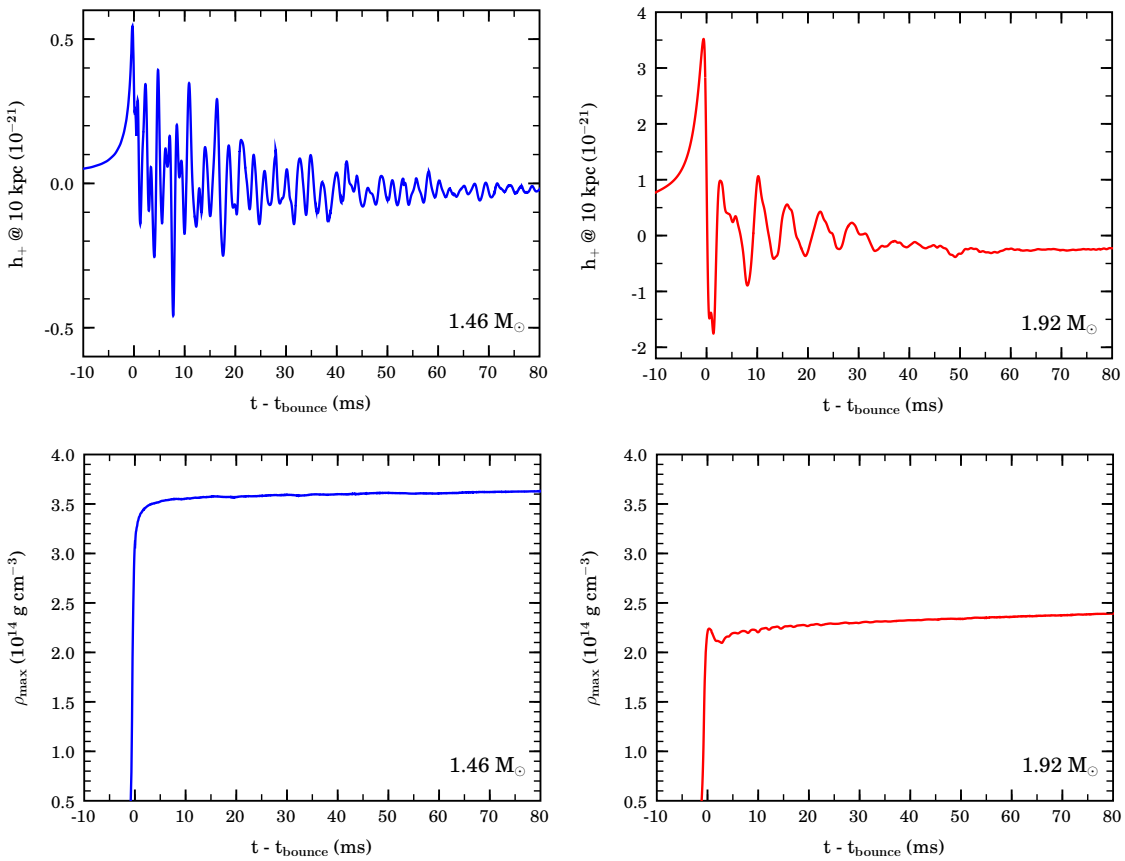

Figure 7.14: Top: Gravitational wave strain h_+ at an observer distance of 10 kpc for the 1.46-$M_\odot$ model (left) and the 1.92-$M_\odot$ model (right). Note the different ordinate scales. Bottom: Evolution of the density maximum ρ_{max} as a function of postbounce time. Note that even in the quickly spinning 1.92-$M_\odot$ model the influence of rotation on the dynamics is small, merely leading to a reduction in ρ_{max}, but not to harmonic-oscillator like postbounce re-expansion–collapse–bounce cycles. However, note that the postbounce variations in the 1.92-$M_\odot$ model waveform are more quickly damped and of lower frequency than those visible in the 1.46-$M_\odot$ model waveform.

support of the inner core is weak in this model, and the very low Y_e leads to a very small inner core mass at bounce of only $\lesssim 0.35\,M_\odot$ with little rotational flatting in this model. For standard massive-star iron core collapse, an M_{ic} between $\sim$0.5–0.7 $M_\odot$ is expected (see, e.g., [64]). As portrayed by the evolution of this model's maximum density ρ_{max}, shown in the lower left panel of figure 7.14, the rebound is very weak. It does not lead to a notable re-expansion of the inner core at core bounce. The upper left panel of figure 7.14 displays the gravitational wave strain as emitted by quadrupolar mass motions in the 1.46-$M_\odot$ model and at an assumed observer location of 10 kpc. The maximum strain amplitude of 5.5×10^{-22} (at 10 kpc) is reached in the positive (slightly prebounce) spike. After bounce, the waveform exhibits high frequency (f $\sim$400–500 Hz), exponentially-damped oscillations with an e-folding time of $\sim$30 ms. The PNS of the 1.46-$M_\odot$ model shows only very weak convective motions [16]. This is confirmed by the waveform which lacks any features/late-time variations that could be associated with aspherical convective overturn.

The described waveform morphology is reminiscent of type-III waveforms that were observed in previous adiabatic studies employing ideal-fluid/hybrid EOSs for low adiabatic Γs around 1.28 [12, 13, 30] (see also §5.1.3). In particular, type-III morphology has been associated with *small* inner core mass and little inner core angular momentum / rotational support, both of which is the case for the 1.46-$M_\odot$ model in this study. Although type-III morphology has been deemed unlikely to obtain in standard rotating iron core collapse [9, 14], it may — as our 1.46-$M_\odot$ model demonstrates — be possible in the AIC context.

As in the 1.46-$M_\odot$ model, the greater angular momentum 1.92-$M_\odot$ white dwarf undergoes fast collapse and reaches core bounce at approximately the same time ($\sim$37 ms) as the 1.46-$M_\odot$ model. Due to the strong and fast deleptonization, rotational support becomes relevant only from the plunge phase of collapse on[9]. The 1.92-$M_\odot$ model is initially in solid-body rotation and, not unlike the 1.46-$M_\odot$ model, most of its rotational energy is initially located at large radii. Hence, as figure 7.13 depicts, the global integral β in this model does not increase until the plunge phase of collapse, when the inner core contracts and spins up very rapidly. Despite its low inner core Y_e at core bounce (see figure 7.12), and due to the significant rotational support at core bounce, the 1.92-$M_\odot$ model has a "regular" inner core mass of $\sim$0.56 $M_\odot$. At core bounce, the 1.92-$M_\odot$ model has reached a β of $\sim$0.14, which steadily increases due to accretion of high angular momentum material to an asymptotic value of $\sim$0.26 at the end of the calculation. These values of β are large enough for the growth of secular and, perhaps, even dynamical rotational nonaxisymmetric instabilities (see, e.g., [19, 21–23, 286, 309, 504] and §6.4). In addition, we find an off-center (by $\sim$1 km) maximum of the density distribution in the 1.92-$M_\odot$ model. This indicates a quasi-toroidal shape of the central regions of this model's PNS and may have relevance in the context of rotational instabilities [23, 309]. The study of the development of nonaxisymmetric structure shall be postponed to future 3D calculations.

The right panels of figure 7.14 show the mass-quadrupole gravitational waveform (top) and the $\rho_{\max}$ evolution (bottom) of the 1.92-$M_\odot$ model from 10 ms prebounce to 80 ms after bounce. In comparison with the 1.46-$M_\odot$ model, the 1.92-$M_\odot$ model reaches a maximum density that is $\sim$60% lower at core bounce. However, owing to its inner core's greater rotational support, its rebound is more pronounced, leading to a significant relaxation (drop in $\rho_{\max}$) in the first postbounce millisecond. The gravitational wave signal is dominated by the large positive spike slightly before bounce with a peak strain of 3.6×10^{-21} (at 10 kpc). This is more than six times greater than the peak strain of the 1.46-$M_\odot$ model. The positive prebounce waveform feature is followed in magnitude by the negative bounce spike that usually dominates the waveform of rotating massive star iron core collapse. The postbounce waveform consists of damped oscillations with frequencies f $\sim$100–200 Hz. While the fluid motions responsible for the postbounce emission are certainly affected by rotation (low frequencies; compare to the 1.46-$M_\odot$ model above), there is no coherent volume-mode type pulsation present that would correlate $\rho_{\max}$ and waveform variations. Note that — as in the 1.46-$M_\odot$ model — we do not observe any significant convective overturn in the 1.92-$M_\odot$ model and hence no convective features in its gravitational waveform.

Considering the waveform morphologies presented in §5.1, we categorize the 1.92-$M_\odot$ waveform as type-III/II transitional, since it exhibits similar morphology to that of the 1.46-$M_\odot$ model while having a more massive inner core, containing more angular momentum and experiencing significant rotational support, leading to a mixture of type-III and type-II (rotationally dominated bounce) behavior.

Gravitational Wave Emission from Anisotropic Neutrino Radiation

As pointed out in §7.1.4 and §7.2.2 not only accelerated aspherical fluid motion, but also anisotropies in the neutrino radiation fields may lead to the emission of gravitational waves at sizable amplitudes. The analysis of the neutrino-induced gravitational wave emission of the nonrotating models of Ott et al. [15] (§7.2.2) has shown that already small anisotropies in the neutrino radiation can lead to the emission of large-amplitude gravitational waves and at low frequencies and leaving behind a static "offset" of spacetime, owing to their intrinsic gravitational wave *memory*.

In figure 7.15 we show for both models at early times (top row) and at the last simulated time (bottom row) color maps of the total neutrino flux in the radial direction, with isodensity contours overplotted as white curves, and velocity vectors as black arrows. Due to the hydrodynamical history of rotating collapse, the PNS is relatively devoid of overlying material in the polar direction, while in the 1.92-$M_\odot$ model a massive ($\sim$0.6 $M_\odot$) and dense (10^6–10^{10} g cm^{-3}) near-Keplerian disk is located at latitudes $\lesssim$40°. Given this configuration, the dynamical effect of a spherically-symmetric neutrino radiation field would be enhanced along the low-density polar direction. This is indeed reflected by the appearance of a strong neutrino-driven wind in the polar direction that does not exist (in both models) in directions within $\sim$ $\pm$40° [16]. In addition, and as figure 7.15 depicts, the radial

[9] A more detailed discussion on the influence of deleptonization in rotating core collapse is presented in §6.3.

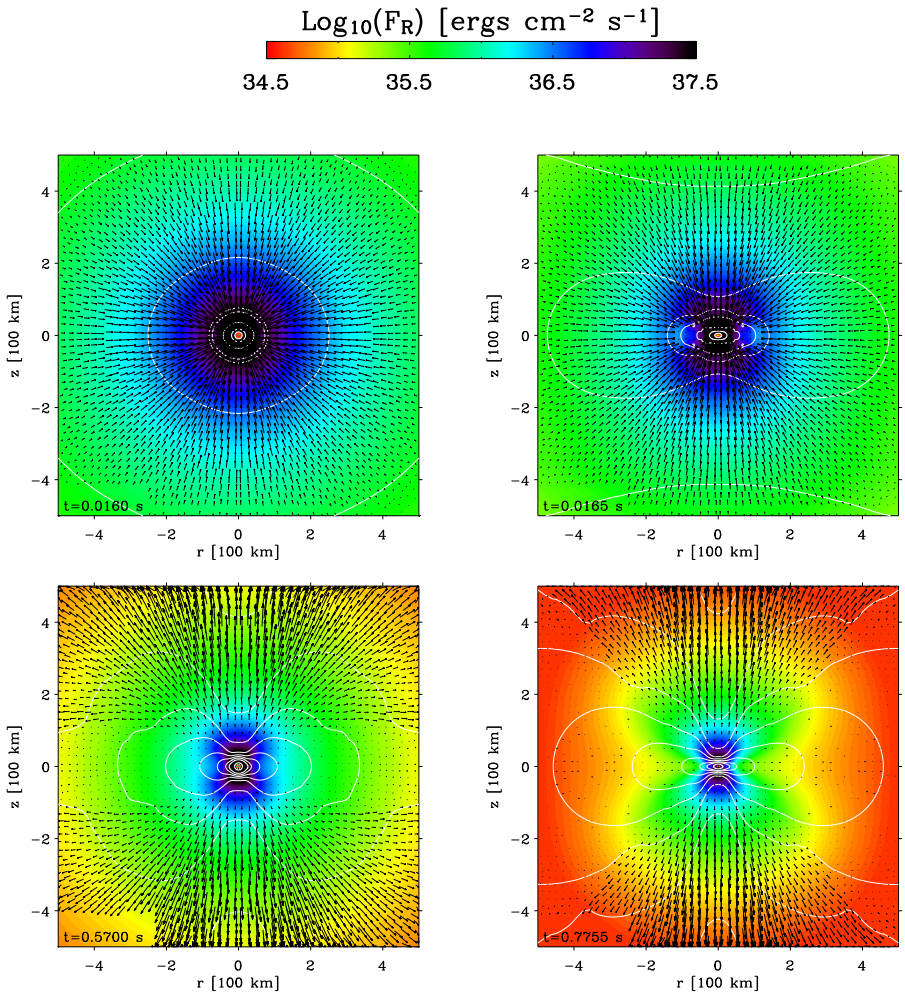

Figure 7.15: Total energy/species-integrated radial neutrino flux soon after bounce (top row) and at the last simulated time (bottom row) for the 1.46-$M_\odot$ model (left column) and the 1.92-$M_\odot$ model (right column). Velocity vectors and isodensity contours (for every decade starting from 10^{14} g cm^{-3}). Note the growing flux anisotropy with time in both models. Also note the oblate-prolate correspondence of matter and neutrino flux anisotropy. At and shortly after core bounce, the neutrino radiation field of the 1.46-$M_\odot$ model is still almost spherically symmetric, while at the end of the simulation its anisotropy is large — almost as large as that of the 1.92-$M_\odot$ model whose PNS is already very quickly spinning and, hence, oblate at and shortly after core bounce. Regions of high flux generally coincide primarily with regions of low density (and correspondingly small neutrinosphere radii [16] and high temperature). This figure has been prepared by L. Dessart and is figure 16 of [16].

neutrino flux from the PNS in both models itself is anisotropic and grows more anisotropic with time. This is due to the rotational flattening of the PNS that leads to a pronounced oblate flattening of the neutrinospheres[10] with polar to equatorial neutrinosphere radii ratios of down to 1/10 [16]. While the angle-dependent neutrino decoupling radius does mitigate the asphericity [87] slightly, the latitudinal variation of the neutrino flux is still very large.

Note that the neutrino radiation field in the 1.46-$M_\odot$ model at 16 ms after core bounce (figure 7.15) is still quite isotropic, while that of the 1.92-$M_\odot$ model already exhibits strong anisotropy with much larger fluxes in the polar regions than near the equator. This difference is readily explained by the different initial rotational configurations of the two models displayed in figures 7.10 and 7.11. The central region of the 1.46-$M_\odot$ model is only very slowly rotating, hence only prolonged accretion of outer white dwarf material with high specific angular momentum leads to the oblate deformation of this model's PNS and the prolate shape of the neutrino radiation field at late times. This is portrayed

[10]The neutrinosphere position is defined by the point at which the optical depth in the radial direction for neutrinos is 2/3.

by the lower left panel of figure 7.15. The 1.92-$M_\odot$ model's PNS, on the other hand, is already spinning very rapidly at and after core bounce, leading to the strongly prolate shape of its neutrino radiation field.

Figure 7.16 depicts the time evolution of the instantaneous neutrino radiation anisotropy parameter α that is defined by equation (7.25). In the 1.46-$M_\odot$ model, we extract α outside the neutrinospheres at an observer radius of 200 km while we choose an observer radius of 300 km in the 1.92-$M_\odot$ model since the neutrinospheres extend out to significantly larger equatorial radii in this model [16]. As pointed out earlier (§7.2.2), our MGFLD approach tends to smooth out anisotropies in the neutrino emission. Hence, the values of α and the amplitudes of the neutrino-induced gravitational waveforms presented in this section may be regarded as lower bounds to the realistic anisotropy/wave amplitudes. Future fully angle-dependent neutrino radiation-hydrodynamics calculations will be required for more reliable estimates of the neutrino radiation anisotropy and the corresponding gravitational wave emission.

The α evolutions of the 1.46-$M_\odot$ and 1.92-$M_\odot$ models are qualitatively quite similar while the latter model reaches up to 8 times larger α. Note that α assumes positive values throughout our model calculations. This is due to the clear prolate deformation of the neutrino radiation field and is in stark contrast to the behavior of α in nonrotating massive star core-collapse models (cf. §7.2.2).

In order to understand the evolution of α presented in figure 7.16, it is useful to consider figure 7.17 that compares the polar and equatorial energy and flavor integrated neutrino luminosities L_ν in the 1.92-$M_\odot$ model. The first peak in α at core bounce correlates with the electron neutrino break-out peak in L_ν that is ∼40% larger at the poles than on the equator. The second increase in α at ∼50–100 km after core bounce coincides with the rise in magnitude and anisotropy of the anti-electron and "μ" neutrino luminosities during that time interval. The slow late-time decay of α can in turn be associated with late-time decrease of the $\bar{\nu}_e$ and "ν_μ" contributions to the total emission.

The neutrino-induced gravitational waveform is obtained by integrating in time the product of α and the total neutrino luminosity L_ν (equation [7.24]). Given the overall small time variation and positive nature of α, the resultant gravitational wave signal should exhibit only slow time variation and should increase monotonically in amplitude. The left panel of figure 7.18 clearly confirms this. At the end of their numerical evolutions, the neutrino-induced h_+ for an observer located on the equator of the source at 10 kpc distance has risen to 2.0×10^{-20} and 4.6×10^{-21} in the 1.92-$M_\odot$ and 1.46-$M_\odot$ models, respectively. Note that these numbers are 6 times larger in the 1.92-$M_\odot$ model and 10 times

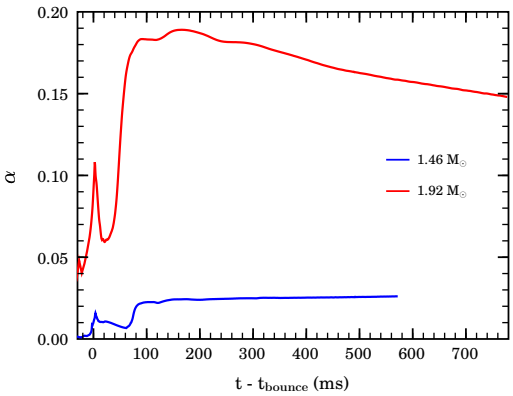

Figure 7.16: Neutrino radiation field anisotropy parameter α (defined by equation (7.25)) extracted at 200 km radius in the 1.46-$M_\odot$ model and at 300 km radius in the 1.92-$M_\odot$ model. Note the spike in α correlated with core bounce in both models. Also note the strong increase in α between 50 and 100 ms after core bounce. This is related to the rise in the $\bar{\nu}_e$ and "$\bar{\nu}_\mu$" emissions from the PNS that generally show greater anisotropies than the ν_e radiation field [16]. See figure 7.17.

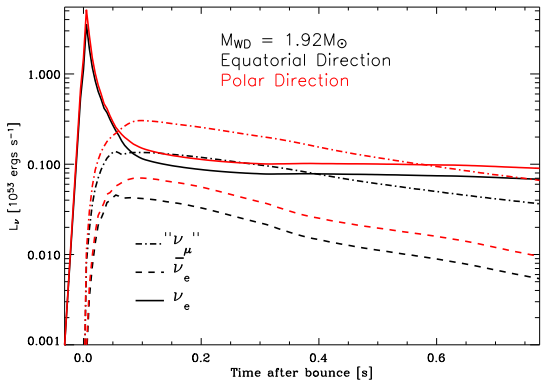

Figure 7.17: Flavor- and angle-dependent neutrino luminosities for the 1.92-$M_\odot$ progenitor at a radius of 400 km. Luminosities shown as solid, dash-dotted, and dashed lines correspond to $\int d\Omega R^2 F_\nu(R,\theta,\epsilon_\nu)$ for the ν_e, $\bar{\nu}_e$ and "ν_μ" neutrinos, respectively. Black corresponds to the equatorial direction ($\theta = \pi/2$) and red corresponds to the polar direction ($\theta = 0$). This figure was prepared by L. Dessart and has been published as part of figure 9 of [16].

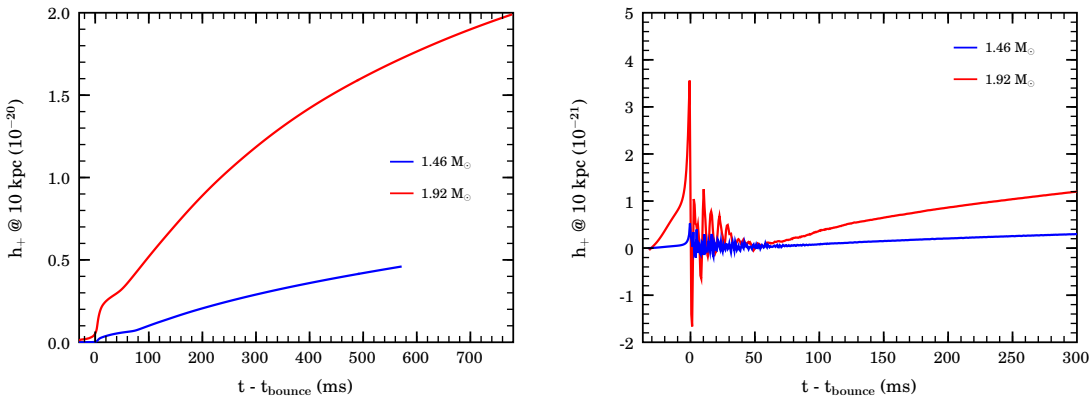

Figure 7.18: Left: Gravitational waveforms due to the anisotropic neutrino radiation in the 1.46-$M_\odot$ and 1.92-$M_\odot$ models as seen by an observer located on the equator in the source coordinate system at 10 kpc distance. Note the low frequency, almost 'DC' character of the neutrino-induced gravitational wave emission. Right: Sum of the matter and neutrino gravitational waveforms. Note that at bounce and early postbounce times the matter wave signal dominates in amplitude, while being slightly offset due to the slowly varying neutrino wave signal. Note the different ordinate scales in the left and right panels. Compare with figure 7.14.

larger in the 1.46-$M_\odot$ model than the maximum amplitudes of the mass-quadrupole gravitational wave signals. However, as the right panel of figure 7.18 shows, the matter signal is dominating in amplitude at early times and is only surpassed in maximum amplitude on a timescale of several hundred milliseconds by the neutrino gravitational wave emission. Importantly, we point out that the mass-quadrupole emission, owing to its much faster time-variation, vastly dominates the energy emission. In the 1.46-$M_\odot$ model, a total energy of 5.7×10^{-10} $M_\odot c^2$ is emitted of which 99.8% is due to aspherical accelerated mass motions. For the 1.92-$M_\odot$ model, we find a total energy emission of 7.0×10^{-8} $M_\odot c^2$ in the form of gravitational waves, of which 98.4% is due to mass-quadrupole wave emission.

7.3.3 Summary and Discussion

We have performed the first set of 2D Newtonian multi-group flux-limited diffusion radiation-hydrodynamics calculations of accretion induced collapse using initial rotational equilibrium configurations [61] set up with accreting-white-dwarf rotation laws [580]. The general results of the simulations are discussed in Dessart et al. [16]. Here we have focussed on the gravitational wave emissions of two progenitor white dwarf models that differ in initial central angular velocity and total white dwarf mass (1.46-$M_\odot$ model $\rightarrow \Omega_c = 0$, 1.92-$M_\odot$ model $\rightarrow \Omega_c = 17.62$ rad s^{-1}). For the first time ever we present gravitational waveform estimates for AIC.

We find that due to the high initial white dwarf central densities of 5×10^{10} g cm^{-3}, electron capture sets in quickly and in a very efficient fashion. This results in fast collapse and small inner core masses. At the time of core bounce the small inner core of the 1.46-$M_\odot$ model is only slightly rotationally deformed. This leads to a weak peak matter gravitational wave signal that qualitatively resembles what has been suggested as a type-III "fast collapse" waveform in previous studies [12, 30]. The 1.92-$M_\odot$ model exhibits greater centrifugal flattening, but experiences strong rotational support only during the plunge phase of collapse, leading to a matter gravitational waveform whose morphology still resembles the above mentioned type-III, but clearly shows the imprint of fast rotation. Therefore we classify it as type-III/II transitional — a type of waveform morphology not published before.

Both AIC models show strong anisotropies in their neutrino radiation fields throughout their postbounce evolution. Our analysis of the gravitational wave emission from anisotropic neutrino radiation fields indicates that the neutrino waveform dominates the amplitudes at postbounce times $\gtrsim$50 ms, but not the total gravitational wave energy emission. The neutrino waveform has an inherent memory effect, leaving behind a constant offset in h once the anisotropic emission subsides (on the timescale of $\sim$10 s). To date, it is not entirely clear how such "DC"-like offsets would be detectable by current and future gravitational wave antennas (but see [283, 617]).

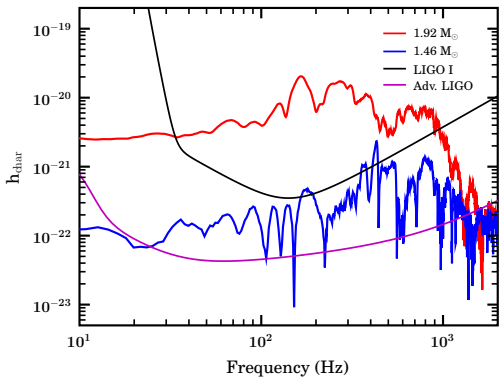

Figure 7.19: Characteristic gravitational wave strain spectra $h_{\rm char}$ computed via equation (3.179) for the mass-quadrupole gravitational wave signals emitted by the two AIC models, if located at 10 kpc distance. For comparison, we have plotted the LIGO I [515] and projected advanced LIGO optimal single-detector burst sensitivities. The advanced LIGO curve has been provided by D. Shoemaker [228]. Unfortunately, not enough data are available for a reliable Fourier transform of the gravitational waves emitted by anisotropic neutrino emission.

Figure 7.19 compares the characteristic gravitational wave strain spectra $h_{\rm char}$ [514] (computed as discussed in §3.8.3) of the two AIC models (at 10 kpc distance) with the LIGO I and advanced LIGO rms strain sensitivity. The latter is defined as $h_{\rm rms} = \sqrt{fS(f)}$, where f is the frequency and $S(f)$ is the optimal noise power spectral density [228, 514, 515]. We include only the mass-quadrupole emission in $h_{\rm char}$ since we are unable to compute reliable Fourier transforms of the neutrino gravitational wave signal due to a lack of sufficient data points[11]. Because of the slowly time-varying neutrino emission, we expect a relevant contribution only at frequencies below $\sim$10 Hz where both current and future LIGO sensitivity is poor.

The 1.46-$M_\odot$ model's characteristic strain spectrum peaks at 430 Hz with a maximum characteristic gravitational wave strain $h_{\rm char}\sim 2.3\times10^{-21}$, while the more centrifugally supported 1.92-$M_\odot$ model has a maximum $h_{\rm char}\sim 2.0\times10^{-20}$ at f$\sim$160 Hz. Based on the comparison with LIGO sensitivities shown in figure 7.19, we surmise that for optimal source–detector orientation, the 1.92-$M_\odot$ model should be comfortably detectable by current and future LIGO-class observatories throughout the Milky Way. The 1.46-$M_\odot$ model may be marginally detectable by the currently operative LIGO I detectors, but should certainly be visible to advanced LIGO throughout the Milky Way, provided favorable source/detector orientation. Note that we find final βs of $\sim$0.06 and $\sim$0.26 in the 1.46-$M_\odot$ and 1.92-$M_\odot$ models, respectively. Both βs may be large enough [20–22, 24, 309, 504] to undergo nonaxisymmetric rotational instabilities which could lead to the prolonged and strong emission of gravitational waves in a narrow frequency band. This deserves further investigation in 3D.

As discussed earlier, Fryer et al. [270] estimated the gravitational wave emission from aspherical accelerated mass motions in the single rotating AIC model of [42]. This model employed a simple, solid-body rotation law and had a final β of $\sim$0.06. They did not consider anisotropic neutrino emission. Our more realistic models yield maximum (matter) gravitational wave strains that are 1.5–2 orders of magnitude smaller than those predicted by [270]. The total energy emission matches within a factor of 2 since our models emit at higher frequencies.

We point out that the results and conclusions presented here on the gravitational wave signature of accretion-induced collapse should be cosindered as preliminary in a variety of aspects. Our calculations are performed in axisymmetry, rely on Newtonian gravity, do not include magnetic field effects, and treat neutrino radiation transport in the MGFLD approximation. We have considered only two initial white dwarf models and for both assumed unusually high initial central densities. A large parameter study in initial rotational configuration and central density will be required to fully understand the systematics of AIC collapse and postbounce evolution, and the corresponding gravitational waveforms. Nevertheless, we believe that our work marks an important step towards realistic models of AICs. Future work will be directed towards improved efficient radiative-transfer methods [616] and the inclusion of magnetic fields in our calculations.

[11] The neutrino waveform is obtained via post-processing of radiation-hydrodynamics data output at 0.5 ms intervals.

Chapter 8

The Greater Picture: Summary and Outlook

The emission of gravitational waves (GWs) from accelerated aspherical mass motions is a central prediction of Einstein's General Theory of Relativity (GR). At the advent of GW astronomy, a burgeoning international array of light-interferometric GW observatories is coming on-line, opening up an entirely new window to the universe.

Ever since the early attempts to detect GWs by Joe Weber, core-collapse supernovae have been deemed — among with compact binary systems[1] — prime candidates for the emission of GWs, at sufficiently high amplitudes to be observable by Earth-based detectors.

Beginning in the 1990s, the efforts to compute the core-collapse supernova GW signature branched into two directions[2]: One group of studies adopted simplified descriptions for progenitor structure, microphysics[3] and discarded neutrino radiation transport in order to perform extensive axisymmetric parameter studies in Newtonian gravity and/or GR. The other group of studies included a detailed treatment of the microphysics, neutrino radiation transport, and employed progenitor structure models from stellar evolutionary calculations. Owing to the complexity and computational cost of such calculations, these studies were limited to Newtonian gravity[4] and a small set of model calculations. Nevertheless, these detailed studies provided us with important insight into supernova physics and showed that the gravitational wave signature of core-collapse supernovae is much more diverse than first assumed. Not only rotating collapse, core bounce and nonaxisymmetric rotational instabilities can lead to significant GW emission, but also postbounce convective overturn, anisotropic neutrino emission, instabilities of the standing accretion shock, and protoneutron star (PNS) pulsations.

In this dissertation, I reported on my work towards bridging between the two aforementioned paradigms. I improved existing numerical tools and combined them with newly implemented ones, in order to connect {3+1} numerical relativity with core-collapse supernova theory.

I performed the first-ever calculations of rotating stellar iron core collapse in {3+1} numerical relativity and GR hydrodynamics. In a first step, these calculations were carried out with simple polytropic initial models and a hybrid polytropic/ideal-fluid equation of state (EOS) for comparison and with previous calculations [12, 18] carried out in the conformal-flatness approximation of GR (CFC)[5]. In agreement with previous comparisons [13, 162], I found excellent agreement of CFC with full GR in rotating stellar iron core collapse.

In a second step, I coupled a finite-temperature nuclear EOS, an approximate scheme for deleptonization during core collapse, and a scheme for including the Fermi pressure of neutrinos to my numerical code and performed the first stellar collapse calculations in multi-dimensional numerical relativity that incorporated microphysics and employed presupernova structure data from stellar evolutionary calculations. These calculations are the most important technical achievement in my

[1] Black hole–black hole, neutron star–neutron star, black-hole–neutron star.

[2] See §2.7 for a detailed historical discussion.

[3] The term microphysics is used here to denote a finite-temperature nuclear EOS and weak interactions, including electron captures on free and bound protons.

[4] And recently approximate GR with a "relativistic" monopole term in the Newtonian potential [95, 551]

[5] CFC: Conformal-Flatness Condition. See §5.2.

work and included all physics that is deemed relevant in the rotating collapse and bounce phase of core-collapse supernovae [3, 64, 83, 276]. I performed a parameter study in the initial rotation rate, degree of differential rotation, degree of deleptonization, and progenitor stellar structure. The results of these calculations (discussed in §6 and summarized in §6.6) provide the to-date most realistic estimates for the GW emission from rotating collapse, bounce, and the early postbounce epoch of core-collapse supernovae. Importantly, I found that even rapidly rotating realistic precollapse iron cores stay axisymmetric through core bounce and may only at postbounce times become subject to nonaxisymmetric rotational instabilities boosting their GW emissions.

The approximation employed for deleptonization was designed for the collapse phase only and can neither capture the important postbounce deleptonization of the PNS nor the important neutrino transport / heating / cooling effects in the postshock region. This is the most important limitation of my {3+1} GR calculations (additional others were discussed in §6.6). Future work must be directed towards more realistic approximations for the postbounce phase to further the applicability of my {3+1} GR approach in the broader core-collapse supernova context.

I supplemented my {3+1} GR hydrodynamic calculations with state-of-the-art axisymmetric Newtonian radiation-hydrodynamic supernova calculations (discussed in §7) that included all relevant neutrino transport effects and in which I focussed on (1) nonrotating and very slowly rotating iron cores that yield little GW emission from core bounce, but significant GW emission at intermediate and late postbounce times from convection, anisotropic neutrino radiation, SASI[6], and PNS g-mode oscillations, and (2) on the GW emission in the accretion-induced collapse (AIC) of rapidly rotating O/Ne/Mg white dwarfs. The most important downside of these calculations is the neglect of magnetic field effects that are of potential importance at postbounce times in a rotating PNS. In particular, the magneto-rotational instability (MRI) [276–278, 606–609, 623] that operates on the shear energy stored in differential rotation might lead to exponential magnetic field amplification on a timescale comparable with the rotation period of the PNS and could result in significant spindown and magneto-hydrodynamic (MHD) effects in the postshock region including, possibly, MHD jet-driven explosions. However, sufficiently realistic multi-dimensional calculations have not yet been performed and the relevance and the rotation dependence of MHD effects are not clear.

The Gravitational Wave Signature of Core-Collapse Supernovae

Based on the combined results of my {3+1} GR and 2D Newtonian calculations, knowledge of the current state of supernova theory and well-founded speculation, I now attempt to summarize the results presented in this dissertation, draw a tentative qualitative and quantitative picture of the core-collapse supernova GW signature and estimate the rate of detectable events.

- **Nonrotating / Slowly Rotating Iron Cores:** Nonrotating or slowly rotating iron cores[7] produce no significant gravitational wave emission related to core bounce (see §6.2, §6.3.5, §7.2, and [95]) unless their precollapse structure is significantly aspherical [265, 271]. At postbounce times, convection and SASI can grow unhindered by rotation and GWs are emitted by accelerated quadrupolar mass motions associated with the SASI-distorted shock, convection in the PNS and neutrino-driven convection in the postshock region. For a galactic supernova at 10 kpc from Earth, dimensionless strains $h \lesssim 5 \times 10^{-23}$ at postbounce times $\lesssim$ 100–200 ms and $h \lesssim 1 \times 10^{-22}$ at times when the SASI has reached non-linear amplitudes are to be expected. The emission is broadband with frequencies in the range of $\sim$100–$\sim$1000 Hz.

  If the neutrino mechanism (see §2.3.2) works, explosion sets in within $\lesssim$ 300 ms after bounce and mutes the GW emission. Even with the non-linear SASI phase taken into account, the total radiated energy is likely to be $\lesssim 10^{-9}\,M_\odot c^2$ [95]. In addition to the GW emission from accelerated aspherical mass motions, convection/SASI induced anisotropies in the neutrino radiation field near the radii at which the neutrinos decouple from the matter and begin to free-stream lead to GW emission. In my calculations (see §7.2), I find maximum dimensionless GW strains (at 10 kpc distance) of $3 \times 10^{-22} \lesssim h \lesssim 2.5 \times 10^{-21}$ emitted at frequencies in the

[6] SASI: Standing Accretion Shock Instability, see, e.g., [27, 73, 86, 90–93, 97–99, 101].

[7] I define a slowly rotating iron core as one that has an initial central period $\gtrsim$ 25 s and yields cold neutron star spin periods in the range of those observed for young pulsars (10–60 ms) [273, 511] without the need for one or multiple (unknown) spindown mechanism(s). Such cores make PNSs with $\beta = T/|W| \lesssim 1\%$ and cold neutron stars with $\beta \lesssim 5\%$.

range of 1–10 Hz and with the characteristic memory effect [265, 281, 283]. Owing to the small temporal variation of the neutrino-induced gravitational waveform, the emitted energies are small, typically $E_{\mathrm{GW},\nu} \lesssim 10^{-12}\,\mathrm{M}_\odot c^2$.

GWs from neutrino-driven nonrotating or slowly rotating core-collapse supernovae will require advanced-LIGO-class detectors to be detectable even if occurring in the Milky Way. The expected event rate is $\sim$1 supernova in 40 years (see §2.2).

If the neutrino mechanism does not work (which could, for example, be the case in massive cores with high outer core accretion rates), the SASI continues to distort the postshock region and modulate accretion downstreams that hit the PNS and in combination with turbulence in the PNS surroundings may excite PNS oscillations (see §7.2 and [10, 26–28]).

If these strong non-linear PNS pulsations obtain, they could lead to prolonged narrow band emission with GW strains in the range $1 \times 10^{-21} \lesssim h \lesssim 5 \times 10^{-20}$ (at 10 kpc; depending on the progenitor; the numbers are inferred from the calculations presented in §7.2) at frequencies of 600–1000 Hz and emitted energies in the range of $2 \times 10^{-8}\,\mathrm{M}_\odot c^2 \lesssim E_{\mathrm{GW}} \lesssim 7 \times 10^{-6}\,\mathrm{M}_\odot c^2$. If the stalled shock is revived by the acoustic power emitted from the pulsating PNS, the star explodes and the oscillations and the GW emission damp out as accretion subsides. This potential explosion mechanism is the so-called "acoustic mechanism" proposed by Burrows et al. [26]. If the star is not exploded, the oscillations and GW emission continue, and upon black hole formation migrate to black-hole quasi-normal modes.

Core-collapse supernovae with strong PNS oscillations may be detectable throughout the Milky Way with the initial LIGOs and throughout the Local Group ($D \lesssim 1\,\mathrm{Mpc}$) with advanced LIGOs. The event rates are $\sim$ 1 in 40 years and $\sim$1 in 17 years for the Milky Way and the entire Local Group, respectively (see §2.2). Large progenitor cores may lead to very massive, extremely energetically pulsating PNSs that could possibly be seen with advanced LIGOs out to the Virgo Cluster ($\sim$10–20 Mpc). The hard upper limit for the detectable event rate is < 5 per year in this case.

If the PNS oscillations do not obtain or do not reach sizable amplitudes, no late-postbounce GW enhancement of the GW emission is expected and without explosion, the PNS eventually collapses quasi-spherically into a black hole.

- **Rapidly Rotating Iron Cores:** Rapidly rotating iron cores deform sufficiently during collapse to emit a strong burst of GWs at core bounce with subsequent GW emission from the non-radial parts of the PNS ring-down pulsations. They stay axisymmetric through collapse, bounce, and the early postbounce phases. Based on the results of the calculations presented in §6.3, I expect dimensionless strain amplitudes in the bounce GW burst in the range $1 \times 10^{-21} \lesssim h \lesssim 1 \times 10^{-20}$ (at 10 kpc), relatively-narrow band emission peaked around frequencies in the interval of $\sim$500–1000 Hz and emitted energies in the range $5 \times 10^{-10}\,\mathrm{M}_\odot c^2 \lesssim E_{\mathrm{GW}} \lesssim 4 \times 10^{-8}\,\mathrm{M}_\odot c^2$. Initial LIGOs should be able to see such core collapse events throughout the Milky Way and advanced detectors out to the Magellanic Clouds. This gives upper limits on the detectable event rate of $\sim$1 in 40 years and $\sim$1 in 30 years for the Milky Way and Milky Way plus Magellanic Clouds, respectively. There is theoretical evidence from stellar evolutionary calculations that progenitor stars with rapidly rotating iron cores make up not more than 1% of all stars above 10 $\mathrm{M}_\odot$ [113, 511].

  An unknown fraction of the rapidly rotating iron cores will not make PNSs rotating rapidly enough to inhibit convection, SASI and/or PNS core oscillations. In the absence of significant MHD effects and rotational instabilities, what I have said above concerning the intermediate and late postbounce emission in the context of nonrotating or slowly rotating iron cores applies for such cores as well.

  All rotating PNSs spin virtually uniformly out to $\lesssim$ 15 km and strongly differentially outside their core regions (see §6.4 and [273]). The faster fraction of the rapidly spinning cores yields PNSs and postshock regions sufficiently fast for rotation to dominate the postshock flow. The strong rotational flattening of the PNS leads to anisotropic neutrino radiation fields and consequential emission of low-frequency GWs. This is discussed below in the context of AIC.

  It is not unlikely [88, 273] that centrifugal effects stabilize the postshock convection at low latitudes and may partially inhibit the SASI and the PNS core oscillations. In this case, neither the neutrino nor the acoustic mechanism might work and such core-collapse supernovae may

rely on MHD processes that tap the PNS rotational kinetic energy to drive the explosion (e.g., [608, 623]).

In the MHD-driven explosion case, the PNS is spun down (see [273] for spindown estimates) and most likely becomes rigidly rotating on a dynamical timescale [278, 609]. In this case, no significant postbounce GW emission is likely to take place unless the PNS spins up sufficiently during its cooling phase to become unstable to the classical secular or dynamical nonaxisymmetric instability[8] at high-$T/|W|$. Quantitative estimates for the GW emission depend on the rotation period, mass and radius of the cooling PNS, and on the duration of the bar-like nonaxisymmetric deformation. Using equation (2.124) on page 42, I estimate for a NS with a period of 1 ms, $R = 10$ km, and $M = 1.4\,\mathrm{M}_\odot$ that is located in the Virgo Cluster at $D = 15$ Mpc, a GW emission at $f_{\mathrm{GW}} = 1000$ Hz with $h \sim 4 \times 10^{-23}$. With $\sqrt{n}$-scaling, the bar-mode instability in this NS would have to last at least for $\sim$100 cycles to become detectable by advanced LIGOs. A galactic bar-mode deformed NS should be easily detectable already by the initial LIGOs. The hard upper limits on the event rates are set by the core-collapse supernova rates given in §2.2. If 1% of all core-collapse supernovae are rapidly rotating, one can expect not more than $\sim$1 supernova in 4000 years in the Milky Way and $\sim$1 supernova in 20 years out to the Virgo Cluster to leave behind a NS that becomes bar-unstable during its cooling epoch.

If MHD effects are not sufficiently strong to explode the supernova at early postbounce times and/or to lead to rapid angular momentum redistribution, a rapidly rotating PNS may be subject to a low-$T/|W|$ instability as discussed in §6.4. The quadrupole components of the nonaxisymmetric deformations then emit GWs quasi-periodically in a narrow frequency range. In my model calculations I found GW strains in the range $2 \times 10^{-21} \lesssim h \lesssim 5 \times 10^{-21}$ (at 10 kpc) and emitted around 930 Hz, beginning at 20–60 ms after core bounce with no sign of decay at the end of my calculations. It is unknown how long the instability can last, but natural end points would be the onset of explosion or black hole formation. The emitted energy and the detectability depend crucially on the amount of GW cycles the nonaxisymmetric deformation lasts. In the optimistic case and assumed emission over a period of 300 ms, I estimated detectability by advanced LIGOs out to the Virgo Cluster. With the above considerations on the event rate of quickly-spinning core-collapse supernovae, $\sim$1 detectable event in 20 years out to the Virgo Cluster and $\sim$1 such event in 4000 years in the Milky Way.

If the shock is neither revived by a MHD mechanism, nor by the neutrino mechanism, nor by the acoustic mechanism, nor by a combination of these mechanisms, then either a presently unexpected mechanism explodes the star, or black hole formation becomes inevitable and occurs (depending on progenitor mass and precollapse density profile) within $\lesssim 1.5$ s after bounce. Provided sufficient angular momentum, a thick accretion disk could form around the black hole and turn the massive dying star into a collapsar-type gamma-ray burst (GRB) with bipolar jets along the axis of rotation powered by accretion and probably driven by magnetic fields and neutrinos [2, 108, 109]. The details of this process and its event rate in the nearby universe are unclear. Observations and theory indicate that GRBs may require low progenitor metallicity to operate [2]. The closest observed GRB was located at $z = 0.16$ and $D \sim$38 Mpc.

Black hole formation from a rotating NS is likely to go along with an energetic burst of GWs with energy emission peaked at frequencies around 10 KHz [123, 624] and characteristic GW strain of $\sim 5 \times 10^{-22}$ at 10 kpc in the LIGO band between $\sim$100–1000 Hz.

- **Rapidly rotating AIC:** The progenitors of AIC related core collapse supernovae are rapidly rotating massive O/Ne/Mg white dwarfs that are pushed over their Chandrasekhar mass limit by accretion from a close companion star. The two model simulations analyzed as part of this work (discussed in §7.3) indicate that AIC proceeds very rapidly owing to very efficient electron captures and resulting in small inner cores and consequently GW emission from core bounce and PNS ring-down (despite their strong rotational flattening) at moderate GW amplitudes in the range $\sim 5 \times 10^{-22} \lesssim h \lesssim 4 \times 10^{-21}$ (at 10 kpc) and with emitted energies of $\sim 6 \times 10^{-10}\,\mathrm{M}_\odot c^2$ in the more slowly rotating model and $\sim 7 \times 10^{-8}\,\mathrm{M}_\odot c^2$ in the faster model. The models show no significant postbounce convection and an early onset of a neutrino-driven explosion. The large oblateness of the postbounce PNS cores leads to significant anisotropies in the neutrino radiation fields that result in GW emission at low frequencies and with small

[8] See §2.7.3. $\beta = T/|W|$ is the ratio of rotational kinetic to gravitational potential energy.

energy content that builds up a significant strain memory [265, 281, 283] of up to $h \sim 2 \times 10^{20}$ at 10 kpc. The corresponding effect in less oblate PNSs will be smaller.

Based on their GW strains and emitted energies, the bounce and PNS ring-down GW signature of AIC has a GW detectability comparable to that of regular rapidly rotating iron core collapse and detection by initial and advanced LIGOs throughout the Milky Way is likely. Detection of the GW emission from axisymmetric bounce and PNS ring-down out to the Virgo Cluster is probably impossible. The AIC event rate is less than 50–100 type Ia (see §7.3) and the galactic type Ia supernova rate is ∼1 in 250 years [44]. This makes at most ∼1 AIC in 12500 years in the Milky Way.

In contrast to the much more extended and more slowly collapsing rotating iron cores, AIC appears to allow more compact and rapidly rotating that can become unstable to the classical high-$T/|W|$ dynamical rotational instability at early postbounce times. The AIC calculations that I considered were carried out in 2D, hence could not investigate the development of non-axisymmetric structure. If the PNS deforms into a persistent bar, detection out to the Virgo Cluster may be possible and based on what is said in §2.2, I estimate an upper limit for the detectable event rate of ∼1 AIC in 100 years.

Conclusions and Outlook

Based on the above results, there is little hope for the detection of GWs from axisymmetric rotating iron core collapse from anywhere outside the Milky Way and the Magellanic Clouds even with advanced LIGO-class detectors. If the current event rates and estimates for the precollapse rotation rates of massive stars are correct, not more than ∼1 detectable event in 4000 years might occur. If rapidly rotating iron cores generically result in nonaxisymmetric postbounce configurations, ∼1 detectable event in 20 years might be a realistic number for advanced LIGOs and is still a factor of 2 better than the event rate for a galactic core-collapse supernova.

The PNS core oscillations are the only GW emission process that may be sufficiently strong to be detectable out to the Virgo Cluster and that does not suffer from the rapid-rotation event rate penalty. It will be the easiest to test by observation, once the advanced LIGO detectors become on-line.

On the other hand, a galactic supernova explosion today would already allow us to draw a number of conclusions concerning the relevance and strength of the various aforementioned GW emission processes. These in turn are tightly linked by supernova theory to various proposed explosion mechanisms and even the absence of a GW signal from a galactic supernova in initial LIGO detector data would be an important hint!

There is always room for surprises. Unless we are extremely lucky, a detected supernova gravitational waveform will most likely look different, possibly very different, from what our best theoretical models, including those presented in this work, tell us. But after a short time of confusion, our experience and theoretical understanding of core-collapse supernovae will enable us to fill in the missing gaps and to revise and improve our theoretical models.

In future work, I plan to focus on the postbounce aspects of the core-collapse supernova gravitational wave signature and work towards improving the microphysics and neutrino radiation transport capabilities of the {3+1} GR code, to enable it to perform longer-term and higher-precision calculations of the nonaxisymmetric postbounce evolution observed in some models.

The long-term perspective and the ultimate goal is the fully self-consistent simulation of collapsar-type GRBs from iron core collapse through black hole formation, jet creation, and ultimate disruption of the stellar envelope, in order to unravel the myths surrounding GRB engine. Such calculations will require computers 100 times faster than today's and {3+1} spacetime evolution codes of unprecedented accuracy and stability in addition to GRMHD and neutrino and photon radiation transport.

Personal Note

The process of writing this dissertation was painful and took about 8 months. I have learned much and would do it again. But not in this life.

I would like to point out that the foundations of this work were laid when I was an exchange student from Heidelberg at the University of Arizona in 2001/2002 and began to collaborate with A. Burrows on core-collapse supernovae. In the search for a code that would enable me to get a hands-on introduction to GR hydrodynamics and spacetime evolution, I came across the freely available GR3D code [625], a product of the NASA Binary Neutron Star Grand Challenge project [626]. The GR3D code enabled me to make my first and at that time still shaky steps in the realm of GR hydrodynamics and only through this code have I become familiar with the CACTUS infrastructure [366] and met my PhD advisor Edward Seidel and the Albert-Einstein-Institut numerical relativity group.

It is important for the progress of science and future generations of scientists to fully disclose our methods and to make our codes freely available and open source.

Appendix A

Constants, Units, and Unit Conversions

For convenience, CACTUS/CARPET/WHISKY set $c = G = M = 1$. The mass unit M can be chosen arbitrarily in vacuum spacetimes. For spacetimes containing matter, hence having a non-zero stress-energy tensor, the choice $c = G = \mathrm{M}_\odot = 1$ is made, $\mathrm{M}_\odot$ being exactly one solar mass.

In table A.2, I display all relevant unit conversions between the (for the astrophysicist intuitive) cgs system, geometric ($c = G = 1$), and $c = G = \mathrm{M}_\odot = 1$ units. All numbers are based on the values of the fundamental physical constants (table A.1) as published by the United States National Institute for Standards and Technology (NIST) [627]

Table A.1: Fundamental Physical Constants used in this work.

Constant	Value	Symbol	Rel. Uncertainty
Speed of light	c	$2.99792458 \times 10^{10}$ cm s^{-1}	0
Gravitational constant	G	$6.6742(10) \times 10^{-8}$ cm^3 g^{-1} s^{-2}	1.5×10^{-4}
Elementary charge	e	$1.60317653(14) \times 10^{-19}$ C	8.5×10^{-8}
Boltzmann constant	k_B	$1.3806505(24) \times 10^{-16}$ erg K^{-1}	1.8×10^{-6}
Avogadro constant	N_A	$6.0221415(10) \times 10^{23}$ mol^{-1}	1.7×10^{-7}
Planck constant	h	$6.6260693(11) \times 10^{-27}$ erg s	1.7×10^{-7}
Atomic mass unit	m_u	$1.66053886(28) \times 10^{-24}$ g	1.7×10^{-7}

Comment: Physical constants used in this work in cgs units. The numbers are taken from the NIST table of fundamental physical constants [627]. The number of significant decimal places is determined by the relative uncertainty of each constant as given by NIST.

Table A.2: Physical Constants and units in cgs, geometric and $c = G = \mathrm{M}_\odot = 1$ units

Dimension / Quantity	cgs	Geometric	$c = G = \mathrm{M}_\odot = 1$
Time	1 s	$3.33564095198 \times 10^{-11}$ cm	2.0296×10^5
Length	1 cm	1 cm	6.7706×10^{-6}
Mass	1 g	7.4261×10^{-29} cm	5.0279×10^{-34}
Density	1 g cm^{-3}	7.4261×10^{-29} cm^{-2}	1.6199×10^{-18}
Energy	1 erg = 1 g cm^2 s^{-2}	8.2627×10^{-50} cm	5.5953×10^{-55}
Specific internal energy	1 erg g^{-1}	$1.11265005605 \times 10^{-21}$	$1.11265005605 \times 10^{-21}$
Solar mass	1.9891×10^{33} g	1.4772×10^5 cm	1.0
Speed of light	$2.99792458 \times 10^{10}$ cm s^{-1}	1.0	1.0
Pressure	1 dyn cm^{-2}	6.6742×10^{-8}	1.8063×10^{-39}

Comment: The number of significant decimal places is determined by the relative uncertainty of the values of the physical constants as given by NIST [627].

Appendix B

Thermodynamic Derivatives

B.1 Speed of Sound and Γ for a Supernova EOS

The relativistic speed of sound is defined as [156, 157]

$$c_s = \frac{1}{h} c_{s,\text{Newt.}} \,, \tag{B.1}$$

where $h = 1 + \epsilon + p/\rho$ is the relativistic enthalpy and $c_{s,\text{Newt.}}$ is the Newtonian speed of sound given by

$$c_s = \sqrt{\left.\frac{\partial p}{\partial \rho}\right|_s} \,. \tag{B.2}$$

The adiabatic index Γ is defined (e.g., [149]) as

$$\Gamma = \frac{\rho}{p}\left.\frac{\partial p}{\partial \rho}\right|_s = \frac{\rho}{p}\, c_s^2 = \left.\frac{\partial \ln p}{\partial \ln \rho}\right|_s \,, \tag{B.3}$$

where the pressure p usually is a function of compositional variables X_i, baryonic rest-mass density ρ, and temperature T, specific entropy s or specific internal energy ϵ. In the following I assume $X_i \equiv Y_e$ and $p = p(\rho, T, Y_e)$, $s = s(\rho, T, Y_e)$, $\epsilon = \epsilon(\rho, T, Y_e)$.

The EOS required in core-collapse supernova calculations consists of a nuclear (nucleons and nuclei), an electron, and a photonic component. The total pressure p and all other thermodynamic variables are the sum of the individual component contributions. The following derivation of Γ for a general EOS with $p = p(\rho, T, Y_e)$ has been worked out by A. Marek, H. Dimmelmeier, and myself.

In order to evaluate equation (B.3), I write out the following differentials:

(i) $p = p(\rho, T, Y_e)$:

$$dp = \left.\frac{\partial p}{\partial \rho}\right|_{T,Y_e} d\rho + \left.\frac{\partial p}{\partial T}\right|_{\rho,Y_e} dT + \left.\frac{\partial p}{\partial Y_e}\right|_{\rho,T} dY_e \,. \tag{B.4}$$

(ii) $s = s(\rho, T, Y_e)$:

$$ds = \left.\frac{\partial s}{\partial \rho}\right|_{T,Y_e} d\rho + \left.\frac{\partial s}{\partial T}\right|_{\rho,Y_e} dT + \left.\frac{\partial s}{\partial Y_e}\right|_{\rho,T} dY_e \,. \tag{B.5}$$

(iii) $p = p(\rho, s, Y_e)$ with $s = s(\rho, T, Y_e)$:

$$dp = \left.\frac{\partial p}{\partial \rho}\right|_{s,Y_e} d\rho + \left.\frac{\partial p}{\partial s}\right|_{\rho,Y_e} ds + \left.\frac{\partial p}{\partial Y_e}\right|_{\rho,s} dY_e \,. \tag{B.6}$$

Inserting (ii) into (iii) yields

$$\begin{aligned} dp &= \left.\frac{\partial p}{\partial \rho}\right|_{s,Y_e} d\rho + \left.\frac{\partial p}{\partial s}\right|_{\rho,Y_e} \left[\left.\frac{\partial s}{\partial \rho}\right|_{T,Y_e} d\rho + \left.\frac{\partial s}{\partial T}\right|_{\rho,Y_e} dT + \left.\frac{\partial s}{\partial Y_e}\right|_{\rho,T} dY_e\right] + \left.\frac{\partial p}{\partial Y_e}\right|_{\rho,s} dY_e \\ &= \left[\left.\frac{\partial p}{\partial \rho}\right|_{s,Y_e} + \left.\frac{\partial p}{\partial s}\right|_{\rho,Y_e} \left.\frac{\partial s}{\partial \rho}\right|_{T,Y_e}\right] d\rho + \left.\frac{\partial p}{\partial s}\right|_{\rho,Y_e} \left.\frac{\partial s}{\partial T}\right|_{\rho,Y_e} dT + \left[\left.\frac{\partial p}{\partial s}\right|_{\rho,Y_e} \left.\frac{\partial s}{\partial Y_e}\right|_{\rho,T} + \left.\frac{\partial p}{\partial Y_e}\right|_{\rho,s}\right] dY_e \,. \end{aligned} \tag{B.7}$$

Via comparison with (i) I obtain:

$$\left.\frac{\partial p}{\partial \rho}\right|_{T,Y_e} = \left.\frac{\partial p}{\partial \rho}\right|_{s,Y_e} + \left.\frac{\partial p}{\partial s}\right|_{\rho,Y_e}\left.\frac{\partial s}{\partial \rho}\right|_{T,Y_e}, \tag{B.8}$$

$$\left.\frac{\partial p}{\partial T}\right|_{\rho,Y_e} = \left.\frac{\partial p}{\partial s}\right|_{\rho,Y_e}\left.\frac{\partial s}{\partial T}\right|_{\rho,Y_e}, \tag{B.9}$$

$$\left.\frac{\partial p}{\partial Y_e}\right|_{\rho,T} = \left.\frac{\partial p}{\partial s}\right|_{\rho,Y_e}\left.\frac{\partial s}{\partial Y_e}\right|_{\rho,T} + \left.\frac{\partial p}{\partial Y_e}\right|_{\rho,s}. \tag{B.10}$$

With the assumption[1] that $\left.\frac{\partial p}{\partial \rho}\right|_{s,Y_e} \approx \left.\frac{\partial p}{\partial \rho}\right|_{s}$ and by combining expressions (B.8) and (B.9) I arrive at

$$\left.\frac{\partial p}{\partial \rho}\right|_{s} = \left.\frac{\partial p}{\partial \rho}\right|_{T,Y_e} - \left.\frac{\partial p}{\partial s}\right|_{\rho,Y_e}\left.\frac{\partial s}{\partial \rho}\right|_{T,Y_e} = \left.\frac{\partial p}{\partial \rho}\right|_{T,Y_e} - \left.\frac{\partial s}{\partial \rho}\right|_{T,Y_e}\left.\frac{\partial p}{\partial T}\right|_{\rho,Y_e}\left(\left.\frac{\partial s}{\partial T}\right|_{\rho,Y_e}\right)^{-1}, \tag{B.11}$$

and

$$\Gamma = \frac{\rho}{p}\left[\left.\frac{\partial p}{\partial \rho}\right|_{T,Y_e} - \left.\frac{\partial s}{\partial \rho}\right|_{T,Y_e}\left.\frac{\partial p}{\partial T}\right|_{\rho,Y_e}\left(\left.\frac{\partial s}{\partial T}\right|_{\rho,Y_e}\right)^{-1}\right]. \tag{B.12}$$

Using

$$\frac{\partial p}{\partial \rho} = \frac{p}{\rho}\frac{\partial \ln p}{\partial \ln \rho}, \quad \frac{\partial s}{\partial \rho} = \frac{1}{\rho}\frac{\partial s}{\partial \ln \rho}, \quad \frac{\partial p}{\partial T} = \frac{p}{T}\frac{\partial \ln p}{\partial \ln T}, \quad \frac{\partial s}{\partial T} = \frac{1}{T}\frac{\partial s}{\partial \ln T}, \tag{B.13}$$

equation (B.12) can be converted to logarithmic derivatives in ρ and T:

$$\Gamma = \left.\frac{\partial \ln p}{\partial \ln \rho}\right|_{T,Y_e} - \left.\frac{\partial s}{\partial \ln \rho}\right|_{T,Y_e}\left.\frac{\partial \ln p}{\partial \ln T}\right|_{\rho,Y_e}\left(\left.\frac{\partial s}{\partial \ln T}\right|_{\rho,Y_e}\right)^{-1}. \tag{B.14}$$

This expression for Γ is directly implemented via standard finite differences in the routines that convert the Shen EOS table (see §3.6.2) into usable form for CACTUS/CARPET/WHISKY. The speed of sound is evaluated via equations (B.1) and (B.3).

B.2 Additional Pressure Derivatives

Besides the relativistic speed of sound, WHISKY requires additional thermodynamic derivatives for the computation of the characteristic information in the local Riemann problems (see appendix C) and for the iterative recovery of the primitive hydrodynamic variables (see §3.5.3). As mentioned above, I assume $p = p(\rho, T, Y_e)$.

$\left.\frac{\partial p}{\partial \rho}\right|_{\epsilon}$ in terms of (ρ, T, Y_e)

First, I assume that $\left.\frac{\partial p}{\partial \rho}\right|_{\epsilon,Y_e} \approx \left.\frac{\partial p}{\partial \rho}\right|_{\epsilon}$, since a change in Y_e typically goes along with a change in the fluid internal energy. Using the pressure differential

$$dp = \left.\frac{\partial p}{\partial \rho}\right|_{T,Y_e} d\rho + \left.\frac{\partial p}{\partial T}\right|_{\rho,Y_e} dT + \left.\frac{\partial p}{\partial Y_e}\right|_{\rho,T} dY_e, \tag{B.15}$$

and "dividing" by $d\rho$ while keeping ϵ and Y_e fixed yields

$$\left.\frac{\partial p}{\partial \rho}\right|_{\epsilon,Y_e} = \left.\frac{\partial p}{\partial \rho}\right|_{T,Y_e} + \left.\frac{\partial p}{\partial T}\right|_{\rho,Y_e}\left.\frac{\partial T}{\partial \rho}\right|_{\epsilon,Y_e}. \tag{B.16}$$

[1] Note that this assumption is well justified since in nonadiabatic stellar iron core collapse a change in Y_e generally goes along with a change in entropy [3, 64, 475].

Here the computation of $\frac{\partial p}{\partial \rho}\big|_{T,Y_e}$ and $\frac{\partial p}{\partial T}\big|_{\rho,Y_e}$ is straightforward from the EOS table. For $\frac{\partial T}{\partial \rho}\big|_{\epsilon,Y_e}$ I make use of the differential of $\epsilon = \epsilon(\rho, T, Y_e)$,

$$d\epsilon = \left.\frac{\partial \epsilon}{\partial \rho}\right|_{T,Y_e} d\rho + \left.\frac{\partial \epsilon}{\partial T}\right|_{\rho,Y_e} dT + \left.\frac{\partial \epsilon}{\partial Y_e}\right|_{\rho,T} dY_e \ . \tag{B.17}$$

Since ϵ and Y_e are kept fixed, this leads to (adopting a cavalier adherence to mathematical rigor)

$$\left.\frac{\partial \epsilon}{\partial \rho}\right|_{T,Y_e} d\rho = -\left.\frac{\partial \epsilon}{\partial T}\right|_{\rho,Y_e} dT \ , \tag{B.18}$$

and

$$\left.\frac{\partial T}{\partial \rho}\right|_{\epsilon,Y_e} = -\left.\frac{\partial \epsilon}{\partial \rho}\right|_{T,Y_e} \left(\left.\frac{\partial \epsilon}{\partial T}\right|_{\rho,Y_e}\right)^{-1} . \tag{B.19}$$

Finally, I can write

$$\left.\frac{\partial p}{\partial \rho}\right|_{\epsilon,Y_e} = \left.\frac{\partial p}{\partial \rho}\right|_{T,Y_e} + \left.\frac{\partial p}{\partial T}\right|_{\rho,Y_e} \left(- \left.\frac{\partial \epsilon}{\partial \rho}\right|_{T,Y_e}\right) \left(\left.\frac{\partial \epsilon}{\partial T}\right|_{\rho,Y_e}\right)^{-1} . \tag{B.20}$$

$\left.\frac{\partial p}{\partial \epsilon}\right|_{\rho}$ in terms of (ρ, T, Y_e)

Assuming $\frac{\partial p}{\partial \epsilon}\big|_{\rho,Y_e} \approx \frac{\partial p}{\partial \epsilon}\big|_{\epsilon}$, I devide equation (B.4) by $d\epsilon$ and write

$$\left.\frac{\partial p}{\partial \epsilon}\right|_{\rho,Y_e} = \left.\frac{\partial p}{\partial T}\right|_{\rho,Y_e} \left.\frac{\partial T}{\partial \epsilon}\right|_{\rho,Y_e} . \tag{B.21}$$

Here $\frac{\partial p}{\partial T}\big|_{\rho,Y_e}$ is readily evaluated and $\frac{\partial T}{\partial \epsilon}\big|_{\rho,Y_e}$ can be written as

$$\left.\frac{\partial T}{\partial \epsilon}\right|_{\rho,Y_e} = \left(\left.\frac{\partial \epsilon}{\partial T}\right|_{\rho,Y_e}\right)^{-1} , \tag{B.22}$$

which is easy to compute from the EOS table.

Finally, I point out that the Newtonian speed of sound for an EOS with $p = p(\rho, \epsilon)$ is given [36] by

$$c_s^2 = \left.\frac{\partial p}{\partial \rho}\right|_{\epsilon} + \frac{p}{\rho^2} \left.\frac{\partial p}{\partial \epsilon}\right|_{\rho} . \tag{B.23}$$

Hence, the speed of sound can be computed via equations (B.20), (B.22), and (B.23) as an alternative to and verification of the approach disscussed in appendix B.1.

Appendix C

Eigenstructure of the GR Hydrodynamic Equations

The knowledge of the eigenstructure – defined as the set of eigenvalues and corresponding eigenvectors – of the three 5×5 Jacobi matrices of the general relativistic Euler equations (2.66),

$$\mathbf{B}^i = \frac{\partial(\sqrt{\gamma}\mathbf{F}^i)}{\partial(\sqrt{\gamma}\mathbf{U})} = \frac{\partial(\mathbf{F}^i)}{\partial(\mathbf{U})} \ , \tag{C.1}$$

as introduced in §2.5, is relevant for the (approximate) solution of the local Riemann problems at cell interfaces when using high-resolution shock-capturing methods.

As stated before in §2.5, the three Jacobi matrices $\mathbf{B}^i$ each have tree unique eigenvalues, one of which is triply degenerate:

$$\lambda^i_0 = \alpha v^i - \beta^i \quad \text{(triply-degenerate)} \tag{C.2}$$

$$\lambda^i{}_{\pm} = \frac{\alpha}{1 - v^2 {c_s}^2} \left\{ v^i(1 - {c_s}^2) \pm \sqrt{{c_s}^2(1 - v^2)\left[\gamma^{ii}(1 - v^2 {c_s}^2) - v^i v^i (1 - {c_s}^2)\right]} \right\} - \beta^i \ , \tag{C.3}$$

where c_s is the local speed of sound. All eigenvalues are real and a set of 5 linearly independent eigenvectors exists. Hence, $\mathbf{B}^i$ are diagonizable:

$$\boldsymbol{\lambda}^i = \mathbf{L}^i \mathbf{B}^i \mathbf{R}^i \ . \tag{C.4}$$

Here $\boldsymbol{\lambda}^i$ is the diagonal matrix of the eigenvalues of Jacobian i and the columns of matrix $\mathbf{R}^i$ are its right eigenvectors, and $\mathbf{L}^i \equiv (\mathbf{R}^i)^{-1}$ is column-composed of the left eigenvectors of $\mathbf{B}^i$.

For $i = 1$ (that is, here for the x coordinate direction in Cartesian coordinates), the complete set of right eigenvectors [158, 628] reads

$$\mathbf{r}^x_1 = \begin{bmatrix} \frac{\kappa}{hW(\kappa - \rho {c_s}^2)} \\ v_x \\ v_y \\ v_z \\ 1 - \frac{\kappa}{hW(\kappa - \rho {c_s}^2)} \end{bmatrix} , \ \mathbf{r}^x_2 = \begin{bmatrix} Wv_y \\ h(\gamma_{xy} + 2W^2 v_x v_y) \\ h(\gamma_{yy} + 2W^2 v_y v_y) \\ h(\gamma_{yz} + 2W^2 v_y v_z) \\ v_y W(2Wh - 1) \end{bmatrix} , \ \mathbf{r}^x_3 = \begin{bmatrix} Wv_z \\ h(\gamma_{xz} + 2W^2 v_x v_z) \\ h(\gamma_{yz} + 2W^2 v_y v_z) \\ h(\gamma_{zz} + 2W^2 v_z v_z) \\ v_z W(2Wh - 1) \end{bmatrix} ,$$

$$\mathbf{r}^x_{\pm} = \begin{bmatrix} 1 \\ hW\left(v_x - \frac{v^x - (\lambda_{\pm} + \beta^x)/\alpha}{\gamma^{xx} - v^x(\lambda_{\pm} + \beta^x)/\alpha}\right) \\ hWv_y \\ hWv_z \\ \frac{hW(\gamma^{xx} - v^x v^x)}{\gamma^{xx} - v^x(\lambda_{\pm} + \beta^x)/\alpha} - 1 \end{bmatrix} . \tag{C.5}$$

Here, $\kappa \equiv \partial P / \partial \epsilon|_{(\rho, Y_i)}$. The right eigenvectors $\mathbf{r}^y$ and $\mathbf{r}^z$ are obtained by exchanging the indices $x \leftrightarrow y$ or $x \leftrightarrow z$ and by a permutation of rows 2 and 3 or 2 and 4, respectively.

For writing out the set of corresponding left eigenvectors, I define the following shortcuts:

$$\tilde{\kappa} \equiv \frac{\kappa}{\rho} \, , \mathcal{K} \equiv \frac{\tilde{\kappa}}{\tilde{\kappa}-c_s^2} \, , \mathcal{V}_\pm^x \equiv \frac{v^x-\lambda_\pm^x}{\gamma^{xx}-v^x\lambda_\pm^x} \, , \mathcal{C}_\pm^x \equiv v_x - \mathcal{V}_\pm^x$$

$$\mathcal{W}^x \equiv 1 - v_x v^x \, , \mathcal{A}_\pm^x \equiv \frac{\gamma^{xx}-v^x v^x}{\gamma^{xx}-v^x\lambda_\pm^x}$$

$$\Gamma_{xx} \equiv \gamma_{yy}\gamma_{zz} - \gamma_{yz}^2 \, , \Gamma_{xy} \equiv \gamma_{yz}\gamma_{xz} - \gamma_{xy}\gamma_{zz} \, , \Gamma_{xz} \equiv \gamma_{xy}\gamma_{yz} - \gamma_{xz}\gamma_{yy}$$

$$\gamma \equiv \det(\gamma_{ij}) = \gamma_{xx}\Gamma_{xx} + \gamma_{xy}\Gamma_{xy} + \gamma_{xz}\Gamma_{xz} \, , \gamma v^x = \Gamma_{xx}v_x + \Gamma_{xy}v_y + \Gamma_{xz}v_z$$

$$\xi \equiv \Gamma_{xx} - \gamma v^x v^x \, , \Delta \equiv h^3 W(\mathcal{K}-1)(\mathcal{C}_+^x - \mathcal{C}_-^x)\xi \tag{C.6}$$

The left eigenvectors for the Cartesian x direction are then given [628] by

$$\mathbf{l}_1^x = \frac{W}{\mathcal{K}-1}\begin{bmatrix} h-W \\ Wv^x \\ Wv^y \\ Wv^z \\ -W \end{bmatrix} \, , \mathbf{l}_2^x = \frac{1}{h\xi}\begin{bmatrix} -\gamma_{zz}v_y + \gamma_{yz}v_z \\ v^x(\gamma_{zz}v_y - \gamma_{yz}v_z) \\ \gamma_{zz}\mathcal{W}^x + \gamma_{xz}v_z v^x \\ -\gamma_{yz}\mathcal{W}^x - \gamma_{xz}v_y v^x \\ -\gamma_{zz}v_y + \gamma_{yz}v_z \end{bmatrix} \, , \mathbf{l}_3^x = \frac{1}{h\xi}\begin{bmatrix} -\gamma_{yy}v_z + \gamma_{zy}v_y \\ v^x(\gamma_{yy}v_z - \gamma_{zy}v_y) \\ -\gamma_{zy}\mathcal{W}^x - \gamma_{xy}v_z v^x \\ \gamma_{yy}\mathcal{W}^x + \gamma_{xy}v_y v^x \\ -\gamma_{yy}v_z + \gamma_{zy}v_y \end{bmatrix} \, ,$$

$$\mathbf{l}_\mp^x = \pm\frac{h^2}{\Delta}\begin{bmatrix} hW\mathcal{V}_\pm^x\xi + \frac{\Delta}{h^2}\left[(1-\mathcal{K})(-\gamma v^x + \mathcal{V}_\pm^x[W^2\xi - \Gamma_{xx}]) - \mathcal{K}W^2\mathcal{V}_\pm^x\xi\right] \\ \Gamma_{xx}(1-\mathcal{K}\mathcal{A}_\pm^x) + (2\mathcal{K}-1)\mathcal{V}_\pm^x(W^2v^x\xi - \Gamma_{xx}v^x) \\ \Gamma_{xy}(1-\mathcal{K}\mathcal{A}_\pm^x) + (2\mathcal{K}-1)\mathcal{V}_\pm^x(W^2v^y\xi - \Gamma_{xy}v^x) \\ \Gamma_{xz}(1-\mathcal{K}\mathcal{A}_\pm^x) + (2\mathcal{K}-1)\mathcal{V}_\pm^x(W^2v^z\xi - \Gamma_{xz}v^x) \\ (1-\mathcal{K})(-\gamma v^x + \mathcal{V}_\pm^x[W^2\xi - \Gamma_{xx}]) - \mathcal{K}W^2\mathcal{V}_\pm^x\xi \end{bmatrix} \, . \tag{C.7}$$

The y and z left eigenvectors are straightforwardly obtained by exchange of indices and permutation of rows.

Appendix D

Rotating Polytrope Model Parameters

Table D.1: Initial model parameters for rotating GR polytropes in equilibrium computed with WHISKY_RNSID (see §3.7.2). The models are named according to the scheme introduced by [30] and the values of β_{initial} are given for $n = 3$ polytropes with central density 10^{10} g cm^{-3} and polytropic $K = 4.9 \times 10^{14}$ [cgs].

Model Name	A (km)	β_{initial} (%)	$\hat{A}$	Axis Ratio	Remarks
A1B1	50000	0.25	30.8335791000	0.9450	
A1B2	50000	0.50	29.2062612000	0.8875	
A1B3	50000	0.90	22.2166923000	0.6650	
A1B4	50000	1.80	—	—	beyond mass shedding
A1B5	50000	4.00	—	—	beyond mass shedding
A2B1	1000	0.25	0.6360404070	0.9725	
A2B2	1000	0.50	0.6265180080	0.9475	
A2B3	1000	0.90	0.6098352960	0.9050	
A2B4	1000	1.80	0.5745211740	0.8200	
A2B5	1000	4.00	0.4943131580	0.6475	
A3B1	500	0.25	0.3215101880	0.9800	
A3B2	500	0.50	0.3200531210	0.9625	
A3B3	500	0.90	0.3173203410	0.9300	
A3B4	500	1.80	0.3122088370	0.8700	
A3B5	500	4.00	0.3016501170	0.7450	
A4B1	100	0.25	0.0654153811	0.9625	$\rho_{\max} = 1.000054\ \rho_c$
A4B2	100	0.50	0.0661612517	0.9300	$\rho_{\max} = 1.000108\ \rho_c$
A4B3	100	0.90	0.0675440136	0.8775	$\rho_{\max} = 1.002626\ \rho_c$
A4B4	100	1.80	0.0707954833	0.7825	$\rho_{\max} = 1.048859\ \rho_c$
A4B5	100	4.00	0.0800146668	0.6250	$\rho_{\max} = 1.307659\ \rho_c$

Appendix E

Mesh Refinement Hierarchies

In this appendix I list all CARPET mesh refinement hierarchies used in the numerical simulations discussed in this dissertation. See §3.4 and [391, 397] for details on CARPET.

Table E.1: Standard 9 level bitant mode refinement hierarchies used in this dissertation. For each refinement level the coordinates of the lower and upper bounds of the refined region are given. Δx is the grid spacing. All units are in $c = G = M_\odot = 1$. A length of 0.24 in these units corresponds to 354.43 m in cgs (see appendix A for details).

	level	lower			upper			Δx	grid points
		x	y	z	x	y	z		
RHI	0	-1966.08	-1966.08	0	1966.08	1966.08	1966.08	122.88	(33x33x17)
	1	-1228.80	-1228.80	0	1228.80	1228.80	1228.8	61.44	(41x41x21)
	2	-614.40	-614.40	0	614.40	614.40	614.40	30.72	(41x41x21)
	3	-307.20	-307.20	0	307.20	307.20	307.20	15.36	(41x41x21)
	4	-184.32	-184.32	0	184.32	184.32	184.32	7.68	(49x49x25)
	5	-92.16	-92.16	0	92.16	92.16	92.16	3.84	(49x49x25)
	6	-38.40	-38.40	0	38.40	38.40	38.40	1.92	(41x41x21)
	7	-19.20	-19.20	0	19.20	19.20	19.20	0.96	(41x41x21)
	8	-9.60	-9.60	0	9.60	9.60	9.60	0.48	(41x41x21)
RHII	0	-1966.08	-1966.08	0	1966.08	1966.08	1966.08	61.44	(65x65x33)
	1	-1228.80	-1228.80	0	1228.80	1228.80	1228.8	30.72	(81x81x41)
	2	-614.40	-614.40	0	614.40	614.40	614.40	15.36	(81x81x41)
	3	-307.20	-307.20	0	307.20	307.20	307.20	7.68	(81x81x41)
	4	-184.32	-184.32	0	184.32	184.32	184.32	3.84	(97x97x49)
	5	-92.16	-92.16	0	92.16	92.16	92.16	1.92	(97x97x49)
	6	-38.40	-38.40	0	38.40	38.40	38.40	0.96	(81x81x41)
	7	-19.20	-19.20	0	19.20	19.20	19.20	0.48	(81x81x41)
	8	-9.60	-9.60	0	9.60	9.60	9.60	0.24	(81x81x41)
RHIII	0	-1981.44	-1981.44	0	1981.44	1981.44	1981.44	46.08	(87x87x43)
	1	-1244.16	-1244.16	0	1244.16	1244.16	1244.16	23.04	(109x109x55)
	2	-622.08	-622.08	0	622.08	622.08	622.08	11.52	(109x109x55)
	3	-311.40	-311.40	0	311.40	311.40	311.40	5.76	(109x109x55)
	4	-184.32	-184.32	0	184.32	184.32	184.32	2.88	(129x129x65)
	5	-92.16	-92.16	0	92.16	92.16	92.16	1.44	(129x129x65)
	6	-38.88	-38.88	0	38.88	38.88	38.88	0.72	(109x109x55)
	7	-19.44	-19.44	0	19.44	19.44	19.44	0.36	(109x109x55)
	8	-9.72	-9.72	0	9.72	9.72	9.72	0.18	(109x109x55)
RHIV	0	-1966.08	-1966.08	0	1966.08	1966.08	1966.08	30.72	(129x129x65)
	1	-1228.80	-1228.80	0	1228.80	1228.80	1228.8	15.36	(161x161x81)
	2	-614.40	-614.40	0	614.40	614.40	614.40	7.68	(161x161x81)
	3	-307.20	-307.20	0	307.20	307.20	307.20	3.84	(161x161x81)
	4	-184.32	-184.32	0	184.32	184.32	184.32	1.92	(193x193x97)
	5	-92.16	-92.16	0	92.16	92.16	92.16	0.96	(193x193x97)
	6	-38.40	-38.40	0	38.40	38.40	38.40	0.48	(161x161x81)
	7	-19.20	-19.20	0	19.20	19.20	19.20	0.24	(161x161x81)
	8	-9.60	-9.60	0	9.60	9.60	9.60	0.12	(161x161x81)

Table E.2: Like table E.1, but for the standard 8 level bitant mode refinement hierarchies used in this dissertation.

	level	lower			upper			Δx	grid points
		x	y	z	x	y	z		
RH8I	0	-1966.08	-1966.08	0	1966.08	1966.08	1966.08	61.44	(65x65x33)
	1	-614.40	-614.40	0	614.40	614.40	614.40	30.72	(41x41x21)
	2	-307.20	-307.20	0	307.20	307.20	307.20	15.36	(41x41x21)
	3	-184.32	-184.32	0	184.32	184.32	184.32	7.68	(49x49x25)
	4	-92.16	-92.16	0	92.16	92.16	92.16	3.84	(49x49x25)
	5	-38.40	-38.40	0	38.40	38.40	38.40	1.92	(41x41x21)
	6	-19.20	-19.20	0	19.20	19.20	19.20	0.96	(41x41x21)
	7	-9.60	-9.60	0	9.60	9.60	9.60	0.48	(41x41x21)
RH8II	0	-1966.08	-1966.08	0	1966.08	1966.08	1966.08	30.72	(129x129x65)
	1	-614.40	-614.40	0	614.40	614.40	614.40	15.36	(81x81x41)
	2	-307.20	-307.20	0	307.20	307.20	307.20	7.68	(81x81x41)
	3	-184.32	-184.32	0	184.32	184.32	184.32	3.84	(97x97x49)
	4	-92.16	-92.16	0	92.16	92.16	92.16	1.92	(97x97x49)
	5	-38.40	-38.40	0	38.40	38.40	38.40	0.96	(81x81x41)
	6	-19.20	-19.20	0	19.20	19.20	19.20	0.48	(81x81x41)
	7	-9.60	-9.60	0	9.60	9.60	9.60	0.24	(81x81x41)
RH8III	0	-1981.44	-1981.44	0	1981.44	1981.44	1981.44	23.04	(173x173x87)
	1	-622.08	-622.08	0	622.08	622.08	622.08	11.52	(109x109x55)
	2	-311.40	-311.40	0	311.40	311.40	311.40	5.76	(109x109x55)
	3	-184.32	-184.32	0	184.32	184.32	184.32	2.88	(129x129x65)
	4	-92.16	-92.16	0	92.16	92.16	92.16	1.44	(129x129x65)
	5	-38.88	-38.88	0	38.88	38.88	38.88	0.72	(109x109x55)
	6	-19.44	-19.44	0	19.44	19.44	19.44	0.36	(109x109x55)
	7	-9.72	-9.72	0	9.72	9.72	9.72	0.18	(109x109x55)
RH8IV	0	-1966.08	-1966.08	0	1966.08	1966.08	1966.08	15.36	(257x257x129)
	1	-614.40	-614.40	0	614.40	614.40	614.40	7.68	(161x161x81)
	2	-307.20	-307.20	0	307.20	307.20	307.20	3.84	(161x161x81)
	3	-184.32	-184.32	0	184.32	184.32	184.32	1.92	(193x193x97)
	4	-92.16	-92.16	0	92.16	92.16	92.16	0.96	(193x193x97)
	5	-38.40	-38.40	0	38.40	38.40	38.40	0.48	(161x161x81)
	6	-19.20	-19.20	0	19.20	19.20	19.20	0.24	(161x161x81)
	7	-9.60	-9.60	0	9.60	9.60	9.60	0.12	(161x161x81)

Table E.3: Like table E.1, but for special 8 level bitant mode refinement hierarchies used in this dissertation.

	level	lower			upper			Δx	grid points
		x	y	z	x	y	z		
RH8IIe	0	-1966.08	-1966.08	0	1966.08	1966.08	1966.08	30.72	(129x129x65)
	1	-737.28	-737.28	0	737.28	737.28	737.28	15.36	(97x97x49)
	2	-368.64	-368.64	0	368.64	368.64	368.64	7.68	(97x97x49)
	3	-184.32	-184.32	0	184.32	184.32	184.32	3.84	(97x97x49)
	4	-92.16	-92.16	0	92.16	92.16	92.16	1.92	(97x97x49)
	5	-46.08	-46.08	0	46.08	46.08	46.0	0.96	(97x97x49)
	6	-23.04	-23.04	0	23.04	23.04	23.04	0.48	(97x97x41)
	7	-11.52	-11.52	0	11.52	11.52	11.52	0.24	(97x97x41)

Table E.4: Like table E.1, but for special 9 level bitant mode refinement hierarchies used in this dissertation.

	level	lower			upper			Δx	grid points
		x	y	z	x	y	z		
RHIIe	0	-2088.96	-2088.96	0	2088.96	2088.96	2088.96	61.44	(69x69x35)
	1	-983.04	-983.04	0	983.04	983.04	983.04	30.72	(65x65x33)
	2	-614.40	-614.40	0	614.40	614.40	614.40	15.36	(81x81x41)
	3	-307.20	-307.20	0	307.20	307.20	307.20	7.68	(81x81x41)
	4	-153.60	-153.60	0	153.60	153.6	153.60	3.84	(81x81x41)
	5	-76.80	-76.80	0	76.80	76.80	76.80	1.92	(81x81x41)
	6	-40.32	-40.32	0	40.32	40.32	40.32	0.96	(85x85x43)
	7	-23.04	-23.04	0	23.04	23.04	23.04	0.48	(97x97x49)
	8	-11.52	-11.52	0	11.52	11.52	11.52	0.24	(97x97x49)
RHIIe2	0	-2088.96	-2088.96	0	2088.96	2088.96	2088.96	61.44	(69x69x35)
	1	-1044.48	-1044.48	0	1044.48	1044.48	1044.48	30.72	(69x69x35)
	2	-614.40	-614.40	0	614.40	614.40	614.40	15.36	(81x81x41)
	3	-307.20	-307.20	0	307.20	307.20	307.20	7.68	(81x81x41)
	4	-153.60	-153.60	0	153.60	153.6	153.60	3.84	(81x81x41)
	5	-76.80	-76.80	0	76.80	76.80	76.80	1.92	(81x81x41)
	6	-46.08	-46.08	0	46.08	46.08	46.08	0.96	(97x97x49)
	7	-24.96	-24.96	0	24.96	24.96	24.96	0.48	(105x105x53)
	8	-11.52	-11.52	0	11.52	11.52	11.52	0.24	(97x97x49)
RHIIeHR	0	-2048.00	-2048.00	0	2048.00	2048.00	2048.00	51.20	(81x81x41)
	1	-1024.00	-1024.00	0	1024.00	1024.00	1024.00	25.60	(81x81x41)
	2	-614.40	-614.40	0	614.40	614.40	614.40	12.80	(97x97x49)
	3	-307.20	-307.20	0	307.20	307.20	307.20	6.40	(97x97x49)
	4	-153.60	-153.60	0	153.60	153.6	153.60	3.20	(97x97x49)
	5	-76.80	-76.80	0	76.80	76.80	76.80	1.60	(97x97x49)
	6	-41.60	-41.60	0	41.60	41.60	41.60	0.80	(103x103x53)
	7	-23.20	-23.20	0	23.20	23.20	23.20	0.40	(117x117x59)
	8	-11.60	-11.60	0	11.60	11.60	11.60	0.20	(117x117x59)

Table E.5: Like table E.1, but for special 9 level octant mode refinement hierarchies used in this dissertation.

	level	lower			upper			Δx	grid points
		x	y	z	x	y	z		
ORHIIIe	0	0	0	0	1935.36	1935.36	1935.36	46.08	(43x43x43)
	1	0	0	0	967.68	967.68	967.68	23.04	(43x43x43)
	2	0	0	0	483.84	483.84	483.84	11.52	(43x43x43)
	3	0	0	0	311.04	311.04	311.04	5.76	(55x55x55)
	4	0	0	0	184.32	184.32	184.32	2.88	(65x65x65)
	5	0	0	0	92.16	92.16	92.16	1.44	(65x65x65)
	6	0	0	0	60.48	60.48	60.48	0.72	(85x85x85)
	7	0	0	0	23.04	23.04	23.04	0.36	(65x65x65)
	8	0	0	0	9.72	9.72	9.72	0.18	(55x55x55)
ORHIIe	0	0	0	0	2088.96	2088.96	2088.96	61.44	(35x35x35)
	1	0	0	0	1228.80	1228.80	1228.8	30.72	(41x41x41)
	2	0	0	0	614.40	614.40	614.40	15.36	(41x41x41)
	3	0	0	0	307.20	307.20	307.20	7.68	(41x41x41)
	4	0	0	0	153.60	153.6	153.60	3.84	(41x41x41)
	5	0	0	0	76.80	76.80	76.80	1.92	(41x41x41)
	6	0	0	0	46.08	46.08	46.08	0.96	(49x49x49)
	7	0	0	0	24.96	24.96	24.96	0.48	(53x53x53)
	8	0	0	0	11.52	11.52	11.52	0.24	(49x49x49)
ORHIIe2	0	0	0	0	2088.96	2088.96	2088.96	61.44	(35x35x35)
	1	0	0	0	1413.12	1413.12	1413.12	30.72	(47x47x47)
	2	0	0	0	706.56	706.56	706.56	15.36	(47x47x47)
	3	0	0	0	307.20	307.20	307.20	7.68	(41x41x41)
	4	0	0	0	153.60	153.6	153.60	3.84	(41x41x41)
	5	0	0	0	76.80	76.80	76.80	1.92	(41x41x41)
	6	0	0	0	46.08	46.08	46.08	0.96	(49x49x49)
	7	0	0	0	24.96	24.96	24.96	0.48	(53x53x53)
	8	0	0	0	11.52	11.52	11.52	0.24	(49x49x49)
ORHIIeHR	0	0	0	0	2048.00	2048.00	2048.00	52.00	(40x40x40)
	1	0	0	0	1228.80	1228.80	1228.8	25.60	(49x49x49)
	2	0	0	0	614.40	614.40	614.40	12.80	(49x49x49)
	3	0	0	0	307.20	307.20	307.20	6.40	(49x49x49)
	4	0	0	0	153.60	153.6	153.60	3.20	(49x49x49)
	5	0	0	0	76.80	76.80	76.80	1.60	(49x49x49)
	6	0	0	0	46.40	46.40	46.40	0.80	(59x59x59)
	7	0	0	0	25.20	25.20	25.20	0.40	(64x64x64)
	8	0	0	0	11.60	11.60	11.60	0.20	(59x59x59)

References

[1] A. Burrows. Supernova Explosions in the Universe. *Nature*, 403:727, 2000.

[2] S. E. Woosley and J. S. Bloom. The Supernova Gamma-Ray Burst Connection. *Ann. Rev. Astron. Astrophys.*, 44:507, 2006.

[3] H. A. Bethe. Supernova mechanisms. *Rev. Mod. Phys.*, 62:801, 1990.

[4] A. Einstein. Zur Allgemeinen Relativitätstheorie. *Preuss. Akad. Wiss. Berlin, Sitzber.*, page 778, 1915.

[5] A. Einstein. Die Feldgleichungen der Gravitation. *Preuss. Akad. Wiss. Berlin, Sitzber.*, page 844, 1915.

[6] A. Einstein. Näherungsweise Integration der Feldgleichungen der Gravitation. *Preuss. Akad. Wiss. Berlin, Sitzber.*, page 688, 1916.

[7] A. Einstein. Über Gravitationswellen. *Preuss. Akad. Wiss. Berlin, Sitzber.*, page 154, 1918.

[8] J. M. Weisberg and J. H. Taylor. The Relativistic Binary Pulsar B1913+16: Thirty Years of Observations and Analysis. In F. A. Rasio and I. H. Stairs, editors, *ASP Conf. Ser. 328: Binary Radio Pulsars*, page 25, 2005.

[9] C. D. Ott, A. Burrows, E. Livne, and R. Walder. Gravitational waves from axisymmetric, rotating stellar core collapse. *Astrophys. J.*, 600: 834, 2004.

[10] C. D. Ott, H. Dimmelmeier, A. Marek, H. . Janka, I. Hawke, B. Zink, and E. Schnetter. 3D Collapse of Rotating Stellar Iron Cores in General Relativity with Microphysics. *Phys. Rev. Lett. submitted*, 2006.

[11] R. Mönchmeyer, G. Schäfer, E. Müller, and R. Kates. Gravitational waves from the collapse of rotating stellar cores. *Astron. Astrophys.*, 246:417, 1991.

[12] H. Dimmelmeier, J. A. Font, and E. Müller. Relativistic simulations of rotational core collapse II. Collapse dynamics and gravitational radiation. *Astron. Astrophys.*, 393:523, 2002.

[13] M. Shibata and Y. Sekiguchi. Gravitational waves from axisymmetric rotating stellar core collapse to a neutron star in full general relativity. *Phys. Rev. D*, 69(8):084024, 2004.

[14] K. Kotake, S. Yamada, and K. Sato. Gravitational radiation from axisymmetric rotational core collapse. *Phys. Rev. D.*, 68(4):044023, 2003.

[15] C. D. Ott, A. Burrows, L. Dessart, and E. Livne. A New Mechanism for Gravitational-Wave Emission in Core-Collapse Supernovae. *Phys. Rev. Lett.*, 96(20):201102, 2006.

[16] L. Dessart, A. Burrows, C. D. Ott, E. Livne, S.-Y. Yoon, and N. Langer. Multidimensional Simulations of the Accretion-induced Collapse of White Dwarfs to Neutron Stars. *Astrophys. J.*, 644:1063, 2006.

[17] H. Dimmelmeier, J. A. Font, and E. Müller. Gravitational Waves from Relativistic Rotational Core Collapse. *Astrophys. J. Lett.*, 560:L163, 2001.

[18] H. Dimmelmeier. *General Relativistic Collapse of Rotating Stellar Cores in Axisymmetry*. PhD thesis, Technische Universität München, 2001.

[19] A. L. Watts, N. Andersson, and D. I. Jones. The Nature of Low $T/|W|$ Dynamical Instabilities in Differentially Rotating Stars. *Astrophys. J. Lett.*, 618:L37, 2005.

[20] M. Saijo, T. W. Baumgarte, and S. L. Shapiro. One-armed Spiral Instability in Differentially Rotating Stars. *Astrophys. J.*, 595:352, 2003.

[21] J. M. Centrella, K. C. B. New, L. L. Lowe, and J. D. Brown. Dynamical Rotational Instability at Low T/W. *Astrophys. J. Lett.*, 550:L193, 2001.

[22] C. D. Ott, S. Ou, J. E. Tohline, and A. Burrows. One-armed Spiral Instability in a Low-T/|W| Postbounce Supernova Core. *Astrophys. J. Lett.*, 625:L119, 2005.

[23] M. Saijo and S. Yoshida. Low $T/|W|$ dynamical instability in differentially rotating stars: diagnosis with canonical angular momentum. *Mon. Not. R. Astron. Soc.*, 368:1429, 2006.

[24] S. Ou and J. E. Tohline. Unexpected Dynamical Instabilities in Differentially Rotating Neutron Stars. *Astrophys. J.*, 651:1068, 2006.

[25] B. Zink, N. Stergioulas, I. Hawke, C. D. Ott, E. Schnetter, and E. Müller. Non-axisymmetric instability and fragmentation of general relativistic quasi-toroidal stars. *Phys. Rev. D. submitted*, 2006.

[26] A. Burrows, E. Livne, L. Dessart, C. D. Ott, and J. Murphy. A New Mechanism for Core-Collapse Supernova Explosions. *Astrophys. J.*, 640:878, 2006.

[27] A. Burrows, E. Livne, L. Dessart, C. D. Ott, and J. Murphy. Features of the Acoustic Mechanism of Core-Collapse Supernova Explosions. *Astrophys. J.*, 655:416, 2007.

[28] A. Burrows, E. Livne, L. Dessart, C. D. Ott, and J. Murphy. *"An Acoustic Mechanism for Core-Collapse Supernova Explosions," "Astronomy with Radioactivities V: From Gamma-Rays to Stardust," held at Clemson University, SC, USA*, 2005.

[29] A. Burrows, E. Livne, L. Dessart, C. D. Ott, and J. Murphy. An acoustic mechanism for core-collapse supernova explosions. *New Astronomy Review*, 50:487, 2006.

[30] T. Zwerger and E. Müller. Dynamics and gravitational wave signature of axisymmetric rotational core collapse. *Astron. Astrophys.*, 320: 209, 1997.

[31] W. Baade and F. Zwicky. Remarks on Super-Novae and Cosmic Rays. *Physical Review*, 46:76, 1934.

[32] F. Zwicky. On Collapsed Neutron Stars. *Astrophys. J.*, 88:522, 1938.

[33] F. Zwicky. On the Theory and Observation of Highly Collapsed Stars. *Physical Review*, 55:726, 1939.

[34] M. Hamuy. Review on the Observed and Physical Properties of Core-Collapse Supernovae. *astro-ph/0301006*, 2003.

[35] D. Arnett. *Supernovae and nucleosynthesis. an investigation of the history of matter, from the Big Bang to the present*. Princeton series in astrophysics, Princeton, NJ: Princeton University Press, 1996.

[36] L. S. Shapiro and S. A. Teukolsky. *Black Holes, White Dwarfs and Neutron Stars*. John Wiley & Sons, New York U. S. A., 1983.

[37] S. E. Woosley and H.-T. Janka. The physics of core-collapse supernovae. *Nature Physics*, 1:147, 2005.

[38] S. E. Woosley, A. Heger, and T. A. Weaver. The evolution and explosion of massive stars. *Rev. Mod. Phys.*, 74:1015, 2002.

[39] R. Minkowski. Spectra of Supernovae. *Publ. Astron. Soc. Pac.*, 53:224, 1941.

[40] A. G. Riess, A. V. Filippenko, P. Challis, A. Clocchiatti, A. Diercks, P. M. Garnavich, R. L. Gilliland, C. J. Hogan, S. Jha, R. P. Kirshner, B. Leibundgut, M. M. Phillips, D. Reiss, B. P. Schmidt, R. A. Schommer, R. C. Smith, J. Spyromilio, C. Stubbs, N. B. Suntzeff, and J. Tonry. Observational Evidence from Supernovae for an Accelerating Universe and a Cosmological Constant. *Astron. J.*, 116:1009, 1998.

[41] A. G. Lyne and F. Graham-Smith. *Pulsar astronomy, Cambridge, U.K.: Cambridge University Press.* Pulsar astronomy / Andrew G. Lyne and Francis Graham-Smith. Cambridge, U.K.; New York : Cambridge University Press, 1998. (Cambridge astrophysics series ; 31), 1998.

[42] C. Fryer, W. Benz, M. Herant, and S. A. Colgate. What Can the Accretion-induced Collapse of White Dwarfs Really Explain? *Astrophys. J.*, 516:892, 1999.

[43] B. Aschenbach. Discovery of a young nearby supernova remnant. *Nature*, 396:141, 1998.

[44] S. van den Bergh and G. A. Tammann. Galactic and extragalactic supernova rates. *Ann. Rev. Astron. Astrophys.*, 29:363, 1991.

[45] E. Cappellaro, R. Evans, and M. Turatto. A new determination of supernova rates and a comparison with indicators for galactic star formation. *Astron. Astrophys.*, 351:459, 1999.

[46] G. A. Tammann, W. Loeffler, and A. Schroeder. The Galactic supernova rate. *Astrophys. J. Suppl. Ser.* , 92:487, 1994.

[47] Y.-H. Chu and R. C. Kennicutt, Jr. Environments and populations of supernova remnants in the Large Magellanic Cloud. *Astron. J.*, 96: 1874, 1988.

[48] R. C. Kennicutt, Jr. and P. W. Hodge. H II regions and star formation in the Magellanic Clouds. *Astrophys. J.*, 306:130, 1986.

[49] E. M. Berkhuijsen. Supernova rate and the number of supernova remnants in M31, M33 and the Galaxy. *Astron. Astrophys.*, 140:431, 1984.

[50] S. M. Gordon, R. P. Kirshner, K. S. Long, W. P. Blair, N. Duric, and R. C. Smith. A New Optical Sample of Supernova Remnants in M33. *Astrophys. J. Suppl. Ser.* , 117:89, 1998.

[51] H. A. Thronson, Jr., D. A. Hunter, S. Casey, and D. A. Harper. Submillimeter continuum emission from galaxies - Star formation and the interstellar medium in the local group dwarf IC 10. *Astrophys. J.*, 355:94, 1990.

[52] F. X. Timmes and S. E. Woosley. Gamma-Ray Line Signals from 26Al and 60Fe in the Galaxies of the Local Group. *Astrophys. J. Lett.*, 481: L81, 1997.

[53] S. van den Bergh and R. D. McClure. Rediscussion of extragalactic supernova rates derived from Evans's 1980-1988 observations. *Astrophys. J.*, 425:205, 1994.

[54] E. de Donder and D. Vanbeveren. The galactic evolution of the supernova rates. *New Astronomy*, 8:817, 2003.

[55] B. C. Reed. New Estimates of the Solar-Neighborhood Massive Star Birthrate and the Galactic Supernova Rate. *Astron. J.*, 130:1652, 2005.

[56] H. Navasardyan, A. R. Petrosian, M. Turatto, E. Cappellaro, and J. Boulesteix. Supernovae in isolated galaxies, in pairs and in groups of galaxies. *Mon. Not. R. Astron. Soc.*, 328:1181, 2001.

[57] F. Mannucci, M. Della Valle, N. Panagia, E. Cappellaro, G. Cresci, R. Maiolino, A. Petrosian, and M. Turatto. The supernova rate per unit mass. *Astron. Astrophys.*, 433:807, 2005.

[58] S. van den Bergh. *The Galaxies of the Local Group*. The galaxies of the Local Group, by Sidney Van den Bergh. Published by Cambridge, UK: Cambridge University Press, 2000 Cambridge Astrophysics Series Series, vol no: 35, 2000.

[59] N. Arnaud, M. Barsuglia, M.-A. Bizouard, V. Brisson, F. Cavalier, M. Davier, P. Hello, S. Kreckelbergh, and E. K. Porter. Detection of a close supernova gravitational wave burst in a network of interferometers, neutrino and optical detectors. *Astroparticle Physics*, 21:201, 2004.

[60] R. B. Tully and J. R. Fisher. *Catalog of Nearby Galaxies*. Catalog of Nearby Galaxies, by R. Brent Tully and J. Richard Fisher, pp. 224. Cambridge, UK: Cambridge University Press, April 1988., 1988.

[61] S.-C. Yoon and N. Langer. On the evolution of rapidly rotating massive white dwarfs towards supernovae or collapses. *Astron. Astrophys.*, 435:967, 2005.

[62] F. S. Kitaura, H.-T. Janka, and W. Hillebrandt. Explosions of O-Ne-Mg cores, the Crab supernova, and subluminous type II-P supernovae. *Astron. Astrophys.*, 450:345, 2006.

[63] S. Chandrasekhar. The Dynamical Instability of Gaseous Masses Approaching the Schwarzschild Limit in General Relativity. *Astrophys. J.*, 140:417, 1964.

[64] G. Martínez-Pinedo, M. Liebendörfer, and D. Frekers. Nuclear Input for Core-collapse Models. *astro-ph/0412091*, 2004.

[65] P. Goldreich and S. V. Weber. Homologously collapsing stellar cores. *Astrophys. J.*, 238:991, 1980.

[66] A. Yahil. Self-similar stellar collapse. *Astrophys. J.*, 265:1047, 1983.

[67] K. A. van Riper. General relativistic hydrodynamics and the adiabatic collapse of stellar cores. *Astrophys. J.*, 232:558, 1979.

[68] K. A. van Riper and J. M. Lattimer. Stellar core collapse. I - Infall epoch. *Astrophys. J.*, 249:270, 1981.

[69] K. A. van Riper. Stellar core collapse. II - Inner core bounce and shock propagation. *Astrophys. J.*, 257:793, 1982.

[70] T. A. Thompson, A. Burrows, and P. A. Pinto. Shock Breakout in Core-Collapse Supernovae and Its Neutrino Signature. *Astrophys. J.*, 592: 434, 2003.

[71] W. D. Arnett. Mass Dependence in Gravitational Collapse of Stellar Cores. *Can. J. Phys.*, 45:1621, 1967.

[72] L. Dessart, A. Burrows, E. Livne, and C. D. Ott. Multidimensional Radiation/Hydrodynamic Simulations of Proto-Neutron Star Convection. *Astrophys. J.*, 645:534, 2006.

[73] R. Buras, H.-T. Janka, M. Rampp, and K. Kifonidis. Two-dimensional hydrodynamic core-collapse supernova simulations with spectral neutrino transport. II. Models for different progenitor stars. *Astron. Astrophys.*, 457:281, 2006.

[74] H. A. Bethe and J. R. Wilson. Revival of a stalled supernova shock by neutrino heating. *Astrophys. J.*, 295:14, 1985.

[75] J. R. Wilson. Supernovae and Post-Collapse Behavior. In J. M. Centrella, J. M. Leblanc, and R. L. Bowers, editors, *Numerical Astrophysics*, page 422, 1985.

[76] S. A. Colgate and R. H. White. The Hydrodynamic Behavior of Supernovae Explosions. *Astrophys. J.*, 143:626, 1966.

[77] A. Burrows, J. Hayes, and B. A. Fryxell. On the Nature of Core-Collapse Supernova Explosions. *Astrophys. J.*, 450:830, 1995.

[78] R. Buras, M. Rampp, H.-T. Janka, and K. Kifonidis. Improved Models of Stellar Core Collapse and Still No Explosions: What Is Missing? *Phys. Rev. Lett.*, 90(24):241101, 2003.

[79] H.-T. Janka and E. Müller. Neutrino heating, convection, and the mechanism of Type-II supernova explosions. *Astron. Astrophys.*, 306: 167, 1996.

[80] A. Mezzacappa, A. C. Calder, S. W. Bruenn, J. M. Blondin, M. W. Guidry, M. R. Strayer, and A. S. Umar. An Investigation of Neutrino-driven Convection and the Core Collapse Supernova Mechanism Using Multigroup Neutrino Transport. *Astrophys. J.*, 495:911, 1998.

[81] M. Liebendörfer, O. E. B. Messer, A. Mezzacappa, and W. R. Hix. General Relativistic Simulations of Stellar Core Collapse and Postbounce Evolution with Boltzmann Neutrino Transport. In J. C. Wheeler and H. Martel, editors, *AIP Conf. Proc. 586: 20th Texas Symposium on relativistic astrophysics*, page 472, 2001.

[82] M. Liebendörfer, A. Mezzacappa, F. Thielemann, O. E. Messer, W. R. Hix, and S. W. Bruenn. Probing the gravitational well: No supernova explosion in spherical symmetry with general relativistic Boltzmann neutrino transport. *Phys. Rev. D.*, 63:103004, 2001.

[83] M. Liebendörfer, M. Rampp, H.-T. Janka, and A. Mezzacappa. Supernova Simulations with Boltzmann Neutrino Transport: A Comparison of Methods. *Astrophys. J.*, 620:840, 2005.

[84] M. Rampp and H.-T. Janka. Spherically Symmetric Simulation with Boltzmann Neutrino Transport of Core Collapse and Postbounce Evolution of a 15 M solar mass Star. *Astrophys. J. Lett.*, 539:L33, 2000.

[85] M. Rampp and H.-T. Janka. Radiation hydrodynamics with neutrinos. Variable Eddington factor method for core-collapse supernova simulations. *Astron. Astrophys.*, 396:361, 2002.

[86] R. Buras, M. Rampp, H.-T. Janka, and K. Kifonidis. Two-dimensional hydrodynamic core-collapse supernova simulations with spectral neutrino transport. I. Numerical method and results for a 15 Mò star. *Astron. Astrophys.*, 447:1049, 2006.

[87] R. Walder, A. Burrows, C. D. Ott, E. Livne, I. Lichtenstadt, and M. Jarrah. Anisotropies in the Neutrino Fluxes and Heating Profiles in Two-dimensional, Time-dependent, Multigroup Radiation Hydrodynamics Simulations of Rotating Core-Collapse Supernovae. *Astrophys. J.*, 626:317, 2005.

[88] C. L. Fryer and A. Heger. Core-Collapse Simulations of Rotating Stars. *Astrophys. J.*, 541:1033, 2000.

[89] C. L. Fryer and M. S. Warren. The Collapse of Rotating Massive Stars in Three Dimensions. *Astrophys. J.*, 601:391, 2004.

[90] J. M. Blondin, A. Mezzacappa, and C. DeMarino. Stability of Standing Accretion Shocks, with an Eye toward Core-Collapse Supernovae. *Astrophys. J.*, 584:971, 2003.

[91] H.-T. Janka, R. Buras, F. S. Kitaura Joyanes, A. Marek, M. Rampp, and L. Scheck. Neutrino-driven supernovae: An accretion instability in a nuclear physics controlled environment. *Nuclear Physics A*, 758:19, 2005.

[92] J. M. Blondin and A. Mezzacappa. The Spherical Accretion Shock Instability in the Linear Regime. *Astrophys. J.*, 642:401, 2006.

[93] S. W. Bruenn, C. J. Dirk, A. Mezzacappa, J. C. Hayes, J. M. Blondin, W. R. Hix, and O. E. B. Messer. Modeling core collapse supernovae in 2 and 3 dimensions with spectral neutrino transport. *Journal of Physics Conference Series*, 46:393, 2006.

[94] K. Kotake, N. Ohnishi, and S. Yamada. Gravitational Radiation from Standing Accretion Shock Instability in Core-Collapse Supernovae. *Submitted to Astrophys. J.*, 2006.

[95] E. Müller, M. Rampp, R. Buras, H.-T. Janka, and D. H. Shoemaker. Toward Gravitational Wave Signals from Realistic Core-Collapse Supernova Models. *Astrophys. J.*, 603:221, 2004.

[96] L. Scheck, K. Kifonidis, H.-T. Janka, and E. Müller. Multidimensional supernova simulations with approximative neutrino transport. I. Neutron star kicks and the anisotropy of neutrino-driven explosions in two spatial dimensions. *Astron. Astrophys.*, 457:963, 2006.

[97] T. Foglizzo and M. Tagger. Entropic-acoustic instability in shocked accretion flows. *Astron. Astrophys.*, 363:174, 2000.

[98] T. Foglizzo. Entropic-acoustic instability of shocked Bondi accretion I. What does perturbed Bondi accretion sound like? *Astron. Astrophys.*, 368:311, 2001.

[99] T. Foglizzo. Non-radial instabilities of isothermal Bondi accretion with a shock: Vortical-acoustic cycle vs. post-shock acceleration. *Astron. Astrophys.*, 392:353, 2002.

[100] T. Foglizzo, P. Galletti, and M. Ruffert. A fresh look at the unstable simulations of Bondi-Hoyle-Lyttleton accretion. *Astron. Astrophys.*, 435:397, 2005.

[101] T. Foglizzo, P. Galletti, L. Scheck, and H. . Janka. Instability of a stalled accretion shock: evidence for the advective-acoustic cycle. *accepted to Astrophys. J.*, 2006.

[102] K. Nakazato, K. Sumiyoshi, and S. Yamada. Gravitational Collapse and Neutrino Emission of Population III Massive Stars. *Astrophys. J.*, 645:519, 2006.

[103] Stuart L. Shapiro and Saul A. Teukolsky. Gravitational collapse to neutron stars and black holes: Computer generation of spherical spacetimes. *Astrophys. J.*, 235:199, 1980.

[104] T. Nakamura, K. Oohara, and Y. Kojima. General relativistic collapse to black holes and gravitational waves from black holes. *Prog. Theor. Phys. Suppl.*, 90:1, 1987.

[105] Y.-I. Sekiguchi and M. Shibata. Axisymmetric collapse simulations of rotating massive stellar cores in full general relativity: Numerical study for prompt black hole formation. *Phys. Rev. D.*, 71(8):084013, 2005.

[106] W. R. Hix, O. E. Messer, A. Mezzacappa, M. Liebendörfer, J. Sampaio, K. Langanke, D. J. Dean, and G. Martínez-Pinedo. Consequences of Nuclear Electron Capture in Core Collapse Supernovae. *Phys. Rev. Lett.*, 91(20):201102, 2003.

[107] A. Heger, C. L. Fryer, S. E. Woosley, N. Langer, and D. H. Hartmann. How Massive Single Stars End Their Life. *Astrophys. J.*, 591:288, 2003.

[108] S. E. Woosley. Gamma-ray bursts from stellar mass accretion disks around black holes. *Astrophys. J.*, 405:273, 1993.

[109] A. I. MacFadyen and S. E. Woosley. Collapsars: Gamma-Ray Bursts and Explosions in "Failed Supernovae". *Astrophys. J.*, 524:262, 1999.

[110] C. L. Fryer. Mass Limits For Black Hole Formation. *Astrophys. J.*, 522:413, 1999.

[111] P. Mészáros. Gamma-ray bursts. *Reports of Progress in Physics*, 69:2259, 2006.

[112] J. Petrovic, N. Langer, S.-C. Yoon, and A. Heger. Which massive stars are gamma-ray burst progenitors? *Astron. Astrophys.*, 435:247, 2005.

[113] S. E. Woosley and A. Heger. The Progenitor Stars of Gamma-Ray Bursts. *Astrophys. J.*, 637:914, 2006.

[114] S. . Yoon, N. Langer, and C. Norman. Single star progenitors of long gamma-ray bursts I: Model grids and redshift dependent GRB rate. *submitted to Astron. Astrophys.*, 2006.

[115] B. F. Schutz. *A First Course in General Relativity*. Cambridge University Press, Cambridge UK, 1985.

[116] C. W. Misner, K. S. Thorne, and J. A. Wheeler. *Gravitation*. San Francisco: W.H. Freeman and Co., 1973.

[117] R. Arnowitt, S. Deser, and C. W. Misner. The dynamics of general relativity. In L. Witten, editor, *Gravitation: An Introduction to Current Research*, page 227. J. Wiley, New York, 1962.

[118] J. W. York. Kinematics and dynamics of general relativity. In L. L. Smarr, editor, *Sources of Gravitational Radiation*, page 83. Cambridge University Press, Cambridge, UK, 1979.

[119] A. Lichnerowicz. L'intégration des équations de la gravitation relativiste et la problème des n corps. *J. Math Pures et Appl.*, 23:37, 1944.

[120] T. W. Baumgarte and S. L. Shapiro. Numerical relativity and compact binaries. *Physics Reports*, 376(2):41, 2003.

[121] J. Thornburg. *Numerical Relativity in Black Hole Spacetimes*. PhD thesis, University of British Columbia, Vancouver, British Columbia, 1993.

[122] F. Herrmann. *Evolution and Analysis of Binary Black Hole Spacetimes*. PhD thesis, Universität Potsdam, 2005.

[123] L. Baiotti. *Numerical relativity simulations of non-vacuum spacetimes in three dimensions*. PhD thesis, SISSA International School for Advanced Studies, Trieste, Italy, 2004.

[124] J. W. York. The initial value problem and dynamics. In Nathalie Deruelle and Tsvi Piran, editors, *Gravitational Radiation*, page 175. North-Holland, Amsterdam, 1983.

[125] R. M. Wald. *General Relativity*. The University of Chicago Press, Chicago, 1984.

[126] N. Ó Murchadha and J. W. York. Gravitational energy. *Phys. Rev. D.*, 10:2345–2357, 1974.

[127] G. B. Cook. Initial data for numerical relativity. *Living Rev. Rel.*, 3:5, 2000.

[128] Y. Choquet-Bruhat and James W. York, Jr. The Cauchy problem. In A. Held, editor, *General Relativity and Gravitation*, volume 1, page 99. Plenum, New York, 1980.

[129] Y. Choquet-Bruhat and J. York. Geometrical well posed systems for the Einstein equations. *C. R. Acad. Sc. Paris*, 321:1089, 1995.

[130] H. Friedrich and G. Nagy. The initial boundary value problem for Einstein's vacuum field equations. *Commun. Math. Phys.*, 201:619, 1999.

[131] S. L. Shapiro and S. A. Teukolsky. Relativistic stellar dynamics on the computer. In J. M. Centrella, editor, *Dynamical Spacetimes and Numerical Relativity*, pages 74–100. Cambridge University Press, Cambridge, England, 1986.

[132] L. Smarr and J. York. Radiation gauge in general relativity. *Phys. Rev.D*, 17:1945, 1978.

[133] B. Gustafsson, H.-O. Kreiss, and J. Oliger. *Time dependent problems and difference methods*. Wiley, New York, 1995.

[134] H. Beyer and O. Sarbach. On the well posedness of the Baumgarte-Shapiro-Shibata-Nakamura formulation of Einstein's field equations. *Phys. Rev. D*, 70:104004, 2004.

[135] C. Gundlach and J.M. Martin-Garcia. Symmetric hyperbolic form of systems of second-order evolution equations subject to constraints. *Phys. Rev. D*, 70:044031, 2004.

[136] C. Gundlach and J. M. Martin-Garcia. Symmetric hyperbolicity and consistent boundary conditions for second-order Einstein equations. *Phys. Rev. D*, 70:044032, 2004.

[137] M. Holst, L. Lindblom, R. Owen, H. Pfeiffer, M. Scheel, and L. Kidder. Optimal constraint projection for hyperbolic evolution systems. *Phys. Rev. D*, 70:084017, 2004.

[138] M. Anderson and R. A. Matzner. Extended Lifetime in Computational Evolution of Isolated Black Holes. *gr-qc/0307055*, 2003.

[139] C. Bona and J. Massó. Hyperbolic evolution system for numerical relativity. *Phys. Rev. Lett.*, 68:1097, 1992.

[140] M. Shibata and T. Nakamura. Evolution of three-dimensional gravitational waves: Harmonic slicing case. *Phys. Rev. D*, 52:5428, 1995.

[141] T. W. Baumgarte and S. L. Shapiro. On the numerical integration of Einstein's field equations. *Phys. Rev. D*, 59:024007, 1999.

[142] A. Abrahams, A. Anderson, Y. Choquet-Bruhat, and J. York. A non-strictly hyperbolic system for the Einstein equations with arbitrary lapse and shift. *C.R. Acad. Sci. Paris*, t. 323, Serie II:835, 1996.

[143] O. Sarbach, G. Calabrese, J. Pullin, and M. Tiglio. Hyperbolicity of the BSSN system of Einstein evolution equations. *Phys. Rev. D*, 66: 064002, 2002.

[144] M. Alcubierre, B. Brügmann, T. Dramlitsch, J. A. Font, P. Papadopoulos, E. Seidel, N. Stergioulas, and R. Takahashi. Towards a stable numerical evolution of strongly gravitating systems in general relativity: The conformal treatments. *Phys. Rev. D*, 62:044034, 2000.

[145] M. Shibata. Axisymmetric Simulations of Rotating Stellar Collapse in Full General Relativity. *Prog. Theor. Phys.*, 104:325, 2000.

[146] J. A. Font, T. Goodale, S. Iyer, M. Miller, L. Rezzolla, E. Seidel, N. Stergioulas, W. M. Suen, and M. Tobias. Three-dimensional general relativistic hydrodynamics. II. Long-term dynamics of single relativistic stars. *Phys. Rev. D*, 65:084024, 2002.

[147] J. W. York. Gravitational degrees of freedom and the initial-value problem. *Phys. Rev. Lett.*, 26:1656, 1971.

[148] J. W. York. Role of Conformal Three-Geometry in the Dynamics of Gravitation. *Phys. Rev. Lett.*, 28:1082, 1972.

[149] D. Mihalas and B. Weibel-Mihalas. *Foundations of Radiation Hydrodynamics*. Dover Publications, Mineola, NY, USA, 1999.

[150] P. G. LeFloch. *Hyperbolic Systems of Conservation Laws*. ETH Zürich Lectures in Mathematics. Birkhäuser, Basel, 2002.

[151] E. F. Toro. *Riemann Solvers and Numerical Methods for Fluid Dynamics*. Springer, Berlin, 1999.

[152] R. J. LeVeque. *Finite Volume Methods for Hyperbolic Problems*. Cambridge University Press, Cambridge UK, 2002.

[153] J. M. Martí, J. M. Ibáñez, and J. M. Miralles. Numerical relativistic hydrodynamics: Local characteristic approach. *Phys. Rev. D*, 43:3794, 1991.

[154] J. M. Ibanez, J. M. Marti, J. A. Miralles, and J. V. Romero. Godonov-Type Methods Applied to General Relativistic Stellar Collapse. In R. D'Inverno, editor, *Approaches to Numerical Relativity*, page 223, 1992.

[155] J. V. Romero, J. M. Ibáñez, J. M. Martí, and J. A. Miralles. A new spherically symmetric general relativistic hydrodynamical code. *Astrophys. J.*, 462:839, 1996.

[156] F. Banyuls, J. A. Font, J. M. Ibáñez, J. M. Martí, and J. A. Miralles. Numerical 3+1 general-relativistic hydrodynamics: A local characteristic approach. *Astrophys. J.*, 476:221, 1997.

[157] J. A. Font. Numerical hydrodynamics in general relativity. *Liv. Rev. Relativ.*, 6:4, 2003.

[158] J. A. Font, M. Miller, W. M. Suen, and M. Tobias. Three-dimensional numerical general relativistic hydrodynamics: Formulations, methods, and code tests. *Phys. Rev. D*, 61:044011, 2000.

[159] S. K. Godunov. *Mat. Sb.*, 47:271, 1959. In Russian.

[160] H. Dimmelmeier, J. A. Font, and E. Müller. Relativistic simulations of rotational core collapse I. Methods, initial models, and code tests. *Astron. Astrophys.*, 388:917, 2002.

[161] H. Dimmelmeier, J. Novak, J. A. Font, J. M. Ibáñez, and E. Müller. Combining spectral and shock-capturing methods: A new numerical approach for 3D relativistic core collapse simulations. *Phys. Rev. D.*, 71(6):064023, 2005.

[162] P. Cerdá-Durán, G. Faye, H. Dimmelmeier, J. A. Font, J. M. Ibáñez, E. Müller, and G. Schäfer. CFC+: improved dynamics and gravitational waveforms from relativistic core collapse simulations. *Astron. Astrophys.*, 439:1033, 2005.

[163] L. Baiotti, I. Hawke, P. J. Montero, F. Löffler, L. Rezzolla, N. Stergioulas, J. A. Font, and E. Seidel. Three-dimensional relativistic simulations of rotating neutron star collapse to a kerr black hole. *Phys. Rev. D*, 71:024035, 2005.

[164] M. Shibata. Axisymmetric general relativistic hydrodynamics: Long-term evolution of neutron stars and stellar collapse to neutron stars and black holes. *Phys. Rev. D.*, 67(2):024033, 2003.

[165] J. M. Martí and E. Müller. Numerical hydrodynamics in special relativity. *Living Rev. Rel.*, 6:7, 2003.

[166] L. D. Landau and E. M. Lifshitz. *Fluid Mechanics*. Course of Theoretical Physics. Butterworth-Heinemann, Oxford, 1987.

[167] É. É. Flanagan and S. A. Hughes. The basics of gravitational wave theory. *New Journal of Physics*, 7:204, 2005.

[168] K. S. Thorne. Multipole expansions of gravitational radiation. *Rev. Mod. Phys.*, 52:299, 1980.

[169] K. S. Thorne. In S. W. Hawking and Israel W., editors, *300 hundred years of gravitation*, Cambridge, Massachusets, 1987. Cambridge University Press.

[170] C. D. Ott. Gravitational Waves from Core-Collapse Supernovae. Diploma thesis, Fakultät für Physik und Astronomie, Ruprecht-Karls-Universität Heidelberg, 2003.

[171] L. Blanchet, T. Damour, and G. Schaefer. Post-Newtonian hydrodynamics and post-Newtonian gravitational wave generation for numerical relativity. *Mon. Not. R. Astron. Soc.*, 242:289, 1990.

[172] G. D. Birkhoff. *Relativity and Modern Physics*. Harvard University Press, Cambridge, Mass., U.S.A., 1923.

[173] E. Balbinski, B. F. Schutz, S. Detweiler, and L. Lindblom. The accuracy of the quadrupole approximation for the gravitational radiation from pulsating stars. *Mon. Not. R. Astron. Soc.*, 213:553, 1985.

[174] M. Shibata and Y.-I. Sekiguchi. Gravitational waves from axisymmetrically oscillating neutron stars in general relativistic simulations. *Phys. Rev. D.*, 68(10):104020, 2003.

[175] F. J. Zerilli. Effective potential for even-parity Regge-Wheeler gravitational perturbation equations. *Phys. Rev. Lett.*, 24(13):737, 1970.

[176] V. Moncrief. Gravitational perturbations of spherically symmetric systems. I. the exterior problem. *Annals of Physics*, 88:323, 1974.

[177] A. Abrahams, D. Bernstein, D. Hobill, E. Seidel, and L. Smarr. Numerically generated black hole spacetimes: Interaction with gravitational waves. *Phys. Rev. D*, 45:3544, 1992.

[178] L. S. Finn and C. R. Evans. Determining gravitational radiation from Newtonian self-gravitating systems. *Astrophys. J.*, 351:588, 1990.

[179] K. Kokkotas and B. Schmidt. Quasi-Normal Modes of Stars and Black Holes. *Living Reviews in Relativity*, 2:2, 1999.

[180] A. Abrahams and C. Evans. Reading off gravitational radiation waveforms in numerical relativity calculations: Matching to linearised gravity. *Phys. Rev. D*, 37:318, 1988.

[181] A. Abrahams and C. Evans. Gauge invariant treatment of gravitational radiation near the source: Analysis and numerical simulations. *Phys. Rev. D*, 42:2585, 1990.

[182] L. Smarr. Gauge conditions, radiation formulae and the two black hole collision. In L. Smarr, editor, *Sources of Gravitational Radiation*, page 245. Cambridge University Press, Cambridge, England, 1979.

[183] L. Smarr, A. Čadež, B. DeWitt, and K. R. Eppley. Collision of two black holes: Theoretical framework. *Phys. Rev. D*, 14(10):2443, 1976.

[184] C. Beetle and L. M. Burko. A Radiation Scalar for Numerical Relativity. *Physical Review Letters*, 89(26):A261101, 2002.

[185] A. Nerozzi, C. Beetle, M. Bruni, L. M. Burko, and D. Pollney. Towards a wave-extraction method for numerical relativity. II. The quasi-Kinnersley frame. *Phys. Rev. D.*, 72(2):024014, 2005.

[186] E. Newman and R. Penrose. An approach to gravitational radiation by a method of spin coefficients. *J. Math. Phys.*, 3:566, 1962.

[187] M. Babiuc, B. Szilágyi, I. Hawke, and Y. Zlochower. Gravitational wave extraction based on Cauchy characteristic extraction and characteristic evolution. *Classical and Quantum Gravity*, 22:5089, 2005.

[188] L. Smarr and James W. York, Jr. Kinematical conditions in the construction of spacetime. *Phys. Rev. D*, 17(10):2529, 1978.

[189] S. W. Hawking and G. F. R. Ellis. *The Large Scale Structure of Spacetime*. Cambridge University Press, Cambridge, England, 1973.

[190] S. Chandrasekhar. *The Mathematical Theory of Black Holes*. Oxford University Press, Oxford, England, 1983.

[191] D. R. Fiske, J. G. Baker, J. R. van Meter, D. Choi, and J. M. Centrella. Wave zone extraction of gravitational radiation in three-dimensional numerical relativity. *Phys. Rev. D*, 71:104036, 2005.

[192] U. Sperhake, B. Kelly, P. Laguna, K. L. Smith, and E. Schnetter. Black hole head-on collisions and gravitational waves with fixed mesh-refinement and dynamic singularity excision. *Phys. Rev. D*, 71:124042, 2005.

[193] W. M. Kinnersley. Type D Gravitational Fields. *Ph.D. Thesis*, 1969.

[194] T. Regge and J. Wheeler. Stability of a Schwarzschild singularity. *Phys. Rev.*, 108(4):1063, 1957.

[195] P. Anninos, D. Hobill, E. Seidel, L. Smarr, and W.-M. Suen. Head-on collision of two equal mass black holes. *Phys. Rev. D*, 52(4):2044, 1995.

[196] K. Camarda and E. Seidel. Numerical evolution of dynamic 3D black holes: Extracting waves. *Phys. Rev. D*, 57:R3204, 1998.

[197] K. Camarda and E. Seidel. Three-dimensional simulations of distorted black holes: Comparison with axisymmetric results. *Phys. Rev. D*, 59:064019, 1999.

[198] M. Campanelli, W. Krivan, and C. O. Lousto. The imposition of Cauchy data to the Teukolsky equation II: Numerical comparison with the Zerilli-Moncrief approach to black hole perturbations. *Phys. Rev. D*, 58:024016, 1998.

[199] A. M. Abrahams, L. Rezzolla, M. E. Rupright, A. Anderson, Peter Anninos, Thomas W. Baumgarte, N. T. Bishop, S. R. Brandt, J. C. Browne, K. Camarda, M. W. Choptuik, Gregory B. Cook, R. R. Correll, C. R. Evans, L. S. Finn, G. C. Fox, R. Gómez, T. Haupt, M. F. Huq, L. E. Kidder, S. A. Klasky, P. Laguna, W. Landry, L. Lehner, J. Lenaghan, R. L. Marsa, J. Massó, R. A. Matzner, S. Mitra, P. Papadopoulos, M. Parashar, F. Saied, P. E. Saylor, Mark A. Scheel, E. Seidel, Stuart L. Shapiro, D. Shoemaker, L. Smarr, B. Szilagyi, Saul A. Teukolsky, M. H. P. M. van Putten, P. Walker, J. Winicour, and Jr J. W. York. Gravitational wave extraction and outer boundary conditions by perturbative matching. *Phys. Rev. Lett.*, 80:1812, 1998.

[200] P. Anninos, J. Massó, E. Seidel, W.-M. Suen, and M. Tobias. Dynamics of gravitational waves in 3D: Formulations, methods and tests. *Phys. Rev. D*, 56:842, 1997.

[201] M. Alcubierre, W. Benger, B. Brügmann, G. Lanfermann, L. Nerger, E. Seidel, and R. Takahashi. 3D Grazing Collision of Two Black Holes. *Phys. Rev. Lett.*, 87:271103, 2001.

[202] L. Baiotti, I. Hawke, L. Rezzolla, and E. Schnetter. Gravitational-wave emission from rotating gravitational collapse in three dimensions. *Phys. Rev. Lett.*, 94:131101, 2005.

[203] M. D. Duez, S. L. Shapiro, and H.-J. Yo. Relativistic hydrodynamic evolutions with black hole excision. *Phys. Rev. D.*, 69(10):104016, 2004.

[204] M. Shibata and Y.-I. Sekiguchi. Three-dimensional simulations of stellar core collapse in full general relativity: Nonaxisymmetric dynamical instabilities. *Phys. Rev. D.*, 71(2):024014, 2005.

[205] M. Shibata, K. Taniguchi, and K. Uryū. Merger of binary neutron stars of unequal mass in full general relativity. *Phys. Rev. D.*, 68(8): 084020, 2003.

[206] M. D. Duez, T. W. Baumgarte, S. L. Shapiro, M. Shibata, and K. Uryū. Comparing the inspiral of irrotational and corotational binary neutron stars. *Phys. Rev. D.*, 65(2):024016, 2002.

[207] M. D. Duez, T. W. Baumgarte, and S. L. Shapiro. Computing the complete gravitational wavetrain from relativistic binary inspiral. *Phys. Rev. D.*, 63(8):084030, 2001.

[208] A. Nagar and L. Rezzolla. TOPICAL REVIEW: Gauge-invariant non-spherical metric perturbations of Schwarzschild black-hole spacetimes. *Classical and Quantum Gravity*, 22:167, 2005.

[209] G. Allen. *Cactus Computational Toolkit Thorn Guide for Thorn* EXTRACT. URL `http://www.cactuscode.org`.

[210] E. Schnetter. *Private communiciation*, 2006.

[211] J. Weber. Detection and Generation of Gravitational Waves. *Phys. Rev. Lett.*, 117:306, 1960.

[212] J. Weber. Evidence for Discovery of Gravitational Radiation. *Phys. Rev. Lett.*, 22:1320, 1969.

[213] V. Fafone. Resonant-mass detectors: status and perspectives. *Classical and Quantum Gravity*, 21:377, 2004.

[214] P. Aufmuth and K. Danzmann. Gravitational wave detectors. *N. J. Phys.*, 7:202, 2005.

[215] B. Schutz. Gravitational Wave Astronomy. *Classical and Quantum Gravity*, 16:A131, 1999.

[216] G. E. Moss, L. R. Miller, and R. L. Forward. Photon-noise-limited laser tranducer for gravitational antenna. *Appl. Opt.*, 10:2495, 1971.

[217] R. Weiss. Electromagnetically coupled broadband gravitational antenna. Technical Report 105, Res. Lab. Electron., 1972.

[218] H. Billing, K. Maischberger, A. Ruediger, R. Schilling, L. Schnupp, and W. Winkler. An argon laser interferometer for the detection of gravitational radiation. *Journal of Physics E Scientific Instruments*, 12:1043, 1979.

[219] P. R. Saulson. *Fundamentals of interferometric gravitational wave detectors*. Fundamentals of interferometric gravitational wave detectors, Singapore: World Scientific Publishers, 1994, xvi, 299 p., 1994.

[220] J. Hough and S. Rowan. Gravitational Wave Detection by Interferometry (Ground and Space). *Living Reviews in Relativity*, 3:3, 2000.

[221] A. Abramovici, W. E. Althouse, R. W. P. Drever, Y. Gursel, S. Kawamura, F. J. Raab, D. Shoemaker, L. Sievers, R. E. Spero, and K. S. Thorne. LIGO - The Laser Interferometer Gravitational-Wave Observatory. *Science*, 256:325, 1992.

[222] D. Sigg. Commissioning of LIGO detectors. *Classical and Quantum Gravity*, 21:409, 2004.

[223] B. Willke, P. Aufmuth, C. Aulbert, S. Babak, R. Balasubramanian, B. W. Barr, S. Berukoff, S. Bose, G. Cagnoli, M. M. Casey, D. Churches, D. Clubley, C. N. Colacino, D. R. M. Crooks, C. Cutler, K. Danzmann, R. Davies, R. Dupuis, E. Elliffe, C. Fallnich, A. Freise, S. Goßler, A. Grant, H. Grote, G. Heinzel, A. Heptonstall, M. Heurs, M. Hewitson, J. Hough, O. Jennrich, K. Kawabe, K. Kötter, V. Leonhardt, H. Lück, M. Malec, P. W. McNamara, S. A. McIntosh, K. Mossavi, S. Mohanty, S. Mukherjee, S. Nagano, G. P. Newton, B. J. Owen, D. Palmer, M. A. Papa, M. V. Plissi, V. Quetschke, D. I. Robertson, N. A. Robertson, S. Rowan, A. Rüdiger, B. S. Sathyaprakash, R. Schilling, B. F. Schutz, R. Senior, A. M. Sintes, K. D. Skeldon, P. Sneddon, F. Stief, K. A. Strain, I. Taylor, C. I. Torrie, A. Vecchio, H. Ward, U. Weiland, H. Welling, P. Williams, W. Winkler, G. Woan, and I. Zawischa. The GEO 600 gravitational wave detector . *Classical and Quantum Gravity*, 19:1377, 2002.

[224] J. Smith. Geo600 sensitivity. URL `http://www.geo600.uni-hannover.de/geocurves/`. November 2006.

[225] M. Ando and the TAMA collaboration. Current status of TAMA. *Classical and Quantum Gravity*, 19:1409, 2002.

[226] F. Acernese, P. Amico, N. Arnaud, D. Babusci, R. Barillé, F. Barone, L. Barsotti, M. Barsuglia, F. Beauville, M. A. Bizouard, C. Boccara, F. Bondu, L. Bosi, C. Bradaschia, L. Bracci, S. Braccini, A. Brillet, V. Brisson, L. Brocco, D. Buskulic, G. Calamai, E. Calloni, E. Campagna, F. Cavalier, G. Cella, E. Chassande-Mottin, F. Cleva, T. Cokelaer, G. Conforto, C. Corda, J.-P. Coulon, E. Cuoco, V. Dattilo, M. Davier, R. DeRosa, L. Di Fiore, A. Di Virgilio, B. Dujardin, A. Eleuteri, D. Enard, I. Ferrante, F. Fidecaro, I. Fiori, R. Flaminio, J.-D. Fournier, S. Frasca, F. Frasconi, L. Gammaitoni, A. Gennai, A. Giazotto, G. Giordano, G. Guidi, H. Heitmann, P. Hello, P. Heusse, L. Holloway, S. Kreckelberg, P. La Penna, V. Loriette, M. Loupias, G. Losurdo, J.-M. Mackowski, E. Majorana, C. N. Man, F. Marion, F. Martelli, A. Masserot, L. Massonnet, M. Mazzoni, L. Milano, J. Moreau, F. Moreau, N. Morgado, F. Mornet, B. Mours, J. Pacheco, A. Pai, C. Palomba, F. Paoletti, R. Passaquieti, D. Passuello, B. Perniola, L. Pinard, R. Poggiani, M. Punturo, P. Puppo, K. Qipiani, J. Ramonet, P. Rapagnani, V. Reita, A. Remillieux, F. Ricci, I. Ricciardi, G. Russo, S. Solimeno, R. Stanga, A. Toncelli, M. Tonelli, E. Tournefier, F. Travasso, H. Trinquet, M. Varvella, D. Verkindt, F. Vetrano, O. Veziant, A. Viceré, J.-Y. Vinet, H. Vocca, and M. Yvert. Status of VIRGO. *Classical and Quantum Gravity*, 21:385, 2004.

[227] URL `http://www.ligo.caltech.edu/advLIGO`. Advanced LIGO.

[228] D. Shoemaker. *Private communiciation*, 2006.

[229] URL `http://lisa.jpl.nasa.gov`. LISA.

[230] A. Einstein and N. Rosen. On gravitational waves. *J. Franklin Inst.*, 223:43, 1937.

[231] C. M. De Witt. *Conference on the Role of Gravitation in Physics*. proceedings of conference at Chapel Hill, North Carolina, January 18-23, 1957. Wright Air Development Center technical report 57-126, United States Air Fors, Wright-Patterson Air Force Base, Ohio, USA., 1957.

[232] H. Bondi. Plane Graviatiational Waves in General Relativity. *Nature*, 179:1072, 1957.

[233] H. Bondi, M. G. J. van der Burg, and A. W. K. Metzner. Gravitational waves in general relativity VII. Waves from axi-symmetric isolated systems. *Proc. R. Soc. London*, A269:21, 1962.

[234] R. K. Sachs. Gravitational waves in general relativity VIII. Waves in asymptotically flat space-time. *Proc. Roy. Soc. London*, A270:103, 1962.

[235] D. Kennefick. *Controversies in the History of the Radiation Reaction Problem in General Relativity*, page 207. The Expanding Worlds of General Relativity, 1999.

[236] W. H. Press and K. S. Thorne. Gravitational-Wave Astronomy. *Ann. Rev. Astron. Astrophys.*, 10:335, 1972.

[237] J. Weber. Observation of the Thermal Fluctuations of a Gravitational-Wave Detector. *Phys. Rev. Lett.*, 17:1228, 1966.

[238] M. Bartusiak. *Einstein's unfinished symphony : listening to the sounds of space-time*, page 90. National Academy Press, Washington DC., 2000.

[239] F. J. Dyson. *Private communication*, 2006.

[240] C. Fryer and K. C. B. New. Gravitational waves from gravitational collapse. *Living Rev. Relativity*, 6:2, 2003.

[241] K. Kotake, K. Sato, and K. Takahashi. Explosion mechanism, neutrino burst and gravitational wave in core-collapse supernovae. *Reports of Progress in Physics*, 69:971, 2006.

[242] K. D. Kokkotas and N. Stergioulas. Gravitational Waves from Compact Sources. *gr-qc/0506083*, 2005.

[243] R. Ruffini and J. A. Wheeler. Relativistic Cosmology and Space Platforms. In V. Hardy and H. Moore, editors, *Proceedings of the Conference on Space Physics, ESRO, Paris, France*, page 45, 1971.

[244] T. X. Thuan and J. P. Ostriker. Gravitational Radiation from Stellar Collapse. *Astrophys. J. Lett.*, 191:L105, 1974.

[245] I. D. Novikov. Gravitational radiation from a star that is contracting into a disk. *Soviet Astron.*, 52:657, 1975.

[246] S. L. Shapiro. Gravitational radiation from stellar collapse - The initial burst. *Astrophys. J.*, 214:566, 1977.

[247] R. Epstein. *The post-Newtonian theory of the generation of gravitational radiation and its application to stellar collapse*. PhD thesis, Stanford University, Stanford, USA, 1976.

[248] R. A. Saenz and S. L. Shapiro. Gravitational radiation from stellar collapse – Ellipsoidal models. *Astrophys. J.*, 221:286, 1978.

[249] R. A. Saenz and S. L. Shapiro. Gravitational and neutrino radiation from stellar core collapse – Improved ellipsoidal model calculations. *Astrophys. J.*, 229:1107, 1979.

[250] R. A. Saenz and S. L. Shapiro. Gravitational radiation from stellar core collapse. III – Damped ellipsoidal oscillations. *Astrophys. J.*, 244: 1033, 1981.

[251] V. Moncrief. Gravitational radiation from the homologous oscillation of compressible Newtonian spheroids. *Astrophys. J.*, 234:628, 1979.

[252] S. Detweiler and L. Lindblom. On the evolution of the homogeneous ellipsoidal figures. II - Gravitational collapse and gravitational radiation. *Astrophys. J.*, 250:739, 1981.

[253] M. S. Turner and R. V. Wagoner. Gravitational radiation from slowly-rotating 'supernovae' - Preliminary results. In L. L. Smarr, editor, *Sources of Gravitational Radiation*, page 383, 1979.

[254] K. A. van Riper. The hydrodynamics of stellar collapse. *Astrophys. J.*, 221:304, 1978.

[255] J. R. Wilson. Unpublished work. 1977.

[256] E. Seidel and T. Moore. Gravitational radiation from realistic relativistic stars: Odd-parity fluid perturbations. *Phys. Rev. D.*, 35:2287, 1987.

[257] H. E. Seidel. Perturbation methods for the calculation of gravitational waves from slightly non-spherical spacetimes with applications to stellar core collapse. *Ph.D. Thesis*, 1988.

[258] E. Seidel, E. S. Myra, and T. Moore. Gravitational radiation from type-II supernovae: The effect of the high-density equation of state. *Phys. Rev. D.*, 38:2349, 1988.

[259] E. Seidel. Gravitational radiation from even-parity perturbations of stellar collapse: Mathematical formalism and numerical methods. *Phys. Rev. D.*, 42:1884, 1990.

[260] E. Müller. Gravitational radiation from collapsing rotating stellar cores. *Astron. Astrophys.*, 114:53, 1982.

[261] E. Müller and W. Hillebrandt. The collapse of rotating stellar cores. *Astron. Astrophys.*, 103:358, 1981.

[262] L. S. Finn. *in Frontiers in Numerical Relativity, ed. C. R. Evans, L. S. Finn, & D. W. Hobill*, page 126. Cambridge University Press, Cambridge, U. K., 1989.

[263] R. Mönchmeyer. *PhD Thesis, unpublished*. PhD thesis, Technische Universität München, 1990.

[264] S. Bonazzola and J. A. Marck. Efficiency of gravitational radiation from axisymmetric and 3 D stellar collapse. I - Polytropic case. *Astron. Astrophys.*, 267:623, 1993.

[265] A. Burrows and J. Hayes. Pulsar Recoil and Gravitational Radiation Due to Asymmetrical Stellar Collapse and Explosion. *Phys. Rev. Lett.*, 76:352, 1996.

[266] S. Yamada and K. Sato. Gravitational Radiation from Rotational Collapse of a Supernova Core. *Astrophys. J.*, 450:245, 1995.

[267] M. Rampp, E. Müller, and M. Ruffert. Simulations of non-axisymmetric rotational core collapse. *Astron. Astrophys.*, 332:969, 1998.

[268] J. D. Brown. Rotational Instabilities in post-Collapse Stellar Cores. In *AIP Conf. Proc. 575: Astrophysical Sources for Ground-Based Gravitational Wave Detectors*, page 234, 2001.

[269] F. Siebel, J. A. Font, E. Müller, and P. Papadopoulos. Axisymmetric core collapse simulations using characteristic numerical relativity. *Phys. Rev. D.*, 67(12):124018, 2003.

[270] C.L. Fryer, D.E. Holz, and S.A. Hughes. Gravitational Wave Emission from Core Collapse of Massive Stars. *Astrophys. J.*, 565:430, 2002.

[271] C. L. Fryer, D. E. Holz, and S. A. Hughes. Gravitational Waves from Stellar Collapse: Correlations to Explosion Asymmetries. *Astrophys. J.*, 609:288, 2004.

[272] K. Kotake, S. Yamada, and K. Sato. Anisotropic Neutrino Radiation in Rotational Core Collapse. *Astrophys. J.*, 595:304, 2003.

[273] C. D. Ott, A. Burrows, T. A. Thompson, E. Livne, and R. Walder. The Spin Periods and Rotational Profiles of Neutron Stars at Birth. *Astrophys. J. Suppl. Ser.* , 164:130, 2006.

[274] K. Kotake, S. Yamada, K. Sato, K. Sumiyoshi, H. Ono, and H. Suzuki. Gravitational radiation from rotational core collapse: Effects of magnetic fields and realistic equations of state. *Phys. Rev. D.*, 69(12):124004, 2004.

[275] S. Yamada and H. Sawai. Numerical Study on the Rotational Collapse of Strongly Magnetized Cores of Massive Stars. *Astrophys. J.*, 608: 907, 2004.

[276] M. Obergaulinger, M. A. Aloy, and E. Müller. Axisymmetric simulations of magneto-rotational core collapse: dynamics and gravitational wave signal. *Astron. Astrophys.*, 450:1107, 2006.

[277] M. Obergaulinger, M. A. Aloy, H. Dimmelmeier, and E. Müller. Axisymmetric simulations of magnetorotational core collapse: Approximate inclusion of general relativistic effects. *Astron. Astrophys.submitted*, 2006.

[278] M. Shibata, Y. T. Liu, S. L. Shapiro, and B. C. Stephens. Magnetorotational collapse of massive stellar cores to neutron stars: Simulations in full general relativity. *astro-ph/0610840, Phys. Rev. D.accepted*, 2006.

[279] M. Herant, W. Benz, W. R. Hix, C. L. Fryer, and S. A. Colgate. Inside the supernova: A powerful convective engine. *Astrophys. J.*, 435:339, 1994.

[280] J. M. Lattimer and T. J. Mazurek. Leptonic overturn and shocks in collapsing stellar cores. *Astrophys. J.*, 246:955, 1981.

[281] R. Epstein. The generation of gravitational radiation by escaping supernova neutrinos. *Astrophys. J.*, 223:1037, 1978.

[282] R. I. Epstein. Lepton-driven convection in supernovae. *Mon. Not. R. Astron. Soc.*, 188:305, 1979.

[283] V. B. Braginskii and K. S. Thorne. Gravitational-wave bursts with memory and experimental prospects. *Nature*, 327:123, 1987.

[284] E. Müller and H.-T. Janka. Gravitational radiation from convective instabilities in Type II supernova explosions. *Astron. Astrophys.*, 317: 140, 1997.

[285] S. Chandrasekhar. *Ellipsoidal Figures of Equilibrium*. Yale University Press, New Haven, USA, 1969. revised edition 1987.

[286] N. Andersson. TOPICAL REVIEW: Gravitational waves from instabilities in relativistic stars. *Classical and Quantum Gravity*, 20:105, 2003.

[287] P. H. Roberts and K. Stewartson. On the Stability of a Maclaurin Spheroid of Small Viscosity. *Astrophys. J.*, 137:777, 1963.

[288] L. Lindblom and S. L. Detweiler. On the secular instabilities of the Maclaurin spheroids. *Astrophys. J.*, 211:565, 1977.

[289] J. L. Friedman and B. F. Schutz. Secular instability of rotating Newtonian stars. *Astrophys. J.*, 222:281, 1978.

[290] S. Chandrasekhar. The Effect of Gravitational Radiation on the Secular Stability of the Maclaurin Spheroid. *Astrophys. J.*, 161:561, 1970.

[291] D. Lai. Secular Bar-Mode Evolution and Gravitational Waves from Neutron Stars. In J. M. Centrella, editor, *AIP Conf. Proc. 575: Astrophysical Sources for Ground-Based Gravitational Wave Detectors*, page 246, 2001.

[292] Y. T. Liu and L. Lindblom. Models of rapidly rotating neutron stars: remnants of accretion-induced collapse. *Mon. Not. R. Astron. Soc.*, 324:1063, 2001.

[293] Y. T. Liu. Dynamical instability of new-born neutron stars as sources of gravitational radiation. *Phys. Rev. D.*, 65(12):124003, 2002.

[294] J. N. Imamura and R. H. Durisen. The Dominance of Dynamic Barlike Instabilities in the Evolution of a Massive Stellar Core Collapse That "Fizzles". *Astrophys. J.*, 549:1062, 2001.

[295] J. N. Imamura, B. K. Pickett, and R. H. Durisen. The Nonlinear Evolution of Massive Stellar Core Collapses That "Fizzle". *Astrophys. J.*, 587:341, 2003.

[296] J. N. Imamura and R. H. Durisen. f-Mode Secular Instabilities in Deleptonizing Fizzlers. *Astrophys. J.*, 616:1095, 2004.

[297] D. Lai and S. L. Shapiro. Gravitational radiation from rapidly rotating nascent neutron stars. *Astrophys. J.*, 442:259, 1995.

[298] J. R. Ipser and R. A. Managan. On the emission of gravitational radiation from inhomogeneous Jacobi configurations. *Astrophys. J.*, 282: 287, 1984.

[299] J. L. Houser, J. M. Centrella, and S. C. Smith. Gravitational radiation from nonaxisymmetric instability in a rotating star. *Physical Review Letters*, 72:1314, 1994.

[300] L. Baiotti, R. De Pietri, G. M. Manca, and L. Rezzolla. Accurate simulations of the dynamical barmode instability in full General Relativity. *Phys. Rev. D.submitted*, 2006.

[301] S. Ou, J. E. Tohline, and L. Lindblom. Nonlinear Development of the Secular Bar-Mode Instability in Rotating Neutron Stars. *Astrophys. J.*, 617:490, 2004.

[302] M. Shibata, T. W. Baumgarte, and S. L. Shapiro. The Bar-Mode Instability in Differentially Rotating Neutron Stars: Simulations in Full General Relativity. *Astrophys. J.*, 542:453, 2000.

[303] M. Saijo. Dynamical bar instability in a relativistic rotational core collapse. *Phys. Rev. D.*, 71(10):104038, 2005.

[304] M. Saijo, M. Shibata, T. W. Baumgarte, and S. L. Shapiro. Dynamical bar instability in rotating stars: Effect of general relativity. *Astrophys. J.*, 548:919, 2001.

[305] N. Stergioulas and J. L. Friedman. Nonaxisymmetric Neutral Modes in Rotating Relativistic Stars. *Astrophys. J.*, 492:301, 1998.

[306] K. C. B. New, J. M. Centrella, and J. E. Tohline. Gravitational waves from long-duration simulations of the dynamical bar instability. *Phys. Rev. D.*, 62(6):064019, 2000.

[307] J. D. Brown. Gravitational waves from the dynamical bar instability in a rapidly rotating star. *Phys. Rev. D.*, 62(8):084024, 2000.

[308] M. Shibata, S. Karino, and Y. Eriguchi. Dynamical instability of differentially rotating stars. *Mon. Not. R. Astron. Soc.*, 334:L27, 2002.

[309] M. Shibata, S. Karino, and Y. Eriguchi. Dynamical bar-mode instability of differentially rotating stars: effects of equations of state and velocity profiles. *Mon. Not. R. Astron. Soc.*, 343:619, 2003.

[310] M. Shibata and S. Karino. Numerical evolution of secular bar-mode instability induced by the gravitational radiation reaction in rapidly rotating neutron stars. *Phys. Rev. D.*, 70(8):084022, 2004.

[311] S. Karino and Y. Eriguchi. Linear Stability Analysis of Differentially Rotating Polytropes: New Results for the m=2 f-Mode Dynamical Instability. *Astrophys. J.*, 592:1119, 2003.

[312] N. Stergioulas. Rotating stars in relativity. *Living Rev. Relativity*, 6:3, 2003.

[313] J. E. Tohline. The collapse of rotating stellar cores - Equilibria between white dwarf and neutron star densities. *Astrophys. J.*, 285:721, 1984.

[314] S. T. Shapiro and A. P. Lightman. Rapidly rotating, post-Newtonian neutron stars. *Astrophys. J.*, 207:263, 1976.

[315] Y. Eriguchi and E. Mueller. Equilibrium models of differentially rotating polytropes and the collapse of rotating stellar cores. *Astron. Astrophys.*, 147:161, 1985.

[316] A. Hayashi, Y. Eriguchi, and M.-A. Hashimoto. On the Possibility of the Nonexplosive Core Contraction of Massive Stars: New Evolutionary Paths from Rotating White Dwarfs to Rotating Neutron Stars. *Astrophys. J.*, 492:286, 1998.

[317] A. Hayashi, Y. Eriguchi, and M.-A. Hashimoto. On the Possibility of the Nonexplosive Core Contraction of Massive Stars. II. General Relativistic Analysis. *Astrophys. J.*, 521:376, 1999.

[318] L. Villain, J. A. Pons, P. Cerdá-Durán, and E. Gourgoulhon. Evolutionary sequences of rotating protoneutron stars. *Astron. Astrophys.*, 418:283, 2004.

[319] Wikipedia. Normal modes. URL `http://en.wikipedia.org/wiki/Normal_mode`. November 2006.

[320] L. Villain and S. Bonazzola. Inertial modes in slowly rotating stars: An evolutionary description. *Phys. Rev. D.*, 66(12):123001, 2002.

[321] K. D. Kokkotas and B. F. Schutz. W-modes - A new family of normal modes of pulsating relativistic stars. *Mon. Not. R. Astron. Soc.*, 255: 119, 1992.

[322] N. Stergioulas, T. A. Apostolatos, and J. A. Font. Non-linear pulsations in differentially rotating neutron stars: mass-shedding-induced damping and splitting of the fundamental mode. *Mon. Not. R. Astron. Soc.*, 352:1089, 2004.

[323] H. Dimmelmeier, N. Stergioulas, and J. A. Font. Non-linear axisymmetric pulsations of rotating relativistic stars in the conformal flatness approximation. *Mon. Not. R. Astron. Soc.*, 368:1609, 2006.

[324] N. Andersson, K. D. Kokkotas, and B. F. Schutz. A new numerical approach to the oscillation modes of relativistic stars. *Mon. Not. R. Astron. Soc.*, 274:1039, 1995.

[325] K. S. Thorne and A. Campolattaro. Non-Radial Pulsation of General-Relativistic Stellar Models. I. Analytic Analysis for L $\geq$ 2. *Astrophys. J.*, 149:591, 1967.

[326] R. Price and K. S. Thorne. Non-Radial Pulsation of General-Relativistic Stellar Models. II. Properties of the Gravitational Waves. *Astrophys. J.*, 155:163, 1969.

[327] K. S. Thorne. Nonradial Pulsation of General-Relativistic Stellar Models. III. Analytic and Numerical Results for Neutron Stars. *Astrophys. J.*, 158:1, 1969.

[328] K. S. Thorne. Nonradial Pulsation of General-Relativistic Stellar Models.IV. The Weakfield Limit. *Astrophys. J.*, 158:997, 1969.

[329] A. Campolattaro and K. S. Thorne. Nonradial Pulsation of General-Relativistic Stellar Models. V. Analytic Analysis for L = 1. *Astrophys. J.*, 159:847, 1970.

[330] J. R. Ipser and K. S. Thorne. Nonradial Pulsation of General-Relativistic Stellar Models.VI. Corrections. *Astrophys. J.*, 181:181, 1973.

[331] S. L. Detweiler and J. R. Ipser. A Variational Principle and a Stability Criterion for the Non-Radial Modes of Pulsation of Stellar Models in General Relativity. *Astrophys. J.*, 185:685, 1973.

[332] S. L. Detweiler. A variational principle and a stability criterion for the dipole modes of pulsation of stellar models in general relativity. *Astrophys. J.*, 201:440, 1975.

[333] S. L. Detweiler. A variational calculation of the fundamental frequencies of quadrupole pulsation of fluid spheres in general relativity. *Astrophys. J.*, 197:203, 1975.

[334] L. Lindblom and S. L. Detweiler. The quadrupole oscillations of neutron stars. *Astrophys. J. Suppl. Ser.* , 53:73, 1983.

[335] P. N. McDermott, H. M. van Horn, and J. F. Scholl. Nonradial g-mode oscillations of warm neutron stars. *Astrophys. J.*, 268:837, 1983.

[336] P. N. McDermott, H. M. van Horn, C. J. Hansen, and R. Buland. The nonradial oscillation spectra of neutron stars. *Astrophys. J. Lett.*, 297: L37, 1985.

[337] P. N. McDermott, H. M. van Horn, and C. J. Hansen. Nonradial oscillations of neutron stars. *Astrophys. J.*, 325:725, 1988.

[338] N. Andersson, Y. Kojima, and K. D. Kokkotas. On the Oscillation Spectra of Ultracompact Stars: an Extensive Survey of Gravitational-Wave Modes. *Astrophys. J.*, 462:855, 1996.

[339] G. Allen, N. Andersson, K. D. Kokkotas, and B. F. Schutz. Gravitational waves from pulsating stars: Evolving the perturbation equations for a relativistic star. *Phys. Rev. D.*, 58(12):124012, 1998.

[340] N. Andersson and K. D. Kokkotas. Towards gravitational wave asteroseismology. *Mon. Not. R. Astron. Soc.*, 299:1059, 1998.

[341] K. D. Kokkotas, T. A. Apostolatos, and N. Andersson. The inverse problem for pulsating neutron stars: a 'fingerprint analysis' for the supranuclear equation of state. *Mon. Not. R. Astron. Soc.*, 320:307, 2001.

[342] O. Benhar, V. Ferrari, and L. Gualtieri. Gravitational wave asteroseismology reexamined. *Phys. Rev. D.*, 70(12):124015, 2004.

[343] V. Ferrari, G. Miniutti, and J. A. Pons. Gravitational waves from newly born, hot neutron stars. *Mon. Not. R. Astron. Soc.*, 342:629, 2003.

[344] L. Gualtieri, J. A. Pons, Miniutti, and G. Nonadiabatic oscillations of compact stars in general relativity. *Phys. Rev. D.*, 70(8):084009, 2004.

[345] V. Ferrari, L. Gualtieri, J. A. Pons, and A. Stavridis. Rotational effects on the oscillation frequencies of newly born proto-neutron stars. *Mon. Not. R. Astron. Soc.*, 350:763, 2004.

[346] V. Ferrari, L. Gualtieri, J. A. Pons, and A. Stavridis. Gravitational waves from rotating proto-neutron stars. *Classical and Quantum Gravity*, 21:515, 2004.

[347] V. Ferrari, G. Miniutti, and J. A. Pons. Gravitational waves from neutron stars at different evolutionary stages. *Classical and Quantum Gravity*, 20:841, 2003.

[348] G. Miniutti, J. A. Pons, E. Berti, L. Gualtieri, and V. Ferrari. Non-radial oscillation modes as a probe of density discontinuities in neutron stars. *Mon. Not. R. Astron. Soc.*, 338:389, 2003.

[349] J. A. Font, H. Dimmelmeier, A. Gupta, and N. Stergioulas. Axisymmetric modes of rotating relativistic stars in the Cowling approximation. *Mon. Not. R. Astron. Soc.*, 325:1463, 2001.

[350] A. Passamonti, M. Bruni, L. Gualtieri, and C. F. Sopuerta. Coupling of radial and nonradial oscillations of relativistic stars: Gauge-invariant formalism. *Phys. Rev. D.*, 71(2):024022, 2005.

[351] D. M. Eardley. Theoretical models for sources of gravitational waves. In N. Deruelle and T. Piran, editors, *Gravitational Radiation*, page 257, Amsterdam, 1983. North-Holland.

[352] E. N. Glass and L. Lindblom. The radial oscillations of neutron stars. *Astrophys. J. Suppl. Ser.* , 53:93, 1983.

[353] J. M. Marti, J. A. Miralles, and J. M. Ibanez. Radial oscillations of warm cores in neutron stars. *Astroph. & Space Sc.*, 139:93, 1987.

[354] U. Sperhake, P. Papadopoulos, and N. Andersson. Non-linear radial oscillations of neutron stars: Mode-coupling results. *astro-ph/0110487*, 2001.

[355] N. Andersson. A New Class of Unstable Modes of Rotating Relativistic Stars. *Astrophys. J.*, 502:708, 1998.

[356] J. L. Friedman and S. M. Morsink. Axial Instability of Rotating Relativistic Stars. *Astrophys. J.*, 502:714, 1998.

[357] N. Andersson, K. D. Kokkotas, and V. Ferrari. The R-Mode Instability in Rotating Neutron Stars. *Int. J. Mod. Phys. D*, 10:381, 2001.

[358] L. Lindblom, B. J. Owen, and S. M. Morsink. Gravitational Radiation Instability in Hot Young Neutron Stars. *Physical Review Letters*, 80: 4843, 1998.

[359] B. J. Owen, L. Lindblom, C. Cutler, B. F. Schutz, A. Vecchio, and N. Andersson. Gravitational waves from hot young rapidly rotating neutron stars. *Phys. Rev. D.*, 58(8):084020, 1998.

[360] L. Lindblom, J. E. Tohline, and M. Vallisneri. Nonlinear Evolution of the r-Modes in Neutron Stars. *Phys. Rev. Lett.*, 86:1152, 2001.

[361] L. Lindblom, J. E. Tohline, and M. Vallisneri. Numerical evolutions of nonlinear r-modes in neutron stars. *Phys. Rev. D.*, 65(8):084039, 2002.

[362] N. Stergioulas and J. A. Font. Nonlinear r-Modes in Rapidly Rotating Relativistic Stars. *Physical Review Letters*, 86:1148, 2001.

[363] P. Arras, E. E. Flanagan, S. M. Morsink, A. K. Schenk, S. A. Teukolsky, and I. Wasserman. Saturation of the r-Mode Instability. *Astrophys. J.*, 591:1129–1151, 2003.

[364] A. K. Schenk, P. Arras, É. É. Flanagan, S. A. Teukolsky, and I. Wasserman. Nonlinear mode coupling in rotating stars and the r-mode instability in neutron stars. *Phys. Rev. D.*, 65(2):024001, 2002.

[365] P. Gressman, L.-M. Lin, W.-M. Suen, N. Stergioulas, and J. L. Friedman. Nonlinear r-modes in neutron stars: Instability of an unstable mode. *Phys. Rev. D.*, 66(4):041303, 2002.

[366] URL `http://www.cactuscode.org/`. Cactus Computational Toolkit home page.

[367] T. Goodale, G. Allen, G. Lanfermann, J. Massó, T. Radke, E. Seidel, and J. Shalf. The Cactus framework and toolkit: Design and applications. In *Vector and Parallel Processing - VECPAR'2002, 5th International Conference, Lecture Notes in Computer Science*, Berlin, 2003. Springer. URL `http://www.cactuscode.org`.

[368] *CactusEinstein Arrangement*. URL `http://www.cactuscode.org`.

[369] URL `http://www.gnu.org/copyleft/lesser.html`. GPL: the GNU Lesser General Public License.

[370] James M. Hyman. The method of lines solution of partial differential equations. Technical Report COO-3077-139, ERDA Mathematics and Computing Laboratory, Courant Institute of Mathematical Sciences, New York University, 1976.

[371] James M. Hyman. A method of lines approach to the numerical solution of conservation laws. Technical Report LA-UR 79-837, Los Alamos National Laboratory, 1979. submitted to Third IMACS International Symposium on Computer Methods for Partial Differential Equations, 20-22 June 1979, Lehigh University, Bethlehem PA 18015, USA.

[372] James M. Hyman. Numerical methodologies for solving partial differential equations. In J. R. Buchler, editor, *NATO Advanced Research Workshop on the Numerical Modeling of Nonlinear Stellar Pulsations: Problems and Prospects*, pages 215–237. Kluwer, Dordrecht, 1989. Also available as Los Alamos National Laboratories Report LA-UR 89-3136.

[373] C. W. Shu and S. J. Osher. Efficient implementation of essentially non-oscillatory shock-capturing schmes, ii. *J. Comput. Phys.*, 83:32, 1989.

[374] C. W. Shu. High Order ENO and WENO Schemes for Computational Fluid Dynamics. In T. J. Barth and H. Deconinck, editors, *High-Order Methods for Computational Physics*. Springer, 1999.

[375] R. Courant, K.O. Friedrichs, and H. Lewy. Über die partiellen Differenzengleichungen der mathematischen Physik. *Math. Ann.*, 100:32, 1928.

[376] B. Gustafsson. On the implementation of boundary conditions for the method of lines. *BIT*, 38(2):293, 1998.

[377] S. Teukolsky. On the stability of the iterated crank-nicholson method in numerical relativity. *Phys. Rev. D*, 61:087501, 2000.

[378] G. Leiler and L. Rezzolla. Iterated Crank-Nicolson method for hyperbolic and parabolic equations in numerical relativity. *Phys. Rev. D.*, 73(4):044001, 2006.

[379] A. Harten. High resolution schemes for hyperbolic conservation laws. *J. Comput. Phys.*, 49:357, 1983.

[380] S. Gottlieb and C. Shu. Total Variation Diminishing Runge-Kutta schemes. *Math. Comp.*, 67:73, 1998.

[381] M. Shibata. Collapse of rotating supramassive neutron stars to black holes: Fully general relativistic simulations. *Astrophys. J.*, 595:992, 2003.

[382] J. Thornburg. A fast apparent-horizon finder for 3-dimensional Cartesian grids in numerical relativity. *Class. Quantum Grav.*, 21(2):743, 2004.

[383] G. Nagy, O. E. Ortiz, and O. A. Reula. Strongly hyperbolic second order Einstein's evolution equations. *Phys. Rev. D*, 70:044012, 2004.

[384] B.. Reimann. *Gauge Conditions in Numerical Relativity*. PhD thesis, Universität Potsdam, 2006.

[385] P. Anninos, G. Daues, J. Massó, E. Seidel, and W.-M. Suen. Singularity avoidance in numerical black hole spacetimes. In R. T. Jantzen, G. M. Keiser, and R. Ruffini, editors, *The Seventh Marcel Grossmann Meeting: On Recent Developments in Theoretical and Experimental General Relativity, Gravitation, and Relativistic Field Theories*, page 637, Singapore, 1996. World Scientific.

[386] C. Bona, J. Massó, E. Seidel, and J. Stela. New Formalism for Numerical Relativity. *Phys. Rev. Lett.*, 75:600, 1995.

[387] M. Alcubierre. Hyperbolic slicings of spacetime: singularity avoidance and gauge shocks. *Class. Quantum Grav.*, 20(4):607, 2003.

[388] D. Bernstein. *A Numerical Study of the Black Hole Plus Brill Wave Spacetime*. PhD thesis, University of Illinois Urbana-Champaign, 1993.

[389] M. Alcubierre, B. Brügmann, P. Diener, M. Koppitz, D. Pollney, E. Seidel, and R. Takahashi. Gauge conditions for long-term numerical black hole evolutions without excision. *Phys. Rev. D*, 67:084023, 2003.

[390] A. P. Barnes, P. G. Lefloch, B. G. Schmidt, and J. M. Stewart. The Glimm scheme for perfect fluids on plane-symmetric Gowdy spacetimes. *Classical and Quantum Gravity*, 21:5043, 2004.

[391] E. Schnetter, S. H. Hawley, and I. Hawke. Evolutions in 3D numerical relativity using fixed mesh refinement. *Class. Quantum Grav.*, 21(6): 1465, 2004.

[392] H.-O. Kreiss and J. Oliger. Methods for the approximate solution of time dependent problems. *Global atmospheric research programme publications series*, 10, 1973.

[393] O. Rinne. *Axisymmetric Numerical Relativity*. PhD thesis, University of Cambridge, Cambridge, United Kingdom, 2006.

[394] M. J. Berger and J. Oliger. Adaptive mesh refinement for hyperbolic partial differential equations. *J. Comput. Phys.*, 53:484, 1984.

[395] M.J. Berger and P. Colella. Local adaptive mesh refinement for shock hydrodynamics. *J. Comput. Phys.*, 82:64, 1989.

[396] T. Plewa. URL `http://flash.uchicago.edu/~tomek/AMR`.

[397] E. Schnetter et al. Mesh Refinement with Carpet. URL `http://www.carpetcode.org/`.

[398] MPI. The message passing interface (mpi) standard. URL `http://www.ncs.anl.gov/mpi/`.

[399] URL `http://www-unix.mcs.anl.gov/mpi/mpich/`. MPICH: ANL/MSU MPI implementation.

[400] G. Burns, R. Daoud, and J. Vaigl. LAM: An Open Cluster Environment for MPI. In *Proceedings of Supercomputing Symposium*, page 379, 1994. URL `http://www.lam-mpi.org/download/files/lam-papers.tar.gz`.

[401] URL `http://www.cactuscode.org/Benchmarks`. Cactus Computational Toolkit home page, Benchmarks.

[402] J. J. Quirk. *An Adaptive Grid Algorithm for Computational Shock Hydrodynamics*. PhD thesis, Cranfield Institute of Technolog, 1991.

[403] European Union Research Training Network on Sources of Gravitational Waves, http://www.eu-network.org.

[404] B. Zink, N. Stergioulas, I. Hawke, C. D. Ott, E. Schnetter, and E. Müller. Formation of Supermassive Black Holes through Fragmentation of Torodial Supermassive Stars. *Phys. Rev. Lett.*, 96(16):161101, 2006.

[405] F. Löffler. *Numerical Simulations of Neutron Star-Black Hole Mergers*. PhD thesis, Universität Potsdam, 2006.

[406] I. Hawke, F. Löffler, and A. Nerozzi. Excision methods for high resolution shock capturing schemes applied to general relativistic hydrodynamics. *Phys. Rev. D.*, 71(10):104006, 2005.

[407] B. Einfeldt. On Godunov-type methods for gas dynamics. *SIAM J. Numer. Anal.*, **25**:294, 1988.

[408] A. Kurganov and E. Tadmor. New High-Resolution Central Schemes for Nonlinear Conservation Laws and Convection-Diffusion Equations. *J. Comput. Phys.*, 160:241, 2000.

[409] A. Lucas-Serrano, J. A. Font, J. M. Ibáñez, and J. M. Martí. Assessment of a high-resolution central scheme for the solution of the relativistic hydrodynamics equations. *Astron. Astrophys.*, 428:703, 2004.

[410] *Cactus Thorn Guide for Thorn* WHISKY. URL `http://www.whiskycode.org`.

[411] B. J. van Leer. Towards the ultimative conservative difference scheme I. the quest for monotonicity. *Lecture Notes in Physics*, 18:163, 1973.

[412] P. Colella and P. Woodward. The Piecewise Parabolic Method (PPM) for Gas-Dynamical Simulations. *J. Comput. Phys.*, 54:174, 1984.

[413] B. J. van Leer. Towards the ultimate conservative difference scheme: IV. A new approach to numerical convection. *J. Comput. Phys.*, 23: 276, 1977.

[414] B. J. van Leer. Towards the ultimate conservative difference scheme. V - A second-order sequel to Godunov's method. *J. Comput. Phys.*, 32:101, 1979.

[415] P. L. Roe. Some contributions to the modelling of discontinuous flows. In R. L. Lee, R. L. Sani, T. M. Shih, and P. M. Gresho, editors, *Large-scale computations in fluid mechanics; Proceedings of the Fifteenth Summer Seminar on Applied Mathematics, La Jolla, CA, June 27-July 8, 1983. Part 2 (A85-48201 23-34). Providence, RI, American Mathematical Society*, page 163, 1985.

[416] J. M. Martí and E. Müller. *J. Comput. Phys.*, 123:1, 1996.

[417] C. B. Laney. *Computational Gasdynamics*. Cambridge University Press, 1998.

[418] J. M. Martí and E. Müller. The analytical solution of the riemann problem in relativistic hydrodynamics. *J. Fluid Mech.*, 258:317, 1994.

[419] L. Rezzolla and O. Zanotti. An improved exact Riemann solver for relativistic hydrodynamics. *J. Fluid Mech.*, 449:395, 2001.

[420] L. Rezzolla, O. Zanotti, and J. A. Pons. An improved exact Riemann solver for multi-dimensional relativistic flows. *J. Fluid Mech.*, 479: 199, 2003.

[421] P. L. Roe. Approximate riemann solvers, parameter vectors and difference schemes. *J. Comput. Phy.*, 43:357, 1981.

[422] A. Harten, P. D. Lax, and B. van Leer. *SIAM Rev.*, 25:35, 1983.

[423] R. Donat and A. Marquina. Capturing shock reflections: an improved flux formula. *J. Comput. Phys.*, 125:42, 1996.

[424] R. Donat, J. A. Font, J. M. Ibáñez, and A. Marquina. A flux-split algorithm applied to relativistic flows. *J. Comput. Phys.*, 146:58, 1998.

[425] M. A. Aloy, J. Mª. Ibáñez, J. Mª. Martí, and E. Müller. GENESIS: A High-Resolution Code for Three-dimensional Relativistic Hydrodynamics. *Astroph. J. Supp.*, 122:151, 1999.

[426] F. Eulderink and G. Mellema. Special relativistic jet collimation by inertial confinement. *Astron. Astrophys.*, 284:654, 1994.

[427] F. Eulderink and G. Mellema. General relativistic hydrodynamics with a roe solver. *Astron. Astrophys.Suppl.*, 110:587, 1995.

[428] *Cactus Thorn Guide for Thorn* CACTUSEINSTEIN/ADMBASE. URL `http://www.cactuscode.org`.

[429] *Cactus Thorn Guide for Thorn* CACTUSEINSTEIN/ADMCOUPLING. URL `http://www.cactuscode.org`.

[430] H.-T. Janka, T. Zwerger, and R. Mönchmeyer. Does artificial viscosity destroy prompt type-II supernova explosions? *Astron. Astrophys.*, 268:360, 1993.

[431] *Cactus Thorn Guide for Thorn* SPACEMASK. URL `http://www.cactuscode.org`.

[432] R. Kippenhahn and A. Weigert. *Stellar Structure and Evolution.* Springer Verlag, Berlin, Germany, 1990.

[433] R. I. Epstein and W. D. Arnett. Neutronization and thermal disintegration of dense stellar matter. *Astrophys. J.*, 201:202, 1975.

[434] T. Plewa and E. Müller. The consistent multi-fluid advection method. *Astron. Astrophys.*, 342:179, 1999.

[435] D. Q. Lamb, J. M. Lattimer, C. J. Pethick, and D. G. Ravenhall. Hot dense matter and stellar collapse. *Phys. Rev. Lett.*, 41:1623, 1978.

[436] D. Q. Lamb, J. M. Lattimer, C. J. Pethick, and D. G. Ravenhall. Physical properties of hot, dense matter: The bulk equilibrium approximation. *Nucl. Phys. A*, 360:459, 1981.

[437] H. A. Bethe, G. E. Brown, J. Applegate, and J. M. Lattimer. Equation of state in the gravitational collapse of stars. *Nucl. Phys. A*, 324:487, 1979.

[438] J. M. Lattimer, C. J. Pethick, D. G. Ravenhall, and D. Q. Lamb. Physical properties of hot, dense matter: The general case. *Nucl. Phys. A*, 432:646, 1985.

[439] J. M. Lattimer and F. D. Swesty. A Generalized Equation of State for Hot, Dense Matter. *Nucl. Phys. A*, 535:331, 1991. URL `http://www.ess.sunysb.edu/dswesty`.

[440] D. G. Ravenhall, C. J. Pethick, and J. R. Wilson. Structure of Matter below Nuclear Saturation Density. *Phys. Rev. Lett.*, 50:2066, 1983.

[441] G. Baym, H. A. Bethe, and C. J. Pethick. Neutron star matter. *Nucl. Phys. A*, 175:225, 1971.

[442] J. K. Perring and T. H. R. Skyrme. The Alpha-Particle and Shell Models of the Nucleus . *Proc. Phys. Soc. A*, 69:600, 1956.

[443] J. Cooperstein. The equation of state in supernovae. *Nucl. Phys. A*, 438:722, 1985.

[444] E. Baron, J. Cooperstein, and S. Kahana. Supernovae and the nuclear equation of state at high densities. *Nucl. Phys. A*, 440:744, 1985.

[445] A. Burrows and J. M. Lattimer. The birth of neutron stars. *Astrophys. J.*, 307:178, 1986.

[446] M. Beiner, H. Flocard, N. van Giai, and P. Quentin. Nuclear ground-state properties and self-consistent calculations with the skyrme interaction (I). Spherical description. *Nucl. Phys. A*, 238:29, 1975.

[447] M. F. El Eid and W. Hillebrandt. A new equation of state of supernova matter. *Astron. Astrophys. Suppl.*, 42:215, 1980.

[448] W. Hillebrandt and R. G. Wolff. Models of Type II Supernova Explosions. In W. D. Arnett and J. W. Truran, editors, *Nucleosynthesis : Challenges and New Developments*, page 131, 1985.

[449] P. Bonche and D. Vautherin. A mean-field calculation of the equation of state of supernova matter. *Nucl. Phys. A*, 372:496, 1981.

[450] P. Bonche and D. Vautherin. Mean-field calculations of the equation of state of supernova matter II. *Astron. Astrophys.*, 112:268, 1982.

[451] Myers, W. D. and Swiatecki, W. J. The nuclear thomas-fermi model. Technical Report LBL-36004, Lawrence Berkeley Laboratory, University of California, 1994.

[452] M. Barranco and J.-R. Buchler. Equation of state of hot, dense stellar matter: Finite temperature nuclear Thomas-Fermi approach. *Phys. Rev. C.*, 24:1191, 1981.

[453] S. Marcos, M. Barranco, and J. R. Buchler. Low-entropy adiabats for stellar collapse. *Nucl. Phys. A*, 381:507, 1982.

[454] R. Ogasawara and K. Sato. Nuclei in Neutrino-Degenerate Dense Matter. II —Hot Case—. *Prog. Theor. Phys.*, 70:1569, 1983.

[455] E. Suraud and D. Vautherin. Thomas-Fermi calculations of hot dense matter. *Phys. Lett. B*, 138:325, 1984.

[456] E. Suraud. A Thomas-Fermi Equation of State of Hot Dense Matter. In D. Bancel and M. Signore, editors, *Problems of Collapse and Numerical Relativity, Proceedings of the NATO Advanced Research Workshop held in Toulouse, November 7-11, 1983, Dordrecht: Reidel, 1984, edited by Daniel Bancel and Monique Signore. NATO Advanced Science Institutes (ASI) Series C, Volume 134*, page 81, 1984.

[457] P.-G. Reinhard. The relativistic mean-field description of nuclei and nuclear dynamics. *Rep. Prog. Phys.*, 52:439, 1989.

[458] Y. Sugahara and H. Toki. Relativistic mean-field theory for unstable nuclei with non-linear σ and ω terms. *Nucl. Phys. A*, 579:557, 1994.

[459] K. Sumiyoshi and H. Toki. Relativistic equation of state of nuclear matter for the supernova explosion and the birth of neutron stars. *Astrophys. J.*, 422:700, 1994.

[460] K. Sumiyoshi, H. Kuwabara, and H. Toki. Relativistic mean-field theory with non-linear σ and ω terms for neutron stars and supernovae. *Nucl. Phys. A*, 581:725, 1995.

[461] R. Brockmann and R. Machleidt. Relativistic nuclear structure. I. Nuclear matter. *Phys. Rev. C.*, 42:1965, 1990.

[462] H. Müther, R. Machleidt, and R. Brockmann. Relativistic nuclear structure. II. Finite nuclei. *Phys. Rev. C.*, 42:1981, 1990.

[463] K. Sumiyoshi, D. Hirata, H. Toki, and H. Sagawa. Comparison of the relativistic mean-field theory and the Skyrme Hartree-Fock theory for properties of nuclei and nuclear matter. *Nucl. Phys. A*, 552:437, 1993.

[464] H. Shen, H. Toki, K. Oyamatsu, and K. Sumiyoshi. Relativistic equation of state of nuclear matter for supernova and neutron star. *Nucl. Phys. A*, 637:435, 1998. URL `http://user.numazu-ct.ac.jp/~sumi/eos`.

[465] H. Shen, H. Toki, K. Oyamatsu, and K. Sumiyoshi. Relativistic Equation of State of Nuclear Matter for Supernova Explosion. *Progress of Theoretical Physics*, 100:1013, 1998.

[466] K. Oyamatsu. Nuclear shapes in the inner crust of a neutron star. *Nucl. Phys. A*, 561:431, 1993.

[467] K. Sumiyoshi, H. Suzuki, S. Yamada, and H. Toki. Properties of a relativistic equation of state for collapse-driven supernovae. *Nuclear Physics A*, 730:227, 2004.

[468] K. Sumiyoshi, S. Yamada, H. Suzuki, H. Shen, S. Chiba, and H. Toki. Postbounce Evolution of Core-Collapse Supernovae: Long-Term Effects of the Equation of State. *Astrophys. J.*, 629:922, 2005.

[469] A. Marek, H.-T. Janka, R. Buras, M. Liebendörfer, and M. Rampp. On ion-ion correlation effects during stellar core collapse. *Astron. Astrophys.*, 443:201, 2005.

[470] D. Swesty. Thermodynamically Consistent Interpolation of Equation of State Tables. *Journal of Computational Physics*, 127:118, 1996.

[471] F. X. Timmes and F. D. Swesty. The Accuracy, Consistency, and Speed of an Electron-Positron Equation of State Based on Table Interpolation of the Helmholtz Free Energy. *Astrophys. J. Suppl. Ser.* , 126:501, 2000.

[472] A. Burrows. *Private Communication*, 2006.

[473] S. A. Bludman and K. A. van Riper. Equation of state of an ideal Fermi gas. *Astrophys. J.*, 212:859, 1977.

[474] J. M. Lattimer, C. J. Pethick, D. G. Ravenhall, and D. Q. Lamb. Physical properties of hot, dense matter: The general case. *Nuc. Phys. A.*, 432:646, 1985.

[475] S. W. Bruenn. Stellar core collapse - Numerical model and infall epoch. *Astrophys. J. Suppl. Ser.* , 58:771, 1985.

[476] M. Liebendörfer. A Simple Parameterization of the Consequences of Deleptonization for Simulations of Stellar Core Collapse. *Astrophys. J.*, 633:1042, 2005.

[477] E. Livne, A. Burrows, R. Walder, I. Lichtenstadt, and T. A. Thompson. Two-dimensional, Time-dependent, Multigroup, Multiangle Radiation Hydrodynamics Test Simulation in the Core-Collapse Supernova Context. *Astrophys. J.*, 609:277, 2004.

[478] F. D. Swesty and E. S. Myra. A Numerical Algorithm for Modeling Multigroup Neutrino-Radiation Hydrodynamics in Two Spatial Dimensions. *submitted to Astrophys. J.*, 2006.

[479] J. Cooperstein. Neutrinos in supernovae. *Phys. Rep.*, 163:95, 1988.

[480] S. A. Bludman, I. Lichtenstadt, and G. Hayden. Homologous collapse and deleptonization of an evolved stellar core. *Astrophys. J.*, 261: 661, 1982.

[481] R. I. Epstein and C. J. Pethick. Lepton loss and entropy generation in stellar collapse. *Astrophys. J.*, 243:1003, 1981.

[482] S. Rosswog and M. Liebendörfer. High-resolution calculations of merging neutron stars - II. Neutrino emission. *Mon. Not. R. Astron. Soc.*, 342:673, 2003.

[483] M. Ruffert, H.-T. Janka, and G. Schaefer. Coalescing neutron stars - a step towards physical models. I. Hydrodynamic evolution and gravitational-wave emission. *Astron. Astrophys.*, 311:532, 1996.

[484] A. Burrows and R. F. Sawyer. Many-body corrections to charged-current neutrino absorption rates in nuclear matter. *Phys. Rev. C.*, 59: 510, 1999.

[485] A. Mezzacappa and S. W. Bruenn. Type II supernovae and Boltzmann neutrino transport - The infall phase. *Astrophys. J.*, 405:637, 1993.

[486] K. Langanke, G. Martínez-Pinedo, J. M. Sampaio, D. J. Dean, W. R. Hix, O. E. Messer, A. Mezzacappa, M. Liebendörfer, H.-T. Janka, and M. Rampp. Electron Capture Rates on Nuclei and Implications for Stellar Core Collapse. *Phys. Rev. Lett.*, 90(24):241102, 2003.

[487] S. A. Bludman and K. A. van Riper. Diffusion approximation to neutrino transport in dense matter. *Astrophys. J.*, 224:631, 1978.

[488] P. Rhodes. Fermi-Dirac function of integral order. *Proc. Royal Soc. Math. Physic. Sci.*, 204:396, 1950.

[489] J. Pons. *Private communiciation*, 2006.

[490] R. C. Tolman. Static Solutions of Einstein's Field Equations for Spheres of Fluid. *Phys. Rev.*, 55:364, 1939.

[491] J. R. Oppenheimer and G. Volkoff. On massive neutron cores. *Phys. Rev.*, 55:374, 1939.

[492] E. M. Butterworth. On the structure and stability of rapidly rotating fluid bodies in general relativity. II - The structure of uniformly rotating pseudopolytropes. *Astrophys. J.*, 204:561, 1976.

[493] W. H. Press, S. A. Teukolsky, W. T. Vetterling, and B. P. Flannery. *Numerical Recipes in C, 2nd. edition*. Cambridge University Press, Cambridge, U. K., 1992.

[494] A. C. Hindmarsh. Odepack, a systematized collection of ode solvers. *IMACS Transactions on Scientific Computing*, 1:55, 1983. URL `http://www.netlib.org/odepack/index.html`. article also available at http://www.llnl.gov/CASC/nsde/pubs/u88007.pdf.

[495] N. Stergioulas. *The Structure and Stability of Rotating Relativistic Stars*. PhD thesis, University of Wisconsin-Milwaukee, Milwaukee, Wisconsin, 1996.

[496] N. Stergioulas and J. L. Friedman. Comparing models of rapidly rotating relativistic stars constructed by two numerical methods. *Astrophys. J.*, 444:306, 1995.

[497] T. Nozawa, N. Stergioulas, E. Gourgoulhon, and Y. Eriguchi. Construction of highly accurate models of rotating neutron stars - comparison of three different numerical schemes. *Astron. Astrophys. Suppl.*, 132:431, 1998.

[498] H. Komatsu, Y. Eriguchi, and I. Hachisu. Rapidly rotating general relativistic stars. I - Numerical method and its application to uniformly rotating polytropes. *Mon. Not. R. Astron. Soc.*, 237:355, 1989.

[499] H. Komatsu, Y. Eriguchi, and I. Hachisu. Rapidly rotating general relativistic stars. II - Differentially rotating polytropes. *Mon. Not. R. Astron. Soc.*, 239:153, 1989.

[500] G. B. Cook, S. L. Shapiro, and S. A. Teukolsky. Rapidly rotating polytropes in general relativity. *Astrophys. J.*, 422:227, 1994.

[501] B. Carter. Killing Horizons and Orthogonally Transitive Groups in Space-Time. *J. Math. Phys.*, 10:70, 1969.

[502] B. Carter. The commutation property of a stationary, axisymmetric system. *Commun. Math. Phys.*, 17:233, 1970.

[503] E. M. Butterworth and J. R. Ipser. On the structure and stability of rapidly rotating fluid bodies in general relativity. I - The numerical method for computing structure and its application to uniformly rotating homogeneous bodies. *Astrophys. J.*, 204:200, 1976.

[504] J.-L. Tassoul. *Theory of Rotating Stars*. Princeton University Press, Princeton U. S. A., 1978.

[505] D. D. Clayton. *Principles of stellar evolution and nucleosynthesis*. Chicago: University of Chicago Press, 1983, 1983.

[506] T. A. Weaver, G. B. Zimmerman, and S. E. Woosley. Presupernova evolution of massive stars. *Astrophys. J.*, 225:1021, 1978.

[507] K. Nomoto and M.-A. Hashimoto. Presupernova evolution of massive stars. *Phys. Rep.*, 163:13, 1988.

[508] S. E. Woosley and T. A. Weaver. The Evolution and Explosion of Massive Stars. II. Explosive Hydrodynamics and Nucleosynthesis. *Astrophys. J. Suppl. Ser.*, 101:181, 1995.

[509] A. Heger, N. Langer, and S. E. Woosley. Presupernova Evolution of Rotating Massive Stars. I. Numerical Method and Evolution of the Internal Stellar Structure. *Astrophys. J.*, 528:368, 2000.

[510] R. Hirschi, G. Meynet, and A. Maeder. Stellar evolution with rotation. XII. Pre-supernova models. *Astron. Astrophys.*, 425:649, 2004.

[511] A. Heger, S. E. Woosley, and H. C. Spruit. Presupernova Evolution of Differentially Rotating Massive Stars Including Magnetic Fields. *Astrophys. J.*, 626:350, 2005.

[512] C. Kochanek. Graviational radiation from colliding clusters: Newtonian simulations in three dimensions. *Astrophys. J.*, 398:234, 1992.

[513] X. Zhuge, J. M. Centrella, and S. L. McMillan. Gravitational radiation from coalescing binary neutron stars. *Phys. Rev. D.*, 50:6247, 1994.

[514] É. É. Flanagan and S. A. Hughes. Measuring gravitational waves from binary black hole coalescences. I. Signal to noise for inspiral, merger, and ringdown. *Phys. Rev. D.*, 57:4535, 1998.

[515] E. Gustafson, D. Shoemaker, K. Strain, and R. Weiss. *LSC white paper on detector research and development*, Technical Report LIGO T990080-00-D, 1999.

[516] H.-J. Yo, T. W. Baumgarte, and S. L. Shapiro. Improved numerical stability of stationary black hole evolution calculations. *Phys. Rev. D*, 66:084026, 2002.

[517] J. M. Bowen and James W. York, Jr. Time-asymmetric initial data for black holes and black hole collisions. *Phys. Rev. D*, 21(8):2047, 1980.

[518] V. Moncrief. Radiation from collapsing relativistic stars. IV - Black hole recoil. *Astrophys. J.*, 238:333, 1980.

[519] M. Shibata. Fully general relativistic simulation of coalescing binary neutron stars: Preparatory tests. *Phys. Rev. D*, 60:104052, 1999.

[520] J. L. Friedman, L. Parker, and J. R. Ipser. Rapidly rotating neutron star models. *Astrophys. J.*, 304:115, 1986.

[521] G. B. Cook, S. L. Shapiro, and S. A. Teukolsky. Spin-up of a rapidly rotating star by angular momentum loss - Effects of general relativity. *Astrophys. J.*, 398:203, 1992.

[522] J. E. Tohline, R. H. Durisen, and M. McCollough. The linear and nonlinear dynamic stability of rotating N = 3/2 polytropes. *Astrophys. J.*, 298:220, 1985.

[523] L. F. Richardson. The Approximate Solution of Various Boundary Problems by Surface Integration combined with Freehand Graphs . *Proceedings of the Physical Society of London*, 23:75, 1910.

[524] M. W. Choptuik. Consistency of finite-difference solutions to Einstein's equations. *Phys. Rev. D*, 44:3124, 1991.

[525] H. Dimmelmeier. *Private communiciation*, 2006.

[526] J. W. Gibbs. Fourier series. *Nature*, 59:200, 1898.

[527] J. W. Gibbs. Fourier series. *Nature*, 59:606, 1899.

[528] N. Stergioulas. *Private communication*, 2006.

[529] E. Seidel. *Private communiciation*, 2006.

[530] E. Müller. TOPICAL REVIEW: Supernova theory and the nuclear equation of state. *Journal of Physics G Nuclear Physics*, 16:1571, 1990.

[531] E. Müller. *in Computational Methods for Astrophysical Fluid Flow. Saas-Fee Advanced Course 27, ed. O. Steiner & A. Gautschy*, page 343. Springer, Berlin, Germany, 1998.

[532] P. Ledoux. On the Radial Pulsation of Gaseous Stars. *Astrophys. J.*, 102:143, 1945.

[533] J. A. Isenberg. *University of Maryland Preprint, unpublished*, 1978.

[534] J. R. Wilson, G. J. Mathews, and P. Marronetti. Relativistic numerical model for close neutron-star binaries. *Phys. Rev. D.*, 54:1317–1331, 1996.

[535] A. Garat and R. H. Price. Nonexistence of conformally flat slices of the Kerr spacetime. *Phys. Rev. D.*, 61(12):124011, 2000.

[536] G. B. Cook, S. L. Shapiro, and S. A. Teukolsky. Testing a simplified version of Einstein's equations for numerical relativity. *Phys. Rev. D.*, 53:5533, 1996.

[537] W. Kley and G. Schäfer. Relativistic dust disks and the Wilson-Mathews approach. *Phys. Rev. D.*, 60(2):027501, 1999.

[538] M. MacCallum D. Kramer, H. Stephani and E. Herlt. *Exact Solutions of Einstein's Field Equations*. Cambridge University Press, Cambridge, 1980.

[539] L. P. Eisenhart. *Riemannian Geometry*. Princeton University Press, Princeton, 1926.

[540] L. Witten. *Gravitation: an Introduction to current research*. New York: Wiley, 1962, edited by Witten, Louis, 1962.

[541] E. Cotton. Sur les variétés à trois dimensions. *Ann. Fac. Sci. Toulouse II*, (1):385, 1899.

[542] M. Miller, P. Gressman, and W.-M. Suen. Towards a realistic neutron star binary inspiral: Initial data and multiple orbit evolution in full general relativity. *Phys. Rev. D*, 69:064026, 2004.

[543] I. Fukuda. A statistical study of rotational velocities of the stars. *Publ. Astron. Soc. Pac.*, 94:271, 1982.

[544] R. H. D. Townsend, S. P. Owocki, and I. D. Howarth. Be-star rotation: how close to critical? *Mon. Not. R. Astron. Soc.*, 350:189, 2004.

[545] W. Huang and D. R. Gies. Stellar Rotation in Young Clusters. I. Evolution of Projected Rotational Velocity Distributions. *Astrophys. J.*, 648: 580, 2006.

[546] W. Huang and D. R. Gies. Stellar Rotation in Young Clusters. II. Evolution of Stellar Rotation and Surface Helium Abundance. *Astrophys. J.*, 648:591, 2006.

[547] H. A. Abt, H. Levato, and M. Grosso. Rotational Velocities of B Stars. *Astrophys. J.*, 573:359, 2002.

[548] A. Heger, S. E. Woosley, N. Langer, and H. C. Spruit. Presupernova Evolution of Rotating Massive Stars and Rotation Rate of Pulsars (Invited Review). In A. Maeder and P. Eenens, editors, *IAU Symposium*, page 591, 2004.

[549] S. Yamada and K. Sato. Numerical study of rotating core collapse in supernova explosions. *Astrophys. J.*, 434:268, 1994.

[550] I. Hachisu. A versatile method for obtaining structures of rapidly rotating stars. *Astrophys. J. Suppl. Ser.* , 61:479, 1986.

[551] A. Marek, H. Dimmelmeier, H.-T. Janka, E. Müller, and R. Buras. Exploring the relativistic regime with Newtonian hydrodynamics: an improved effective gravitational potential for supernova simulations. *Astron. Astrophys.*, 445:273, 2006.

[552] S. W. Bruenn, K. R. De Nisco, and A. Mezzacappa. General Relativistic Effects in the Core Collapse Supernova Mechanism. *Astrophys. J.*, 560:326, 2001.

[553] P. Ledoux. Stellar Models with Convection and with Discontinuity of the Mean Molecular. *Astrophys. J.*, 105:305, 1947.

[554] E. Böhm-Vitense. Über die Wasserstoffkonvektionszone in Sternen verschiedener Effektivtemperaturen und Leuchtkräfte. Mit 5 Textabbildungen. *Zeitsch. für Astrophys.*, 46:108, 1958.

[555] W. Keil, H.-T. Janka, and E. Müller. Ledoux Convection in Protoneutron Stars—A Clue to Supernova Nucleosynthesis? *Astrophys. J. Lett.*, 473:L111, 1996.

[556] J. Cooperstein, H. A. Bethe, and G. E. Brown. Shock propagation in supernovae: Concept of net ram pressure. *Nucl. Phys. A*, 429:527, 1984.

[557] A. Burrows. Convection and the mechanism of type II supernovae. *Astrophys. J. Lett.*, 318:L57, 1987.

[558] A. Burrows and J. M. Lattimer. Convection, type II supernovae, and the early evolution of neutron stars. *Phys. Rep.*, 163:51, 1988.

[559] D. S. Miller, J. R. Wilson, and R. W. Mayle. Convection above the neutrinosphere in Type II supernovae. *Astrophys. J.*, 415:278, 1993.

[560] E. Müller and H.-T. Janka. Multi-Dimensional Simulations of Neutrino-Driven Supernovae. *Rev. Mod. Astron.*, 7:103, 1994.

[561] S. W. Bruenn, E. A. Raley, and A. Mezzacappa. Fluid Stability Below the Neutrinospheres of Supernova Progenitors and the Dominant Role of Lepto-Entropy Fingers. *ArXiv Astrophysics e-prints*, 2004.

[562] T. Shimizu, S. Yamada, and K. Sato. Three-dimensional simulations of convection in supernova cores. *Publ. Astron. Soc. Jap.*, 45:L53, 1993.

[563] S. Yamada, T. Shimizu, and K. Sato. Convective Instability in Hot Bubble in a Delayed Supernova Explosion. *Progress of Theoretical Physics*, 89:1175, 1993.

[564] J. B. Hartle and J. L. Friedman. Slowly Rotating Relativistic Stars. VIII. Frequencies of the Quasi-Radial Modes of an N = 3/2 Polytrope. *Astrophys. J.*, 196:653, 1975.

[565] T. A. Weaver, S. E. Woosley, and G. M. Fuller. Neutron-Rich Silicon Burning and the Final Fate of Massive Stars. In *Bulletin of the American Astronomical Society*, page 957, 1982.

[566] A. Marek. The effects of the nuclear equation of state on stellar core collapse and supernova evolution. Diploma thesis, Technische Universität München, 2003.

[567] H. C. Spruit and E. S. Phinney. Birth kicks as the origin of pulsar rotation. *Nature*, 393:139, 1998.

[568] C. A. Meakin. *Hydrodynamic Modeling of Massive Star Interiors*. PhD thesis, The University of Arizona, Tucson, Arizona, 2006.

[569] C. A. Meakin and D. Arnett. Active Carbon and Oxygen Shell Burning Hydrodynamics. *Astrophys. J. Lett.*, 637:L53, 2006.

[570] J. W. Murphy, A. Burrows, and A. Heger. Pulsational Analysis of the Cores of Massive Stars and Its Relevance to Pulsar Kicks. *Astrophys. J.*, 615:460, 2004.

[571] D. Lai and P. Goldreich. Growth of Perturbations in Gravitational Collapse and Accretion. *Astrophys. J.*, 535:402, 2000.

[572] J. A. Pons, S. Reddy, M. Prakash, J. M. Lattimer, and J. A. Miralles. Evolution of Proto-Neutron Stars. *Astrophys. J.*, 513:780, 1999.

[573] P. M. Motl, J. E. Tohline, and J. Frank. Numerical Methods for the Simulation of Dynamical Mass Transfer in Binaries. *Astrophys. J. Suppl. Ser.* , 138:121, 2002.

[574] E. Livne. An implicit method for two-dimensional hydrodynamics. *Astrophys. J.*, 412:634, 1993.

[575] K. S. Thorne. Gravitational Waves. In E. W. Kolb and R. D. Peccei, editors, *Particle and Nuclear Astrophysics and Cosmology in the Next Millenium*, page 160, 1995.

[576] T. Piran. Gravitational Radiation and Supernovae. In J. C. Wheeler, T. Piran, and S. Weinberg, editors, *Supernovae, Jerusalem Winter School for Theoretical Physics*, page 303, 1990.

[577] K. D. Kokkotas. High-frequency sources of gravitational waves. *Classical and Quantum Gravity*, 21:501, 2004.

[578] D. Lynden-Bell and J. E. Pringle. The evolution of viscous discs and the origin of the nebular variables. *Mon. Not. R. Astron. Soc.*, 168:603, 1974.

[579] A. S. Endal and S. Sofia. The evolution of rotating stars. II - Calculations with time-dependent redistribution of angular momentum for 7- and 10-solar-mass stars. *Astrophys. J.*, 220:279, 1978.

[580] S.-C. Yoon and N. Langer. Presupernova evolution of accreting white dwarfs with rotation. *Astron. Astrophys.*, 419:623, 2004.

[581] K. C. B. New and J. M. Centrella. Rotational Instabilities and Centrifugal Hangup. In J. M. Centrella, editor, *AIP Conf. Proc. 575: Astrophysical Sources for Ground-Based Gravitational Wave Detectors*, page 221, 2001.

[582] C. C. Lin and F. H. Shu. On the Spiral Structure of Disk Galaxies. *Astrophys. J.*, 140:646–+, 1964.

[583] D. Lynden-Bell and A. J. Kalnajs. On the generating mechanism of spiral structure. *Mon. Not. R. Astron. Soc.*, 157:1, 1972.

[584] A. Toomre. Theories of spiral structure. *Ann. Rev. Astron. Astrophys.*, 15:437, 1977.

[585] F. H. Shu. *Physics of Astrophysics, Vol. II*. Physics of Astrophysics, Vol. II, by Frank H. Shu. Published by University Science Books,, 1992.

[586] J. C. B. Papaloizou and D. N. C. Lin. Theory Of Accretion Disks I: Angular Momentum Transport Processes. *Ann. Rev. Astron. Astrophys.*, 33:505, 1995.

[587] D. N. C. Lin and J. E. Pringle. A viscosity prescription for a self-gravitating accretion disc. *Mon. Not. R. Astron. Soc.*, 225:607, 1987.

[588] N. I. Shakura and R. A. Sunyaev. Black holes in binary systems. Observational appearance. *Astron. Astrophys.*, 24:337, 1973.

[589] J. W. Woodward, J. E. Tohline, and I. Hachisu. The stability of thick, self-gravitating disks in protostellar systems. *Astrophys. J.*, 420: 247–267, 1994.

[590] J. E. Tohline and I. Hachisu. The breakup of self-gravitating rings, tori, and thick accretion disks. *Astrophys. J.*, 361:394–407, 1990.

[591] E. Balbinski. A new shear instability in rotating, self-gravitating, perfect fluids. *Mon. Not. R. Astron. Soc.*, 216:897, 1985.

[592] P. J. Luyten. The dynamical stability of differentially rotating, self-gravitating cylinders. *Mon. Not. R. Astron. Soc.*, 242:447, 1990.

[593] A. L. Watts, N. Andersson, H. Beyer, and B. F. Schutz. The oscillation and stability of differentially rotating spherical shells: the normal-mode problem. *Mon. Not. R. Astron. Soc.*, 342:1156, 2003.

[594] A. L. Watts, N. Andersson, and R. L. Williams. The oscillation and stability of differentially rotating spherical shells: the initial-value problem. *Mon. Not. R. Astron. Soc.*, 350:927, 2004.

[595] F. H. Shu, S. Tremaine, F. C. Adams, and S. P. Ruden. Sling amplification and eccentric gravitational instabilities in gaseous disks. *Astrophys. J.*, 358:495, 1990.

[596] J. Binney and S. Tremaine. *Galactic dynamics*. Princeton, NJ, Princeton University Press, 1987, 747 p., 1987.

[597] J. C. B. Papaloizou and J. E. Pringle. The dynamical stability of differentially rotating discs with constant specific angular momentum. *Mon. Not. R. Astron. Soc.*, 208:721, 1984.

[598] J. C. B. Papaloizou and J. E. Pringle. The dynamical stability of differentially rotating discs. II. *Mon. Not. R. Astron. Soc.*, 213:799, 1985.

[599] J. C. B. Papaloizou and J. E. Pringle. The dynamical stability of differentially rotating discs. III. *Mon. Not. R. Astron. Soc.*, 225:267, 1987.

[600] P. Goldreich, J. Goodman, and R. Narayan. The stability of accretion tori. I - Long-wavelength modes of slender tori. *Mon. Not. R. Astron. Soc.*, 221:339, 1986.

[601] R. V. E. Lovelace, H. Li, S. A. Colgate, and A. F. Nelson. Rossby Wave Instability of Keplerian Accretion Disks. *Astrophys. J.*, 513:805, 1999.

[602] H. Li, J. M. Finn, R. V. E. Lovelace, and S. A. Colgate. Rossby Wave Instability of Thin Accretion Disks. II. Detailed Linear Theory. *Astrophys. J.*, 533:1023–1034, 2000.

[603] H. Li, S. A. Colgate, B. Wendroff, and R. Liska. Rossby Wave Instability of Thin Accretion Disks. III. Nonlinear Simulations. *Astrophys. J.*, 551:874, 2001.

[604] J. Tohline. *Private Communication*, 2006.

[605] T. Summerscales, A. Burrows, L. S. Finn, and C. D. Ott. Maximum Entropy for Gravitational Wave Data Analysis: Inferring the Physical Parameters of Core-Collapse Supernovae. *Astrophys. J. submitted.*, 2006.

[606] S. A. Balbus and J. F. Hawley. A powerful local shear instability in weakly magnetized disks. I - Linear analysis. II - Nonlinear evolution. *Astrophys. J.*, 376:214, 1991.

[607] S. A. Balbus and J. F. Hawley. The Stability of Differentially Rotating Weakly Magnetized Stellar Radiative Zones. *Mon. Not. R. Astron. Soc.*, 266:769, 1994.

[608] S. Akiyama, J. C. Wheeler, D. L. Meier, and I. Lichtenstadt. The Magnetorotational Instability in Core-Collapse Supernova Explosions. *Astrophys. J.*, 584:954, 2003.

[609] T. A. Thompson, E. Quataert, and A. Burrows. Viscosity and Rotation in Core-Collapse Supernovae. *Astrophys. J.*, 620:861, 2005.

[610] E. Schnetter, P. Diener, E. N. Dorband, and M. Tiglio. A multi-block infrastructure for three-dimensional time-dependent numerical relativity. *Classical and Quantum Gravity*, 23:553, 2006.

[611] J. von Neumann and R. D. Richtmyer. *J. Appl. Phys.*, 21:232, 1950.

[612] W. H. Press, B. P. Flannery, Saul A. Teukolsky, and W. T. Vetterling. *Numerical Recipes*. Cambridge University Press, Cambridge, England, 1986.

[613] A. Burrows, S. Reddy, and T. A. Thompson. Neutrino Opacities in Nuclear Matter. *to be published in Nucl. Phys. A*, 2004.

[614] E. Müller and M. Steinmetz. Simulating self-gravitating hydrodynamic flows. *Comput. Phys. Commun.*, 89:45, 1995.

[615] M. S. Turner. Gravitational radiation from supernova neutrino bursts. *Nature*, 274:565, 1978.

[616] I. Hubeny and A. Burrows. A New Algorithm for 2-D Transport for Astrophysical Simulations: I. General Formulation and Tests for the 1-D Spherical Case. *Astrophys. J. submitted*, 2006.

[617] A. Buonanno, G. Sigl, G. G. Raffelt, H.-T. Janka, and E. Müller. Stochastic gravitational-wave background from cosmological supernovae. *Phys. Rev. D.*, 72(8):084001, 2005.

[618] K. Nomoto and Y. Kondo. Conditions for accretion-induced collapse of white dwarfs. *Astrophys. J. Lett.*, 267:L19, 1991.

[619] L. R. Yungelson and M. Livio. Type IA Supernovae: an Examination of Potential Progenitors and the Redshift Distribution. *Astrophys. J.*, 497:168, 1998.

[620] A. R. King and J.-P. Lasota. Spin evolution and magnetic fields in cataclysmic variables. *Astrophys. J.*, 378:674, 1991.

[621] J. P. Ostriker and J. W.-K. Mark. Rapidly rotating stars. I. The self-consistent-field method. *Astrophys. J.*, 151:1075, 1968.

[622] S. E. Woosley and E. Baron. The collapse of white dwarfs to neutron stars. *Astrophys. J.*, 391:228, 1992.

[623] S. Akiyama and J. C. Wheeler. The Nonmonotonic Dependence of Supernova and Compact Remnant Formation on Progenitor Rotation. *Astrophys. J.*, 629:414, 2005.

[624] R. F. Stark and T. Piran. Gravitational-wave emission from rotating gravitational collapse. *Phys. Rev. Lett.*, 55:891, 1985.

[625] URL `http://wugrav.wustl.edu/research/codes/GR3D/`. GR3D.

[626] URL `http://wugrav.wustl.edu/research/projects/final_report/nasafinal3.html`. NASA Binary Neutron Star Grand Challenge Project.

[627] P. J. Mohr and B. N. Taylor. CODATA recommended values of the fundamental physical constants: 2002. *Rev. Mod. Phys.*, 77:1, 2005.

[628] J.M. Ibáñez, M.A. Aloy, J.A. Font, J.M. Martí, J.A. Miralles, and J.A. Pons. In E.F. Toro, editor, *Godunov methods: theory and applications*, New York, 2001. Kluwer Academic/Plenum Publishers.

[629] Python. URL `http://www.python.org`.

[630] J. Hunter. Matplotlib. URL `http://matplotlib.sourceforge.net`.

[631] P. Barrett, J. Hunter, J. T. Miller, J.-C. Hsu, and P. Greenfield. matplotlib – A Portable Python Plotting Package. In P. Shopbell, M. Britton, and R. Ebert, editors, *ASP Conf. Ser. 347: Astronomical Data Analysis Software and Systems XIV*, page 91, 2005.

Acknowledgements

First and foremost, I thank my parents for their continuous love and support and for having given me the endurance and ambition necessary for carrying out this work.

I am deeply indebted to Edward Seidel for enabling me to carry out this work at the AEI, for the scientific freedom that he has always given me and for being virtually always available via instant messenger despite his very busy schedule and almost always different timezones. I am also deeply indebted to Adam Burrows from whom I have learned most of what I know about supernova physics and who has always provided me with his scientific insight and advice.

I am very grateful to my closest collaborators in the general relativistic part of this work, Harald Dimmelmeier, Erik Schnetter, and Ian Hawke. They have gone with me through all stages of this work and have carefully read and copyedited this dissertation. I also acknowledge important help from and discussions with Andreas Marek and Hans-Thomas Janka who provided me with the equation of state table that I employed in my {3+1} GR calculations. I thank Nikolaos Stergioulas for helpful and stimulating discussions and for providing his initial model solver for use in this work.

I thank Eli Livne for his help with the VULCAN/2D code and for many scientific discussions. I also wish to thank Luc Dessart for his help with IDL, the AIC simulation data, the VULCAN code, and for many stimulating discussions during my visits to Steward Observatory at the University of Arizona.

I am grateful to Thomas Radke for his invaluable help with CACTUS, CARPET, and his careful proofreading of two chapters of this dissertation. I would also like to thank Ralf Kähler for his help with the Amira visualization package and Steve White for his help with CACTUS and CARPET and for many interesting discussions.

It is a pleasure to acknowledge helpful, sometimes controversial, but always stimulating scientific discussions with Joel Tohline, Shangli Ou, Luciano Rezzolla, Ewald Müller, Burkhard Zink, Bernard Schutz, Wolfgang Hillebrandt, Toni Font, Wolfgang Duschl, Pablo Cerdá-Durán, José Pons, Nils Andersson, Todd Thompson, Jeremiah Murphy, Rolf Walder, Jonathan Thornburg, Denis Pollney, Luca Baiotti, Frank Herrmann, Michael Koppitz, Frank Löffler, Tilman Vogel, Joachim Frieben, Sascha Husa, Anil Zenginoglou, Carsten Schneemann, Thorsten Kellermann, Horst Beyer, Anna Watts, Steve Brandt, and Manuel Tiglio.

It is a pleasure to thank Kurt Just, Kika Ernst, and Christian Reisswig for extensive proofreading of this dissertation and for helpful discussions.

I thank the Albert-Einstein-Institut and the Max-Planck-Gesellschaft for financial support that enabled me to carry out this work. I also thank the Center for Computation & Technology at Louisiana State University (LSU), Baton Rouge and the Max-Planck-Institut für Astrophysik, Garching for hosting me many times for productive visits. I acknowledge partial support during my visits to the MPA by the Sonderforschungsbereich/Transregio 7 "Gravitationswellenastronomie" of the Deutsche Forschungsgemeinschaft.

I thank my friends, fellow PhD students and fellow astrophysicists Thomas Marquart, Benjamin Darwin Oppenheimer, and Casey Meakin for stimulating discussions and their support.

Finally, I would like to thank Magdalena Marschall for her love, her kindness and support.

The numerical calculations presented in this work were carried out on the Peyote Intel Xeon cluster at the Albert-Einstein-Institut, on the Supermike Intel Xeon cluster and on the Santaka SGI Prism Intel Itanium 2 machine at LSU, on the Jacquard AMD Opteron cluster at the National Energy Research Scientific Computing Center (NERSC), on the Cobalt SGI Altix Intel Itanium 2 system and on the Mercury Intel Itanium 2 cluster at the National Center for Supercomputing Applications (NCSA), and on the Grendel AMD Opteron cluster of Steward Observatory, University of Arizona.

Most of the figures in this dissertation were generate with the `Python` [629] based `matplotlib` plotting package [630, 631].